
Crystallography-microstructure-relations of hierarchical lath martensite from a micromechanical point of view

DISSERTATION

zur Erlangung des akademischen Grades

Doktor der montanistischen Wissenschaften

an der Montanuniversität Leoben

im Fachgebiet

Mechanik und Mathematik

ausgefertigt am

Institut für Mechanik (Montanuniversität Leoben)

Centre des Matériaux (MINES ParisTech)

vorgelegt von

Dipl.-Ing. Manuel Petersmann

geboren am 09.01.1990 in Bodensdorf

Betreuer der Arbeit:

Professor Thomas Antretter (Montanuniversität Leoben)

Professor Georges Cailletaud (Mines ParisTech)

Eidesstattliche Erklärung

Ich erkläre an Eides statt, dass ich diese Arbeit selbständig verfasst, andere als die angegebenen Quellen und Hilfsmittel nicht benutzt und mich auch sonst keiner unerlaubten Hilfsmittel bedient habe.

Affidavit

I declare in lieu of oath, that I wrote this thesis and performed the associated research myself, using only literature cited in this volume.

Date: 14. 04. 2018

Unterschrift Verfasser/in
Manuel, Petersmann
Matrikelnummer: 00935137

Crystals are like people, it is the defects in them which tend to make them interesting.

Colin Humphreys

Peut-être trouvera t-on que c'est de cette figure des grains et de leur arrangement que dépendant la ductilité des Metaux et celles de quelques autre matières.

Reaumur, 1724

Wer die Geometrie begreift vermag in dieser Welt alles zu verstehen

Gallileo Gallilei

Acknowledgements

The studies underlying this thesis have been conducted at the Institute of Mechanics at University of Leoben and the Centre des Matériaux at MINES ParisTech in the frame of the COMET research project A.1.14, operated by the Materials Center Leoben Forschung GmbH.

Particular thanks go to Prof. Thomas Antretter for the provided freedom in the choice of the pursued research, the fruitful discussions and nice teamwork over the past years. The given confidence has helped me to explore research directions based on personal preference.

Further, I acknowledge the atmosphere created by the people at the Centre des Matériaux (Paris) during my one year stay there from summer 2015 to 2016. Particular thanks go to Prof. Georges Cailletaud, who despite his tight schedule and many professional obligations always took the time to answer my questions during my stay.

Last but not least I would like to express my thanks to all the people outside of the scientific scope, namely my friends and my family. Especially, my soon to be wife Catrin for the support and sacrifice she made to help me accomplish this goal. Thank you all for your invaluable support and enrichment of my life!

Financial support by the Austrian Federal Government (in particular from Bundesministerium für Verkehr, Innovation und Technologie and Bundesministerium für Wissenschaft, Forschung und Wirtschaft) represented by Österreichische Forschungsförderungsgesellschaft mbH and the Styrian and the Tyrolean Provincial Government, represented by Steirische Wirtschaftsförderungsgesellschaft mbH and Standortagentur Tirol, within the framework of the COMET Funding Programme is gratefully acknowledged.

Dedicated to everyone who finds fun in science

Contents

Abbreviations	xiv
Symbols	xxiii
Abstract	xxiv
Résumé	xxv
Zusammenfassung	xxvi
1 Motivation and Scope of the Thesis	1
1.1 Hierarchical Microstructure of Highly Dislocated Lath Martensite	5
2 Introduction	13
2.1 Classifications of Phase Transformations in Steels	13
2.1.1 Thermodynamic Classification	14
2.1.2 Structural Classification	16
2.1.3 Kinetic Classification	20
2.2 From Composition via Processing to Microstructure	23
2.2.1 Alloying Elements, Metallurgical Hardening Relations and Steel Types	23
2.2.2 Heat- and/or Mechanical Treatments and Transformation Diagrams (Kinetic Experiments)	28
2.2.3 Dependencies of Transformation Modes and Morphologic- Crystallo- graphic Differences of Martensites in Steels	34
2.2.4 Mutual Couplings Between Phase Transformation and Plasticity . .	39
2.3 Modelling Strategies	44
2.3.1 A Question of Scale - Discrete vs Continuous (Phenomenological) View of Materials	44
2.3.2 Multi-scale Modelling Methods (MMM) and Current Developments .	45
3 Crystallographic Aspects of Martensite	53
3.1 Preliminaries: Lattice-Bases, -Correspondence, -Symmetry	54
3.2 Properties of Dislocations	56
3.3 Stacking Faults and Twins	60
3.4 Texture, Orientation Relationships and Related Topics	63
3.5 Crystallographic Theories for Martensite Formation	69
3.5.1 Continuum and Lattice Perspective of Compatibility	70

3.5.2	Structural Stretch Tensors	73
3.5.3	Crystallographic Continuum Compatibility	77
3.5.3.1	Invariant lines	77
3.5.3.2	Invariant Plane Strain (IPS) - Generalities	79
3.5.3.3	IPS including Slip (Reconstructive)	83
3.5.3.4	IPS by Transformation Twinning (Purely Displacive)	85
3.5.4	Theories Considering Continuous Features of Orientation Relationships and Kinematics of Sphere Packings	86
3.5.5	Interfaces, Lattice Defects at Interfaces, their Characterisation and Resulting Theories of Lattice Coherency	88
3.6	Relations between Oriented Crystallographic Variables	99
3.7	Overview of Important Slip and Boundary Sliding Mechanisms for Lath Martensite	100
3.8	The Composite Block Model for Dislocated Lath Martensite of Qi and Khachaturyan (CBQK)	107
3.9	Average Compatibility Relations for Homogeneous Boundary Conditions	110
3.10	Generalization & Unification of Discrete and Continuum Methods for the Hierarchical Microstructure of Dislocated Lath Martensite	111
3.10.1	Lath Level	112
3.10.1.1	Incremental Formulation of Shearing	112
3.10.1.2	Rotations During the Transformation and Lattice Correspondence	113
3.10.1.3	Selection Criteria for Lath Level Solutions	115
3.10.2	Block Level: Restrictions, Selection Criteria and Optimization	116
3.10.3	Martensite Calculator - Code Structure and Case Example	117
4	Scale Transition Strategies	131
4.1	Homogenization	131
4.2	Possible Microstructure Discretization Levels for the Hierarchical Structure of Lath Martensite	134
4.3	The Eshelby Tensor, Inclusions, Inhomogeneities and the Equivalent Inclusion Method (EIM)	136
4.4	Localization - Scale Transition Rules for Non-linear Behavior	139
5	Experimental Characterisation	143
5.1	MarvalX12 - Material Data	143
5.2	Macroscopic TRIP Experiments	144
5.3	Kinetics	146
5.4	Impact of Thermal Transformation Cycling on the Microstructure	149
5.5	Microstructure Characterization by Orientation Imaging Microscopy	150
5.5.1	Many Grains	155
5.5.2	Block Details	169
6	Constitutive Description of Dislocated Lath Martensite Formation	173
6.1	Continuum Kinematics and Classes of Continuum Models	173
6.2	Assumptions and Consequences	176
6.3	Generalities for Multi-Variant for Phase Transformations	178

6.4	Thermodynamic (Extremum) Principles	184
6.4.1	Energetic / Equilibrium Thermodynamics, Thermostatistics	186
6.4.2	Dissipative / Non-equilibrium / Irreversible Thermodynamics	188
6.4.3	Couplings	189
6.5	Some Remarks on Size Effects in Metals	190
6.6	Constitutive Relations for Plastic Deformation	192
6.6.1	Flow Formulations and Yield Surfaces	193
6.6.1.1	Plastic and Viscoplastic Flow, Deformation and Temperature Rate Dependencies	193
6.6.1.2	Macroscopic Relations	196
6.6.1.3	Microscopic Relations	198
6.6.2	Evolution Equations for Hardening Variables	201
6.7	Constitutive Relations for the Phase Transformation	207
6.7.1	Differences in Nucleation and Growth Theories	207
6.7.2	Semi-empirical and Phenomenological Kinetics Fit Functions	210
6.7.3	Aspects of Discrete Transformation Strains in Mean Field Models	212
6.7.4	Variant-Variant Interaction	213
6.7.5	Structural Model for Martensite Nuclei	215
6.7.6	Transformation Driving and Dragging Forces and "Flow" Formulation Incorporating Nucleation and Growth	217
6.8	Model Parameter Calibration by Inverse Fitting	219
7	Summary and Outlook	221
	List of Figures	224
	List of Tables	234
A	Related Scale Bridging Concepts	236
A.1	Continuum Theory of Dislocations	236
A.2	Relations between Thermodynamic Potentials, Kinetic Rate Factors and Statistical Mechanics	240
B	Implicit Formulation of a Phenomenological Macro Model	243
C	Code	251
C.1	Programs, Codes, Libraries Related to the Topic	251
C.2	Eshelby Tensor Ellipsoid - Matlab	254
C.3	Selected Zebfront Code	256
C.3.1	Micro-Meso Model Dislocation Densities Explicit in Zebfront	256
C.3.2	Macro Model Explicit and Implicit in Zebfront	260

Abbreviations

Steel:

AHSS	Advanced High-Strength Steels
CCT	Continuous Cooling Diagram
DBTT	Ductile Brittle Transition Temperature
DPS	Dual Phase Steels
DSA	Dynamic Strain Aging (Microscopic mechanism inducing PLC)
HSLA	High Strength Low Alloy
HSS	High Strength Steel
PLC	Portevin-LeChatelier effect
PH	Precipitation Hardenable
QP	Quenching & Partitioning
(A/C)TMP	Advanced/Controlled Thermomechanical Processing
TTT	Time Temperature Transformation diagram
TRIP	Transformation Induced Plasticity
TWIP	Twinning Induced Plasticity

Experimental:

APT	Atom Probe Tomography
DSC	Differential Scanning Calorimetry
DTA	Differential Thermal Analysis
ECCI	Electron Channeling Contrast Imaging
EBSD	Electron Back Scattered Diffraction
FIB	Field Ion Beam
LSCM	Laser Scanning Confocal Microscopy
OIM	Orientation Imaging Microscopy

Crystallographic:

CBR	Cauchy Born Rule
(C)DP /DC	(Coherent) Dichromatic Pattern / Dichromatic Complex
CSL	Coincidence Site Lattice
CRSS	Critically Resolved Shear Stress
E2EM	Edge to Edge Model
GND	Geometrically Necessary Dislocations
HAGB	High Angle Grain Boundary
HP	Habit Plane
HPV	Habit Plane Variant
(IP)GB	(Inter Phase) Grain Boundary
ILS	Invariant Line Strain
IPS	Invariant Plane Strain
KAM	Kernel Average Misorientation
LAGB	Low Angle Grain Boundary
LCV	(Lattice) Correspondence Variant
LEDS	Low Energy Dislocation Structures
LI(S/D)	Lattice Invariant Shear/Deformation
MDF	Misorientation Distribution Function
OR	Orientation Relationship
ODF	Orientation Distribution Function
PTMC	Phenomenological Theory of Martensite Crystallography
SFE	Stacking Fault Energy
SF(E/T)S	Stress Free (Eigen/Transformation) Strain
SSD	Statistically Stored Dislocations
TOL	Theory of O-Lattice (or O-Line)
TM	Topological Models
UFG	Ultra Fine Grained

Other:

BVP	B oundary V alue P roblem
CAS	C omputer A lgebra S ystem
CNT	C lassical N ucleation T heory
CPFEM	C rystal P lasticity F inite E lement M odelling
(D)DD	(D) iscrete) D islocation D ynamics
DIC	D igital I mage C orrelation
DMR	D igital M aterial R epresentation
EIM	E quivalent I nclusion M ethod
FFT	F ast F ourier T ransform
GBE	G rain B oundary E ngineering
(G/I)P	G auß/ I ntegration P oint
ICME	I ntegrated C omputational M aterials E ngineering
KUBC	K inematic U niform B oundary C onditions
MD	M olecular D ynamics
PDF	P robability D istribution F unction
PBC	P eriodic B oundary C onditions
PAG	P rior A ustenite G rains
RVE	R epresentative V olume E lement
SMA	S hape M emory A lloy
SUBC	S tatic U niform B oundary C onditions
SVE	S tatistical V olume E lement
TEP	T hermodynamical E xtremum P inciples
LTC	L ocal T ransformation C riterion
GTC	G lobal T ransformation C riterion

Symbols

$i, j, k, l,$	Indices for tensor notation
Sup-/Superscripts	and phase and domain symbols
Ω	domain designator
\mathcal{L}	symbol for Bravais lattice
\odot, \perp	sub-/superscript symbols for screw and edge dislocation respectively
I, M	superscripts for inclusion and matrix respectively
L, B	superscripts for martensite lath and block respectively
ext	superscript for externally applied, e.g. load σ^{ext}
γ, a	face centred cubic (f.c.c) phase in steel (austenite)
α	body centred cubic (b.c.c) phase in steel
α', m	particularly emphasising b.c.c or b.c.t (tetragonal) martensite
ε	hexagonal close packed (h.c.p) epsilon martensite
Scalars	
\mathcal{L}	Any function plus constraints added with Lagrange multipliers
V, P	volume, pressure (analogy to $\underline{\varepsilon}, \underline{\sigma}$ in thermodynamic relations of solids)
$s, S(U, \underline{\varepsilon})$	Entropy JK^{-1}
$e, E, u, U(S, \underline{\varepsilon})$	inner/internal energy; for gases $U(S, V)$
$H(S, \underline{\sigma}) = U + \underline{\sigma} : \underline{\varepsilon}$	Enthalpy; for gases $H(S, P)$
$F(T, \underline{\varepsilon}) = U - TS$	Helmholtz free energy (often denoted as A)
$G(T, \underline{\sigma}) = H - TS$	Gibbs free energy
Ψ, Φ	Common symbols for generalized Helmholtz and Gibbs potentials comprising interface-, interaction/mixing- energies etc.

$\Delta G_{\gamma \rightarrow \alpha'}$	free energy difference between austenite and martensite $G_{\alpha'} - G_{\gamma}$
$\Delta s_{\gamma \rightarrow \alpha'}$	specific entropy difference between austenite and martensite
$\Omega_{\sigma}, \Omega_{\varepsilon}$	dissipation / inelastic potential
\mathcal{D}	dissipated energy / dissipation
$c_{\sigma}, c_{\varepsilon}$	specific heat capacities at constant strain or stress
λ_H	specific latent heat $\text{J K}^{-1} \text{g}$, hence $\rho \lambda_H = \text{J K}^{-1} \text{cm}^3$
p_i, P_{ij}	probability of state i ; transition probability from state i to state j
\mathfrak{R}	kinetic rate factor
b	length of dislocation burgers vector $ \mathbf{b} $
h	step height of interface step / ledge
d_{hkl}	normal distance between $\{hkl\}$ lattice planes
g	number of lattice planes (usually multiplied with d_{hkl})
a_{γ}, a_{α}	lattice parameter of cubic systems
$c_1, c_2, c_3 \dots$	empirical coefficients determined by an inverse fitting procedure
T_m	melting temperature of alloy
T_r	recrystallization temperature of alloy
$A_s, A_f = A_{c1}, A_{c2}$	austenite start/finish temperature (c..."chauffage")
$M_s, M_f = A_{r1}, A_{r2}$	martensite start/finish temperature (r..."refroidissement")
M_d	highest temperature at which martensite form due to applied stress
T, \dot{T}	temperature, cooling/heating rate
k_B	Boltzmann constant $1.38064852 \times 10^{-23} \text{J K}^{-1}$
N_a	Avogadro constant $6,022140857 \cdot 10^{23} \text{mol}^{-1}$
R	Ideal Gas constant $k_B \cdot N_a = 8,3144598 \text{J K}^{-1} \text{mol}^{-1}$
ω_A	mean atomic attempt frequency
v_s	speed of Sound $\approx \sqrt{G/\rho} \approx 1000 \text{m s}^{-1}$ for steel (transversal wave)
L, l_0	general mean free path, e.g. for dislocation motion
m	Schmidt factor or strain rate sensitivity
κ	lattice curvature or gradient energy coefficient
η	order parameter of phase transformation
λ_i	eigenvalues of specific matrix
λ, λ^i	Lagrange multipliers (=plastic multipliers in plasticity)
γ^{sf}	stacking fault energy J m^{-2}
w^{sf}	separation width of stacking fault partials

σ^{ie}	general interface energy
σ^{bcc}	coherent twin boundary energy $\approx 0.2 \text{ J m}^{-2}$
σ^{hcp}	interface energy of stacking fault $\approx 0.0115 \text{ J m}^{-2}$
ξ	total phase fraction of martensite $\xi = \sum_i \xi^i$
$\varphi_1, \Phi, \varphi_2$	Euler angles of Bunge's convention (z, x', z'')
θ	general angle (e.g. Lode angle)
θ_{CP}	smallest angle between $\{111\}_\gamma$ and $\{110\}_\alpha$
θ_{KS}	smallest angle between $\langle 110 \rangle_\gamma$ and $\langle 111 \rangle_\alpha$
θ_{HP}	angle between lath habit plane and close packed direction
θ_{ILS}	angle between block habit plane and close packed direction
θ_{Rot}	rotation angle of rotation matrix: $\arccos(\text{tr}(\mathbf{R}) - 1)/2$
$I_1, I_2, I_3,$	invariants of the Cauchy stress tensor $\boldsymbol{\sigma}$
$\sigma_I, \sigma_{II}, \sigma_{III}$	principal stresses of $\boldsymbol{\sigma}$
J_2, J_3	2.,3. invariants of the stress deviator (mechanical invariants)
J	determinant of mapping (Jacobian), here $\det(\mathbf{F})$
$\sigma^{\text{Mises}}, \sigma^{\text{eq}}$	equivalent Mises stress, $(3J_2)^{1/2} = (3/2 \boldsymbol{s} : \boldsymbol{s})^{1/2}$
σ_y	yield strength of macroscopic tensile test ($= \sigma^{\text{eq}}$)
σ^{mean}	mean stress (negative pressure), $\sigma^{\text{mean}} = -p = 1/3 \text{tr}(\boldsymbol{\sigma})$
τ	general shear stress
τ_c	critically resolved shear stress (CRSS) for slip or twinning
$\varepsilon^{\text{eq}}, p$	equivalent plastic strain
γ_0, ε_0	reference strain rate [s^{-1}]
ρ_{gnd}	geometrically necessary dislocation density
μ	shear Modulus or twin variant fraction (often also chemical potential)
K	compression Modulus
ν	Poisson's ratio
f	yield surface / yield function / load-function
Vectors	
\mathbf{X}	position vector in undeformed reference configuration
\mathbf{x}	$\mathbf{x} = \mathbf{x}(\mathbf{X}, t)$ position vector in deformed current configuration
\mathbf{u}, u_i	vector of displacements

\mathbf{a}_i	lattice vectors (=conventional basis for cubic lattices)
\mathbf{b}	Burgers vector of dislocation
\mathbf{b}_p	Burgers vector of partial dislocation
\mathbf{s}, s_i	slip direction $\parallel \mathbf{b}$ for edge and $\perp \mathbf{b}$ for screw dislocation segment
\mathbf{m}, m_i	slip plane normal (commonly given in miller indices)
$\boldsymbol{\xi}, \xi_i$	dislocation line direction
\mathbf{t}	lattice translation vector
$K_1, K_2, \boldsymbol{\eta}_1, \boldsymbol{\eta}_2$	twinning elements: twin plane normals, twinning shear directions
\mathbf{h}	geometrically / "macroscopically" invariant plane (habit-plane) normal
\mathbf{d}	direction of shape deformation
\mathbf{k}	direction of lath (needle) long dimension
\mathbf{n}	normal vector of local terrace plane of an irrational interface
\mathbf{v}	arbitrary vector lying in an (averaged) interface plane (probe vector)
$\boldsymbol{\omega}$	Frank-Rodriguez vector
ξ^i	phase (volume) fraction of individual martensite symmetry variant i
τ^i	resolved shear stress on slip system i
γ^i	vector of accumulated slips
$\boldsymbol{\alpha}_i,$	thermodynamic fluxes
\mathbf{K}_i	thermodynamic forces
\mathbf{K}_c^i	transformation threshold or hardening contributions
Second order tensors	and matrices
\mathbf{I}	identity matrix, δ_{ij} (Kronecker delta)
$\mathbf{A}^A, \mathbf{A}^M$	assembly of lattice vectors into a matrix
g_{ij}, \mathbf{G}	metric tensor of crystal lattice
$\mathbf{C}^{AM}, \mathcal{P}$	lattice correspondence
$\mathbf{F}, \tilde{\mathbf{F}}$	total deformation gradient $\mathbf{F} = \frac{\partial \mathbf{x}(\mathbf{X}, t)}{\partial \mathbf{X}}$
$\mathbf{F}^e, \mathbf{F}^p, \mathbf{F}^{\text{tr}}$	elastic, plastic, transformation part of deformation gradient
\mathbf{C}	Cauchy Green tensor ($\mathbf{F}^T \mathbf{F}$)
\mathbf{U}	symmetric positive definite matrix (pure stretch in an orthonormal basis)
\mathbf{U}_S	structural stretch tensor; for steels the Bain strain \mathbf{B}

$\mathbf{R}, \mathbf{R}[e, \theta]$	rotation matrix, axis angle pair representation
\mathbf{S}	(simple) shear matrix
$\underline{\boldsymbol{\sigma}}$	total Cauchy stress tensor in a material point
$\underline{\mathbf{p}}$	hydrostatic part of Cauchy stress tensor, $1/3 \text{tr}(\underline{\boldsymbol{\sigma}})\mathbf{I}$
$\underline{\boldsymbol{s}}$	stress deviator, $\text{dev}(\underline{\boldsymbol{\sigma}}) = \underline{\boldsymbol{\sigma}} - \underline{\mathbf{p}}$
\mathbf{n}	derivative of macroscopic load/yield function w.r.t $\underline{\boldsymbol{\sigma}}$
$\underline{\mathbf{X}}^i$	generalized force/stress, e.g backstress
$\underline{\boldsymbol{\alpha}}^i$	generalized flux/strain, e.g. conjugate to back stress
$\boldsymbol{\alpha}, \alpha_{ij}$	dislocation density tensor, or thermal expansion tensor
$\underline{\boldsymbol{\beta}}^i$	phenomenological strain variable
$\underline{\boldsymbol{\varepsilon}}^{\text{te}} = \underline{\boldsymbol{\varepsilon}}^{\text{th}} + \underline{\boldsymbol{\varepsilon}}^{\text{el}}$	thermoelastic (reversible), elastic, thermal strains
$\underline{\boldsymbol{\varepsilon}}^{\text{p}}, \underline{\boldsymbol{\varepsilon}}^{\text{vp}}, \gamma_{ij}$	(visco-) plastic strain (in the limiting case of negligibly small rate dependence $\underline{\boldsymbol{\varepsilon}}^{\text{p}} \approx \underline{\boldsymbol{\varepsilon}}^{\text{vp}}$)
$\underline{\boldsymbol{\varepsilon}}^*, \underline{\boldsymbol{\varepsilon}}^{\text{tr}}$	stress free (geometrical view) transformation- or eigenstrain
$\underline{\boldsymbol{\varepsilon}}^{\text{trip}} = \underline{\boldsymbol{\varepsilon}}^{\text{tr}} + \underline{\boldsymbol{\varepsilon}}^{\text{p}}$	total transformation induced plasticity strain
$\underline{\boldsymbol{\varepsilon}}^c \mathbf{I}$	coherently stressed / constrained eigenstrain of Eshelby inclusion
$\underline{\boldsymbol{\varepsilon}}(c)$	compositional eigenstrain
\mathbf{m}^i	Schmidt tensor of slip system i
$\underline{\boldsymbol{\chi}}, \chi_{ij}$	generalized material gradient
h_{ij}, a_{ij}	interaction matrix between slip systems
h_{ij}^{sv}	interaction matrix between martensite variants and slip systems
h_{ij}^{yy}	interaction matrix between martensite variants
$\underline{\boldsymbol{\Sigma}}$	global homogenized stress tensor
$\underline{\mathbf{E}}, \underline{\mathbf{E}}^e, \underline{\mathbf{E}}^p \dots$	Either global homogenized strain tensors or specifically denoting large deformation (Green-Lagrange) strains
Third order tensors	
ϵ_{ijk}	permutation- / Levi-Civita-symbol $\mathbf{e}_i \cdot (\mathbf{e}_j \times \mathbf{e}_k)$

Fourth order tensors

$$\underline{\underline{\mathbf{I}}} = \frac{\partial A_{ij}}{\partial A_{kl}} = \delta_{ik}\delta_{jl} \quad \text{fourth order identity tensor}$$

$$\underline{\underline{\mathbf{I}}}^{\text{sym}} \quad 1/2 (\delta_{ik}\delta_{jl} + \delta_{il}\delta_{jk}) \text{ components of } \underline{\underline{\mathbf{I}}} \text{ acting on symmetrical tensors}$$

$$\underline{\underline{\mathbf{I}}}^{\text{skw}} \quad 1/2 (\delta_{ik}\delta_{jl} - \delta_{il}\delta_{jk}) \text{ fourth order asymmetric identity tensor}$$

$$\underline{\underline{\mathbf{K}}} = 1/3 \delta_{ij}\delta_{kl} \quad \text{spherical/isotropic projection tensor}$$

$$\underline{\underline{\mathbf{J}}} = \underline{\underline{\mathbf{I}}}^{\text{skw}} - \underline{\underline{\mathbf{K}}} \quad \text{deviatoric projection tensor}$$

$$\underline{\underline{\mathbf{C}}} = C_{ijkl} \quad \text{elasticity (stiffness) tensor}$$

$$\underline{\underline{\mathbf{M}}} = M_{ijkl} = \underline{\underline{\mathbf{C}}}^{-1} \quad \text{compliance tensor}$$

$$\underline{\underline{\mathbf{S}}} = S_{ijkl} \quad \text{Eshelby tensor}$$

$$\underline{\underline{\mathbf{D}}} \quad \text{Dual to Eshelby tensor}$$

Abstract

Highly dislocated lath martensite is an essential microstructure component of many multi-phase advanced high-strength steels (AHSS) such as dual-phase-, transformation / twinning induced plasticity and precipitation hardened steels. In the last decade novel experimental microstructure characterisation methods based on lattice diffraction phenomena enabled to obtain a clearer picture of the overall microstructural state of lath martensite, revealing that under certain circumstances it forms a hierarchical microstructural arrangement where the smallest units (laths) group to definite blocks that again assemble definite packets. Beside this general trend, the exact microstructure formation during transformation is highly sensitive on the materials processing history as well as temperature rates and external loadings during transformation. Modelling of the transformation necessitates a multi-scale description and a multitude of experimental data for the model verification. Since transformation induced plasticity results from accommodation processes of the highly anisotropic transformation strains at the microscale, the morphological aspects, i.e. the crystallographic variants related to the lattice change of the transformation must be taken into account. This work is motivated by experimental data obtained from electron backscattering diffraction measurements necessary to calibrate stress sensitive constitutive relations formulated at the microscale for their use in finite element models. In order to be able to accomplish such a goal (i) there must be a definite link between the experimental data and variables of the model and (ii) the model must comprise microstructurally and micromechanics motivated relations. However, for none of these two problems a generally accepted strategy exists up to date. Based on the requirements for the microstructure of a thermally cycled and mechanically loaded maraging steel forming a lath martensitic microstructure, first a unification of crystal plasticity and the crystallographic theory of martensite formation is proposed for point (i). For point (ii) phenomenological scaling relations for non-local effects as well as constitutive laws for the stress dependence of the transformation, dislocation plasticity, nucleation and coupling effects fitting this framework are advised.

Résumé

La martensite à haut degré de dislocation présentant une structure en lattes est un composant essentiel de la microstructure de nombreux aciers multi-phase à très haute résistance dont propriétés sont à côté d'autres facteurs, tels que le durcissement par précipitation, pour une large part en raison du effet d'écrouissage induit par un changement de phase. Dans la dernière décennie, de nouvelles méthodes expérimentales de caractérisation microstructurale, basées sur des phénomènes de diffraction en réseau cristallin, ont découvert que dans certaines circonstances, la martensite forme un arrangement microstructural hiérarchique, où les plus petites unités (des lattes) se regroupent en blocs qui, à leur tour, s'assemblent en paquets définis. En plus de cette tendance générale, la structure définitive de la microstructure au cours de la transformation est très sensible au traitement des matériaux avant la transformation ainsi qu'aux vitesses de changement de température et de contraintes externes pendant la transformation. La modélisation de la transformation nécessite une description à plusieurs échelles et une variété de données expérimentales pour la vérification du modèle. Puisque la plasticité induite par la transformation résulte des processus d'accommodation des souches de transformation hautement anisotropes à l'échelle microscopique, les aspects morphologiques, c'est-à-dire les variations cristallographiques liées au changement de réseau pendant la transformation, doivent être pris en compte à cette échelle. Le but de ce travail est d'utiliser des données provenant d'expériences de rétrodiffusion électronique pour calibrer différents modèles théoriques. Deux aspects sont essentiels pour la mise en œuvre : (i) Il doit y avoir un lien précis entre les données expérimentales et les variables du modèle et (ii) le modèle doit être basé sur les relations microstructurales (géométriques et micromécaniques). A ce jour, il n'existe pas encore de stratégie générale pour ces deux points. À partir d'un modèle de microstructure d'un acier maraging formant une microstructure martensitique à lattes, thermo-cyclé et chargé mécaniquement, on propose d'abord une unification de la plasticité cristalline et de la théorie cristallographique de la martensite, ce qui résout le point (i). Pour le point (ii), les relations de transition d'échelle phénoménologiques pour tenir compte de l'effet non local caractéristique des contraintes et des lois de comportement pour la dépendance à l'intensité de la transformation, la plasticité de dislocation, la nucléation et les effets de couplage adaptés à ce cadre sont développés.

Zusammenfassung

Lattenmartensit mit hoher Versetzungsdichte ist ein wichtiger Gefügebestandteil vieler hochfester mehrphasiger Stahlkonzepte, die durch einen hohen Grad transformationsinduzierter Plastizität und andere Mechanismen wie Ausscheidungshärtung ihre Festigkeit steigern. Durch neuartige experimentelle Charakterisierungsmethoden basierend auf Elektronenrückstreubeugung am Kristallgitter fand man im letzten Jahrzehnt heraus, dass Martensit unter bestimmten Umständen eine Mikrostruktur bildet, die einer gewissen hierarchischen Struktur folgt in welcher ähnlich orientierte Martensitlatten zu definierten Blöcken und diese wiederum zu definierten Paketen zusammengefasst werden können. Neben diesem generellen Trend ist die Transformation höchst sensitiv bezüglich der Verfahrensvorgeschichte sowie der Temperaturrate und externer Belastungen während der Umwandlung. Die Modellierung der Transformation erfordert eine multi-skalige Beschreibung und vielfältige experimentelle Daten zur Modellverifikation. Da der Effekt der transformationsinduzierten Plastizität auf der Akkommodation der stark anisotropen Dehnungen zufolge der Phasentransformation auf der Mikroskala basiert, müssen charakteristische morphologische Aspekte auf dieser Skala berücksichtigt werden. Die Motivation dieser Arbeit ergibt sich daraus Daten aus Experimenten der Elektronenrückstreubeugung für die Kalibrierung verschiedener theoretischer Modelle zu verwenden. Für die Umsetzung sind zwei Aspekte entscheidend: (i) Es muss eine eindeutige Beziehung zwischen den experimentellen Daten und den Variablen des Modells bestehen und (ii) das Modell muss auf geometrischen und mikromechanischen Beziehungen der Mikrostruktur basieren. Allerdings existiert für keinen der beiden Punkte eine allgemein akzeptierte Strategie. Ausgehend von den Anforderungen der Mikrostruktur eines maraging Stahls, die durch wiederholte Umwandlung nach mehreren thermischen Zyklen by gleichzeitiger mechanischer Belastung entstanden ist, wird zunächst eine generalisierte Theorie der martensitischen Umwandlung vorgeschlagen, die ein Bindeglied für (i) darstellt. Im Bezug auf (ii) wurden phänomenologische Skalenübergangsregeln zur Berücksichtigung nicht-lokaler Einflüsse und Konstitutivgesetze für die Spannungsabhängigkeit der Transformation, Versetzungsentwicklung, Nukleation und Kopplungseffekte zwischen ihnen verglichen und weiterentwickelt.

Chapter 1

Motivation and Scope of the Thesis

Lath martensite is one of the main constituents in many advanced steel grades with widespread applications. In the last decade the investigation of its microstructure experienced a scientific renaissance, which has two reasons. First, orientation imaging microscopy (OIM) devices became affordable for institutions all over the world and accompanying software became more user friendly, which triggered a plentitude of microstructure investigations. Particularly, the influence of diverse processes on the final microstructure is still investigated. Second, new methods to evaluate OIM data were developed for studying in particular internal boundaries / interfaces as well as lattice strains and their gradients.

Nowadays the scientific trend strongly develops towards learning algorithms (machine / reinforcement learning, neuronal networks etc.) and it is just a matter of time until OIM data will be used to calibrate industrial processes. On the other hand, deterministic, semi-empirical material modelling has already proven itself a valuable tool for describing the behavior of steels in certain cases. Furthermore, finite element models, as treated in this thesis, are able to account for the influence of internal and external stresses, which are known to have a substantial influence on the microstructural evolution, especially when a phase transformation is involved. In the author's opinion one of the future challenges will be to combine both approaches. For instance finite element models could be used to generate data relatable to the information obtained by OIM, providing a stronger statistical basis neuronal networks can be trained with.

Alternatively, the OIM data can be used for the calibration of micromechanically motivated constitutive models. While this has already been done in the case of plastic texture development in the framework of crystal plasticity a comprehensive modelling approach of the martensitic transformation texture is still lacking. While in principle, models with a large number of model parameters allow to describe complex material behavior under various conditions, the challenge in the use of a wide variety of (possibly interdependent) parameters lies in the validation of the correct response of the model when one parameter is altered. From the physical point of view this means that the effect of any of the parameters should be verifiable by an experimentally observed behavior.

Especially models considering the coupling between the phase transformation and plasticity often need a considerable amount of material parameters. Therefore, at least for the plastic deformation of the austenite a model with many parameters motivated from dislocation dynamics simulations, but without any fitting parameters is considered. This is of interest for determining the role of each of the respective mechanisms, i.e. the transformation and classical plasticity in TRIP steels. Such investigations are valuable, because they cannot be carried out experimentally.

Macroscopic constitutive laws have been successfully applied to estimate macroscopic stresses due to the transformation, but their internal variables generally do not relate to microstructural characteristics. While macroscopic models are usually calibrated against macroscopic stress strain curves under various conditions there are only a few micromechanical tests to calibrate micromechanical models. Furthermore, as opposed to macroscopic data, the mechanical behavior of such tests usually strongly varies due to size effects not making it statistically representative.

The aim of this thesis is to bring together aspects of the martensitic transformation that will eventually enable to utilise orientation imaging microscopy data of highly dislocated martensite microstructures in steels for the calibration of micromechanically motivated finite element constitutive frameworks.

Contrary to the constitutive framework for plastic deformation due to dislocation motion, take Orowan's equation for dislocation bowing (Equation 2.3) as an example, there are very few fundamental equations for martensite that have a mechanistic character. This

manifests itself in the fact that micromechanical approaches to the formation of martensite are more the exception than the rule.

The solid state phase transformation community seems to be split into groups following either purely diffusive or displacive theories for phase transformations in steels. One significant distinction between the two is that mainly the former has been applied to alloy design. This is due to the fact that diffusional transformations are closer to thermodynamical equilibrium (although still quite far away) for which generally accepted models exist. However, from the point of view of tuning material properties by specialised microstructures, the catch-phrase is "microstructure property relationship", material processing routes far away from equilibrium are more suitable.

The major point of this work is to review and extend the current understanding of lath martensite from the point of view of its experimental characterization and its crystallographic description to eventually set up a constitutive framework general enough to account for most effects related to thermomechanical processing. Considering a description starting at the lowest scale incorporating nanoscale parameters such as the Burgers vector of interfacial dislocations seems to be necessary as very recently emphasised by Levitas 2018, who even designates them as as a new dimension in a "phase diagram". For that reason, the key physical mechanisms of nucleation and elasto-plastic accommodation on the lowest level must be well-understood under various (processing) conditions.

The thesis is organized as follows: First, experimental and specific numerical works dealing with the topic are briefly reviewed. In chapter 2 a general introduction to the several classifications of the phase transformation phenomenon in steels is provided. Also a general overview of common steel types and processing routes is given and modelling strategies are discussed emphasising the multi scale nature of the problem.

Then in chapter 3 crystallographic aspects related to martensite are treated. Since a major characteristic of lath martensite is its strong coupling with plasticity, the nomenclature on defects like dislocations, stacking faults and twins is briefly introduced. In this chapter also the theoretical ground is laid for the understanding of how martensite is characterised in terms of OIM data and which problems are still insufficiently explained. Then crystallographic theories of martensite in terms of geometrical continuum relations as well as from the point of view of interface kinematics are reviewed. Emphasis is laid on the interplay between crystallographic relations and the three dimensional morphology of martensite

domains. Particularly, a refined set of possible "boundary" glide systems based on the structured arrangement of laths to sub-blocks and blocks is discussed based on all foregoing considerations.

Afterwards, the existing concepts are unified and extended in a manner of most generality. The proposed framework combines the kinematics of crystal plasticity, and the crystallographic theories of martensite and is formulated as an optimization problem with a variable amount of constraints that can be motivated based on experimental findings. More precisely a theory of blocks built of laths is presented. This is the main result of the thesis in terms of pushing the boundaries of the current knowledge.

In chapter 4 aspects of homogenization and localization as well as inclusion theory are provided. Even though lath martensite forms strongly coupled with dislocation plasticity its formation is still highly influenced by non-local strain energy contributions. The issue is as always in multi-scale problems the trade-off between enough detail to depict the heterogeneity due to nucleation and interfaces dictating the microstructural evolution, while concurrently approaching as closely as possible the scale of a representative volume element. The idea of (on average) fitting the non-linear evolution of stresses during the phase transformation in terms of a modified phenomenological scale transition rule termed β -rule is finally adopted to fit the hierarchical microstructure of lath martensite.

chapter 5 provides information on the experimental characterisation on the mechanical behavior and the kinetics of martensite. Also the effect of thermal transformation cycling on the microstructure of a precipitation hardenable maraging steel exhibiting the phenomenon of transformation induced plasticity upon moderate cooling rates is studied using orientation imaging microscopy. On the one hand statistical data characterising martensite over many grains is discussed. On the other hand the ability to quantitatively measure the finest possible features such as dislocation cells lying on the edge of the resolution of the electron backscattering diffraction method is presented.

The last chapter is devoted to the finite element modelling of martensite. General frameworks of implementation as well as kinematic and thermodynamic approaches for martensite are reviewed in order to obtain a full understanding of the variety of this topic. Plasticity is discussed in terms of size effects, hardening, flow and yield formulations. Finally, constitutive relations for martensite are reviewed. Essential parts a micromechanical model

incorporating crystallographic variants should comprise are discussed. Possibilities for exploiting the geometrical information obtained in the crystallographic study to formulate constitutive equations at the single crystal level are presented. For parameter fitting on OIM data currently no general framework exists and given the complexity of the investigated microstructure at hand finding such a framework would go beyond the scope of this work. However, essential groundwork is laid throughout the work to prospectively tackle this problem. A full model should eventually represent the spatial and statistical distribution of crystallographic variant fractions resembling the hierarchical assembly of lath martensitic steels as characterised by EBSD methods.

In this work no attempt is made to set up a full model incorporating all the features that influence the stabilisation, nucleation, growth, accommodation and homogenization. However, key aspects such a model should contain are elaborated which will serve as an essential input for future modelling approaches.

1.1 Hierarchical Microstructure of Highly Dislocated Lath Martensite

Only in recent years electron back scattering diffraction (EBSD) methods with a resolution just high enough to contrast some finer features of the microstructure of dislocated lath martensite while recording several grains became generally available. Multiple studies then revealed that dislocated lath martensite arranges in a three level hierarchical microstructure pattern within grains, as sketched in Figure 1.1.

1. First, bundles of laths form blocks (regions of low crystallographic misorientation). Either bi-variant blocks (consisting of sub-blocks as in Figure 1.2) or single variant blocks.
2. Second, blocks, separated by irregular high-angle boundaries, stack to packets, i.e. a lath group with the same plane parallel relationship with the close packed plane in austenite namely $\{111\}_\gamma \parallel \{011\}_{\alpha'}$ (4 $\{111\}_\gamma$ CP groups).
3. Third, packets partition a grain.

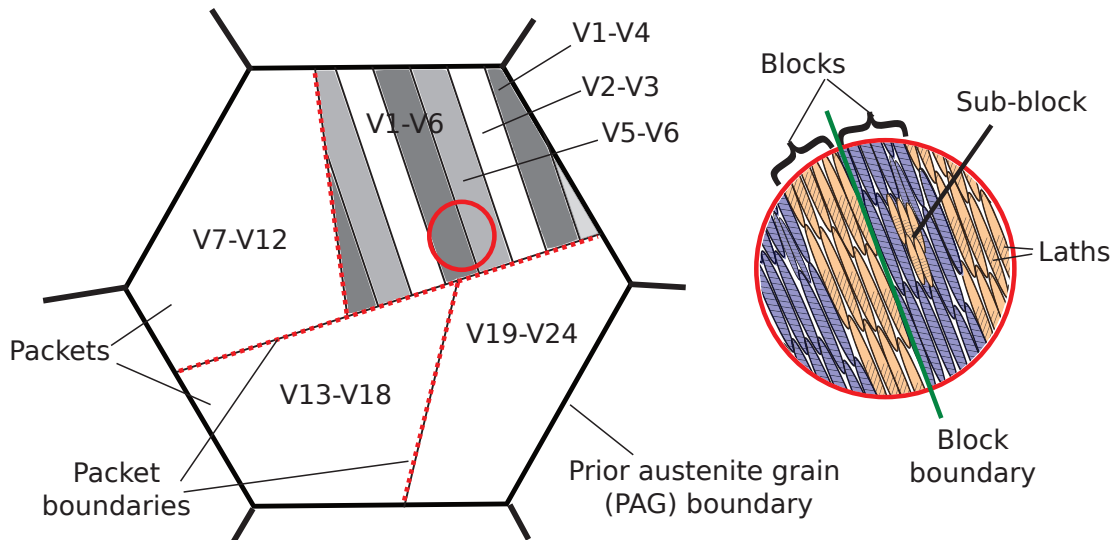


FIGURE 1.1: Redraw of highly idealised schematic commonly found in the literature, showing the hierarchical microstructure of dislocated lath martensite. Laths form (composite) blocks (bi-variant or single variant), blocks stack to packets and packets partition a grain. The variant notation (pairings) is that of Morito et al. 2003. A broader classification is found in Figure 1.3.

Morito et al. 2003; Morito et al. 2006a use the term sub-blocks for blocks which are fully surrounded by another block (i.e. they form an inclusion in the other block). Their boundaries are hence sub-block boundaries. In the case of bi-variant blocks often, also the term sub-units is used for a small cluster (mainly) of single laths. However some authors refer to sub-units as sub-blocks. A consequence of this organized structure is for example that "effective grain sizes" for strength, plasticity and failure (crack propagation) are substantially different Guo et al. 2004; Galindo-Nava et al. 2015.

Since martensite blocks are separated by high angle grain boundaries restricting slip transmission, the effective grain size in martensitic microstructures is usually defined as the block size.

A comparative study between block boundary and sub-block boundary strengthening by means of micro tensile testing has been carried out by Du et al. 2016a; Shibata et al. 2010; Mine et al. 2013 and complemented by crystal plasticity simulations of individual laths by Mine et al. 2013; Kwak et al. 2016.

In general it might be distinguished between mild / plain (Morito et al. 2003) carbon steels and alloy steels (Morito et al. 2006a; Kitahara et al. 2006). In plain / mild carbon steels (0.0026-0.61%) generally the size of the blocks and packets decreases with increasing C content. Between 0.0026 -0.38%C, packets consist of well developed parallel blocks forming

in pairs (two orientation / correspondence variants) with definite orientation relations (the same Bain strain but two specific KS orientations, hence also bi-variant blocks), showing a certain misorientation (namely the lowest possible - theoretically 10.5°). There are three blocks with different orientations in a packet (all three Bain strains). Especially, for carbon free steels and low isothermal transformation temperatures or continuous cooling paths this is the preferred microstructure. The lath structure observed via TEM of a high alloy steel similar in alloy design to the MarvalX12 (model material used in this work) is shown in Figure 1.2.

The 2 variants have very regular / straight sub-block boundaries (habit planes of the lath boundaries) of type $\bar{1}65)_{\alpha'}$ and $(165)_{\alpha'}$, corresponding approximately to $(575)_{\gamma}$ and $(755)_{\gamma}$ in the case of a Kurdjumov–Sachs orientation relation (see section 3.4). Due to their regularity and the fact that fine austenite films may be retained at these boundaries block boundary sliding has been studied by Du et al. 2016b using a micromechanical testing device. Maresca 2015 incorporated this behavior in a crystal plasticity modelling approach.

In carbon alloy $>0.61\%C$, packets consist of fine blocks whose width is a few μm . Each block consists of laths of a single orientation / correspondence variant and blocks of all the six variants are distributed randomly in the packet. The higher the carbon content gets the less regular / straight the block boundaries become.

A possible interpretation of blocks and packets becoming is as follows: In low carbon alloys, laths in a large block are formed by autocatalysis and significant plastic accommodation occurs in the austenite matrix. However, the higher the carbon content gets, the more difficult it becomes to accommodate the strain of martensite in the austenite matrix, because austenite becomes harder (called composite effect in Nagayama et al. 2001, solid solution hardening of C and work hardening due to TRIP) and it must be kept in mind that C stabilizes the austenite leading to lower lower M_s temperatures. For self-accommodation, it is necessary that blocks and packets size decreases and all variants in a packet appear, resulting in the formation of blocks and packets with small size and random distribution of variants.

Furuhara et al. 2006; Morito et al. 2010 studied the carbon and temperature dependency of the hierarchical structure for Fe-9Ni-(0.15-0.5)C and classified it as shown in Figure 1.3. The packet size and block thickness decreases with increasing cooling rate, although the

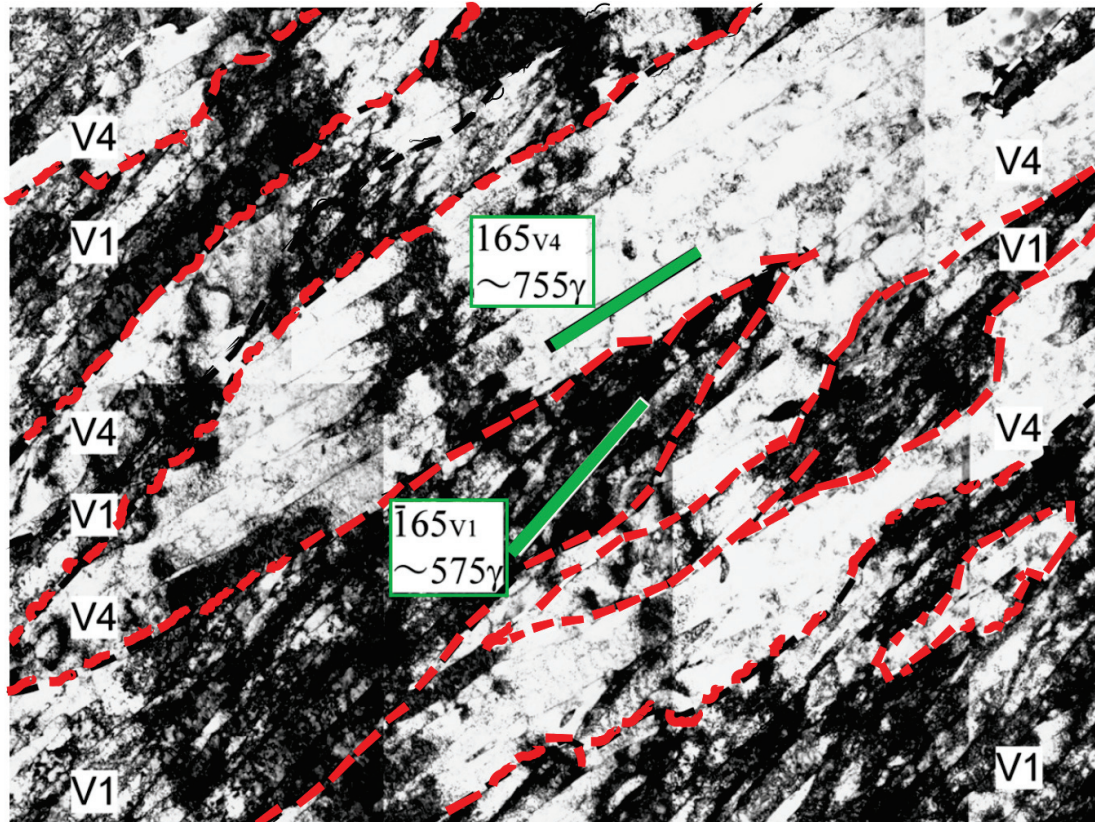


FIGURE 1.2: Lath structure of 18Cr-8Co-5Mo, see Table 1.1 Morito et al. 2006a. large block made up of sub-blocks V1 and V4 (alternating black and white contrast). The sub-block boundaries are marked as dashed red lines. Note the difference in the lath boundary directions in V1 and V4. The habit planes were identified as $(\bar{1}65)_\alpha$ and $(165)_\alpha \approx (575)_\gamma$ and $(775)_\gamma$ for V1 and V4, respectively.

sub-block thickness does not change. This trend has also been observed in upper Bainite Lambert-Perlade et al. 2004. The dependence of variant-pairings on temperature and carbon content has been investigated in Stormvinter et al. 2012; Takayama et al. 2012.

Also the prior austenite grain size (PAGS) affects the maximum plate or lath size, i.e. the larger the austenite size the bigger the maximum plate or lath size. However Morito et al. 2006b found that the lath size is practically independent of the prior-austenite grain size. This suggests that if the formation of blocks is well understood material models may attain a certain universality / maturity.

Similarly, the average number of packets has been shown to be proportional to the PAGS Morito et al. 2006a; Morito et al. 2005; Morito et al. 2013. Particularly, Morito et al. 2005 reported that not all blocks formed in Fe-0.2C-1.5Mn-0.15V when the prior-austenite grain size is lower than $\approx 5-10 \mu\text{m}$. This is a crucial point, since many recent investigations on the hierarchical structure found in the literature are reported for grain sizes much larger

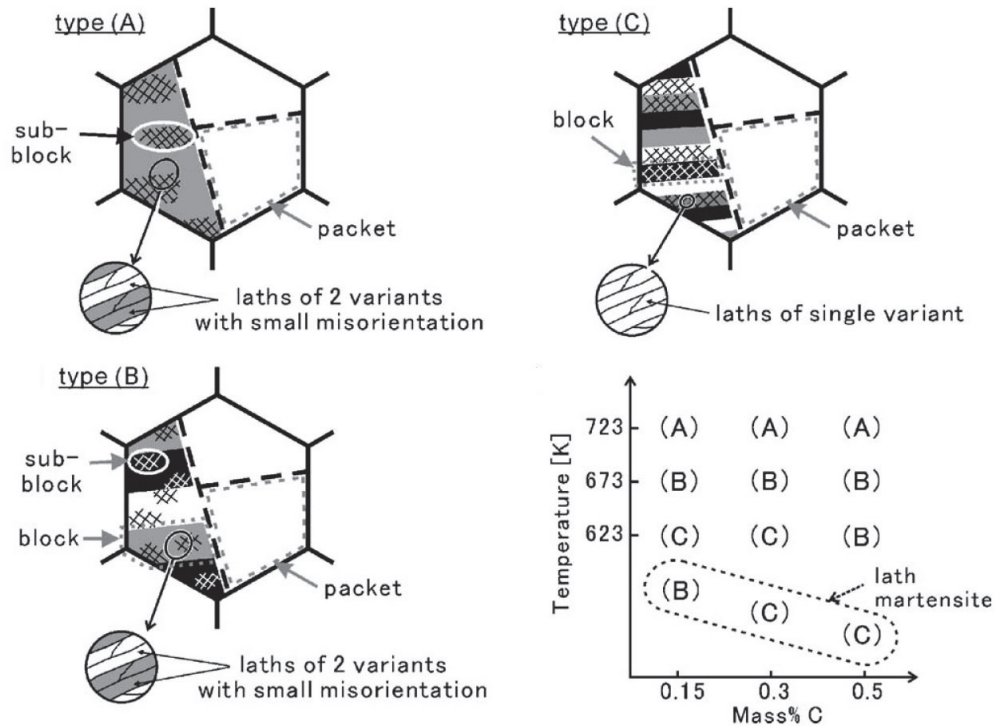


FIGURE 1.3: Crystallographic characteristics of upper bainite and lath martensite sub-structures in Fe-9Ni-(0.15-0.5)C alloys according to Furuhashi et al. 2006

than in our specimen of the MarvalX12, see Table 1.1. Note, however, that these large grain sizes studied in the literature are generally too large, to be favourable in typical industrial applications. An example of the situation in the MarvalX12 for a small grain size is given in 1.4.

Note, that it is not only the PAG that has an influence, but also the plastic heterogeneity of the austenite. Their effect is similar, namely they both influence the degree of facilitated nucleation (cf. strain induced transformation). A combined study of PAG and austenite heterogeneity for a 15Cr-9Mn-Ni-Cu stainless steel has been carried out by Kisko et al. 2013. To sum up, all recrystallization, recovery and grain growth at high temperatures influence the later nucleation behavior of martensite.

Recently, 3D EBSD reconstructions of stacked images obtained by removing some surface with a field ion beam between EBSD recordings have been realized by Morito and co-workers. This way they studied the three-dimensional morphology of sub-blocks, see Morito et al. 2009 as well as whole packets, see Morito et al. 2013 packets. For the packets a higher irregularity for the smaller grain size can be observed, however no information on the history of the specimen before annealing is given.

Morsdorf et al. 2015; Morsdorf et al. 2016 emphasised the importance of transformation sequence and multitude of plasticity mechanisms. The martensite domains formed in the early stage of transformation are much coarser, have a relatively low dislocation density and are subjected to a stronger autotempering during the quenching process in comparison to later transforming thinner laths with higher dislocation densities. The stronger autotempering process is explained by the evolving stress state of the austenite and martensite, where the stress state at later stages of the transformation is sufficient to (mechanically) stabilize the austenite (c.f. retained austenite). The consequence is a significant scatter in local yield strength even within the bounds of a single prior austenite grain. Packet boundaries are asymmetric, since laths on one side (which formed earlier in the sequence of martensitic transformation) lie parallel to the packet boundary, while on the other side laths end with their short edges at the packet boundary. This effect adds to the crystallographic misorientation of $\approx 40 - 60^\circ$ that also exists across packet boundaries.

steel	Cr	Ni	Mo	Al	Ti	C	Si	Mn
MarvalX12 ¹	12.15	9.05	2.03	0.7	0.35	<0.01	0.05	0.03
Fe-18Ni-8Cr / 304 ²	18.16	8.03	-	-	-	0.05	0.61	0.95
Fe-5Ni-C ³	-	5	-	-	-	0.13	-	-
Fe-18Ni-8Co ⁴	-	18.51	5.8	0.063	0.72	0.003	0.006	0.02
Fe-3Mn ⁵	-	-	-	0.009	0.021	0.0049	0.14	3.14
Fe-9Ni ⁶	0.01	9	-	0.02	-	0.046	0.23	0.64
Fe-12Mn ⁷	0.023	0.01	<0.01	-	-	0.009	<0.01	12.23
AISI 1030	-	-	-	-	-	0.34	0.2	0.6
AISI 4140	1.0	-	0.21	-	-	0.42	0.22	0.8

steel	austenitization	$D_{\text{grain}} [\mu\text{m}]$	cooling process
MarvalX12 ¹	TA03 - 1373 K for 1.8 ks	16 ± 3	air cooled with 1 K s^{-1}
	TR32, TR25 1113 K for 1.8 ks	14 ± 3	air cooled with 1 K s^{-1}
Fe-18Ni-8Cr / 304 ²	1273K	27	air cooled
Fe-5Ni-C ³	1173 K for 0.36ks	25	water quenched
Fe-3Mn ⁴	1473K for 0.6ks	350	water quenched
Fe-18Ni-8Co ⁵	1473K for 3.6ks	660	water quenched
Fe-9Ni ⁶	1473K for 7.2ks	50-100	water quenched
Fe-12Mn ⁷	1473K for 5.4ks; 1273K for 18ks	100	quenched to 448K, reaut., quenched
AISI 1030	1423 K for 10.8ks	80	water quenched
AISI 4140	1423 K for 10.8ks	120	water quenched

TABLE 1.1: Top: Chemical compositions (wt%) of some steel types for which a hierarchical microstructure is reported. ¹Nagayama et al. 2001, ²Shintani et al. 2011, ³Morsdorf et al. 2015, ⁴Morito et al. 2006a, ⁵Morito et al. 2006a, ⁶Kinney et al. 2014, ⁷Kinney et al. 2017. Bottom: Emphasis on the difference on processing conditions of steel specimen for which a hierarchical microstructure is reported. Austenitization temperatures and holding times, approximate resulting grain sizes, specification of cooling process.

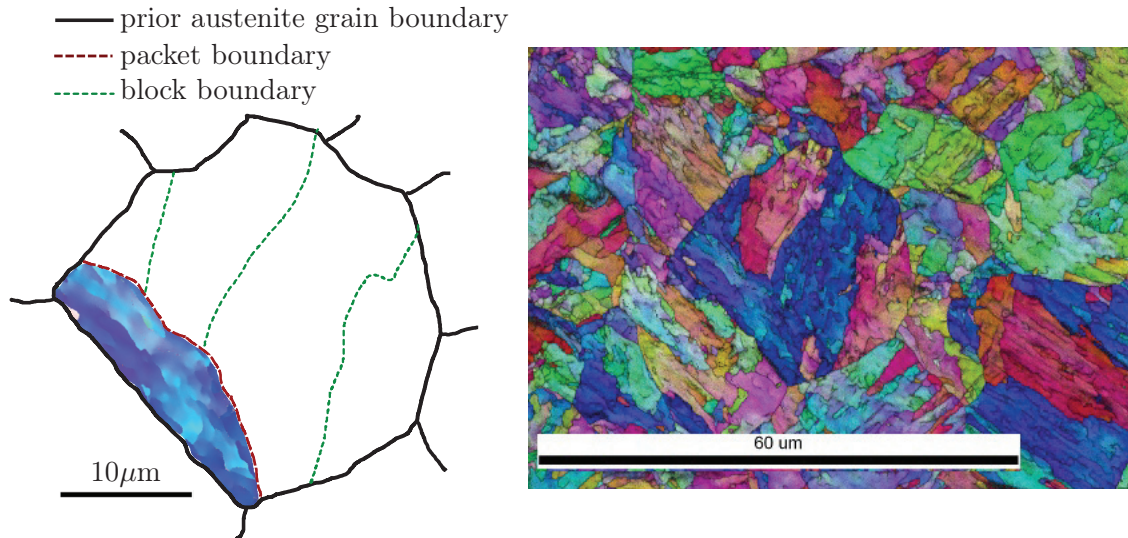


FIGURE 1.4: Exemplary orientation imaging microscopy image of hierarchic structure for small grain size of MarvalX12 (specimen TR32 see Table 1.1). Color code: inverse pole figure; grayscale: fit. One dominant packet (four visible blocks in the 2D representation) and a minor packet consisting of just one single block (redundant terminology). In the minor packet (single block) the inverse pole figure colour contrast is zoomed on the left. Bright/dark regions indicate a bi-variant block structure, however, TEM is required to resolve it, see Figure 1.2.

An overview of all scales addressed in this work is given in Figure 1.5. The range of scales effecting the material behavior leads to a discretisation problem in modelling. The question is how to take into account microstructural complexity (and hence the description of the evolution of driving and dragging forces) without resolving it in detail. In this work, strains for the laths are worked out and strategies are presented to obtain homogenized strains for the bi-variant blocks (section 3.10). A modified form of a phenomenological localisation (strain transition) rule is proposed for obtaining the stresses of each phase locally (section 4.4). Interestingly, with the rise of gradient methods (section 6.1) instabilities are now numerically manageable and approaches in this direction are made, see section 6.3 and subsection 6.7.1.

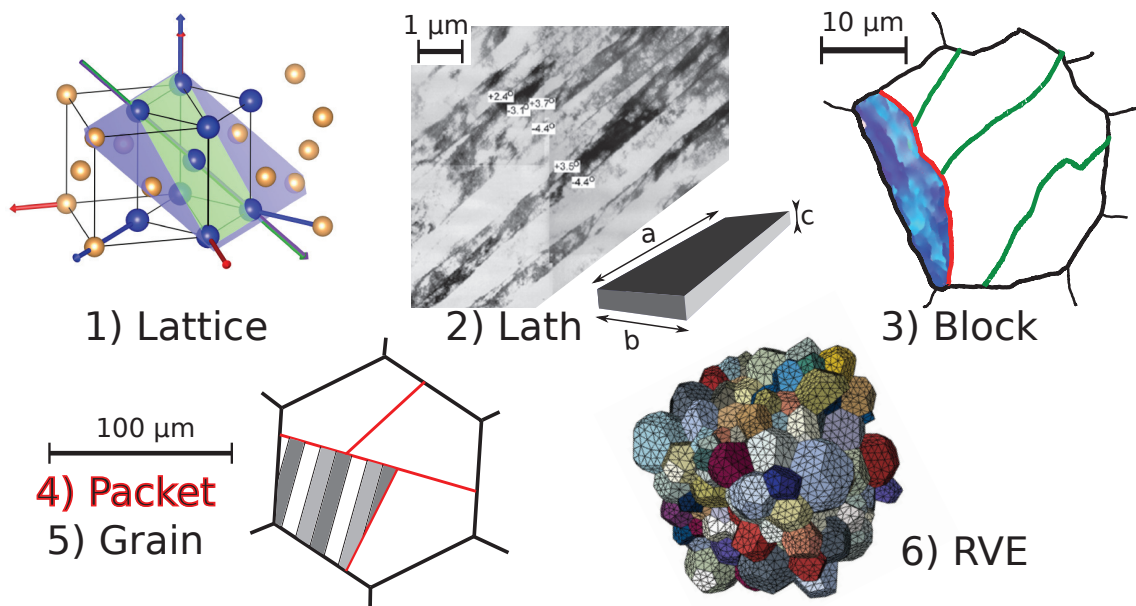


FIGURE 1.5: Scales addressed in this work. Starting from considerations on the lattice kinematics and the 3D structure and arrangement of laths into blocks suitable strains are worked out. The idea is to construct a microstructure sensitive combination of a mean-field full-field model, that e.g. recovers the variant distribution into packets.

Chapter 2

Introduction

2.1 Classifications of Phase Transformations in Steels

The solid state phase transformations in steels has been classified from three perspectives. First, from a thermodynamic perspective (see Ehrenfest 1933b; Ehrenfest 1933a, second from a structural perspective (see Buerger 1951 and more recently J. Hirth et al. 2011; M.-X. Zhang et al. 2009) and third from the point of view of kinetics (see Roitburd et al. 1979; Kaufman et al. 1958). The main point of this section is that it is insufficient to classify a system solely based on one of these three points of view.

Selection and arrangement (morphology) in phase transformations depends on thermodynamic, kinematic and kinetic constraints. Kinematic factors include restrictions on the lattice-invariant deformations (e.g. twinning/slip) and the influence of the interface mobilities (e.g. ledge/smooth). Once kinematic constraints are specified for a given phase transformation, thermodynamics (energy minimization of surface/strain energy, dissipation maximization) determines the direction and kinetic constraints determine the morphology.

Three extreme cases of martensite growth modes have been defined by G. B. Olson et al. 1986:

- (i) An almost purely thermoelastic, hence reversible (see subsection 2.1.1) formation as in shape-memory alloys (SMAs).
- (ii) An elastic-plastic formation, where plasticity cannot immediately follow the initially very fast growth that is dictated by nucleation (e.g. high carbon or > 20 wt% Ni lenticular

martensites/ characteristic midrib).

(iii) A formation that is fully coupled to plastic accommodation, where growth occurs via organized disclination (cf. J. Hirth et al. 2013; generalization of dislocations to interfaces) motion on semi-coherent interfaces with a defect structure that enables a high interface mobility (glissile interface), see Maresca et al. 2017. (ii) and (iii) are non-thermoelastic hence irreversible, see subsection 2.1.1. The latter is the case for dislocated lath martensite, see subsection 2.2.3. According to Roitburd 1990 it constitutes a relaxed state, i.e. it has the lowest transformation barrier, resulting in the comparatively high martensite start (M_s) temperatures. It is envisioned (see Figure 3.10) that screw dislocations swipe the interface and cause a growth of the lath, therefore providing an easy growth mechanism because additional atoms can be added easily to the step of the screw (see section 3.2 and subsection 3.5.5).

The question of growth mechanism is one of the central features of a martensitic transformation, again emphasizing the importance of the martensitic interface (see chapter 3).

2.1.1 Thermodynamic Classification

According to Ehrenfest 1933a the order of a transformation is the degree of derivative of the free energy with respect to some thermodynamic variable at which the first discontinuity occurs. For instance $\Delta V \neq 0$ or $\Delta S \neq 0$ and exchange of latent heat $\Delta H = T\Delta S$ occurs.

Except in quite exotic cases a discontinuity occurs at the latest in the second derivative. Therefore, it is often considered sufficient to merely investigate the first derivative w.r.t. field parameters of the system. If it is zero the transition is also called continuous (hence it must be second order). In continuous transitions critical points are important (critical phenomena) and corresponding physical laws show some commonalities (universality). On the contrary, a non-zero first derivative indicates the presence of a first-order phase transition. Examples of a typical first order transformations are any recrystallization or decomposition (see Khachaturyan 1983). However, this classification has turned out neither to be sufficiently ample nor precise (Müller 2013).

A broader classification scheme is to denote first-order phase transitions as those involving latent heat and second-order ones as those without latent heat (e.g. already used by Landau 1937 in the first sentence of his seminal paper).

In contrast to SMAs that are said to behave thermoelastically, i.e. they show a reversible or enantiotropic (see Müller 2013) transformation and therefore have a low hysteresis (e.g. Ni-Mn-Ga, Fe-Pd, see Seiner et al. 2016), the phase change upon cooling in steels is accompanied by a volume dilatation between +0.5-4%. This volume change leads to a stress distribution of dominating tension in the austenite and compression in the martensite, most easily deduced by Barlows formula (Kesselgleichungen). Due to the heterogeneity of a polycrystal and kinematic constraints of lattice deformation modes this volume change can never be accommodated purely elastically (non-thermoelastic / reconstructive / irreversible / monotropic / only kinetically stable, but thermodynamically unstable at any condition; high hysteresis), but is always accompanied by some degree of plastic deformation (dislocation motion). "Irreversible" also means that martensite, once formed, cannot reorientate to another martensite variant or even transform back into austenite. In high carbon steels, beside plastic deformation, irreversibility is also due to carbide precipitation after transformation. For reversible processes $dS = \delta Q/T = 0$.

In a martensitic reaction, the extra strain energy is tolerated because some degree of coherency is essential to the mechanism of transformation, and alternative forms of transformation with smaller strain energies do not take place because their rates are much slower (see Christian 1965). Artemev et al. 2001 define the ratio of strain energy produced to driving force to characterise the degree of self accommodation, i.e. the potential to form optimal structures minimizing the strain energy. M. Cohen et al. 1992 denote martensitic transformations where the kinetics and morphology are not dominated by strain energy as quasi-martensitic (e.g. in the antiferromagnetic Mn-Ni alloy).

Since this work specifically deals with a cubic martensite phase, at this point the thermodynamic difference to "classical" tetragonal martensite is shortly outlined. The difference between a b.c.c and b.c.t (martensite) crystal structure is the thermodynamic preference for ordering of carbon atoms within one interstitial sub-lattice of b.c.c. Zener 1948 pointed out that an indirect, strain-induced interaction between the carbon atoms causes this spontaneous ordering. Based on his work, Kurdjumov et al. 1975 developed a model for the order-disorder transition using elasticity theory. However, it could not explain the mechanically driven b.c.c-b.c.t transition that can be observed (see Djaziri et al. 2016). It is often stated that for carbon contents above ≈ 0.6 wt% the crystal lattice becomes b.c.t because of the extreme supersaturation of solid solution carbon. However, it must be emphasised

that this is by no means generally valid, but strongly depends on alloying elements and process routes.

Finally it is pointed out that historically there has always been a discrepancy between the energies calculated in the framework of classical nucleation theory CNT (equilibrium thermodynamics) and corresponding nucleation rates. Particularly, calculated energies were too high (see e.g. M. Cohen 1972; Roitburd 1990) comparable to the problem of theoretical yield strength without the concept of dislocations. As we will see, the theory is far from complete, but considerable progress has been made by employing a multi-scale view.

2.1.2 Structural Classification

Solid-state phase transformations are frequently classified as either reconstructive or displacive see e.g. Christian 1994; Authier 2003. In a chemical bond model, an entirely displacive transformation means that a lattice change occurs just by distorting the lattice locally without breaking chemical bonds (bonds are merely distorted). Hence, each atom moves relative to its neighbours by less than an interatomic distance. As a corollary of this, the number of atoms must be conserved in any incremental volume. Displacive transformations are characterised by small values of heat (few J g^{-1}) and a symmetry relation between the parent and product phase (e.g. in the simplest case a group-subgroup relation, see subsection 3.5.2, leading to a correspondence between symmetry elements). Bhattacharya et al. 2004; Conti et al. 2004 argues that in order for a transformation to be reversible the symmetry group of both the parent and product phase have to be included in a common finite symmetry group (known as weak transformations).

Reconstructive, most generally means that bonds are broken and reformed at some point in the course of a transformation. In the reconstructive limit (commonly termed "diffusional" transformation), atoms move on average several thousand interatomic distances. Since diffusion is thermally activated, diffusional transformations have a tendency to occur at higher temperatures. In the displacive limit, neighbouring atomic bonds are never broken, hence atoms do not make a single diffusive jump. However between these two limiting cases, statistical measures for broken bonds or the average/maximum travel distance of atoms by diffusion cannot have not been specified. Here the terms diffusional-displacive

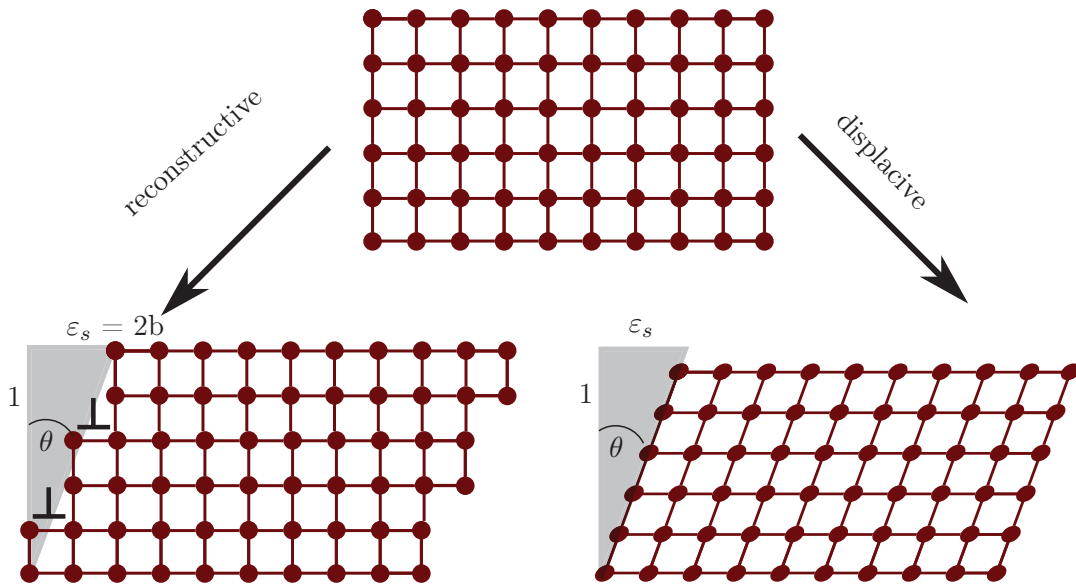


FIGURE 2.1: Comparison of schematic atomic movements according to notions of displacive (pure shear) and reconstructive transformation in the case of a simple shear. A controversy of this notion is that although twinning in steels is generally considered to be displacive the result is still a cubic crystal and not e.g. a rhombohedral (cf. for instance the cubic to monoclinic transformation in NiTi). The contraction due to the pure shear is compensated by a lattice stretch during transformation. ε_s are the shear magnitude. Lower-left: Schematic of two step dislocations producing a shear magnitude of two times their Burgers vector.

or bainitic as well as massive transformation are commonly used. Particularly, in bainitic transformations, long range diffusion (of carbon) and displacive transformation occur sequentially.

Some solid solutions transform very rapidly to a new single-phase structure with the same composition as the original phase (composition invariant). When a reaction of this type exhibits nucleation and growth rather than martensitic characteristics, it is usually called a massive transformation. In steels, however the growth (kinetics) is very fast and comparably to classical (i.e. tetragonal, twinned with high contents of austenite stabilizing elements especially carbon) martensite formation, which is why the transformation is nevertheless called martensitic. In a massive transformation, specific short range diffusion (only surface diffusion; diffusion length up to two lattice parameters; also excluding interstitial carbon/nitrogen long range diffusion) plays a profound role for mobility and nucleation of such interfaces, enabling the change of crystal structure, at constant composition by means of coordinated diffusional jumps across matrix boundaries, controlled/permitted by

the structure of these boundaries (elaborated in subsection 3.5.5). An important question arising for massive transformations is to what extent, details regarding the atomic structure and/or transport of atoms from one phase to the other at the interface (atomic mechanism of the transformation) are important to quantify the overall transformation process. For example the effect of solute drag, which is well-studied for diffusional transformations, is not entirely clear for massive transformations. For instance the new phase forms with the same composition as the parent phase, but behind a steep pile-up of the minority component in the parent phase (solute drag in bainite).

In a fully reconstructive transformation diffusion occurs during nucleation and growth (e.g. all types of ferrite, Pearlite). In Widmanstätten ferrite high internal stresses strongly enhance diffusion giving it some displacive characteristic. In bainite, carbon diffusion plays a significant role for nucleation, but may be negligible during the comparably short growth duration of a transforming domain (relative to the time needed for any significant diffusion).

Features like habit planes (HPs), growth directions and orientation relationships (ORs) are common to most of both reconstructive and displacive transformations (herein referred to as crystallographic features). Howe 2006 points out that both martensitic and diffusional transformation products can follow the phenomenological theory of martensite crystallography (PTMC) and invariant-line theories (treated in section 3.5), so that determination of orientation relationships, habit planes and surface relief are no longer sufficient to define a transformation as martensitic. A distinguishing feature occurring in martensitic transformations only is the formation of a pair or group of certain domains that are in contact with each other, reflecting the mutual accommodation of the shape change.

Considering all possibilities of transformation types, differences in the ORs are generally more subtle compared to morphological features. Martensitic transformation products are inevitably plate-, lens- or even lath-shaped to minimise the strain energy associated with the transformation, whereas reconstructive diffusional transformations may show a similar morphology but can also be e.g. spheres or cubes, depending on the governing factor(s). If the governing factor is lowering the interface energy this may be done by maximising atom matching across the interface. In certain cases of interfaces and possible mechanism(s) discussed in chapter 3, even a one dimensional matching of close-packed or nearly close-packed rows of atoms is sufficient to do so. The consequence of this is that the orientation relationships in these diffusional transformations often exhibit exact parallelism

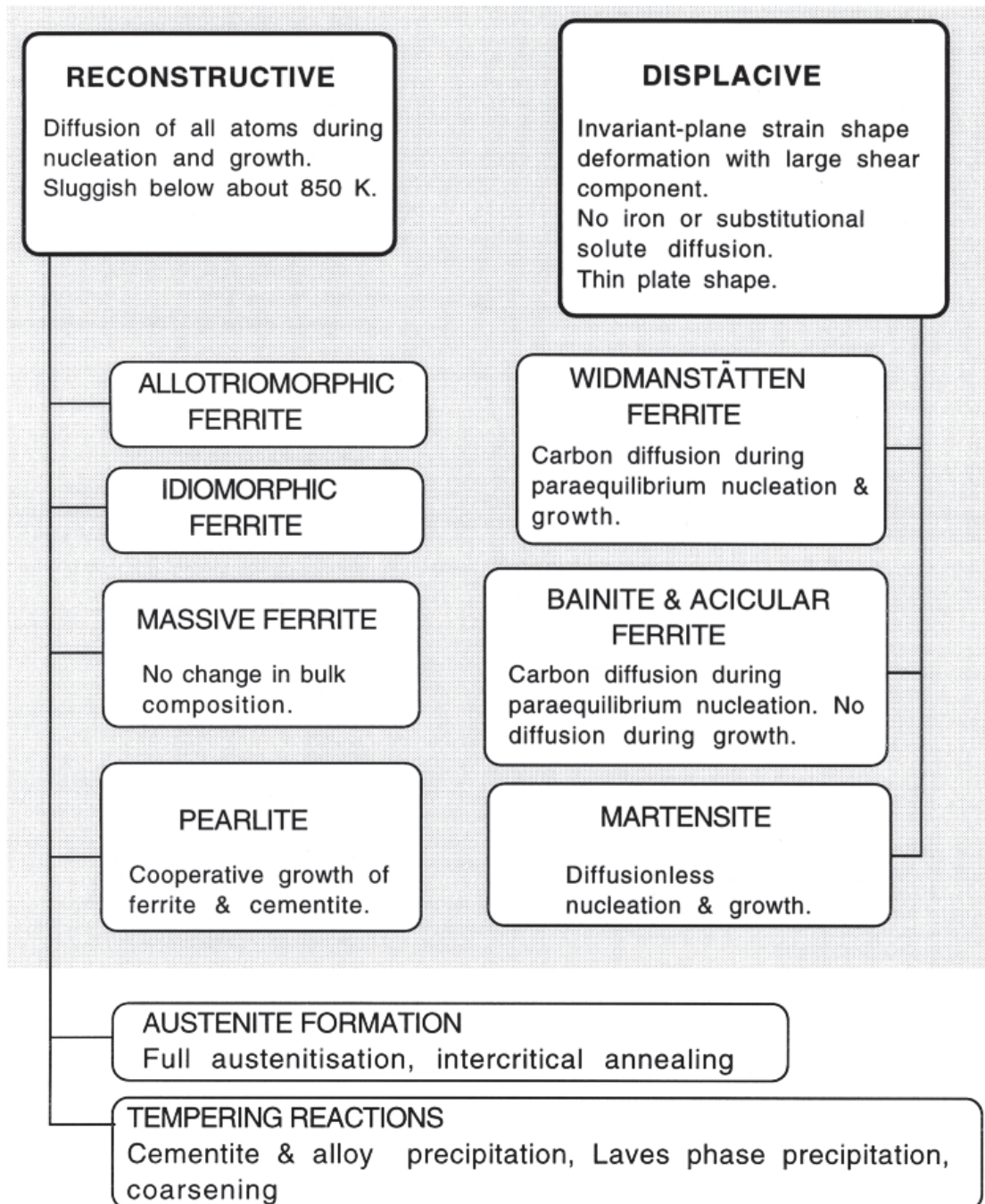


FIGURE 2.2: Structural classification after H. K. D. H. Bhadeshia et al. 1990. Note, that generally there is no strict boundary on these terms. For instance the term massive ferrite is rarely found in the literature and is normally called lath or dislocated martensite. The figure reflects the split of the scientific field into "displacivists" and "diffusionists".

of (nearly) close-packed directions. ORs of displacive martensitic transformations on the other hand, are generally not exactly parallel to each other- a minor difference, that should be considered in the determination of the transformation character.

The importance of an incoherent interface has been discussed by Massalski et al. 2006. Again several terms from mineralogy and crystallography enter the discussion. In an "allotriomorphic" transformation the forming shape does not reflect internal crystalline symmetries, neither of the product phase nor of the parent phase. "Idiomorphic" (or euhedral) means that the domain shapes of the newly forming phase reflect the symmetry of the crystal. Note that the term idiomorphic in mineralogy is actually used under conditions, where a crystal grows at a free surface and not embedded in a matrix as in a solid state transformation. In steels ferrite is often classified as being either idiomorphic or allotriomorphic, see Figure 2.2. The term "diamorphic" comes from interface theory, specifically bi-crystals and emphasises that both sides of the interface (the parent and product phase) have a strong influence. Particularly, such transformations show a definite orientation relation. A topotactic reaction is a chemical solid-state reaction such that the orientations of the product crystals are determined by the orientation of the initial crystal, see Müller 2013 (resulting in a topotactic texture).

2.1.3 Kinetic Classification

In order to emphasize the influence of kinetics we start with an unusual limiting example. Notably, for high amounts of alloying elements (not regarded as steel anymore) and complex systems (Fe + 5 elements and more) cooling rates in the order of 10^6 K/s from the melt enable to form amorphous metallic glass. Such materials are indeed being investigated, but up to now only a few applications justify their high cost. Most metallic glasses can only be produced as thin layers and the record for so called bulk or massive metallic glasses is somewhere around 7 cm in diameter. Obviously, the limiting factor here is the inertia of the heat flow. A similar problem exists for martensite. In practical terms the result is a characterisation of hardenability (see the next section). Industrially relevant maximal cooling rates, e.g. by water quenching, for real component sizes are always below 10^3 K/s (see Hasan et al. 2012). Contrary to bulk metallic glasses where high cooling rates are sought, in additive manufacturing they are a problem for carbon containing steels due to martensite embrittlement.

According to the operative nucleation kinetics Roitburd et al. 1979 classify martensitic transformations as athermal or isothermal. Especially the term athermal often is used in a misleading way in the literature. E.g. it is often found that: The transformation develops without any thermal activation. Which actually means that the transformation is not triggered by thermal fluctuations at constant temperature (i.e. is time independent at constant temperature). Also (Novikov 2002): "The transformation mostly depends on temperature (undercooling)", which more precisely means the extent of the transformation is only dependent on the degree of undercooling.

Athermal martensite is characterised by diffusionless nucleation and growth. It occurs because of the existence of an easy growth mechanism (twinning), not requiring atomic diffusion, which leads to the rapid production of a new phase and a net lowering of the free energy. In other words, athermal martensites in most cases exhibit twinned microstructures and have a steeper kinetics slope. Athermal behaviour is typical for steels containing higher amounts of austenite stabilizer (particularly carbon). The transformation starts at lower temperatures with an initial transformation burst due to an autocatalytic effect on both the nucleation rate and self-accommodation.

Generally, the term athermal is better seen as the opposite of isothermal. Isothermal means that a discernible time dependency at constant temperature exists. Particularly, it has been claimed that nucleation rates are higher, hence kinetics is nucleation controlled in the case of isothermal transformations, see Thadhani et al. 1986. Steels showing comparatively high transformation start temperatures for low constant cooling rates mainly transform massively and exhibit a similar nucleation controlled kinetics. Note, that both terms are very imprecise, since no such thing as normalized cooling rates and conditions are described in this context, making comparisons questionable.

To ultimately emphasize the variety of phenomena to consider for a classification an overview of the characteristics due to H. K. D. H. Bhadeshia et al. 1990; Christian 1965 is given in Table 2.1.

comment / product phase	α'	α_{lb}	α_{up}	α_a	α_w	α	α_i	P
Nucleation and growth reaction	✓	✓	✓	✓	✓	✓	✓	✓
Plate morphology	✓	✓	✓	✓	✓	x	x	x
IPS shape change with shear component	✓	✓	✓	✓	✓	x	x	x
Diffusionless nucleation	✓	x	x	x	x	x	x	x
Reconstructive diffusion during nucleation	x	✓	✓	✓	✓	x	x	x
Often nucleates intragranularly on defects	✓	x	x	✓	x	x	✓	x
Diffusionless growth	✓	✓	✓	✓	x	x	x	x
Reconstructive diffusion during growth	x	x	x	x	x	✓	✓	✓
Atomic correspondence (all atoms) during growth	✓	✓	✓	✓	x	x	x	x
Atomic correspondence, during growth for atoms in substitutional sites	✓	✓	✓	✓	✓	x	x	x
Bulk redistribution of X atoms during growth	x	x	x	x	x	≈	≈	≈
Local equilibrium at interface during growth	x	x	x	x	x	≈	≈	≈
Local paraequilibrium at interface during growth	x	x	x	x	✓	≈	≈	x
Diffusion of carbon during transformation	x	x	x	x	✓	✓	✓	✓
Carbon diffusion-controlled growth	x	x	x	x	✓	≈	≈	≈
Cooperative growth of ferrite and cementite	x	x	x	x	x	x	x	✓
High dislocation density	✓	✓	✓	✓	≈	x	x	x
Incomplete-reaction phenomenon	x	✓	✓	✓	x	x	x	x
Necessarily has a glissile interface	✓	✓	✓	✓	✓	x	x	x
Always has an orientation with the Bain region	✓	✓	✓	✓	✓	x	x	x
Grows across austenite grain boundaries	x	x	x	x	x	✓	✓	✓
High interface mobility at low temperatures	✓	✓	✓	✓	✓	x	x	x
Displacive transformation mechanism	✓	✓	✓	✓	✓	x	x	x
Reconstructive transformation mechanism	x	x	x	x	x	✓	✓	✓

TABLE 2.1: Characteristics of transformation product (low temperature phase) in steel. due to H. K. D. H. Bhadeshia et al. 1990; Christian 1965. consistency (✓) and inconsistency (x) of phenomenon or theory stated on the left. ≈ means that both cases have been observed. Considered products are: martensite (α'), lower bainite (α_{lb}), upper bainite (α_{up}), acicular (chaotic) ferrite (α_{ac}), Widmanstätten ferrite (α_w), allotriomorphic ferrite (α), idiomorphic ferrite (α_i), pearlite (P)

2.2 From Composition via Processing to Microstructure

In this section the common terminology for martensitic or partially martensitic steels is elaborated. An overview of the effect of alloying elements and heat treatments is given and morphological differences are worked out. Books for this topics are e.g. that by Bain et al. 1966; Totten et al. 1997; H. Bhadeshia et al. 2006; Haldar et al. 2009; Pereloma et al. 2012; Krauss 2015.

2.2.1 Alloying Elements, Metallurgical Hardening Relations and Steel Types

Steels solely alloyed with carbon, so-called plain/mild carbon steels are labelled after their carbon content as (numbers in wt%): low-: to 0.3, medium-: 0.3-0.6, high-:0.6-1 and ultra high 1.25-2.1 carbon steels. However, steels are also termed as carbon steel when no minimum content is specified or required for the most common alloying elements. Carbon is an interstitial that resides in the tetrahedral interstice of the f.c.c lattice although the octahedral interstice is larger because of elastic anisotropy $E_{111} = 276$ GPa, $E_{100} = 130$ GPa.

The f.c.c. austenite possess a maximum C-solubility of 2.1 wt% (8.8 at%) at 1147°C and 0.8 wt% or (3.6 at%) at 723°C. That of N is 2.8 wt% (10.3 at%) at 650°C and decreasing to 2.3 wt% (8.7 at%) at 590°C. Ferrite possesses a maximum C solubility of 0.022 wt % (even much lower at room temperature). Note that cementite (Fe_3C) has 6.7 wt%.

Another way to classify plain carbon steels is by stating whether the carbon content is below or above that yielding a fully eutectic microstructure (fully pearlitic steel): Hypoeutectoid-C: 0.022-0.77wt% and Hypereutectoid $C > 0.77\text{wt}\%$ steels respectively. Note that carbon generally has a negative effect on weldability, see subsection 2.2.3.

Plain/mild carbon steels are of a particular interest to the steel industry due to a good balance of properties and price. They have a relatively simple ferritic microstructure, that is especially sought for its ductility. Compared to high strength low alloy (HSLA) steels, forming them requires $\approx 30\%$ less power. They are widely produced and used. They commonly serve as example material that is compared to other materials in the course of material selection.

Conventional low- to high-strength steels include interstitial (mainly C and N) free (IF), ultra low carbon (ULC), bake hardened (BH), and HSLA steels. BH steels have a simple ferritic microstructure and are hardened by solid solution strengthening. Bake hardening occurs at $\approx 200^\circ\text{C}$, where diffusion of carbon to certain dislocation structures is possible and results in a stabilising/pinning effect (C assembles in so-called Cottrell clouds Cottrell 1964). In principle those also form at lower temperatures, however this requires significantly more time (cf. Portevin-Le Chatelier effect; dynamic strain aging - DSA / Dynamische Reckalterung in German, refers specifically to the microscopic mechanism). Special techniques are employed to keep carbon in solution through processing until it is released during baking process.

Conventional high strength steel (HSS) also include: -) Low alloy steels ($< 8\%$ alloying elements). The total alloy content can range from 2.07% up to levels just below that of stainless or inox steel (cf. French inoxidable), containing a minimum of 10.5% Cr (EN 10088-1:2005). -) High alloy steels, e.g. for extreme corrosion, heat and wear resistance.

During the 20th century the automotive industry, which is especially concerned about formability, weldability and weight reduction, triggered the development of new steel types, due to the possibility to tune the mechanical properties of each car component. New experimental methods opened the way to investigate microstructure–property relations for purposes of tailoring the microstructure to specific needs. Generally, such tailored microstructures are referred to as advanced high strength steels (AHSS). First, un- or microalloyed steels were used. AHSS offer high work- and bake hardening capabilities, allowing an increased formability and opportunities for optimization of part geometries, as opposed to HSS. Their high strain / work-hardening capacity also results in a high toughness [Energy/Volume], i.e. resistance to localized necking and fracture. This is important for a high energy absorption in the event of a crash.

Next, the effects of alloying elements on the chemical driving and dragging forces for the f.c.c \rightarrow b.c.c transformation are outlined. Depending on the direction of the transformation an element is a stabilizer if the transformation is retarded e.g. for $\gamma \rightarrow \alpha$ a γ -stabilizer delays this transformation.

Austenite / f.c.c stabilizer: Ni, Mn, C, N - γ -field is expanded, but its range of existence is cut short by solid solution (=intermetallic compound) formation.

Ferrite / b.c.c stabilizer: B, Si, Al, Be, P and strong carbide forming elements Cr, Ti, Mo, V, Ta, Zr, Nb. The effect of silicon is indirect since it retards the formation of carbides during quenching, thus preventing austenite decomposition. The main effect of carbide forming elements is to bind C, hindering its diffusion.

Al, Nb, Ti and V in small amounts (0.03 wt% to 0.10 wt%) inhibit grain growth at the austenitizing temperature since they are present as highly dispersed carbides, nitrides or carbonitrides (Al only as nitride), which only fully go into solution at or near the melting temperature. The main role of minor alloying additions is to form fine dispersions of carbonitrides that are i) controlling the austenite grain size, if out of solution during austenitization and ii) precipitate in both austenite and ferrite during cooling from the solution treatment temperature.

In metallurgy, the ability of a steel to form martensite on quenching is referred to as the hardenability. This is merely a practical term, not reflecting any physical principle. Porter et al. 2009 writes: "The primary aim of adding alloying elements to steels is to increase the hardenability, that is, to delay the time required for the decomposition into ferrite and pearlite. This allows slower cooling rates to produce fully martensitic structures". Several definitions of hardenability exist and are discussed along with typical tests e.g. in Krauss 2015, chapter 16 therein. A common test (particularly for welded materials) to study the stress accumulation of a transforming material under constrained is due to Satoh 1972. In the Satoh test a rigidly constrained tensile specimen is cooled and the stress that accumulates is monitored.

Ultimately, the distinction into five hardening mechanisms in metallurgy (shortly outlined subsequently) all boil down to the fact that dislocation motion is hindered. The actual mechanism how this happens (internal stresses, dislocation-interface, -precipitate, -substitutional element interaction will be elaborated in the course of this work, for now some general macroscopic relations are given.

1) Grain (domain)-size (Hall-Petch:)

$$R^{hp} = k_y / \sqrt{c_1} \quad (2.1)$$

where k_y is a constant and c_1 is a microstructure distance, e.g. proportional to the average high angle interface boundary distance (commonly the grain size, also the martensite packet

size, see section 1.1). Note that the dimension of k_y is $MPam^{-1/2}$, i.e. it can be seen as a fracture toughness.

2) Work hardening (Taylor hardening)

$$\sigma = \sigma_0 + c_1 \mu b \sqrt{\rho} \quad (2.2)$$

where μ is the shear modulus, b is the length of the Burgers vector, ρ is the dislocation density, σ_0 is a dislocation free yield stress and c_1 (often denoted α) is a constant, $\approx 0.2-0.35$ dependent on the material (variations are much below the accuracy of its experimental determination as pointed out by U. Kocks et al. 2003). Note that, due to its unit of length ($\sqrt{m/m^3}$), $\sqrt{\rho}$ may be considered as the characteristic obstacle spacing in the glide plane or in a more general view the mean spacing between dislocations.

3) Precipitation hardening: It must be differentiated between Dislocation bowing around precipitates or cutting. Bowing:

$$\tau^{\text{orowan}} = c_1 \mu b / L \quad (2.3)$$

τ^{orowan} (glide resistance or Orowan by-pass stress) describes the bowing of dislocations around particles, with $c_1 \approx \pi r$, L is the spacing between pinning points and can be related to the grain size in the case of undeformed polycrystalline metals or the separation of HAGBs in the case of heavily deformed metals (or packet boundaries in low carbon steels) or LAGBs. Note that above a critical threshold depending on the particles coherency the dislocation cuts the particle. The strength decreases again and is given by: $\pi r \gamma / bl$ with γ the surface energy. A good work for complex 9-12 Cr steels (similar to the one mainly studied in this thesis) is by Holzer 2010.

4) solid solution strengthening and 5) transformation hardening. After these steels are often classified as:

1. Solid-solution-strengthened steels
2. High strength low alloy (HSLA) steels: Hardening by precipitation (e.g. fine dispersion of alloy carbides) or grain refinement. Most HSLA steels have directionally sensitive properties. An industrially relevant grain size is in the range of $8 - 12 \mu m$.

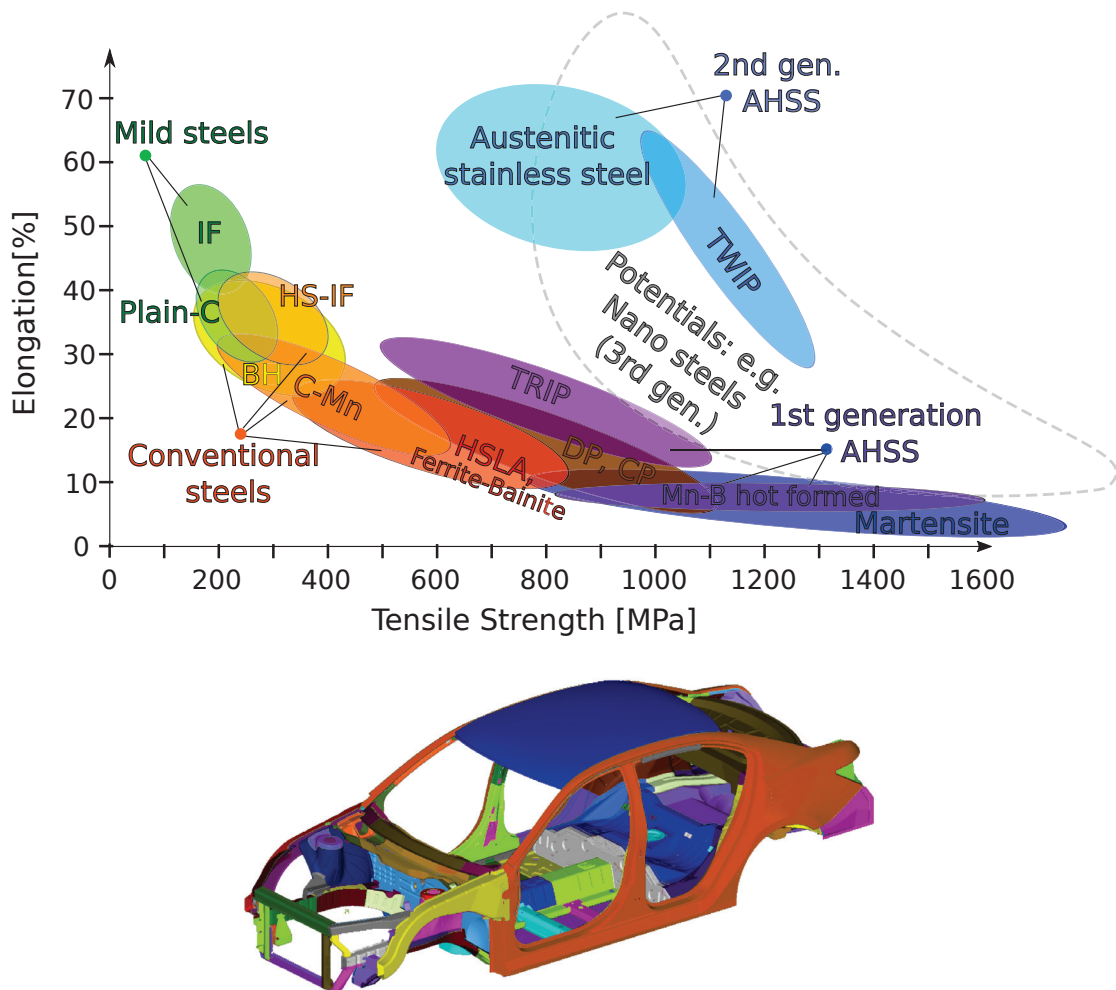


FIGURE 2.3: Above: Strength-ductility trade-off in steels. Current research involves "How to get off the banana?" when referred to variety of steels. Below, typical vehicle body recoloured from Nanosteel 2017. The colouring of the individual parts corresponds to the diagram. Nowadays, illustrations of properties like the above one can easily be plotted with a larger variety of steels from any material selection software, such as CES (Cambridge Engineering Selector) see EduPack 2007 as has been done e.g. by S. Kalidindi 2015.

Ultra fine grained (UFG) microstructures can be obtained by (advanced) thermo-mechanical processing ((A)TMP) or severe plastic deformation (SPD) methods.

3. Transformation-hardened steels: Steels with a microstructure including martensite, bainite and retained austenite, i.e. untransformed austenite stabilized by carbon and/or high internal compressive stresses \rightarrow incomplete reaction phenomenon). AHSS include: dual-phase (ferrite and martensite) steels, transformation induced plasticity (TRIP) steels (see subsection 2.2.4), complex-phase steels and martensitic steels.

TRIP steels use higher quantities of carbon than Dual Phase steels to obtain a sufficient carbon content for stabilizing the retained austenite phase to below ambient temperature. There are several varieties of TRIP steels. Large quantities of austenite-stabilizing elements, lead to fully austenitic steels transforming to martensite when stressed. When the austenite is a minor phase in the microstructure retaining its potential to transform martensitic during straining, the steel is also said to be TRIP assisted (usually low alloy steels).

2.2.2 Heat- and/or Mechanical Treatments and Transformation Diagrams (Kinetic Experiments)

In this section, first some specifics of time temperature transformation (TTT) and continuous cooling transformation (CCT) diagrams are introduced since they are the most common way to experimentally investigate kinetic features of phase transformations in steels. First, process routes of steels where carbon plays a crucial role in some way are covered. Then, steels with 0.2 wt% C and less, forming dislocated lath martensite mainly dealt with in this thesis, are specifically treated. The mechanical treatments of these steels will be discussed in the next section.

Transformation diagrams provide information about non-equilibrium kinetic features including: the nature of transformation, i.e. reconstructive or displacive isothermal, athermal or mixed kinetic characteristics, stability of phases (start and finishing temperatures) under isothermal or continuous transformation conditions, transformation rate.

Microstructural evolution comprises a variety of phenomena (occurring partly simultaneously) that influence each other. These phenomena are: recovery, recrystallization, grain-growth, transformation, precipitation, texture (preferred orientation) evolution, fibrous texture (mechanical fibering) evolution etc. Most importantly, all this processes have their own kinetics. A mere temperature dependence of transformation kinetics is mainly studied either by quenching to a particular temperature followed by isothermal transformation (TTT) or utilising a constant cooling (rate) until the transformation is finished (CCT).

Note, that both TTT and CCT diagrams are strongly dependent on the specific chemical composition as well as the initial state of the material (texture, grain size, microstructure

heterogeneity etc.). Heterogeneous austenite leads to an earlier start as well as a later finish for both the martensitic and bainitic transformations.

The oldest but probably still most popular technique in industry to determine TTT is the salt bath techniques combined with metallography and hardness measurements. CCT diagrams are often used when heat treating steel to test different temperature rates (see e.g. Z. Zhang et al. 1995). CCT diagrams are often more convenient than TTT diagrams just because it is easier to cool materials at a certain rate than to quickly cool down to a certain temperature followed by holding it constant. Methods to determine transformation diagrams comprise: dilatometry, measurements of electrical resistivity or magnetic permeability, in-situ diffraction techniques utilising X-rays or neutrons, acoustic emission, thermal measurement techniques, density measurement techniques and thermodynamic predictions. Further experimental aspects are given in chapter 5.

Other cases of time dependent diagrams include cases where transformation occurs under an applied load. If the cooling stage is preceded by deformation, the phase transformation diagram may be called a DCCT diagram. There are time temperature embrittlement (TTE) diagrams dealing with temper embrittlement, time temperature-precipitation (TTP) diagrams (mainly isothermal) showing conditions under which various nitrides, carbides or intermetallic phases precipitate in a wide variety of steels, time-temperature-sensitization (TTS) diagrams showing intergranular attacks after sensitization treatments (especially important for stainless steels) etc.

As detailed in subsection 2.2.3 the carbon content strongly influences the microstructure and the microstructure in turn determines the degree of carbon partitioning between martensite and austenite as e.g. investigated by Toji et al. 2014. Hardness changes during tempering are also very dependent on carbon content. Figure 2.4 shows three common processing routes for steels entailing fully or partially displacive transformations, where carbon plays a crucial role. These are discussed subsequently.

To form martensite with these steels the cooling rate must be high enough to inhibit diffusion and the undercooling must be large enough to trigger an athermal, displacive transformation. For some materials that do not enable martensite by water quenching to room temperature, it can nevertheless be obtained by further cooling e.g. with liquid

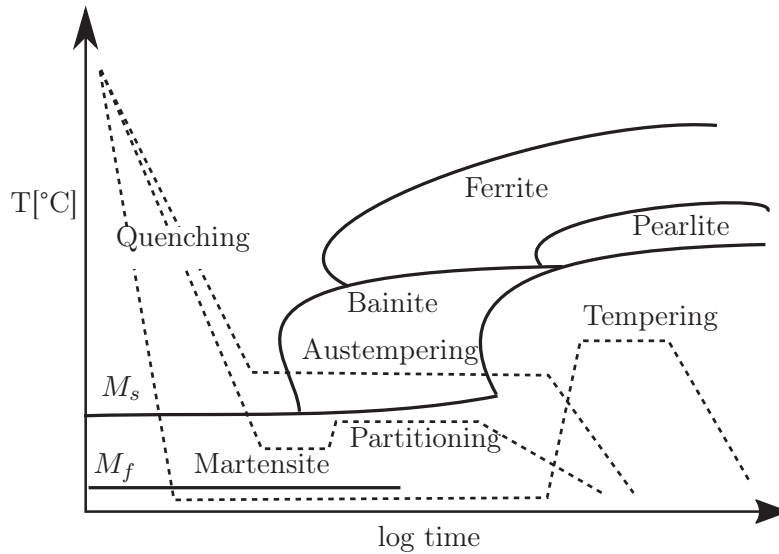


FIGURE 2.4: Three common processing routes for steels with $\approx 0.2\text{wt}\%C$ content, entailing displacive or partially displacive transformations. All processes start with quenching (Q) to a certain temperature. If quenched under M_f , the fully martensitic part is tempered afterwards (Q & T). If quenched until slightly above M_s and transformed isothermally in the bainite region this is called "austempering" (Q & A). Quenching between M_s and M_f , followed by raising the temperature slightly below M_s (partitioning) to enrich the remaining austenite with carbon has been proposed by Speer et al. 2003; L. Wang et al. 2013 (Q & P)

hydrogen. The martensite remains stable at room temperature due to the irreversibility of the transformation.

Since this kind of martensite is very hard and brittle a subsequent heat treatment (tempering) is necessary. The high hardness is caused by the rapid distortion of the crystal structure that leads to an extreme solid solution strengthening of substitutional as well as interstitial atoms (solute trapping or just trapping), accompanied by very high internal stresses. Thermodynamical trapping means that a component is transferred across a moving interface against its chemical driving force.

Often carbide particles can be observed in the martensite forming first. This martensite shows the tendency of tempering during the remainder of the quench due to high residual stresses after transformation, giving rise to an increased diffusivity of interstitials. Note, that all tempering processes occurring during and automatically after the quenching are denoted as autotempering.

On reheating the as-quenched martensite H. Bhadeshia et al. 2006 identify four different tempering effects in overlapping temperature intervals i) precipitation of ϵ -iron carbide

$\leq 250^\circ\text{C}$

ii) decomposition of retained austenite $200\text{--}300^\circ\text{C}$

iii) replacement of ε -iron carbide by cementite $200\text{--}350^\circ\text{C}$; martensite loses tetragonality

iv) $\geq 350^\circ\text{C}$ coarsening of cementite; recrystallization of ferrite.

Heating to even higher temperatures can lead to a reverse transformation, i.e. so-called reversed (or reverted) austenite. This austenite is chemically and morphologically different from retained austenite because more stabilizing elements are dissolved. Leem et al. 2001 found for a Fe-13Cr-7Ni-3Si steel that with increasing heating rate A_s and A_f increased but stabilized due to a change from diffusional to displacive character of the reverse transformation. The stable austenite film thickness increases slightly with alloying content. Speaking of reverted austenite, a "thinner is less stable" relation has been reported by M.-M. Wang et al. 2014 for nanometer broad retained films of austenite. Recent TEM investigations by D. Kim et al. 2012 report retained austenite layers with thicknesses around 20 nm in quenched martensite. Secondary hardening (i.e. the formation of alloy carbides that are even more stable than cementite) of all alloy steels does not start until reaching a temperature range of $500\text{--}600^\circ\text{C}$ (depending on the diffusivity of the alloying element), because below this temperature diffusion is insufficient to allow alloy carbides to nucleate.

The second treatment depicted in Figure 2.4 is the Q&P process suggested by Speer et al. 2003. It creates steel microstructures with retained austenite by promoting thicker austenitic layers. The process involves quenching austenite below the martensite-start temperature, followed by a partitioning treatment to enrich the remaining austenite with carbon, thereby stabilizing it at room temperature. However, upon mechanical loading the retained austenite may transform. Hence this treatment is among others used to obtain TRIP steels (see subsection 2.2.4). Another, typical processing route used to produce cold-rolled TRIP steels is continuous annealing at galvanizing lines.

The third processing route in Figure 2.4, where austenite is quenched into a salt bath followed by an isothermal transformation to bainite is called austempering.

For some steels containing less than ≈ 0.2 wt% C (strongly depending on other alloying elements) high enough cooling rates to produce fully martensitic structures practically cannot be reached. However, for specific compositions and upon plastic deformation, for other steels (like the steel treated within this thesis, see chapter 5), even if the carbon concentration is almost zero, a relatively fast transformation compared to purely athermal

martensites, accompanied by a high degree of plastic deformation (relaxed state) can already be induced upon imposing (very) modest cooling rates of less than 1 K/s. These high rates are why the transformation is regarded martensitic, although it is not displacive (massive ferrite). A characteristic CCT diagram of such a steel is depicted in Figure 2.5. These steels form a characteristic lath microstructure specifically treated in subsection 2.2.3, section 1.1. Interestingly, during fast quenching of such steels with $C \leq 0.2$ wt%, the majority (up to 90%) of the carbon segregates to dislocations and lath boundaries, but with slower quenching some precipitation of cementite occurs.

High-resolution TEM studies of laths and their boundaries revealed how they might be used to tailor the microstructure of the martensite blocks to control properties (grain/lath boundary engineering see e.g. Raabe et al. 2013). In particular, re-heating the steel triggers the precipitation of austenite phase along the lath boundaries, which lays the ground to develop three important processes as described by Morris 2016:

- (1) A treatment at a low temperature within the two-phase region (intercritical tempering) where thermally stable precipitates of austenite form along the lath boundaries. This austenite breaks up the alignment of laths within the block and significantly improves low-temperature toughness. It is widely used to process steels for low-temperature use.
- (2) A treatment at a higher temperature within the two-phase region (intercritical annealing) produces interlath austenite that re-transforms on cooling. The result is “dual-phase” steel, with blocks in which laths of fresh martensite alternate with laths of well-tempered martensite. These steels have tailored work-hardening characteristics that produce very good tensile elongation. They are widely used in the automotive industry.
- (3) A treatment that uses an intercritical anneal followed by reversion to the austenite phase and subsequent quenching (the “QLQ” treatment) produces a dislocated martensite structure in which adjacent laths are different Kurdjumov-Sachs (KS) orientation variants (see section 3.4) of the martensite, leading to exceptional combinations of strength and toughness.

A classical example where the heat treatment is optimized w.r.t. the steel’s hardening behaviour are maraging steels (martensitic + aging). These steels possess a superior strength and toughness without a significant drawback in ductility. They are nearly free of carbon and possess a high percentage of Ni (12-25 wt%) or Mn (9-15 wt%) mainly stabilizing the austenite and some secondary alloying elements that give this steel its strength by forming

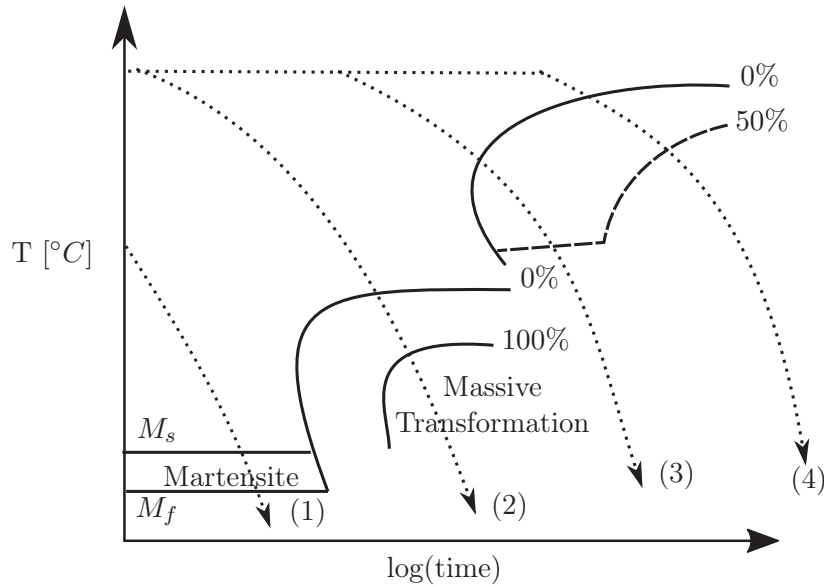


FIGURE 2.5: Typical CCT of a steel with $< 0.2C$ and alloyed such that highly dislocated lath martensite occurs. (1)-(4) different cooling rates \dot{T} . (1) fully martensitic microstructure, (2) massive transformation, (3) Widmannstätten ferrite, (4) Slow cooling leads to precipitation of equiaxed ferritic grains.

very fine intermetallic precipitates like Ni_3Mo , Ni_3Ti , Laves phase (close packed $MeMe_2$). While for the higher contents of austenite stabilizers, the austenite remains stable during processing, for the lower contents quenching only provides enough driving force to produce martensite.

Manganese steels with $\approx 13\%$ Mn and 0.8 to 1.25 % C are called Hadfield steels (also Mangalloys). Even higher Mn concentrations enable stable austenite at room temperature. Due to the temperature dependence of the deformation mode twinning is now energetically favourable, leading to so-called TWIP (twinning induced plasticity) steels. In fact, the manganese content is so high that TWIP steel may not even be considered as steel any more, but rather as an advanced alloy.

There are many potential benefits offered by appropriate thermo-mechanical processing (TMP), particularly if the same properties can be achieved by optimizing the microstructure without the addition of alloying elements, especially rare earth elements and minor metals, cf. Lin et al. 2012. For instance segregations (inclusions) introduced during casting are refined and distributed more uniformly. Commonly, the nomenclature denoting deformation treatments use a prefix indicating the state of the microstructure (hence also

whether the transformation has already taken place). The prefix *mar-* indicates a fully martensitic state e.g. *maraging*, *marstraining* or *marforming*, and treatments of austenite prior to transformation have the prefix *aus-*, e.g. *ausforming*. TMP of steel may be distinguished depending on its occurrence before, during or after transformation.

After (*marforming*): The martensite is cold worked prior to tempering to induce a dislocation substructure that a.o. improves the distribution of temper carbides, cf. Lin et al. 2012.

During (*advanced or controlled TMP*): E.g. controlled rolling or isoforming if the temperature is held constant). Deformation below the recrystallisation region divides the grains into several blocks separated by deformation bands caused by a plastic instability (locally only a limited number of slip systems is active). In case the finish rolling temperature is at or just above the recrystallisation temperature T_r , the quenching starts from a fine-grained, equi-axed austenite and the process is called recrystallization controlled, whereas if the finish rolling temperature is below T_r , the quenching is done from deformed austenite and the process is called “controlled rolling” (CR).

Before (*ausforming*): Plastically deforming a steel, while it is in the austenite temperature range refines the microstructure through dynamic recrystallisation (deformation in the recrystallisation region). At higher C contents and temperatures spheroidal carbides form within a ferrite matrix. Lin et al. 2012 point out that ausforming alone is confined to stainless steels. For TRIP steels, *aus-* and *marforming* are commonly combined. The high strength of TRIP steels is thus due to the combined effect of grain boundary strengthening, solid solution strengthening and dislocation hardening.

2.2.3 Dependencies of Transformation Modes and Morphologic-Crystallographic Differences of Martensites in Steels

Keeping in mind all the dependencies of the transformation (i.e. composition as well as mechanical and thermal processing history, including the fact that everything is rate dependent), it is actually not suitable to make predictions on morphological characteristics based on a reduced set of information. This should always be kept in mind, as explained in the following section as well as all other literature.

Ferrous martensites may be roughly divided into three morphological types: lath-, lens- and thin-plate martensite see Figure 2.6. Austenite stabilizing elements (mainly C see

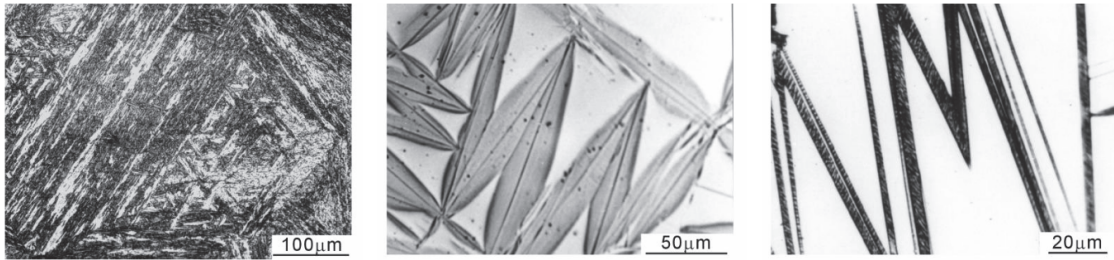


FIGURE 2.6: The three different morphologies of ferrous martensites. Left: highly dislocated laths forming blocks and packets (Fe-9Ni-0.15C), Middle: Lenticular martensite (Fe-29Ni-0.26C), Right: Thin-plate, fully internally twinned morphology (Fe-31Ni-0.23C). (Images from Maki 1999; Maki 2012)

subsection 2.2.1) dictate M_s and whether the deformation mechanism is slip or twinning. Note that a higher content of austenite stabilizing elements favours twinning. Note also that slip and twinning is temperature dependent, where twinning is favoured at lower temperatures, see Figure 2.7. Generally, the more twins appear, the lower is the dislocation density. Furthermore, the following trends can be observed:

1. temperature: dislocation motion is thermally activated, thus low temperature promotes twinning
2. strain rate: plasticity is strain rate sensitive, hence high strain rates favour twinning, fully twinned structures are observed in explosive tests.
3. stacking fault energy: lowering stacking fault energy makes twinning easier (a stacking fault is the smallest possible twin, see section 3.3)
4. grain size: a lower grain size makes twinning more difficult (however it may still appear at nano grain size if the material generally has a high tendency to form twins).
5. most lath martensites are b.c.c. and most plate ones are b.c.t., however this is no general rule. The only difference between tetragonal and cubic martensite is that in the former the $\{011\}_\gamma$ mirror planes are transformed into $\{011\}_\alpha$ and in the later into $\{112\}_\alpha$.

If investigating possible twinning modes is of interest, the material should be deformed at a very low temperature and very high strain rate. Combined plastic slip and twinning has

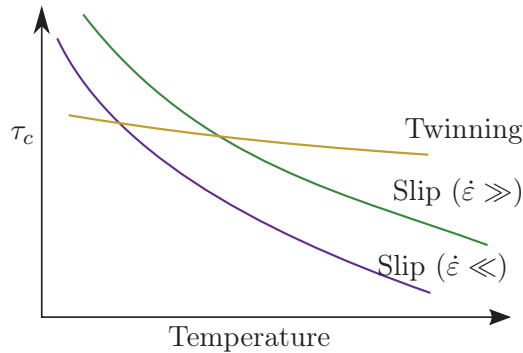


FIGURE 2.7: Schematic dependency of critical stress τ_c for deformation modes (slip and twinning) enabling the phase transformation.

been argued to be active in high temperature shape-memory alloys, cf. Karaman et al. 2000.

Krauss et al. 1971 introduced the terminology 'lath' and 'plate' martensite based on light microscopy studies. Expressed in terms of ellipsoids this corresponds to prolate and oblate ellipsoids (note however that they are not space-filling). Denoting the dimensions of martensite domains as a , b and c , experiments as well as theoretical considerations suggest that characteristic dimensions for individual dislocated laths as well as bundles of them are $a < b \ll c$ (see Figure 3.10) and $a \ll b \approx c$ for twinned plates.

Wayman 1972 described variants forming long stretched, but narrow laths in low carbon steels ($< 0.2-0.3\% \text{C}$) as winglets of an airplane. The long morphology of the lath suggests that beside the close-packed plane also the close-packed direction is preserved. The laths or plates are heavily dislocated to an extent that individual dislocations are very difficult to observe in thin-foil electron micrographs. The dislocation density in dislocated lath martensite can be as high as $10^{12} \text{ cm}^{-2} = 10^{16} \text{ m}^{-2}$. With rising carbon content P. Zhang et al. 2016 already reported the first appearance of fine twins (about 5–10 nm) around about 0.2 wt% C (at regions of locally higher carbon) for a 0.2C-0.85Mn-1.08Cr steel as observed in the TEM.

Between ≈ 0.4 and 0.8 wt% C (depending on other alloying elements etc.) both lens/lenticular martensite containing both internal twins and dislocations as well as lath martensite coexist, i.e. the transition from a highly dislocated to a twinned microstructure occurs very gradual. A distinct feature in the case of plate martensite is the midrib, which is reported to be the first forming unit consisting of many transformation twins Shibata et al. 2008;

Shibata et al. 2009. The midrib is more heavily attacked by etchants, owing to its apparent higher state of distortion compared to the rest of the plate.

The opposite of "perfectly" dislocated lath martensite, is thin-plate martensite obtained for high amounts of austenite stabilizing elements or $C \approx > 1\%$. Plate-like martensites accommodate in non-parallel, zig-zag ("butterfly") or triangular arrangements due to the higher stresses produced and generally have lower M_s temperatures than dislocated lath martensites.

In the case of plate martensite the size of the unit is determined by the free mean transformation path between strong obstacles (grain boundaries, precipitates, other plates) to grow. Lath martensites do not partition grains as do plates, but instead, typically form a hierarchical structure of bi-variant blocks that stack to packets, see section 1.1.

Since lath martensite already transforms at higher temperatures, it offers the advantage of a better formability/ easier thermo-mechanical processing. This point is also interesting for Ti-base alloys forming a lath martensite microstructure (see D. Banerjee et al. 2013; S. Banerjee et al. 2010; Mayer et al. 2016).

Historically, lath martensites have been studied first by TEM revealing their incoherent interfaces. However, TEM observation of steel has some limitations. The b.c.c phase is ferromagnetic at room temperature, hence magnetic interference between the ferromagnetic specimen and the objective lens magnetic field occurs. Using TEM to observe a thin-foil steel sample therefore results in image distortion, deflection of the electron beam, and temporary bending of the sample due to the magnetism of the ferrous iron phase (Hata et al. 2015). The magnetic field can be reduced by a thinner foil, however, then only very limited morphological features can be observed.

R. Davies et al. 1970 pointed out that in the Fe-Ni System, magnetic properties also have a profound influence on the formation and morphology of martensite. They found that ferromagnetic austenite is a necessary but not sufficient condition for lenticular martensite. If Ni is the only alloying element, lenticular martensite only appears above 30 wt% otherwise the hierarchic / block structure persists. Table 2.2 gives an overview of microstructural features of martensite in steel.

exemplary steel composition	habit-plane/OR	defect structure
Fe-($< 0.3 - 0.4$ C), low γ^{sf}	$\{111\}_{\gamma}$ (ε -mart), $\{\bar{1}\bar{1}2\}_{\gamma}$, $\{557\}_{\gamma}$ - KS - needles/laths	high dislocation density (high plastic accommodation during growth) in both γ and α' , laths of 2 variants with small misorientation (nearly parallel)
Fe-0.4-0.6 C	mixture of habit planes of laths and plates	Blocks are not very parallel, laths of single variants within Blocks Lambert-Perlade et al. 2004; Furuhashi et al. 2006
Fe-(0.5 – 1.4 C) Fe-(2.8-8 Cr)-(1.1-1.5 C)	$\{225\}_{\gamma}$ Baur et al. 2017 lenticular plates, pronounced primary and secondary size difference	mixed fine $\{112\}$ twins in the middle and dislocations at the interface of the lens (twinned α' and slip in γ)
Fe-1.78 C Greninger et al. 1949	$\{259\}_{\gamma}$ plate	mixed fine twins near the invariant plane and more dislocations near the interface of the plate (elastic/plastic)
Fe-(27 – 34 Ni)-(0.4 – 1.2C)	$\{259\}_{\gamma}$ plate - NW	mainly twinned
C and or Ni steels with a Volume ratio 1.04; Fe-(7-10% Al)-2% C	$\{3\ 10\ 15\}_{\gamma}$ thin plate - NW Wechsler et al. 1953	twinned laminate of fine (112) extending through the whole cross-section of the plate

TABLE 2.2: Overview of typical habit planes, orientation relations and defect structures in steels (c.f Nishiyama et al. 1978; Porter et al. 2009). Note, that actually for a lath no definite plane is defined. From top to bottom: Dislocation density and M_s tendentially decrease. γ^{sf} ...stacking fault energy (SFE). Orientation relations (ORs) such as Kurdjumov-Sachs (KS) and Nishiyama-Wassermann (NW) are listed in section 3.4

As for slip and twinning some morphological transition dependencies are described:

For higher SFEs the tendential evolution of habit planes is $\{557\}_{\gamma} \rightarrow \{225\}_{\gamma} \rightarrow \{259\}_{\gamma}$ or $\{3\ 10\ 15\}_{\gamma}$ with decreasing the transformation temperature and increasing the yield strength of austenite. This evolution is depicted in Figure 2.8 in an inverse pole figure

(cf. subsection 5.5.1). R. G. Davies et al. 1971 report that if the yield strength of the austenite is > 207 MPa the habit plane is $\{259\}_\gamma$ and if it is < 207 MPa it is either $\{111\}_\gamma$ (see e.g. P. Kelly et al. 1990) or $\{225\}_\gamma$ depending on the plastic resistance of the b.c.c phase. Laverroux et al. 1974 demonstrated a lath-to-plate morphological transition via precipitation hardening (with Ta) in Fe-Ni and Fe-Ni-Co alloys even though M_s was increasing (also see Talonen 2007).

There is a connection between the morphology and the isothermal nucleation rate implying that the morphology is determined very early in the martensite formation process, i.e. by thermally activated interfacial motion.

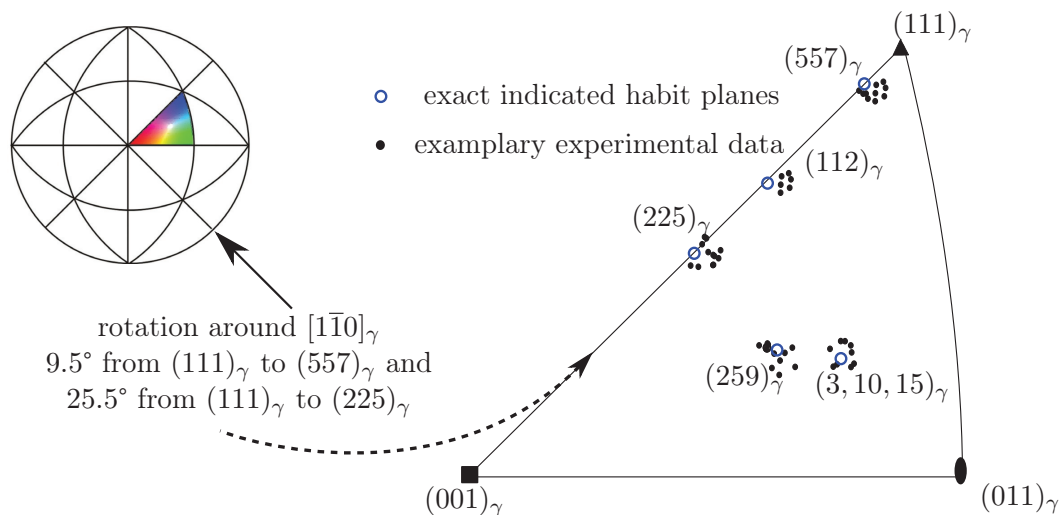


FIGURE 2.8: Typical habit planes illustrated in the usual stereographic projection of the fundamental zone (equivalent by point group symmetry) highlighted in colour of the cubic system. Interestingly, habit planes of lath martensite are commonly found to be of the form (xyx)

2.2.4 Mutual Couplings Between Phase Transformation and Plasticity

To sum up it is emphasised that TRIP is an intricate process that requires all strain components e.g. also thermal strains to be correctly modelled.

Two factors should be kept in mind in the following discussion:

First, in general the interaction between the plastic deformation of austenite and the martensitic transformation is twofold (see e.g. Kouznetsova et al. 2007; Cherkaoui et al. 1998). On the one hand, the plastic deformation of austenite is known to promote the transformation by creation of additional nucleation sites for the transformation, on the other hand the work hardening effect leads to the mechanical stabilization of austenite,

thus retarding the transformation.

Second, applied stresses are significant due to both, a general free energy (strain energy) dependency (cf. tension-compression asymmetry) as well as the role of dislocations in both nucleation and growth mechanisms.

Subsequently, some terminology is defined and discussed since some terms are used ambiguously in the literature. The ambiguity is due to a phenomenological macroscopic view. In the author's opinion it can be avoided if the problem is viewed at the microscale.

The first term is transformation induced plasticity or shortly TRIP. Some authors misleadingly use the term plasticity for the total inelastic deformation (trip-strain $\underline{\epsilon}^{\text{trip}}$), i.e. transformation and plastic deformation summed up as inelastic deformation or transformation plasticity. This may be due to a macroscopic, characterisation of the experimental results with a kind of metallurgical variable ($\underline{\epsilon}^{\text{trip}}$) incorporating the concept of plastic accommodation of the transformation strain in the framework of classical phenomenological plasticity. This concept was first adopted by Greenwood et al. 1965 and later by J. B. Leblond et al. 1989 including the martensitic volume fraction and stress deviator effects. The assumptions are that the trip strain rate $\dot{\underline{\epsilon}}^{\text{trip}}$ i) follows the stress deviator and ii) is solely governed by the rate of transformation $\dot{\xi}$, which is in turn iii) merely controlled only by a heuristic function $\Phi(\xi)$ (often referred to as "saturation function")

$$\dot{\underline{\epsilon}}^{\text{trip}} = \frac{3}{2} \left(\underline{s} - \underline{X} \right) \kappa \frac{d\Phi}{d\xi} \dot{\xi} \quad (2.4)$$

Sometimes also the TRIP constant / Greenwood-Johnson coefficient κ is assumed to be a function of the volumetric strain. In general, such a description has limited predictive capabilities.

Others, however, refer merely to the irreversible plastic part, stating that the transformation part $\underline{\epsilon}^{\text{tr}}$ is fully reversible upon reverse transformation as in SMAs. If the transformation is thermally cycled, these authors call the TRIP strain the magnitude of irreversible plastic deformation after several cycles, when the loop has stabilised in the sense that the increase of this additional irreversible plastic deformation stays constant (the initial deformation rate may be much higher). In the experimental studies this thesis is built on (see Nagayama et al. 2000; Nagayama et al. 2001; Nagayama et al. 2002; Tanaka et al.

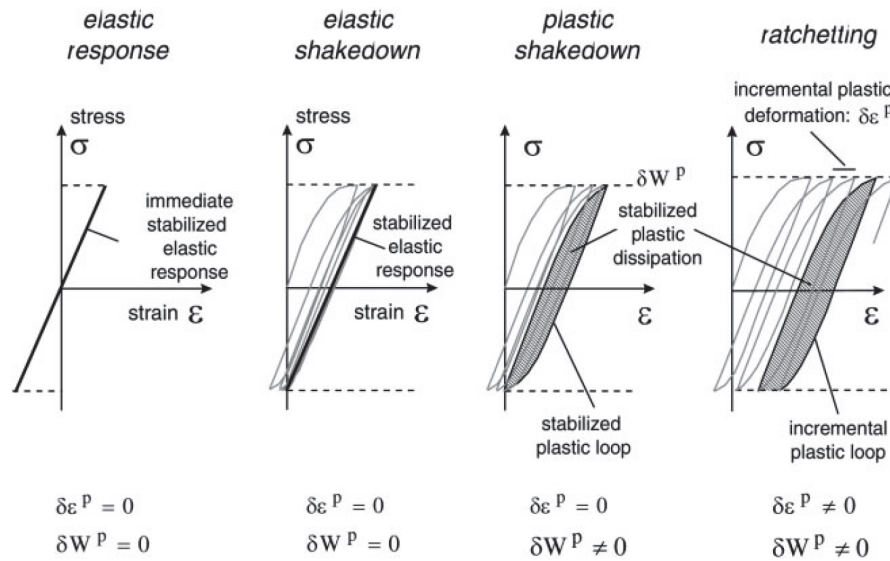


FIGURE 2.9: Asymptotic behaviours under cyclic loading after Fouvry et al. 2001. Elastic shakedown: An elastic behaviour, after possibly an initial plastic strain. Plastic shakedown: An extended hysteresis loop, with a periodic plastic loading between two fixed values. Ratchetting: Accumulation of inelastic deformation, eventually leading to failure.

2003) however, this is referred to as ratchetting strain ϵ^{rat} following classical ratchetting appearing under cycling (plastic) loading conditions.

Remarkably, possible behaviours of thermal transformation cycling are similar to imposed elastic or plastic deformation cycling, as depicted in Figure 2.9. Particularly, it must be clear what is meant by stabilization of the loop, i.e. whether elastic or plastic shakedown or ratchetting occurs. For instance for SMAs it may be found that: ...the total deformation loop after several cycles stabilizes to a definite cycle that is not expanding or moving any more in stress space.

Other terms commonly occurring in conjunction with the plastic-transformation coupling are the Magee effect (after Magee 1966) as well as the Greenwood-Johnson effect (after Greenwood et al. 1965).

The Magee effect (or variant orientation effect, note that Magee investigated a Fe-31Ni lenticular martensite steel) corresponds to a preferred orientation in the transformation strain due to variant selection (for the term variant see subsection 3.5.2 and variant selection ??). This selection is due to the local stress state (which generally is a superposition of the internal as well as applied stress) as well as specific variant nuclei (specific shear bands). In terms of the structural stretch tensor (see subsection 3.5.2) the whole deviatoric and in terms of plastic slip (as an integral part of the transformation) the shear components

are particularly important. When martensite is formed, deformation incompatibilities, e.g. near grain boundaries, are dominant in determining the local stress state.

The Greenwood Johnson effect (plastic accommodation effect) means that plasticity occurs in the presence of an external load, even if this load is well below the yield strength of the material. Again, this is due to the generation of internal stresses (J. Leblond 1989 calls them micro stresses) due to the volume change between martensite and austenite that trigger plastic flow in the weakest phase. Since neither effect makes any reference to any particular mechanism in terms of nucleation, dislocations or variant accommodation they are used quite general which may lead, as pointed out, to misunderstandings.

Apparently, there is a controversy on the proportional contributions due to the Magee (plastic strain) and Greenwood Johnson (transformation strain) effect, which in the authors opinion remains insufficiently investigated to the present day. Obviously, it is experimentally very difficult to impossible to study of the variations of plasticity associated with the amount of martensite formed under various loading paths. For this purpose, modelling depicts a vital tool in predicting this values.

Next the terms "stress-assisted" and "strain-induced" martensite transformation introduced by G. B. Olson et al. 1986 are widely used. They are illustrated in Figure 2.10, where the temperature dependence of the critical stress causing a martensitic transformation is schematically represented.

A transformation is stress-assisted if transformation is triggered upon loading (below the yield strength) between M_s and M_s^σ . In steels M_s increases with both tensile and compressive loading. In a transformation with positive volumetric change generally a macroscopic tensile loading has a slightly stronger effect. However, in general it is the anisotropy of the structural stretch tensor that locally determines what stress state is more favourable.

Strain induced martensite (or transformation induced by plastic deformation - J. B. Leblond et al. 1989, or plastic strain induced transformation - Cherkaoui et al. 2000b) is associated with the creation of nucleation sites for martensite due to the heterogeneity of plastic strain (dislocation pile-ups, dislocation dipoles, intersection of slip bands etc. often collectively termed shear-bands). First the plastic deformation of the austenite aids the transformation by the formation of energetically favourable nucleation sites for the martensite as e.g. described by M. Cohen 1972; G. Olson et al. 1972 and second, the internal stress due to

the dislocations pile-ups produces an additional mechanical driving force (cf. backstress).

Macroscopically, the concept of backstress has proven to be useful for the description of the unloading behaviour of TRIP steels F. D. Fischer et al. 2000; Fischlschweiger et al. 2012. However, such models heavily depend on inverse parameter fitting do not possess much predictive capabilities outside their calibration range.

The upper temperature limit for the strain-induced transformation is denoted as M_d . At this temperature even the highest plastic deformation does not produce a suitable state of enhanced nucleation and sufficient internal stress to trigger any transformation.

From a macroscopic view the strain induced transformation is also referred to as dynamic softening. Note, that a awareness of the overall mechanisms (particularly their time and length scales) leading to such a behavior is required. Particularly, its an elastic (shear) instability that facilitates local nucleation, see subsection 6.7.1 causing a strain evolution that manifests itself in a macroscopic softening. However, the transformed state is always more "hardened" (b.c.c. with no densest packed planes, TRIP effect leading to more dislocations, cf. Taylor hardening). Especially in chromium-nickel steels the transformation

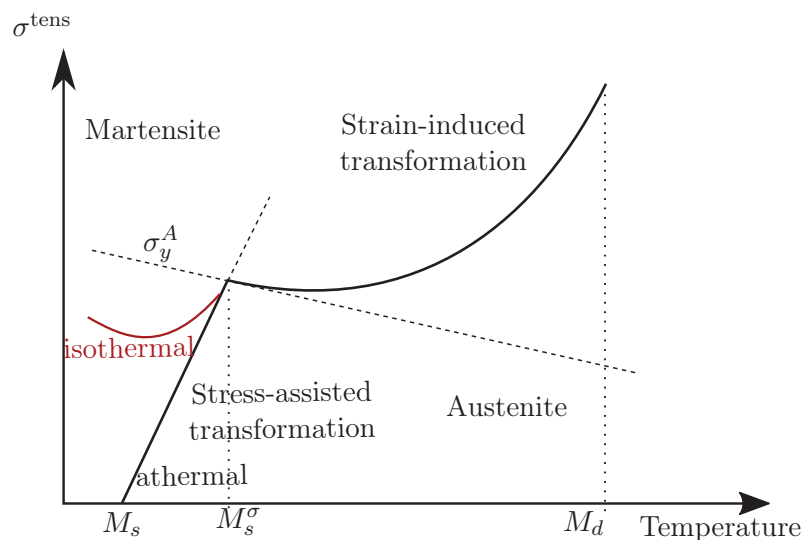


FIGURE 2.10: Schematic illustration of the critical stress σ_c to initiate martensitic transformation as a function of temperature after G. Olson et al. 1972. σ_y^A is the temperature dependent yield strength of austenite. The red line shows the behavior for martensites showing isothermal transformation characteristics.

from f.c.c. to b.c.c. proceeds mainly via an intermediate h.c.p. ϵ -martensite. The lattice is transformed via a shear resulting from partial dislocations. Therefore, an important

nucleation site in austenitic stainless steels are bundles of overlapping stacking faults as found by J. Venables 1964; J. A. Venables 1962 in 18Cr-8Ni ($>\approx 10\%$ Cr-equivalent) and mechanical twins (see section 3.2).

Lecroisey et al. 1972 found that although austenitic Fe-Ni and Fe-Ni-Cr alloys exhibited rather comparable chemical driving forces $\Delta G_{\gamma\rightarrow\alpha'}$, the former showed a significantly lower difference between the M_s and M_d temperatures, i.e., higher stability against the strain-induced martensitic transformation. This was explained in terms of the lower stacking fault energy (SFE, see section 3.2) of the Fe-Ni-Cr alloys, which enables the generation of energetically favourable nucleation sites (shear band intersections), and thus, the occurrence of the strain-induced α' -martensite transformation at much higher temperatures.

2.3 Modelling Strategies

The following section starts with a short historic note on continuum and discrete modelling methods and outlines current trends. Discrete methods are only marginally touched, the focus is on continuum models, especially multi-scale frameworks (see also Phillips 1998; Phillips 2001; Luscher 2010) solved using the finite element method. Then possibilities of multi-scale modelling methods are discussed with varying degrees of discretisation, i.e. from approaches directly in the integration / Gauß point (IP / GP) to very discrete model geometries (see also Böhm 1998).

2.3.1 A Question of Scale - Discrete vs Continuous (Phenomenological) View of Materials

In the 18th century Pierre-Simon Laplace (1749-1827) coined the idea that one can describe material behaviour knowing the interaction potentials and the distances between molecules. Claude Navier (1785-1836) and Augustin-Louis Cauchy (1789-1857) adopted this notion to establish the equations of elastic equilibrium. Opposed to that, Georges Green (1783-1841) suggested a purely phenomenological theory relying directly on the magnitude of the forces and the movements at the observed scale, disregarding microstructure. This approach is nowadays called 'continuum mechanics'. For a historical development of continuum

mechanics in the last century see Maugin 2013 and earlier the introduction of Timoshenko et al. 1940.

Continuum mechanics is a phenomenological field theory, which does not neglect some discrete properties of matter. For instance symmetries are incorporated by the principle of Curie-Neumann stating that the symmetry of physical properties must reflect the symmetry group of the underlying crystal lattice. The question of an application limit of continuum mechanics is strongly problem specific and can therefore not unambiguously be answered.

Despite the longer history of continuum mechanics, phenomenological modelling is by far not completed, but still supplemented by:

- capturing highly non-linear geometrical and physical effects
- modelling/analysing coupled field-problems (multiphysics)
- extending phenomenological models by including significant structural effects

On the discrete side, with the growing computational power of the last centuries now everyone has the (at least theoretical) possibility to conduct ab-initio studies on their computers, making it the fastest growing discipline of materials science. Direct interactions between atoms and even their electrons can be considered, at least given the approximation of density functional theory.

2.3.2 Multi-scale Modelling Methods (MMM) and Current Developments

The main motivation for using MMM is to account for the coupling between different geometrical scales, e.g for polycrystalline materials: the macroscale (structural problem), mesoscale (grain structure) and microscale (individual grains, ideally single crystals, cf. the classification of residual stresses into Type I to III). Microstructural heterogeneity is especially important to understand processes like crack growth.

Depending on the problem at hand it may be useful to differentiate between static or evolving geometries (e.g. microstructure), or speaking in industrial terms (except in cases where the application requires microstructural changes), property and processing models. Processing models predict the internal structure of materials under some processing conditions, either directly (such methods are shortly discussed at the end of this section) or

through a correlation with continuum state variables (like in this thesis). Property models predict a material's performance under some operating conditions, given a description of its internal structure.

Constitutive modelling can be applied on any continuum scale, however material parameters of lower scales are harder to obtain, which is why MMM is often used to extract parameters from macroscopic experimental data. A rather coarse classification into three levels is as follows:

1. Level 1: Phenomenological (macroscopic) hardening variables, no neighbouring effects, homogeneous continuum with unknown internal characteristics, material parameters are calibrated by fitting experimental tests, these models have little to no predictive power outside their calibration zone as pointed out by Cailletaud et al. 2016.
2. Level 2: Mean- / uniform field approaches have many possible variations in discreteness of geometry and combinations with constitutive models. Constitutive equations for each phase. Microfields within each constituent of an inhomogeneous material are approximated by their phase averages $\langle\sigma\rangle$ and $\langle\varepsilon\rangle$. Commonly piecewise (phase-wise) uniform stress and strain fields are employed. Better "rules of mixtures", relaxation methods (commonly stated for martensite), localization or homogenization functions are discussed in chapter 4. Mean / uniform field models, are implicitly multi-scale. This work falls into this category as a micromechanical thermodynamic model of the martensitic transformation modelled in terms of a continuous distribution of volume fraction of martensitic variants rather than a discrete (geometrically resolved) microstructure.
3. Level 3: Full-field, explicit representation of discrete microstructural features, mutual influences of neighbouring material points are a result of the global equilibrium calculation.

Note that the term micromechanic model sometimes is ambiguous since it is not clear whether a micromechanically motivated mean-field constitutive model or a full-field model on the microscale is meant.

If intergranular hardening is low, the presence of various grains is not the crucial point of the modelling as pointed out by Cailletaud 1992. Therefore, some authors already introduce "grain averages" at the integration point level (condensed methods), see e.g. Mahnken et al. 2015; Lange et al. 2015. The challenge is to adequately describe interactions between average units without resolving them spatially. Roters 2011 refers to all kinds of simulations with more than one crystal assigned to one integration point as large scale crystal plasticity finite element modelling (CPFEM). In terms of the resolved model geometry (volume elements) the following approaches may be distinguished (also see section 4.1):

i) Periodic field approaches: The geometry is limited to space filling tessellations. Utilising finite elements the mesh must be periodic and setting up periodic boundary conditions often is tedious. Furthermore, if there is no suitable pre-conditioner of the total stiffness matrix implemented when multi-point constraint equations are specified, calculations may take significantly longer. In recent years periodic cells have more efficiently been solved fast fourier transformation (FFT). This method also has the advantage to directly operate on a voxelized image of the microstructure and it is 1-2 orders of magnitude faster than conventional FEM. However, there are drawbacks at discontinuities such as interfaces, see ???. Which numerical method is better suited overall for homogenization will become apparent with future research. In terms of literature see Moulinec et al. 1995; Suquet 1997; Lebensohn 2001; Kochmann et al. 2016.

ii) Windowing approaches: Only the properties of a small region in the bulk of a volume element (window) is evaluated (integrated over). Typically, this window is too small to be representative. Accordingly, windowing methods describe the behaviour of individual inhomogeneous samples rather than of inhomogeneous materials and give rise to apparent rather than effective macroscopic responses. The advantage is that (almost) no boundary conditions (except of a statically determinate support) must be specified for the volume element.

iii) Embedded approaches: The volume element is split into a local heterogeneous core region (motif) region and an outer embedding region (matrix). In the core region a full-field approach is utilized. In the outer region often a reduced model is applied.

iv) Concurrent schemes: These involve two-way (bottom–up and top–down see Figure 2.11) couplings between models located at different scales. In case the finite element method is used at both scales to solve the entire problem as a nested boundary value problem (BVP) Feyel 2003 called this FE^2 . A finite element submodel is employed at each integration point, i.e. no explicit material law is used on the higher scale, but the full constitutive behaviour is determined concurrently at the lower scale. The lower scale volume element is coupled to a homogeneous model on the higher scale via appropriate coupling conditions (which may conveniently be implemented via the boundary conditions of the lower scale volume element). The drawback is that the lower scale BVP must be solved at each macroscopic iteration. Above that it must be considered that the higher scale requires the consistent tangent moduli representing the current local material stiffness. Computational improvements in terms of hardware usage (adoption of algorithms suitable for graphics cards' central processing units, GPUs) has e.g. been done by Savage et al. 2015; Fritzen et al. 2016. In addition, asymptotic homogenization allows directly coupling FE models on the macro- and microscales.

Another efficient alternative, namely micro-sphere models have been introduced e.g. by Miehe et al. 2004; Ostwald et al. 2010 where the consistent tangent operator used in 3d is obtained from an average overall integration of points on a micro-sphere.

Finally, the uniform and nonuniform transformation field (TFA) analysis should be mentioned Suquet 1997; J. Michel et al. 2003; Fritzen et al. 2010; Dvorak 2012. Though the idea is very similar to FE^2 (localization, constitutive equations at the local scale, homogenization), the realization is technically very different, since the local problem is used to derive concentration and influence tensors, see e.g. *Z-set: Multiscale Materials Modelling V8.6* n.d.

Since multi-scale approaches like the micromechanical analysis of polycrystals with single crystal models, or even condensed polycrystal models are computationally very demanding, model reduction techniques (resulting in so-called meta-models) recently gained momentum, see e.g. J.-C. Michel et al. 2016.

Finally, it must be pointed out that despite the strength of utilising volume elements with a detailed geometry for homogenizing stationary microstructures, they become even more computationally demanding if the microstructure evolves. The three main methods that are found in the literature for finite element calculations on simulating evolving microstructures

are: vertex or front-tracking models, the phase field method (microscopic phase field theory for martensite see e.g. Y. U. Wang et al. 2001; Levitas 2014; Düsing et al. 2016; Yeddu et al. 2017) and the level set method. Constitutive equations are either based on Landau polynomials for the energy barrier or thermodynamic theory. The phase-field method has become especially popular since no tracking of the interface is required. However, there is often a discrepancy between the real and numerical interface widths. Often this parameter is chosen such that the numerical procedure is stable, disregarding its strong physical meaning, see Levitas et al. 2016. The problem is that with an interface width $\approx 1 \text{ nm}$, resolution of the order parameter (see subsection 6.7.6) variation requires at least three grid cells. Therefore, only single nanocrystals or polynanocrystals can be treated, while the grain sizes in typical engineering materials are $10 - 1000 \mu\text{m}$ as pointed out by Levitas et al. 2004.

As far as the modelling of the evolution of interfaces are concerned, it must be pointed out that the important mechanisms are actually taking place on an atomic scale. It is therefore often criticized to treat such problems within a continuum framework (e.g. Tschopp et al. 2008)

Multi-scale approaches are not limited to continuum micromechanics. Especially the capability of FEM to handle highly complex constitutive descriptions has been used to build hierarchical approaches that employ, among others, material models based on discrete dislocation plasticity, see e.g. Zaiser 2001; Zaiser et al. 2014; Vattré et al. 2014, as well as links between continuum and atomistic descriptions, see e.g. Tadmor et al. 2011. Also the stochastic finite element method must be mentioned at this point, see e.g. Stefanou 2009.

Another approach providing at least complementary information on the overall behaviour of microscopically heterogeneous solids is the explicit statistical formulation, where an RVE is viewed as a member of an ensemble from which ensemble averages are estimated and used to represent the corresponding macroscopic constitutive parameters, as well as the material response. Variational bounding methods also fall into this category. The notion of statistical models of intermittent flow is particularly appealing to capture rate processes (kinetics). See Groma 1997; Groma et al. 2003 for dislocation descriptions, Zaiser et al. 2006; Hochrainer et al. 2007; Hochrainer et al. 2014 for the concept of lifted dislocations in the framework of continuum dislocation dynamics (suitable coarse grained

physical dislocation density models) and E. R. Oberaigner et al. 2011 (statistical physics approach) for phase transformations.

In a statistical framework, normally the thermal noise is irrelevant, therefore the entropic term in the free energy ($-TS$) can be neglected (except e.g. for climb). A problem of the "classical statistical physics" approach is that it is basically defined for ideal cases (e.g. ideal gas) in equilibrium (thermostatistics see subsection 6.4.1). Problems to be solved, for an extension of this theory to dislocations and phase transformations are: Long range interactions and dissipative motion (no Hamiltonian system).

As illustrated in Figure 2.11 the industrial demand to quickly achieve goals lead to a top-down approach from "performance" to "processing". On the other side, a fuller picture generally is achieved with a bottom-up strategy. However, it is best to calibrate in both directions. In some cases upscaling is not essential.

There are many principles possessing predictive capabilities without the need to scale up, such as quantum engineering of the bond structure at material interfaces to resist defect nucleation or migration. A popular method to calculate interface- and stacking fault energies as well as critical shear stresses ("energy landscapes") is the embedded atom method Daw et al. 1984. Paragon examples for top-down developments based on experience and empirical correlations are Ni-base super alloys and Titanium alloys, see McDowell 2008.

In recent years this approach has been challenged by the Integrated Computational Materials Engineering (ICME) paradigm, see the books by Horstemeyer 2012; S. Kalidindi 2015. ICME combines both bottom-up and top-down modelling and simulation strategies which aims at reducing the time to market of innovative products (Matouš et al. 2017). The microstructure is effectively a design variable in concurrent design of material and product. Consequently, there is a need for:

-) Microstructure-sensitive parameters of macroscale models to enable preliminary design searches.
-) An exact determination of microstructural characteristics, i.e. topology, distribution and crystallography, due to phase transformation, see Capriz 2013.

To close this section an outlook on the possible influence of machine learning on this research area is discussed. Machine learning generally means that a computer algorithm is applied to data to find out patterns hidden in the data. The predictive power beside the

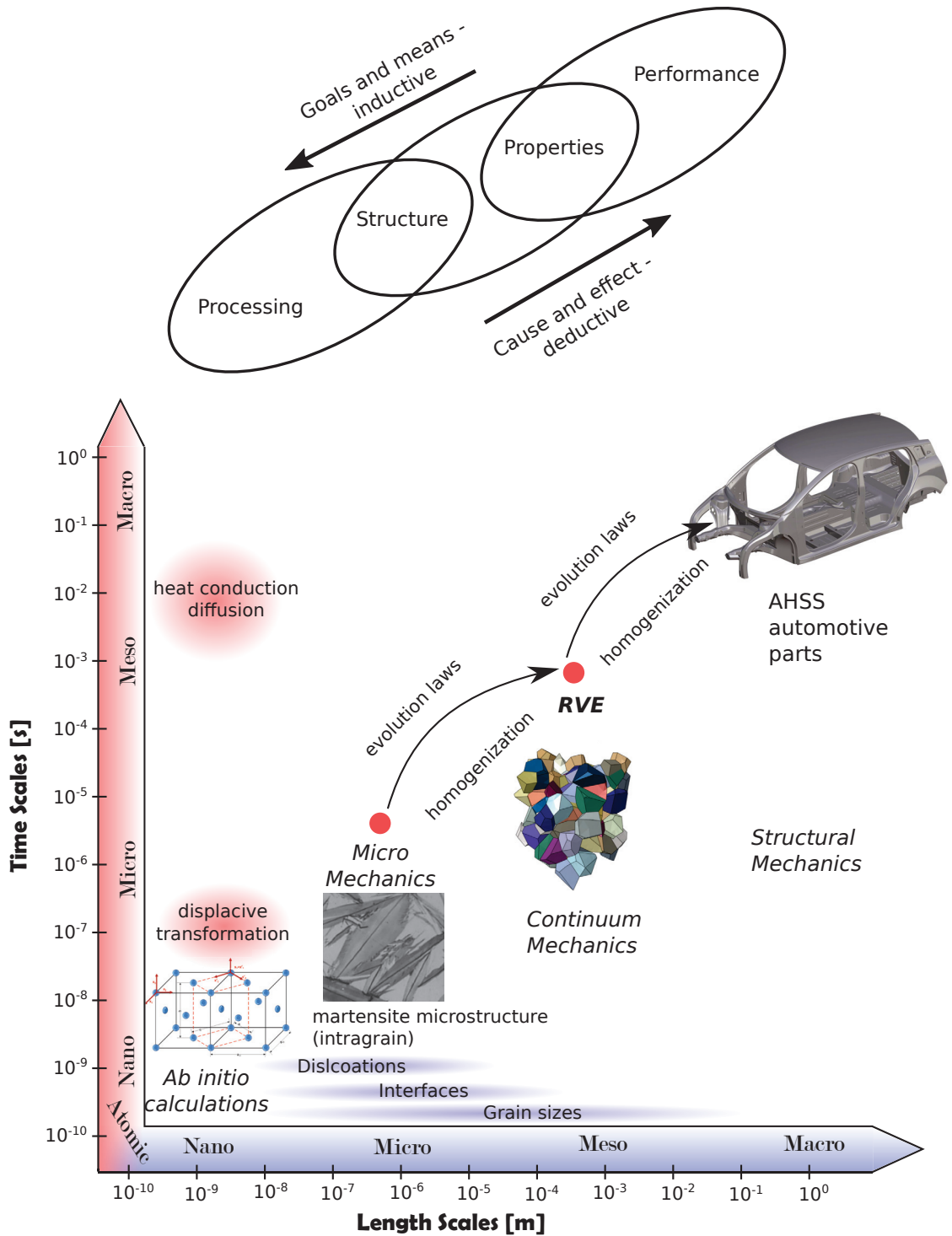


FIGURE 2.11: Top: Top-down and bottom-up interactions arising from the interplay of industrial needs and scientific methods (according to G. B. Olson 1997). Bottom: Overview of ideas on various length scales treated in this thesis. Starting from considerations on the unit cell level a mean-field approach incorporating a detailed description of interactions between deformation mechanisms during the phase transformation and a suitable scale-transition rule is developed on the grain-scale. Simulation of a representative volume element (see section 4.1) enables to approach the macroscale.

flexibility of the algorithm then largely depends on the amount and quality of the data. It is often emphasized that the biggest difference between machine learning and modelling (as employed in this thesis) is that the latter approach emphasizes inference. The future question that remains to be answered is whether experimental data is sufficient in terms of variety and reliability so that machine learning can be applied for the prediction of complex material behaviour involving highly coupled physical phenomena.

Chapter 3

Crystallographic Aspects of Martensite

Concepts like that of an orientation relation, lattice correspondence and an effective deformation gradient require a thorough understanding of the differences and commonalities between lattice and continuum coherency.

The process of nucleation of lath martensite is closely linked to interface dislocations G. B. Olson et al. 1981. Since dislocations have to be nucleated at free surfaces or interfaces such as grain- or phase boundaries these boundaries obviously play a special role if the phase transformation is accompanied by plasticity.

In this work exclusively linear maps are utilised, particularly affine transformations / maps (preserving straight lines) and coordinate transformations / change of basis. The latter are mainly utilised to switch between two (mainly orthonormal) bases such as conventional crystallographic bases. Physically this corresponds to a passive transformation as opposed to an active transformation which actually changes the physical position of an object.

Particularly, the deformation gradient \mathbf{F} will be used in this chapter. According to the polar decomposition theorem any quadratic, real (or complex: in the following the complex terminology is given alongside in brackets) matrix (such as \mathbf{F}) can be decomposed as

$$\mathbf{F} = \mathbf{R}\mathbf{U} \tag{3.1}$$

where \mathbf{U} is a positive semi-definite symmetric (hermitian / self-adjoint) matrix and \mathbf{R} a orthogonal (unitary) matrix. In any orthonormal basis \mathbf{U} is a pure strain and \mathbf{R} a rotation.

As to the term similarity: Geometric similarity means that two objects can be mapped into each other by rotating, translating, scaling and reflecting.

Matrix similarity more generally means that given two matrices $\mathbf{A}, \mathbf{B} \in n \times n$ (quadratic), they are similar if: $\mathbf{B} = \mathbf{P}^{-1}\mathbf{A}\mathbf{P}$, with $\mathbf{P} \in n \times n$ and \mathbf{P} invertible. Similar matrices represent the same linear operator with respect to (possibly) different bases and share all properties of their shared underlying operator such as eigenvalues, rank, trace, characteristic polynomial, etc.

3.1 Preliminaries: Lattice-Bases, -Correspondence, -Symmetry

To start with some mathematical preliminaries are provided here to avoid confusion. A Bravais lattice \mathcal{L} is determined by linearly independent lattice vectors \mathbf{a}_i representing discrete translation operations under which the lattice (a pattern of points) is invariant / periodic. The metric tensor (used for measuring lengths and angles) is given by:

$$g_{ij} = \mathbf{a}_i \cdot \mathbf{a}_j \quad (3.2)$$

If $g_{ij} = \delta_{ij} = \mathbf{I}$ then the basis is orthonormal (orthogonal and normalized vectors). A mapping \mathbf{W} between orthonormal bases is a rotation (orthogonal matrix \mathbf{R} , $\det(\mathbf{R}) = +1$). The components of \mathbf{R} are directional cosines. The metric of the dual space / reciprocal lattice is the inverse of g_{ij} . The reciprocal lattice / dual space follows from the periodicity condition of any local physical property, see e.g. Khachatryan 1983.

In our case of a f.c.c to b.c.c transformation both sets of lattice vectors are orthogonal. If additionally the lattice vectors are normalized as is usually done for calculations in the cubic system) both become orthonormal. For lattices the distinction of conventional (commonly an orthonormal basis) and primitive basis (generally shortest lattice vectors) should be kept in mind (see e.g. Müller 2013). Given two lattices \mathcal{L}^A and \mathcal{L}^M and the assembly of their lattice vectors into matrices \mathbf{A}^A and \mathbf{A}^M

$$\mathbf{A}^A = \mathbf{C}^{AM} \mathbf{A}^M \quad (3.3)$$

where the non-singular matrix \mathbf{C}^{AM} is called the correspondence matrix from A to M (cf. change of basis). Note, that it is important whether the lattice vectors are assembled as row or column vectors. \mathbf{C}^{AM} links corresponding lattice planes and lines. Historically, lattice correspondences have been found by inspection of unit cells. The principal axes of the lattice deformation are then parallel to rational crystallographic axes of the parent structure, even though there is no theoretical necessity for the principal axes to be rational lattice vectors. Obviously, a lattice correspondence is not unique. Especially, there are many possibilities when the primitive cells differ appreciably in size.

Comprehensive information on symmetry and group properties of lattices can be found in Müller 2013 (comprehensive reference for space groups), Pitteri et al. 1998 (particularly twinning), Sutton et al. 1995 (particularly crystalline interfaces), Authier 2003 (relations between physical properties and crystal symmetries). In the following some particular aspects useful for this will be pointed out:

A geometric symmetry operation / isometry is a distance preserving mapping that does not change appearance. Particularly, a mapping \mathbf{W} is called an isometry if $\det(\mathbf{W}) = \pm 1$ and

$$g_{mn} = g_{ij}W_{mi}W_{jn} \quad \mathbf{G} = \mathbf{W}^T \mathbf{G} \mathbf{W} \quad (3.4)$$

The set of all symmetry operations is called space group. The space group is the largest group because it includes translational symmetries. A point group is the set of all symmetry operations that keeps at least one point fixed (translations are excluded). After Euler's theorem, any displacement of a rigid body which leaves one of its points fixed may be produced by a rotation of the body through an angle $\theta < 180^\circ$ about an axis through that point. Point group determination follows a definite scheme where certain symmetries are ruled out in a stepwise procedure. Nowadays this is automated e.g. in any electron back scattering diffraction (EBSD) software. For crystallographic calculations often inversion symmetries are excluded (the handedness of coordinate system is not allowed to change). The resulting group is called the Laue Group.

The (bulk) free energy of a crystal is pictured as an scalar valued anisotropic tensor function (see e.g. Itskov 2015), invariant w.r.t. the symmetry group. Particularly, it is distinguished between material symmetry and frame indifference, i.e. no change of the free energy after

active rotation in the symmetry group and no change after coordinate transformation (passive rotation) within the symmetry group, respectively.

The high-temperature phase almost always has a higher symmetry than the low-temperature phase. The number of elements in a group \mathcal{G} often denoted as $|\mathcal{G}|$ is called the *order* of the group. The theorem of Lagrange, which follows directly from the co-set decomposition of a finite group states that if \mathcal{G} is a finite group and \mathcal{H} is a subgroup, i.e. $\mathcal{H} < \mathcal{G}$, then the $|\mathcal{H}|$ is a divisor of \mathcal{G} . This relation is useful for solid state phase transformations, where one lattice whose operations form a group changes into another lattice whose symmetry operations form a subgroup of the former. The number of non-equivalent lattices then is G/H . Often the term variant is used. A group theoretical description of martensite has recently given by Sowa 2017. Y. Gao et al. 2016 recently did a group theory description of the transformation pathway degeneracy in structural phase transformations.

3.2 Properties of Dislocations

To Love (1927) we owe the name of "dislocation" spelled equally in English and French. Classical books on the topic are Friedel 1964; Hull et al. 2001; J. P. Hirth et al. 1968; Kostorz et al. 2013.

Dislocations are line defects in the material forming closed loops inside the material. The introduction of the Burgers vector \mathbf{b} enables a distinction of dislocations due to its relative orientation to the dislocation line $\boldsymbol{\xi}$. Different parts of the loop are of different character (edge, mixed, or screw) and of different sense, but have the same Burgers vector. Any mixed dislocation line segment can be split up into screw and edge parts. The Burgers vector of a single dislocation or the Burgers vector content of multiple dislocations is the difference of the coordinates of a closed path around these dislocation lines in a strained state of the lattice to those of an unstrained (ideal) reference lattice, see e.g. J. P. Hirth et al. 1968. Nowadays, such mapping procedures are implemented in atomistic simulation codes, see e.g. Stukowski et al. 2012 (for the continuum case see Equation A.3).

Edge dislocation: $\mathbf{b} \perp \boldsymbol{\xi}$, i.e. tensile, compressive and shear stress fields may be present the polarity of the dislocation may be positive or negative depending on which side of the half plane it exists.

Screw dislocation: $\mathbf{b} \parallel \boldsymbol{\xi}$, i.e. any plane for which \mathbf{b} is a zone axis is a possible glide plane. Screw dislocations do not climb, however, they may slip in any plane containing the dislocation (cross slip). An important factor in view of phase transformations is that screw dislocations provide an easy growth mechanism because additional atoms and unit cells can be added easily to the step / ledge of the screw. The stresses and displacements due to a screw dislocation are calculated under the assumption of antiplane shear, see e.g. Voss et al. 2018.

A slip system is specified by its slip direction \mathbf{s} (given by $\mathbf{b}/|\mathbf{b}|$ for edge dislocation segments and $\mathbf{b}/|\mathbf{b}| \times \mathbf{m}$ for screw dislocation segments) and slip plane normal \mathbf{m} . If the Burgers vector of a dislocation loop lies in the loop plane, the loop is glissile / conservative (no mass transport required). In the opposite case, it is sessile / non-conservative (requires mass transport). We will retrieve this nomenclature in the case of interfaces in subsection 3.5.5 because the mobility of interfaces depends on the mobility of dislocations in the interface. The continuum shear deformations of homogenized volume elements sheared by continuously distributed, straight screw (\odot) and edge dislocations (\perp) are given by

$$\mathbf{S}_i^\perp \text{ or } \mathbf{S}_i^\odot = \mathbf{I} + \varepsilon_s \frac{\mathbf{s}_i}{\|\mathbf{s}_i\|} \otimes \frac{\mathbf{m}_i}{\|\mathbf{m}_i\|} \quad (3.5)$$

where ε_s is the shear magnitude. Note that a simple shear is a special case of an invariant plane strain (IPS, see Equation 3.25). Caution is advisable concerning the definitions of the vectors in the dyad when comparing different literature since some authors define both vectors as unit vectors, H. Bhadeshia 1987, while others directly take the Miller indices, Khachaturyan 1983, which changes of course the interpretation of the pre-factor of the dyadic product.

For cubic lattices a simple shear can conveniently be written using Miller indices instead of unit vectors. The spacing of adjacent slip planes (normal vector \mathbf{m}) in the cubic lattice is $d_{(hkl)} = a_{\text{cubic}}/\sqrt{h^2 + k^2 + l^2}$. Sketching the deformation of simple shear, and by using the intercept-theorem (cf. Figure 2.1) it can easily be shown that

$$\frac{1}{\varepsilon_s} = \frac{g \cdot d_{(hkl)}}{\|\mathbf{b}\|} \quad (3.6)$$

where $\|\mathbf{b}\|$ is the norm of the slip system's Burgers vector, e.g. for $\mathbf{b} = a_\alpha/2\langle 110 \rangle$, this means $\|\mathbf{b}\| = a_\alpha/\sqrt{2}$ and g can be interpreted in an idealized way as the average number

of glide planes between evenly spaced, straight (non-kinked) dislocations of the same glide system. Equation 3.6 can be used to switch between the representation of the dyadic shear term utilizing normalized vectors (Equation 3.5) or Miller indices resulting in

$$\mathbf{S}^\perp = \mathbf{I} + \frac{1}{g_i} \mathbf{b}_i \otimes \mathbf{m}_i \quad (3.7)$$

as found in Khachaturyan 1983; Qi et al. 2014 where \mathbf{b}_i and \mathbf{m}_i are the vectors of Miller indices of the Burgers vector and the slip plane normal respectively. Qi et al. 2014 call the pre-factor $(1/g_i)$ "slip density".

It can be shown that only 5 of the 12 $\{111\}\langle 110 \rangle$ slip systems in f.c.c. are independent in terms of constituting any arbitrary deformation: There can only be two independent slip directions on one and the same plane, which reduces the number from 12 to 8. From these 8, it is a simple practical exercise to show that 5 of them suffice to write down all the others.

In f.c.c. crystals plastic slip is predominantly activated by shear stresses. This is commonly decided by the Schmid factor m (Schmid et al. 1968) coming from the relation:

$$\tau = F^{\text{tens}}/A' = \sigma^{\text{tens}} \cos(\theta^1) \cos(\theta^2) = \sigma^{\text{tens}} m \quad 0 < m < 0.5 (\theta^1 = \theta^2 = 45^\circ)$$

with τ being the resolved shear stress, A' the projected area of the slip plane in the direction of the force and θ^1 and θ^2 the angles between the slip plane normal \mathbf{m} as well as the slip direction \mathbf{s} and the force direction, respectively (corollary $\sigma_y \leq 2\tau_c$). The ratio of tensile yield strength of a polycrystal σ_y and the critical resolved shear stress (CRSS) τ_c of a single crystal is the Taylor factor M

$$\frac{\sigma_y}{\tau_c} = M \quad (3.8)$$

For f.c.c. polycrystals M is in the range of 2.7 – 3.2 depending on the degree of texture. Nowadays EBSD software can be used to determine it more accurately as e.g. done by Steinmetz et al. 2013. In crystal plasticity both the dyad $\mathbf{m} \otimes \mathbf{s}$ and the strain due to simple shear (last term in a finite strain setting

$$\underline{\mathbf{m}} = \frac{1}{2} (\mathbf{m} \otimes \mathbf{s} + \mathbf{s} \otimes \mathbf{m} + |\mathbf{s}| \mathbf{m} \otimes \mathbf{m}) \quad (3.9)$$

are often called Schmid tensor. For a general stress state the resolved shear stress is obtained as:

$$\tau^i = \boldsymbol{\sigma} : \mathbf{m}^i \quad i = 1 \dots 12 \quad (3.10)$$

While in f.c.c. metals normal strains are basically negligible, already for b.c.c. and h.c.p. metals they must be taken into account (so-called non-Schmid effects).

Short segments of the dislocation line with $\boldsymbol{\xi}$ normal to the glide plane are termed jogs (when the normal component extends over only a single interplanar spacing d they are called unit jogs or for brevity just jogs, and over more than one interplanar spacing 'superjog'). Kinks are steps in the dislocation line lying in the glide plane. Dislocations required for compatible deformation of various parts of the crystal are called geometrically necessary dislocations (also see section 6.5).

Dislocations accumulating by trapping each other in a random way are called statistically stored dislocations. Dislocations intersecting another glide plane are called forest dislocations with respect to the glide plane they intersect. With a reasonable approximation, the intersection with a forest dislocation can be treated as point obstacle in the glide plane. When two attractive dislocations gliding in different slip planes cross each other, they can reduce their total energy by reacting to form a third dislocation segment called a junction. This junction lies at the intersection of the two dislocation slip planes. It is usually not mobile (if it is immobile it is also referred to as lock) and therefore represents a barrier to further dislocation motion, until the local stress is raised to a critical value such that the junction is destroyed and dislocation crossing occurs. A dislocation dipole consists of two parallel dislocations with parallel and opposite Burgers vectors. Consequently, the elastic-strain energy of the pair is localized in the vicinity of the pair (St. Venant's principle) in analogy to the localization of the electrostatic energy of an electric dipole. The specific line energy of a dislocation segment is normally estimated as Hull et al. 2001

$$E_{\text{el}}^{\text{dis}} = c_1 l \mu b \frac{1}{4\pi} \ln \left(\frac{R}{r_0} \right) \quad (3.11)$$

where l denotes the length of the dislocation segment, b the magnitude of the Burgers vector, R a characteristic length for the size of the strain field (outer cut-off radius, e.g. given by Equation 6.35), and r_0 the dislocation core radius (in the range of b) and c_1 a material dependent parameter, related to the Poisson's ratio ν that differs for a screw

($c_1 = 1$) and edge dislocation ($c_1 = (1 - \nu)^{-1}$). Equation 3.11 is often approximated by $E_{el}^{dis} \approx 1/2\mu b^2$ [J m⁻¹], Frank 1951 proposed that dislocations will decompose according to:

$$|\mathbf{b}_1|^2 > |\mathbf{b}_2|^2 + |\mathbf{b}_3|^2 \quad (3.12)$$

Screw segments annihilate much easier than edge segments (Kubin et al. 2009). In general these annihilations leave dislocation segments in the cross-slip plane, which are called collinear superjogs (the term ‘‘collinear’’ indicates that they have the same Burgers vector as the primary dislocations), see Devincere et al. 2007.

However, in a b.c.c. lattice the mobility of a screw dislocation is much smaller than that of an edge dislocation. Consequently, screw dislocations are dominant in small samples, since edge dislocations easily reach the surface where they annihilate. A common way to estimate dislocation densities is by using a proposal by Stibitz 1936

$$\rho = \frac{L}{V} = \frac{E^{el}}{1/2\mu b^2} \quad E^{el} = \frac{3E}{2(1 - 2\nu^2)} \varepsilon^2 \quad \text{with} \quad \varepsilon = \frac{\Delta d}{d} \quad (3.13)$$

where d is the interplanar lattice spacing and Δd is the peak broadening in X-ray or neutron diffraction, see e.g. Christien et al. 2013. The author concedes that an estimation obtained this way is quite inaccurate. Other methods are based on line / peak broadening analysis of X-ray diffraction patterns, see e.g. Ungár et al. 1996; Scardi et al. 2004.

3.3 Stacking Faults and Twins

A comprehensive discussion on stacking faults is found in Christian 1965. Denoting A, B and C as the possible layer positions in a projection normal to the close-packed layers the stacking sequence in f.c.c. is any of ABCABCABC = CBACBACBA = CABABCAB and that in h.c.p. ABABAB = BCBCBC = CACACA. A stacking fault is any deviation of these arrangements, e.g. in f.c.c. ABCACABCA (one B removed). Note, the stacking sequence of a twin



where the twin plane is marked. Frank 1951 classified stacking faults as intrinsic or extrinsic. For intrinsic faults generated by removing one atomic layer, the atomic pattern of each half of the crystal extends right up to the composition plane (a boundary containing

atoms shared by both lattices), whereas for extrinsic faults (adding one layer to many), the composition plane is an atomic plane which does not belong to the lattice structure on either side of it. Note that intrinsic and extrinsic faults may be regarded formally as mono-layer and two layer twins respectively. Stacking faults are the basic defects of deformation twins (Christian et al. 1995a; Mahajan et al. 1973), in phase transformations, and in the formation of dislocation barriers by intersecting dislocations. In deformation twinning the lattice symmetry is not reduced and the deformation on each side of the coherent interface is a simple (reconstructive) shear. They share many features, such as their nucleation mechanisms with transformation twins, i.e. twinning deformation as a result of a phase transformation treated in subsection 3.5.3.4.

According to Equation 3.12 intrinsic stacking faults form in f.c.c. crystals as a consequence of the dissociation of $\mathbf{b} = a_\gamma/2\langle 110\rangle\{111\}$ perfect dislocations into two $\mathbf{b} = a_\gamma/6\langle 211\rangle\{111\}$ partial dislocations (Shockley partial dislocations) lowering the dislocation's energy. Alternatively the decomposition of a perfect $\mathbf{b} = a_\gamma/2\langle 110\rangle\{111\}$ into one Shockley partial and an immobile Frank partial $\mathbf{b} = a_\gamma/3\langle \bar{1}11\rangle$ ($\mathbf{b} \perp \mathbf{m}$) forming a pole, is possible. However, the Shockley partial can move around the pole forming a stacking-fault, known as the pole mechanism for twinning. Both mechanisms are depicted in Figure 3.1.

The stacking fault energy γ^{sf} (SFE) is composition and stress dependent. The SFE quickly and non-linearly drops to almost zero with increasing alloying content. The rate of the drop depends on the ratio of the number of valence electrons to the number of alloy atoms. The SFE controls the distance two partials can separate, i.e. the width of the stacking fault. A low SFE leads to widely dissociated partial dislocations, which cannot cross slip. As a result pronounced planar slip and a high strain rate hardening occur. High SFEs

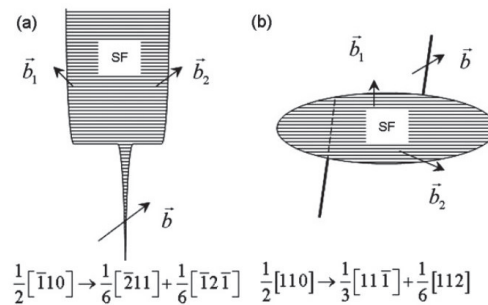


FIGURE 3.1: Dislocation dissociations into partials to produce stacking faults. a) two Shockley partials, b) (immobile) pole mechanism for twinning.

facilitate cross slip of screw dislocations, providing extra ductility. The temperature dependence of stacking fault energy (increase with higher temperature) has been qualitatively investigated experimentally in Rémy et al. 1978. This is important for hot rolling, where stacking fault ribbons are narrowed, facilitating dislocation cross-slip.

SFE can be determined from first principle calculations (e.g. Lu et al. 2016) or measuring distances between single dislocations. The SFE determines the mobility of partial dislocations at interfaces. Geissler et al. 2014 points out that in general the SFE is a quantity that can only be determined with a high degree of uncertainty from ab-initio calculations and always needs experimental verification.

U. Kocks et al. 2003 point out that dynamic recovery, characterizing the strongly temperature- and rate-dependent decrease of the hardening rate at larger strains (stage III), is almost independent of diffusion, but strongly coupled to the SFE (directly proportional, indicating that cross slip is an important factor).

With decreasing SFE, the plasticity mechanisms change from: i) dislocation glide ($\approx 45 \text{ mJ m}^{-2}$) to ii) dislocation glide in conjunction with mechanical twinning to iii) dislocation glide in conjunction with martensitic phase transformation, see Curtze et al. 2010. In the range of $15\text{-}45 \text{ mJ m}^{-2}$ deformation twinning results in an increased strain hardening rate due to twin boundaries acting as obstacles for dislocations. If the SFE falls below $15\text{-}20 \text{ mJ m}^{-2}$ very fine α' as well as ϵ -martensite is observed.

Twin formation involves the passage of $\mathbf{b} = a_\gamma/6\langle 11\bar{2} \rangle$ Shockley partials on every $\{111\}$ plane, while the formation of ϵ -martensite (f.c.c. \rightarrow h.c.p. transformation) is achieved through the passage of $\mathbf{b} = a_\gamma/6\langle 11\bar{2} \rangle$ Shockley partials on every second $\{111\}$ plane. The terminology of twinning elements is visualized in Figure 3.2.

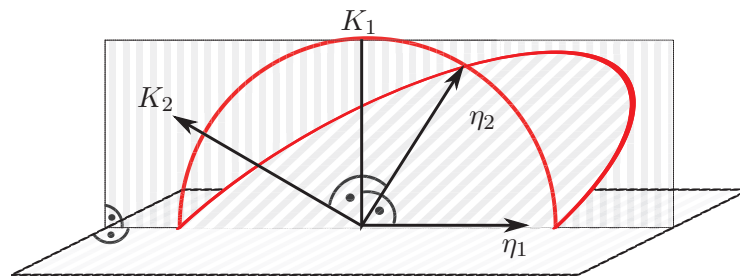


FIGURE 3.2: Terminology of twinning elements. For a type I twin K_1 is the twin plane normal η_1 the twinning shear direction. η_2 points in the direction of the invariant line and is the twinning shear direction of a type II twin (K_2 is its twin plane normal).

3.4 Texture, Orientation Relationships and Related Topics

Texture means the distribution of crystallographic orientations of a polycrystalline sample.

The processing of steel involves five stages of texture development (Jonas 2009):

- i) austenite deformation (during hot rolling)
- ii) austenite recrystallization (during and after hot rolling)
- iii) the transformation (on cooling after rolling, see e.g. Tomida et al. 2013; Tomida 2018)
- iv) ferrite deformation (during warm or cold rolling)
- v) static recrystallization during annealing after cold rolling.

In this section the theory for the characterisation of orientation imaging microscopy (OIM) data is shortly outlined. A particular emphasis is laid on stage iii) from above. First the lattice rotations are parameterizations, since in OIM everything is limited to rotations (orientation of lattice). Then discrete orientation relations are discussed and the concept of lattice correspondence variants (LCVs) / orientational variants is introduced. Correlations between the 12 $\{111\}_\gamma$ slip systems in f.c.c. and these variants are established. Next, texture representations and problems of commonly used orientation spaces are pointed out. Then distribution functions are discussed. Finally, austenite reconstruction methods are mentioned. An emphasis is laid on the correlation of all these concepts with morphology, an aspect, that in the authors opinion, has not yet been given enough attention in the case of high dislocation densities. The reference coordinate system used in OIM as well as particularities and practical problems related to lath martensite are found in section 5.5.

Parametrizations of rotations (all resulting in rotation matrices) are:

- i) Euler angles: Sequential plane rotations around coordinate axes. Unfortunately, a multitude of different conventions exist. In this work the convention after H. Bunge 1982 is employed $\varphi_1, \Phi, \varphi_2$ around ($3 = z, 1' = x', 3'' = z''$, see ??). This is the most used convention in OIM, e.g. *TSL OIM Analysis Manual* n.d.).
- ii) Axis-angle representation: 4-parameter axis $[u, v, w]$ - angle θ pair. The 4 parameters can be reduced to three using the Rodriguez formula

$$\boldsymbol{\omega} = \tan(\theta/2) [u, v, w] \quad (3.14)$$

As e.g. pointed out by He et al. 2005 the singularity associated with the ω approaching infinity as $\theta \rightarrow \pi$ can be avoided by confining to the fundamental zone. iii) Quaternions, see e.g. Mason et al. 2008; Patala et al. 2012.

Given two orientations \mathbf{R}_A and \mathbf{R}_M their misorientation / orientation distance is given by

$$\Delta\mathbf{R}_{AM} = \mathbf{R}_A\mathbf{R}_M^{-1} \quad (3.15)$$

Although orientation relations ORs between phases are most often tabulated as discrete sets of parallel crystallographic directions (see Table 3.1 for those common in steels), the set of measured ORs does not consist of discrete values but of a continuous distribution of values around some maxima. These maxima correspond to a higher packing density in the interface region between the parent and the product phase. The magnitude of variation depends on the process history of the austenite and the amount of plasticity triggered by the transformation that is in turn system dependent and may be referred to as “plastic trace of the transformation mechanism” Cayron 2017. Generally, the final texture becomes more sharp with increasing alloy content Ray et al. 1990 (lower stacking fault energy). In order to formally distinguish between martensite variants (and in further consequence determine their relative contributions, see e.g. K. Verbeken 2009), definite bounds of misorientations around discrete crystallographic directions must be introduced.

Note that the parallel plane relationship $\{111\}_\gamma || \{011\}_\alpha$ (CP1,...,CP4) is always almost exactly satisfied, but the direction relation varies. Note, that the reason for the parallelism of the directions is atomic row matching in the longitudinal direction of the transforming domain, see Howe 1997 p.190-192 therein. Utilizing these parallel relations so-called lattice correspondence / orientational (KS-,NW-...) variants may be defined by pure rotations, see Table 3.3). However, microstructural morphology is not characterised by rotations alone but also needs stretches. Particularly, the full deformation will have certain (geometric or kinematic) characteristics as elaborated in the next section.

Name	Orientation Relationship	# variants
Kurdjumov et al. 1930 (KS)	$\{111\}_\gamma \parallel \{011\}_{\alpha'} \quad \& \quad \langle \bar{1}01 \rangle_\gamma \parallel \langle \bar{1}\bar{1}1 \rangle_{\alpha'}$	24
Nishiyama 1934 (NW)	$\{111\}_\gamma \parallel \{011\}_{\alpha'} \quad \& \quad \langle 11\bar{2} \rangle_\gamma \parallel \langle 0\bar{1}1 \rangle_{\alpha'}$ or equivalently ... $\& \langle 10\bar{1} \rangle_\gamma \parallel \langle 100 \rangle_{\alpha'}$	12
Pitsch 1962 (P)	$\{100\}_\gamma \parallel \{011\}_{\alpha'} \quad \& \quad \langle 110 \rangle_\gamma \parallel \langle 111 \rangle_{\alpha'}$	12
Greninger et al. 1949 (GT) and GT'	$\{111\}_\gamma \parallel \{110\}_{\alpha'} \quad \&$ half-way between KS and NW directions ... $\langle 123 \rangle_\gamma \parallel \langle 133 \rangle_{\alpha'}$ (GT) ... $\& \langle 133 \rangle_\gamma \parallel \langle 123 \rangle_{\alpha'}$ (GT')	2×12
ε -martensite OR	$\{111\}_\gamma \parallel \{0001\}_\varepsilon \quad \& \quad \langle \bar{1}01 \rangle_\gamma \parallel \langle \bar{1}\bar{1}20 \rangle_\varepsilon$ $\{110\}_{\alpha'} \parallel \{0001\}_\varepsilon \quad \& \quad \langle \bar{1}11 \rangle_\gamma \parallel \langle \bar{1}\bar{1}20 \rangle_\varepsilon$	Consequently $\gamma \rightarrow \varepsilon \rightarrow \alpha'$ results in KS

TABLE 3.1: Overview of commonly stated (idealised) orientation relationships between f.c.c. austenite, b.c.c. martensite and h.c.p ε -martensite in steel. Three dots indicate that the plane relation is the same, only that of the directions changes. Both Pitsch and NW are 5.26° from KS ($\{111\}_\gamma$ in-plane rotation). These relations are quite idealised considering that orientation relations are not discrete but follow some distribution and most interfaces are irrational.

While the KS, NW and Pitsch give rational orientation relationships (predominantly coherent interfaces), GT and GT' are irrational, a term used for morphological features such as habit planes and long directions that cannot be expressed in terms of low-index, Miller indices (W.-Z. Zhang et al. 2005; M.-X. Zhang et al. 2009). One complication associated with this "rational" versus "irrational" nomenclature in relation to morphological features, such as habit planes or long directions, is that in the interest of brevity, simplicity and convenience, a number of published experimental and theoretical results for irrational habit planes or long directions have been purposely expressed in terms of the nearest low-index plane or direction (as in Table 2.2). However, as pointed out in M.-X. Zhang et al. 2009 (p.7 therein) for an exact specification of an orientation relationship the full rotation matrix must be given.

Some commonly found texture components are:

Cube $\{100\}(001)_\gamma$, ($\varphi_1 = 0, \Phi = 0, \varphi_2 = 0$)

Goss: $\{110\}\langle 001\rangle$ ($\varphi_1 = 0^\circ, \Phi = 45^\circ, \varphi_2 = 90^\circ/0^\circ$)

Brass: $\{110\}\langle 112\rangle_\gamma \rightarrow \{332\}\langle 113\rangle_\alpha$ ($\varphi_1 = 35^\circ, \Phi = 45^\circ, \varphi_2 = 90^\circ/0^\circ$)

Copper: $\{112\}\langle 111\rangle_\gamma \rightarrow \{113\}\langle 110\rangle_\alpha$ ($\varphi_1 = 60^\circ, \Phi = 32^\circ, \varphi_2 = 65^\circ$).

The reason for the names of "copper" and "brass" (Cu with up to 40% Zn) has to do with changes in texture with alloying. Ray et al. 1990 report that *Brass* and *Copper* are the major transformation texture components inherited by α from γ in deformed austenite such as controlled rolled steels. The texture of recrystallized austenite is made up predominantly of the *Cube* component. Three-dimensional representations of some important crystallographic plane-direction in pairs Euler space (Bunge convention) can be found in H.-J. Bunge et al. 1969.

In the author's opinion there is a substantial problem in utilizing Euler angles and hence the Euler orientation space to quantify transformation variants, since one orientation is represented by many points in the asymmetric region of Euler space, i.e. $0 \leq \phi_1 \leq 2\pi$; $0 \leq \Phi \leq \pi$; $0 \leq \phi_2 \leq 2\pi$ (multiple combinations of angles yield the same rotation, see Hansen et al. 1978). Two cubic symmetries induce a sectioning (plane partitioning) of this region into $2 \times 4 = 8$ symmetrically (and geometrically) equivalent subregions. However, there are $2 \times 4 \times 3$ symmetrically equivalent regions and the further reduction is geometrically non-linear (see Figure 3.3, upper-left therein). For the representation of the ODF in the case of (at least) orthorhombic sample symmetry mostly the subregion $0 \leq \phi_1 \leq \pi/2$; $0 \leq \Phi \leq \pi/2$; $0 \leq \phi_2 \leq 2\pi$ is used although this region generally contains each orientation 3 times (Multiplicity = 3).

One-point statistics contain information regarding the probability of finding a particular local state at a single point sampled from the material. This information is best captured as distribution functions over the local state space. In OIM this state space is the orientation space resulting in an orientation distribution function (ODF) describing the frequency of occurrence of particular orientations

$$f(y) = \frac{\Delta Z}{Z} \quad (3.16)$$

where y , Z and ΔZ are the orientation, the total volume of the considered domain (although normally obtained from a 2D OIM image) and the volume-fraction, having a crystal orientation within Δy around y , respectively. The minimum occurring negative value of

the calculated $f(y)$ will be approximately equal to the absolute error of the calculation as pointed out in H. Bunge 1982, p. 221 therein.

Other commonly used distributions are e.g. the crystallite distribution function (constant orientation within each grain e.g. kernel average misorientation - KAM), the boundary

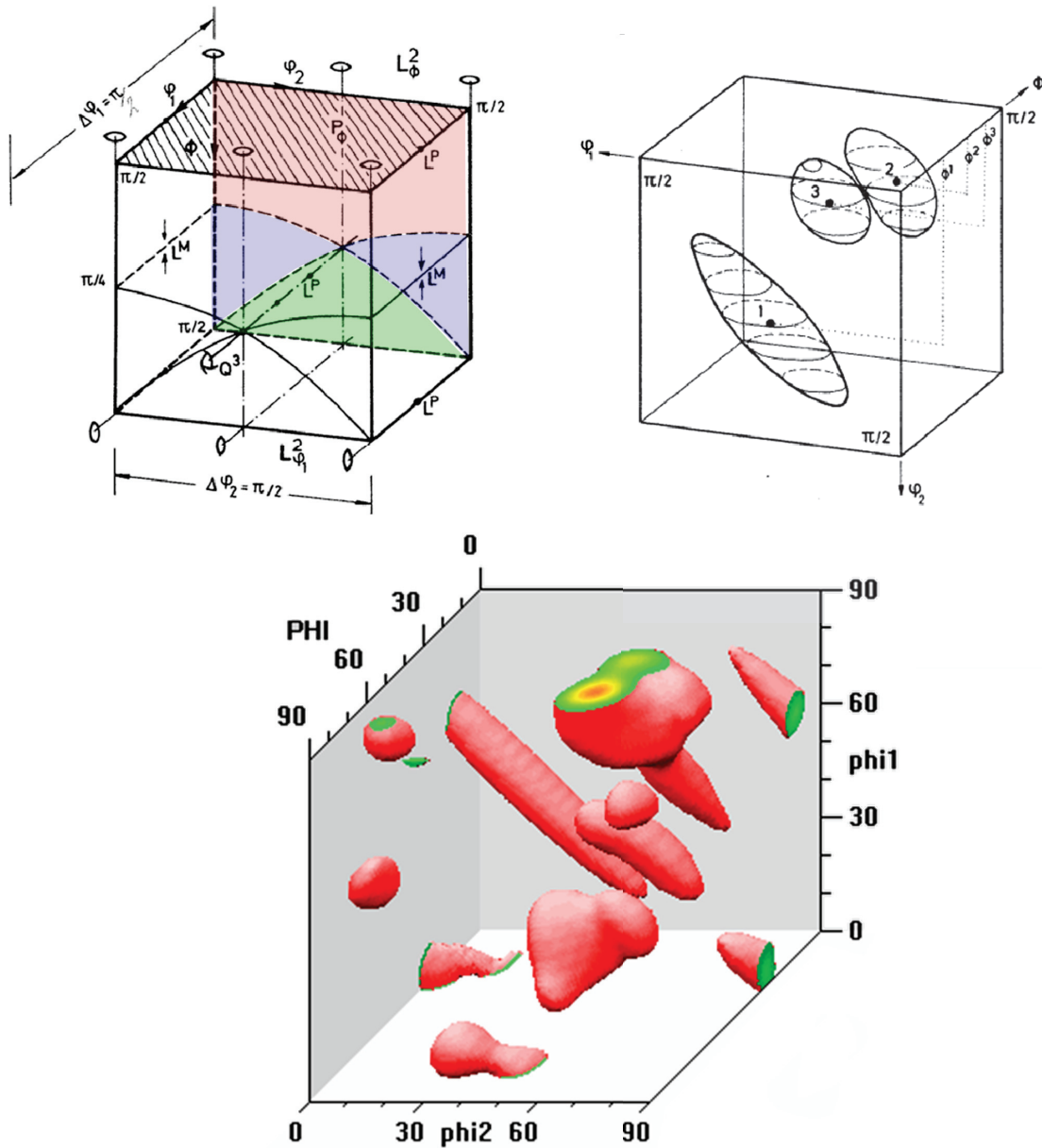


FIGURE 3.3: Upper-left: asymmetric region of full Euler space (one-sixteenth) taken from Hansen et al. 1978. Upper-right: Surfaces representing the same misorientation of three symmetrically equivalent components of the orientation $\{123\}$ (634) (taken from Hansen et al. 1978) illustrating the non-linearity of the Euler-space. Bottom: Major texture components of MarvalX12 (TR32 specimen see section 5.1).

distribution function (y then is the orientation of the 2D boundary), the direction distribution function (y is a vector) and the misorientation distribution function (MDF, cf. Equation 3.15), which is particularly useful for the identification of martensite variants. Also combined properties can be studied using

$$f(y_1, y_2) = \frac{\Delta Z}{Z} \quad (3.17)$$

Examples are a grain-size-ODF where dZ now indicates the volume fraction of crystal orientation within Δy_1 around y_1 , and a grain size δy_2 around y_2 , see Fullwood et al. 2010. Interestingly, although for martensite there are some significant correlations between morphology and orientation relations, the author merely found some preliminary works by Iwamoto et al. 2000; Iwamoto et al. 2002 studying these correlations using light microscopy images. Nowadays such an approach would be very powerful in conjunction with OIM data.

Finally, high temperature austenite texture reconstruction methods, i.e. given a measured texture at room temperature drawing conclusions about the material's state before transformation are discussed. In general this "untransformation procedure" is of considerable potential value for the study of texture development in high temperature phases, such as hot rolled austenite, where the direct measurement of texture is handicapped by experimental difficulties. Reconstruction of austenite grains particularly is a challenge i) from fully transformed states where no retained austenite is present and ii) if the material is thermomechanically processed (Notably, for the MarvalX12 studied in this work both applies). As far as point ii) is concerned also it is pointed out that the reconstruction works better for a lower dislocation density, i.e. as long as the transformation is well-characterised by a set of ORs (which is mainly the case for coherent transformations, see subsection 3.5.3).

Initial studies assumed that the initial austenite is homogeneous (which obviously is not the case in general). A reconstruction method of the parent texture given the daughter texture expressed in terms of the coefficients of generalized spherical harmonics as well as the misorientation distribution function (MDF) of the daughter phase was already discussed by Sargent 1974; Kallend et al. 1976.

Cayron 2007 treated the transformation texture problem using the misorientations (called operators therein) between the lattice correspondence variants - LCVs (cf. group multiplication table, see e.g. Müller 2013) and wrote the python program ARPGE, also see

section C.1. In Cayron 2006 he described the character of these operators forming a groupoid (as opposed to a group). Beside considering theoretical ORs, his reconstruction was based on the use of average orientations within inherited grains.

Conversely, Miyamoto et al. 2010 proposed a reconstruction method using the local orientation of every pixel, pointing out that a reconstruction on a local (i.e., pixel-based) scale is preferable because it allows the orientation gradient within martensite domains grains to be taken into account in the reconstruction process in highly deformed steels. L. Germain et al. 2012 considered irrational orientation relations in the reconstruction process noting some improvements for low alloyed steels with $C < 0.2$ wt%. Finally, Bernier et al. 2014 combined the features of orientation relationship refinement, the local pixel-by-pixel analysis and the nuclei identification and spreading strategy. A reconstruction strategy exploiting the hierarchical microstructure of lath martensite, specifically the notion of packets has been proposed by Zachrisson et al. 2013.

3.5 Crystallographic Theories for Martensite Formation

The words continuity, coherency and compatibility are used synonymously in this section. In the literature coherency is commonly used in crystallography / materials science, compatibility in continuum mechanics and continuity in mathematics. The description of compatibility is a question of scale.

Apparently, due to the multi-scale nature of microstructure deformations, the same framework of linear mappings is applied on many different scales. Here, the lowest and second lowest scales where it has been applied are treated. Particularly, the lower scale is essentially a 2D representation of the higher scale near an (assumed) planar interface. If a homogeneous deformation describes the deformation at a higher scale, its rotational part (\mathbf{R}) can often be neglected (since microstructure formation averages it out). In a crystallographic description on the micro and sub-micro scale however, \mathbf{R} is the rotation the transforming domain of a lattice (e.g. inclusion) has to undergo while the surrounding matrix remains invariant. Therefore, its characterisation is crucial (it is important to emphasize that it is not a rigid body rotation). In general, while a variety of criteria have been considered for validating crystallographic calculations, surprisingly that of \mathbf{R} has not been given enough significance. It is generally, advised to search for solutions where the

rotation is negligibly small (either directly as a result of compatibility or due to a suitable homogenization process).

Furthermore, the fact that each deformation component in a multiplicative decomposition of the deformation gradient \mathbf{F} (as elaborated in the following sections) is large, the order of the decomposition plays a role. Normally it cannot be based on physical grounds (also see section 6.1) which beside simplicity is another reason why an additive decomposition is preferred.

3.5.1 Continuum and Lattice Perspective of Compatibility

The state of compatibility of enclosed particles is usually defined in terms of the continuum concept of continuity of displacements and tractions across the interface. Any global minimum of strain energy corresponds to a stress-free configuration further away from the particle (no far field stresses). Again, it is the scale at which the problem is described that defines what is "far".

Continuum theories postulate that the crystals need not fit together on an atomic scale provided that the atomic misfit does not accumulate, so that there is an average fit at a higher scale. Whether this theory is appropriate depends on the nature of the interfaces and the absolute size of domains for which the assumption of a homogeneous deformation is justified. In the continuum treatment the problem reduces to a geometric one (geometric constructions of invariant planes, invariant lines using strain ellipsoids, see e.g. Wayman 1964; Christian 1965), dealt with in subsection 3.5.3. Beside the geometric description, a structural stretch tensor \mathbf{U}_S based on the Cauchy-Born Rule (CBR) (elaborated in subsection 3.5.2) is another postulate in the continuum picture.

Note that also an inhomogeneous deformation like lattice invariant shear / deformation LIS / LID is considered as macroscopically homogeneous resulting in the matrix form of Equation 3.5. Therefore the continuum theory is basically a "continuum plasticity" matrix description superimposed on a lattice, although the lattice invariant deformation is interpreted in terms of discrete slip or twinning events. The only difference to crystal plasticity is that the evolution of the plastic strain does not evolve incrementally, but each active shear is taken as a single matrix operation. Therefore, the order of the matrix operations does matter. Particularly the rotational term usually comes last, which often cannot be physically justified.

In any case atom movements during transformation are homogeneous only over a localized region (e.g. it may be found in optical microscopy that scratches on surfaces remain straight lines). An adjacent region is formed by a different deformation in a way that accommodates the neighbouring deformation. The following three points, as also pointed out by G. B. Olson et al. 1986 should be considered:

1. The rotational part of the crystallographic mapping \mathbf{R} accompanying the transformation of an enclosed particle will tend to minimize rotation of directions of maximum dimension.
2. An inclusion will maximize and minimize its dimension in directions of minimum and maximum distortion (specified by the eigenvectors of \mathbf{U}) respectively.
3. An inclusion which minimizes surface energy will adopt a morphology which maximizes the coincidence of lattice sites in its interface. The probability of a site coincidence along a particular plane or direction scales with the packing density.

Only principles 1 and 2 are considered in the continuum theory. In the theory of martensite formation the deformation, motivated by the experimentally observed morphology of martensite, forming martensite domains are argued to be, or at least to be close to, an invariant strain (IPS see subsection 3.5.3.2; limiting case of an infinitely thin, plate inclusion), where the invariant plane generally is called habit-plane. Then in analogy to lattice correspondence- / orientational (e.g. KS- or NW-variants, see section 3.4) symmetry considerations lead to habit plane variants (HPVs). As opposed to lattice correspondence variants, habit plane variants incorporate the full shape transformation including stretches.

In highly dislocated lath martensite, beside the definition as plane of a plate-shaped crystal, the habit plane has been defined as the average plane of a semi-coherent plane glissile interface on the atomic interface / level (Maresca et al. 2017) and the average interface orientation on the higher block / packet level.

From a discrete lattice viewpoint the state of coherency of enclosed particles is controlled by the extent of lattice-invariant deformations that relax these displacements and tractions. They in turn are governed by the coherency of interfaces, defined in terms of the discrete lattice concept of continuity of corresponding crystal planes and lines across interfaces. If coherency at interfaces cannot be achieved additional dislocations are necessary locally at

the interface (semi-coherent / commensurate interfaces). Christian 1965 points out that: "The motion of a coherent boundary produces a macroscopic change of shape which is specified by the lattice correspondence. If the boundary is incoherent, there is no correspondence and no shape change when it moves." The evolution of the correspondence (cf. update of glide system orientation in large strain crystal plasticity) should be investigated. The vital question in this regard is to which extent the interface can accommodate, which in turn depends on the amount of diffusional component of the transformation, the type of interface or the types of defects forming the interface, the difference of the compliances of the accompanied phases etc. Theories that have been developed to tackle this problem at the discrete lattice scale (they define a local correspondence at the interface) are elaborated in subsection 3.5.5. Note that such theories should be applied for the phase field method at the crystallographic level.

For irregular and fine microstructures, such as in the case of lath martensite, it is difficult to quantify a compromise between surface and strain energies. Note that the relative importance of these factors is influenced by a size-dependent surface to volume ratio of crystal domains, varying significantly (relative to each other) on a low scale. Considering the fine microstructural features of lath martensite the continuum theory has been criticised to produce unrelaxed configurations at the interface, see e.g. R. Pond et al. 2003. However, the scale of the discrete interface approaches is too low to be used in a continuum model at the grain scale (individual martensite laths / subunits). Unfortunately, no attempt to homogenize results of discrete interface approaches to a higher scale has yet been followed. In this work, such a homogenization approach is attempted utilizing averaged compatibility conditions, see section 3.9.

In accordance with the discussion between continuum and lattice coherency in subsection 3.5.1, Sutton et al. 1995 define macroscopic and microscopic geometrical degrees of freedom (DOFs) for an interface. The macroscopic DOFs determine the particular OR and interface of a bicrystal (see Figure 3.9). The microscopic DOFs describe the atomic structure of the interface. They are determined by relaxation processes. Macroscopic DOFs specify BCs far from the interface and the microscopic DOFs adjust in such a way as to minimize the free energy of the system subject to BCs.

Crucial differences between continuum and discrete interface theories are given here ex ante. First, essentially many of the differences come down to the definition of bases /

coordinate systems for the two regions separated by an interface and how they are related to each other (correspondence). Historically (up to today) in the continuum theories a constant correspondence (Bain correspondence) has been assumed and all calculations are carried out in the coordinate frame of the parent lattice. Essentially, this assumption is a sufficient one if the interface is (and remains) a coherent one during transformation (rotation of the interface and hence partitioning of deformation is not necessary).

Only Cayron 2015 proposed a model with varying correspondence subsection 3.5.4, but never emphasised it (took a fixed value in the end). In the discrete theories the selection of a reference basis is one of the key points of the solution process. Beside the assumption of an invariant parent reference, a median reference basis (equal partitioning between interfaces; reference lattice halfway rotated between the two lattices) and a coherently strained interface unit (a so-called terrace plane), which is found from the study of dichromatic patterns / complexes introduced in subsection 3.5.5), is emphasised. Continuum theories additionally require a specification of deformation modes e.g. allowed slip (highly ambiguous) or twin systems (less ambiguous) and yield a strain based on geometrical arguments. Results must be checked a posteriori against experimental data as outlined in section 3.10. Discrete interface theories on the other hand require an coherent reference state (e.g. specified by an orientation relation) and yield lattice invariant deformation modes.

3.5.2 Structural Stretch Tensors

The Cauchy-Born rule (CBR) is a easy way of correlating changes in positions of atomic or molecular theories to descriptions of deformations in continuum theories. A homogeneous deformation gradient \mathbf{F} is applied to a reference set of lattice vectors giving another possible set of lattice vectors in the deformed crystal. If \mathbf{F} does not contain any plastic / lattice invariant / inhomogeneous deformation its positive definite symmetric part \mathbf{U} (stretch part / structural stretch tensor / "natural" lattice deformation) in steels is widely known as the Bain strain \mathbf{B} after Bain et al. 1924, transforming a f.c.c. into a b.c.c. or b.c.t. lattice. The question of validity of the CBR is e.g. discussed in Ericksen 2008. Therein, it is pointed out that although extensive plastic deformation takes place in the f.c.c. \rightarrow b.c.c. transformation the CBR is valid in the sense that the Bain strain is generally accepted for characterising the transition.

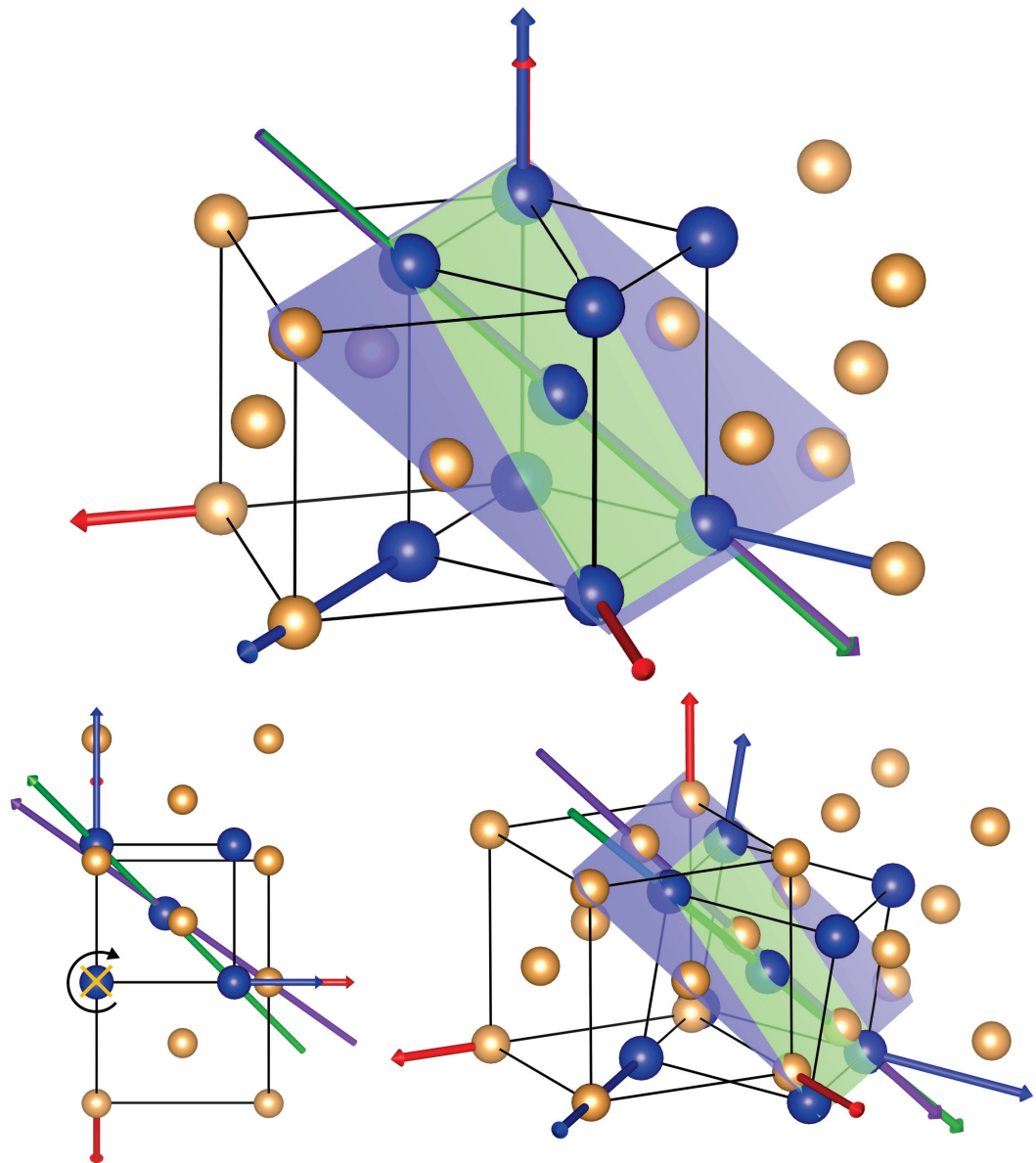


FIGURE 3.4: Bain strain \mathbf{B} model. Golden atoms (f.c.c) remain invariant. Top: Initial b.c.t unit cell, that can be drawn into two neighbouring f.c.c unit cells (Bain OR, blue atoms coincide with golden ones). Lower-Left: $\langle 100 \rangle_{\text{bcc}}$ projection after application of \mathbf{B} morphing b.c.t \rightarrow b.c.c. Lower-right: Other view of right illustrating that a rotation around a specific $\langle 100 \rangle_{\text{bcc}}$ aligns $\{111\}_{\gamma} \parallel \{011\}_{\alpha'}$ (violet \parallel green plane), as e.g. pointed out by Maresca et al. 2017. Graphics have been produced with VESTA (Momma et al. 2011).

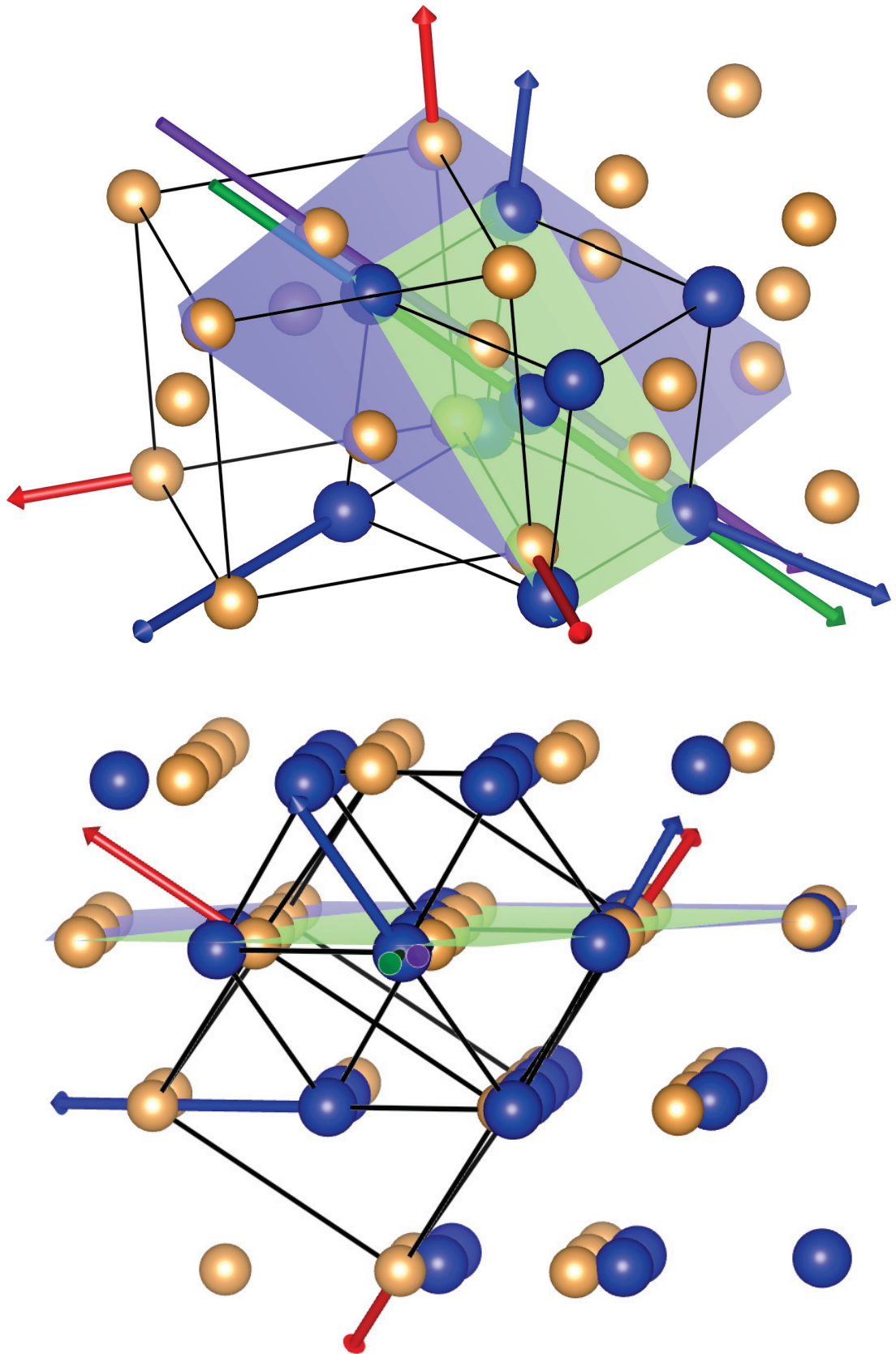


FIGURE 3.5: Two views of a Kurdjumov-Sachs OR, i.e. after application of the in-plane rotation aligning $\langle 110 \rangle_\gamma \parallel \langle 111 \rangle_{\alpha'}$ (violet \parallel green arrow). Experimentally, a distribution of the in-plane rotation angle θ_{KS} with a maximum between the KS and NW directions is observed. In the lower picture the correlation between row / edge matching between the phases as emphasised in subsection 3.5.5 and the KS directions is illustrated (slightly tilted projection along these directions).

The correspondence matrix $\mathbf{C}^{\alpha\gamma}$ as well as the Bain-strain \mathbf{B} can be directly derived from Figure 3.4 (top) in terms of a linear combination of parent phase basis vectors (red) to form the product phase basis vectors (blue). One possibility in accordance with Figure 3.4 is:

$$\mathbf{C}^{AB} = \begin{bmatrix} 1/2 & -1/2 & 0 \\ 1/2 & 1/2 & 0 \\ 0 & 0 & 1 \end{bmatrix} \quad (3.18)$$

$$\mathbf{B}_3 = \begin{bmatrix} \sqrt{2} \frac{a_\alpha}{a_\gamma} & 0 & 0 \\ 0 & \sqrt{2} \frac{a_\alpha}{a_\gamma} & 0 \\ 0 & 0 & \frac{a_\alpha}{a_\gamma} \end{bmatrix} \stackrel{\text{MarvalX12}}{=} \begin{bmatrix} 1.1311 & 0 & 0 \\ 0 & 1.1311 & 0 \\ 0 & 0 & 0.7998 \end{bmatrix} \quad (3.19)$$

with a_α , a_γ lattice parameters. If the factor $\sqrt{2}$ is already taken into account in $\mathbf{C}^{\alpha\gamma}$ it automatically represents the orientation relation (rotation) $\{100\}_\gamma \parallel \{011\}_{\alpha'}$ $\langle 100 \rangle_\gamma \parallel \langle 011 \rangle_{\alpha'}$ referred to as Bain orientation relation (OR). Since the Bain OR is practically never observed, but rather the Kurdjumov-Sachs OR illustrated in Figure 3.5, it should become clear that a lattice correspondence does not imply an OR, but that additional lattice rotations arise.

There are methods to identify most favourable correspondences in terms of maximum principal deformation or of some norm of the total deformation, see Chen et al. 2016; K. Koumatos et al. 2016. It is an interesting fact that the Bain deformation involves the absolute minimum of overall atomic movements in generating the b.c.c. from the f.c.c. lattice K. Koumatos et al. 2016 (except maybe for only a couple of atoms Chen et al. 2016), i.e. there is an inherent size effect.

A crucial point to keep in mind is that there is no investigation of the CBR or optimality of the structural stretch tensor that permits a varying degree of plastic shear (which apparently favours the transformation by offering an easy nucleation mechanism). It would be interesting to see how the optimum changes in terms of an energy norm.

The selection of the lattice correspondence is the first step in any crystallographic continuum theory. Note that without lattice invariant deformation, the correspondence automatically fixes the directions of the principal axes and the magnitudes of the principal strains of the lattice deformation.

Note that $\mathbf{C}^{\alpha\gamma}$ in general only describes the displacements of a fraction of atoms to define the new lattice. The remaining atoms may shuffle in various ways giving rise to different space group symmetries, but it is the linear / homogeneous transformation (deformation gradient) that relates to macroscopic deformation and therefore to conditions of continuum compatibility Chen et al. 2016. Christian 1997 notes that in general there is more than one plausible set of shuffles, so that the final site of every atom cannot always be specified unambiguously.

3.5.3 Crystallographic Continuum Compatibility

Note that the eigenvalues λ_i of a symmetric matrix \mathbf{A} (equivalent to its singular values in this special case) are the square roots of the eigenvalues of the matrix $\mathbf{A}^T \mathbf{A}$. Also note that

$$\mathbf{F}^T \mathbf{F} = (\mathbf{R}\mathbf{U})^T (\mathbf{R}\mathbf{U}) = \mathbf{U}^T \mathbf{R}^T \mathbf{R} \mathbf{U} = \mathbf{U}^T \mathbf{U} = \text{''}\mathbf{U}^2\text{''} \quad (3.20)$$

hence $\lambda_i^2(\mathbf{F}) = \lambda_i(\mathbf{F}^T \mathbf{F})$.

Note that some authors Khachaturyan 1983; Qi et al. 2014; Christian 1965 use the $\lambda_i^2(\mathbf{F})$, while others (J. Ball et al. 1987; Bhattacharya 2003) denote the eigenvalues of the matrix \mathbf{U}^2 as λ_i .

3.5.3.1 Invariant lines

In an invariant line strain (ILS), as the name suggests, a line remains geometrically invariant (undistorted and unrotated). A ILS is always accompanied by a plane strain. Plane strain means that the normal vector of a plane is undistorted and unrotated (however rotation around the plane vector as well as distortion in the plane is allowed). One eigenvalue λ_i of \mathbf{F} must be one ($\lambda_i = 1$) **or** exactly one is smaller or larger one (equivalently one principal strain $\lambda_i^2 - 1$ be zero, **or** has the opposite sign from the other two). The Bain strain (Equation 3.19) even defines a cone of undistorted lines because two eigenvalues are equal.

Practically, applying any deformation to a (unit) vector \mathbf{x} , i.e. $\mathbf{F}\mathbf{x} = \mathbf{x}'$ the rotation (written as axis-angle pair)

$$\mathbf{R} [\mathbf{x} \times \mathbf{x}', \arccos(\mathbf{x} \cdot \mathbf{x}')] \quad (3.21)$$

rotates the line back to its initial orientation. Additional deformation in general is necessary in order for it to be completely invariant, i.e. also unstretched.

Any ILS can be decomposed into two invariant plane strains (IPS, see subsection 3.5.3.2), with the invariant line lying at the intersection of the invariant planes.

$$\mathbf{F}^{\text{ILS}} = \mathbf{F}_1^{\text{IPS}} \mathbf{F}_2^{\text{IPS}} = \mathbf{S}_1 \mathbf{S}_2 \quad (3.22)$$

In the case that the two IPSs have the same invariant-plane, or the same displacement direction, then their combined effect is simply another IPS.

Particularly, morphing the lattice with two simple shears provides for a common nucleation model. This line of thinking already started by Kurdjumov et al. 1930 proposing a two-shear nucleation model (two consecutive plastic shears that directly morph austenite into martensite). Burgers 1934 deduced a double shear theory assuming hard spheres for a zirc-alloy. His model was applied by Bogers et al. 1964 for the f.c.c-h.c.p.(ϵ -martensite) transformation. J. A. Venables 1962 was one of the first to study this model using TEM. Later, it was thermodynamically described by G. B. Olson et al. 1976a; G. B. Olson et al. 1976b; G. B. Olson et al. 1976c (Burgers-Bogers-Olson-Cohen Model, cf. stacking fault model). The model has recently been supported by in-situ HRTEM experiments Yang et al. 2015; Yang et al. 2017.

Dahmen 1982 used the ILS assumption for studying orientation relations for precipitations in the Fe-Cu system based on the experimental observation that they form very long and fine precipitates.

In Nishiyama et al. 1978; Christian et al. 1995b; H. Bhadeshia 1987 (also elaborated in subsection 3.5.5) it is pointed out that an ILS has a kinematic role (the interface must remain mobile / glissile) for the formation of ferrous martensite laths if the moving interface is formed by dislocations. Therefore the factorization

$$\mathbf{F}^{\text{ILS}} = \mathbf{F}_1^{\text{IPS}} \mathbf{S}_1 \quad (3.23)$$

is sometimes argued to fulfil both the mobility as well as the IPS criterion. However, nothing is said about how to form $\mathbf{F}_1^{\text{IPS}}$ in the first place, which is generally not possible without further shears conflicting the mobility argument.

3.5.3.2 Invariant Plane Strain (IPS) - Generalities

Cermelli et al. 1994 denote the relative deformation between two regions on either side of an interface undergoing homogeneous deformations \mathbf{F}_1 and \mathbf{F}_2 as coherency tensor \mathbf{H} (also misfit)

$$\mathbf{H} = \mathbf{F}_2^{-1}\mathbf{F}_1 \quad (3.24)$$

Note that if only rotational contributions are considered (e.g. for rotated lattices), this corresponds to the misorientation already introduced in Equation 3.15. Also the interface defect operator in Equation 3.38 is defined in analogy (the only difference being that in general translations are included).

The interface is an invariant plane or the relative deformation \mathbf{H} is an invariant plane strain (IPS) \mathbf{F}_{IPS} if:

$$\text{rank}(\mathbf{F}_1 - \mathbf{F}_2) = 1 \quad \text{or} \quad \mathbf{F}_1 - \mathbf{F}_2 = \varepsilon_0 \mathbf{d} \otimes \mathbf{h} \quad (3.25)$$

where \mathbf{d} gives the direction / is collinear with the ("macroscopic") shape deformation (shearing), \mathbf{h} is the interface normal (both unit vectors) and ε_0 is the magnitude of deformation in direction \mathbf{d} . Experimental evaluation of the shape strain normally comes from a surface relief measurement. However, it should be kept in mind that the stress state at the surface is substantially different than in the bulk, so that higher magnitudes of deformation ε_0 may be tolerable. Typical values for ε_0 are in the range between 0.2-0.5 for steels.

Since self-accommodation is of importance it must be pointed out that for Equation 3.25, by construction if the shape strain tends towards zero $|\varepsilon_0| \rightarrow \det(\mathbf{F}_{\text{IPS}}) - 1 = \varepsilon_0(\mathbf{d} \cdot \mathbf{h})$ this corresponds to an optimal accommodation (in the unloaded, untextured case). The stress free fit, i.e. perfect self-accommodation is theoretically only possible if the volume does not change during transformation i.e. $\det(\mathbf{F}_{\text{IPS}}) = 1$ and hence $|\varepsilon_0| \rightarrow 0$ and $\mathbf{H} \rightarrow \mathbf{I}$.

Equation 3.25 is also referred to as Hadamard compatibility condition (continuous change of homogeneous deformation). Note that simple shears $\{\mathbf{S}_i\}$ are special cases of an IPS, i.e. $\{\mathbf{S}_i\} \subseteq \{\mathbf{F}_{\text{IPS}}^i\}$ ($\mathbf{d} \perp \mathbf{h} \implies \Delta V = 0$). As opposed to plastic deformation for evolving strains during phase transformation in general $(V - V_0)/V_0 = \det(\mathbf{F}_{\text{IPS}}) - 1 = \varepsilon_0(\mathbf{d} \cdot \mathbf{h}) \neq 0$.

Considering the polar decomposition theorem a particular basis can be found by multiplying with rotations, where Equation 3.25 is of the form:

$$\mathbf{R}\mathbf{U}_1 - \mathbf{U}_2 = \varepsilon_0 \mathbf{d} \otimes \mathbf{h} \quad (3.26)$$

If plastic deformation is included, it should be noted that the pure stretch \mathbf{U} does not coincide with the structural stretch tensor \mathbf{U}_S , but also includes the stretch part from the plastic shear! (also the rotation includes a component due to the plastic shear).

Following J. Ball et al. 1987; Bhattacharya 2003, denoting the eigenvalues of the matrix $\mathbf{C} = \mathbf{U}_2^{-T} \mathbf{F}_1^T \mathbf{F}_1 \mathbf{U}_2^{-1}$ (cf. Equation 3.24 and Equation 3.20) as $\lambda_{i(c)}$, solutions to Equation 3.25 exist if the $\lambda_{i(c)}$ (sorted in ascending order) fulfil

$$\lambda_{1(c)} < 1, \quad \lambda_{2(c)} = 1, \quad \lambda_{3(c)} > 1 \quad (3.27)$$

(equivalently one principal strain $\lambda_{i\mathbf{F}}^2 - 1 = 0$ **and** the other two have opposite signs). Explicit formulae to obtain \mathbf{d} , \mathbf{h} and ε_0 in the most general case expressed in terms of the eigenvalues (λ_i) and corresponding eigenvectors have been worked out e.g. by J. Ball et al. 1987; Khachaturyan 1983; Bhattacharya 2003 on the premise that the matrix \mathbf{C} does not comprise a rotational part. The rotation \mathbf{R} is obtained by rearranging Equation 3.26 and inserting \mathbf{d} , \mathbf{h} and ε_0 . There are 4 solutions due to sign changes in general, however often these are degenerate (as in the case of the cubic to cubic transformation where solutions come in pairs).

A twin is characterised by two symmetry related structural stretch tensors \mathbf{U}_1^S and \mathbf{U}_2^S corresponding to energy wells (see Figure 6.2) without requiring any lattice invariant deformation. The variable parameter of the twinning shear is either the twin plane normal vector (typically denoted as K1) or twin direction $\boldsymbol{\eta}_1$ (selection of one fixes the other). The two \mathbf{U}_i^S can, but need not be different. If the two \mathbf{U}_i are equal the choice of K1 and $\boldsymbol{\eta}_1$ is severely restricted. Either K1 (defined in the parent phase) must be a mirror plane or the $\boldsymbol{\eta}_1$ direction must be derived from a two-fold symmetry axis of the parent matrix (Mallards law, see e.g. Bhattacharya 2003). Importantly, this is the case in the cubic system.

From Figure 3.2 it is evident that mathematically / from a continuum perspective the shear due to slip and a twinning lamellae is equivalent, if the twin plane ($K1$) corresponds to the slip plane \mathbf{m} and the twinning shear deformation ($\boldsymbol{\eta}_1$) is parallel (edge dislocation)

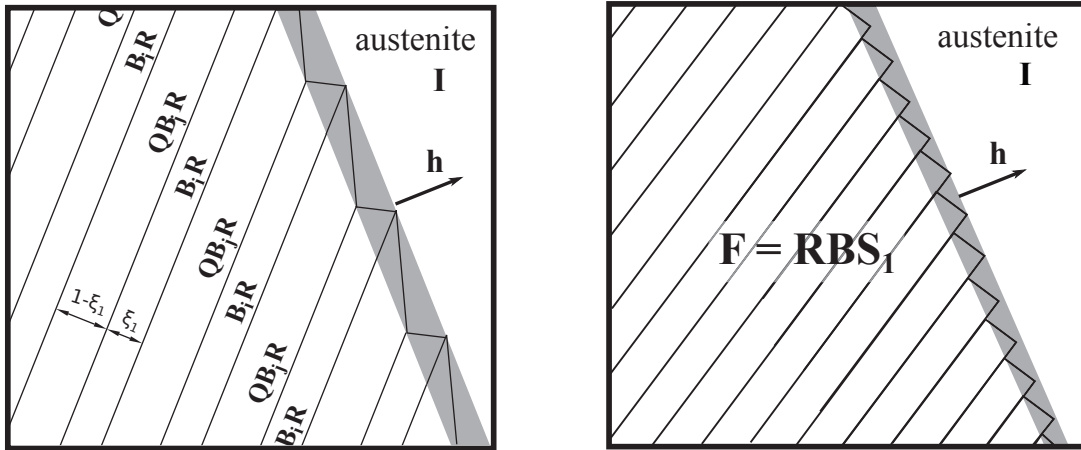


FIGURE 3.6: Formal equivalence of an invariant plane strain on one side of an interface, constructed (left) by a twinned laminate of alternating stretches (modulated / adaptive martensite) or (right) by one homogeneously distributed, straight dislocation lines. In the former case an IPS can be obtained by varying ξ_1 (cf. Equation 3.30), in the latter by ε_s (cf. Equation 3.5). Generally, the variety of ILSs/ILPs solutions using shears is much larger, but the scale at which the concept of a homogeneous shear applies is much smaller than as a consequence of a twin laminate.

or normal (screw dislocation) to the Burgers vector, cf. Equation 3.5. Notably, the same holds for a laminate of twins, where the overall shear magnitude is determined by the fraction of each twin lamella, cf. Figure 3.6 and Equation 3.30.

The matrix \mathbf{C} (modification of its eigenvalues to Equation 3.27) in general is constructed using a combination of structural stretch tensors \mathbf{U}_i^S (e.g. the Bain strain Equation 3.19), rotations \mathbf{R}_i and slip shears \mathbf{S}_i as outlined in the next sections.

Note that since purely geometrical arguments are used, for each solution it must be checked a-posteriori whether it is reasonable by comparing it against experimental results such as orientation relations, habit plane orientation etc. Particularly, recalling the principles mentioned in subsection 3.5.1, in the author's opinion, a final check of the resulting \mathbf{R} has not received enough attention in the case of lath martensite.

Subsequently, a short historical review is given in order to better understand the diverse literature. In the case of martensite, the seminal works by Wechsler et al. 1953 for the $\{3\ 10\ 5\}_\gamma$ habit plane between austenite and a twinned martensite laminate (proposed for high carbon, twinned b.c.t. martensite steels) and Bowles et al. 1954, allegedly proposed independently, remain most cited. The latter introduced a dilation parameter $\det(\mathbf{F}_{\text{IPS}}) - 1 = \varepsilon_0(\mathbf{d} \cdot \mathbf{h})$ normal to the habit plane in order to account for the volume change since

they do not presuppose the Bain strain. After their treatment the field split into two groups. The first added plasticity in a continuum averaged sense (continuously smeared slip resulting in a homogeneous, simple shear, Wayman 1964; Christian 1965; H. Bhadeshia 1987) in analogy to what is done in crystal plasticity. A drawback of such an approach is that the obtained set of possible solutions merely fulfilling the IPS condition is vast if any combination of arbitrary shears is allowed. Solutions then are selected according to experimentally observed microstructural features (i.e. via an inverse approach).

The other (more mathematical) group limited the range of linear mappings such that plastic deformations are excluded (Ericksen-Pitteri neighborhood, see Pitteri et al. 1998) and generalized the notion of (rank-one) compatible deformations in the framework of non-linear elasticity (e.g. compatible laminates of twins). Particularly in the works of J. Ball et al. 1987; Kohn 1991; Bhattacharya 2003 it is argued that the main crystallographic characteristics are derived by energy minimization for elastic materials at finite strains (often referred to as mathematical theory of martensitic microstructure). As the global minimum of energy corresponds to a stress-free configuration, the problem reduces to the geometric one. Again it must be emphasised that slip is not considered in this theory!

While this framework may be more limited in deformation modes compared to slip (at least without considering higher order laminates / macro twins, see e.g. J. Ball 2004; Mühlemann et al. 2015; Petersmann et al. 2017b) the advantage is that the twin-laminate shear magnitudes follow directly from the requirement of compatibility.

Note that the plastic shear incorporated in theory is the same as in crystal plasticity, which in turn is normally incorporated under the premise of maximum dissipation, see subsection 6.4.2. It is, however, difficult to incorporate this principle for the selection of the integral shear(s) since the selection is a compromise between both energy minimization and dissipation maximisation. Notably, dissipation mainly emanates from the movement of the incoherent interface, references can be found at the end of subsection 6.4.2.

3.5.3.3 IPS including Slip (Reconstructive)

Despite austenite is considered the easier deformable phase the austenite-martensite interface is always described with austenite remaining unaffected by deformation, i.e. represented by \mathbf{I} , i.e.

$$\mathbf{RB}_i \prod_j \mathbf{S}_j - \mathbf{I} = \mathbf{F}_{\text{IPS}} - \mathbf{I} = \varepsilon_0 \mathbf{d} \otimes \mathbf{h} \quad (3.28)$$

It is argued that since the transformation takes place in the interface the shears \mathbf{S}_i can be selected from both sides of it, i.e. slip systems of both the austenite and martensite. Crocker 1965; Nishiyama et al. 1978; P. M. Kelly 1992 found that the $\{557\}_\gamma$ habit plane of individual laths can be explained utilising $\mathbf{F}_{\text{IPS}} = \mathbf{RBS}_2\mathbf{S}_1$. Iwashita et al. 2011 used the additive decomposition (small strain) and Miller-index representation of shears following Khachatryan 1983 to obtain a similar result. Note that more than two shears are generally very unlikely since the dislocations would intersect each other and make the interface immobile / sessile (see subsection 3.5.5). In subsection 3.5.3.4 utilizing the continuum analogy between slip and twinning the formalism to obtain this HP from a hierarchy of twinned laminates is outlined.

The invariant parent phase - slipped martensite theory is very successful in the case of f.c.c–h.c.p. transformation such as the high temperature transformation in titanium alloys, particularly titanium-aluminides (\mathbf{BS}_1) see Mayer et al. 2016 or the transformation in cobalt base alloys, see Weikensteiner, Petersmann et al. 2018 (in preparation). Figure 3.7 shows the accordance of the theoretical orientation of habit planes with calculated ones in Ti-Al-3Mo.

A factor to bear in mind is that the lattice-invariant shear is an integral part of the transformation, i.e. it does not proceed independently before or after the lattice change has occurred. According to Wayman 1964 for relaxed lath martensite it is of utmost importance to distinguish between the lattice invariant shear, which is a part of the transformation mechanism, and plastic deformation arising from distortion of the martensitic phase itself. However, the latter contribution has up to now not been considered at the continuum theory as above, although new developments in the theory of crystalline interfaces use this concept as well, see subsection 3.5.5.

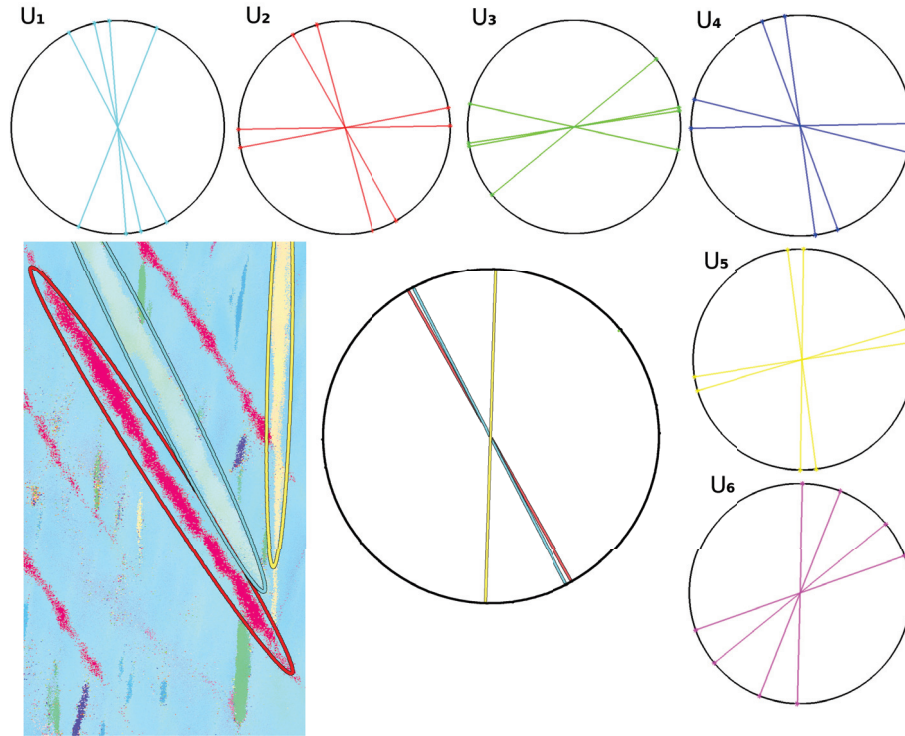


FIGURE 3.7: Traces of calculated habit planes of martensite with the surface recorded via EBSD (given in terms of a lattice vector) taken from Mayer et al. 2016. The color-code in the EBSD mapping and the traces correlates. U_1-U_6 denote the symmetry variants of the structural stretch tensor. Note, that in general four IPS solutions occur together. In this case the other phase easily enables a determination of the relative orientations and only a small amount of plastic slip is necessary in order to enable an invariant plane strain.

A partitioning of the deformation between martensite and austenite has been recently observed by J. Liu et al. 2017 in an in-situ TEM study. The obvious extension of the current theory therefore is

$$RB_i \prod_j \mathbf{S}_j - \prod_k \mathbf{S}_k = \mathbf{F}_1^{\text{IPS}} - \mathbf{F}_2^{\text{IPS}} = \varepsilon_0 \mathbf{d} \otimes \mathbf{h} \quad (3.29)$$

Here the \mathbf{S}_j may be selected from both phases whereas the \mathbf{S}_k are exclusively austenite systems. The latter could be identified by studying the role of the atomic interface structure on the nucleation of glissile dislocations from a low energy, atomically flat, incoherent f.c.c – b.c.c. interface. Such studies have already been carried out by R. Zhang et al. 2011; R. Zhang et al. 2012 particularly for the KS orientation relationship. Such an ansatz may also explain why neighbouring domains form subsequently instead of simultaneously.

3.5.3.4 IPS by Transformation Twinning (Purely Displacive)

Mühlemann et al. 2015 explained the $\{557\}_\gamma$ habit plane in terms of hierarchical twinning / twins within twins / a second order laminate, i.e. a double shear in the algebraic sense. The general idea is the following: If $\det(\mathbf{U}_i^S) = 0$ (in this case Equation 3.44 is automatically fulfilled), the limit of an energy minimising sequence is given by (see Figure 3.6)

$$\mathbf{F} = (1 - \xi_1)\mathbf{U}_1^S + \xi_1\mathbf{R}\mathbf{U}_2^S \quad (3.30)$$

This is taken as an average / total shape deformation (laminate deformation). For a cubic to tetragonal transformation there exist at most 24 twinned-laminate to austenite solutions (Hane et al. 1998). Using Equation 3.26, one \mathbf{U}_i^S can be eliminated from Equation 3.30. Note that for two different \mathbf{U}_i there are 4×2 possibilities (exchange of \mathbf{R} and ξ_1). Using $\mathbf{U}_i^S = \mathbf{B}_i$ yields e.g.

$$\mathbf{F} = \mathbf{B}_i + \xi_1\boldsymbol{\eta} \otimes \mathbf{K} = \mathbf{B}_i (\mathbf{I} + \xi_1\mathbf{B}_i^{-1}\mathbf{K} \otimes \boldsymbol{\eta}) = \mathbf{B}_i\mathbf{S}_{\xi_1} \quad (3.31)$$

$$\text{where } \mathbf{S}_{\xi_1} = \mathbf{I} + \xi_1\mathbf{B}_i^{-1}\boldsymbol{\eta} \otimes \mathbf{K} = \mathbf{I} + \langle 1\bar{1}0 \rangle_\alpha \otimes \{110\}_\alpha \text{ is a simple shear} \quad (3.32)$$

If the same formalism is repeated once again the macroscopic deformation of twins within twins (double shear) is obtained as

$$\mathbf{F} = \mathbf{B}_1 + \xi_1\boldsymbol{\eta} \otimes \mathbf{K} + \xi_2\boldsymbol{\eta}_{\xi_1} \otimes \mathbf{K}_{\xi_1} = \mathbf{B}_1\mathbf{S}_2(\xi_1, \xi_2)\mathbf{S}_1(\xi_1) \quad (3.33)$$

$$\text{where } \mathbf{S}_2 = \mathbf{I} + \xi_2\mathbf{B}_1^{-1}\boldsymbol{\eta}_{\xi_1} \otimes \mathbf{S}_1^{-T}\mathbf{K}_{\xi_1} \quad (3.34)$$

The results are identical to the double shear case using specific twinning shears ($\{112\}_\gamma$) in subsection 3.5.3.3, but the origin is different. Due to this analogy the twin shear direction of the laminate is often argued to be also active for the plastically sheared case. Their ansatz is supported by recent TEM studies P. Zhang et al. 2016; Man et al. 2018. Recently, K. Koumatos et al. 2018 (re-)published their work with a Matlab toolbox and an emphasis on this analogy (plastic doubleshear). However, they still did not check their results against Equation 3.44.

Bartel et al. 2009; Bartel et al. 2010; Hackl et al. 2014 (cf. lamination theory) present a slightly weaker version of the above construction by introducing the notion of a quasiconvex hull and the direct specification of a (semi-empirical) fluctuation field that is derived

from the displacement field by perturbation (hence automatically fulfilling compatibility). Explicit formulae have been derived for second order laminates that can be readily used in evolution equations (also see Hackl et al. 2008a; Peigney 2016).

Other rank-one constructions like wedge or diamond shapes can be found in Bhattacharya 2003. The basic idea is to construct coupled compatibility equations (in those cases there are points that must full-fill 3 and more equations simultaneously).

3.5.4 Theories Considering Continuous Features of Orientation Relationships and Kinematics of Sphere Packings

The following crystallographic models present interesting characteristics, in particular they do not presuppose any macroscopic criterion of inelastic deformation. Orientation relations are taken as inputs in these theories. An advantage of these theories is that statistical information about orientation relations is readily obtained by two-dimensional EBSD measurements.

It is anticipated that in these theories few to nothing is said about morphology although arguments are based on lamination, similar to twinned microstructures.

Muehlemann et al. 2016 proposed to relax the initial postulate of an invariant plane strain to an unrotated plane strain for the calculation of transformation strains / habit plane variants. Their framework provides a one-to-one correspondence to orientational / correspondence variants. The work also gives a good overview of operators relating these variants.

As e.g. pointed out in K. Verbeken 2009 the poles in the pole figures of highly dislocated lath martensite steels exhibiting transformation induced plasticity are not discrete but continuous. This may be because both the Nishiyama Wassermann (NW) and Kurdjumov-Sachs (KS) OR (see Figure 3.4) together characterise 36 coherent transformations simultaneously occurring in steels, see e.g. Guo et al. 2004. Cayron et al. 2010 interpreted these continuous features in terms of the formation mechanism and proposed a two-step theory (via the intermediate h.c.p. ϵ - martensite phase). Their approach was reviewed by H. Bhadeshia 2011 pointing out that the continuous features are an artefact of the high dislocation density leading to a spread in diffracted intensity. He also pointed out that even if such predictions may be statistically representative on the meso scale they

should not be used in models considering crystallographic mechanisms. Cayron et al. 2011 correctly pointed out that the resolution of modern EBSDs ($\approx 1^\circ$) is quite high compared to the continuous features appearing in an interval of $\approx 5^\circ$.

Next, Cayron 2015 studied the way the atoms move by treating them as rigid spheres obeying rolling kinematics. The idea is to directly construct a displacive distortion that gives the final OR, i.e. the orientation relation implies the "natural deformation", contrary to other models where the lattice correspondence has to be assumed. Cayron 2015 classifies this transformation as "angular-distortive" and calls the resulting mappings distortional variants. The question is what orientation relation is considered as final configuration. If the KS OR is considered the model yields the same results as initially proposed by Jaswon et al. 1948. If the NW OR is considered, the result of the model coincides with that proposed in Bogers et al. 1964. A problem in the model is that the volume change is overestimated due to the hard sphere assumption (up to 8%). The model predicts the $\{225\}$ habit plane (commonly observed in martensites exhibiting butterfly morphology) as a composite block ($\xi = 0.5$) of two KS distortional variants, see Cayron et al. 2016 and the $\{557\}_\gamma$ habit plane as a composite block ($\xi = 0.5$) of two NW distortional variants, see Baur et al. 2017. Note that these two habit-planes occur in steels where twinning is predominant (the transformation is displacive in character). The $\{557\}_\gamma$ also occurs in dislocated lath martensite (see section 1.1), but not as a composite block. Furthermore, the results are equivalent to the twinned continuum theory for displacive transformations. Contrary to other theories the ratio of the lattice parameters does not play a role due to the rigid sphere assumption.

Summarizing this approach is interesting regarding displacive transformations, cf. Figure 2.1 particularly for the prediction of new twinning modes, see Cyril 2018. The author believes, however, that for highly reconstructive transformations such as the f.c.c. – b.c.c. accompanied by a phonon soft mode instability (see subsection 6.7.1) the "shear paradigm" (Cayron 2017) should still be followed.

3.5.5 Interfaces, Lattice Defects at Interfaces, their Characterisation and Resulting Theories of Lattice Coherency

Sutton et al. 1995; Howe 1997 distinguish between homogeneous interfaces, such as grain boundaries (GBs), twin boundaries, stacking faults and heterogeneous interfaces separating two crystals of different composition, different Bravais lattice or both. Heterogeneous interfaces, are further divided into coherent, semi-coherent / commensurate (some translation vectors, not necessarily primitive, of the two adjoining lattices are equal, leading to one- or two-dimensional periodic arrangements of dislocations in the interface plane) and incoherent / incommensurate (e.g. high angle grain boundaries - HAGBs). According to M. Cohen et al. 1992 the term semi-coherent / commensurate is generally used for a transforming domain undergoing sufficient plastic relaxation by slip or twinning in order to form an IPS.

In general, coherency requires the adjacent crystals to be strained. Very approximate expressions for this (purely elastic) coherency / misfit strain / disregistry that are commonly found are $\varepsilon = (\mathbf{a}_i - \mathbf{a}_j) / \langle a_j \rangle$ or $(\mathbf{a}_i - \mathbf{a}_j) / |a_j|$, where the \mathbf{a}_i are translation vectors of the lattice. The matching of rows of atoms (in the laths' $\langle 110 \rangle_\gamma$ long directions) in the f.c.c. – b.c.c. interface seems to be of high importance. Notably, an exact matching between a $(111)_\gamma$ and $(110)_\alpha$ monolayer can be reached if $\eta_3 = a_\alpha / a_\gamma = 0.9185$ or $a_\gamma / a_\alpha = r = 1.0887$ by rotating the monolayers through 5.26° , see Howe 1997 p.190-192 therein.

The degree of coherency of homophase low-angle tilt and twist grain boundaries LAGB ($\theta < 15^\circ$) can be described through dislocation based models and is characterised by the spacing between dislocations within the interface plane. If the misorientation angle of the interface is greater than 15° , the cores of the interfacial dislocations become too densely packed for an individual distinction, requiring a different description of the interface structure.

In the mid-1980s high-resolution TEM (HRTEM / phase contrast imaging allowing to view the atomic structure), became available to reveal the atomic structure of transformation interfaces, in particular interface steps (ledges in surface sciences see e.g. Shiflet et al. 1994)

associated with both diffusional and martensitic transformations (also see Figure 3.10). In-situ heating studies revealed how such steps propagated along the interfaces, e.g. Christian 1965; Mahon et al. 1989; Howe 1997.

Subsequently, the development of the defect theory of interfaces is outlined. Remarkably, much has already been theoretically predicted before observations of martensitic interfaces by means of HRTEM revealed that the interface of individual laths of martensite comprises coherent terraces reticulated by arrays of interfacial defects.

The Frank-Bilby-Bollmann equation Equation 3.35 arises from the incompatibility of the shape and lattice deformations. \mathbf{b}^c is the effective / net (misfit / anticompatibility, see Table 3.2) dislocation Burgers vector of the interface ("surface-dislocation" after Bullough et al. 1956) crossing a vector \mathbf{v} (probe vector) in this interface. \mathbf{b}^c is not unique because of the multiplicity of affine deformations which will generate one lattice from another. Bilby's original derivation starts with the dislocation density tensor and is somewhat cumbersome. An easier way to obtain the final equation based on circuit mapping through an interface can e.g. be found in Christian 1965 (p. 364-365 therein) or Nishiyama et al. 1978 (p.408 therein). In any case the result is:

$$\mathbf{b}^c = (\mathbf{F}_{\text{ref} \rightarrow \text{A}}^{-1} - \mathbf{F}_{\text{ref} \rightarrow \text{M}}^{-1}) \mathbf{v} = (\mathbf{F}_{\text{A} \rightarrow \text{ref}} - \mathbf{F}_{\text{M} \rightarrow \text{ref}}) \mathbf{v} \quad (3.35)$$

The matrices $\mathbf{F}_{\text{ref} \rightarrow \text{A}}^{-1}$ and $\mathbf{F}_{\text{ref} \rightarrow \text{M}}^{-1}$ represent the homogeneous deformations necessary to transform the reference crystals into their coherent forms. While initially the unstrained / natural lattice has been considered as reference, recent treatments prefer a coherently strained reference as elaborated subsequently. $(\mathbf{F}_{\text{ref} \rightarrow \text{M}}^{-1} - \mathbf{F}_{\text{ref} \rightarrow \text{A}}^{-1})$ is the terrace coherency strain $\mathbf{E}_{\text{ref} \rightarrow \text{c}}$. \mathbf{v} is a random / probe vector in the interface. Examples of coherency strains and related coherency dislocation networks are found in J.M. Howe 2009.

Taking the parent structure as reference lattice Equation 3.35 is equivalent to the "O-lattice" construction proposed by Bollmann 1971. A conceptual difference is that Bollmann considers solutions as discrete ($\mathbf{v} \rightarrow \mathbf{x}^o \in \text{O-lattice space}$), whereas Frank and Bilby envision continuous distributions of dislocations (although they are always quantized in the interface).

In this case the algebra is that of an invariant line. For the O-lattice and resulting cell structure treatment see e.g. W.-Z. Zhang et al. 1993a; W.-Z. Zhang et al. 1993b. This

is the most general but least quantitative theory. The equation may also be formulated in reciprocal space (plane vectors) where it is referred to as $\Delta\mathbf{g}$ method, see W.-Z. Zhang et al. 2005. Note that interfacial dislocations in crystalline solids are ‘quantized’ by the discrete lattice, and truly continuous dislocation distributions are not possible.

Despite exhaustive plastic deformation the interface velocity is only slightly lower in ferrous lath martensites than in twinned plate martensite ($\approx 1/3$ of the speed of sound Thadhani et al. 1986). The semi-coherent / commensurate interface must be such that the interfacial dislocations can glide as the interface moves (non-conservative climb is not permitted or can be excluded because it is too slow compared to the high interface velocity). It follows that the Burgers vectors \mathbf{b} (one set of continuously distributed straight dislocations) or the effective / net dislocation content of the interface \mathbf{b}^c must not lie in the interface plane unless the dislocations are screws. However, Schoen et al. 1971 point out that the net burgers vector \mathbf{b} is not parallel to the net dislocation line ξ_i , because an array of pure screw dislocations is not stable. Conservative interfaces may be termed glissile in the sense in which this term is used for dislocation lines.

The line vectors of the interfacial dislocations must lie along an invariant-line, i.e., a line which joins the parent and product crystals without any rotation or distortion. For any distortion along the dislocation line other dislocations would be needed to accommodate that misfit. It would then be necessary to have more than one set of non-parallel dislocations in the interface. These non-parallel dislocations can intersect to form jogs which render the interface sessile. Therefore the choice of slip systems in other theories should be restricted due to the argument of interface mobility by imposing the requirement that the invariant line should be contained in a particular set of slip planes: $ILS_{\mathbf{F}} \in \mathbf{m}_i$.

An edge to edge meeting of slip planes was first proposed by Frank 1953 (shortly before the continuum theories) to explain the high-index, i.e. $\{225\}_{\gamma}$, habit plane of martensite in steel. As this habit plane contains the close-packed $(110)_{\gamma}$ direction of the product lattice, Frank suggested that close-packed planes of the two lattices meet edge to edge in the interface along close-packed rows. The relation regarding a martensite lath is illustrated in Figure 3.8. The aspect of edge to edge matching is particularly emphasised by M.-X. Zhang et al. 2005 known as the edge to edge model (E2EM) also popular for diffusional transformations.

The terminology for dislocations at the interface is diverse as shown in Table 3.2. A coherent interface can contain partial dislocations, so-called transformation / coherency dislocations. They are partial dislocations of both the parent and product crystal lattices and consequently their motion is constrained by fault energy. This forces the dislocations to remain in the interface / maintain their periodicity as the interface moves and determines the nature of their motion as individual defects G. B. Olson et al. 1979; G. B. Olson et al. 1986. They maintain continuity (lattice correspondence) of the lattice, are capable of conservative climb or glide during the transformation, but their motion is restricted to the plane of the dislocation loop since they form stacking faults. The strain energy associated with coherency dislocations can be reduced by misfit / anticoherency dislocations, generally having lattice Burgers vectors and producing a lattice-invariant deformation which disrupts the uniformity of the lattice correspondence across the interface, and thereby reduces coherency (they produce steps / ledges. The anticoherency dislocations move as conventional dislocations.

Various names	misfit- (Frank) / anticoherency- (G. B. Olson et al. 1979) / primary- (Christian 1965) / accommodation- / intrinsic- (H. Bhadeshia 1987) / inherent dislocations; dislocations are a necessary	transformation- (Bilby) / coherency- (G. B. Olson et al. 1979) / secondary- (Christian 1965) / extrinsic (H. Bhadeshia 1987) / extraneous dislocations.
Function	Continuum deformation by lattice invariant shear of martensite required for reducing the long range / global strain energy. Enables the total shape-deformation of the habit-plane to be an or close to an ILS / IPS.	enable transformation by providing a suitable nucleation (SFEs) and growth (SFE remains in the interface) mechanism; preserve lattice correspondence across the interface (maintain the coherency of the interface).
Lattice coherency	generally reduce coherency and disrupt uniformity of lattice correspondence	Maintain coherency and lattice correspondence
Burgers vector	Except for twinning dislocations (LIS) perfect dislocation (lattice) \mathbf{b}	partial \mathbf{b}
Motion	conservative glide (as stacking fault partial), climb by diffusion	Motion restricted within plane of the dislocation loop. However, both conservative climb and glide possible in that plane.

TABLE 3.2: Overview of terminology of dislocations at semi-coherent / commensurate interfaces.

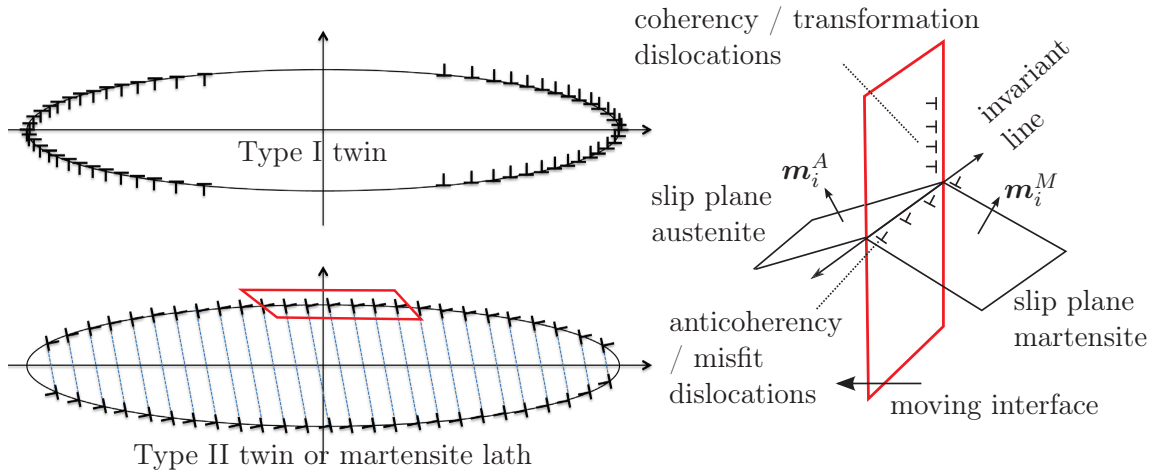


FIGURE 3.8: Left: modified from J. Hirth et al. 2016. Upper-left: low nucleation rate, high growth rate. Lower-left: high nucleation rate, low growth rate. According to J. Hirth et al. 2016 this tendency even applies for twinning. Right: magnification of glissile interface. Slip systems meet edge to edge along an invariant line. Also see Figure 3.10.

Sandvik et al. 1983 pointed out that in the f.c.c. \rightarrow b.c.c. transition, transformation /coherency dislocations may be difficult to resolve in Fe-alloys, because their Burgers vector can be small and the dislocations are very closely spaced.

Solving the Frank–Bilby–Bollmann equation, i.e. determining $\mathbf{b}^c = -\mathbf{E}_{\text{ref} \rightarrow \text{c}} \mathbf{v}$ (coherency dislocation content) by an iterative procedure, is referred to as topological model (TM) by R. Pond et al. 2007; J. Hirth et al. 2013; R. Pond et al. 2015.

As for all crystallographic theories the determination of a suitable reference lattice for an interface is not unambiguous, especially when it contains arrays of dislocations. It is most convenient to take one of the two lattices as reference lattice, particularly if the motion of an interface by dislocation glide is considered. For metallic systems, where the isotropic uniform elastic approximation normally holds a so-called "median lattice" rotated half way between the two is also often used. For a determination of the coherent reference state in an anisotropic treatment see, Abdolrahim et al. 2016.

In the topological method, the key assumption is the existence of a reasonably coherent "terrace plane" with sufficiently small coherency strains, see R. Pond et al. 2007; J.M. Howe 2009. Considerations on inter-penetrating lattice sides as subsequently outlined serve as perfect reference lattices for lattice circuit mapping and hence for determining these terrace planes, see J. Hirth et al. 2013. According to a terrace plane (reticulated by steps) has been selected the misfit strain is deduced from the lattice parameters.

After J. Hirth et al. 2013 \mathbf{v} cannot be established until the final interface plane is known, i.e. until the partitioning of rotations has been determined.

In Figure 3.9 an overview of the microscopic study of interfaces starting from bicrystals, i.e. two non interpenetrating lattices, here austenite (A) and martensite (M), according to J. Hirth et al. 2013 is given. Generally, the symmetry of the bicrystal is lower than the symmetries of the component crystals (dissymmetrization after R. C. Pond et al. 1983). The first stage of dissymmetrization is by interpenetrating the two lattices of the bicrystal forming a dichromatic pattern / complex (DP / DC). Note, that so-called *moiré patterns*, are formed analogously by two sets of parallel lines that are inclined relatively to each other. DPs are distinguished according to their coherency as follows:

- no coherency strains are present - natural DP (NDP).
- coherency strains but no rotations - commensurate DP (CDP, mostly coherent).
- coherency strains and rotations (RCDP).

Reference spaces must represent all the symmetry operations of both crystals, hence the use of DPs representing unions of both space groups. DPs with 3-D periodicity have symmetries belonging to the classical space groups. These DPs are known as coincidence-site lattices (CSLs) in the grain boundary literature. Predictions of the morphology of precipitates, where the interface energy dominates is mainly based on finding the optimum interphase boundaries with a high density of near coincidence sites (NCSs), see M.-X. Zhang et al. 2009.

The inverse density of coincident side lattice (CSL) points is defined as

$$\Sigma = \frac{\text{Volume unit cell of CSL}}{\text{Volume unit cell crystal lattice}} \quad (3.36)$$

for low angle boundaries $\Sigma \approx 1$ ($\Sigma 1$). Twins are characterised by $\Sigma 3$. In the case of highly relaxed, dislocated lath martensite, beside $\Sigma 1$ boundaries the coherent $\{111\}_\gamma$ and the symmetric incoherent $\{112\}_\gamma$ $\Sigma 3$ (90° from the former $\{111\}_\gamma$) twin boundary is important. Note that the CSL theory applies to lattice sites, not atom positions. In reality there will be dislocations at interface and atoms wont be at the CSL points. Remarkably, the positions of the atoms at the GB can be described by one out of seven polyhedra (Bernard structures)

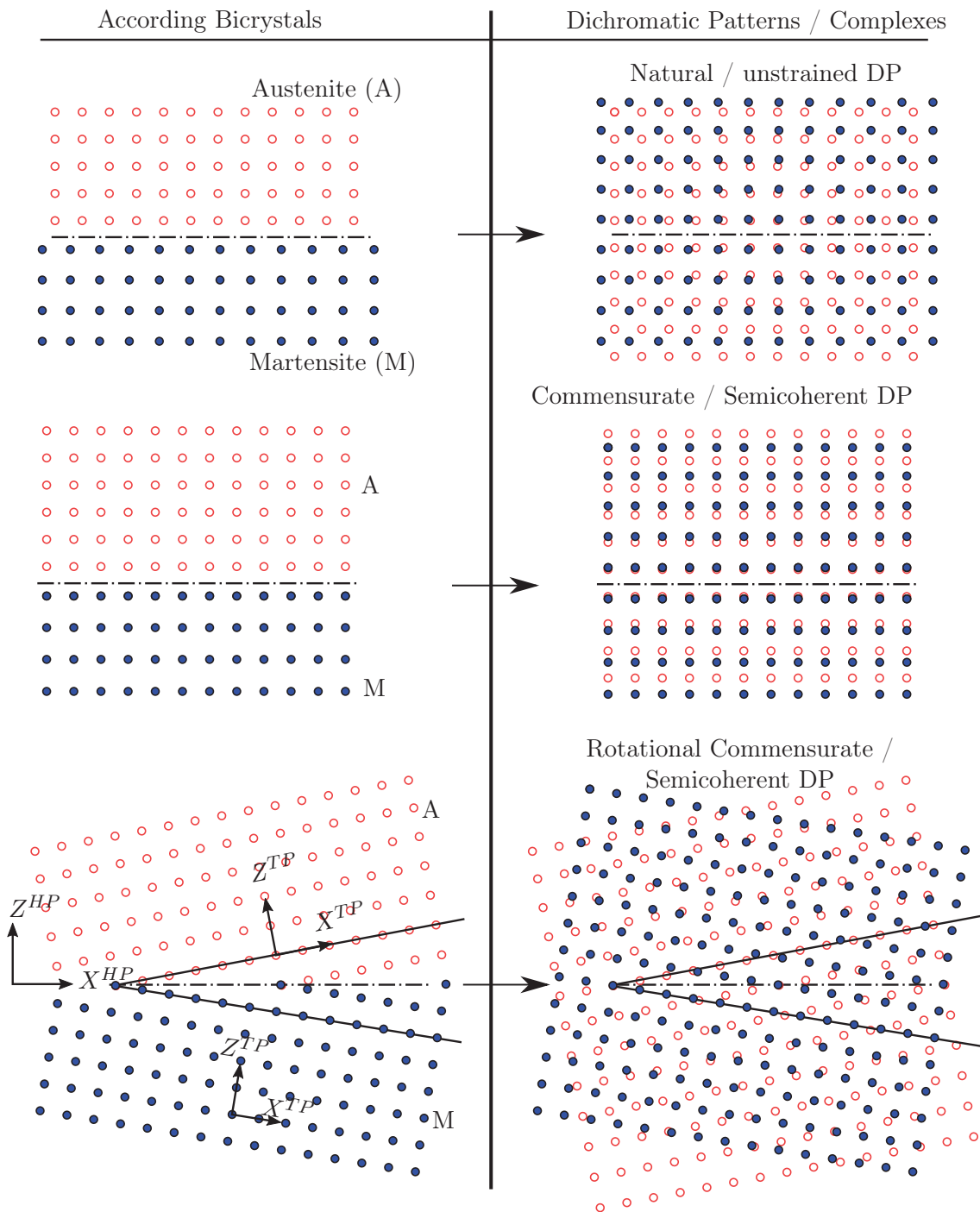


FIGURE 3.9: Interface terminology following J. Hirth et al. 2013. Indices of austenite (A) and martensite (M) lattice. For interfacial defects the suggested reference space is the dichromatic complex / pattern (union of the space groups of both A and B). Left column: Bicrystal, i.e. same as on the right but the atoms on the other side of the interface are not shown. Bottom: The total rotation, is partitioned between the two crystals with respect to the initial (coherently strained) terrace plane. The subscripts HP and TP mark the habit plane and terrace plane bases respectively.

that correspond to dislocations. Evidence strongly suggests that in all except f.c.c metals, material properties are related to the two surfaces that make up the boundary, not the CSL structure. The existence of low energy boundaries for e.g., $\Sigma 3$ and $\Sigma 11$ boundaries is “coincidental” (although probable due to the high symmetry). Bollmann et al. 1972 reported CSL boundaries in stainless Cr-steels.

Using the concept of configurational Kienzler et al. 2000 and virtual (cf. method of virtual displacements) / image force J. P. Hirth et al. 1968 showed that single dislocations in a perfect homogeneous continuum tend to move towards free surfaces or interfaces. Following this line of thinking a defect near interfaces and free surfaces may be split into step / ledge (free surface) as well as screw and edge dislocation components (bulk behavior). Such a general characterisation of a generic line defect at interfaces has been given by J. Hirth 1994.

J. Hirth 1994 obtained a formal definition of a step / ledge vector of a free surface, equivalently to a Burgers vector by a-posteriori circuit mapping of a closed path crossing the interface. He gave the combined defect at the interface the name ‘disconnection’.

The topological character of an admissible defect that can be superimposed on a certain reference structure is given by a combination of symmetry operators, one from each of the bicrystal (J.M. Howe 2009). Using the matrix formalism for symmetry operators (Seitz symbol of the mappings) set out in the International Tables for Crystallography (Hahn 1987),

$$\mathcal{W} = (\mathbf{W}, \mathbf{t}) \quad (3.37)$$

where \mathbf{W} is a linear mapping and \mathbf{t} is a lattice translation vector. As already mentioned in subsection 3.5.3.2 the operator characterising an interface defect is defined in analogy to the misorientation (Equation 3.15, only rotations) and the incoherency tensor (general deformation without translation, Equation 3.24) with the only difference now translations are included. Using the notation of Hirth, Pond, Howe The operator characterising a defect in the interface is therefore given by:

$$\mathcal{Q}_{ij} = \mathcal{W}(A)_i \mathcal{W}^*(M)_j^{-1} \quad (3.38)$$

with $\mathcal{W}(A)_i$ and $\mathcal{W}^*(M)_j^{-1}$ as the operators given in the basis / coordinate frame of austenite (A), indicated by an * for the martensite (M) operator. Possibilities of distinct

defects that can arise in a given interface depend on the extent of symmetry breaking during dissymmetrization. Equation 3.38 is equivalent to the Frank–Bilby–Bollmann equation (Equation 3.35), in which $\mathscr{W}(A)_i$ and $\mathscr{W}^*(M)_j^{-1}$ represent the vector \mathbf{v} after mapping into the natural reference of austenite and martensite, respectively.

First, special cases are considered. A perfect dislocation (transformation/anticoherency dislocation) in austenite therefore becomes $\mathcal{Q}_{ij} = (\mathbf{I}, \mathbf{b}(A))$. Interface dislocations arise in the case where dislocations from both crystals coincide at the interface and either translation or point symmetry is broken leading to $\mathbf{t} = \mathbf{b} = \mathbf{b}(A)_i - \mathbf{b}^*(M)_j$. These are the defects considered in the continuum theories for geometrical shearing (LIS). Their motion along an interface cannot produce transfer of material between the phases. J. Hirth et al. 1996 define the "overlap" step / ledge height, h associated with a general defect given by Equation 3.38 to be the smaller of $\mathbf{n} \cdot \mathbf{t}(A)_i$ and $\mathbf{n} \cdot \mathbf{t}^*(M)_j$ where \mathbf{n} is the unit normal vector of the local terrace plane (of a generally irrational interface) pointing into austenite. (Initially the ledge / step vector of interface defect \mathbf{l} has been defined independently, later the direction of \mathbf{l} was specified via the terrace plane vector \mathbf{n}). Pure interface steps / ledges $\mathcal{Q}_{ij} = (\mathbf{I}, \mathbf{0})$, ($\mathbf{b} = 0, h \neq 0$) occur in the special case where the adjacent crystals have some symmetry in common. No dislocation character arises i.e. no misfit is accommodated.

In the general case of a disconnection ($\mathbf{b} \neq 0, h \neq 0$). The differential flux due to long range diffusion accompanying dislocation climb is proportional to the normal component of the Burgers vector $b_n = \mathbf{b} \cdot \mathbf{n}$. and the differential flux due to step / ledge movement $\propto h$ (most generally also the difference in density between the crystals). The long range stress field is solely proportional to the dislocation portion characterized by \mathbf{b} . An overview of this terminology regarding a martensite lath is shown in Figure 3.10.

For the mobility of line defects at interfaces and hence for the interface itself to be sufficiently mobile the line defects must have translational (or if the stacking fault energy is very high, near translational) character, i.e. $\mathbf{t} \in$ dichromatic complex (DC). Otherwise a stacking fault forms. Equivalently to dislocations, there are perfect and partial disconnections depending on whether the dislocation and step / ledge part are translation vectors of the lattice.

When the disconnections contain only edge Burgers vector components by lying in the terrace plane, there is exact agreement between the geometrical treatment and the topological model. The transformation distortion is an invariant plane strain. However, for the

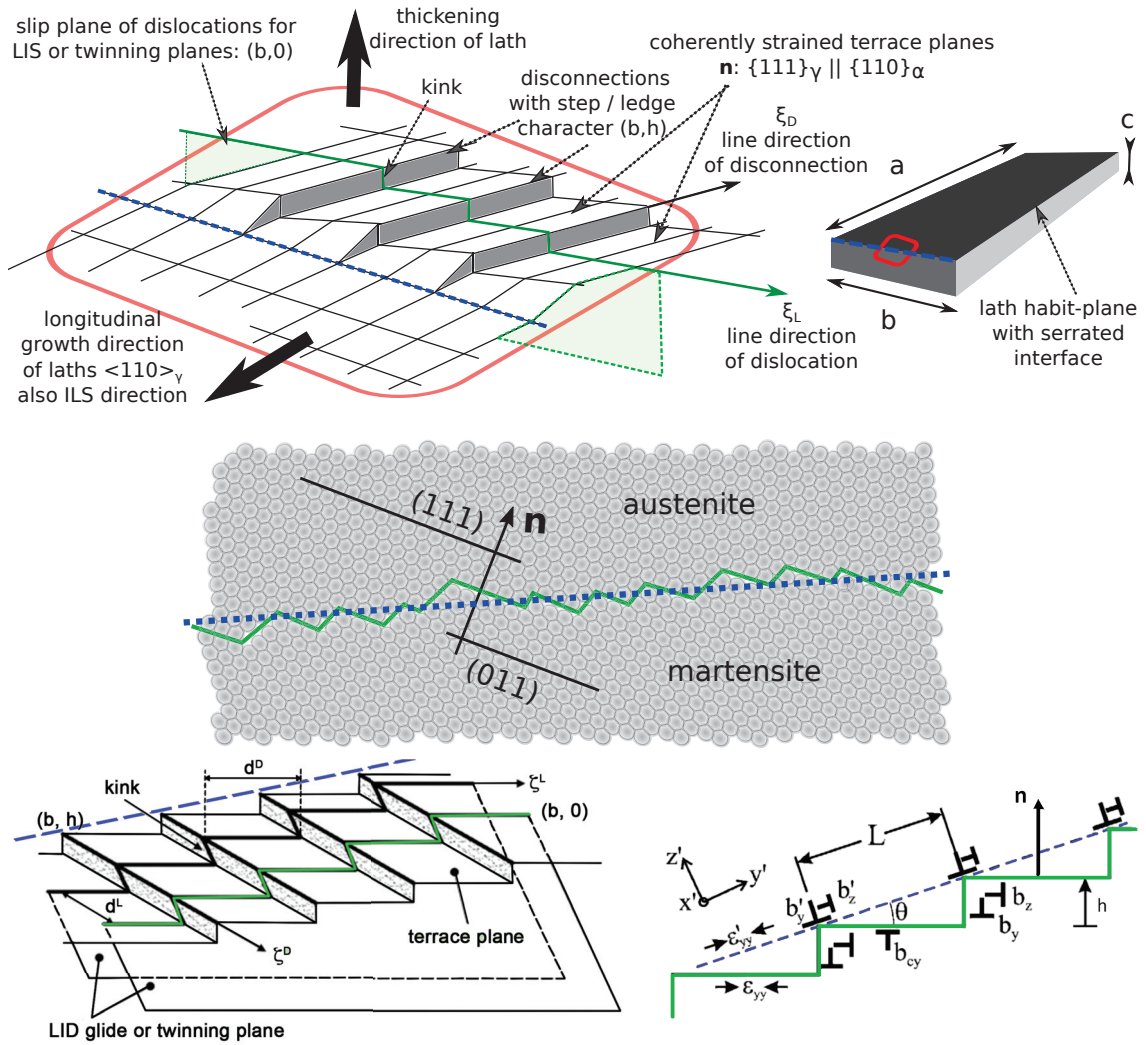


FIGURE 3.10: Red, green and blue colors mark correspondences between the images. Upper-left: Habit structure of martensite laths along the lines of Christian 1965. Frank 1953 proposed a longitudinal growth by screw dislocations ($\mathbf{b} \parallel \xi_D = \xi_L$). Topological characterisation and notion of disconnection and terrace plane after J. Hirth et al. 2011. Recent MD simulations (e.g. Maresca et al. 2017 particularly Figure 5 therein) support this view and reveal the nature of the two shears. Upper-right: Characteristic dimensions of a lath. Center: Interface cross section showing orientation relation (terrace plane). Lower-left: Schematic of habit plane interface cross section as found in publications of J. Hirth et al. 2013. Lower-right: Habit-plane and terrace-plane systems.

transformation case when there is also a Burgers vector component normal to the terrace plane, the distortion is planar but it is not exactly an invariant plane strain, but contains rotational components.

It must be kept in mind that the interface predicted by the TM does in general not predict a lattice-matched plane on a larger scale than the crystallographic one. In other words almost nothing is said about microstructure morphology. However, the framework leads to an interface, which is invariant in a physical sense since its structure does not change on average during transformation by lateral motion of the disconnections (which produces a plane strain / invariant line deformation). Thus, the habit plane from a purely geometrical treatment may produce unrelaxed interfaces in case the interface is stepped while the TM interface is fully relaxed on the atomic scale. The near-distortion field predicted by the TM is argued to be important since it not only relates to the interfacial energy, but also to the mechanism of transformation and hence kinetics.

Considering the nature of disconnections an analysis of the diffusional flux during the transformation on an atomic scale has been performed by G. B. Olson et al. 1986; R. Pond et al. 2007; J.M. Howe 2009. Summarizing there are up to five requirements in the TM: i) the composition, ii) the interface, iii) the defect, iv) the defect's mobility (generally greater if $|\mathbf{b}|$ and h have small magnitudes) and v) the requirement that if more than one set of defects is present their defect intersections must also be glissile (network requirement) Christian 1994; R. Pond et al. 2007; R. Pond et al. 2003.

Most of the models outlined here are comprised in the open source program PTCLab by Gu et al. 2016; W.-Z. Zhang et al. 2016 (also see section C.1). A comprehensive overview of the mechanical characterisation of such interfaces can be found in Fressengeas 2017.

3.6 Relations between Oriented Crystallographic Variables

Now that the underlying principles of stretch tensors, orientations relations and their importance in view of morphology and interface mobility have been elaborated it is time to give an overview of the crystallographic relations commonly reported for the hierarchical microstructure of lath martensitic steel. Here symmetry-related structural stretch tensors are the Bains (B_1) and KS-OR variants are denoted as V_i . Figure 3.11 illustrates the relation between the V_i in relation to the slip systems in austenite depicted on an unfolded Thompson tetrahedron. In Table 3.3 an overview of the grouping of variants in terms of crystallographic relations is given. Particularly the close packed plane group (short CP) marks packets and misorientations are calculated between V_1 and other variants based on the assumption of an ideal K-S OR.

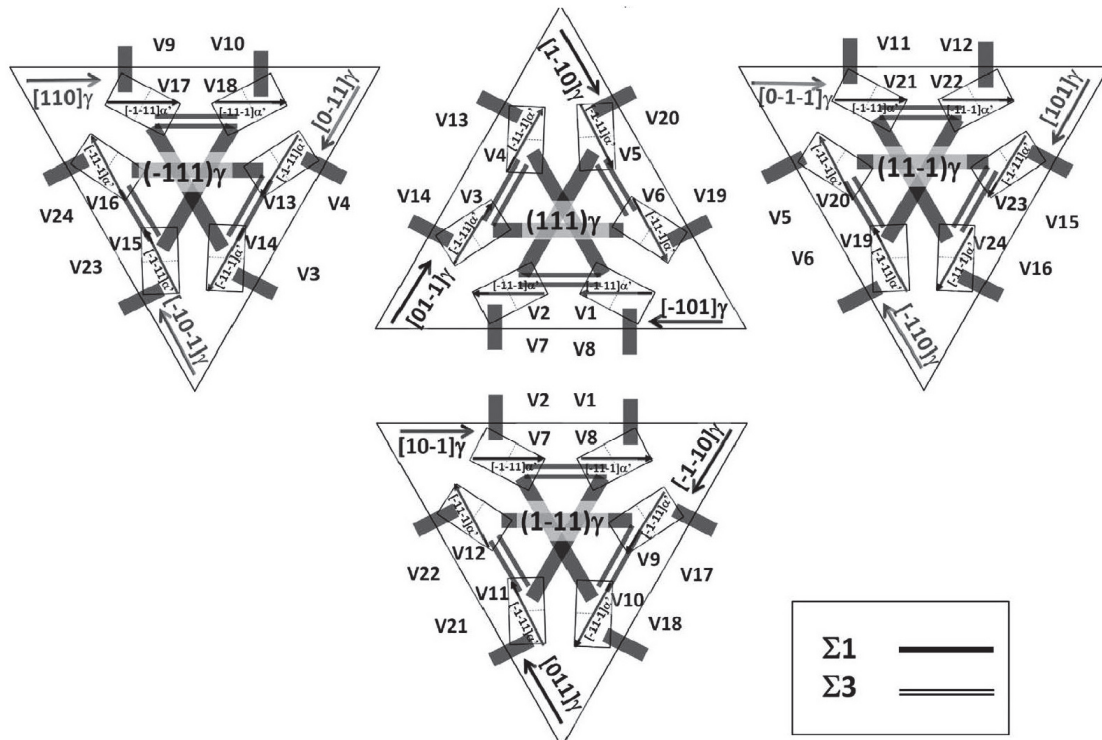


FIGURE 3.11: Connections between the 24 KS-OR variants. The four triangles are the $\{111\}_\gamma$ slip planes oriented as an "unfolded" Thompson tetrahedron. The slip / KS-direction relation and variant number due to Morito et al. 2006a are shown on each plane. The lines mark special interfaces (CSL see subsection 3.5.5) between the variants: $\Sigma 1$ is a low angle boundary and $\Sigma 3$ a (coherent) twin boundary, see e.g. S. Zhang et al. 2012 for a Fe-13Cr-9Ni stainless steel similar to the MarvalX12. Variants connected by $\Sigma 1$ belong to the same Bain correspondence (see subsection 3.5.2).

Variant no.	Plane parallel	Direction parallel	CP group	Bain group	Misorientation from V1 (°)
V1	$(111)_\gamma // (011)_\alpha$	$[\bar{1}01]_\gamma // [\bar{1}\bar{1}1]_\alpha$	CP1	B1	–
V2		$[\bar{1}01]_\gamma // [\bar{1}1\bar{1}]_\alpha$		B2	60.0
V3		$[01\bar{1}]_\gamma // [\bar{1}\bar{1}1]_\alpha$		B3	60.0
V4		$[01\bar{1}]_\gamma // [\bar{1}1\bar{1}]_\alpha$		B1	10.5
V5		$[\bar{1}\bar{1}0]_\gamma // [\bar{1}\bar{1}1]_\alpha$		B2	60.0
V6		$[\bar{1}\bar{1}0]_\gamma // [\bar{1}1\bar{1}]_\alpha$		B3	49.5
V7	$(1\bar{1}1)_\gamma // (011)_\alpha$	$[10\bar{1}]_\gamma // [\bar{1}\bar{1}1]_\alpha$	CP2	B2	49.5
V8		$[10\bar{1}]_\gamma // [\bar{1}1\bar{1}]_\alpha$		B1	10.5
V9		$[\bar{1}\bar{1}0]_\gamma // [\bar{1}\bar{1}1]_\alpha$		B3	50.5
V10		$[\bar{1}\bar{1}0]_\gamma // [\bar{1}1\bar{1}]_\alpha$		B2	50.5
V11		$[011]_\gamma // [\bar{1}\bar{1}1]_\alpha$		B1	14.9
V12		$[011]_\gamma // [\bar{1}1\bar{1}]_\alpha$		B3	57.2
V13	$(\bar{1}11)_\gamma // (011)_\alpha$	$[0\bar{1}1]_\gamma // [\bar{1}\bar{1}1]_\alpha$	CP3	B1	14.9
V14		$[0\bar{1}1]_\gamma // [\bar{1}1\bar{1}]_\alpha$		B3	50.5
V15		$[\bar{1}0\bar{1}]_\gamma // [\bar{1}\bar{1}1]_\alpha$		B2	57.2
V16		$[\bar{1}0\bar{1}]_\gamma // [\bar{1}1\bar{1}]_\alpha$		B1	20.6
V17		$[110]_\gamma // [\bar{1}\bar{1}1]_\alpha$		B3	51.7
V18		$[110]_\gamma // [\bar{1}1\bar{1}]_\alpha$		B2	47.1
V19	$(111)_\gamma // (011)_\alpha$	$[\bar{1}10]_\gamma // [\bar{1}\bar{1}1]_\alpha$	CP4	B3	50.5
V20		$[\bar{1}10]_\gamma // [\bar{1}1\bar{1}]_\alpha$		B2	57.2
V21		$[0\bar{1}\bar{1}]_\gamma // [\bar{1}\bar{1}1]_\alpha$		B1	20.6
V22		$[\bar{1}\bar{1}0]_\gamma // [\bar{1}\bar{1}1]_\alpha$		B3	47.1
V23		$[101]_\gamma // [\bar{1}\bar{1}1]_\alpha$		B2	57.2
V24		$[101]_\gamma // [\bar{1}1\bar{1}]_\alpha$		B1	21.1

TABLE 3.3: Overview of the twenty-four KS orientation variants (orientational / lattice correspondence variants - LCVs). The individual Bains (compression axes), parallel plane (CP) relations defining packets and theoretical misorientations w.r.t. variant V1 are given. Note that all misorientations in a packet belong to a $\langle 110 \rangle_\alpha$ direction. The 10.5° and 14.9° misorientations are semi coherent $\Sigma 1$ coincidence side lattice CSL interfaces. $V_i - V_{i+1}$ are related by a 60° rotation around a specific $\{111\}_\gamma$ and form a $\Sigma 3$ twin boundary (this is the characteristic Type I twin solution).

3.7 Overview of Important Slip and Boundary Sliding Mechanisms for Lath Martensite

The lath geometry can become very pronounced as Fe-20Ni-5Mn with lath dimensions of $a : b : c = 0.3 : 2.8 : 100 \mu m$ Wakasa et al. 1981. Sandvik et al. 1983 investigated the same steel in TEM and found that individual laths contained a high density of screw dislocations with $\xi = \mathbf{b}$ along the four $\langle 1\bar{1}0 \rangle_\gamma \approx \langle 111 \rangle_\alpha$ (in KS OR) directions with a predominance of one of them. Note that the net continuum shear deformation of straight, parallel screw dislocations with $\langle 111 \rangle_\alpha$ Burgers vector gliding in the plane $\{110\}_\alpha$ is

$$\mathbf{I} + \frac{1}{m}(\mathbf{b} \times \mathbf{m}) \otimes \mathbf{m} = \mathbf{I} + \langle 1\bar{1}2 \rangle_\alpha \otimes \{110\}_\alpha \quad (3.39)$$

Sandvik et al. 1983 assumed a correspondence of this effect with the lath's long direction (several μm) which, however, can not be determined in a thin foil used for transmission electron microscopy. Particularly, they stated: "Information concerning the long direction

of a lath in terms of the accurate variant of the austenite-martensite orientation relationship would be very valuable". Recently, Qiu et al. 2014 proposed a method to determine the habit plane in TEM based on an accurate measurement of the foil thickness. P. Kelly et al. 1990 showed that the lath long direction indeed is the close packed direction $\langle 1\bar{1}0 \rangle_\gamma$. Sandvik et al. 1983 noted that austenite dislocation arrays associated with the straight and irregular lath interfaces are very different, suggesting that the thickening of a lath takes place mainly in one direction away from the initial straight interface. Generally, the dominance of screw dislocations is interesting because they have a much higher tendency to annihilate than edge dislocations. This has e.g. been confirmed by Shintani et al. 2011 reporting a decrease in the relative contribution of screw dislocations with increasing deformation.

Wittridge et al. 2001 points out that there is a one to one correspondence between the $2 \times 12 \{111\}_\gamma || \{011\}_\gamma$ (perfect dislocation) slip shears and the 24 KS-variants as illustrated in Figure 3.11. Note that the unit cells of the f.c.c. and b.c.c. phases in KS OR are related by a 90° rotation about a $\langle 112 \rangle$ axis. In analogy Jonas et al. 2005 established a connection between the 12 NW-variants and Shockley partial dislocations.

For modelling the effective behavior of the hierarchical arrangement two pseudo-single crystal slip families have been considered by Schastlivtsev et al. 1999; Mine et al. 2013; Kwak et al. 2016, again exploiting the KS OR, some $\{110\}_{\alpha'}$ systems act on the same planes as f.c.c. slip systems parallel to the austenite-martensite interface assumed as

1. $\{111\}_\gamma \langle 0\bar{1}1 \rangle_\gamma = \{110\}_{\alpha'} \langle \bar{1}11 \rangle_{\alpha'}$ referred to as "in-lath-plane" slip system family and
2. $\{0\bar{1}1\}_\gamma \langle 0\bar{1}1 \rangle_\gamma = \{112\}_{\alpha'} \langle 111 \rangle_{\alpha'}$ "out-of-lath-plane" slip system family, as also illustrated in Figure 3.12. Maresca et al. 2014 although mentioning characteristic laths' dimensions, merely considered lath cross-sections normal to the lath long directions and studied the influence of inter-lath retained austenite in a (essentially) two-dimensional (1 continuum element thick model - "2.5" dimensional) crystal plasticity model.

In the case of single laths, TEM studies Sandvik et al. 1983; Moritani et al. 2002; Ogawa et al. 2004 show that the habit plane deviates from rational lattice directions (hence is irrational) due to the semi-coherent, serrated nature of the glissile interface, with a typical misorientation $\theta : 9.5^\circ < \theta < 19.5^\circ$ about $\langle 110 \rangle_\gamma$, thus lying between $\{575\}_\gamma$ and $\{121\}_\gamma$ Maresca et al. 2017. Note that the habit plane generally is of the form $\{xyx\}_\gamma$, hence only 12 apparent habit planes exist, although there are 24 variants of the orientation relationship.

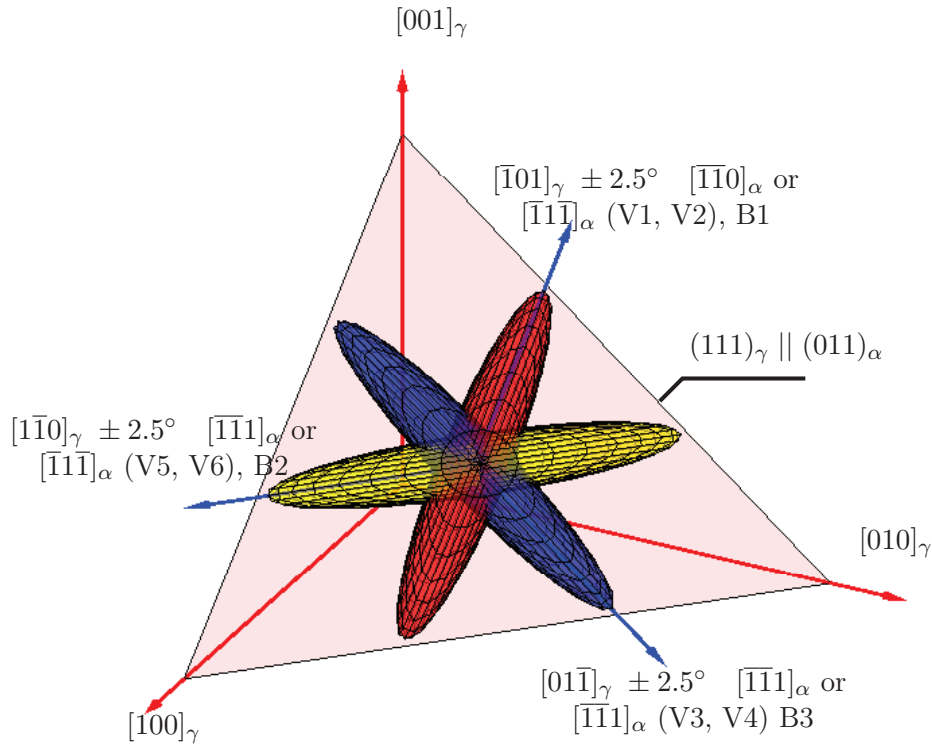


FIGURE 3.12: Sketch of relative orientation between single laths (here illustrated as ellipsoids with half axis lengths $a < b \ll c$ with $a \parallel \mathbf{k}$ the close packed γ and invariant line direction and $b \parallel \mathbf{h}$ the habit plane) of a packet relative to austenite crystal system (also see Figure 3.11). The given pairs are actually twin pairs, which are related by a 60° rotation around $[1\bar{1}1]$ ($\Sigma 3$ boundary). However, the reported pairing in this block of lath martensite is V1-V4, V3-V6, V2-V5. The theoretical lattice misorientation between these pairs is 10.5° ($\Sigma 1$ boundary, experimentally smaller, see Stormvinter et al. 2012).

In a three-dimensional setting, in fact, the pseudo slip system consisting of the habit-plane of the lath and its long direction should be considered for lath sliding. Assuming a habit plane of type $\{575\}_\gamma$ then the possible lath habit plane long-direction systems in agreement with the variant pairings observed experimentally are given in Table 3.4. Consistently, the notation due to Morito et al. 2006a is used (cf. the V1-V4 KS-variant pairing in Figure 1.2).

There are 12 $\{557\}_\gamma$ habit planes. However, as pointed out in subsection 3.5.3.2 it must be considered that the habit plane solutions come in pairs. Furthermore, certain coherency conditions have to be fulfilled. The $(557)_\gamma$ habit plane of the packet CP1 would correspond to the KS direction of the variant pairing V5-V6 which are both highly misoriented ($> 49.5^\circ$) and have no coherence relation (except the very weak $\Sigma 11$) to both variants V1 and V4, see Table 3.3. This may be the reason why not all three permutations of habit planes are realized in a block. In other words the pairings in a block are dictated by the coherency

packet	lath long-direction habit-plane boundary sliding systems		
CP1 $(111)_\gamma$	V1,V2: $[\bar{1}01] (575)_\gamma$	V3,V4: $[01\bar{1}] (755)_\gamma$	V5,V6: $[\bar{1}\bar{1}0] (557)_\gamma$
CP2 $(\bar{1}\bar{1}1)_\gamma$	V7,V8: $[10\bar{1}] (5\bar{7}5)_\gamma$	V9,V10: $[\bar{1}\bar{1}0] (5\bar{5}7)_\gamma$	V11,V12: $[011] (7\bar{5}5)_\gamma$
CP3 $(\bar{1}11)_\gamma$	V13,V14: $[0\bar{1}\bar{1}] (7\bar{5}5)_\gamma$	V15,V16: $[\bar{1}0\bar{1}] (575)_\gamma$	V17,V18: $[110] (557)_\gamma$
CP4 $(11\bar{1})_\gamma$	V19,V20: $[\bar{1}10] (557)_\gamma$	V21,V22: $[0\bar{1}\bar{1}] (75\bar{5})_\gamma$	V23,V24: $[101] (57\bar{5})_\gamma$

TABLE 3.4: Sub-block boundary sliding systems: each habit plane of a certain packet forms with a certain lath long direction a pseudo slip system. Note that within a block only two such systems are active due to the pairings forming coherent low angle CSL interfaces e.g. V1-V4, V3-V5, V2-V5 in packet $(111)_\gamma$, see Table 3.3

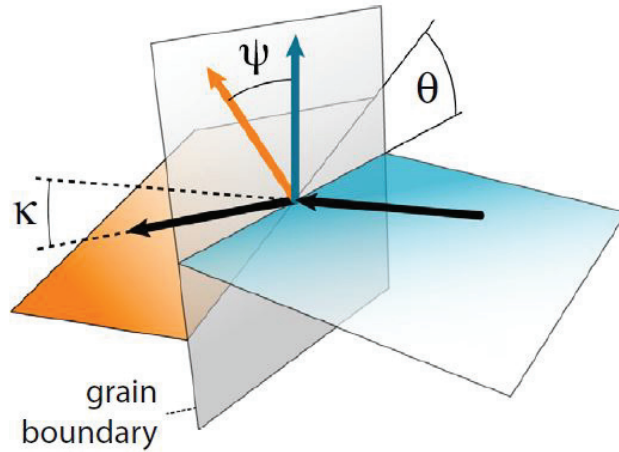


FIGURE 3.13: Geometry of slip transfer across a grain boundary taken from Bieler et al. 2014. Horizontal (orange and blue) planes signify slip or twinning planes on either side of the boundary. κ is the angle between slip directions, ψ is the angle between plane normals, and θ is the angle between plane traces on the boundary.

stresses of the low angle semi-coherent interfaces. The slip direction is given by $\langle 110 \rangle_\gamma$. Particularly, the slip direction on a specific habit plane is given by the KS direction, which is normal to the HP.

B. Liu et al. 2012 carried out discrete dislocation simulations of dislocation penetrations through low angle grain boundaries (LAGBs) and found that coherent boundaries are hardly penetrable. This may be the reason why martensite laths stop to grow, limited by the developing coherency stress preventing the interface dislocations from to move in a glissile manner. Slip transfer across interfaces, has recently been reviewed by Bieler et al. 2014. Figure 3.13 illustrates the three angles which are commonly used to formulate a slip transfer condition. A matlab toolbox to study such effects has been developed by Mercier et al. 2015 (see section C.1).

Recent molecular dynamic works investigate the mobility and defect structure of the

f.c.c. – b.c.c. interface. B. Wang et al. 2013; Ou et al. 2016; Maresca et al. 2017; Karewar et al. 2018. Such investigations are highly sensitive w.r.t. the initial configuration of atoms in the model. Except in Karewar et al. 2018 (using a Meyer-Entel potential), all of them use an embedded atom potential. The simulated cell is always a f.c.c. – b.c.c. bi-crystal of several nm thickness with periodic boundary conditions. A RVE of that size is certainly not large enough to investigate accommodation effects (also not taken into account with a mere bi-crystal RVE). However, valuable insights of the kinematics and interface defect structure (e.g. related slip systems) of the semi-coherent interface necessary for a glissile interface are gained.

Ou et al. 2016 found that growth of the b.c.c. phase follows the faulting mechanism proposed by G. B. Olson et al. 1976b based on the Bogers et al. 1964 model. B. Wang et al. 2013 reported that shear deformation is crucial in order to move the f.c.c. – b.c.c. interface. This must be considered in conjunction with the shear instability occurring during the transformation and the local shear stress fields of screw dislocations which produce local shear stress fields again emphasising their importance.

Karewar et al. 2018 investigated the effect of pre-existing defects on the transformation mechanism with the result that all well-known nucleation and transformation models could be recovered depending on the pre-existing defect type and arrangement.

Maresca et al. 2017 relaxed many initial configurations with CP relation and varying angles between close packed directions. Particularly, they constructed atomistic interfaces in pure Fe guided by the experimental observation that the step direction is always close to $\langle \bar{1}01 \rangle_\gamma$. A difficulty in such an approach is bringing together both lattices as close as possible while not removing too much or too few atoms, i.e. to find a stable configuration with minimum energy that does not emit defects into the bulk phases.

They found two sets of defects: First, screw dislocations as those initially proposed by Frank 1953 sketched in Figure 3.10 with Burgers vector $a_\gamma/2\langle 101 \rangle$, one dislocation per step independent of step height lying next to the steps, with a stacking fault between partials lying on the $\{111\}_\gamma$ terrace.

Second, there are (kinked) screw dislocations with $a_\alpha/2[1\bar{1}1]_\alpha$ Burgers vector gliding on $(\bar{1}01)_\alpha$ in the b.c.c. phase with a line direction in the interface (see Maresca et al. 2017 Fig. 5 therein). These dislocations, forming edge-character kinks where they cross the steps, reside exclusively in the already rearranged b.c.c. phase and accommodate the angle

between ideal KS directions.

They assign \mathbf{S}_1 as the $a_\alpha/2[1\bar{1}1]_\alpha$ ($\bar{1}01$) $_\alpha$ slip system, i.e. the shear due to the screw dislocations ($\approx \langle 110 \rangle_\gamma$ $\{1\bar{1}1\}_\gamma$ in KS), of the second set of defects as above) and assume that the slip magnitude is fixed by the geometry, hence depending only on the orientation relation, which enables them to work out an explicit expression for \mathbf{S}_1 . They also assign \mathbf{S}_2 as $a_\gamma/2[\bar{1}01]; (111)_\gamma$ corresponding with their first set of defects as above.

They point out that both, experiments and simulations, show step heights h of multiples of $d_{111} = a_\gamma/\sqrt{3}$ in the same material cf. Figure 3.10. Accordingly, it seems that the average step height must be taken into account in a theory for calculating transformation strains. Maresca et al. 2017 denote β (similar to our g) as the average interface step height h normalized by $a_\gamma/\sqrt{3}$ and propose that a further selection criterion should be that $\beta > 1$ in accordance with experiments and simulations. The shear strain ε_s^3 is then the shear strain due to one f.c.c. screw dislocation Burgers vector per step divided by the average step height, i.e. $\varepsilon_s^3 = b/h = 1/\beta\sqrt{3/2}$. Note that contrary to Equation 3.6 (where it is assumed that slip plane is normal to the initially flat interface equal to the later terrace plane \mathbf{n}), here the slip plane is parallel to the terrace plane, hence $1/\varepsilon_s = gd_{111}/b = h/b$ (see Figure 3.14). Eventually, they set $\mathbf{F} = \mathbf{RBS}_2\mathbf{S}_1$ and determine β such that it becomes an IPS. Although not explicitly stated their assumptions lead to the shear magnitudes $\varepsilon_s^3 = 0.33$ (fixed by β ; assuming they use normed vectors in the shear dyad; for Miller indices it would be 0.8 which is unreasonable) and $\varepsilon_s^2 = 0.1$ (fixed by OR).

Finally, an overview of slip systems that have been considered for the plastic shear deformation that is an integral part of the transformation strain is given in Table 3.5.

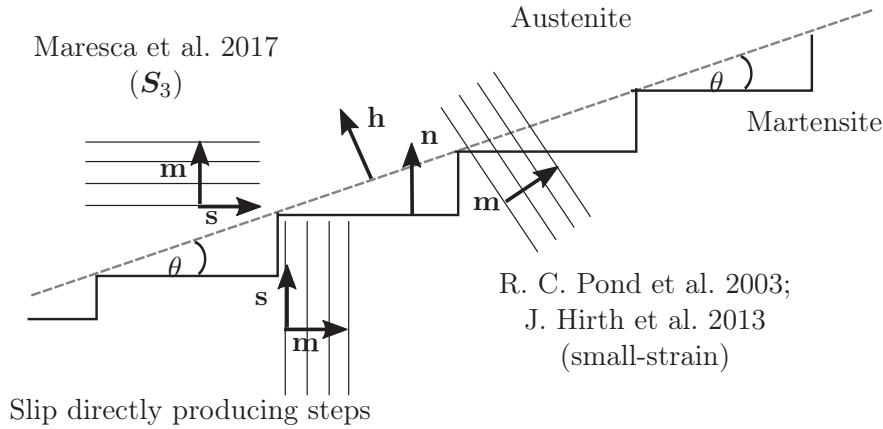


FIGURE 3.14: The habit-plane (normal vector \mathbf{h}) is usually of type $\{xyx\}_\gamma$ and $10^\circ < \theta < 20^\circ$ from $\{111\}_\gamma$, i.e. between $\{557\}_\gamma$ and $\{112\}_\gamma$. \mathbf{n} terrace plane vector (usually $\{111\}_\gamma$). Illustration of different assumptions of relative slip plane alignment with stepped interface. The inter-penetrating lines indicate the general treatment as outlined in subsection 3.5.5. Accommodation of coherency strains is most efficient if the slip direction \mathbf{s} is parallel / \mathbf{m} is normal to the terrace plane. Conversely, the rotation necessary to achieve an invariant plane strain is most efficient if \mathbf{s} is normal / \mathbf{m} is parallel to the habit-plane.

$\{110\}_\alpha \langle 111 \rangle_\alpha$	#6 × 2	classical/preferred b.c.c. type Qi et al. 2014; Khachaturyan 1983
$\{112\}_\alpha \langle 110 \rangle_\alpha$	#12 × 1	classical/preferred b.c.c. type (Pitsch Path Sowa 2017) e.g. used by Lambert-Perlade et al. 2004
$\{112\}_\alpha \langle 111 \rangle_\alpha$	#12 × 1	classical/preferred b.c.c., e.g. Qi et al. 2014; Nishiyama et al. 1978 p.356 therein.
$\{110\}_\alpha \langle 110 \rangle_\alpha$	#6 × 1	"regenerative slip" see Qi et al. 2014; Khachaturyan 1983 also Nambu et al. 2013 (NW-Path Sowa 2017). This shear is unlikely to occur directly as such, but is equivalent to equal amounts of shears in two $\{111\}_\alpha$ directions in a specific $\{110\}_\alpha$ plane.
$\{111\}_\alpha \langle 110 \rangle_\alpha$	#4 × 3	proposal due to MD model Maresca et al. 2017. A dissociation reaction of this type of defect has been discussed by J. Cohen et al. 1962.
$\{111\}_\gamma \langle 110 \rangle_\gamma$	#4 × 3	classical/preferred f.c.c. type. Note that the dissociation of this type of dislocation into two stacking fault partials (two $\langle 11\bar{2} \rangle_\gamma$ directions on the same $\{111\}_\gamma$ plane) plays an important role for nucleation Bogers et al. 1964; G. B. Olson et al. 1976b; R. Zhang et al. 2012.
$\{112\}_\gamma \langle 111 \rangle_\gamma$	#12 × 1	P. M. Kelly 1992
$\{112\}_\gamma \langle 101 \rangle_\gamma$	#12 × 2	P. M. Kelly 1992

TABLE 3.5: Overview of lattice invariant shear (LIS) systems proposed for the f.c.c. → b.c.c. transformation in steels.

3.8 The Composite Block Model for Dislocated Lath Martensite of Qi and Khachaturyan (CBQK)

Khachaturyan 1983 describes the f.c.c.-b.c.c. martensite transformation with a double slip approach assuming small plastic strains due to slip, justifying an additive decomposition of multiple slips. The assumption is reasonable, since slip should be as small as possible. Moreover, with this approximation the order of the shears does not matter.

$$\mathbf{A}_D = \mathbf{S}_2 \mathbf{S}_1 \approx \mathbf{I} + \frac{1}{m_1} \mathbf{b}_1 \otimes \mathbf{m}_1 + \frac{1}{m_2} \mathbf{b}_2 \otimes \mathbf{m}_2 \quad (3.40)$$

Khachaturyan 1983 initially proposed the system $\langle 101 \rangle_\alpha \{ \bar{1}01 \}_\alpha$ twice (these are not standard slip systems in b.c.c, but these slips can be made by a combination of two $\mathbf{a}/2\langle 111 \rangle_{\alpha'}$ dislocations. Particularly the right combination restores the lattice, see Khachaturyan 1983 p.183 therein, which is why he refers to it as "regenerative slip" (also called "pencil glide" in the literature).

Adopting the observation of hierarchical stacking of Bi-KS-variant blocks Morito et al. 2003; Morito et al. 2006a; Kinney et al. 2014 in the latter observed for 9Ni steel, Qi et al. 2014 reformulated the framework of Khachaturyan 1983 for tetragonal twinned martensite (two symmetry related Bain variants, no slip, opposite and equal rotations to close the gap between them) to one Bain strain, that is split into two KS OR-variants by mirror symmetric double-slip in the laths (sub-blocks) $(\mathbf{A}_D, \mathbf{A}_D^{(hkl)})$ and are rejoined by opposite and equal rotations $(\mathbf{R}, \mathbf{R}^{-1})$. The model is henceforth abbreviated as CBQK (composite block Qi Khachaturyan) model. The deformation gradient of a block in the CBQK model is

$$\bar{\mathbf{F}}_{\text{IPS}}^{\text{Block}} = \mathbf{I} + \varepsilon_0^{\text{B}} \mathbf{d}^{\text{B}} \otimes \mathbf{h}^{\text{B}} = \mathbf{R}_B \frac{1}{2} \{ \mathbf{R}^{-1} \mathbf{A}_D + \mathbf{R} \mathbf{A}_D^{(hkl)} \} \mathbf{B} \quad (3.41)$$

where $\bar{\mathbf{F}}_{\text{IPS}}^{\text{Block}}$ denotes the average IPS deformation of the block and $\mathbf{A}_D^{(hkl)}$ denotes the mirrored deformation of \mathbf{A}_D relative to the plane (hkl) . Qi et al. 2014 chose as mirror planes the two highly symmetric plane families $\{001\}_\alpha$ and $\{011\}_\alpha$. Although not explicitly mentioned, the idea is rooted in the prism matching model of B. Bilby et al. 1960 also see Nishiyama et al. 1978 p.402 therein. Note, that the rotations, $(\mathbf{R}, \mathbf{R}^{-1})$ are chosen such that mapped directions of these vectors are rotated back to their initial direction, (i.e. the initial planes stay connected). This assumption is discussion in subsection 3.10.1.2.

They consider the four slip system types resulting from combinations of $\{110\}_\alpha$ and $\{112\}_\alpha$ planes and the $\langle 111 \rangle_\alpha$ and $\langle 110 \rangle_\alpha$ slip vectors, see Table 3.5.

Using the lattice parameters for 9Ni steel of $a_\gamma = 3.56 \text{ \AA}$ and $a_\alpha = 2.869 \text{ \AA}$ the Bain strain tensor (Equation 3.19) becomes

$$\mathbf{B}_3 = \begin{bmatrix} 1.1397 & 0 & 0 \\ 0 & 1.1397 & 0 \\ 0 & 0 & 0.8059 \end{bmatrix} \quad \mathbf{E}_{\text{Bain}} = \begin{bmatrix} -0.3505 & 0 & 0 \\ 0 & -0.3505 & 0 \\ 0 & 0 & -0.6753 \end{bmatrix}$$

Their best solution utilizes the same active slip systems as initially proposed by Khachaturyan, i.e. two of the $\langle 101 \rangle \{\bar{1}01\}_\alpha$ type (both with a shear magnitude of $\varepsilon_s \approx 0.13$). This is discussed at the end of their work. Subsequently, some aspects of the ansatz in Equation 3.41 are discussed.

First, all characteristics of individual laths are omitted. Instead an average IPS condition for the block is directly approached, arguing that a stacking of blocks on the same CP does not cause significant internal strains. This argument is very promising, but simultaneously suitable conditions for the individual laths as well the compatibility between them should be checked. Also note that using the average deformation of the block to calculate an OR for comparison with classical ORs inevitably leads to inaccuracies.

Second, equal volume fractions of both sub-blocks are implicitly assumed ($\xi = 0.5$). On the one hand, it has been observed that within a given block, one of the two sub-blocks may have a size larger than the other, on the other hand the dominating sub-block may be switched around inside different blocks of a packet, such that on average sub-blocks nevertheless appear with equal amounts in a given packet Morito et al. 2006a. Analogously to twinning, the assumption of equal volume fractions in the blocks may be linked to the fact that for a macro-twin the volume fractions of each of the twinned regions must necessarily be equal Mühlemann et al. 2015. Summarizing, equal volume fractions may be justified, but also highly restrict possible solutions.

Third, they justify their assumption of mirror related shears (same shear magnitudes) based on the argument that: "...the variants (sub-blocks) in the block should remain (on average) joined on a low-index mirror plane in order to avoid a dense distribution of high-energy interfaces inside the block" (Qi et al. 2014). This may be compared to a large (macro)

twin that is additionally highly dislocated, i.e. mirror symmetry or twin-like compatibility is conserved between two KS-variants. Although Morito and co-workers recently pointed out that lath martensite and upper bainite can be identified by a higher frequency of near twin block boundaries Morito et al. 2015, the interface structure of blocky lath martensite generally is highly heterogeneous, involving many other interface types. Furthermore, TEM investigations and calculations for individual laths indicate that their habit plane is between $\{557\}_\gamma$ and $\{112\}_\gamma$.

They employ five selection criteria: i) The shear magnitude in the laths (equal shear magnitudes for both slips). ii) The deviation angle of the CP parallel plane relation henceforth denoted as θ_{CP} . They point out that experimental results show that $\theta_{CP} \approx 0$ in the case of low-carbon steels. iii) The deviation angle of the direction relation in KS orientation (θ_{KS}). iv) The deviation angle of the average block habit plane with the close packed plane in austenite θ_{HP} . v) The shape strain of the block ε_0^B .

Finally, their best solution for $\overline{\mathbf{F}}_{IPS}^{Block}$ is discussed. The smallest eigenvalue corresponds to an eigenvector collinear with $[\overline{110}]_\gamma$ (a close packed direction), which is very reasonable. The same vector is also the rotation axis of its rotational part, with an angle of rotation of 10° , which is highly unfavourable unless the block itself is lath shaped, which is not observed experimentally. The absolute difference of its determinant to that of the Bain strain is 0.4% volumetric change ($\det \overline{\mathbf{F}}_{IPS}^{Block} - \det \mathbf{B} = \Delta V^{err} = 0.004 = 0.4\%$). At the first sight this value is deceptively small but, in terms of strain energy this corresponds to about 2 GPa due to hydrostatic stresses ($G = 210$ GPa, $\nu = 0.33 \rightarrow K = 550$ GPa; hence $K\Delta V^{err} \approx 2$ GPa).

They point out that their best solution is only optimal (within their considerations) within a short interval of the parameter $\eta_3 = a_\alpha/a_\gamma$. For their optimal solution the range of $\eta_3 = [0.805 - 0.8185]$, otherwise deviations $> 1\%$ occur from the CP relation. More importantly, the deviation of the habit plane jumps for values $\eta_3 > 0.81$ from ≈ 0 to $> 5^\circ$. Using the lattice parameters of the MarvalX12 yields $\eta_3 = 0.7998$ and their optimal solution already gives a deviation of the parallel plane relation of $\approx 3\%$, see Qi figure 12a therein,

which is not optimal anymore.

$$\mathbf{E}_{\text{IPS}}^{\text{QKCM}} = \begin{bmatrix} -0.3797 & 0.1189 & -0.0013 \\ 0.1189 & -0.3797 & -0.0013 \\ -0.0013 & -0.0013 & -0.6304 \end{bmatrix}$$

3.9 Average Compatibility Relations for Homogeneous Boundary Conditions

As pointed out in subsection 3.5.1 adjacent regions of martensite are formed by a different deformation, in a way that: i) is compatible to the first deformation and ii) accommodates (compensates) it. The so-called average compatibility or minor relations C. Morrey 2009; Bhattacharya 1992; Bhattacharya 2003) will be of great importance for the discussion of accommodation in the blocks. The general case arises from the consideration of sequences of deformations and their behavior (e.g. finite oscillation characterised by certain probabilities - so-called Young-Measures) on imposing certain limits. Here we consider the special case of homogeneous boundary conditions. Particularly, for a microstructure involving matrices $\mathbf{F}_1, \mathbf{F}_2 \dots \mathbf{F}_N$ in the volume fractions $\xi_1, \xi_2 \dots \xi_N$, satisfying the boundary condition corresponding to a homogeneous deformation $\bar{\mathbf{F}}$ on the boundary $\partial\Omega$, the following is true (see e.g. Bhattacharya 1992; James et al. 2000; Bhattacharya 2003):

$$\bar{\mathbf{F}} = \sum_i^N \xi_i \mathbf{F}_i \quad (3.42)$$

$$\text{cof } \bar{\mathbf{F}} = \sum_i^N \xi_i \text{ cof}(\mathbf{F}_i) \quad (3.43)$$

$$\det \bar{\mathbf{F}} = \sum_i^N \xi_i \det(\mathbf{F}_i) \quad (3.44)$$

Obviously a special case of the minors relations occurs if none of the \mathbf{F}_i entail a volume change ($dV = 0$), since then Equation 3.44 is automatically fulfilled. The theory of twinning in subsection 3.5.3.4 is based on this fact and by locally ensuring Equation 3.43. Noteworthy at this point are certain conditions of "super compatibility", for twinned microstructures based on Equation 3.30. Beside the rank-one connection, cf. Equation 3.27,

two further constraints are set up so that the system of constraints reads:

$$\begin{aligned}\lambda_2 &= 1 \\ 0 &= \boldsymbol{\eta} \cdot \mathbf{U}_S \operatorname{cof}(\mathbf{U}_S^T \mathbf{U}_S - \mathbf{I}) K \\ 2 &\leq \operatorname{tr}(\mathbf{U}_S^T \mathbf{U}_S) + \det(\mathbf{U}_S^T \mathbf{U}_S) - 1/4 |\boldsymbol{\eta}|^2 |K|^2\end{aligned}\tag{3.45}$$

where $\boldsymbol{\eta}$ and K are twinning elements, see Figure 3.2. Under these conditions an invariant plane ($\lambda_2 = 1$) between a twinned laminate and an undeformed region is possible for every choice of $\xi_1 \in [0, 1]$ cf. left image of Figure 3.6. Materials fulfilling these conditions have been shown to have exceptional properties like a vanishingly small hysteresis as a consequence of a generally small strain energy by good accommodation, see e.g. Chen et al. 2013; Song et al. 2013.

3.10 Generalization & Unification of Discrete and Continuum Views for the Hierarchical Microstructure of Dislocated Lath Martensite

Calculating transformation strains based on a crystallographic theory fully specifies the orientation relation (lattice strain) and the parameters of the transformation shape strain (incorporating the Bain and plastic slip strain) of all symmetry related variants often referred to as the crystallographic set H . Bhadeshia 1987; Bhadeshia et al. 2009; Chintia et al. 2013; Giri et al. 2017.

Experimental data provides characteristic constraints, which can be considered directly in the optimization of the crystallographic set, which normally refers to the individual lath level (see subsection 3.10.1.1). If a particular crystallographic set is used in a model, the predictions of the model (e.g. the variant fractions) then can be compared to measurements of associated variant distributions by means of quantitative metallography, orientation distribution functions, habit plane measurements etc., providing additional data a model can be fit to.

Here a generalized two-level theory of blocks out of laths (forming sub-blocks) is sought. Up to now the two microstructure levels have only been considered independently and

without a statistical characterisation within the framework of the phenomenological theory of martensite crystallography. Particularly, a twin laminate spans the same length scale as a block in the CBQK model (section 3.8), which is the only block-level model for slipped martensite to date.

To obtain a more general framework, the constraint of mirror symmetric plastic shears with equal shear magnitudes in the laths forming a block and the constraint of equal variant fractions on the block level are dropped. However, then a mere search for IPS or ILS solutions in a brute force manner as done up to now leads to an unmanageable amount of solutions, already at the lath level. Therefore, in subsection 3.10.1.1 an incremental strategy in analogy to crystal plasticity is followed, with the only difference that the criterion for the incremental evolution (or more generally the cost function that is optimized) will be different.

The role of lattice rotations on the lath level is discussed and emphasised in subsection 3.10.1.2. Then the minors relations (section 3.9) and suitable side conditions on the block level are used to construct as well as compare blocks as linear mixtures of lath level solutions. At this stage the DOFs are the phase fractions of deformation gradients at the lath level. Also for this level an optimization framework is proposed, see subsection 3.10.2. Everything is implemented as an object oriented code into the computer algebra system MATLAB. The structure of the program is outlined in subsection 3.10.3.

The framework, is very flexible and can be adopted to new theoretical and experimental findings, either in terms of a cost function at the lath or block level or as a side constrain for ruling out solutions. Note that finding a cost function that fulfills experimentally required constraints can be seen as optimal in terms of both energy minimization and dissipation maximization.

3.10.1 Lath Level

3.10.1.1 Incremental Formulation of Shearing

To deal with the freedom of plastic shear magnitudes, an incremental framework is considered. In each (plastic) increment the plastic deformation from a set of deformations

$\{\Delta\mathbf{S}_i(\Delta\varepsilon_s)\}$ (all with equal incremental slip magnitude $\Delta\varepsilon_s$) that extremizes a certain cost function is chosen.

In the case, where the lath deformations are supposed to be close to invariant plane strains, it is reasonable to propose that the deviation of λ_2 of the matrix $\mathbf{C} = (\mathbf{F}^{\text{Lath}})^T \mathbf{F}^{\text{Lath}}$ from 1 is minimal, i.e.

$$\Delta\mathbf{S}_j = \min_{\{\Delta\mathbf{S}_i(\Delta\varepsilon^p)\}} \{\lambda_2 - 1\} \quad (3.46)$$

Also, only combinations of two shears are considered, in accordance with the literature Maresca et al. 2017; P. M. Kelly 1992. Consequently, $\{\Delta\mathbf{S}_i(\Delta\varepsilon^p)\} = \{\Delta\mathbf{S}_1, \Delta\mathbf{S}_2\}$. Assuming e.g. five increments, \mathbf{F}^{Lath} then could be of the form

$$\mathbf{F}^{\text{Lath}} = \mathbf{R}\mathbf{B}\Delta\mathbf{S}_2\Delta\mathbf{S}_2\Delta\mathbf{S}_1\Delta\mathbf{S}_2\Delta\mathbf{S}_1 \quad (3.47)$$

Note that up to now the PTMC was written as $\mathbf{F}^{\text{Lath}} = \mathbf{I} + \varepsilon_0 \mathbf{d} \otimes \mathbf{h} = \mathbf{R}\mathbf{B}\mathbf{S}_2\mathbf{S}_1$, where the magnitudes of the two shears were varied.

The solution process starts with a relatively large shear increment and the increment becomes smaller (cut-back) when the solution approaches the cost function optimum (e.g. $\lambda_2 = 1$). Following such a strategy introduces another mechanistic aspect beside the IPS condition to this theory, weakening the criticism that the crystallographic theory of martensite is a mere a-posteriori theory. The procedure also automatically leads to small values of ε_s (which is interpreted as a favourable mechanism Crocker 1965; P. M. Kelly 1992; Qi et al. 2014; Mayer et al. 2016). Notably, any other property can be minimized or maximized incrementally. Here, without neither explicitly resolving geometries nor considering stresses the proposed cost function seems the most suitable. It corresponds to strain energy minimization. Dissipation maximization can e.g. be introduced by incrementally calculating the stress in an inclusion using Eshelby's solution and Equation 4.15. In a full-field model energy or dissipation within an RVE or a combination of both can be extremized this way.

3.10.1.2 Rotations During the Transformation and Lattice Correspondence

In the theory of martensite crystallography the deformation due to plasticity is often denoted as lattice invariant shear (LIS). Intuitively it is understood that the structure of the

lattice remains invariant as e.g. depicted in Figure 2.1. However, the lattice invariance even is meant literally in the sense that the lattice directions also remain invariant, i.e. they do not rotate. This corresponds to the case of a constant lattice correspondence (usually the Bain correspondence cf. Equation 3.18). However, the shears involved in the lattice change induce a lattice rotation, which is not taken into account using a constant correspondence.

Considering the case where the shear direction is perpendicular to the coherent interface, see Figure 3.14 (also in Figure 2.1) the angle of rotation to return the interface to its initial state is $\theta = \arctan(\varepsilon_s)$ (cf. Equation 3.21). This rotation is the same as that applied by Qi et al. 2014 ($(\mathbf{R}, \mathbf{R}^{-1})$) in the model presented in section 3.8. Conversely, the rotation obtained from the polar decomposition of the same shear solely yields a rotation angle of $\theta = \arctan(\varepsilon_s/2)$. This rotation may be argued to be a consequence of the elastic as well as plastic partitioning of the deformation as elaborated previously in this chapter. On the other hand, consider a screw dislocation with Burgers vector in the interface. Homogenization of an array of such screw dislocations gives a shear deformation lying in the interface, i.e. the two phases would only rotate relative to each other in the interface plane. Note, that this rotation is not reflected by the rotations $(\mathbf{R}, \mathbf{R}^{-1})$ of the model in section 3.8 meant to match the planes, but is nevertheless obtained from the polar decomposition of the shear.

The phenomenological theory of martensite crystallography including plastic slip (subsubsection 3.5.3.3) does not consider the rotation of the lattice during the high plastic shear deformation, but defines any shear in an invariant lattice system of the initial austenite. This is remarkable since the sum of typical shear magnitudes due to plastic slip is in the range of $\varepsilon_s = 0.2-0.4$ corresponding to $6^\circ/11^\circ - 11^\circ/21^\circ$ (polar or reverse-rotation angle, respectively).

Therefore, an update of the lattice orientation during deformation (transformation) in analogy to large strain crystal plasticity is proposed. The crucial point is how to choose the rotation to update the lattice orientation. In this work the rotation obtained from the polar decomposition of the plastic shear (\mathbf{Q}) to incrementally update the lattice orientation is used. Particularly, in each increment the shear direction and slip plane normal are updated according to:

$$\frac{\mathbf{s}'_i}{\|\mathbf{s}'_i\|} \otimes \frac{\mathbf{m}'_i}{\|\mathbf{m}'_i\|} = \mathbf{Q}^T \left(\frac{\mathbf{s}_i}{\|\mathbf{s}_i\|} \otimes \frac{\mathbf{m}_i}{\|\mathbf{m}_i\|} \right) \mathbf{Q} \quad (3.48)$$

Note that slight variations in terms of the discrete ORs are less significant from the viewpoint of continuum modelling (e.g. CRSS) than the directional dimensions of these strains.

3.10.1.3 Selection Criteria for Lath Level Solutions

In a next step, the multitude of lath solutions that converged to the optimum of the lath cost function for slip are assessed. Particularly, solutions that do not fulfil a given set of constraints are discarded.

The magnitude of plastic slip $\sum \varepsilon_s^i$ generally should be low. On the other hand it is also important to check for a glissile transformation mechanism, i.e., an invariant line. Consequently, these two aspects have to be assessed together. Particularly, the invariant line should be a $\langle 110 \rangle_\gamma$ direction according to experimental findings and the fact that it is the most densely packed direction. Here the smallest angle between the final invariant plane and a $\langle 110 \rangle_\gamma$ direction denoted as θ_{ILS} is evaluated. The Burgers vector content due to Equation 3.35 should be evaluated as additional selection criterion, see e.g. P. M. Kelly 1992; Gu et al. 2011; Maresca et al. 2017, resulting in an average dislocation spacing or an interface step height. However, it must be pointed out that both quantities generally depend on the relative orientation of the interface and the active slip systems (also the history of their relative orientation). Also the deviation from a perfect parallel CP plane relation (misorientation angle θ_{CP}) and from a perfect parallel KS direction is checked (θ_{KS}).

Lath habit-planes should be of type $\{xyx\}_\gamma$ and for the composition and processing of our steel they are estimated to lie between $\{557\}_\gamma$ and $\{225\}_\gamma$. Lath shape strains ε_0^{L} should be small. The resulting strain energy strongly depends on the shape of the transforming domain, see e.g. Khachaturyan 1983. The experimentally better investigated shape is that of the laths, whereas the blocks generally follow no such strict shape, see e.g. Morito et al. 2013 (HC specimen therein). Therefore, the information of the shape of the laths should be considered in the selection of the solutions. According to principle 2 in subsection 3.5.1 the eigenvector corresponding to the smallest eigenvector should be in the lath's long direction. Rotations must be small. Particularly, any rotation comprised in the final solution that cannot be based on physical grounds such as a consequence of a shear deformation must be small.

3.10.2 Block Level: Restrictions, Selection Criteria and Optimization

Given an array of crystallographic sets on the lath level the block level is approached using the average compatibility relations with homogeneous boundary conditions $\bar{\mathbf{F}} \rightarrow \mathbf{F}^B$. Particularly, following Qi et al. 2014 it is assumed that a composite block, on average, deforms homogeneously and in turn forms approximately an invariant plane strain with the austenite. For instance Qi et al. 2014; Kinney et al. 2014; Kinney et al. 2016 assume that composite blocks themselves have invariant plane strain characteristics on the close packed plane $\{111\}_\gamma$ enabling their stacking to packets. Generally, also austenite could be considered in this mixture, however, the homogenized deformation should be restricted to one block classified by a particular Bain strain orientation.

Admissible residuals for the deviations from the relations Equation 3.43 and Equation 3.44 ($\Delta \det_{\max}$) are set. Particularly, to characterise the deviation from Equation 3.43 a matrix norm must be defined. Here, the sum of absolute values of a matrix denoted as $d1$ (hence the allowed residual is denoted as $\Delta d1_{\max}$) is used for that purpose since it was found that it yields values similar to the determinant's deviation. Furthermore, it is required that \mathbf{F}^B merely entails a negligible net rotation. Further conditions between lath level solutions can easily be specified but are omitted for simplicity.

The above restrictions leave some space for the optimization of the additional degree of freedom ξ_1 at this level. The cost function f now acts on the linear mixture of properties P_i

$$\min_{\xi} f(P^B) = \min_{\xi} f(\xi_1 P_1^L + (1 - \xi_1) P_2^L) \quad (3.49)$$

A minimization of the shape strain has been proposed by Furuhashi et al. 2010 (the function f then is the vector norm $\|\cdot\|$).

$$\min_{\xi} \|\varepsilon_0^B \mathbf{d}^B\| = \min_{\xi} f(\xi_1 \|\varepsilon_0^L \mathbf{d}_1^L\| + (1 - \xi_1) \|\varepsilon_0^L \mathbf{d}_1^L\|) \quad (3.50)$$

Mühlemann et al. 2015 suggested for an invariant determinant that

$$\min_{\xi} \left| (\bar{\mathbf{F}}_{\text{IPS}}^B)^T \bar{\mathbf{F}}_{\text{IPS}}^B - \mathbf{I} \right|^2 = \min_{\xi} |\mathbf{E}^B|^2 \quad (3.51)$$

where $|A|^2 = \sqrt{A: A} = \sqrt{\text{Tr}(A^T A)}$ denotes the Frobenius norm of a matrix, should be minimized as a measure of strain energy. However, this neglects the rotation part of $\bar{\mathbf{F}}_{\text{IPS}}^B$

(rotation of inclusion). Although only lath mixtures forming blocks with negligible net rotations are considered, it must additionally be checked that

$$\min_{\xi} \left| \overline{\mathbf{F}}^{\text{B}} - \mathbf{I} \right|^2 = \left| \mathbf{H}_{\text{IPS}}^{\text{B}} \right|^2 \quad (3.52)$$

Equation 3.50 and Equation 3.52 can be conveniently be formulated and solved as least squares problems. Equation 3.51 has been solved with a simple line search with an initial value of $\xi_1 = 0.5$.

3.10.3 Martensite Calculator - Code Structure and Case Example

The open source, object-oriented Matlab code "Martensite Calculator" for the calculation and specific selection of solutions for invariant plane strains as well as invariant line strains has been developed and is available online (see section C.1). The basic idea behind the code structure is shown in Figure 3.15 and the graphical user interface in Figure 3.16.

Next, a case study utilizing the lattice parameters of MarvalX12 is presented. All slip systems from Table 3.5 are considered, i.e. a total of 84 systems in austenite and 48 systems in martensite (both slip directions of a system are counted separately). All possible pairings are considered. The number of pairs given by $N_{\text{pair}} = N(N - 1)/2 = 12090$. The number

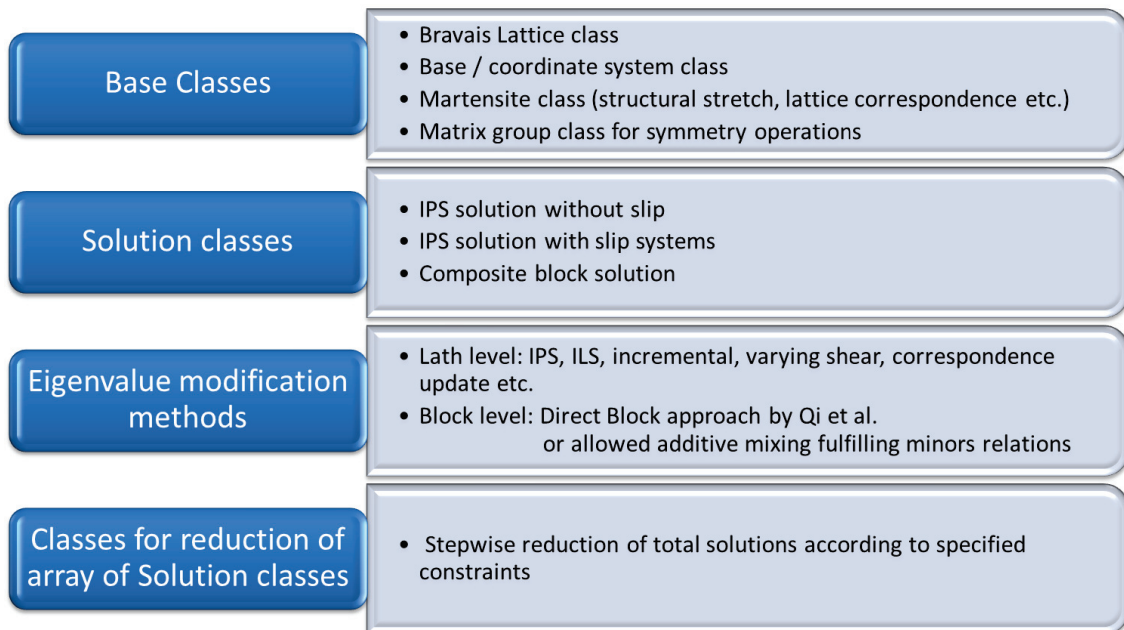


FIGURE 3.15: Basic code structure of Martensite Calculator

of theoretically possible habit planes cannot be larger than two times this value (recall that solutions come in pairs for the cubic to cubic transformation). All calculations are carried out in the austenite basis. Therefore, the slip systems of martensite are transformed into that coordinate system accordingly.

The calculation loops over all possible combinations of slip systems identified. Combinations of two shears are used to compute the net transformation matrix of the smallest microstructural features, i.e. martensite laths \mathbf{F}_{IPS}^L according to Equation 3.28. Particularly, the plastic slip magnitudes ε_s^i are incrementally increased such that a cost function is optimized. Note that not all combinations of slip-systems are able to optimize the cost function (see subsection 3.10.1.3), i.e. they do not converge against an invariant plane strain. All solutions for combinations of slip systems that converge against the utilised cost function optimum are gathered for further consideration. In practice a solution is converged if $1 - \lambda_2 < a$ given allowable residual (here chosen as 10^{-6}).

In a next step the set of all possible solutions is reduced according to reasonable constraints (cf. subsection 3.10.1.3). Particularly, the following constraints are specified for reducing the total number of solutions:

The maximum deviation of a perfect CP plane relationship is $\theta_{CP}^{L-\max} = 2^\circ$.

The maximum deviation of a perfect parallelism of KS OR directions is $\theta_{KS}^{L-\max} = 5.5^\circ$.

The final invariant habit plane should not be further away from $\{111\}_\gamma$ than $\theta_{HP}^{L-\max} = 20^\circ$.

The maximal allowable value of the sum of the two active shear magnitudes $\varepsilon_s^{\max} = 0.4$

The maximum allowable value for the lath shape strain $\varepsilon_0^{L-\max} = 0.65$ and the maximum deviation of the closest packed austenite direction to the already identified invariant plane $\theta_{ILS}^{\max} = 3^\circ$.

In the case of an updated lattice correspondence the total number of solutions found is 16558. Then sequentially filtering out for $\theta_{HP}^{L-\max}$, θ_{CP}^{\max} , θ_{KS}^{\max} , θ_{ILS}^{\max} , ε_s^{\max} , $\varepsilon_0^{L-\max}$ the solutions are reduced to 7733, 2235, 1930, 1197, 1048 and 1023 respectively.

In the case of a constant lattice correspondence the total number of solutions found is 19576. Then the solutions are successively reduced to 9828, 3216, 3140, 688, 652, 620, 620 with the same sequence of selection criteria. Interestingly, while the total number of solutions found without a correspondence update increases, the final number after all reductions have been applied is almost half of that with an incrementally updated lattice correspondence.

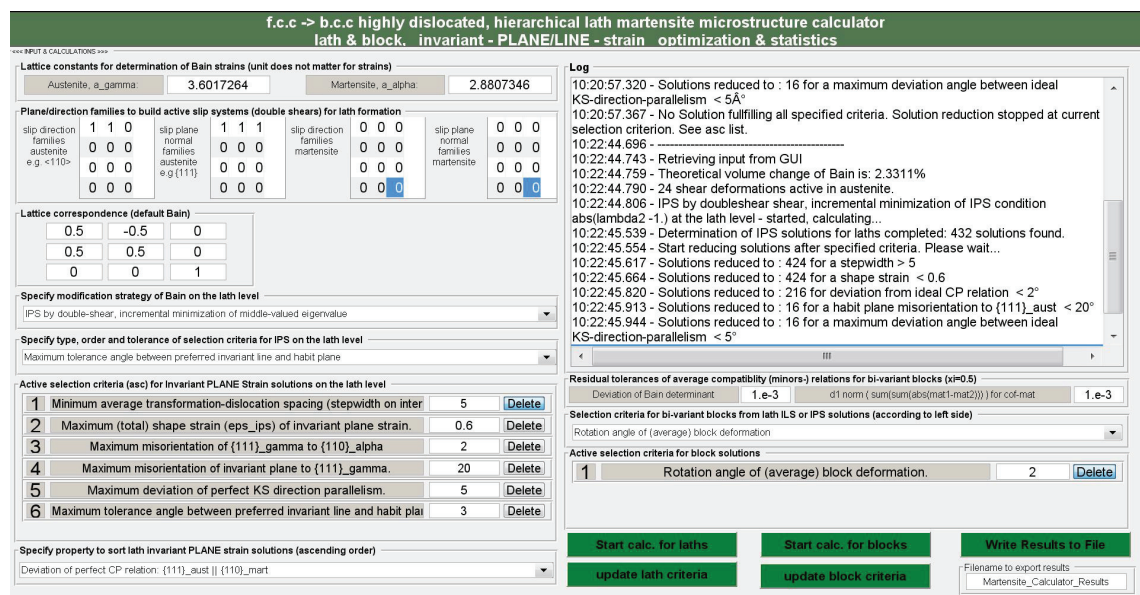


FIGURE 3.16: Graphical user interface of written Matlab toolbox. Input parameters are the lattice parameters and possible slip systems (either in austenite or martensite). A default lattice correspondence is proposed but may also be changed. A set of predefined selection criteria with user defined tolerances can be specified. A log informs the user about errors or calculation activities. After lath solutions have been calculated, optionally composite solutions can be constructed from lath solutions. The results can be written to a text file.

It was also noticed that the well-known linear-dependence of slip deformations, plays a significant role in reducing possible solutions (same overall deformation) due to the nature of the algorithm. A reduction of solutions by a factor of about 2.5 was observed. Nevertheless, all solutions of equal (within some tolerance) deformation but different active slip systems are subsequently considered as individual solutions. Note that this fact may explain the strong heterogeneity of sub-blocks upon high plastic deformation.

Next the evolution of selected solutions after application of the above constraints is visualized with each quantity that has been used in the constraints. In the following two cases the classical constant Bain lattice correspondence and that of an updated correspondence due to the incremental shearing will be presented alongside.

In Figure 3.17 the evolution of the number of solutions with the larger shear magnitude as well as the sum of both shear magnitudes is illustrated. The results indicate that for most of the reasonable solutions one shear generally is much larger than the other. Referring to the previous discussion on slip systems, one shear is mainly necessary to rotate the lath to its habit plane (accommodation transformations), while the other reduces coherency strains in the interface (transformation dislocations). While in the case of using an incrementally

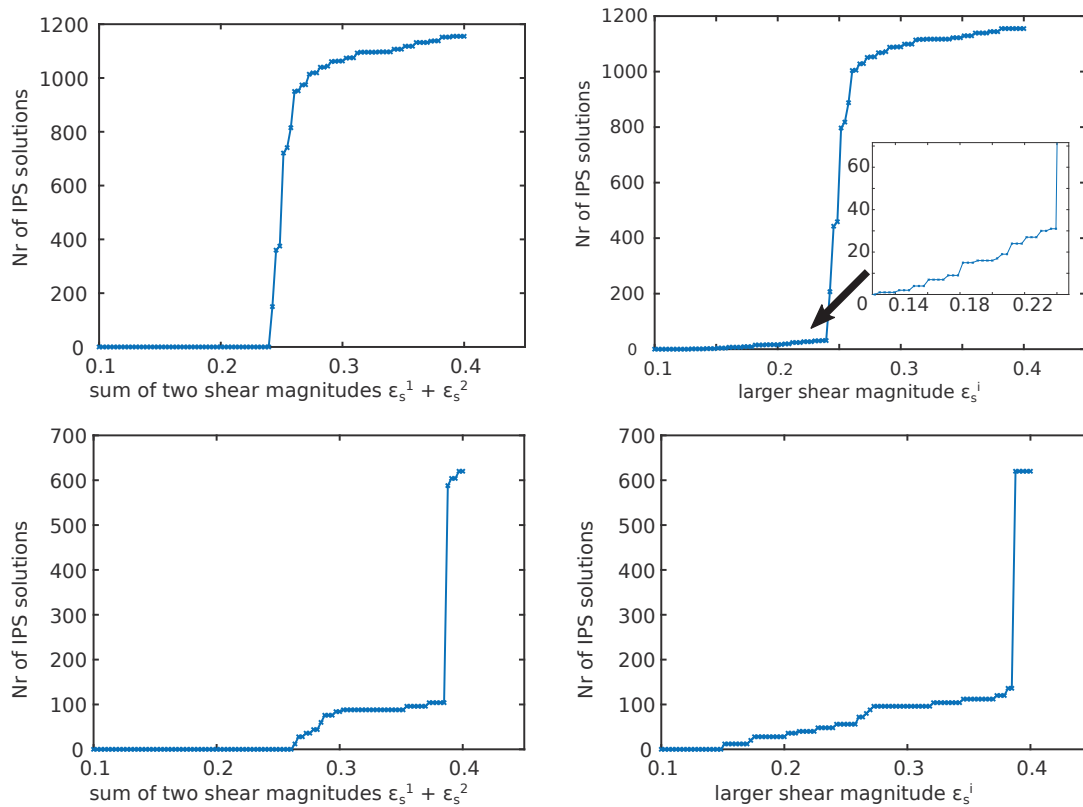


FIGURE 3.17: Evolution of selected habit plane solutions dependent on the larger shear magnitude (right) as well as the sum of both plastic shear magnitudes respectively (left). Top: Correspondence update. Bottom: Constant Bain correspondence. In both cases the results indicate that for most solutions one shear is substantially larger than the other. Also both cases show a strong increase in solutions above a specific value. However, in the case of an updated lattice correspondence the total required shear magnitude is generally lower.

updated lattice correspondence above a certain shear magnitude the possible number of solutions increases from almost zero very fast to its final value. Without a correspondence update the number of solutions first increases to a fraction of the total solutions and then jumps discontinuously to the final value. In general this means, that active lattice rotations during the transformation facilitate accommodation by providing more possibilities of forming an invariant plane strain, which may be one of the reasons of the exceptional properties of lath martensites.

Figure 3.18 illustrates the evolutions of the reduced set of solutions as a function of the habit plane shape strain ε_0^L as well as of the necessary domain rotation in order for its formation. It can be seen that most solutions are found for shape strains in the range of 0.3 to 0.45 which are quite typical values. In terms of lattice rotations this corresponds to

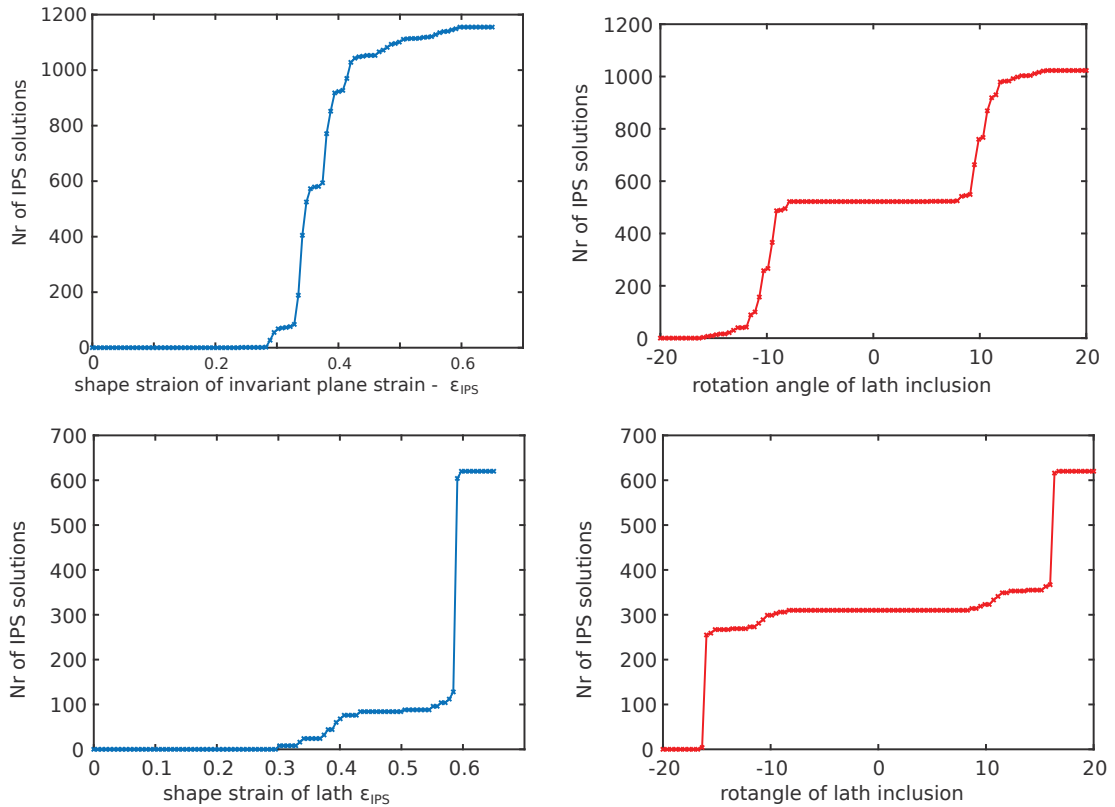


FIGURE 3.18: Progression of selected habit plane solutions depending on their shape strains ϵ_0^L as well as the rotation angle the inclusion must undergo in order to form an invariant plane strain. Top: Correspondence update. Bottom: Constant Bain correspondence. Due to the considered cost function that is optimized incrementally it can be seen that the shape strain has exactly the same progression as the rotation. The right column also illustrated the algorithms ability to find the same number of solutions due to opposite shear directions leading to opposite rotations, which may be interesting for lattices with lower symmetry.

an angular range of about 10° to 12° from $\{111\}_\gamma$, corresponding to the well-known $\{557\}_\gamma$ habit plane type of individual laths.

The difference between an updated and a constant lattice correspondence is similar as in the aforementioned, due to the almost identical nature of ϵ_0^L and $\sum \epsilon_s^i$ in the case of highly dislocated martensite. In the constant case the number of solutions first rises gradually and then shows a jump to comparatively high values. However, in the updated case now clearly 3-4 small plateaus of solutions can be identified in a range where the number of solutions increases significantly (ϵ_0^L between 0.28 and 0.42). These correspond to a distinct type of active slip systems (and their combinations) enabling the transformation.

Next, the dependence of the selected solutions on the misorientation from a perfect Kurdjumov-Sachs orientation relation is investigated. The results are depicted in Figure 3.19. Here the

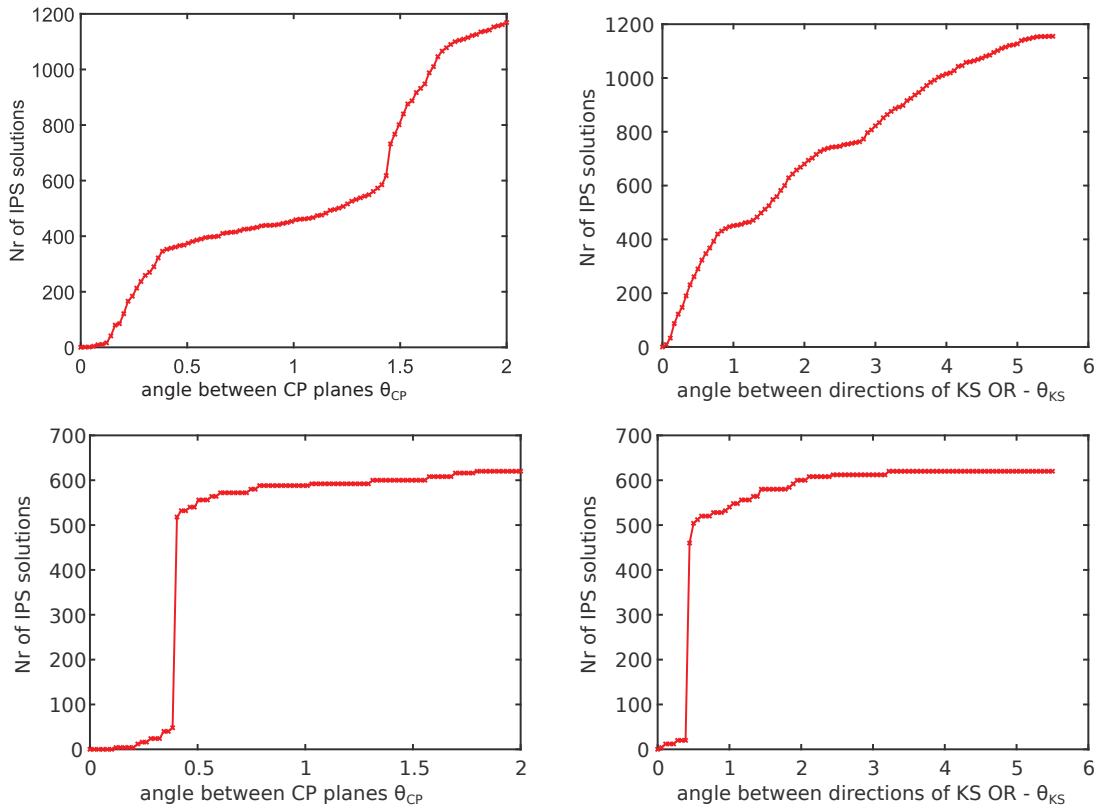


FIGURE 3.19: Dependence of results on misorientation of CP planes (θ_{CP}) and deviation ideal KS direction parallelism θ_{KS} . θ_{CP} is reported to be almost zero. Top: Correspondence update. Bottom: Constant Bain correspondence. In both cases the calculations almost have a plateau for $\theta_{CP} > 0.5^\circ$, so it is reasonable to assume that it is smaller than 0.5° . As opposed to previous dependencies Right: The deviation of the ideal KS direction from the calculated one shows a continuous evolution in accordance with the continuous features of pole figures observed experimentally.

situation is different from previous trends since now the constant correspondence case generally leads to a higher number of solutions at low optimization values (seen as favourable). This is interesting since for an updated lattice correspondence the solutions start to rise earlier, but than saturate again contrary to the constant correspondence case where discontinuous jumps occur at $\theta_{CP} > 0.4^\circ$ as well as $\theta_{KS} > 0.3^\circ$.

Figure 3.20 illustrates the dependence of selected solutions on (i) the misorientation of their habit plane normals and the nearest close packed plane in austenite ($\{111\}_\gamma$) designated as θ_{HP} as well as (ii) the dependence on the angle between the habit plane and the nearest close packed direction in austenite ($\langle 110 \rangle_\gamma$) which normally is experimentally observed to be collinear with the lath's long dimension. For both a constant and an updated lattice correspondence the first solutions are realized $> 5^\circ$. In the case of an updated correspondence there are generally more solutions with smaller deviations between $\langle 110 \rangle_\gamma$ and the lath's

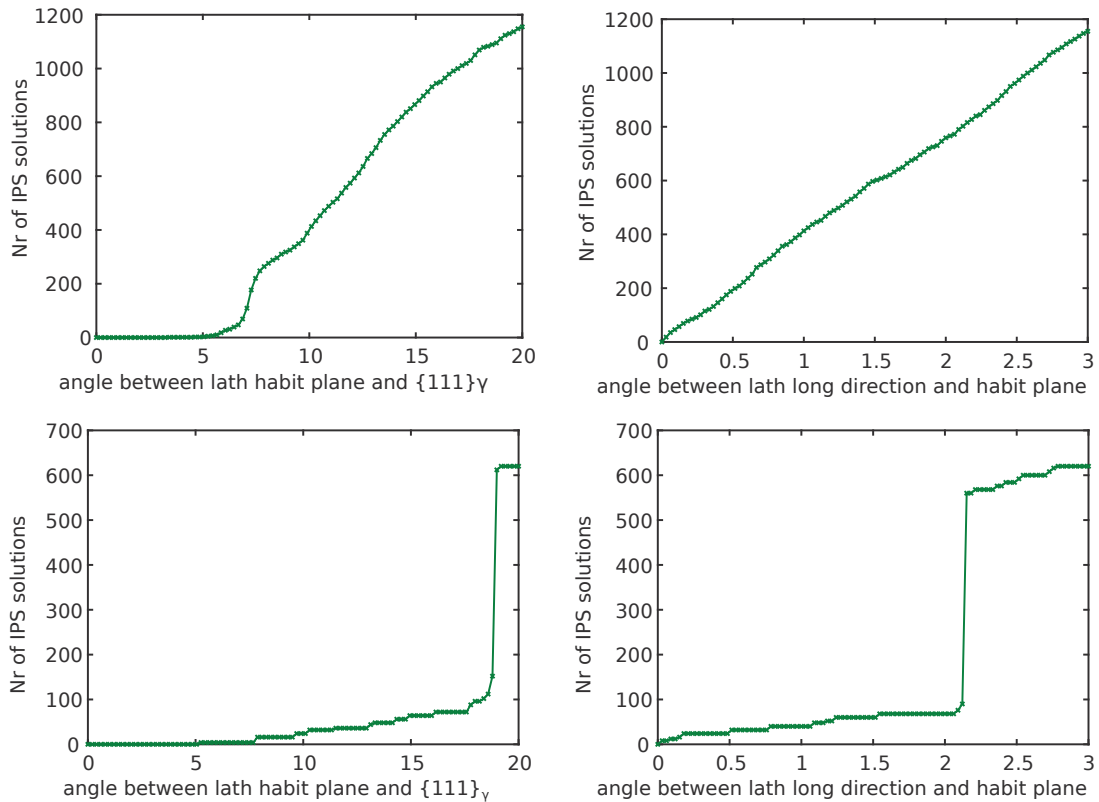


FIGURE 3.20: Left: Effect of misorientation between the laths' habit planes and the nearest close packed plane in austenite. Right-column: Smallest angle between preferred invariant line direction ($\langle 110 \rangle_\gamma$) and habit plane of solutions. Top: Correspondence update. Bottom: Constant Bain correspondence.

habit plane. This is also important since the lath's long direction favourably constitutes the direction of an invariant line strain providing a glissile transformation mechanism.

A major advantage of the object oriented programming approach to the current problem is that it can be easily searched for solutions fulfilling a set of properties. In order to enable an easy visual representation here the discussion is confined to the case of a two-variable dependence and continue with the number of possible solutions. However, it should be noted that any combination of variables may be visualised this way with the goal to investigate a possible correlation. Figure 3.21 shows the number of solutions fulfilling simultaneously a restriction on θ_{CP}^L and ε_0^L . The limiting curves for the highest value of the second variable is recovered in the previous figures showing merely one dependence, while now additionally the evolution in dependence on the second variable is visible.

Actually, if the specified limits for a reasonable selection of lath solutions are not clear a-priori they can be investigated by plotting the data of the whole set of solutions.

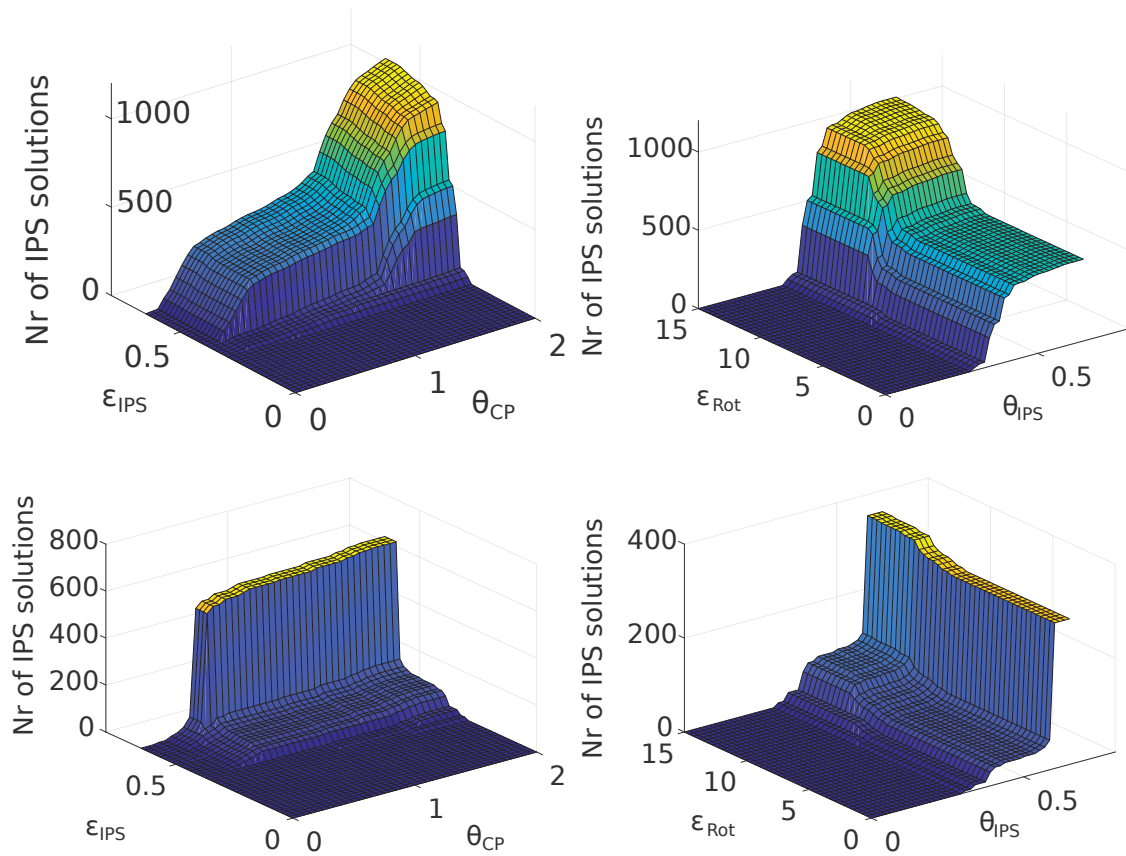


FIGURE 3.21: Visualization of combined property dependences of the number of total habit plane solutions on ϵ_0^L and θ_{HP}^L in the previous example. Left-column: $\epsilon_0^L < \text{threshold}$ and $\theta_{\text{HP}}^L < \text{threshold}$. Right-column: $\epsilon_0^L < \text{threshold}$ and $\theta_{\text{Rot}}^B < \text{threshold}$. Top: Correspondence update. Bottom: Constant Bain correspondence.

The next essential step is the construction of block deformations by means of a reasonable mixture of lath level solutions. Since the laths are elongated in shape, but nevertheless undergo a rotation to accomplish the final orientation relation a major role of block formation is to compensate individual rotations of sub-blocks of laths. Also it was tested to what extent linear mixtures of deformations can obey the minors relations. It should be noted that it is generally known that the minors relations pose too severe restrictions on lattices, so that only in rare cases exact solutions are possible (e.g. Bhattacharya 2003). Therefore, as elaborated in subsection 3.10.2, tolerances are defined under which any solution is found. In order to avoid regarding mixtures of almost equal deformations now the set of solutions is reduced by a criterion for equality of deformation. For this purpose three angles between initial and deformed mutually orthogonal vectors as well as three deformation stretch measures in these directions are defined for each lath deformation gradient respectively. Then two mappings are compared by their difference in angle and

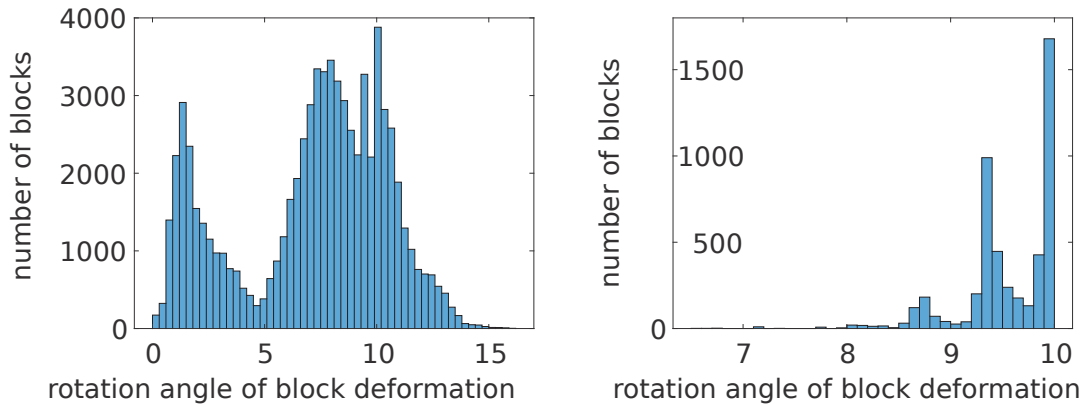


FIGURE 3.22: Overview of rotation angles of composite block deformations at a phase fraction of $\xi_1 = 0.5$. Left: All possible combinations of lath solutions. It can be seen that there are about 400 composite blocks with a rotation angle near 0° which can be seen as optimal in terms of accommodation. Right: Composite blocks reduced by minors relations with $\Delta d_{1_{\max}} = 0.003$ and $\Delta \det_{\max} = 0.003$ showing no blocks with low angles.

stretch measure. This corresponds to a check of similarity of parallel-epipeds. Tolerances of 3° and 1% difference in stretch were applied. Then all possible linear mixtures with $\xi_1 = 0.5$ are constructed from the lath solutions. While in general there are some blocks that do not exhibit a net rotation it turns out that there are none with additional lower bounds on the minors relations as illustrated in Figure 3.22. However, this merely indicates that no optimally accommodated state exists in steels.

This is one reason why the transformation is irreversible.

Beside the compensation of the net rotation of the mapping for composite blocks (a tolerance of $\theta_{\text{Rot}}^{\text{B-max}} = 1^\circ$ is used) the following further constraint is considered: Experimentally it is found that the blocks are oriented close to $\{111\}_\gamma$, hence a limit of $\theta_{\text{HP}}^{\text{B-max}} < 5^\circ$ is specified. Also, it must be pointed out that the sum of two invariant plane strains again yields an IPS. Therefore, a specification of the IPS condition (Equation 3.27) is a relatively weak selection criterion. Practically setting a tolerance of 10^{-3} does not lead to fewer solutions.

The number of pairings using the reduced set of lath solutions in the case of an updated lattice correspondence is 522753 whereas it is 191890 in the case of no lattice correspondence update. Applying the above constraints leaves 1400 solutions in the first case and 2 solutions in the second case.

Figure 3.23 shows the 1400 composite block rotation angles of case 1. It can be seen that the rotation of the composite block is most efficiently compensated at $\xi_1 = 0.5$. Also

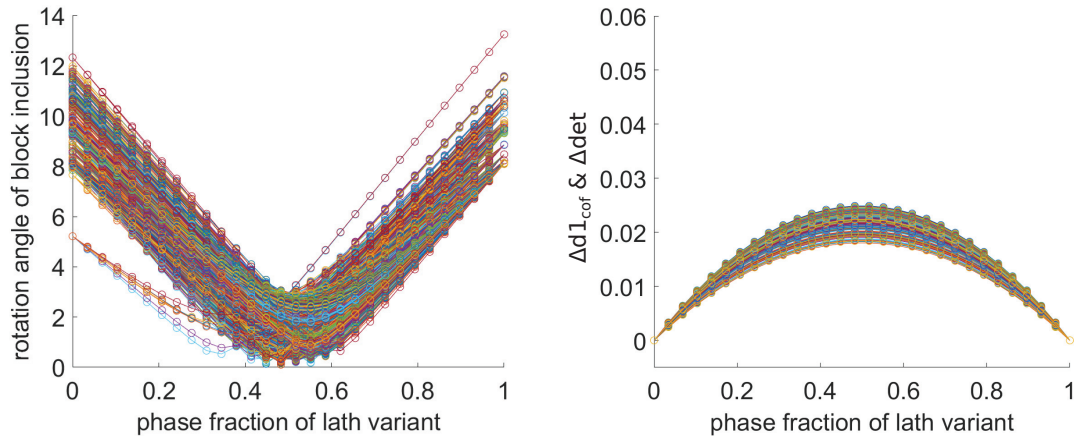


FIGURE 3.23: Left: Net rotation angle of linearly mixed block strain as a function of ξ_1 . It can be seen that almost all minima of the rotation angle are between $\xi_1 = 0.4$ to 0.6 . Right: Residuals of minors relations as a functions of ξ_1 .

the evolution of the residuals for the minors relations over the mixing weight ξ_1 for block mappings concurrently fulfilling the constraints of $\theta_{\text{Rot}}^{\text{B-max}} = 1^\circ$ and $\theta_{\text{HP}}^{\text{B-max}} < 5^\circ$ is shown. Hence the rotation angle is most effectively compensated in the range $\xi_1 = 0.4 - 0.6$ for most composite blocks. Figure 3.24 shows the evolution of the habit plane orientation as a function of ξ_1 for two randomly chosen blocks respectively as well as for all blocks simultaneously in the range of ξ_1 where the rotation minimum occurs.

To further optimize the lath fraction ξ_1 of the block the procedure elaborated in subsection 3.10.2 is applied. The results are shown in Figure 3.25. The range of optimised properties suggests to set the following limits for a further selection: $\varepsilon_0^{\text{B}} < 0.22$, $|\mathbf{H}^{\text{B}}|^2 < 0.21$ and $|\mathbf{E}_{\text{IPS}}^{\text{B}}|^2 < 0.42$, which leads to 27 very similar deformation gradients. All of them have an optimized ξ_1 in the range $0.485 - 0.5$. Consequently the optimized solution in the case of an updated lattice correspondence is

$$\mathbf{F}_{\text{upd}}^{\text{B}} = \begin{bmatrix} 1.0744 & 0.0761 & 0.0023 \\ 0.0685 & 1.0817 & 0.0026 \\ 0.0076 & 0.0035 & 0.8672 \end{bmatrix} \pm \begin{bmatrix} 0.0065 & 0.0125 & 0.0020 \\ 0.0112 & 0.0060 & 0.0024 \\ 0.0094 & 0.0095 & 0.0008 \end{bmatrix}$$

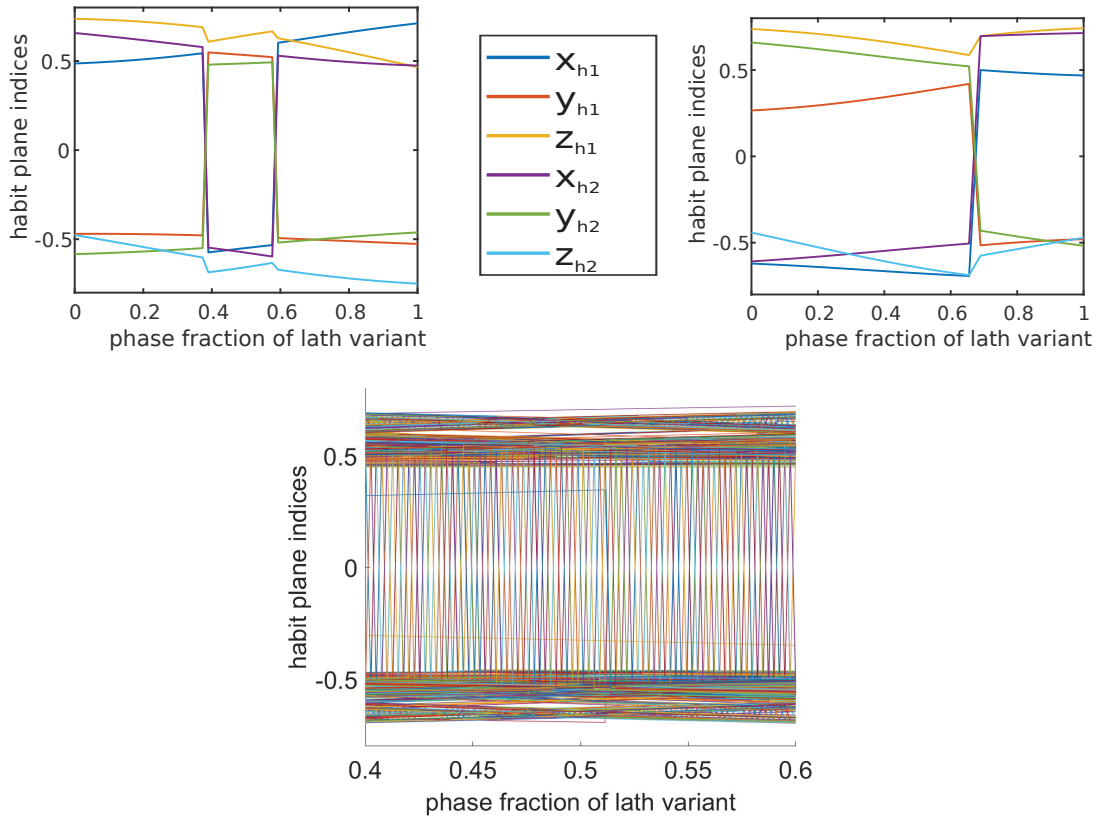


FIGURE 3.24: Top: Evolution of block habit plane orientation (plane normal vector components) of two randomly selected linear mixtures of lath habit plane solutions. Bottom: Full spectrum of plots over all unrestricted linear mixtures of laths to blocks in the range of favourable rotation. The results indicate that there exists a continuous spectrum of block habit planes that are oriented similarly.

The better solution of the two, constructed from lath solutions without lattice correspondence update (the one with the smaller ε_0^B is

$$\mathbf{F}^B = \begin{bmatrix} 1.0745 & 0.0831 & 0 \\ 0.0731 & 1.0816 & 0 \\ 0 & 0 & 0.8672 \end{bmatrix}$$

The lath solutions that build \mathbf{F}^B both use two slip systems of the type $\langle 100 \rangle_\gamma \{211\}_\gamma$. The shear magnitudes for both laths are $\varepsilon_s^1 = 0.115$ and $\varepsilon_s^2 = 0.17$ respectively. The block habit plane normal is made up by permutations of $\mathbf{h}^B = [0.525 \pm 0.15, 0.54 \pm 0.1, 0.645 \pm 0.005]_\gamma$ (plus varying sign) and that of the individual laths $\mathbf{h}^L = [0.589, -0.657, 0.476]_\gamma$. The overall shape strain of the block is $\varepsilon_0^B = 0.18$ (as can also be seen from Figure 3.25).

On the other hand in the laths that build $\mathbf{F}_{\text{upd}}^B$ preferentially only one slip system is active, namely $\langle 110 \rangle_\gamma \{211\}_\gamma$ with $\varepsilon_s^1 = 0.2463 \pm 0.005$. In some cases there is a small second

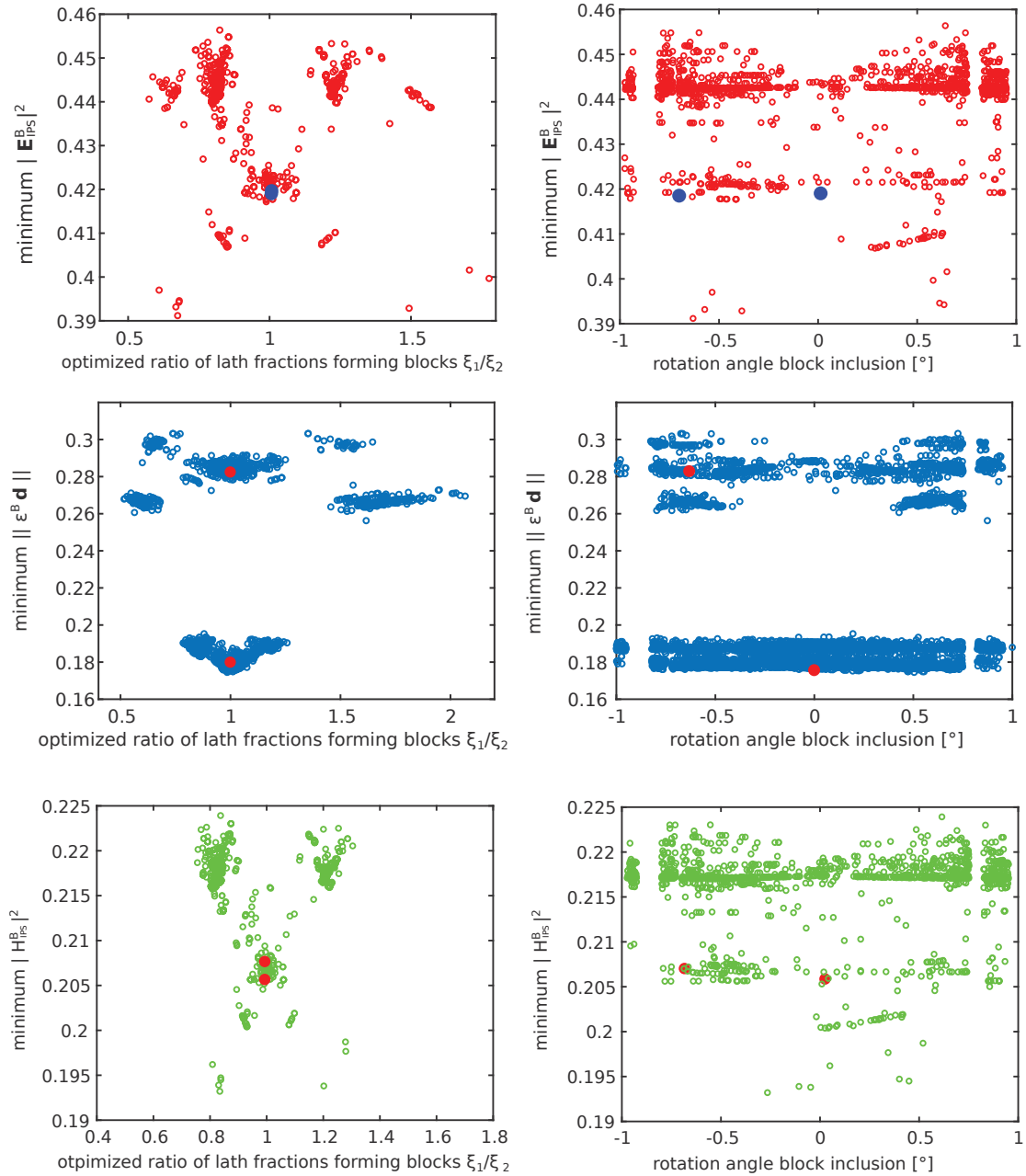


FIGURE 3.25: Block optimization by means of variation of ξ_1 . Three cost functions are considered. Top: Frobenius norm of the Green-Lagrange strain. Center: Minimized shape deformation magnitude. Bottom: Frobenius norm of the displacement gradient for verifying that the remaining small rotation has little influence on the results. The levels of the optimized quantities are still quite different, suggesting new limits for a further reduction of optimal solutions. Marked points are the only two remaining solutions without correspondence using the same constraints.

slip active in martensite on the $\langle 111 \rangle_\alpha \{101\}_\alpha$ system with $\varepsilon_s^2 = 0.02$. The block habit plane normal within the optimal solutions is $\mathbf{h}^B = [0.52, 0.55, 0.65]\gamma$ and that of individual laths $\mathbf{h}_{\text{upd}}^L = [0.54 \pm 0.01, 0.53 \pm 0.01, 0.645 \pm 0.005]\gamma$. The overall shape strain of the block is $\varepsilon_{0\text{upd}}^B = 0.18$. Remarkably the habit planes of the composite blocks are almost equal, although the lath solutions they are built of differ significantly. The small strain as well as Green-Lagrange deformation tensors of the block are

$$\varepsilon_{\text{IPS}}^B = \begin{bmatrix} 0.0814 & 0.0728 & 0.0050 \\ 0.0728 & 0.0889 & 0.0031 \\ 0.0050 & 0.0031 & -0.1271 \end{bmatrix} \quad \mathbf{E}_{\text{IPS}}^B = \begin{bmatrix} -0.4128 & 0.0790 & 0.0047 \\ 0.0790 & -0.4042 & 0.0030 \\ 0.0047 & 0.0030 & -0.6190 \end{bmatrix}$$

compared to that of the Bain strain

$$\varepsilon_{\text{Bain}} = \begin{bmatrix} 0.1311 & 0 & 0 \\ 0 & 0.1311 & 0 \\ 0 & 0 & -0.2002 \end{bmatrix} \quad \mathbf{E}_{\text{Bain}} = \begin{bmatrix} -0.3603 & 0 & 0 \\ 0 & -0.3603 & 0 \\ 0 & 0 & -0.6801 \end{bmatrix}$$

The eigenvectors of all these deformation measures are within 2° of

$$\left[\begin{array}{c|c|c} 1 & 0 & 1 \\ 1 & 0 & \bar{1} \\ 0 & \bar{1} & 0 \\ \hline 1.1506 & -1.1329 & 1.0057 \end{array} \right]$$

where the last line lists the eigenvalues of $\mathbf{F}_{\text{upd}}^B$. This result suggests that blocks have an elongated shape such as sheaves of Bainite in the direction in which almost no stretching occurs, here $[1\bar{1}0]\gamma$. The other two strain components are almost equal in magnitude, but opposite in sign. This circumstance and the fact that blocks accommodate in packets suggests the block arrangement as schematically depicted in Figure 3.26.

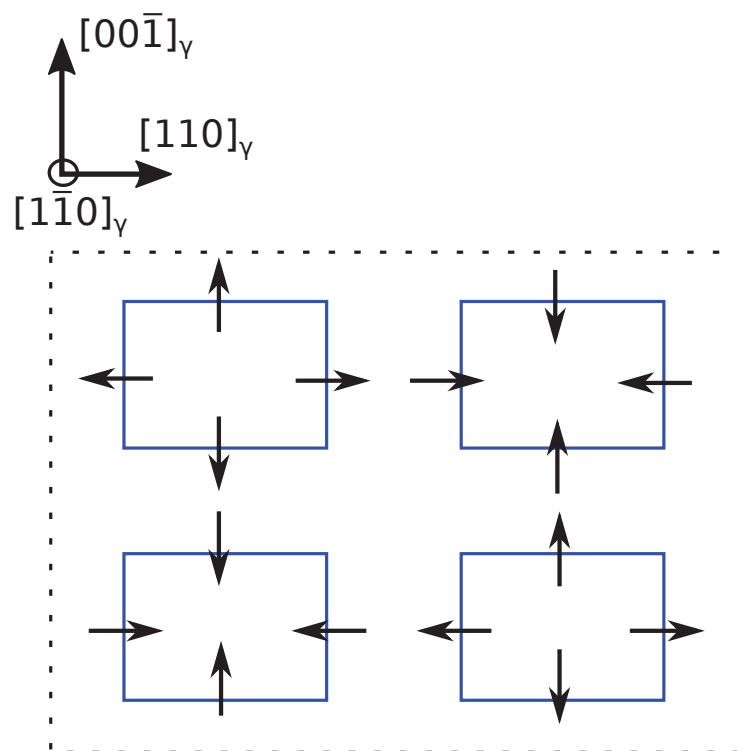


FIGURE 3.26: The previous calculations suggest the following microstructural arrangement of blocks. Shown are sections normal to the largest dimension of the blocks. Up to now a stacking in only one direction has been suggested since the blocks have been envisioned as plates.

Chapter 4

Scale Transition Strategies

Fortunately, the elastic behavior of steel is approximately isotropic, therefore the lengthy discussion of effective moduli of heterogeneous materials, their bounds and determination can be omitted. The interested reader is referred to Maugin 1992; Nemat-Nasser et al. 2013; Qu et al. 2006; Dvorak 2012.

Here Cauchy continua are treated. For generalizations see the works of Forest and co-workers, Jänicke et al. 2009 (micromorphic), Luscher et al. 2010 (second gradient).

4.1 Homogenization

First, recall the Voigt upper and Reuss lower theoretical bounds of effective properties. For polycrystals the equivalents to these bounds are the iso stress model (equal resolved shear stress on the slip system with the highest Schmid factor) by Sachs 1928 satisfying the stress equilibrium condition across the grains but violating the compatibility condition between them, and the iso-strain / full constraint (uniform / constant plastic strain through polycrystal) model by Taylor 1938 violating the stress equilibrium condition but satisfying the compatibility condition among differently oriented grains. Bishop et al. 1951 first presented an incremental formulation of Taylor's model to describe the different loading paths and to show their extreme features for the yield stress of polycrystalline materials.

Microstructurally motivated (lamination theory) Voigt upper bounds have been derived by Bartel et al. 2009; Bartel et al. 2011.

Homogenization methods are based on integration over short length scales ("coarse grain-
ing" in the physics community. The local stress is $\underline{\boldsymbol{\sigma}}(\mathbf{x}) = \underline{\underline{\mathbf{c}}}(\mathbf{x}) : \underline{\boldsymbol{\varepsilon}}^{\text{el}}(\mathbf{x})$. The macroscopic
/ global stress and strain $\underline{\boldsymbol{\Sigma}}$ and $\underline{\mathbf{E}}$ are understood as:

$$\underline{\boldsymbol{\Sigma}} = \langle \underline{\boldsymbol{\sigma}} \rangle = \frac{1}{V} \int_V \underline{\boldsymbol{\sigma}}(\mathbf{x}) dV \quad (4.1)$$

$$\underline{\mathbf{E}} = \langle \underline{\boldsymbol{\varepsilon}} \rangle = \frac{1}{V} \int_V \underline{\boldsymbol{\varepsilon}}(\mathbf{x}) dV \quad (4.2)$$

If the boundary value problem (BVP) of a volume e.g. under a prescribed mean strain $\underline{\mathbf{E}}$
can be solved, for each point \mathbf{x} a (concentration) tensor $\underline{\underline{\mathbf{A}}}(\mathbf{x})$ can be found such that

$$\underline{\boldsymbol{\varepsilon}}(\mathbf{x}) = \underline{\underline{\mathbf{A}}}(\mathbf{x}) : \underline{\mathbf{E}} \quad \text{hence}$$

$$\underline{\boldsymbol{\Sigma}} = \left\langle \underline{\underline{\mathbf{c}}}(\mathbf{x}) : \underline{\boldsymbol{\varepsilon}}^{\text{el}}(\mathbf{x}) \right\rangle = \left\langle \underline{\underline{\mathbf{c}}}(\mathbf{x}) : \underline{\underline{\mathbf{A}}}(\mathbf{x}) : \underline{\mathbf{E}} \right\rangle = \underline{\underline{\mathbf{C}}}^{\text{eff}} : \underline{\mathbf{E}} \quad (4.3)$$

It must be emphasised that $\underline{\underline{\mathbf{C}}}^{\text{eff}}$ is not the mean value of the elastic tensor!

Note, that from a mere mathematical point of view homogenization via an volume element
is generally an ill posed problem. At the microscale suitable boundary conditions (BCs)
have to be defined. The four standard / commonly used types of boundary conditions are:
i) Kinematic uniform boundary conditions (KUBC), i.e. a homogeneous strain at the model
boundary.

$$\mathbf{u} = \underline{\mathbf{E}}\mathbf{x} \quad \forall \mathbf{x} \in \text{boundary } \partial V \quad (4.4)$$

Solution of the boundary value problem yields the (microscopic) stress field and by av-
eraging the effective stress. ii) Static / stress uniform boundary conditions (SUBC) are
understood as applying a uniform stress tensor on the model boundary (with outer normal
 \mathbf{n}), i.e.:

$$\underline{\boldsymbol{\sigma}} \cdot \mathbf{n} = \underline{\boldsymbol{\Sigma}} \cdot \mathbf{n} \quad \forall \mathbf{x} \in \text{boundary } \partial V \quad (4.5)$$

iii) Mixed boundary conditions. iv) Periodic boundary conditions (PBC)

$$\mathbf{u} = \underline{\mathbf{E}}\mathbf{x} + \mathbf{v} \quad \forall \mathbf{x} \in \text{boundary } \partial V \quad (4.6)$$

where \mathbf{v} denotes a periodic fluctuation (same value on opposing sides of periodic model

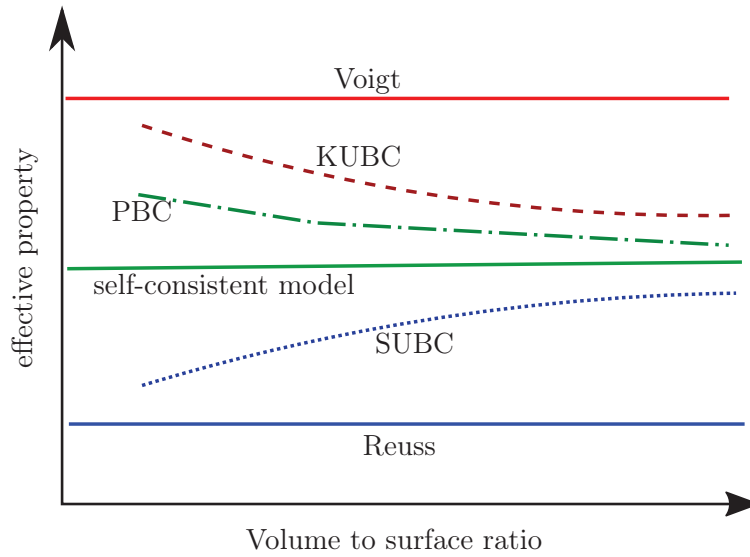


FIGURE 4.1: Schematic, showing the influence of several kinds of boundary conditions on the effective bulk properties of a micromechanical model. An representative volume element is defined as the volume above which the effective properties obtained from KUBCs and SUBCs coincide.

mesh). Generally, PBCs give better approximations than KUBC and SUBC. However, for many technologically relevant materials a small improvement in accuracy is often not worth the effort as pointed by Schneider et al. 2017; Bargmann et al. 2018. It should also be noted, that the stiffness matrix of the global finite element problem loses its band structure by utilizing PBCs.

All types of the a.m. BCs fulfil the Hill-Mandel principle of macro-homogeneity or energy equivalence condition (as in Nemat-Nasser et al. 2013)

$$\langle \boldsymbol{\sigma}^* : \boldsymbol{\varepsilon}' \rangle = \boldsymbol{\Sigma} : \boldsymbol{E} \quad (4.7)$$

with $\boldsymbol{\sigma}^*$ being a divergence free stress field and $\boldsymbol{\varepsilon}'$ a compatible strain field. In statistical theories such as that due to Kröner this condition is viewed as an ergodic hypothesis.

The non-uniform / inhomogeneous case of the above types of boundary conditions as well as the corresponding generalized Hill-Mandel condition for bending are found in Besson et al. 2009 p.296 therein.

For the sake of completeness symmetry BCs commonly applied for components with symmetries are mentioned. They constrain the normal displacement components at the unit cells' surfaces, leaving tangential displacements free. This enforces the condition that pairs

of faces must stay parallel throughout the deformation history. Antisymmetry (or point symmetry) boundary conditions require the presence of centers of point symmetry (“pivot points”) and are, accordingly, even more limited in terms of the microgeometries that they can handle. In contrast to symmetry boundary conditions, however, unit cells employing antisymmetry BCs on all faces are subject to few restrictions with respect to the load cases that can be handled.

To ensure that the homogenization scheme is efficient, separability of scales must hold Besson et al. 2009, i.e. it is required that:

size of the heterogeneities \ll size of the modelled volume \ll size of the final structure

By definition, if the model volume is of sufficient size for a proper representative volume element (RVE) the lower and upper estimates and bounds on the overall elastic properties will coincide, defining the effective behavior. McDowell 2010 points out that it is often tacitly assumed that the RVE size for evolving microstructures is the same as used to study stationary properties. However, since evolution is highly sensitive to local configurations of microstructure attributes, the RVE for such evolutionary responses must often be quite larger than for stationary problems.

If the RVE size is too large or the microstructure very complex the concept of statistically similar RVE (SSRVE), see Schröder et al. 2011; Balzani et al. 2014 may be useful. For microstructures usually an n -point probability function S_n is defined, representing the probability that n points (e.g. given by their 2D coordinates x_i, y_i) are located in phase r , see e.g. Torquato 2013. S_n then is obtained from an ensemble average over indicator functions (0 or 1).

4.2 Possible Microstructure Discretization Levels for the Hierarchical Structure of Lath Martensite

At this point the recent progress in Voronoi tessellation codes able to reproduce statistical microstructure data must be emphasised (Gueninchault 2017; Quey et al. 2018). For instance the open source code Neper provides an easy of achieving several levels of multiscale discretizations. References to this and other useful codes can be found in section C.1.

To capture the whole range of the hierarchical microstructure of dislocated lath martensite the several levels of geometrical discretization for a RVE are possible. The least discretised version is a polycrystal RVE that explicitly resolves PAGs with a single orientation. The advantage in using such a model is that intra grain features are more a result of the model than given a priori. The problem of not explicitly resolving the next lower level of microstructure, i.e. packet boundaries, is that it is difficult to create a model that reproduces the spatial distribution of all 24 martensite variants into packets. It is not clear whether this can be achieved with a mere integration point model that considers all variants. If such a model exists then its model parameters lie in a very small range. Particularly, in order to achieve a spatial patterning the material point behavior of each martensite variant must be strongly coupled to the global equilibrium problem based on reasonable assumptions. A major difficulty is to describe the effect of spatial arrangement in an average manner. The potential of depicting reasonable variant patterning by allowing local softening behavior (instability) should be investigated. A gradient based finite element framework that considers variant fractions of neighbouring integration points would certainly facilitate this problem.

If packet boundaries are resolved from the beginning, the drawback is that to date no general strategy seems to exist for their selection. The author assumes that the behavior of packet formation resembles that of subgrain formation (e.g. Sedláček et al. 2002; Kratochvíl 2014). Since the sectioning of grains into packets already occurs in the early stages of the transformation, the selection of packet boundaries may be modelled explicitly. The advantage of this level of discretization contrary to packet interactions is, that sub-packet morphology follows a more well-arranged / regular / organized structure allowing for a more reasonable formulation of block interactions.

Finally, there are also studies explicitly resolving packet and block boundaries, see Sun et al. 2018. While the results are certainly interesting they provide almost no freedom for microstructure evolution.

Different geometrical sectioning schemes of grains to packets have been proposed by Osipov et al. 2009. Working out their physical significance still remains an open issue. For codes to generate microstructure meshes see section C.1.

4.3 The Eshelby Tensor, Inclusions, Inhomogeneities and the Equivalent Inclusion Method (EIM)

In linear elasticity the boundary value problem of inclusions is commonly solved by using Greens functions and assuming an infinite solid as well as small deformations.

First some common terminology is provided:

Eigenstrain denotes non-elastic strains such origination from (anisotropic) thermal expansion, transformation strain of phase transformation, plastic strain or misfit strain. The shape change the domain / inclusion (I) would undergo if it were separated from the surrounding elastic solid is called the stress free eigenstrain. However, due to the constraint by a surrounding a matrix (M) both the inclusion and the matrix will be stressed.

Inclusion: same elastic constants of matrix and some domain, where the domain has an eigenstrain.

Inhomogeneity: different elastic constants of matrix and domain, where the domain has no eigenstrain. Furthermore, it must be distinguished between elastic strains due to accommodation or external loading $\boldsymbol{\sigma}^{\text{ext}} \Leftrightarrow^{\text{ext}} \boldsymbol{\varepsilon}^{\text{el}}$.

Here some results for the isotropic inclusion are presented. Remarkably, it turns out that the stresses and strains are uniform inside the ellipsoid (in both isotropic and anisotropic cases).

$$\varepsilon_{ij}^{\text{cl}} = S_{ijkl}\varepsilon_{kl}^* = -P_{ijmn}C_{ijkl}\varepsilon_{kl}^* = -P_{ijmn}\boldsymbol{\tau}_{mn}^* \quad (4.8)$$

For an ellipsoidal inclusion with a uniform, constant (stress free) eigenstrain ε_{kl}^* in a homogeneous infinite matrix, the Eshelby tensor S_{ijkl} is a constant, i.e. independent of \boldsymbol{x} . Hence the stress and strain fields inside the inclusion are uniform. $\varepsilon_{ij}^{\text{cl}}$ the constrained strain inside the inclusion, P_{ijmn} is called the Hill polarization tensor (Hill 1983) and $\boldsymbol{\tau}_{mn}^*$ the stress polarization (stress caused by the eigenstrain).

Eshelby's tensor is symmetric in the first and second pair of indices (minor symmetries), but in general it is not symmetric with regard to an exchange of these pairs (no major symmetry). If a tensor has minor and major symmetries it is referred to as super symmetric (see e.g. Itskov 2015).

$$S_{ijkl} = S_{jikl} = S_{ijlk} = S_{jilk} \neq S_{klij} \dots$$

In case of an isotropic material and a general ellipsoid, its components depend only on Poisson's ratio ν , the ratios of the principal axes (entering via elliptic integrals solved via an integrated Matlab function, see section C.2) and their orientation with respect to some Cartesian coordinate system. If additionally a spherical inclusion is considered the dependence on the principal axes and their orientation vanishes (geometric isotropy) and a closed form solution solely in terms of ν is possible. τ_{mn}^* must not be confused with the stress in the inclusion, given by

$$\boldsymbol{\sigma}^I = \boldsymbol{\sigma}^c - \boldsymbol{\sigma}^* = \underset{\sim}{\mathbf{C}} \left(\underset{\sim}{\boldsymbol{\varepsilon}}^{\text{cl}} - \underset{\sim}{\boldsymbol{\varepsilon}}^* \right) = \underset{\sim}{\mathbf{C}} : \left(\underset{\sim}{\mathbf{S}} - \underset{\sim}{\mathbf{I}}^{\text{sym}} \right) \underset{\sim}{\boldsymbol{\varepsilon}}^* = -Q_{ijkl} \varepsilon_{kl}^* \quad (4.9)$$

After Qu et al. 2006 Q_{ijkl} can be viewed as the dual / conjugate of the stress polarization tensor P_{ijkl} . One can also show that

$$\underset{\sim}{\mathbf{C}} : \left(\underset{\sim}{\mathbf{S}} - \underset{\sim}{\mathbf{I}}^{\text{sym}} \right) = \left(\underset{\sim}{\mathbf{I}}^{\text{sym}} - \underset{\sim}{\mathbf{S}}^T \right) : \underset{\sim}{\mathbf{C}} \quad \text{and} \quad \underset{\sim}{\mathbf{C}} \underset{\sim}{\mathbf{S}} = \underset{\sim}{\mathbf{S}}^T \underset{\sim}{\mathbf{C}} \quad (4.10)$$

Equation 4.10 are relations that are often necessary for the manipulation of expressions. Since the stress inside an ellipsoidal inclusion is a constant, the total strain energy, as well as that of the matrix and inclusion respectively are given as

$$E_{\text{I}}^{\text{el}} = \frac{1}{2} \underset{\sim}{\boldsymbol{\sigma}}^I : (\underset{\sim}{\boldsymbol{\varepsilon}}^{\text{cl}} - \underset{\sim}{\boldsymbol{\varepsilon}}^*) V^I \quad (4.11)$$

$$E_{\text{M}}^{\text{el}} = -\frac{1}{2} \underset{\sim}{\boldsymbol{\sigma}}^I : \underset{\sim}{\boldsymbol{\varepsilon}}^{\text{cl}} V^I \quad (4.12)$$

$$E_{\text{tot}}^{\text{el}} = -\frac{1}{2} \underset{\sim}{\boldsymbol{\sigma}}^I : \underset{\sim}{\boldsymbol{\varepsilon}}^* V^I \quad (4.13)$$

The interaction energy of the constrained elastic field with another superimposed field (e.g. an external stress field $\boldsymbol{\sigma}^{\text{ext}}$) leads to an interaction energy inside the inclusion of

$$E_{\text{int}} = - \int_V \underset{\sim}{\boldsymbol{\sigma}}^{\text{ext}} : \underset{\sim}{\boldsymbol{\varepsilon}}^* dV \quad (4.14)$$

The fields outside Ω are no longer uniform, however, their values at points adjoining the interface $\partial\Omega$ can be found Walpole 1969; Hill 1983; Suvorov et al. 2002 using interface operators.

For instance Cherkaoui et al. 2000b; Cherkaoui et al. 2000a used this concept to derive energy dissipation considering interface movement based on the assumption of incremental

homogeneous and isotropic ellipsoidal growth of martensite.

$$\mathcal{D}^i = \underline{\underline{\sigma}}^I : \underline{\underline{\epsilon}}^{*i} + \frac{\xi^i}{2} \underline{\underline{\epsilon}}^{*i} : \underline{\underline{C}} : \left(\underline{\underline{I}} - \underline{\underline{S}}^i \right) \underline{\underline{\epsilon}}^{*i} + \frac{\xi^i}{2} \underline{\underline{\epsilon}}^{*i} : \underline{\underline{C}} : \underline{\underline{S}}^i : \underline{\underline{\epsilon}}^{*i} + \quad (4.15)$$

With $\underline{\underline{S}}^i$ it is possible to distinguish several modes of growth such as homotectic- $\underline{\underline{S}}^i = 0$, plane- and lath-growing, see Cherkaoui et al. 2000a.

Another consequence of the homogeneous stress and strain field inside the inclusion is that an inhomogeneous inclusion / inhomogeneity can be treated as a homogeneous inclusion with initial eigenstrain (if present) plus equivalent eigenstrain, as proposed by J. D. Eshelby 1957. This approach is known as the equivalent inclusion method (EIM). The idea of the EIM is to adopt the eigenstrain of an inclusion such that the stress field of an inhomogeneity is obtained. Note that particular simplifications arise for voids or liquid inclusions since then the stress inside is zero or purely hydrostatic.

The framework of the inhomogeneity also involves cracks, and dislocations, see J. P. Hirth et al. 1968. If vacancies are introduced when the solid is under load, the stress and strain fields of a crack or void of the same shape are obtained. This picture leads directly to Eshelby's energy-momentum tensor of elasticity (J. D. Eshelby 1999), or, as it is more widely known in modern fracture mechanics, Rice's J-integral.

The inhomogeneity is not treated here but can be found in the literature (e.g. J. D. Eshelby 1957; J. Eshelby 1961; Maugin 1993; Nemat-Nasser et al. 2013; Qu et al. 2006 p.87 therein. Extensions to elastic anisotropy have been made by Mura 1987.

The most general form of the EIM is the inhomogeneous inhomogeneity (Qu et al. 2006):

$$\underline{\underline{C}}^I : \left(\text{ext} \underline{\underline{\epsilon}}^{\text{el}} + \underline{\underline{\epsilon}}^c - \underline{\underline{\epsilon}}^p - \underline{\underline{\epsilon}}^* \right) = \underline{\underline{C}}^M \left(\text{ext} \underline{\underline{\epsilon}}^{\text{el}} + \underline{\underline{\epsilon}}^c - \underline{\underline{\epsilon}}^p \right) \quad (4.16)$$

where the plastic strain $\underline{\underline{\epsilon}}^p$ can also be considered as stress free eigenstrain. Using Eshelby's solution first an equivalent eigenstrain $\underline{\underline{\epsilon}}^{**}$ is calculated. This then can be used to show that the following relation holds:

$$\underline{\underline{\sigma}}^I = \underline{\underline{\sigma}} + \underline{\underline{C}} \left(\underline{\underline{S}}^{-1} - \underline{\underline{I}}^{\text{sym}} \right) : \left(\underline{\underline{\epsilon}} - \underline{\underline{\epsilon}}^I \right) \quad (4.17)$$

where $\underline{\underline{C}} \left(\underline{\underline{S}}^{-1} - \underline{\underline{I}}^{\text{sym}} \right) = \underline{\underline{H}}$ is known as Hill's constraint tensor (as in Qu et al. 2006 p.88-90) / (elastic-plastic) accommodation tensor (as in Besson et al. 2009 p.242).

4.4 Localization - Scale Transition Rules for Non-linear Behavior

Localisation is the inverse operation of homogenization. A common method for localisation is the self-consistent scheme. This means that inclusions are embedded in a homogeneous medium / matrix which is given weighted average homogeneous properties. Assuming a homogeneous (linear) elastic medium / matrix (HEM) Eshelby's solution can directly be applied as proposed by Kröner 1961 for grains (index g), considering the plastic strain as stress free eigenstrain.

$$\underline{\underline{\sigma}}^g = \underline{\underline{\sigma}}^{\text{ext}} + 2\mu(1 - c_1) \left(\underline{\underline{\varepsilon}} - \underline{\underline{\varepsilon}}^p \right) \quad (4.18)$$

where c_1 is a coefficient related to the Eshelby tensor for the spherical inclusion in an isotropic matrix (only depending on the Poisson's ratio). Often $2(1 - c_1)$ is taken as one. The next step was taken by Hill 1965, who adopted the above concept and described the plastic flow by solving successive linear problems at each loading increment. This leads to an implicit problem since the HEM property is not known a-priori. This model was extended by Berveiller et al. 1978 to obtain elastic-plastic local tangent tensors under the simplifying assumptions of isotropic elasticity, spherical inclusions with constant volume in line with volume preservation in plasticity and monotonic loadings (analytical integration possible).

In any case, if a linear scale transition rule is used the resulting phase stresses are over-estimated. Therefore a nonlinear scale transition has been proposed for describing plastic deformation in a polycrystalline aggregate (Cailletaud 1987; Cailletaud 1992; Cailletaud et al. 1994; Hoc et al. 2001; Hlilou et al. 2009; Cailletaud et al. 2016). The starting point is

$$\underline{\underline{\dot{\sigma}}}^g = \underline{\underline{\dot{\sigma}}}^{\text{ext}} + \underline{\underline{C}}^{\text{eff}} : \left(\underline{\underline{S}}^{-1} - \underline{\underline{I}}^{\text{sym}} \right) : \left(\underline{\underline{\dot{E}}} - \underline{\underline{\dot{\varepsilon}}}^g \right) = \underline{\underline{\dot{\sigma}}}^{\text{ext}} + \underline{\underline{H}} : \left(\underline{\underline{\dot{E}}} - \underline{\underline{\dot{\varepsilon}}}^g \right) \quad (4.19)$$

A pragmatic approach is to move the non-linear evolution of $\underline{\underline{C}}^{\text{eff}}$ (cf. Equation 4.3) to a corrective term $\underline{\underline{\beta}}$.

$$\underline{\underline{\sigma}}^g = \underline{\underline{\sigma}}^{\text{ext}} + \underline{\underline{C}} : \left(\underline{\underline{S}}^{-1} - \underline{\underline{I}}^{\text{sym}} \right) : \left(\underline{\underline{\beta}} - \underline{\underline{\beta}}^g \right) \quad (4.20)$$

Note, that here the elasticity tensor $\underline{\underline{C}}$ basically is a model parameter. Commonly it is simply replaced by a scalar (e.g. the shear modulus μ), otherwise it must at least be checked against theoretical bounds. An extension to anisotropic elasticity can be found in Cailletaud et al. 2016. The global plastic accommodation variable $\underline{\underline{\beta}}$ is calculated as:

$$\underline{\underline{\beta}} = \sum_g \xi^g \underline{\underline{\beta}}^g \quad (4.21)$$

The task is then to find a suitable evolution equation for $\underline{\underline{\beta}}$, which has the status of a localization state. The idea is to introduce a corrective term depending on plastic strains (in analogy to non-linear kinematic hardening or a recovery term in plasticity) as

$$\dot{\underline{\underline{\beta}}}^g = \dot{\underline{\underline{\epsilon}}}^g - \underline{\underline{D}} : (\underline{\underline{\beta}}^g - \delta \underline{\underline{\epsilon}}^g) \|\dot{\underline{\underline{\epsilon}}}\| \quad (4.22)$$

The $\underline{\underline{\beta}}^g$ are "kinematic-like" scale transition variables that are directly linked to the mechanical behavior of the geometry of material domains. The coefficients $\underline{\underline{D}}$ (which is also sometimes replaced by a simple scalar) and δ are not exactly material coefficients, but scale transition parameters, which should be fitted from finite element computations on realistic polycrystalline aggregates.

$\underline{\underline{D}}$ is an accommodation tensor and may be calculated for a predefined shape, see e.g. Sai et al. 2006 for the case of an infinite cylinder. For a relation of $\underline{\underline{D}}$ with $\underline{\underline{S}}$ see Weinberger et al. 2005 (Equation 2.7. therein). Commonly, instead of a tensor a scalar D is employed and seen as a fitting variable representing the a.m. heterogeneous behaviour, i.e. the "kinematic-like" interaction is a result of the optimization procedure of the parameter calibration. Note that for $D = 0$ the model coincides with Kröner's model Equation 4.18. According to Cailletaud et al. 2003, in the case of f.c.c. polycrystals, the single parameter D is enough to get a reliable estimation of the behavior of the polycrystal.

Ben Naceur et al. 2016 use the term with the coefficient δ in combination with linear kinematic hardening to model the ratchetting behavior of a 304 stainless steel. Chaboche 2008 points out that macroscopically 4.22 is very similar to a nonlinear kinematic hardening (combined with a linear kinematic hardening).

Due to its explicit formulation iteration procedures like in classical self-consistent approaches are not required. The model can be seen as phenomenologically self-consistent, offering a large choice for defining inter-phase plastic contributions, see *Z-set: Multiscale Materials Modelling V8.6* n.d. Figure 4.2 provides an conceptual overview of several homogenization / localization schemes including the β -rule in the case of a two-phase composite.

In the present framework the beta rule is employed within the grains for the forming martensite microstructure. Particularly, as shown in section 5.5 for small grain sizes martensite blocks play have the character of grains. Therefore the index g is dropped and a (austenite) and m are introduced. Furthermore, it will be distinguished between symmetry related variants in the martensite with the index i so that the resulting set of equations becomes:

$$\underline{\beta} = (1 - \xi)\underline{\beta}^a + \sum_g \xi^i \underline{\beta}_i^m \quad (4.23)$$

$$\dot{\underline{\beta}}^a = \dot{\underline{\varepsilon}}^a - D\underline{\beta}^a \|\underline{\varepsilon}^a\| \quad (4.24)$$

$$\dot{\underline{\beta}}_i^m = \text{dev}(\dot{\underline{\varepsilon}}_i^{*m}) - \underline{D}^a : \underline{\beta}_i^m \|\text{dev}(\underline{\varepsilon}_i^{*m})\| \quad (4.25)$$

$$\underline{\sigma}^a = \underline{\sigma}^{\text{ext}} + \mu \left(\underline{\beta} - \underline{\beta}^a \right) + K\xi \frac{\Delta V}{3} \underline{I} \quad (4.26)$$

$$\underline{\sigma}_i^m = \underline{\sigma}^{\text{ext}} + \mu \left(\underline{S}_i^{i-1} - \underline{I}^{\text{sym}} \right) : \left(\underline{\beta} - \underline{\beta}_i^m \right) - K\xi \frac{\Delta V}{3} \underline{I} \quad (4.27)$$

Note that only the deviatoric part of the transformation strains lead to a nonlinear evolution, whereas the contribution due to spherical strain part is linear in the phase fraction ξ (K is the compression modulus). Note that the $\underline{\beta}$ -rule gives an exponential saturation of a strain like variable, where strain is directly proportional to the phase fraction ξ , and the most popular kinetic equation (Equation 6.67) has exactly the same exponential saturation character. Petersmann et al. 2017a, showed that the progression of Equation 6.67 can be explained by evolution of the strain energy in a martensitic transformation that is governed by elastic accommodation (hence behaves auto-catalytic in terms of energy minimization

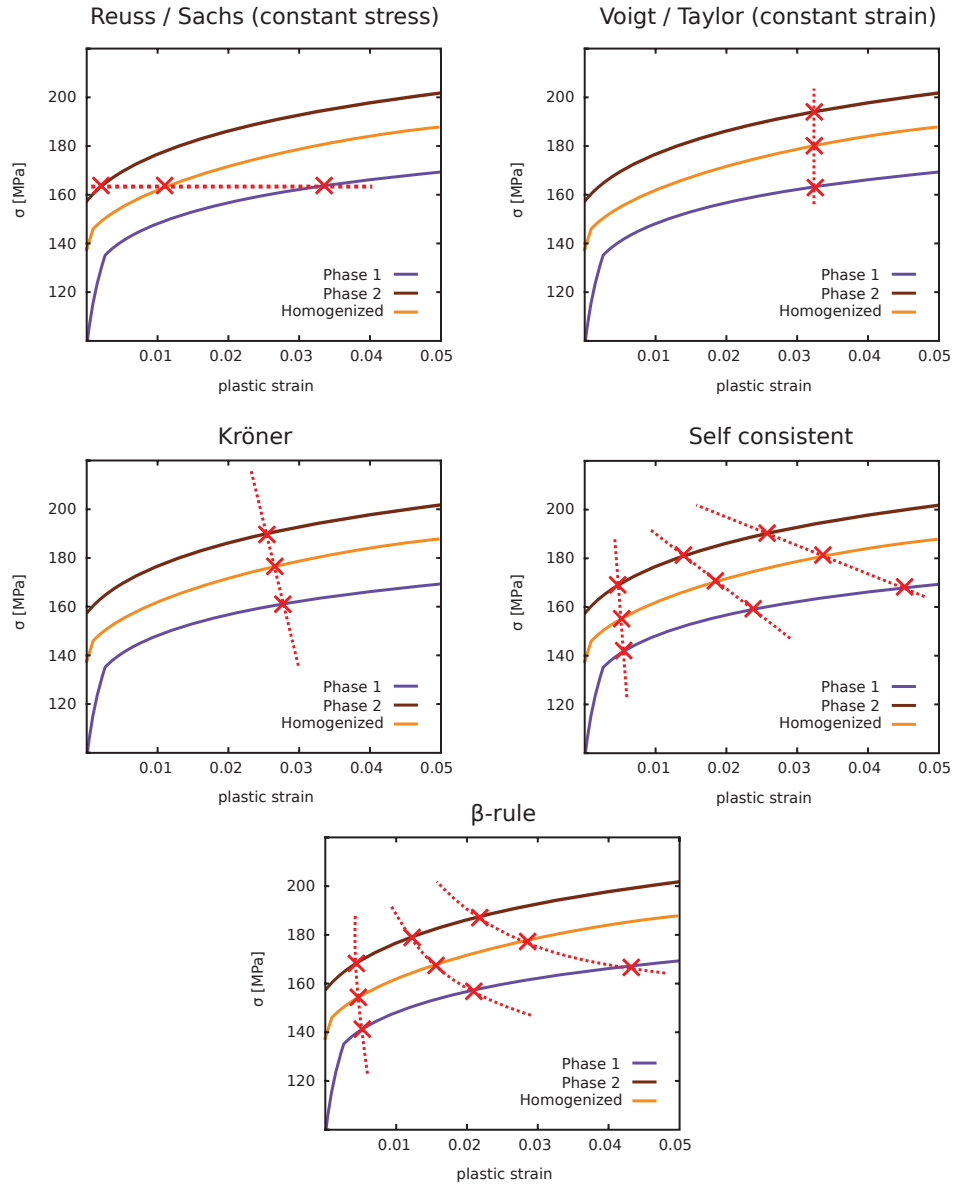


FIGURE 4.2: Schematic interpretation of scale transition rules. Particularly, the evolution of this models under an evolving microstructure is emphasized.

by optimal selection of martensite transformation strain). This provides a physical argument to use the β -rule, which was initially proposed as a phenomenological stress scaling law for plastic behavior, in a mean-field description of martensite.

Finally, it should be mentioned that the according flux variable conjugate to β^i as well as the dissipation contribution are given by

$$\tilde{\mathbf{X}}_i^\beta = \frac{\partial \Psi}{\partial \beta^i} \quad \mathcal{D}^\beta = \tilde{\mathbf{X}}_i^\beta : \dot{\beta}^i \quad (4.28)$$

Chapter 5

Experimental Characterisation

This chapter is organized as follows. First, essential material data to this work is given for MarvalX12. Then a short overview of TRIP experiments is given and the characteristic kinetic features are described. This work focuses on the microstructural changes that lead to as well as accompany the TRIP effect. Therefore, as a next step the effect of thermal cycling on the microstructure is outlined. Finally, a detailed orientation imaging microscopy investigation is carried out.

5.1 MarvalX12 - Material Data

According to a recent nature publication by Morris Jr 2017 the two basic classes of steels that have survived the multi-property selection process to become key competitors for ultra high strength steel applications are secondary hardening steels and maraging steels. Among the latter is the precipitation hardened (PH) 13Cr–8Ni high-strength stainless steels, which is similar in composition to the MarvalX12 investigated in this work. The composition of the MarvalX12 is found in Table 5.1.

The MarvalX12 has a molar mass of $M_{\text{marval}} = 56.22$ g/mol (linear rule of mixtures) compared to that of pure iron, which is $M_{\text{Fe}} = 55.845$ g/mol. Thermal expansion coefficients

Cr	Ni	Mo	Al	Ti	C	Si	Mn	P	S	N
12.15	9.05	2.03	0.7	0.35	<0.01	0.05	0.03	0.009	<0.002	0.0045

TABLE 5.1: Alloying components of Marval X12 (wt%), $\sum \approx 24.2\%$ hence Fe-75.8 %

of austenite and martensite are:

$$\alpha_\gamma = 19.6 \times 10^{-6} K^{-1} \quad \alpha_\alpha = 11.37 \times 10^{-6} K^{-1}$$

The lattice parameters for the maraging steel were measured at "Deutsche Elektronen-Synchrotron" (DESY) in Hamburg at room temperature and linearly extrapolated to the transformation temperature ($M_s = 150 \pm 10^\circ$ C depending on grain size and prior annealing temperature) using the above thermal expansion coefficients of the pure phases resulting in $a_\gamma = 3.6017 \text{ \AA}$ and $a_\alpha = 2.8807 \text{ \AA}$.

In the austenitic state the MarvalX12 has a yield strength of merely 170 MPa (before transformation and precipitation hardening). Furthermore, its hardening behavior is almost linear. Interestingly, Goto et al. 2000, suggest that the linear-like hardening behavior is a consequence of texture evolution, based on polycrystalline plasticity calculations. For comparison, low alloy steels have typical yield strengths in the range of 500-1980 MPa, stainless steels 280-500 MPa and mild steel ≈ 220 MPa (Bower 2009). Macroscopic tensile yield strengths may be found in Lemaitre et al. 1994; Lemaitre 2001

The precipitation behavior of the MarvalX12 has been investigated by Leitner et al. 2011. Particularly, an ordered β -NiAl precipitate of spherical shape and uniform distribution within the matrix is mainly responsible for its precipitation hardening. Also for Ti-containing maraging steels the hexagonal η -phase ($\text{Ni}_3(\text{Ti},\text{Al})$) precipitate is characteristic. Ping et al. 2005 found precipitate sizes of about 2–4 nm and inter-particle distances are about several nanometers (less than 10 nm) in a compositionally similar 13Cr–8Ni–2.5Mo–2Al steel. Notably, the plasticity framework incorporating mean free paths in subsection 6.6.2 can easily be extended to account for precipitates if reliable data is available.

5.2 Macroscopic TRIP Experiments

Recent studies focused on the macroscopic behavior of the the MavalX12. Particularly, a broad spectrum of mechanical tests investigating its structural hardening behaviour (uniaxial monotonic tension, compression, torsion and thermal cycling) are already documented

Nagayama et al. 2000; Nagayama et al. 2001; Nagayama et al. 2002; Tanaka et al. 2003. Similar studies have recently, been carried out by Loewy et al. 2016.

Specimens are, after machining, heated up to 1100°C in air, held there for 30 min., and air-cooled to RT. The material has been initially rolled and the ensuing texture cannot fully be removed even upon heating to 1200°C . An image of a specimen is shown in Figure 5.1.

Prior to all tests, the specimens were heated to at least 840°C at a heating rate of 0.5 K/s and held there for 30 min. to ensure full austenitization. The specimens are then cooled down to room temperature at a cooling rate of 2 K/s until about 50° above M_s (which lies in the range of $150 \pm 10^{\circ}\text{C}$) and at a lower cooling rate of 0.2 K/s from there in order to set an accurate timing of load changing before the start of the transformation. The strain evolution during transformation under various constant loading conditions is depicted in Figure 5.2.

For a prior annealing at 840°C an additional applied tensile strain of 29 MPa (due to an internal backstress) is necessary to close the transformation hysteresis, see Figure 5.2. The martensite start temperature and the backstress depend on the grain size (Bohemen et al. 2017) and on the prior annealing (time and temperature) lowering the effect of strain-induced transformation. Different combinations of annealing times and temperatures have been studied. For example, to close the transformation loop after annealing at 1100°C for 30 min requires an additional tensile loading of 11 MPa, whereas for annealing at 1200°C for 20 min 12 MPa are required. Finally, the importance of biaxial tension and compression is emphasised in the light of recent experiments (Petegem et al. 2016; Polatidis et al. 2018) and simulations (Erinosho et al. 2016; Upadhyay et al. 2016).

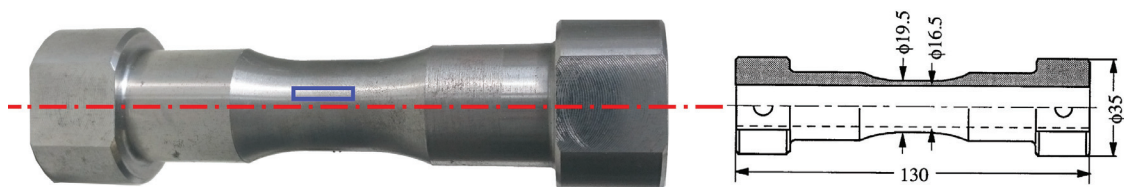


FIGURE 5.1: Thin-walled tubular specimen used in the mechanic characterisation. Samples are machined with surfaces obtained from a longitudinal cut in the blue marked area of the gauge length. Dimensioning plan taken from Nagayama et al. 2001.

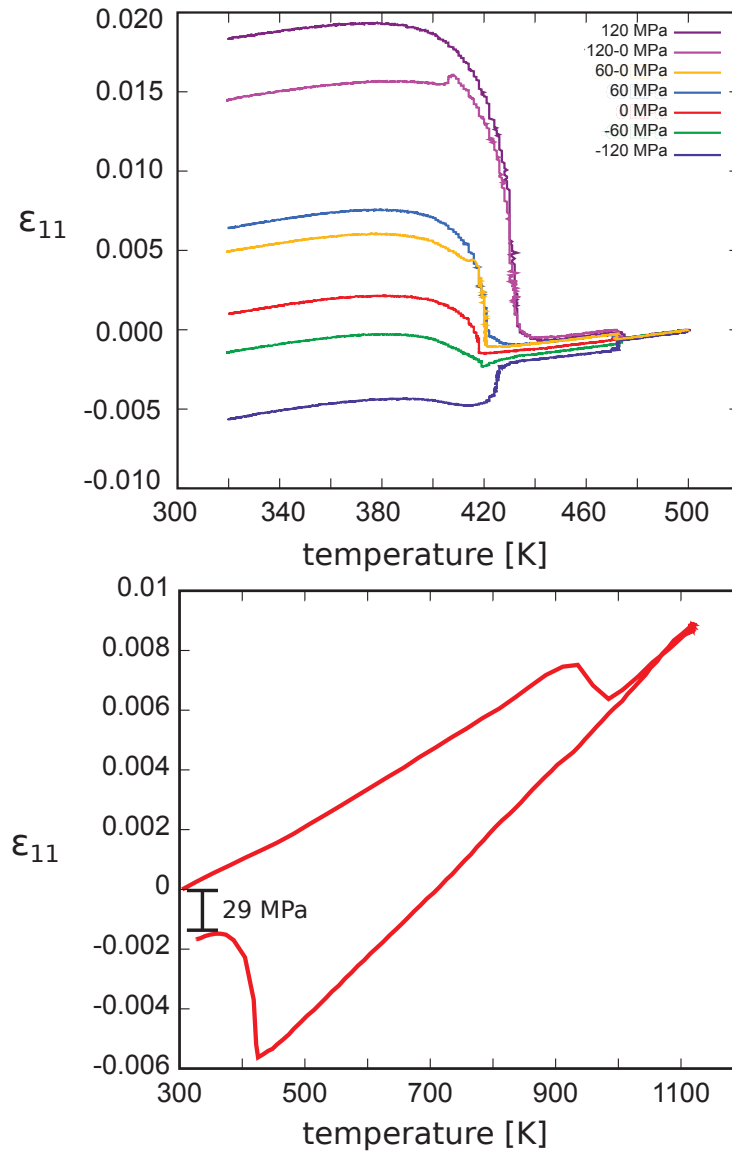


FIGURE 5.2: Top: Strain evolution due to transformation under various constant loading conditions. Bottom: Strain evolution of one thermal cycle without loading. 29 MPa additional tensile loading were found to be necessary to close the transformation loop for the 840° C prior annealing.

5.3 Kinetics

Phase fraction measurement can be done via dilatometry, magnetometry (Holmquist et al. 1995 similar composition to MarvalX12), resistance measurements, X-ray diffraction (evolution of Debye Scherrer Rings) Tian et al. 2017; Wiessner et al. 2017; Villa et al. 2018a; San Martin et al. 2012 (similar composition to MarvalX12), differential scanning calorimetry (DSC), laser ultrasonics (shock pulse detection), neutron depolarization Van der Zwaag 2012 etc. Note that in DSC experiments of steels a slightly increasing heat

flow rate up to the Curie temperature occurs due to the change of magnetic properties. Interestingly, in the macroscopic tensile strain curve of Figure 5.4 a weak deformation change between 800° and 900° C, which is near to the Curie temperature for this steel, can be observed upon cooling.

In dilatometric measurements commonly a linear relation between the martensite phase fraction and the axial strain is assumed. Additionally, a lever rule similar to that used for the calculation of phase fractions in phase diagrams can be used to assess the transformed phase fraction ξ as a function of temperature. The lever rule gives only an approximate value of the transformed volume. This is due to the fact that the method neglects the differences in the specific volumes of different phases and the partition of atoms between phases. Another source of uncertainty is connected with the superposition of dilation signals originating from several phases Pietrzyk et al. 2012. Furthermore, dilatometric measurements may overestimate the phase fraction due to the initial strong variant orientation effect. Basically the kinetics can also be obtained from the work hardening rate $\partial\sigma^{\text{tens}}/\partial\varepsilon^{\text{tens}}$ in a stress controlled test, see e.g. Kisko et al. 2013 Figure 2. therein. In this work also the effect of a more heterogeneous austenite leading to a steeper initial kinetics (higher strain-induced nucleation effect) is illustrated.

The MarvalX12 merely requires a cooling rate of as low as 0.2 K/s to obtain a fully martensitic state (similar to a massive transformation), as opposed to e.g. high carbon steels that require water quenching. The kinetics curve varies between the two upper curves in Figure 5.3 within our experimental data. The kinetics curve is neither sigmoidal nor C-shaped, but has characteristics. Loewy et al. 2014 obtained a similar kinetics investigating a Fe-18Ni-9Co-3-5Mo steel (samples of 90 and 180 μm grain size) using dilatometry. Particularly, they observed staggered transformation rate maxima indicating an elastic accommodation behavior, see Figure 5.3.

Although no specific experiments have been conducted for the isothermal transformation behavior, the literature strongly suggests that the MarvalX12 shows isothermal kinetic characteristics. For recent state of the art kinetic studies of primarily martensites showing isothermal kinetic characteristics, see the works of Villa 2013; Villa et al. 2014; Villa et al. 2018a; Villa et al. 2018b.

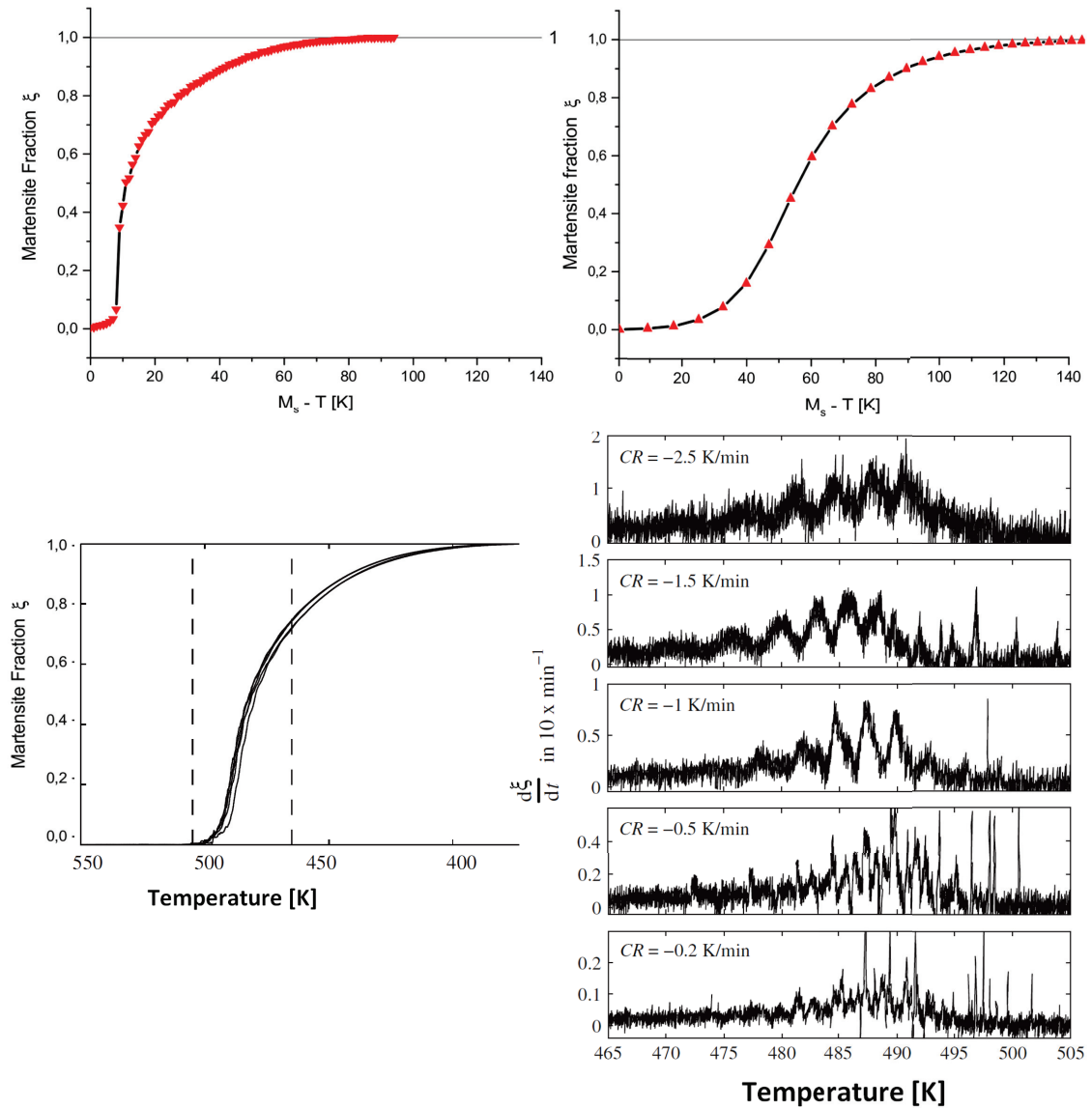


FIGURE 5.3: The kinetics of the MarvalX12 is relatively independent on the cooling rate, but varies strongly with the grain size and austenite heterogeneity both macroscopically characterised by an effective stress in the works cited at the beginning of section 5.2. In the experimental data available the kinetics varies between the upper-right (higher annealing temperature, measured via dilatometry) and upper-left (lower annealing temperature, transformation under load and lever-rule like calculation). The lower images taken from Loewy et al. 2014 illustrate that the transformation rate for a steel of similar composition and kinetics exhibit staggered rate maxima in the indicated temperature interval. This behavior indicates the presence of an elastic accommodation effect, although the transformation is strongly coupled with plasticity.

5.4 Impact of Thermal Transformation Cycling on the Microstructure

In the works cited at the beginning of section 5.2 the macroscopic strain evolution during thermal transformation cycling has been investigated. Therein, the remaining strain in a full thermal cycle has been termed ratchet strain due to the backstress formalism employed. However, the mechanism is quite different to what is normally understood under ratchetting (cf. subsection 2.2.4) considering the full temperature cycle and phase transformation involved. In Figure 5.4 the macroscopic strain evolution is depicted. It can be seen that the axial ratchet strain in the first cycle is much larger than in the following cycles and martensite start decreases slightly with each cycle. A possible explanation is that during each cooling the TRIP effect produces a high density of dislocations. Upon heating they partially first recrystallize and then recover. However, the time the specimen is hold in the austenitic state is too low for material to reach its initial state before the next cooling starts, eventually triggering TRIP again. However, the higher dislocation density, the higher the driving force for recrystallization and recovery. Therefore, if the rates of temperature changes and holding times are kept the same a steady state is reached.

Taleb et al. 2006 investigated a 16MND5 HSLA steel and performed similar cyclic experiments for a bainitic transformation but applied a tensile load during each cycle, with the result that they obtained a positive ratchetting strain evolution, with a total accumulated

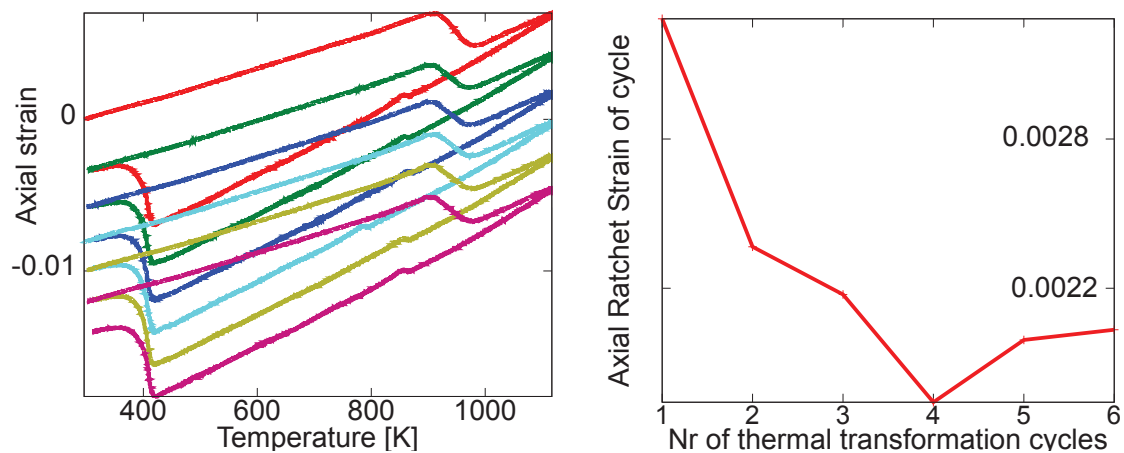


FIGURE 5.4: Strain evolution during thermal cycling (specimen TR32), without an applied load during transformation. Top: full temperature range. Bottom: Strain difference between start of heating and end of cooling for each cycle, respectively.

strain of almost +1.8% after six cycles as opposed to -1.4% shown in Figure 5.5.

Taleb et al. 2006 also conducted tests, with one unloading cycle and a significant plastic deformation in austenitic state (assuming that no stress-assisted or strain-induced effects occur) in the second cycle (between +5 and -10% plastic strain) before bainitic transformation. Interestingly, with initial plastic straining and without applied stress during the transformation a positive plastic strain lead to a negative (but very small; -0.1%) TRIP strain during bainitic transformation and vice versa (+0.2%). Also the kinetics changed significantly. They also report that this result is contrary to the behavior caused by a martensitic transformation in the same steel, see Taleb et al. 2002.

Kisko et al. 2013 specifically studied the influence of grain size on the strain induced martensite formation in tensile straining of an austenitic 15Cr–9Mn–Ni–Cu stainless steel. Orientation imaging microscopy studies on the effect of the thermally cycled transformation have been conducted only very recently by Chiba et al. 2017; Hidalgo et al. 2016. Figure 5.5 is taken from the latter work and illustrates the microstructural changes within four cycles of a Fe-0.3C-1.5Si-3.5Mn steel. Note that all of the specimens that will be considered in the next section have been cycled with ≥ 4 cycles after which the grain size is reported to not change significantly any more.

5.5 Microstructure Characterization by Orientation Imaging Microscopy

In this work three specimens have been investigated. All of them have been cycled at least 4 times such that their resulting block size (grain) size stays approximately constant. Two of them are annealed at 840°C and one at 1100°C for 30 minutes respectively. Of the specimens annealed at the lower temperature one (designated TR25) is loaded with a tensile load of 120 MPa and the other (designated TR32) with a torsion of 120 MPa (\approx only shear stress). The specimen annealed at the higher temperature (designated TA03), is not loaded during transformation. Two sets of EBSD recordings have been carried out. In the first set a larger area comprising many grains has been recorded and is evaluated statistically. In the second set of recordings only a specific block is recorded respectively with a higher voltage and finer step size (30 nm). Attention is directed to the very fine

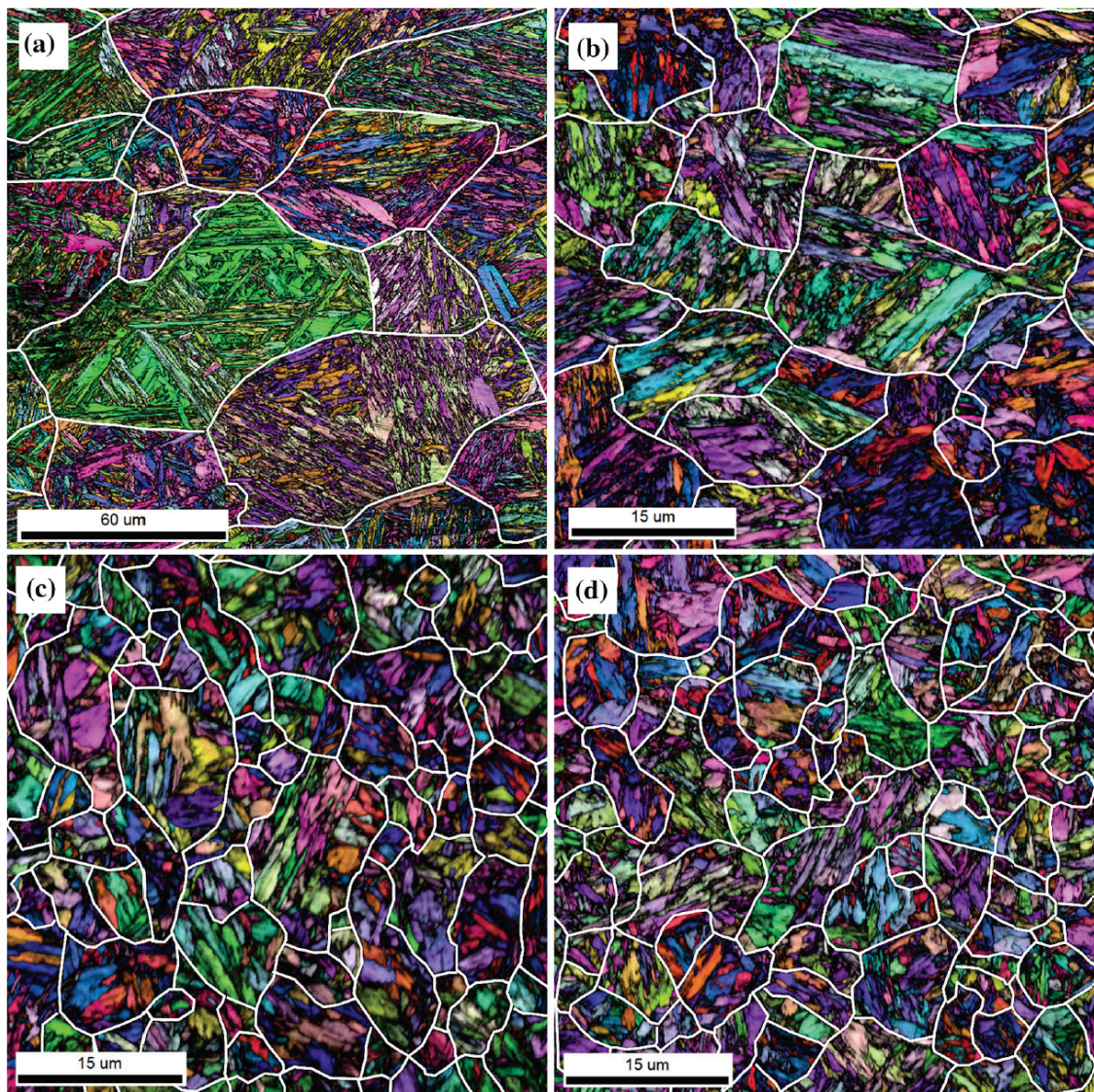


FIGURE 5.5: Taken from Hidalgo et al. 2016. Colour-code: inverse pole figure, grayscale: image quality. (a)-(d) Cycle 1-4. Note that in (a) a larger scale is used. White lines represent misorientation of rotating angle between 20° and 47° argued to represent prior austenite grain (PAG) boundaries.

substructure of martensite, being at the limit of the possible resolution of the electron back scattering diffraction method.

From the tension-torsion specimen (see Figure 5.1) longitudinal cuts are made in the area of the gauge length. The samples are then polished and etched. It should be noted that there are specific methods to particularly etch the grain boundaries, however these methods are dedicated to specific chemical compositions and mainly for the austenite.

The typical resolution of the EBSD measurements is above the expected dimensions of inter-lath retained austenite films. EBSD scans confirmed the prior assumption that there is no noteworthy amount of retained austenite in the samples at room temperature. Particularly, the few spurious films indexed as austenite in the sample are with high certainty merely indexing errors near high angle boundaries. S. Zhang et al. 2012 mention some retained austenite in a similar steel composition (Fe C-0.018 Si-0.29 Mn-0.8 P-0.003 S-0.002 Ni-9.05 Cr-12.95 0.49) utilizing a cooling rate of 0.45 K/s without going further into detail.

The interaction volume of the electron beam has a typical bulb / pear shape and depends on the applied voltage. The lower the applied voltage the weaker the received signal resulting in longer recording times. Phase identification is done by comparing reflection patterns (so-called Kikuchi bands) resulting from the overlap of two diffraction cones, on a detector, see Figure 5.6. The middle of a band corresponds to the trace of the diffracting plane. Characteristic patterns are correlated with known patterns. The coherent signal forming the Kikuchi bands comes from the first ≈ 10 nm of the surface. Therefore the sample must be crystalline and without excessive plastic deformation. Note that plastic deformation always occurs due to the specimen preparation. Therefore, before the recordings some of the polished surface was removed using a soft field ion beam (FIB) method referred to as "ion slicing".

The area that is scanned for each pixel is called step size. In the current recordings a step size of 50 nm has been used. The raw data of orientation imaging microscopy assigns to each pixel an orientation (a matrix) describing the rotation from a reference coordinate system to the identified lattice system. The orientation of the reference system w.r.t. the specimen as well as the orientation for all the orientation imaging microscopy (OIM) images that will follow is shown in Figure 5.6. Several clean-up routines can be performed on the raw data. A common routine is "dilation", where regions of slight misorientation are expanded to correct the indexing errors at high angle boundaries. Another strategy is to filter data which does not fulfil certain quality criteria.

For EBSD image mapping styles it must be distinguished between a style for the image's grayscale (GS) as well as its colour-code (CC). Note that due to the non-linearity and ambiguity of the Euler-angle space, it has been pointed out that by using some prevailing CCs some details are lost and new CCs have been proposed recently, see e.g. Nolze et al. 2016. Subsequently a short notation will be used for designating the mapping style

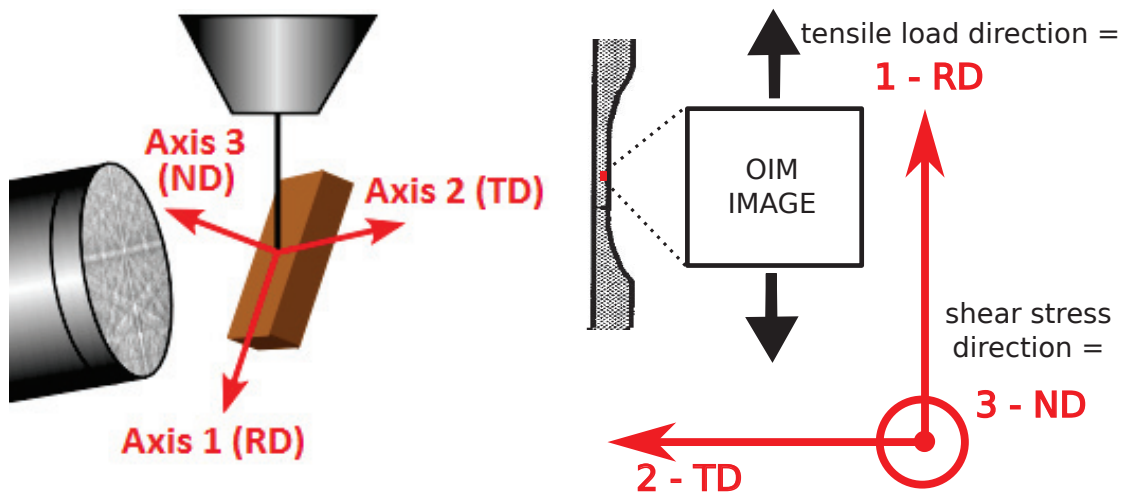


FIGURE 5.6: Left: Schematic arrangement of electron source, specimen and with reference coordinate system in the used OIM software and EBSD detector (image taken from *TSL OIM Analysis Manual* n.d.). Terminology from the characterization of rolling texture: 1 - Rolling direction (RD), 2 - Transverse Direction (TD) and 3 - Normal direction (ND). Right: Orientation of the coordinate system in the images provided in this work and its relative alignment with the sample (indicated by an extract of the gauge length) and its external loading during transformation.

of images, i.e. GS or CC followed by the actual style. The first GS mapping style is, image quality (IQ). It is a parameter generally quantifying the crystallographic uniformity within the interaction volume and how plane a specific area is. The IQ is useful for gaining some insight into the distribution of strain in a microstructure (*TSL OIM Analysis Manual* n.d.). Figure 5.7 shows an EBSD recording of the specimen that has been shear loaded during transformation (TR32) with GS-IQ indicating a strong heterogeneity. Another GS mapping style is "fit". A fit parameter is determined as part of the indexing procedure. It has been found that the best contrast can be achieved using this mapping style (for details see *TSL OIM Analysis Manual* n.d.), whereas the commonly used overlay with IQ leads to very dark images.

The *grain shape orientation* as used in the next section is shown in Figure 5.8. What actually constitutes a grain in OIM is specified by the user. Mainly the grain maximum misorientation angle is important at this point. A common default in most OIM programs is 5° . However, for the identification of bi-variant blocks constituting the role of grains in a fully lath martensitic microstructure a tolerance angle of 11° is specified, since this is slightly larger than 10.5° which is the lowest theoretical lattice misorientation between sub-blocks in bi-variant blocks, see Table 3.3. Finally, it must be mentioned that for all evaluations of grains it is commonly distinguished between area and number weighted averages. These

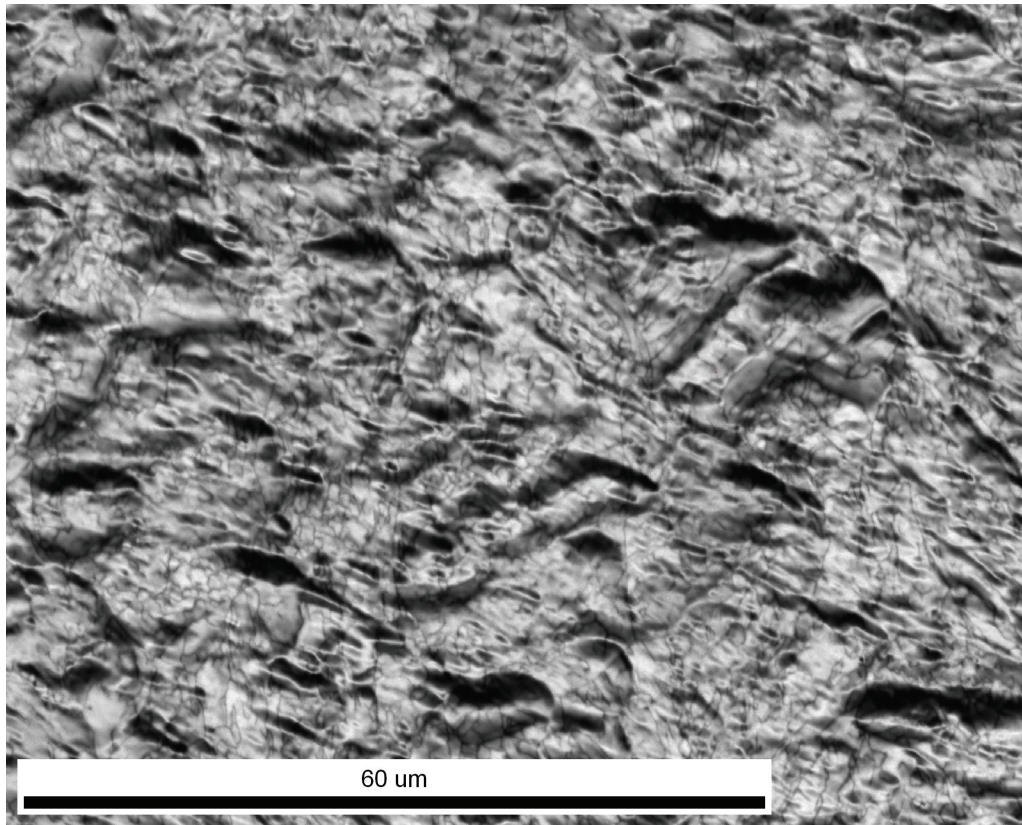


FIGURE 5.7: Sample T32, GS-IQ, lower left quarter of Figure 5.9. The sample surface is not very flat even after ion slicing. This indicates a high degree of dislocations and hence internal stresses.

two values are only close to one another if the grain size (block size) is uniform. Since this is not generally the case in our samples, the area weighted evaluation is preferred.

Finally, some mentionable OIM studies of martensite are shortly reviewed. Malet et al. 2009 studied variant selection in hot-rolled, bainitic, TRIP-aided steels, reporting that hot deformation (general prior plastic deformation) generally reduces the number of packets that form. Miyamoto et al. 2012; Miyamoto et al. 2013 studied ausformed lath martensite (Fe-0.15C-3Ni-1.5Mn-0.5Mo, Fe-25Ni-0.5C, average grain size $\approx 150\mu m$) and found that all six variants belonging to the packet whose $\{011\}_\alpha$ plane is nearly parallel to the primary slip plane in $\{111\}_\gamma$, are formed preferentially. At very high plastic strains ($> 30\%$), the six variants of the packet nearly parallel to the secondary $\{111\}_\gamma$ slip plane are formed. Especially among the two packets those variants nearly perpendicular to the compression axis were selected. The effect of stress on variant selection has also been investigated by Mishiro et al. 2013. Tomida et al. 2013 found that the transformation texture is near the initial plastic texture and reproduces even after a phase transformation cycle. Kinney

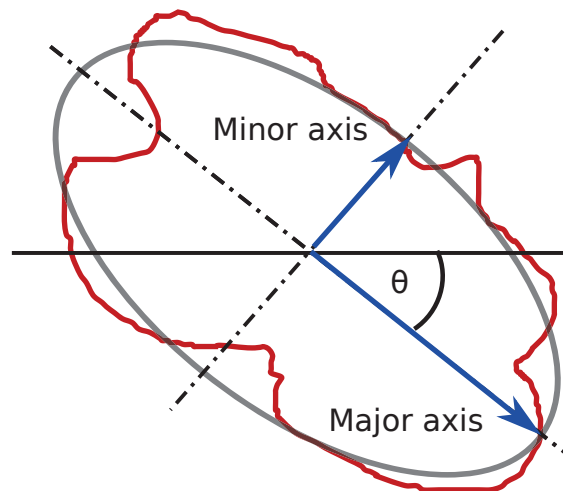


FIGURE 5.8: Definition of grain shape in the OIM software is determined by fitting an ellipse to points making up a grain (red line marks the grain boundary). $0 < \theta < 180^\circ$ gives the grain shape orientation, i.e. the angle between the major axis of fitted ellipse and the horizontal direction (2 in Figure 5.6).

et al. 2016 studied the martensite formed from twinned prior austenite regions (annealing twins, indistinguishable from an IPF map). Giri et al. 2017; Chintha et al. 2013 used the crystallographic set (see section 3.10) to qualitatively identify martensite variants from OIM data. However, the studies are limited to single grains. A characterisation incorporating many grains automatically using a crystallographic set is still a long way of.

5.5.1 Many Grains

In this section an overview of the microstructures of the three specimens as well as some statistics is provided over an area comprising ≈ 100 prior austenite grains (PAG). The average prior austenite grain size (PAGS) of all three specimen was found to be $\approx 15 \mu\text{m}$ estimated from the fully transformed microstructure. The actual grain size i.e. the block size is about one quarter of that, but blocks are much more elongated in shape than PAGS.

The colour-code (CC) used in this section is the inverse pole figure (IPF) mapping style. Note that the difference between a pole figure and an inverse pole figure is that a pole figure shows a particular specified crystal direction relative to the sample frame, while the inverse pole figure shows a particular sample direction relative to a lattice reference frame. Thus, for instance a [001] inverse pole figure shows which crystal direction in the crystal lattice is aligned with the normal (3,ND see Figure 5.6) of the sample reference frame. In

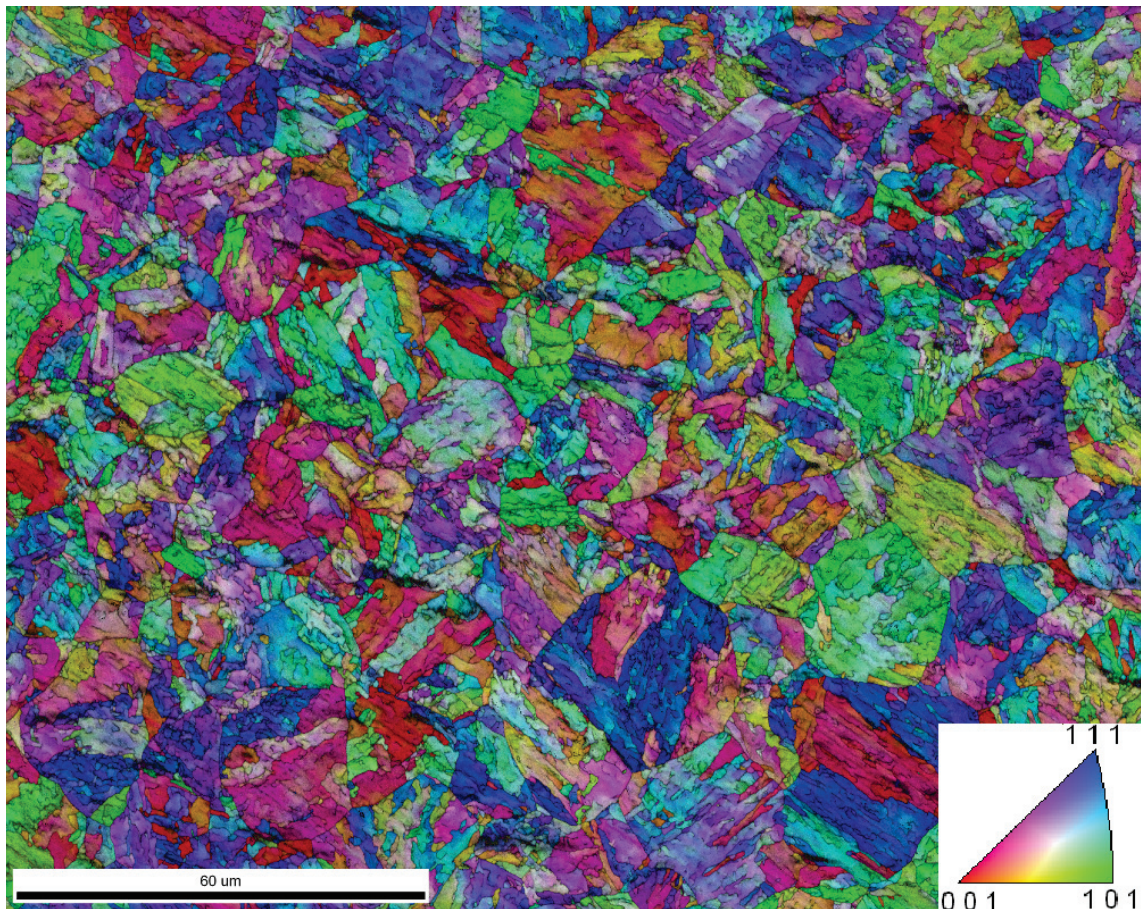


FIGURE 5.9: Specimen TR32 - transformation under 120 MPa torsion loading, CC: inverse pole figure (IPF), GS: fit. A visible orientation contrast from bottom right to top left can be noticed. Particularly, sub-block features oriented in this direction are more elongated than in any other direction. The torsion loading leads by far to the highest heterogeneity within individual blocks.

fact this is the default inverse pole figure mapping in most programs. Furthermore, the default of symmetry inversion is used, i.e. all points indexed on the southern hemisphere are mirrored to the northern hemisphere.

Subsequently an overview of the microstructures of the specimens TR32 (torsion), TR25 (tension) and TA03 (higher annealed) will be given. For the inverse pole figure CC the sample direction in all figures is chosen to be the normal direction $[001]$ since no significant improvement of orientation contrast could be achieved in changing this value, not even for the tensile specimen, where some alignment with the $[100]$ stress direction was expected.

The microstructure of the sample that was loaded in torsion during transformation (approximately pure shear stress) is shown in Figure 5.9 looks like it has been directionally keyed (roughened) at an angle of $\theta = 45^\circ$ from the horizontal. Considering that the shear

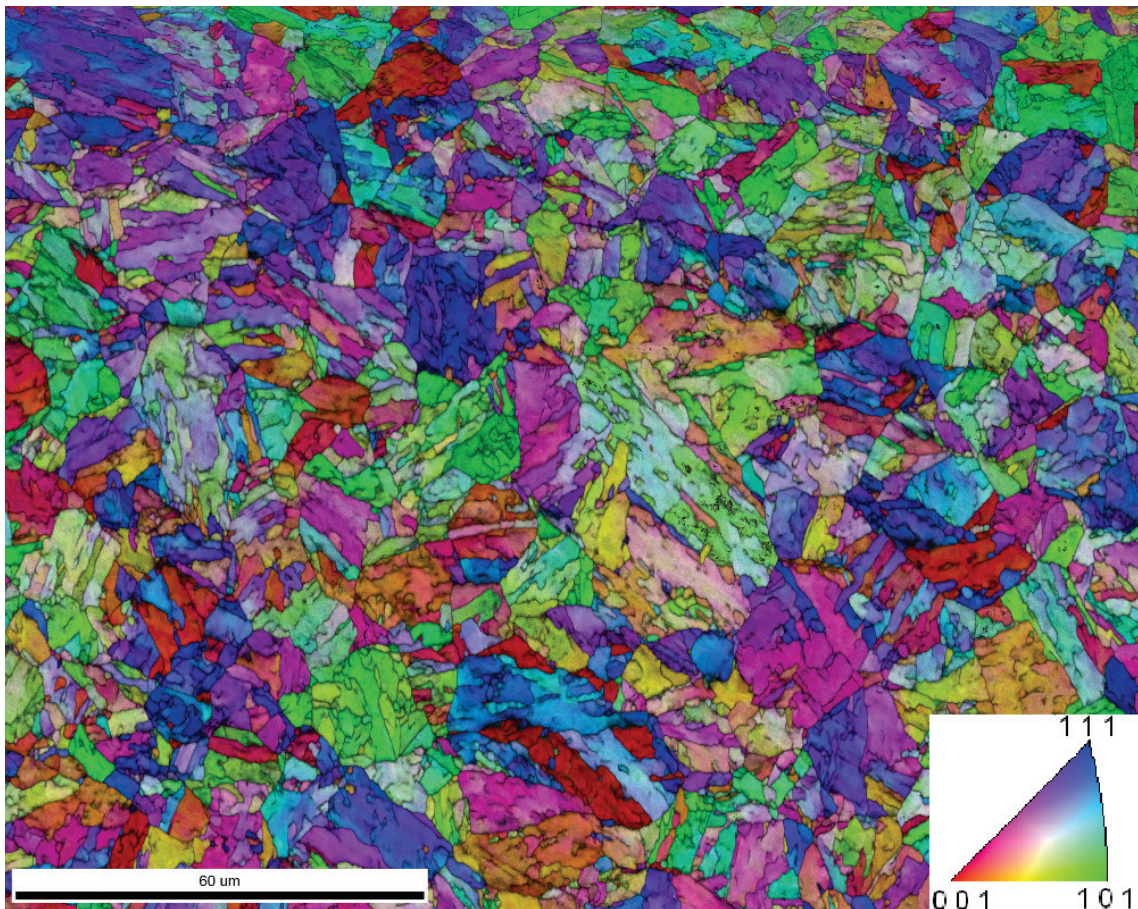


FIGURE 5.10: Specimen TR25 - transformation under 120 MPa tensile loading, CC: IPS, GS: fit. Contrary to the sheared sample no preferred block orientation is visible and heterogeneity within blocks is lower.

plane normal is parallel with the upwards direction in this figure this visible texture indicates a transformation front contrary to a completely homogeneous transformation over the whole gauge length of the specimen. This phenomenon is well-known from NiTi alloys (e.g. J. Shaw et al. 1997). Also sub-block features are far more heterogeneous than in the other two samples indicating a higher dislocation density.

Figure 5.10 gives an overview of the tensile loaded sample during transformation (TR25). The GS contrast due to the fit mapping style is less pronounced than in the torsion sample. The same was observed for the IQ contrasts.

Finally in Figure 5.11 specimen TA03 (annealed higher than TR32 and TR25) is shown. The orientation contrast between neighbouring regions is sharper (misorientation gradients between similarly oriented regions are smaller), as is expected due to the effect of more pronounced recrystallization and recovery phenomena.

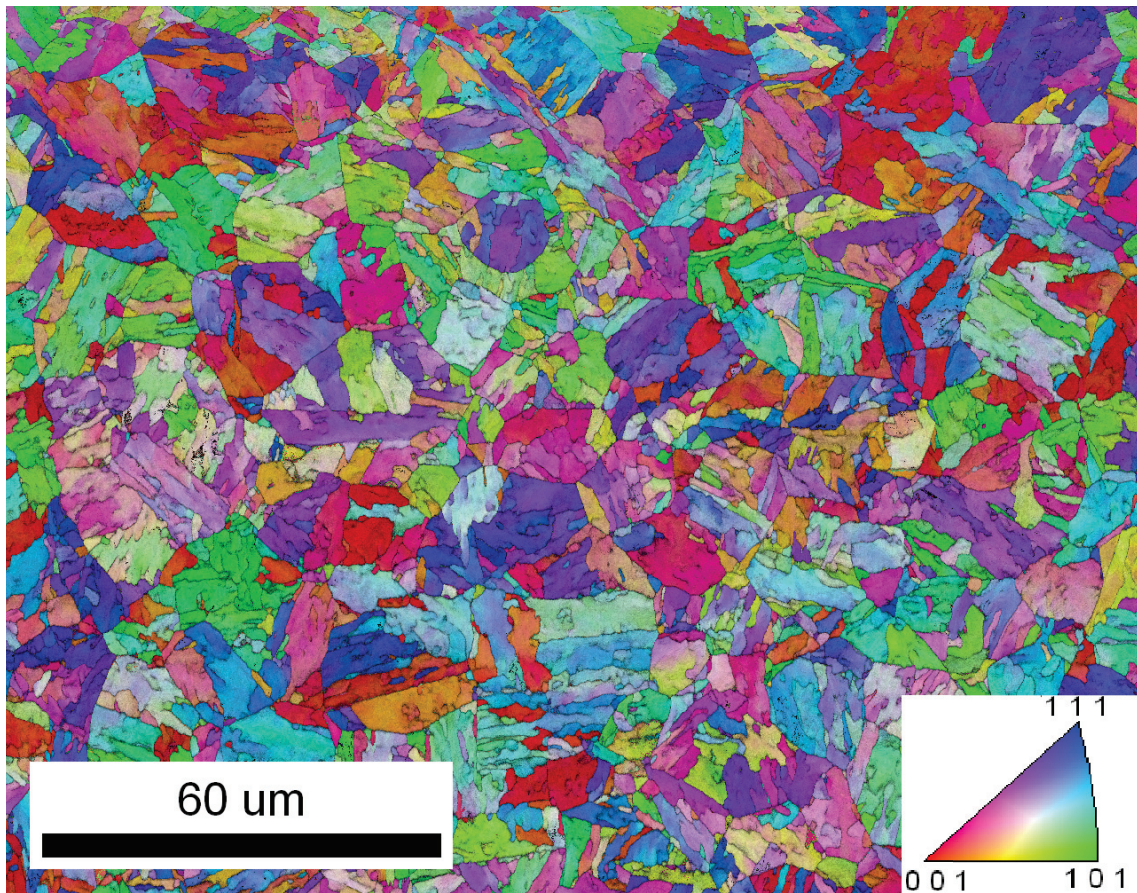


FIGURE 5.11: TA03 higher annealed, CC-IPF, GS:FIT - Same options for GS as for TR32 and TR25. The GS contrast of this image is distinctly different than from TR32 and TR25. This is due to the annealing at higher temperature significantly reducing the dislocation density.

Next, the specimens' textures are investigated utilising pole figures and inverse pole figures (IPFs). Particularly, an ODF is constructed by fitting data using spherical harmonics. Note that a very high series rank in the harmonic expansion is computationally expensive if the processed data set is very large. While pole figures and inverse pole figures (IPFs) utilising one average orientation per grain weighted by the grain area are suitable to characterise block selection, in our severely dislocated specimens they exhibit deviations from the overall state of the ODF obtained by fitting all the available data points (≈ 5 million) that have been recorded per image. This indicates strong orientation gradients within domains classified as grains and hence a large overall heterogeneity of the microstructure. Orientation gradients also depend to some degree on the ability of the OIM software to reconstruct grains. These circumstances are depicted in the following IPFs and pole figures. Note that the IPF representations are shown without *inversion symmetry*.

The Gaussian smoothing value given in the following images is associated with the width

of a Gaussian distribution (recall that an orientation distribution function deals with probabilities) weighting in order to get rid of negative values which are otherwise unavoidable in the fitting procedure, see H. Bunge 1982; *TSL OIM Analysis Manual* n.d.

Furthermore, in the case here it is important not to assume any sample symmetries (triclinic) providing the most generality to identify variant selection in terms of lattice orientation since it may happen that two shape strains become symmetry related although different slip systems act during their formation.

Specimen TA03 is considered first since it depicts the reference of an unloaded transformation. The IPFs shown in Figure 5.12 underline the visual impression obtained in Figure 5.11, namely that for specimen TA03 there is little difference between using the average orientation of areas defined as grains or the full data range. There is a pronounced lack of inversion symmetry for the 3/ND/[001] direction, which should be investigated further. However, since this would require to go into depth of the general indexing procedure of Kikuchi patterns this aspect is not followed further at this point.

The textures of the loaded samples significantly differ from that of TA03 due to the combined effect of loading during, as well as lower annealing temperature before, transformation. Figure 5.13 shows the IPF of the torsion sample (TR32). This specimen shows the most pronounced difference between the IPF using merely one (average) orientation per block defined by 11° and all data points, i.e. this microstructure is the most heterogeneous. Nevertheless, there are distinct maxima observed in the TD and ND direction. Notably, both maxima are not distributed around a single direction but around directions ranging from $\langle 101 \rangle_\alpha$ up to 20° towards $\langle 100 \rangle_\alpha$. Interestingly, the highest values of the maxima are almost not affected, although the shear loading changes the position and shape of the maxima. Particularly, the difference is about 10 % (1.51 to 1.66).

Finally, Figure 5.14 corresponds to the tensile strained specimen. The difference of a grain average and whole data evaluation is between that of TA03 and TR32. A characterisation of this specimen using the reduced grain average is still not exact enough, hence a full evaluation should certainly be preferred. The most distinct feature of this sample is that the maximum in the [100] loading direction accumulates near $\langle 111 \rangle_\alpha$ and $\approx \langle 225 \rangle_\alpha$. Moreover, the preference of a certain orientation is most pronounced in the case of this specimen (note that the intensity is 2.8, which is about 60 % larger than for TA03 and TR32).

While inverse pole figures are very useful to characterise the overall lattice orientation in

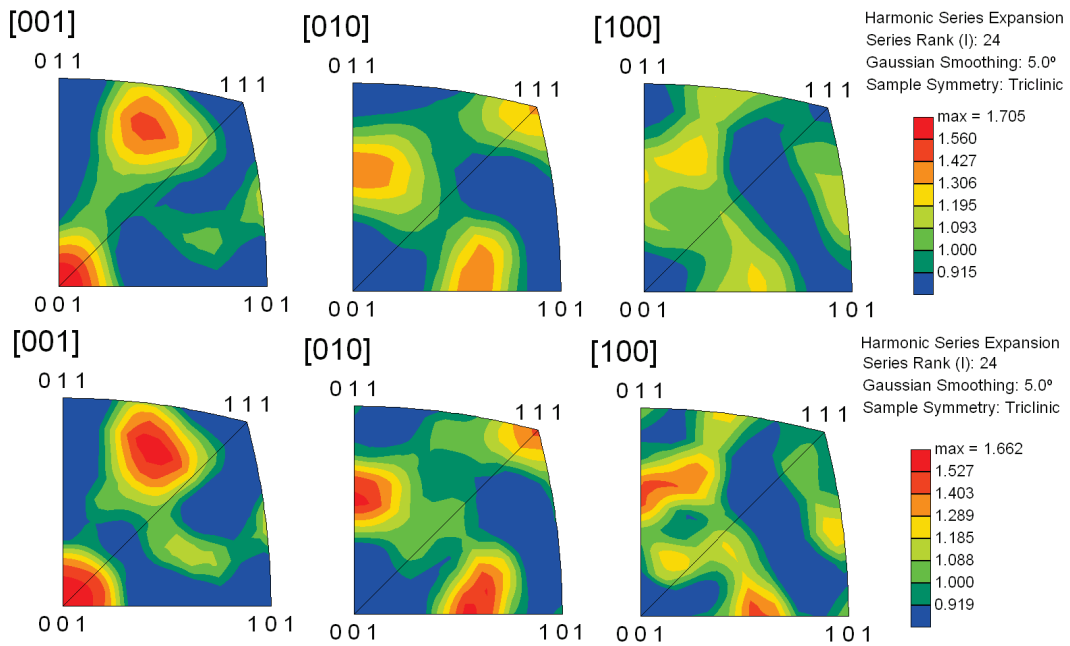


FIGURE 5.12: $\langle 100 \rangle$ IPFs of specimen TA03. Top: IPFs constructed with one average orientation per reconstructed grain defined by a misorientation of 11° . Bottom: IPFs using all data points. It can be seen that the reduced texture evaluation reproduces the full texture very well. Interestingly, in the 3/ND/[001] direction corresponding to the tangential specimen direction there is a texture peak of $\langle 100 \rangle_\alpha$. One possibility is that this is the Bain compression axis, but this would be counter intuitive since without any other deformation mechanism this axis would preferably be oriented towards the free surface in [010] sample direction. So it must be an artifact of the transformation texture developed during the thermal cycling. As expected in an unloaded transformation there is almost no difference between the [010] and [100] IPFs.

the sample they cannot be used for individual variant identification. In the authors opinion also the full Euler space should not be used for individual variant characterisation due to its drawbacks elaborated in section 3.4. It has been tried to find correlations between the bi-variant block structure and texture representations in full Rodriguez space, but no direct trend could be observed. Eventually, pole figures turned out to be most useful for the task of qualitatively characterising the martensite variant distribution.

Again grain average point wise data weighted by the grain area is compared to a fit of all the available data points. Stereographic projections are employed. Alternatively, equal angle and equal area projections are commonly used. Note that there is a small difference between the latter two and the stereographic projection, while the equal angle and equal area projection almost yield identical results. Eventually, this might play a role for quantitative variant identification over larger scanned areas. Figure 5.15 gives an overview of the texture in the sample TA03. Generally, it is found that variants can approximately be identified

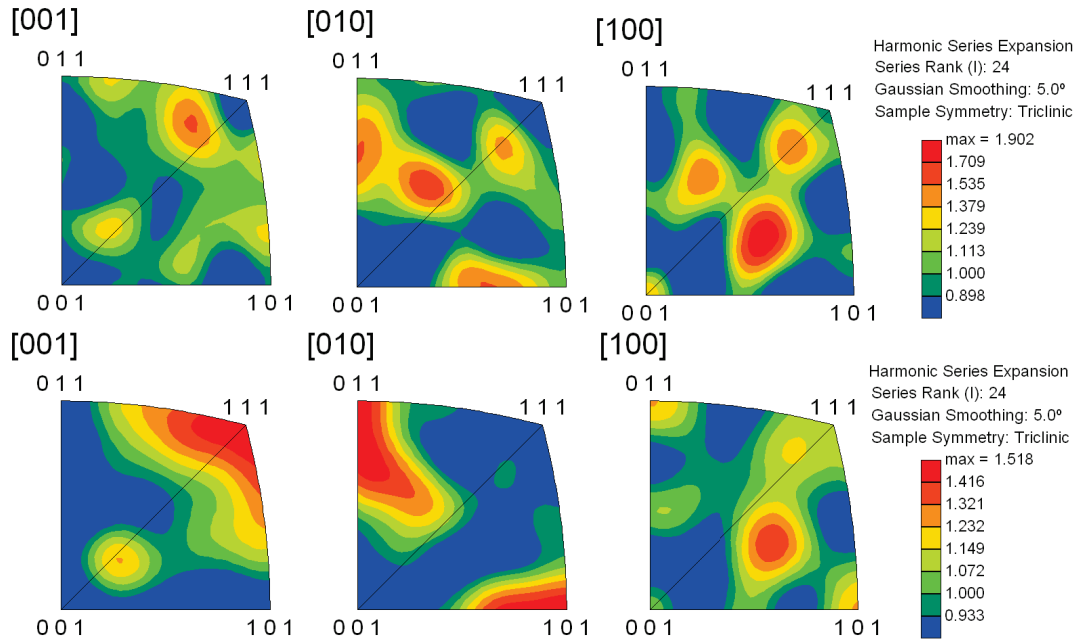


FIGURE 5.13: $\langle 100 \rangle$ IPFs of specimen TR32. Direction of maximum shear stress is $[001]$. Top: IPFs constructed with one average orientation per reconstructed grain defined by a misorientation of 11° . Bottom: IPFs using all data points. The two evaluations differ significantly indicating strong gradients within blocks. Therefore, evaluating all data points should be preferred. There is a preference of $\langle 111 \rangle_\alpha \approx \langle 110 \rangle_\gamma$ to align with the direction of maximum shear and $\langle 011 \rangle_\alpha \approx \langle 111 \rangle_\gamma$ to align with the direction of the free surface.

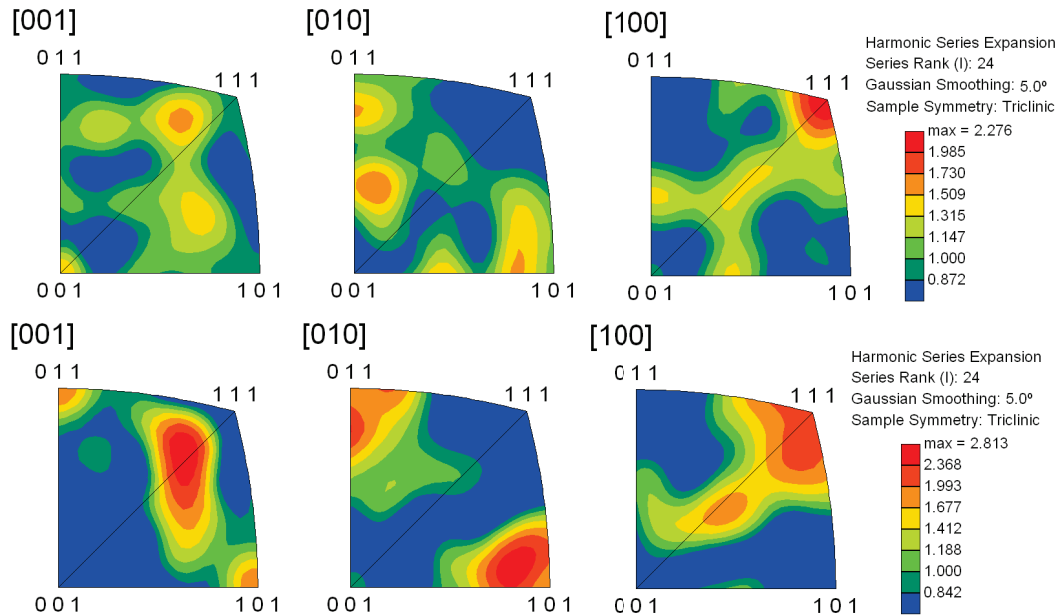


FIGURE 5.14: $\langle 100 \rangle$ IPFs of specimen TR25. Direction of tensile loading is $[100]$. Top: IPFs constructed with one average orientation per reconstructed grain defined by a misorientation of 11° . Bottom: IPFs using all data points. $\langle 111 \rangle_\alpha$ preferably is oriented in the loading direction and the absolute values of all the occurring maxima are much more pronounced than in the shear and unloaded samples.

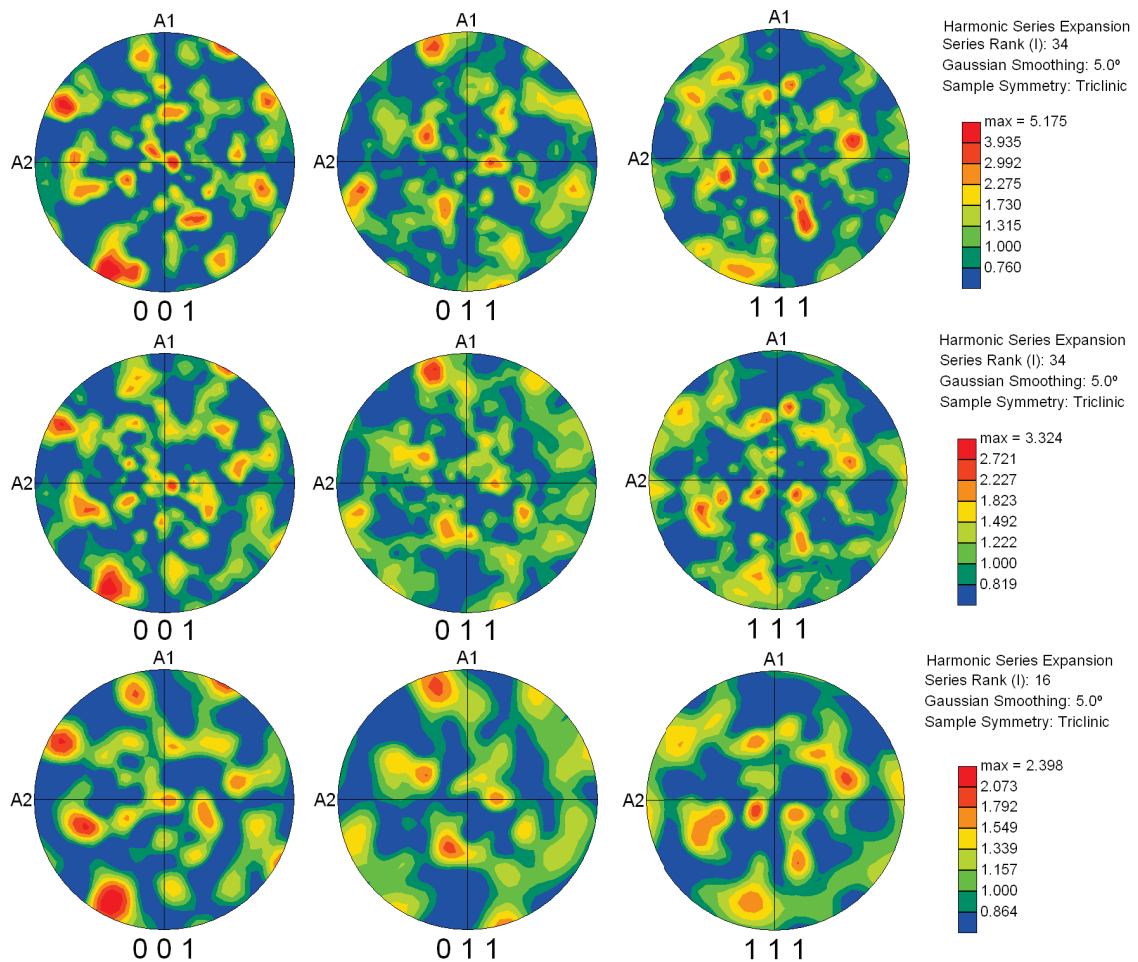


FIGURE 5.15: Pole figures of sample TA03 (stereographic projections). Top row: one point per grain area weighted with grains defined by 5° misorientation. Middle row: one point per grain area weighted with grains defined by 11° . Note that the highest possible rank of 34 is used. Bottom row: fit of all scanned data points with harmonic series rank 16. The 11° resolution for the grains should be preferred over the 5° grain resolution since it depicts the overall state of texture much better. However, the 5° resolution is useful to identify bi-variant pairs forming blocks. Interestingly, maxima in the $\langle 001 \rangle_\alpha$ pole figure are concentrated on the left hand side, cf. the lack of inversion symmetry in Figure 5.12.

by grouping the maxima of the pole figures to 12 main spots corresponding to 12 bi-variant blocks with a maximum misorientation of 11° . In cases where the 12 variants cannot be identified it is helpful to simultaneously regard the pole figures obtained from all data points as well as from average grain (defined by 5° misorientation) orientations weighted by the grain area for a characterisation of variant selection in terms of lattice orientation.

Figure 5.16 shows pole figures for the specimens TR32 and TR25. The pole figures of the tensile loaded specimen (TR25) exhibits symmetries. This can be explained by the fact that the load direction lies within the specimen's cut surface (A1/LD direction).

Conversely, this is not the case for the sheared sample. This observation poses the question whether the same trend would be observed if a cut of the cylinder's cross section (containing the maximum shear direction) instead of a longitudinal one, were investigated. Also it puts in question the common assumption that the distribution obtained from area data is representative for the three dimensional state. Note that this assumption is only valid for fully randomly distributed grain or variant orientations.

Merely using lattice orientation data for the characterisation of martensite is insufficient. It is really the interplay of lattice orientation, martensite domain morphology and interface character that determines the properties of the microstructure and hence macroscopic properties. Therefore, subsequently differences in interface characteristics are investigated.

Figure 5.17 shows the boundary character distribution of the three specimens. Therein it is distinguished between low ($< 15^\circ$), high ($> 15^\circ$) and special low energy coincidence side lattice boundaries. Note, all CSL boundaries are high angle boundaries. It can be seen that external loading during the transformation has a profound effect on this distribution. For a better interpretation the absolute values of these interface types must be known. These are as follows: For TA03 the total interface length in the recorded area is 4.43 cm - 1.37 cm thereof are low and 3.06 cm are high angle boundaries of which again about half are CSL boundaries (≈ 1.5 cm). For TR25 the values are 4.40 cm total, 2.37 cm low and 1.66 high with about two-fifth being CSL boundaries (≈ 1.05 cm) and for TR32: 4.74 cm, 2.36 cm low, 2.38 cm high with about one third CSL boundaries (≈ 0.77 cm).

As a next step the distribution of misorientations is investigated. Results for all three samples are shown in Figure 5.18. All three specimens show quite a pronounced peak exactly at 30° , although this has not been classified as any special theoretical boundary, cf Table 3.3. It is also noted that upon coarsening the data two times (coarsening means removing every other point in each row and every other row from the data) the peak at 30° shrinks significantly. This indicates that it belongs to very fine microstructural features. Another interesting aspect is that there are significantly less 60° boundaries in the sample that transformed under shear loading. These results play a role for grain boundary engineering by loading during the transformation.

Finally, in order to obtain a more complete microstructural picture, an attempt is made to incorporate the martensite domain morphology, which is experimentally most difficult to

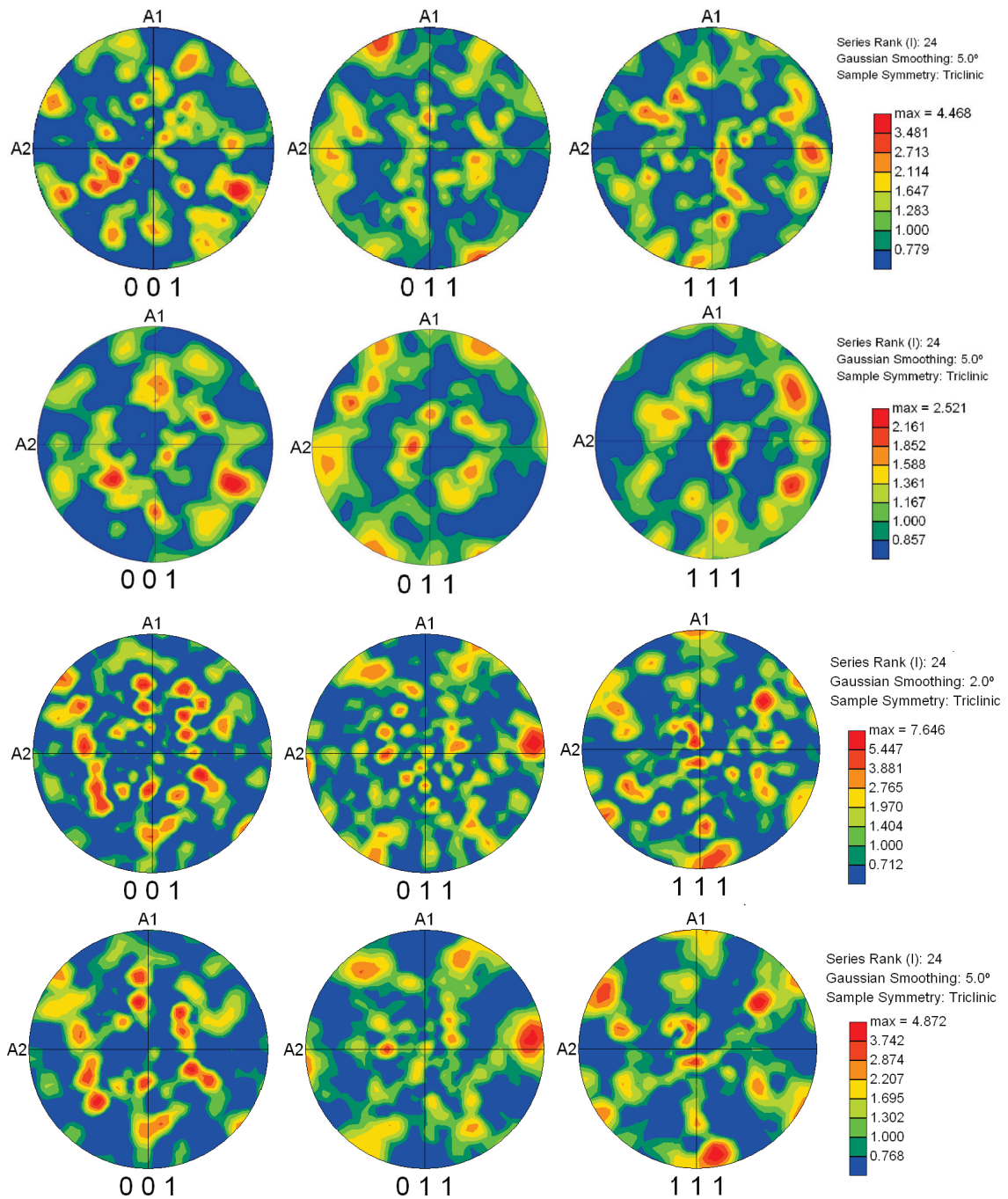


FIGURE 5.16: Pole figures of TR32 and TR25 (stereographic projections). Grain average orientation, with grains defined by a misorientation of 11° , weighted by the grain area for TR32 (top row) and TR25 (3rd row) respectively. Fit of all data points for TR32 (second row) and TR25 (bottom row). As for the IPFs for the torsion sample the reduced texture representation fails to be representative of the whole data. The texture for the tensile loaded sample is very sharp

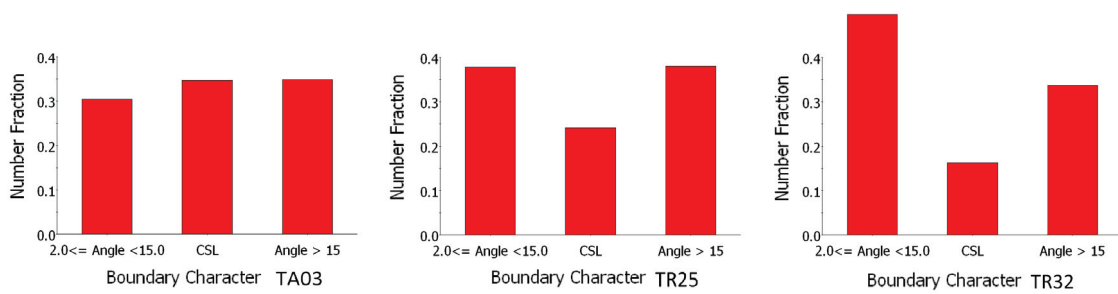


FIGURE 5.17: Boundary/interface character distribution in the three samples. It is distinguished between low and high angle boundaries, where for the latter additionally coincidence site lattice boundaries are distinguished. In shear deformation significantly more low angle boundaries are formed and the number of CSL boundaries decreases most significantly.

characterise. Particularly the effect of grain shape orientation has been considered. Such an approach has e.g. been followed by Nambu et al. 2013 for PAGS of $\approx 100 \mu\text{m}$, where the martensite domains are much more elongated than in the thermally cycled specimen considered in this work. Again the two definitions of grains by a misorientation of 5° as well as 11° are considered. The results are shown in Figure 5.19 for 5° and Figure 5.20 for 11° . It can be seen that by defining a grain with a misorientation of 11° the maxima are more pronounced. Note that this is not an effect due to the smaller amount of data points since area weighting is considered rendering this effect negligible. Particularly, Figure 5.20 is in accordance with the expectations of block selection under load.

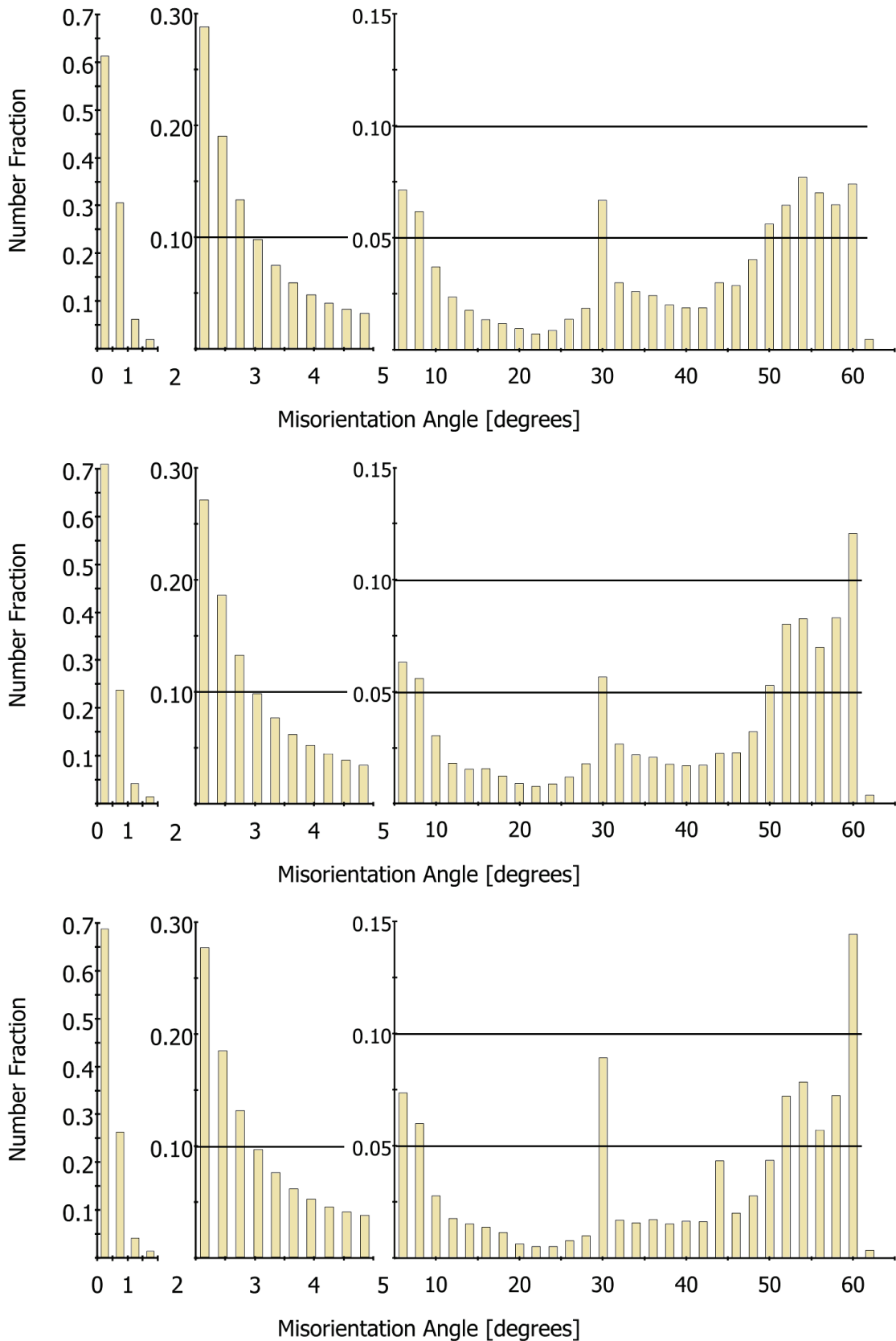


FIGURE 5.18: Distributions of misorientations in the three samples. The sum of the number fractions of each of the individual intervals ($0^{\circ}\text{-}2^{\circ}, 2^{\circ}\text{-}5^{\circ}, 5^{\circ}\text{-}60^{\circ}$) = 1, i.e. even small differences between the same intervals are very pronounced. Top: TR32, Middle: TR25, Bottom: TA03. Deviations in the second interval seem to be the lowest between the three specimen. Interestingly, all samples show a peak around 30° , where no special boundaries are reported (cf. Table 3.3). Therefore, this peak must be a result of the transformation cycling.

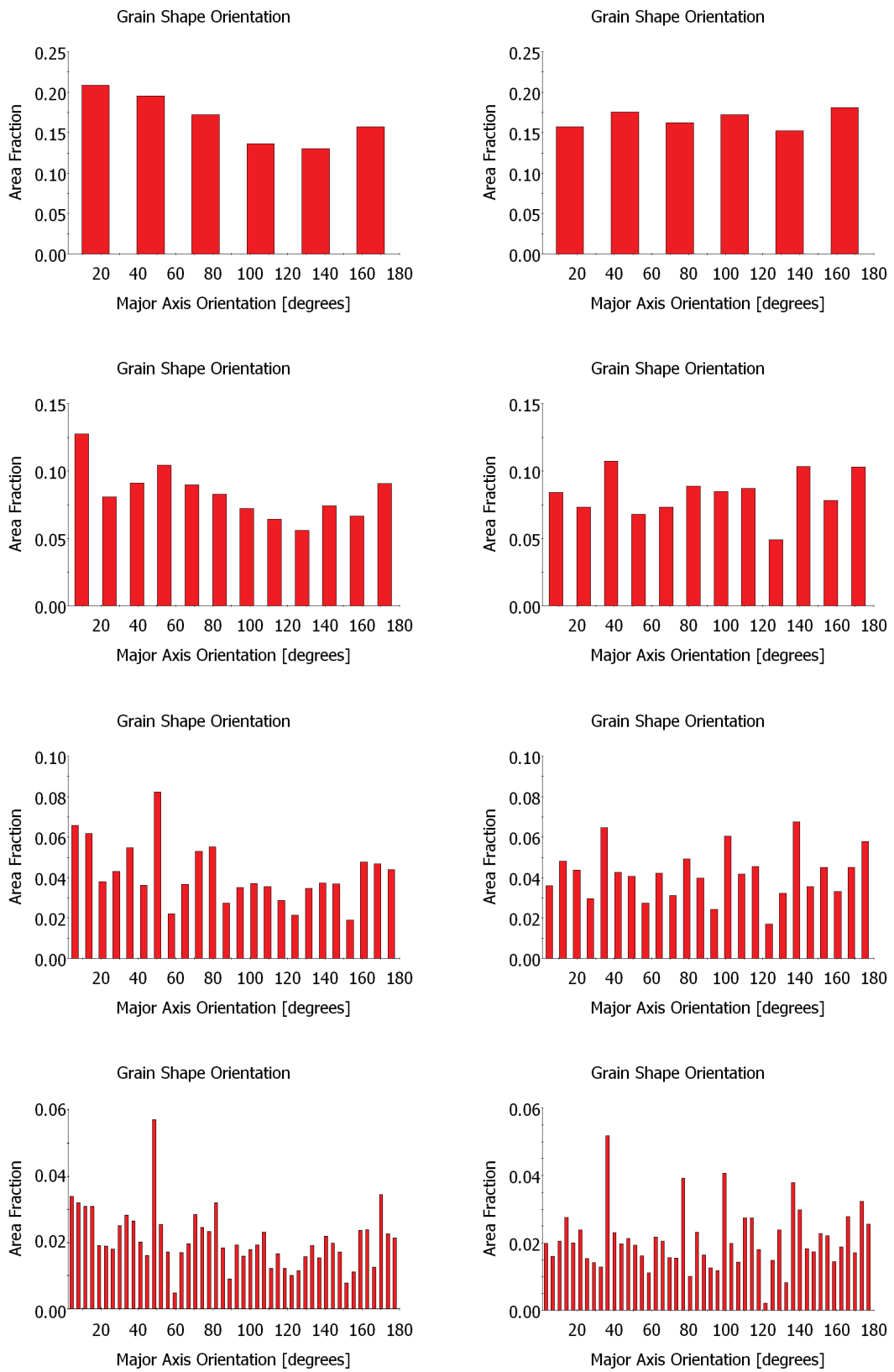


FIGURE 5.19: Distribution of grain shape orientation, cf. Figure 5.8. Grains are defined by connected regions with a misorientation of 5° . Several levels of discretisation are shown for a better characterisation. Left column: specimen transformed under 120 MPa tensile loading (TR25). Right-column: specimen transformed under 120 MPa shear loading (TR32).

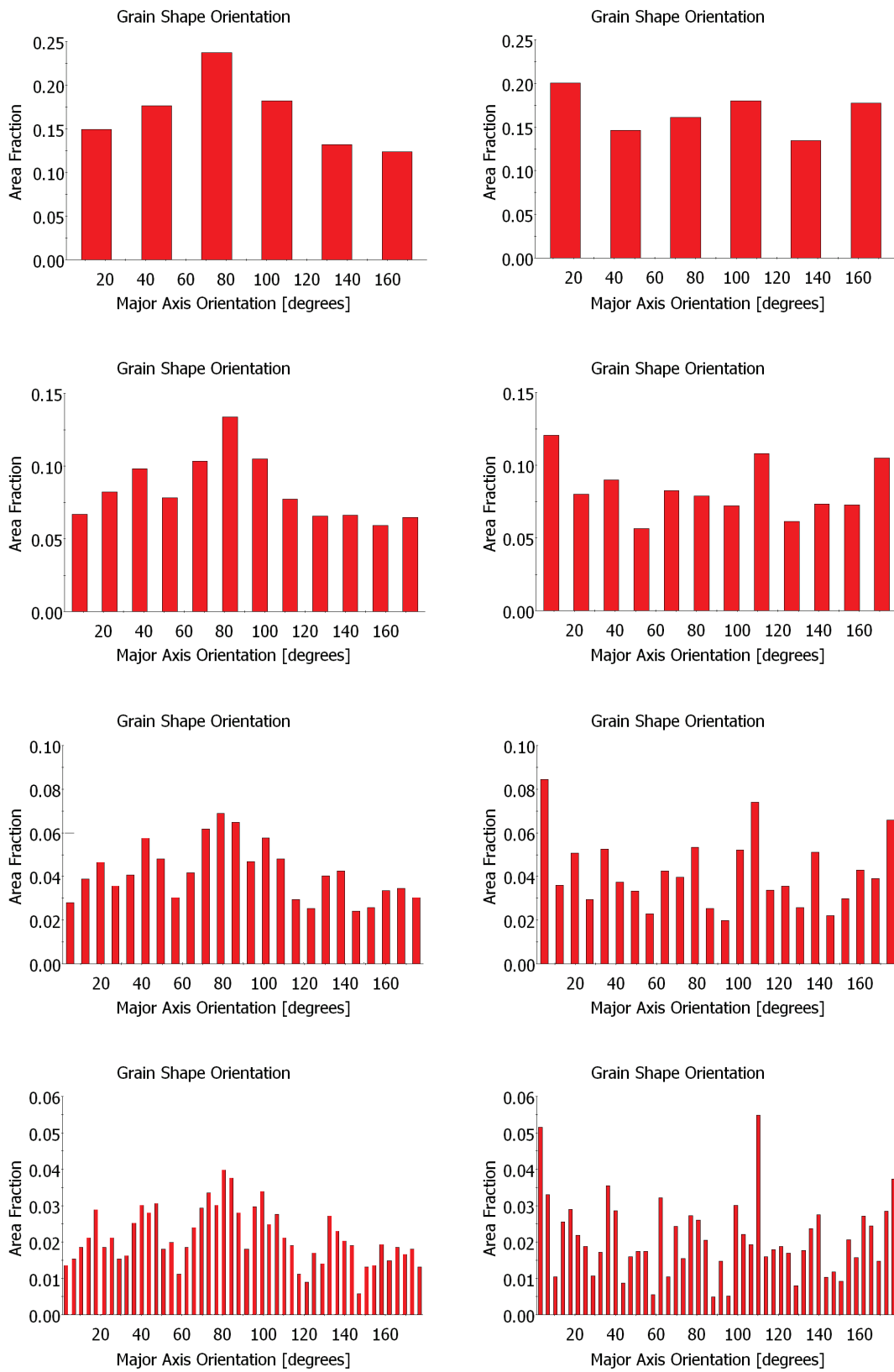


FIGURE 5.20: Grain shape orientation, cf. Figure 5.8 with several discretisation levels. Left column: specimen transformed under 120 MPa tensile loading (TR25). Right column: specimen transformed under 120 MPa shear loading (TR32). Grains are defined as connected regions with a misorientation of 11° .

5.5.2 Block Details

For the characterisation of the substructure of individual blocks such as small twins and dislocation cells, electron backscattering diffraction (EBSD), electron channelling imaging contrast imaging (ECCI), X-ray and synchrotron Bragg diffraction and transmission electron microscopy (TEM) has been used. A discussion of habit plane examination using TEM can be found in M.-X. Zhang et al. 2009. Du et al. 2016b points out that due to the almost identical orientation of sub-blocks their boundaries are invisible in EBSD maps.

Figure 5.21 taken from the literature (Morito et al. 2006a) depicts a regular block arrangement of a steel microstructure with a similar composition as the MarvalX12. Furthermore, it is known that the prior austenite grain size (PAGS) is $320 \mu\text{m}$ and martensite has been obtained by water quenching. Some aspects are important to keep in mind in the following. First, the arrangement of blocks is much more regular with a PAGS much larger than in the case investigated here, i.e. the hierarchical microstructure of lath martensite exhibits an inherent size effect.

Second, a common way to reconstruct a few austenite grains consists in taking a representative pole figure (such as that in Figure 5.21) or ODF, transform it according to an appropriate orientation relationship (KS or NW) and compare it with theoretical pole figures for this OR. Obviously, this approach is not suitable for the determination of an overall variant distribution. References on automatized reconstruction methods are found at the end of section 3.4.

Third, the resolution in Figure 5.21 is about two magnitudes lower than what is possible nowadays. Today often the term high resolution electron back scattering diffraction (HREBSD) is encountered in the literature. Actually, the term does not refer to directly recorded higher resolution, but a signal processing technique. Particularly, some regions of interest (ROI) are extracted and their intensity distributions are cross correlated using a cross correlation function (XCF) in order to achieve a higher angular resolution. According to Wilkinson et al. 2006 this technique is insensitive to hydrostatic strain changes (no change in the angle between Kikuchi bands).

Now the sub-block heterogeneous features of the three specimens are investigated. For this purpose a more sensitive colour coding than in the previous section is chosen to visualize

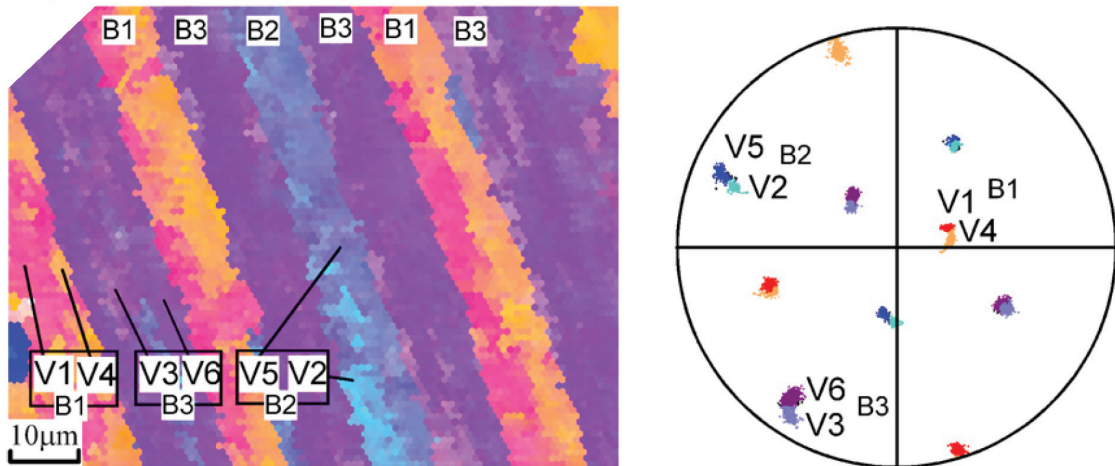


FIGURE 5.21: Left: Typical regular block arrangement of 18Cr-8Ni-5Mo with large $320 \mu\text{m}$ PAGS from Morito et al. 2006a. The data either has been coarsened or the resolution of common EBSD systems at the time of recording was significantly lower than for more modern systems. Right: according pole figure. Such pole figure representations are commonly used to reconstruct grains by comparing them with theoretical pole figures.

lattice orientation gradients more clearly. In addition to that the density of geometrically necessary dislocations (GNDs) is calculated from the local misorientation. The GND density is given in terms of $1 \times 10^{12} \text{ m}^{-2}$. The calculation method is according to Field et al. 2005 and considers both edge and screw dislocations. Two evaluation parameters can be specified. (i) a maximum misorientation, above which orientation gradients are not considered for the GND calculation (the program default is 5°). (ii) the number of nearest neighbours over which the orientation gradient and hence the density of GNDs is calculated. Complementary studies on GNDs in steels may be found in Calcagnotto et al. 2010; Konijnenberg et al. 2015.

Figure 5.22 depicts the fine sub-block features of a block from the microstructure of specimen TR25 (tensile loaded). The heavy plastic deformation due to the repeated TRIP effect involves block-substructure sliding and rotation as indicated by the observed dislocation tangles arranged as dislocation cell walls. This mechanism of rearrangement is highly effective to reduce the strain energy compared to the random distribution of dislocations, resulting in a more (thermodynamically) stable state.

In Figure 5.23 and Figure 5.24 similar evaluations have been carried out with varying maximum misorientation angle for the GND density for the specimens TR32 (torsion) and TA03 (higher annealed).

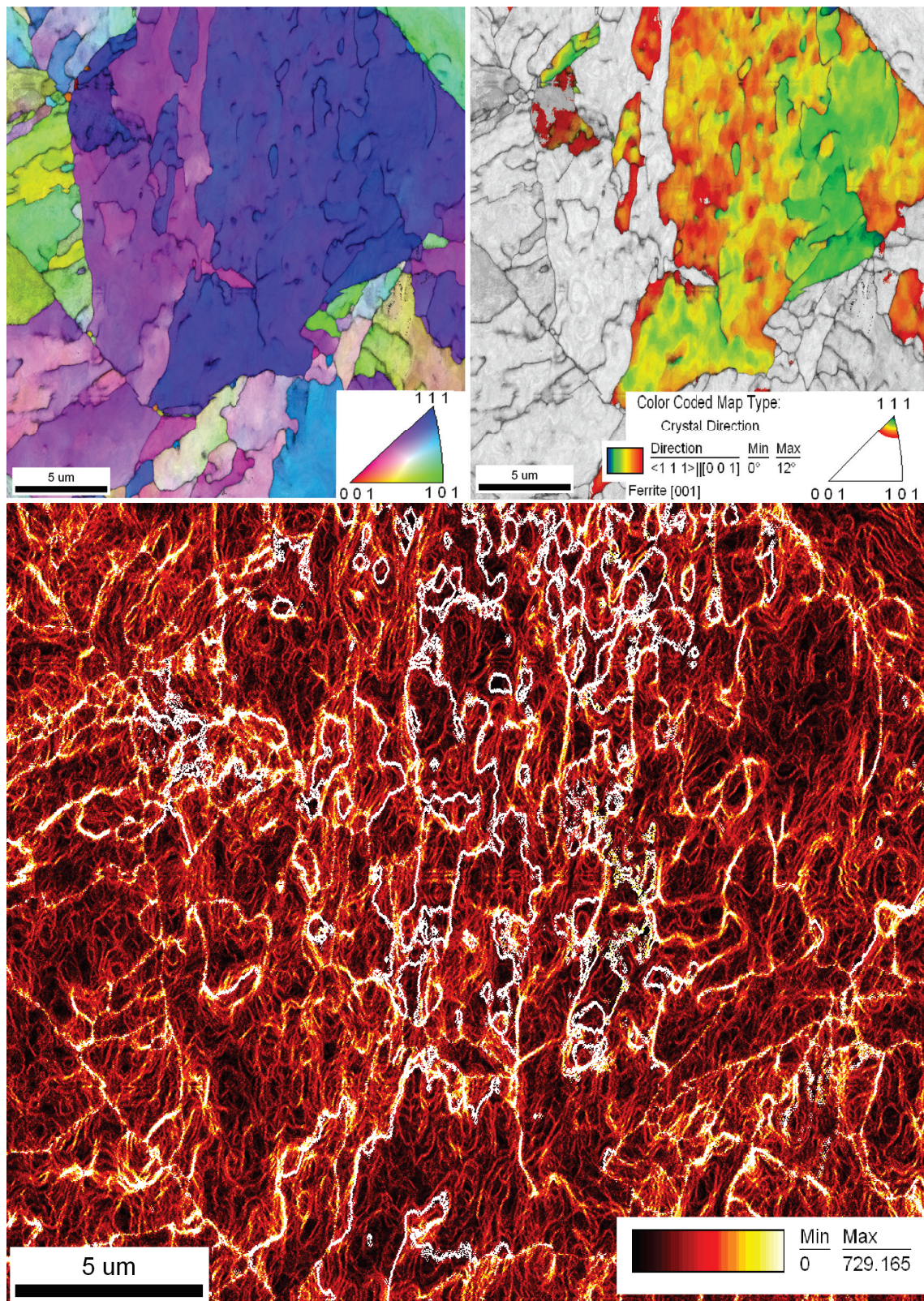


FIGURE 5.22: Specimen TR25 tensile specimen: Upper-left: GS: fit, CC: IPF. Upper-right: CC: [001] IPF with crystal direction $\langle 111 \rangle_{\alpha}$ and colouring up to 12° misorientation indicating bi-variant block-structure. The GND density is evaluated by first nearest neighbour analysis and considering misorientations up to 5° (larger misorientations are ignored). GND density is, given in multiples of $1 \times 10^{12} \text{ m}^{-2}$.

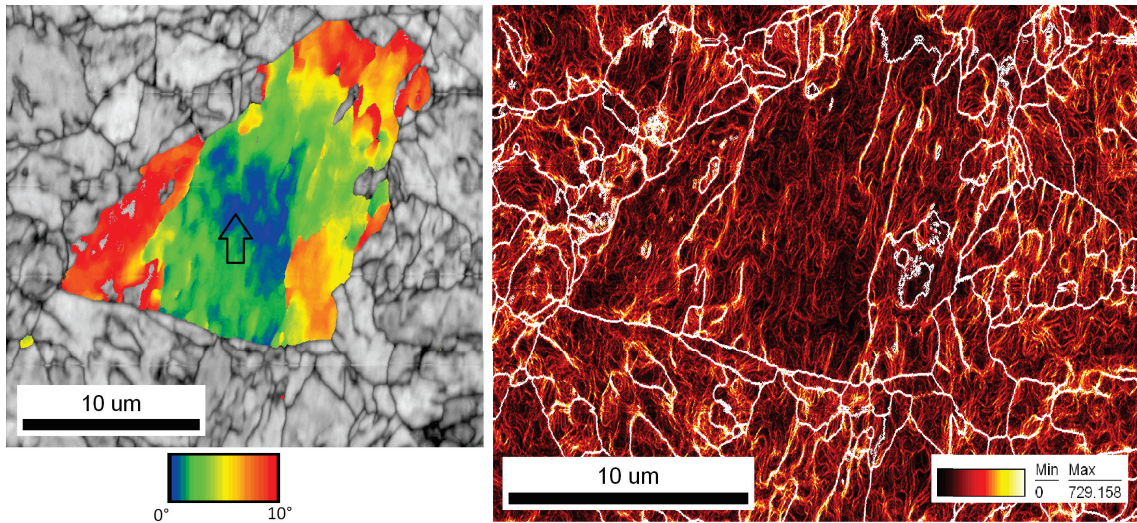


FIGURE 5.23: Specimen TR32 (shear loaded). Left: Local misorientation with maximum of 11° with respect to marked point in grain. Right: GND density evaluated with a maximum considered misorientation of 60° (larger misorientations are ignored) and second nearest neighbours analysis. The GND density is given, in multiples of $1 \times 10^{12} \text{ m}^{-2}$

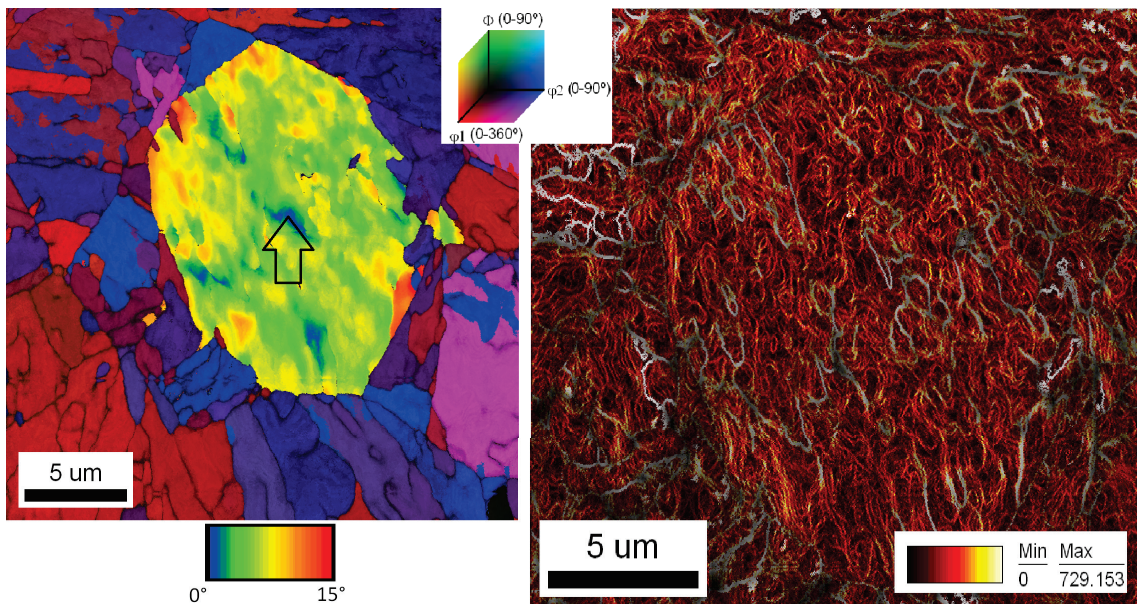


FIGURE 5.24: TA03: Left: Euler angle colouring background and local misorientation with maximum of 15° relative to marked point in the middle of the block. Right: GND density with maximum considered misorientation of 15° (larger misorientations are ignored) and first nearest neighbours gradient calculation. The GND density is given in multiples of $1 \times 10^{12} \text{ m}^{-2}$. Here the GND density is overlaid with an image quality gray-scale contrast Note that at this resolution the grain boundaries can be anticipated by the image quality contrast.

Chapter 6

Constitutive Description of Dislocated Lath Martensite Formation

The focus of this work, from a modelling point of view, is on plastic deformations and lattice changes (accompanied by some positive volumetric change) enabled by dislocation motion as well as their mutual couplings. Microstructurally motivated constitutive relations are sought.

6.1 Continuum Kinematics and Classes of Continuum Models

For the mean field approach developed in this work an engineering / linearised / small / infinitesimal definition of strain is utilized corresponding to an additive decomposition of the total strain $\underline{\epsilon}$. Note that common strain functions are defined, such that for small strains but arbitrary rotations (e.g. in plasticity), all strain measures are the same to the order of approximation. However, the crystallographic deformation due to the phase transformation $\underline{E}^{\text{tr}}$, discussed in chapter 3 in general is not small. Therefore, a large / finite / quadratic / non-linear strain formulation is employed for the transformation strains. A mean field description is employed, i.e. an implicit homogenization of the mechanical

fields weighted with of variant phase fractions ξ^i evolving incrementally for the respective transformation tensors.

$$\underline{\varepsilon} = \underbrace{\underline{\varepsilon}^{\text{te}}}_{\text{reversible}} + \underbrace{\underline{\varepsilon}^{\text{in}}}_{\text{irreversible}} = (\underline{\varepsilon}^{\text{el}} + \underline{\varepsilon}^{\text{th}}) + (\underline{\mathbf{E}}^{\text{tr}} + \underline{\varepsilon}^{\text{P}}) \quad (6.1)$$

with thermoelastic / reversible (elastic plus thermal strains) and inelastic / irreversible (transformation and plastic strains). Equation 6.1 can be extended by taking into account a compositional eigenstrain $\underline{\varepsilon}(c)$. The simplest linear assumption on atomic concentration is known as Vegard's law. At this point also the idea of a lattice continuum as formulated by Mesarovic 2016 is mentioned, which is especially interesting if strong compositional changes occur.

The deformation gradient is a compatible field derived from the displacement vector field. Compatibility conditions are particular cases of integrability conditions and were first derived for linear elasticity by Barré de Saint-Venant in 1864 and proved rigorously by Beltrami in 1886. The conditions for small and large strains respectively are:

$$\begin{aligned} \text{Incompatibility}(\varepsilon_{ij}) &= \text{Inc}(\varepsilon_{ij}) \epsilon_{pmk} \epsilon_{qnj} \varepsilon_{jk, nm} = \nabla \times \underline{\varepsilon} \times \nabla = 0 \\ \epsilon_{qnj} F_{jk, n} &= \text{curl } \mathbf{F} = \nabla \times \mathbf{F} = 0 \end{aligned}$$

i.e. one equation in 2D and 6 Equations in 3D. B. A. Bilby et al. 1955 and Kröner 1958 independently proposed the decomposition of the deformation gradient into elastic and plastic parts.

$$\mathbf{F} = \mathbf{F}^e \mathbf{F}^p \quad (6.2)$$

The idea of Mandel 1972 was that after application of \mathbf{F}^p the lattice directions remain unchanged (isoclinic intermediate configuration, only valid for single crystals). For phase transformations the decomposition

$$\mathbf{F} = \mathbf{F}^e \mathbf{F}^p \mathbf{F}^{\text{tr}} \quad (6.3)$$

having two intermediate configurations is commonly used, see e.g. the works by Levitas et al. 2009a; Addessio et al. 2016. Clayton 2010; Clayton et al. 2014 proposed an extension of Equation 6.2 accounting for local lattice distortion due to defects. It should be noted

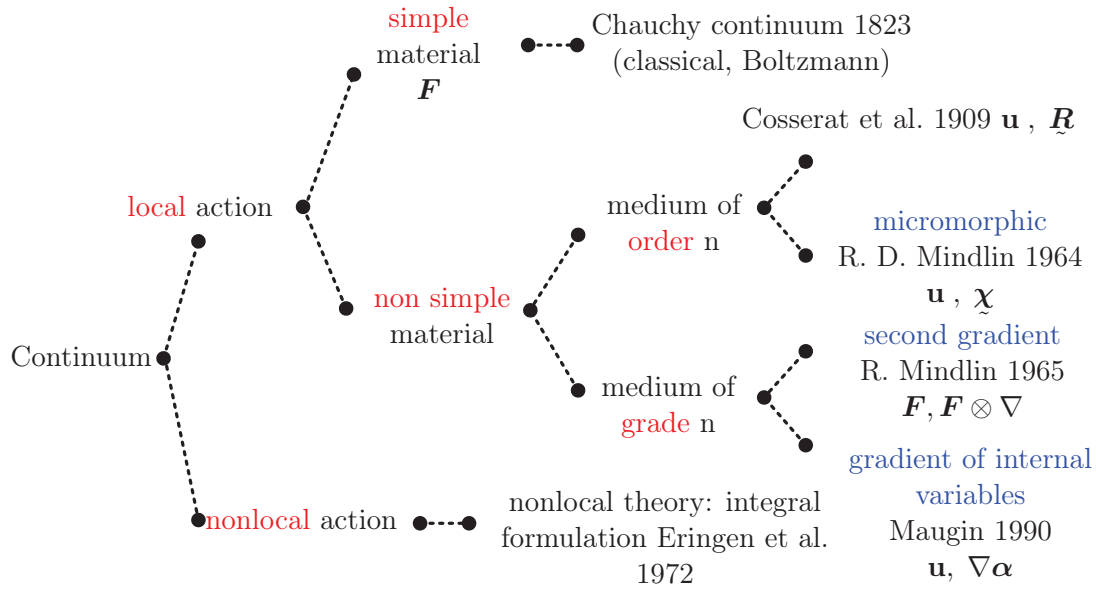


FIGURE 6.1: Terminology of generalized continua. Reproduced after Forest et. al: CISM 2017 - Mesoscale Models: From Micro-Physics to Macro Interpretation. Not explicitly drawn are microstrain theories (negligible micro rotations as a complementary to the Cosserat continuum). Second gradient approaches are probably necessary to describe the deformation of a martensite lath. A typical example of a gradient of internal variable is a gradient of the plastic strain in (phenomenological) strain gradient models.

however, that the actual physical mechanism of deformation is not unambiguously captured utilising multiplicative decomposition (mathematically the order of multiplications does matter), whereas in reality the mechanisms appear simultaneously. This is a crucial point of this work also stressed in section 3.5. This may also be the reason why many authors like S. Kalidindi et al. 1992; Roters et al. 2012 (DAMASK see section C.1) prefer an additive decomposition in mean field models incorporating crystallographic variants.

Next, the term *simple* material as used in the next section is elaborated: After C. Truesdell et al. 1960; C. Truesdell et al. 1965 a material is *simple* at the point \mathbf{X} if and only if its response to homogeneous deformations in a neighbourhood of \mathbf{X} uniquely determines its response to every deformation at \mathbf{X} . For the sake of completeness higher order continua (see e.g. Altenbach et al. 2013; Maugin 2016) are mentioned at this point. An overview of the generalizations is given in Figure 6.1. R. Mindlin 1965 proposed that not only \mathbf{F} should be followed, but also the lattice directions (\mathbf{d}, \mathbf{D} directors in original paper).

$$\mathbf{d} = \chi \mathbf{D} \quad (6.4)$$

If $\chi = \chi_{ij}$ contains non-negligible rotations and stretches the theory is called micromorphic. If either stretches or rotations can be neglected, the Cosserat continuum and the so-called microstrain theory are obtained (see Figure 6.1). The most popular way for metals is to link the plastic strain gradient to geometrically necessary dislocations (GNDs), see section 6.5. Interestingly, by the time these theories were developed there was no way of experimental verification. But nowadays the determination of lattice curvature (gradient of rotation) has become a standard method (the result is e.g. a GND density), see section 5.5.

6.2 Assumptions and Consequences

The following assumptions are made in this work (also see, C. Truesdell et al. 1960; C. A. Truesdell et al. 1965; Lemaitre et al. 1994; Besson et al. 2009; Bower 2009; Bertram et al. 2015):

- i) The local state/action principle, which assumes that the thermodynamic state and resulting local behaviour in a given point depends only on the current values of the corresponding state variables (observable and internal) defined in this point, and not on the surroundings. In a finite element framework without heat conduction and diffusion, the only interaction that arises between integration points is due to the stress or strain evolution from the global solution of the equilibrium problem. Also commonly mentioned along this line of argumentation is the principle of determinism, stating that the current value of any physical variable can be determined from knowledge of the present and past values of all other variables.
- ii) The principle of material simplicity elaborated in the previous section.
- iii) Principle of frame indifference / objectivity stating that any constitutive law should be independent on whatever external frame of reference is used. Practically, this is achieved either by transforming orientation dependent properties properly or by formulating laws depending on tensor invariants, see e.g. Boehler 1987; Zheng 1994 for the latter.
- iv) Material symmetry: A constitutive relation must respect any symmetries that the material possesses.

v) The laws of thermodynamics (1. law: conservation of energy, Equation 6.5, 2. law: dissipation inequality Equation 6.6) and balance equations (conservation of mass, Equation 6.7 and momentum, Equation 6.8), in total 6 scalar equations, must be fulfilled. For derivations see one of the a.m. works. The weak / local formulation reads:

$$\rho \frac{d\dot{e}}{dt} = \nabla \cdot \mathbf{q} + \boldsymbol{\sigma} : \dot{\boldsymbol{\varepsilon}} + r \quad (6.5)$$

$$\rho \frac{ds}{dt} + \nabla \cdot \left(\frac{\mathbf{q}}{T} \right) + \frac{\mathbf{r}}{T} \geq 0 \quad (6.6)$$

$$\frac{\partial \rho}{\partial t} + \nabla \cdot (\rho \mathbf{u}) = 0 \quad (6.7)$$

$$\nabla \cdot \boldsymbol{\sigma} + \rho \mathbf{f} = \rho \ddot{\mathbf{u}} \quad (6.8)$$

where r represents inner heat sources or sinks, \mathbf{q} is the vector of heat flux and \mathbf{f} is the vector of body forces (hence often denoted as \mathbf{b}). Number of unknowns: energy e – (1), density ρ – (1), velocity v_i – (3), σ_{ij} – (6) (in terms of the symmetric Cauchy stress otherwise 9) yielding a total of 11 unknowns. Therefore $11 - 6 = 5$ constitutive relations must be added. Furthermore, initial and boundary conditions must be defined. Summing up, the following equations and conditions must be satisfied simultaneously:

1. equilibrium or balance equations (mostly in weak/local formulation as above), also known as principle of virtual work in the continuum mechanics community (e.g. Maugin 1980)
2. compatibility
3. constitutive equations
4. boundary conditions

If the problem is solved in terms of displacements (e.g. most finite element methods) compatibility is satisfied automatically. Note that, although time cannot be used explicitly in the constitutive equations, the direction of time is related to the increase of entropy according to the second principle of thermodynamics.

In addition, it is a good idea to ensure that the material satisfies the Drucker-Hill stability criteria (see Drucker 1957; Hill 1958):

$$d\boldsymbol{\sigma} : d\boldsymbol{\varepsilon} > 0 \quad \text{with external load, positive work}$$

$$d\boldsymbol{\sigma} : (d\boldsymbol{\varepsilon} - d\boldsymbol{\varepsilon}^{\text{el}}) = d\boldsymbol{\sigma} : d\boldsymbol{\varepsilon}^{\text{p}} \geq 0 \quad \text{for plastic deformation cycle}$$

Materials that fail to satisfy these criteria are likely to present difficulties (i.e. non-uniqueness / bifurcations or singularities) during the solution process causing convergence problems.

6.3 Generalities for Multi-Variant for Phase Transformations

A constitutive law must allow us to calculate the current stress as a function of the whole history of deformation of the continuum. State variables describe the current state of the system and it is distinguished between observable (mechanical: $\boldsymbol{\sigma}$, $\boldsymbol{\varepsilon}$, thermal: T , S , magnetic, electric fields) and internal variables $\boldsymbol{\alpha}_i$, \mathbf{K}_i , describing the internal structure of materials. Notably, as indicated above for the mechanical and thermal fields, each field is characterised by a pair of (conjugate / associated) variables and there are relations between the observable and internal variables. Internal variables are not directly coupled to the observable variables in the sense that they do not participate in "external" work. They operate in an "internal" work and are responsible for the irreversible (dissipative) nature of a process or for a storage of energy (E. Oberaigner 1993). Generally, relations between state and internal variables may be algebraic relations, integral equations or differential equations. Lemaitre et al. 1994 note that for non-linear phenomena often power functions are used, but for phenomena, which asymptotically saturate, exponential functions are preferred. In Lemaitre 2001 it is pointed out that they should result from observations at a microscale and from a homogenization process. In this work, following this advice, a detailed experimental as well as computational analysis of the microstructure yields logical functions with regard to the mechanisms introduced at the microscale.

Following the concept of a generalized force \mathbf{Z} and flux \mathbf{z} any potential \mathbf{P} may be defined by

$$\delta\mathbf{P} = -\mathbf{Z}\delta\mathbf{z} \tag{6.9}$$

Since each field is characterised by a pair of variables, there are always two potentials. One depends on a generalized force and one on a generalized flux (also called primal and dual variables). Forces and fluxes are conjugate pairs (energy conjugates), i.e. their inner product must yield an energy. In general, conjugate pairs can be defined with respect to any thermodynamic state function. Conjugate pairs related to entropy are often used in the analysis of irreversible processes. The Legendre transform is used to change between conjugate state variables. In thermomechanics it is mainly used to switch between potentials described as a function of $\boldsymbol{\varepsilon} \leftrightarrow \mathbf{P}_\varepsilon$ or $\boldsymbol{\sigma} \leftrightarrow \mathbf{P}_\sigma$. For instance exchanging $\boldsymbol{\sigma}$ with $\boldsymbol{\varepsilon}$ in the potential, the transformation is of the form:

$$\mathbf{P}_\varepsilon = \sup \{ \dot{z} : Z - \mathbf{P}_\sigma |_Z \} \quad (6.10)$$

the transformed potential therefore depends on the time derivative of the state variables of the former. As usual forces are obtained by deriving potentials w.r.t. fluxes (often referred to as Coleman-Noll procedure), i.e. thermodynamical forces (here denoted \mathbf{K}^i) associated to the fluxes (here $\boldsymbol{\alpha}^i$) are defined by:

$$\mathbf{K}^i = - \frac{\partial \mathbf{P}}{\partial \boldsymbol{\alpha}^i} \quad (6.11)$$

For the progress of a process the thermodynamic forces must reach a threshold \mathbf{K}_c^i value as a generalization of a yield- / load - surface / function / criterion / condition. For instance assuming a potential formulated in terms of $\boldsymbol{\sigma}$ this condition becomes:

$$f(\boldsymbol{\sigma}, \mathbf{K}^i, T) = \mathbf{K}^i(\boldsymbol{\sigma}, T, \boldsymbol{\alpha}^i) - \mathbf{K}_c^i(T, \boldsymbol{\alpha}^i) = 0 \quad (6.12)$$

For a process to progress this condition must be permanently fulfilled leading to the consistency condition

$$\dot{f} = \frac{\partial \mathbf{K}^i}{\partial \boldsymbol{\sigma}} \dot{\boldsymbol{\sigma}} + \frac{\partial \mathbf{K}^i}{\partial \boldsymbol{\alpha}^i} \dot{\boldsymbol{\alpha}}^i + \frac{\partial \mathbf{K}^i}{\partial T} \dot{T} - \frac{\partial \mathbf{K}_c^i}{\partial T} \dot{T} - \frac{\partial \mathbf{K}_c^i}{\partial \boldsymbol{\alpha}} \dot{\boldsymbol{\alpha}}^i = 0 \quad (6.13)$$

Equation 6.13 sometimes is directly expressed with second derivatives of the initial potentials (the matrix of second derivatives is called Hessian matrix). The interest of these approaches is to provide natural schemes for the choice of evolution equations and the type of internal variables, as e.g. pointed out by Cailletaud 2010. Lemaitre et al. 1994 (p. 194

therein) note that the framework $f(\boldsymbol{\sigma}, \dots)$ is not suitable for softening behaviours, but only materials with monotonically increasing hardening. Softening behaviour should be treated in a $f(\boldsymbol{\varepsilon}, \dots)$ formalism, as e.g. by Idesman et al. 2005; Esfahani et al. 2018.

After Halphen et al. 1975 a model is called generalized standard / fully associated iff both the flow rule and the evolution equations for the internal variables are derived from the same potential. If only the flow rule is derived from a potential the model is called simply associated and if neither the flow rule nor the evolution equations are derived from a potential it is called non-associated. The latter are practically indispensable in soil- and geomechanics (generally granular matter), see e.g. Houlsby et al. 2007.

Generally, the loading-unloading conditions are the following (Besson et al. 2009):

$$\text{elastic behaviour} \quad f < 0 \quad (6.14)$$

$$\text{elastic unloading} \quad f = 0 \quad \text{and} \quad \dot{f} < 0 \quad (6.15)$$

$$\text{plastic flow} \quad f = 0 \quad \text{and} \quad \dot{f} = 0 \quad (6.16)$$

Additionally, the stress has to be determined in such a way that it does not depart from the yield surface during plastic deformation processes. This requirement leads to an additional constraint, known as the consistency condition $\dot{f} = 0$ (during plastic yielding only!). The consistency conditions are often commonly written using Macaulay brackets, i.e. $\langle f \rangle$ meaning that $\langle f \rangle = f$ if $f > 0$ and $\langle f \rangle = 0$ if $f \leq 0$ (Heaviside function).

At this point it has to be anticipated that in plasticity (and most micromechanical models nowadays), in addition to $f \leq 0$ it is assumed that intrinsic dissipation is maximised (normality rule / maximum dissipation principle / Hills principle of maximum power, see subsection 6.4.2), i.e.

$$\mathcal{L}(\mathbf{Z}) = \mathbf{Z}\dot{\mathbf{z}} - \lambda f \quad (6.17)$$

where \mathbf{Z} is the vector of forces, $\dot{\mathbf{z}}$ the vector of fluxes, λ is a Lagrange multiplier. Since $\partial\mathcal{L}/\partial\mathbf{Z}$ must be zero for an extremum, this leads to the flow-rule of rate-independent plasticity (Equation 6.37). The loading unloading conditions (Equation 6.14) can also be formulated in terms of λ

$$\lambda \geq 0 \quad f \leq 0 \quad \lambda f = 0 \quad (6.18)$$

which are simultaneously the Karush-Kuhn-Tucker conditions of convex non-linear optimization / programming, see e.g. Jirasek et al. 2002; Ottosen et al. 2005; Besson et al. 2009; J. Simo et al. 2006. Note that a more general consistency condition incorporating λ is $\lambda \dot{f} = 0$ (if $f = 0$). The above conditions are the main reason why it is often stressed that the yield surface must be convex. Note that mathematically in this context the above conditions are sufficient, but not necessary. Convexity is generally defined as:

$$\forall x_1, x_2 \in X, \forall t \in [0, 1] : \quad f(tx_1 + (1-t)x_2) \leq tf(x_1) + (1-t)f(x_2) \quad (6.19)$$

(\leftrightarrow strict convexity). From a thermodynamical point of view, convexity of f also is a sufficient condition that dissipation is positive, if f additionally includes the origin (see e.g. Lemaitre et al. 1994. However, convexity does not seem to have a physical significance, see Glüge et al. 2017. Convexity of a potential guarantees stability and therefore uniqueness of the solution. Interestingly, as far as phase transformations are concerned convexity studies started from a mere elastic point of view utilizing the direct method of calculus of variations. As a result it was found that the governing potentials tend not to be convex, not even quasiconvex. For several notions of convexity see the works of J. M. Ball 1976; Carstensen et al. 2002; S. Bartels et al. 2004; Heinen et al. 2007; Govindjee et al. 2007. Generally, the probability of the existence of a convex potential at the microscale is diminished by the strong interactions between heterogeneities, necessitating nonlocal formulations. For a schematic energy landscape as imagined on the microscale see Figure 6.2. Non-quasiconvex energy densities are problematic from the mathematical and algorithmic viewpoint as the existence of minima of such functionals cannot be guaranteed, see e.g., C. B. Morrey et al. 1952; C. Morrey 2009; Dacorogna 1982; Dacorogna 2007; Silhavy 1997 for a comprehensive treatise in this regard. Equilibrium states following from such energy densities can, therefore, be regarded as unstable, causing bifurcations and thus additional numerical problems. For a short introduction to bifurcations with this regard, e.g. differentiation between continuous or discontinuous (shear bands, Lüders Bands) see Ottosen et al. 2005 or for a comprehensive treatment Bigoni 2012.

The initiation of microstructure usually follows from a loss of stability. This can be modelled using a strain softening formalism, i.e. purposefully introducing a short softening / instability stage followed by a higher hardening stage, see e.g. Beissel et al. 1996; J. A. Shaw 2000. The case of martensite and its variants in this manner has been treated by

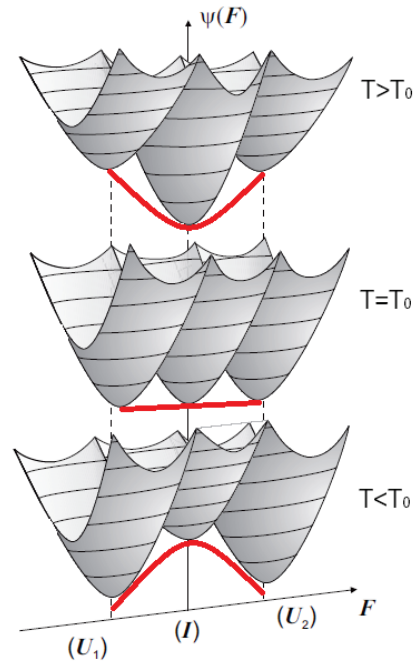


FIGURE 6.2: Schematics of energy "wells" from Wilmanns 2010. Red lines indicate the general trend for various temperatures around the equilibrium temperature T_0 see subsection 6.4.1. The wells are separated by activation barriers. \mathbf{I} stands for the untransformed parent phase, the \mathbf{U}_i are structural stretch tensors or more generally shape strains (see section 3.5) of the product phase.

Levitas and co-workers (Idesman et al. 2005; Esfahani et al. 2018). Such an approach is able to produce a microstructure evolution similar to the phase field method (see also Yalcinkaya et al. 2011; Yalcinkaya et al. 2012 for plastic instabilities, specifically Mazière et al. 2015; Mazière et al. 2017 for Lüders band formation). Without further considerations, numerical problems are of course an issue. It remains to be studied in more detail whether neglecting mathematical rigour (e.g. by loss of convexity) nevertheless produces physically reasonable results under various conditions.

Notably, the energy minimizing approach in the mathematical community has also been followed first in the continuum modelling community. It has been argued by Siredey et al. 1999; X. Gao et al. 2000 to extend the free energy by the obvious constraints on the phase fractions $\xi^i, 1 - \xi$ (interpreted in terms of mass conservation).

$$\xi^i \geq 0 \quad \sum_i \xi^i \leq 1 \quad (6.20)$$

to extent the free energy utilizing Lagrange multipliers as

$$\mathcal{L} = \Psi - \sum_i \lambda^i (-\xi^i) - \lambda^0 (\xi - 1) \quad (6.21)$$

At this point the generality of the Lagrange multiplier method is emphasized. It is found in many problems that allow a similar formulation such as multi-surface / multi-mechanism plasticity, see e.g. J. C. Simo et al. 1988; Cailletaud et al. 2018. The evolution vector of phase fractions is obtained in analogy to rate-independent plasticity elaborated above. Note that in contrast to plasticity, in such models also other norms than the Frobenius / 2-norm are used. A common assumption is to use only the maximum value (infinity-norm) of the incremental phase fraction vector in each increment, as followed e.g. by Lagoudas 2008. This may be interpreted as a smaller time scale, where only one transformation event is treated at a time.

Also note that for non-differential (non-smooth) yield surfaces (e.g. due to a multi-surface / mechanism formalism) the notion of a subdifferential must be introduced (see e.g. Moreau 1977). Generally, whether a minimum or a maximum is obtained utilizing the formalism of Lagrange multipliers must be checked explicitly.

Note that the constraints in Equation 6.20 are mostly inactive during the calculations (the system is over-constrained) and the conditions can also be ensured directly. Govindjee et al. 2001 first implemented the resulting set of equations implicitly (Backward-Euler) with an elastic time step and described an active-set-strategy utilizing a numerical iterative procedure for the determination of the residuals. They described and visualized the transformation surface and applied the algorithm to SMAs ($\Delta V = 0$). Mahnken et al. 2015 followed this line of implementation, adding Mises-plasticity (radial return) and (to the authors knowledge) were among the first using crystallographic transformation strains typical for steels ($\Delta V = 0.5 - 4\%$). In their work they point out that although the constraints are mainly inactive during the transformation process (i.e. $\dot{\mathcal{L}} \approx \dot{\Psi}$) they achieve a better numerical stability following this approach. It remains unclear, whether this formalism is necessary for the determination of variant fractions. An alternative numerical approach for this problem, which also has first been applied in crystal plasticity, has been presented by Schmidt-Baldassari 2003 and employed by Bartel et al. 2011; Auricchio et al. 2014 for multi-variant phase transformations. The strategy consists in replacing the Kuhn-Tucker complementarity inequality conditions, by a complementarity function after

A. Fischer 1992 resulting in a non-linear equality constraint where an active set search can be omitted, which is a fundamental advantage when dealing with many coupled evolution equations. Numerical studies on the flexibility of (almost) equal models, utilizing a plastic or viscoplastic solution strategy should be carried out.

Next, the alternative approach of variational constitutive updates recently gaining momentum is shortly mentioned. The formalism is not only interesting due to its more direct physical interpretation (all unknown variables follow from minimizing a certain potential), but also due to efficient numerics (e.g. a symmetric tangent matrix is always obtained). A historical note is found in Besson et al. 2009 6.3.1 therein. The governing functional J in the variational approach is of the general form

$$J(\mathbf{P}(\mathbf{x})) = \int f(\mathbf{P}(\mathbf{x}, \nabla \mathbf{P})) d\mathbf{x} \quad (6.22)$$

and leads via variation of the parameters

$$J(\mathbf{P}(\mathbf{x}) + \delta \mathbf{P}) - J(\mathbf{P}(\mathbf{x})) \approx \int \frac{\delta J}{\delta \mathbf{P}} \delta \mathbf{P} d\mathbf{x}$$

to the Euler-Lagrange equation

$$\frac{\delta J}{\delta \mathbf{P}} = \frac{\partial f}{\partial \mathbf{P}} - \nabla \frac{\partial f}{\partial \nabla \mathbf{P}} \quad \text{with} \quad \dot{\mathbf{P}} = -M \frac{\delta J}{\delta \mathbf{P}}$$

i.e. rates are proportional to "distance" from equilibrium. The coefficient(s) M are the mobility (normally assumed constant). A good introduction to variational calculus is found in Gelfand et al. 2000. Two famous examples of $f(\Psi)$ are the Ginzburg et al. 1950 (Ginsburg in German) the Cahn et al. 1958 equation (for diffusional problems) as elaborated in subsection 6.7.1. The topic of constitutive updates is treated in Hackl 1997; Ortiz et al. 1999 and more recently by Mosler et al. 2009b; Mosler et al. 2009a; A. Bartels et al. 2015, Miehe 2011. Hackl et al. 2014,

6.4 Thermodynamic (Extremum) Principles

For an introduction to this topic in conjunction with constitutive modelling see Malvern 1969; Lemaitre et al. 1994; Silhavy 1997; Besson et al. 2009; Kurth et al. 2013.

First it should be noted, that we are interested in thermodynamic states far from equilibrium (those are the interesting ones in terms of microstructure tuning). In the literature the used framework is often called extended irreversible thermodynamics. Particularly, there is no need for introducing local equilibria (as in classical irreversible thermodynamics).

In this thesis no effects due to the conduction of heat are treated (i.e. only isothermal processes are considered). Note that for realizing the limit case of an isothermal austenite-martensite $A \rightarrow M$ (exothermic transformation) transformation in experiments sufficient heat extraction must be secured in order for this approximation to be justified ($M \rightarrow A$ endothermic transformation).

Note that especially in material science equilibrium thermodynamics / thermostatics / rational thermodynamics is much better documented, e.g. in the discussion of phase diagrams or classical nucleation theory. Typically, the Gibbs free energy $G(\boldsymbol{\sigma})$ is used in this context (Porter et al. 2009; Christian 1965). Conversely, since most finite element codes are formulated in terms of strains, the governing potential to minimize is the generalized Helmholtz free energy $\Psi(\boldsymbol{\varepsilon})$.

By contrast, for modelling the temporal evolution of physical processes non-equilibrium or irreversible thermodynamics must be utilised. Onsager 1931 proposed a pseudo-potential of dissipation, furnishing the complementary laws of evolution for the variables. Here we consider two inelastic potentials, one depending on the stress Ω_σ and one on the strain Ω_ε . Carstensen et al. 2002 calls Ω_ε inelastic potential and its Legendre transform the dissipation functional. Lemaitre 2001 points out that such potentials may be identified from the observation of flow by integration. A popular example is Norton's creep law $\dot{\varepsilon}(\sigma) = \left(\frac{\sigma}{K}\right)^n$ yielding

$$\Omega_\sigma = \frac{K}{n+1} \left(\frac{\sigma}{K}\right)^{n+1} \quad (6.23)$$

Equivalently, Equation 6.67 could be used for athermal martensite formation, although this seems to have never been proposed. For such an approach, however, it generally has to be verified a-posteriori if the second law is fulfilled. Alternatively, Ω may be chosen from the class of homogeneous functions of degree n , for which it can be shown that dissipation is always positive (see e.g. Ottosen et al. 2005 p.568 therein).

6.4.1 Energetic / Equilibrium Thermodynamics, Thermostatistics

Subsequently, free energy terms in conjunction with phase transformation models are elaborated. In a mean field framework, considering its implicit multi-scale character, elastic, thermal and chemical energies each can have various contributions. Homogenization and localization strategies to quantify these contributions are discussed in chapter 4. Note that in this work particle transfer (in the thermodynamical sense) is neglected. For the remaining thermal and elastic contributions the following explicit terms stemming from different mechanisms may be found:

$$\Psi = \underbrace{\Psi^{\text{el}} + \Psi^{\text{th}}}_{\text{cf. "classical Work"}} + \underbrace{\Psi^{\text{chem}}}_{\text{cf. Heat } Q} + \Psi^{\text{p}} + \Psi^{\text{ie}} + \Psi^{\text{int}} \dots \quad (6.24)$$

Ψ^{el} commonly denotes the strain energy due to the average global / external stress state $\boldsymbol{\sigma}^{\text{ext}}$. Ψ^{th} commonly denote strain energies due to thermal strains $\propto \boldsymbol{\alpha}(T - T^{\text{ref}})$. Ψ^{int} (often also Ψ^{mix} as by Govindjee et al. 2000; Bartel et al. 2011) indicates homogenized quantities at each material point. It can have various origins such as contributions due to the mixture of at least two phases or interactions between crystallographic variants. Interpretation of these contributions can be twofold. In terms of hardening they depict geometric constraints on the one hand and a stabilization by stresses on the other. However, stresses may also have an autocatalytic character on the transformation (especially for isochoric $\Delta V = 0$ transformations like in SMAs).

Ψ^{chem} accounts for the temperature dependence of Ψ (it may also denote a dependency on composition / chemical potential which is neglected here). Note the relation:

$$\left(\frac{\partial \delta Q_{\text{rev}}}{\partial T} \right)_{\varepsilon} = T \left(\frac{\partial S}{\partial T} \right)_{\varepsilon} = T \left(\frac{\partial^2 \Psi}{\partial T^2} \right)_{\varepsilon} = c_{\varepsilon} \quad (\text{specific heat capacity}) \quad (6.25)$$

The notion $\partial \delta Q_{\text{rev}}$ is used on purpose to indicate that Q is a path function and depends on more variables than just T (obviously, it strongly depends on ξ). After Dulong-Petit the specific heat capacity $c \approx 3R$ for most metals. Particularly, the value for iron $\approx 3.5R$ and that for steels $3.4 - 3.8R$. Mostly, a constant value is used for c , resulting in integrated form ($\int_{T_0}^T$) in a free energy contribution $\rho c_{\varepsilon} (1 - \ln(T/T_0))$. Note that a determination of the latent specific heat λ_h in analogy to e.g. a solid-liquid transition is difficult since a variety of plastic dissipative phenomena producing heat occur simultaneously during the

phase transformation in a TRIP steel (see e.g. Bever et al. 1973; Chaboche 1993; Anand et al. 2015).

Ψ^{ie} are contributions due to interface energies, which again are an inherent result of a multi-scale concept (elastic as well as chemical contributions on a lower scale). If the interface structure is well characterized or very regular, phenomenologically introducing a Ψ^{ie} term is an easy way to introduce a size effect into the model via variation of the area to volume ratio see e.g. Petersmann et al. 2017a. The influences of interface surface stress and composition dependency have both been treated in a tensorial formalism by Grinfeld 1991.

In the literature often a Clapeyron relation in analogy to gases is found:

$$\frac{d\sigma}{dT} = \frac{\Delta S}{\Delta V} = \frac{\Delta S}{V_0(\det(\mathbf{F}) - 1)} = \frac{\Delta Q}{TV_0(\det(\mathbf{F}) - 1)} \quad (6.26)$$

However, the problems for solids are: i) Due to heterogeneous microstructures σ strongly varies locally. ii) This equation assumes is thermodynamic equilibrium ($G_{\alpha'} - G_{\gamma} = \Delta G_{\gamma \rightarrow \alpha'} = 0$), which is no longer valid for martensite in steel (where $\Delta V > 0$).

In thermodynamic equilibrium the temperature T_0 between two phases is defined as $\Delta G_{\gamma \rightarrow \alpha'}(T_0) = 0$. For thermoelastic martensites T_0 often is approximated by averages of martensite and austenite transformation start and finishing temperatures: M_s , M_f , A_s , A_f e.g.

$$T_0 = \frac{M_s + A_f}{2} \quad (6.27)$$

as in Tong et al. 1974. If λ_h is known, for relaxed non-thermoelastic martensite exploiting the fact that in the initial stage ($\xi \ll 1$) self accommodation effects are small a good approximation is obtained by

$$T_0 = M_s + \frac{(\Delta\Psi_{\gamma \rightarrow \alpha'} + \mathcal{D})/V^m}{\rho\lambda_h(M_s - M_f)\xi} \quad (6.28)$$

where \mathcal{D} is the internal dissipation discussed in the next section. $\Delta\Psi + \mathcal{D}$ is obtained from the volume average of a full-field finite element simulation resolving a single martensitic domain (needle, lath, plate) embedded in an austenitic matrix with a suitable transformation eigenstrain. V^m is the volume corresponding to the martensite fraction ξ .

To the authors opinion not enough effort is made to quantify relative contributions to the free energy. A major improvement to this topic could be achieved if a whole transformation cycle, see section 5.4 is modelled. Particularly, the reverse transformation of martensite to austenite has been modelled using the equilibrium framework, see Ghosh et al. 2016 by assuming that the stored energy produced by plastic deformation increases the free energy of the austenite until it exceeds that of the normally more unstable δ -ferrite (at about 1500°).

For the sake of completeness it is mentioned that application of a magnetic field (raises M_s because it thermodynamically favours the formation of the ferromagnetic b.c.c. phase) which plays a role in induction-hardening or arc-welding process.

6.4.2 Dissipative / Non-equilibrium / Irreversible Thermodynamics

In section 6.3 the principle of thermodynamic orthogonality/ maximum dissipation/ maximum entropy production, i.e.

$$\dot{z} = \operatorname{argmax}\{\mathcal{D} = Z \cdot \dot{z}\} \quad (6.29)$$

has already been used to obtain a framework for evolution equations. Note that i) it is an associated principle, an axiom, no physical rule, but a class of models and ii) it unconditionally satisfies the dissipation inequality $\mathcal{D} \geq 0$. In a dissipative system the total energy cannot increase.

Some names associated with this principle occurring in materials modelling literature are (in chronological order): W. William Thomson a.k.a Baron Kelvin, Helmholtz, Rayleigh, Onsager 1931; Prigogine 1955, Casimir, P. Germain 1973; Ziegler 1987. Application of this principle in context of solid state phase transformations have extensively been treated by Levitas 1998 and co-workers (e.g. Idesman et al. 2005; Levitas et al. 2009a), who commonly refer to it as "postulate of realizability. Interestingly, even dissipation minimization has been proposed by Prigogine, see e.g. Hackl et al. 2008b. Thermodynamic extremum principles (TEPs) for irreversible processes have been reviewed by Hillert et al. 2006; F. Fischer et al. 2014.

The fundamental dissipation inequality is obtained by replacing r in Equation 6.6 with Equation 6.5. If it is expressed using Ψ it is known as the Clausius-Gibbs-Duhem inequality. Here additionally the additive decomposition of strains is used to obtain

$$\begin{aligned} 0 \leq \mathcal{D} &= \boldsymbol{\sigma} : \dot{\boldsymbol{\varepsilon}} - \rho(\dot{\Psi} + s\dot{T}) - \mathbf{q} \cdot \frac{\nabla T}{T} \\ &= \left(\boldsymbol{\sigma} - \rho \frac{\partial \Psi}{\partial \boldsymbol{\varepsilon}^{\text{el}}} \right) : \dot{\boldsymbol{\varepsilon}}^{\text{el}} + \boldsymbol{\sigma} : \left(\dot{\boldsymbol{\varepsilon}}^{\text{p}} + \dot{\boldsymbol{\varepsilon}}^{\text{tr}} \right) - \rho \frac{\partial \Psi}{\partial \boldsymbol{\alpha}^i} \dot{\boldsymbol{\alpha}}^i - \rho \frac{\partial \Psi}{\partial \mathbf{d}^j} \dot{\mathbf{d}}^j - \frac{\mathbf{q}}{T} \nabla T \end{aligned} \quad (6.30)$$

Individual contributions go by various names. Disregarding all thermal contributions leaves the Clausius-Planck inequality. A stronger condition of the inequality may be introduced by requiring that also individual (e.g. mechanical and thermal) parts must be greater than zero.

In Carstensen et al. 2002 and references therein the functional to be minimized is the increment in the elastic (bulk) energy plus the dissipated energy, i.e. both a.m. principles are unified which he calls the principle of minimum total power / least-action-principle.

The ratio of dissipated heat to plastic work is commonly referred to as Taylor-Quinney coefficient β (after Taylor et al. 1932; Taylor et al. 1934) and may be defined in integral or differential form:

$$\beta_{\text{diff}} = \frac{\dot{Q}}{\dot{W}^p} \quad \beta_{\text{int}} = \frac{\int \dot{Q} dt}{\int \dot{W}^p dt} \quad (6.31)$$

Berbenni et al. 2013 developed a micromechanics-based model for shear-coupled interface migration in bicrystals. Bluthè et al. 2017 presents an energetic approach for a sliding inclusion accounting for plastic dissipation at the interface utilizing conformal maps / complex algebra. Phase field models with interface stresses (and hence dissipation) can be found in Levitas et al. 2016; Ask et al. 2018; *Z-set: Multiscale Materials Modelling V8.6* n.d.

6.4.3 Couplings

Thermodynamic state couplings formally result from potential terms involving the product of two state variables in the free energy

$$\frac{\partial^2 \Psi}{\partial z^i \partial z^j} \neq 0 \quad (6.32)$$

Interesting in this context are the Maxwell-relations (of thermodynamics), obtained by equating cross derivatives see e.g. Rice 1971 for solids. Popular examples are the Peltier and Seebeck effect (electric field gradient causes heat flow and temperature gradient causes electric current). Maybe the most widely used coupling in structural mechanics is that between deformation and damage.

Dissipative / evolution couplings result when the potential is the sum of several potential functions, e.g. slip systems in crystal plasticity (also multi-surface / mechanism models, see Besson et al. 2009; Cailletaud et al. 2018)

$$\dot{z} = \sum_i \frac{\partial \Omega_i}{\partial Z} \quad (6.33)$$

Another example is an additional potential that describes recovery. In the macro model in Appendix B an evolution coupling between the phase fraction of martensite and a phenomenological backstress is employed.

6.5 Some Remarks on Size Effects in Metals

A still open problem in continuum modelling is to depict length scale effects in plasticity by means of suitable deformation measures. Explanations involve dislocation pile-ups at microstructural obstacles, a too small bulk volume for dislocation multiplication (e.g. by the Frank Read mechanism) to take place, etc.

Size effects may be categorized according to the underlying mechanisms or origins (cf. ICTAM presentation Marc Geers 2016):

1. statistical size effects: these result from microstructural heterogeneity,
2. first-order (first moment) size-effects: related to the influence of the ratio between microstructural size (e.g. grain- or phase domain size) and the characteristic specimen/component dimensions, e.g. slip system orientations (texture effects), elastic anisotropy.
3. second-order (second moment) size effects: typically induced by lattice curvature in metals or dislocation pile-ups, modelled phenomenologically as backstress(es) or by a strain gradient (crystal) plasticity approach.

Strain/Work hardening is a result of an increase in dislocation density (=total dislocation line length), as well as of deformation substructure formation such as sub-grain and cell-structures formation, see e.g. U. Kocks et al. 2003; Sedláček et al. 2002; Kratochvíl 2014. There exists an empirical relationship also known as the ‘law of similitude’ linking the flow stress τ_c to the characteristic wavelength / cell size / spacing of dislocation walls \bar{d}^{cell} of dislocation patterns (see e.g. Sauzay et al. 2011).

$$\bar{d}^{cell} = c_1 \mu b / \tau_c \quad (6.34)$$

where c_1 is a material parameter approximately independent of material and deformation conditions (k_0 in Table 6.3). Combining this with the Taylor relation (Equation 2.2) yields

$$\bar{d}^{cell} = c_2 \frac{1}{\sqrt{\rho}} \quad (6.35)$$

with ρ the dislocation density c_2 a combined constant typically in the order of 10, see Zaiser et al. 2014. The author found values in the range 2-15. Another important aspect that should be kept in mind is that most modelling approaches neglect dislocation transport. A framework where dislocation movement is taken into account by transport equations between elements in analogy to diffusion is provided by the software DAMASK, see section C.1 (also see Kords 2013).

Next the continuum concept of backstress is discussed. The macroscopic metallurgical expression explaining the grain-size influence is the Hall-Petch relation. The standard explanation on a microscale is dislocation pile-ups at microstructural obstacles resulting in long range stresses. Upon load reversal the flow (reverse motion of dislocations) in the opposite direction becomes easier (Bauschinger effect). In terms of a continuum theory the concept of effective stress is utilised, e.g. shear-stress $\tau^{eff} = \tau^i - x^i$ with τ^i being the resolved shear stress on the slip system i , x^i a slip system backstress.

According to McDowell 2008 the backstress is inherently a multi-scale concept. i) It is a reflection of the lack of statistical homogeneity / nonuniform distribution of stresses between grains at this scale.

ii) The backstress originates from the inelastic bowing / by-pass of dislocations on precipitates or martensite variants, dislocation interactions, differential yielding and the dislocation arrangement in walls and cells.

iii) The backstress should capture lattice curvature effects and may therefore be formulated in a gradient framework, see subsection 6.6.2.

Kröner 1969; Kröner 1972 (statistical theory of dislocations) proposed that the information be given in terms of n-point dislocation correlation tensor functions. The first correlation function is the ensemble average of the tensor product of the dislocation line $\boldsymbol{\xi}(\boldsymbol{x})$ and Burgers vectors $\boldsymbol{b}(\boldsymbol{x})$.

$$\boldsymbol{\alpha} = \langle \boldsymbol{b} \otimes \boldsymbol{\xi} \rangle \quad (6.36)$$

(The dislocation density is an invariant of the next higher correlation function). A discussion of this quantity and its relation to the continuum theory of dislocations is given in section A.1.

6.6 Constitutive Relations for Plastic Deformation

This section is organized as follows. First, general flow relations and differences between plasticity and viscoplasticity are worked out. Yield-surfaces / -criteria / load functions and hardening formulations are discussed afterwards, starting with macroscopic yield criteria, followed by microscopic formulations. This corresponds to the chronological evolution of plasticity in constitutive models rather than a systematic scale direction. Evolution equations for internal variables for plasticity are simultaneously discussed on both scales. Often the microscopic formalism is a generalization of a relation which also holds on the macroscopic level (e.g. Taylor relation) to individual slip systems.

A short note on the elastic regime for steels: Strictly speaking steel does not behave purely elastic until the yield strength. Hence the Young's modulus is actually a cord modulus (varying slope during loading and unloading).

6.6.1 Flow Formulations and Yield Surfaces

6.6.1.1 Plastic and Viscoplastic Flow, Deformation and Temperature Rate Dependencies

In plasticity the flow rule is derived from the normality rule (Equation 6.17) and consistency condition.

$$\underline{\dot{\boldsymbol{\varepsilon}}}^p = \sum_i \lambda^i \frac{\partial f^i}{\partial \underline{\boldsymbol{\sigma}}} = \sum_i \lambda^i \underline{\boldsymbol{n}}^i \quad (6.37)$$

Most macroscopic models use a single yield surface, e.g. Mises yield criterion. In crystal plasticity λ becomes the rate of shear on the slip system $\dot{\gamma}^i$ (plastic multiplier). The yield surface is defined as a superposition of yield criteria and can in this way be considered as multi-surface / -mechanism model (cf. Equation 6.33). Possible sharp edges of the yield surface lead to (numerical) bifurcations, introducing a mesh dependency.

Considering the ambiguity of slip system selection due the linear dependence of their deformations up to now no generally accepted rule exists for their selection. Commonly slip system selection is a result of a numerical perturbation (at least six stress or strain evaluations hence computationally expensive). The problem is even more pronounced if b.c.c. crystals are involved where Schmid's law does not hold any more.

In plasticity necessarily a mechanical threshold stress (MTS), i.e. an initial plus an optional evolving hardening term is present. Hardening formulations are generally found in the flow rule in a multiplicative or additive fashion. Viscoplastic formulations can also be used without the need of a threshold. In viscoplasticity λ is replaced by $\dot{p} = c_1 \|\dot{\boldsymbol{\varepsilon}}^{\text{vp}}\|$ (Frobenius norm, c_1 chosen such that it yields 1 in the inner product with the yield stress) i.e. the length of the plastic strain path in the plastic strain space (dependent on all hardening parameters, current stress state etc.), which is integrated numerically during the simulation. The flow behaviour is derived from an inelastic potential Ω .

$$\underline{\dot{\boldsymbol{\varepsilon}}}^{\text{vp}} = \sum_i \frac{\partial \Omega}{\partial f^i} \frac{\partial f^i}{\partial \underline{\boldsymbol{\sigma}}} = \dot{p} \underline{\boldsymbol{n}} \quad (6.38)$$

where $\partial \Omega / \partial f$ is referred to as viscosity function. Contrary to rate independent plasticity the stress state can lead to a point outside the yield surface (hence also called overstress

model as often attributed to Perzyna and Duvaut-Lions). Obviously, the flux is then proportional to this excess stress. Besson et al. 2009 point out that the viscoplastic framework offers many opportunities to write a model by choosing the viscosity function, whereas in the plasticity framework, the expression of the yield surface f fully determines the flow intensity.

Note that in viscoplasticity the plastic flow is no longer time independent. Under an applied load viscoplastic models can exhibit creep behaviour. They are also used for time effects without any macroscopic deformation, such as recovery or ageing. From the point of view of this thesis they are suitable to model phase transformations (e.g. Turteltaub et al. 2005), systems exposed to high temperatures or strain rates (recall that the formation of martensite itself is close to the speed of sound in metals), as well as to investigate stability. A model combining these effects has been presented by Addessio et al. 2016.

Examples of macroscopic flow relations that can be rearranged and integrated to obtain a viscoplastic potential Ω , together with characteristic tests for their determination have been described by Chaboche 2008. Two popular examples are:

$$\sigma = \sigma_y + K(p)(\varepsilon^P)^m \quad (\varepsilon^e \ll \varepsilon^P; K = \text{const: Ramberg-Osgood equation}) \quad (6.39)$$

$$\sigma = K(p)(\varepsilon^P)^m(\dot{\varepsilon}^P)^{c_1} \quad \text{Integration leads to Andrade's law for primary creep} \quad (6.40)$$

where $K(p)$ is a function of the accumulated viscoplastic strain p (representing the state of the material) and $\sigma - \sigma_y$ is an effective stress. Since Equation 6.40 is commonly used to fit macroscopic tests under various strain rates, the factor m is commonly called strain rate sensitivity and may be obtained as

$$m = \partial \ln \dot{\varepsilon} / \partial \ln \dot{\sigma} \quad (6.41)$$

Note that there is no exact definition of strain rate sensitivity. It only means that the flow behaviour changes with the rate of the applied load. It is important to realize that the strain rate sensitivity is highly sensitive on dynamic strain aging - DSA (macroscopically - Portevin-Le Chatelier effect - PLC), see e.g. Cooman et al. 2018 section 6 therein.

Note that if a low value is chosen for m , for instance, ≤ 0.01 the stress change obtained for a quite large variation of strain rate is so low that the resulting stress-strain curves lie in a

very narrow band. This is a way of building a time-independent behaviour in the framework of viscoplastic equations. In crystal plasticity, this so-called viscous regularization (in the numerical sense) has the advantage that the edges of the yield surface are not sharp anymore but smoothed out, resulting in a better conditioning of the problem. Obviously, the physical drawback is accuracy (however the loss of accuracy is small for $m \leq 0.01$). Another regularization method is to add gradients, i.e. to formulate a generalized continuum model (see Figure 6.1).

Strain rate sensitivity changes as a function of temperature. As a rule of thumb a non-negligible rate dependence for steels occurs at $\approx T > 1/3 T_m$ i.e. around above 500° C. Mainly dislocation based (plastic) deformation mechanisms, including grain boundary sliding exhibit a strain-rate dependence. For instance, it is a well known fact that the rate sensitivity increases the finer the grain size becomes. Consequently nanocrystalline materials exhibit the most pronounced change in strength for higher loading-rates.

After Boyce et al. 2009, factors for m for high strength and high toughness steels are similar, ranging from $m = 0.004 - 0.007$. Values are quite low compared to most metals which typically fall in the range of $m = 0.02 - 0.2$. Generally a non-linear trend is observed: the strain rate sensitivity is small at slow strain-rates and rises with increasing strain-rate. Specifically these alloys only exhibit approx a 10% increase of strength when strain-rates are increased from quasi static to 200 s^{-1} , and their work hardening is essentially unaffected by strain rate, contrary to other metallic alloys. Chaboche 2008 studied a stainless steel (316L) and, observed a saturation of the rate effect in the high rate regime at 550° C. At low strain rates ($< 10^{-10} \text{ s}^{-1}$) a rapid drop in the stress due to static recovery phenomena occurs.

In the literature temperature dependence is found as an Arrhenius coefficient (see Equation A.16), beside the reference strain rate or as an exponent e.g. as in U. F. Kocks 1976.

$$\dot{\varepsilon}^P = \dot{\varepsilon}_0 \left(\frac{\sigma}{K} \right)^{V_A/k_b T} \quad (6.42)$$

V_A is referred to as activation volume, which however varies experimentally so much that it can be seen as a fit parameter. Note that (at least for metals) the deformation rate and temperature dependence are to some extent both due to the fact that diffusional effects are temperature and time dependent. The question of equivalence of rate and temperature

dependency for metals has been investigated by Zener et al. 1944 (Zener–Hollomon parameter). The importance of thermal activation in plasticity is discussed in Caillard et al. 2003.

6.6.1.2 Macroscopic Relations

Comprehensive information on that topic can be found in Altenbach et al. 2014; Ottosen et al. 2005. First, the Hencky-Mises relations (Equation 6.43) for proportional / monotonic loading where $\boldsymbol{\sigma}(\boldsymbol{\alpha}, t)$ increases monotonically as a function of time are given (enabling an analytical integration). They provide easily experimentally accessible quantities from one dimensional tensile/compression tests (see Lemaitre et al. 1994 p.241 and p.242 for an existence theorem for proportional loading). Equivalence between any multiaxial state represented by σ^{eq} can be compared to the uniaxial case represented by σ^{tens} , this is why σ^{eq} is called the equivalent stress in the von Mises sense. Similarly ε^{eq} can be used to express any multiaxial evolution of strain (under proportional loading) in a manner equivalent to the measured uniaxial hardening law:

$$\sigma^{\text{eq}} = \sqrt{3J_2} = \sqrt{\frac{3}{2} \boldsymbol{s} : \boldsymbol{s}} \quad \varepsilon_{\text{p}}^{\text{eq}} = \int_0^t p \, dt = \sqrt{\frac{2}{3} \boldsymbol{\varepsilon}^{\text{p}} : \boldsymbol{\varepsilon}^{\text{p}}} \quad (6.43)$$

Macroscopic yield surfaces are formulated using invariants (mainly of $\boldsymbol{\sigma}$ or \boldsymbol{s}). The yield

	Uniaxial tension	Simple shear (torsion)
σ^{eq}	σ^{tens}	$\sqrt{3} \tau^{\text{tors}}$
$\varepsilon^{\text{eq}} = p$	$\varepsilon^{\text{tens}}$	$\approx \gamma / \sqrt{3}$

TABLE 6.1: Equivalent-Mises stress and strain in proportional / monotonic uniaxial tension/compression and and shear (approximately pure torsion) see Shrivastava et al. 2012; Pardis et al. 2017

surface for every isotropic material can be represented by the three invariants of the stress tensor. Commonly, yield surfaces are visualized in three dimensions using the three principal stresses $\sigma_I, \sigma_{II}, \sigma_{III}$ or 3 arbitrary invariants (or functions thereof) as "coordinates". Here the (principal) invariants of the Cauchy stress tensor are denoted as I_1, I_2, I_3 and those of the stress deviator J_2, J_3 (mechanical invariants)

For many metals the behaviour in tension and compression is similar, and the main influence on plasticity and failure is represented by J_2 . This is reflected in the extensive use of

the Mises-, J_2 -, or octahedral shear stress yield criterion.

On the other hand, the flow stresses of high strength steels are larger in uniaxial compression than in uniaxial tension. This phenomenon is known as strength-differential effect (see Spitzig et al. 1975) or tension-compression asymmetry.

The mechanical behaviour of pressure sensitive materials, where volumetric changes occur (e.g. granular materials, but also in martensite in steel) depends on the mean stress $-\sigma^{\text{mean}} = \text{pressure} = 1/3 \text{tr}(\boldsymbol{\sigma})$. It is rather simple to extend the Mises surface to incorporate the mean stress (see e.g. Drucker-Prager model). However, differences are often observed between the material behaviour in triaxial compression and in triaxial tension (often a triaxiality factor is defined as $I1/J2$). A representation of this difference requires the use of J_3 . Mahnken et al. 2008 correctly point out that no common agreement exists concerning the best strategy to take into account individual loading scenarios.

For yield surfaces where the normal to the yield surface is coaxial with the projection to the origin (circular yield surfaces like the Mises-criterion) very efficient algorithms exist in the literature, by reducing the problem to a scalar equation, which is solved by a Newton iteration procedure. This is referred to as "Radial Return" method first proposed by Krieg et al. 1976. If J_3 is included the coaxiality of the yield surface normal and the projection to the origin is lost.

Lode 1926 first studied the influence of σ_{II} (middle valued principal stress) on metals. Later the following relation was found (Nayak et al. 1972) by geometric considerations in the $\sigma_I, \sigma_{II}, \sigma_{III}$ coordinate system (see e.g. Ottosen et al. 2005):

$$\text{trig}(\sigma_{II}) \approx \frac{3\sqrt{3}}{2} \frac{J_3}{J_2^{3/2}} = \text{trig}(3\theta) \quad (6.44)$$

where the function $\text{trig}()$ may be one of the following: $\cos()$, $\sin()$, $-\sin()$. Depending on trig the range of θ is different for different stress states. In honour of Lodes work the angle θ was denoted as Lode angle. Macroscopic models for the martensitic transformation have been proposed utilising this quantity e.g. Hallberg et al. 2007; Beese et al. 2012; Fischlschweiger et al. 2012 (the tangent matrix required for an implicit implementation of the latter model is given in Appendix B). Together with the two axial coordinates / invariants (orthogonal

projections of the stress state onto the hydrostatic axis and the deviatoric plane):

$$(\mathbf{I} / \|\mathbf{I}\|): \boldsymbol{\sigma} \quad \text{and} \quad (\underline{\mathbf{s}} / \|\underline{\mathbf{s}}\|): \boldsymbol{\sigma} \quad (6.45)$$

the set of so-called Lode invariants/coordinates (cylindrical coordinates) is obtained.

Experimental yield surfaces of metallic alloys determined after plastic deformation exhibit an affine deformation (expansion or contraction = isotropic hardening or softening, translation = kinematic hardening softening, rotation, shear) but also distortions exceeding an affine deformation that follow the actual loading path, sometimes also referred to as differential hardening, see e.g. Shi et al. 2013. Translations and expansions are depicted by isotropic and kinematic hardening. A common anisotropic extension is a quadratic form generalization of the Mises criterion

$$\boldsymbol{\sigma}^{\text{eff}} = (\boldsymbol{\sigma} : \underline{\underline{\mathbf{B}}} : \boldsymbol{\sigma})^{1/2} \quad (6.46)$$

The number of independent components of the tensor $\underline{\underline{\mathbf{B}}}$ depend on the material symmetry. Also for plastic deformation, $B_{jjkl} = 0$ must hold in order to ensure plastic incompressibility Besson et al. 2009. $\underline{\underline{\mathbf{B}}}$ may also be used to describe initial anisotropic texture (see section 3.4) see e.g. Teodosiu 1997; Canova et al. 1985; Lemaitre 2001. A popular model of this type depicting the orthotropic form of initial anisotropy in polycrystalline parts arising from the processing method (rolling, drawing, extrusion) is due to Hill 1990. An orthotropic material has different initial yield stresses for axes lying parallel and normal to the direction in which it has been worked. Often also transversely isotropic properties are reported, meaning that the elastic characteristics remain invariant for all pairs of directions symmetric w.r.t. an axis (e.g. wrought / drawn wires, rods or bars). General anisotropic cases are treated in Boehler 1987; Schröder et al. 2008.

As a conclusion, while in general a macroscopic yield surface may be found it is however hard to accurately describe the evolution of the yield surface using invariants.

6.6.1.3 Microscopic Relations

Many equations in this section are generalizations of propositions that can also be found for the macroscale, to slip systems $i = 1 \dots 12$ (for the $\{111\}\langle 011 \rangle$ f.c.c.). For instance inversion

of Equation 6.40 leads to the flow formulation of the model by Méric et al. 1991 initially proposed for nickel base super alloys:

$$\dot{\underline{\epsilon}}^p = \sum_i \frac{\partial \Omega}{\partial f^i} \frac{\partial f^i}{\partial \underline{\sigma}} = \sum_i \left\langle \frac{|\underline{\sigma} : \underline{m} - x^i| - R^i - \sigma_y/M}{K} \right\rangle^n \underline{n} = \sum_i \dot{\gamma}^i \underline{m}^i \text{sign}(\tau_{\text{eff}}^i) \quad (6.47)$$

where σ_y/M is the initial yield stress. The model has three possibilities to introducing a hardening: i) Through isotropic hardening parameters R^i , ii) increasing K (drag stress), iii) coupling with kinematic hardening (backstresses x^i). Specific forms of x^i and R^i will be discussed in the next section.

Whereas the total strain tensor $\underline{\dot{\epsilon}}$ is symmetric, $\underline{\dot{\epsilon}}^p$ is generally not. If the latter is to be equated to the macroscopic tensor, the antisymmetric part must be compensated by a crystal lattice rotation in the opposite sense. However, there are special orientations for which the antisymmetric part and hence the lattice rotation becomes zero (see e.g. H. J. Bunge 1970).

For certain cases of multiple slip (idealization with M equivalent slip systems) conversions between macro and micro parameters can be found in Cailletaud 2010.

Often $\dot{\gamma}^i$ is calculated by using the following assumption (commonly referred to as Orowan relation in the literature)

$$\dot{\gamma}_m^i = \rho^i b^i v_{\text{eff}}^i \quad (6.48)$$

$\dot{\gamma}_m^i$ is the mobile dislocation density and v_{eff}^i the effective dislocation velocity (see Equation 6.49). Note that the determination of the mobile density is still a major topic of discussion. In most models all dislocations are considered as mobile in the flow relation. Interestingly, Groma 2017, a Hungarian compatriot of E. Orowan mentioned that this relation has never been proposed by Orowan in this form and that it may rather be seen as a definition of dislocation density than a constitutive law. Based on Equation 6.48 flow rules, often referred to as physical approaches (e.g. by Teodosiu 1997; Lemaitre 2001; Wong et al. 2016) have been proposed. v_{eff}^i comes from the theory of thermally activated dislocation movement taking the form

$$v_{\text{eff}}^i = \omega_A L \exp \left[-\frac{\Delta G_{\text{ta}}^i}{k_B T} \right] \text{sign}(\tau_{\text{eff}}^i) \quad (6.49)$$

ω_A is an attempt frequency, L is an average effective barrier spacing / mean free path / average jump distance (e.g. Equation 6.52). Ma et al. 2012 use Equation 6.35 with a forest dislocation density, i.e. a dislocation cell diameter for L . $\omega_A L$ often is condensed into one coefficient (e.g. v_0 in Wong et al. 2016). A comprehensive compilation of literature on this equation can be found in Kubin 2013. The range of ω_A spans approximately one order of magnitude. The Debye frequency is given by $\nu^{DB} = \left(\frac{3N}{4\pi V}\right)^{1/3} v_s \approx 10^{13} s^{-1}$, where N/V is the number of atoms N in the volume V (number density) and v_s is the speed of sound of shear waves ($\approx \sqrt{\mu/\rho}$). ν^{DB} is an upper bound for an atomic vibration frequency. Interestingly it is in the exact same order of magnitude as in Eyrings theory for chemical reactions $k_B T/h \approx 10^{13} s^{-1}$, with h being Planck's constant. On the other hand Busso et al. 1996 use $\omega_A = v_s/b \approx 3 \cdot 10^{12} s^{-1}$.

Since the energy that a dislocation must overcome by its thermal activation ΔG^{ta} is far too complex to be obtained in closed form, often a phenomenological relation representing a typical barrier encountered by a dislocation is used, see e.g. W. F. Kocks 1975

$$\Delta G_{ta}^i = G_0 \left\{ 1 - \left(\frac{|\tau^i - x^i| - \tau_c^i}{\hat{\tau}} \right)^{c_1} \right\}^{c_2} \quad (6.50)$$

where $0 < c_1 < 1$ and $1 < c_2 < 2$ define the profile of the short-range barrier to the dislocation, $\hat{\tau}$ is the stress above which dislocations can be mobilized without the assistance of thermal activation (e.g. solid solution strength τ_{sol} as used by Wong et al. 2016). x^i is a slip system backstress. Often the parameters $\{c_1, c_2\} = 1$. G_0 is the energy required for a dislocation to overcome the barrier solely by its thermal activation and is given by Lemaitre 2001 p.391 as $G_0 = \hat{\tau} L \lambda b$, with λ the average effective barrier dimension, e.g. particle radius. Often the temperature dependence of $\hat{\tau}$, x^i , τ_c^i are scaled with the temperature dependence of the elastic shear modulus $\mu(T)/\mu(T^{ref})$.

The parameters must be tuned within their reasonable physical range to reflect experimentally measured relations between strain rate and stress for the slip system. Note that by combining Equation 6.49 and Equation 6.50 the expression $\exp(x) - \exp(-x) = 2 \sinh(x)$ i.e. a hyperbolic sine appears that is also often found in the literature.

The above equations are often approximated by a power law with fewer parameters, see e.g. Hutchinson 1976; Peirce et al. 1982 (first crystal plasticity computations) as.

$$\dot{\gamma}^i = \dot{\gamma}_0 \left\| \frac{\tau^i}{\tau_c^i} \right\|^n \text{sign}(\tau^i) = \dot{\gamma}_0 \left(\frac{\tau^i}{\tau_c^i} \right) \left\| \frac{\tau^i}{\tau_c^i} \right\|^{n-1}$$

i.e. a viscoplastic model without any threshold and multiplicative but no additive hardening. $\dot{\gamma}_0$ (slip) or (macro viscoplastic) $\dot{\epsilon}_0$ is a reference strain rate and n is a rate exponent.

Finally, the role of lath / sub-block boundary sliding is emphasized. Particularly, Schmid tensors can be constructed using the geometrical information of the lath habit-planes and lath long directions, see section 3.7 in order to formulate lath boundary sliding.

6.6.2 Evolution Equations for Hardening Variables

In dislocation density based models the evolution of the dislocation density as a function of the accumulated slip on each slip system is most commonly expressed by (see e.g. Teodosiu 1997; Tabourot et al. 1997):

$$\dot{\rho}^i = \frac{1}{b} \left(\sum_j \frac{1}{L_j} - \sum_j y_j^{\text{hkl}} \rho^i \right) \dot{\gamma}^i \quad (6.51)$$

with a generalization of the mean free path for dislocation motion L . y_j^{hkl} are orientation dependent lengths (Kubin 2013 p.79 therein) describing recovery (in a more general description it should be differentiated between dynamic and static recovery). The mean free path due to dislocations in f.c.c. metals is given by:

$$\frac{1}{L} = \frac{\tau_c}{\mu b K_{hkl}} \quad (6.52)$$

$K_{hkl} = 7.3 - 7.5$, see e.g. U. Kocks et al. 2003. The average athermal passing stress τ_c is calculated after Franciosi et al. 1982 with a slip system generalization of Taylor's relation (Equation 2.2):

$$\tau_c^j = \mu b \sqrt{\sum_i h_{ij} \rho^i} \quad (6.53)$$

The slip system interaction matrix h_{ij} will be discussed at the end of this section.

A slip-variant interaction matrix h_{ij}^{sv} can be formulated based on geometrical considerations, e.g. as $h_{ij}^{sv} = \xi^i c_1 (1 - \mathbf{h}^i \cdot \mathbf{m}^i)$ with the same geometrical considerations as in Equation 6.59. Furthermore, the stereographic relation by Fullman 1953 is commonly used (e.g. Allain et al. 2004; Wong et al. 2016), eventually yielding the following contribution to the mean free path.

$$\frac{1}{L_j^{sv}} = \sum_N h_{ij}^{sv} \frac{\xi^i}{t(1 - \xi)} \quad (6.54)$$

Queyreau et al. 2010 proposed an additional mean free path based on Orowan's loop mechanism/description for impenetrable particles assuming circular precipitates, which may be of interest for modelling precipitation hardenable steels. Data on L for this contribution may be obtained from atom probe tomography studies. Considerations on incorporating dislocation cell structures (e.g. dislocation cell wall diameter from Equation 6.35) via L are found in Castelluccio et al. 2017. Also Roters and co-workers follow such line of thinking and additionally consider several types of mobile and immobile dislocations Steinmetz et al. 2013; Wong et al. 2016.

An interesting approach is that by Carson et al. 2017 who proposed to use a combination of diffraction- and mechanics-based metrics, which may be particularly interesting in combination with the extensive habit plane characterisation of this work.

Méric et al. 1991 and also Besson et al. 2009 propose a hardening law of the type:

$$\tau_c^j = c_1 c_2 \sum_i h_{ij} \rho^i \quad \text{and} \quad \dot{\rho}^i = (1 - c_2 \rho^i) \dot{\gamma}^i \quad \text{resulting in} \quad (6.55)$$

$$\tau_c^j = c_1 \sum_i h_{ij} (1 - \exp(-c_2 \gamma^i)) \dot{\gamma}^i \quad (6.56)$$

where c_2 is the convergence rate to a saturation value c_1 . In Cailletaud 2009; Cailletaud 2010 it is pointed out that the phenomenological law in Equation 6.55 and Equation 6.51 have the same nature.

Next, kinematic hardening / backstress evolution is discussed. The simplest model is Prager's linear kinematic hardening Prager 1949, in which the evolution of the kinematic backstress $\underline{\mathbf{X}}$ is collinear with the evolution of the plastic strain

$$\underline{\mathbf{X}} = \frac{2}{3} C \underline{\boldsymbol{\varepsilon}}^p \quad (6.57)$$

For cyclic deformation, linear kinematic hardening does not produce ratchetting and Chaboche 2008 points out that (multi) linear kinematic hardening always leads to shakedown (a stabilization of the cyclic loop). For a method to model ratchetting in combination with linear kinematic hardening, see section 4.4. Non-linear kinematic hardening has first been proposed by Armstrong-Frederick in a company intern report that has only been officially published in Frederick et al. 2007. It became popular through the works of Lemaitre et al. 1994 and co-workers. The idea is to construct a plastic strain path dependence of the yield surface shift and consider a dynamic recovery term proportional to the norm of the plastic strain rate. Macroscopic relations can be found in Appendix B. The non-linear case always leads to ratcheting (see Figure 2.9) under a non-zero mean stress (Chaboche 2008). Possible extensions to backstress formulations include a temperature rate term in the evolution equation of the backstress.

In Méric et al. 1991 and also Besson et al. 2009 the formalism has been generalised to several slip systems

$$\dot{\alpha}^i = \text{sign}(\tau^i - x^i)\dot{\gamma}^i - c_1\alpha^i\dot{\gamma}^i \quad \text{and} \quad \dot{x}^i = c_2\alpha^i \quad (6.58)$$

with x^i scalar backstress variables and c_1 as the convergence rate to the asymptotic value of x^i given by c_1/c_2 and α^i being the generalized slip system strain conjugate to x^i . This is an effective way to phenomenologically take into account 2nd order/moment effects.

Barlat et al. 2011 and coworkers (e.g. Kitayama et al. 2013) propose a generalization of Equation 6.51 with reversible / fluctuating dislocation densities.

Devincre et al. 2015 propose a grain internal Hall-Petch relation, calibrated by MD simulations using the distance to the next grain boundary and the angle between the slip system and the boundary.

Backstress formulations based on GNDs can be found in Bayley et al. 2006 and references therein. The main problem is to obtain slip system GND densities ρ_{gnd}^i as discussed in section 6.5. Notably, in statistically inhomogeneous situations of small scale plasticity the backstress is sensitive to microstructural details. Since in this work the geometrical details of martensite are worked out, it is proposed to substitute the saturation constant by an expression incorporating martensite variant fractions and information on the geometrical relations between martensite domains and slip systems. For oblate martensite domains

(plate martensite) then the slip system backstress is a function of the slip plane normal, the habit plane normal and the variant phase fraction, i.e. $x^i(\xi^j, |\mathbf{m}^i \cdot \mathbf{h}^j|)$. Particularly, the following form is proposed

$$c_1 \rightarrow c_1^i = c_3 \sum_j \xi^j (1 - |\mathbf{m}^i \cdot \mathbf{h}^j|) \quad (6.59)$$

For prolate (lath- and needle-like) martensite domains additionally the lath long direction \mathbf{k} that is also the direction of the invariant line strain could be considered resulting in

$$c_1 \rightarrow c_1^i = c_4 \sum_j \xi^j [(1 - |\mathbf{m}^i \cdot \mathbf{h}^j|) + (1 - |\mathbf{m}^i \cdot \mathbf{k}^j|)] \quad (6.60)$$

It should be noted, that the coupling between the variant phase fractions ξ^i and slip system backstresses x^i also highly influences variant selection if the flow rule incorporates a nucleation criterion that links the accumulated plastic strains on certain slip systems with certain martensite variants (see subsection 6.7.6). Similarly, considerations on martensite variants could lead to a formalism that enable a decomposition into slip system specific GND densities, enabling a unique decomposition of Equation A.8.

The total dissipation in any of the above cases is of the general form:

$$\mathcal{D} = \boldsymbol{\sigma} : \dot{\boldsymbol{\varepsilon}}^p - \sum_i x^i \dot{\alpha}^i - \sum_i \tau_c^i \dot{\rho}^i \quad (6.61)$$

For the free energy density several forms have been proposed, but in general it strongly depends on the specific problem at hand as elaborated by Berdichevsky 2006.

Finally, the interaction matrix h_{ij} is discussed. Here it contains both self-hardening on each system and the latent hardening between the systems / cross hardening / off-diagonal terms. It is reported that cross hardening may be responsible that some systems may not become active at all. A common assumption according to Taylor 1938 is to assume "isotropic hardening," i.e. all $h_{ij} = 1$. Franciosi et al. 1982; Franciosi 1983 first tried to experimentally determine h_{ij} for f.c.c. and b.c.c.. Franciosi 1985 also observed an increasing degree of anisotropy with decreasing stacking fault energy (SFE) and proposed a linear dependence of the h_{ij} with the SFE.

	A2	A3	A6	B2	B4	B5	C1	C3	C5	D1	D4	D6
A2	SH	Copl	Copl	CS	GJ	GJ	HL	GJ	LC	HL	LC	GJ
A3		SH	Copl	GJ	HL	LC	CJ	GS	GJ	LC	HL	GJ
A6			SH	GJ	LC	HL	LC	GJ	HL	GJ	GJ	CS
B2				SH	Copl	Copl	HL	LC	GJ	HL	GJ	LC
B4					SH	Copl	LC	HL	GJ	GJ	CS	GJ
B5						SH	GJ	GJ	CS	LC	GJ	HL
C1							SH	Copl	Copl	CS	GJ	GJ
C3								SH	Copl	GJ	HL	LC
C5									SH	GJ	LC	HL
D1										SH	Copl	Copl
D4											SH	Copl
D6												SH

TABLE 6.2: Slip system interactions, naming convention after Franciosi et al. 1982. Slip planes $(\bar{1}11)$, (111) , $(\bar{1}\bar{1}1)$, $(1\bar{1}\bar{1})$ are named A, B, C, D respectively and slip directions $[011]$, $[0\bar{1}1]$, $[101]$, $[\bar{1}01]$, $[\bar{1}10]$, $[110]$, as 1 2 3 4 5 6 respectively. The 12 slip systems are A1, A3, A6, B2, B4, B5, C1, C3, C5, D1, D4, D6.

SH: Self hardening, Copl: Coplanar / inplane reaction (same glide plane), CS: Colinear / cross slip (same Burgers vector), HL: Hirth Lock (orthogonal Burgers vectors) syst pair with normal slip directions, GJ: Glissile junctions formation, LC: Lomer-Cottrell sessile locks formation

There are three interactions belonging to forest / junction forming slip systems: The Hirth- / orthogonal- and Lomer Cottrell-Lock as well as glissile junctions. Parallel / non-contact dislocation interactions (i.e. the same glide plane) incorporate the two types of coplanar (different \mathbf{b}) and self (same \mathbf{b}) interactions. Colinear / cross slip interactions lead to annihilations. The general form of the interaction matrix h_{ij} is given in Table 6.2.

In Table 6.3 values for the h_{ij} from discrete dislocation (DD) simulations of Kubin et al. 2008; Devincere et al. 2008 are given. It is seen that four interaction strengths have similar values (self, coplanar, glissile and Lomer), while the Hirth type of interaction is weaker and the collinear interaction much larger (preventing the activation of collinear slip under normal conditions). h_{ij} (a_{ij} in Devincere's notation adopted in the following) of active slip systems can approximately be replaced by a average value (≈ 0.35).

A multiplicative, logarithmic correction term (due to bowing of dislocations) for the line tension effect (or line tension drift as in Sauzay et al. 2011) has been devised by Devincere et al. 2006 based on the results of large-scale DD simulations (in these simulations a reference total forest density of the order of $\rho_{\text{ref}} = 1 \times 10^{12} m^{-2}$ has been assumed). This term only applies to the three interaction coefficients related to interactions between junction-forming / forest slip systems. Simulations indicated that long-range stresses contribute globally to

about one-fifth of the critical stress, hence the interaction coefficients are eventually written as $\sqrt{a_{ij}} = c_f^i \sqrt{a_{ij}^{\text{ref}}}$ with

$$c_f^i = 0.2 + 0.8 \frac{\ln\left(1/b\sqrt{a_{\text{ref}}\rho_f^i}\right)}{\ln(1/b\sqrt{a_{\text{ref}}\rho_{\text{ref}}})} \quad (6.62)$$

Similarly, interaction parameters for pure b.c.c. α -iron are determined by Queyreau et al. 2009.

Also, evolution equations for dislocation densities have been proposed in Kubin et al. 2008; Devincre et al. 2008. First, the evolution of forest densities is given. Using the short notation $\rho_f^i = \sum_{j \in f^i} \rho^j$ for the total density of junction-forming forest obstacles for system i , the storage rate induced by active forest slip systems f^i is given by:

$$d\rho^i = \frac{p_0 k_0}{b} \frac{1}{\sqrt{\sum_j a_{ij}(\rho^j + \rho_{jct}^{\rightarrow i})}} \left(\frac{\rho^i}{\rho^i + \rho_{jct}^{\rightarrow i}} \right) \left(\sum_{j \in f^i} \sqrt{a_{ij}\rho^j} \right) \left(1 - \frac{\rho_{jct}^{\rightarrow i}}{\rho_f^i} \right) d\gamma^i \quad (6.63)$$

Evolution of junction density (Devincre et al. 2008 16 or B.5 and B.6 therein)

$$d\rho_{jct}^{\rightarrow i} = \frac{\kappa_0 p_0 k_0}{b} \frac{\rho^i \sum_{j \in f^i} \sqrt{a_{ij}}}{\sqrt{\sum_j a_{ij}(\rho^j + \rho_{jct}^{\rightarrow i})}} \left(1 - \frac{\rho_{jct}^{\rightarrow i}}{(n-1)\rho^i} \right) d\gamma^j \quad (6.64)$$

with n being the number of active slip systems, hence $(n-1)$ is the number of forest systems seen by system i . Note that $\kappa_0 = \rho_{jct}^i/\rho_0^i$ has been shown by DD simulations to be almost constant, Devincre et al. 2008. The evolution of parallel dislocation densities is controlled by:

$$d\rho^i = \left\{ \frac{\sqrt{a_0'} \rho^i}{K_I} + \frac{\sum_{j \in \text{cop}(i)} \sqrt{a_{\text{cop}} \rho^j}}{K_{\text{cop}}} \right\} d\gamma^i \quad (6.65)$$

The set of equations Equation 6.62 - Equation 6.65 have been implemented (independently and as part of the model in subsection C.3.1). The independent version has been used in conjunction with the flow rule in Equation 6.48 to investigate the energy and dissipation of the formation of a single martensite lath (sub-block unit) in a full-field model. Particularly, utilizing the calculated eigenstrains from subsection 3.10.3 the influence of morphology (shape parameters) of single martensite laths as well as composite bi-variant blocks has been investigated based on energy minimization / dissipation maximization.

a'_0	a_{cop}		a_{orth}	a_2 (glissile)	a_3 (Lomer)	a_{colin} (colinear)
0.122	0.122		0.07	0.137	0.122	0.625
p_0	k_0	κ_0	K_{112}	K_{111}	K_{001}	$K_I = K_{\text{copla}}$
0.117	1.08	0.225	10.42	7.29	4.6	180

TABLE 6.3: Values of the dimensionless coefficients determining the critical stress and the storage rate in f.c.c. crystals for a reference dislocation density $\rho_{\text{ref}} = 1 \times 10^{12} m^{-2}$ as given by Devincere et al. 2008 and references therein.

6.7 Constitutive Relations for the Phase Transformation

In this section first differences in nucleation theories are worked out. Second, the most common equation based phenomenological kinetic relations are discussed. Third, driving and dragging forces / hardening relations (and their evolutions) for a transformation criterion / yield condition are outlined. Finally, the unification of these concepts should naturally lead to suitable evolution equations and hence transformation kinetics.

6.7.1 Differences in Nucleation and Growth Theories

This section shortly summarizes as well as extends the work of M. Cohen et al. 1992 chapters 8-10 therein (8 non-linear physics, 9 nucleation, 10 growth). The key issues of martensitic nucleation theory are depicted in Figure 6.3. Classical nucleation assumes a critical nucleus / embryo structure i.e. a region of martensite showing all features of a fully grown domain of the product phase, hence the order parameter $\eta = 1$. Practically, in most cases a free energy is expressed for an inclusion (mainly without external stresses) and minimized w.r.t. its geometric parameters. Extremisation of the energy leads to an energy barrier (and profile) that must be overcome, afterwards spontaneous growth occurs. At this point the difference between a global consideration on a RVE level (global transformation condition - GTC) corresponding to the strong form or merely a local consideration at integration point level (local transformation condition - LTC) corresponding to the weak form must be kept in mind. Early approaches following this concept (e.g. Kaufman et al. 1958) lead to negligible nucleation rates. Only subsequently, pre-existing defects interacting with the nucleus were considered, but in some cases theoretical nucleation rates were still far from realistic ones.

Several (possibly pre-existing) types of defects are: dislocation pile-ups or junction networks, stacking faults, grain boundaries. Particularly, triple junctions appear to play a

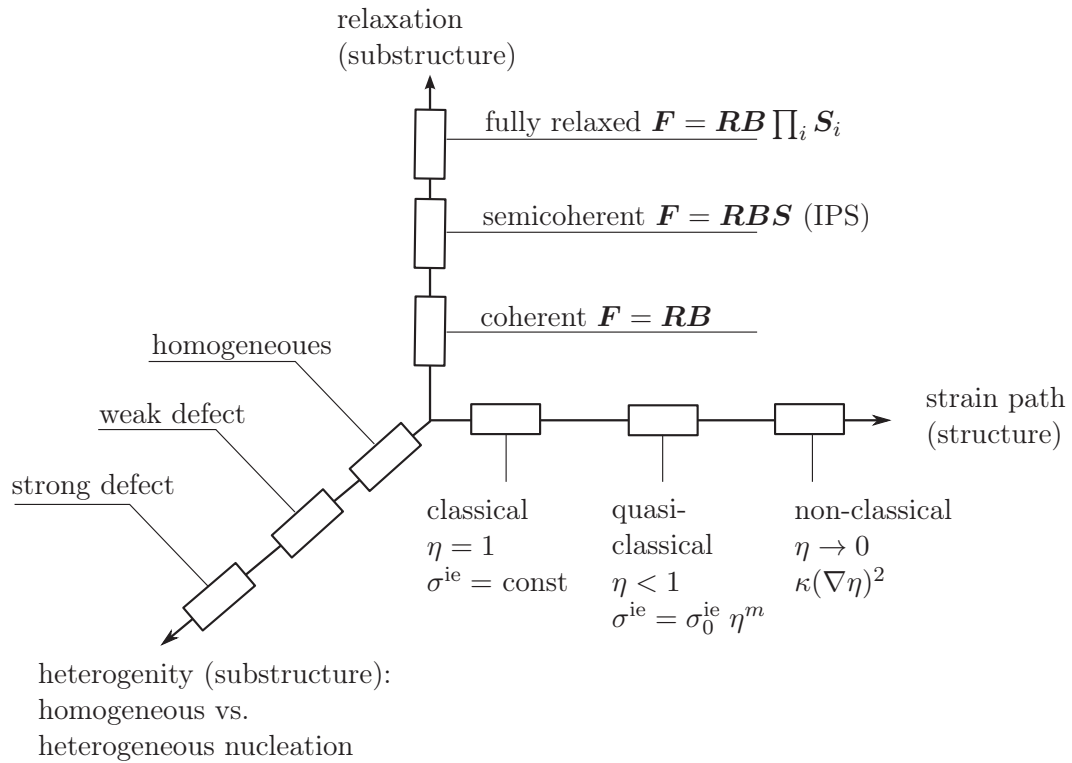


FIGURE 6.3: Parameter space for martensitic nucleation according to M. Cohen et al. 1992, chapter 9 therein. η is a strain order parameter, σ^{ie} a interface energy, m is a critical exponent. the initial substructure heterogeneity strongly varies depending on the processing history and evolves during transformation. Defect strength refers to the stabilization of a nucleus. Non-classical extensions depict softening phenomena.

role. The crucial question is what constitutes a critical stage in the growth of a martensite domain of any morphology. Semi-coherent martensite interfaces with their arrays of dislocations or twins merely exacerbate the problem.

Therefore, in contrast, quasi-classical nucleation admits intermediate nuclei configurations / strain embryos, i.e. a partially displaced lattice along the reaction path (hence "strain- or reaction path" model according to Cohen) between the parent and product structure with $\eta < 1$. Recently, the reaction path model has been applied by Ma et al. 2015 by minimizing the difference in shape strain between plastically deformed regions and the full shape strains of an invariant plane strain (IPS) by means of an optimization problem.

The case $\eta = 0$ depicts a lattice instability of the parent phase. A possible interpretation of the difference between lath and plate martensite is: If the instability is pronounced then lattice coherency (bi-variant Σ_1 connected laths formed by plastic deformation - shear martensite) is favoured over two Bain strains displacively forming a twin ("schiebungs-"

martensite). The non-classical framework stems from an atomistic description of lattice vibrations further utilised in Landau theory and statistical mechanics. Softening of elastic constants (soft phonon-mode / lattice spinoidal) due to anharmonic effects near M_s nowadays is a fruitful area for ab-initio calculations. A characteristic feature of b.c.c. iron is that it develops a reduction of the shear stiffness constant $c' = (c_{11} - c_{12})/2$, which profoundly impacts dislocation behaviour. An elastic instability, driven by spin fluctuations, near the $\gamma \rightarrow \alpha$ transition point has e.g. been predicted by Dudarev et al. 2008 in ab initio calculations of b.c.c. iron. However the methodology still is not mature enough to make quantitative predictions for highly alloyed composites. Particularly it is difficult to describe all effects simultaneously, but attempts in this direction are made, see e.g. Dong et al. 2017. Interestingly, often the lack of macroscopic experimental evidence for this behaviour is criticised, but obviously due to the rapid and locally random transformation of even single crystals such an observation may be tricky. On the other hand, the concept of elastic / lattice softening is already used in practice, e.g. by Edalati et al. 2012 to obtain highly ductile nanostructured materials. A recent experimental investigation of the evolution of soft-phonon modes in Fe-Pd SMA has been done by Seiner et al. 2016. Generally, observation of homogeneous nucleation is a strong indicator for non-classical nucleation.

The notion of non-classical nucleation leads to the phenomenological Landau theory where the free energy is an expansion in an order parameter η , which is nothing more than an appropriate, measurable quantity apt to account for the essential differences of the parent and product phase. For martensitic transformations the order parameter η either is a phase fraction or a strain (the latter is especially useful for second order transitions). It is $\eta = 1$ in martensite (m), $\eta = 0$ in austenite (a) and $\eta = \varepsilon^a/\varepsilon^m$ for a,m mixtures. M. Cohen et al. 1992 merely considered the shear strain component. Recently, the angle of rotational distortion between the phases has been suggested by Cayron 2015 for ferrous martensite.

If the order parameter is strain, its variation of the interface may be described in analogy to the Cahn-Hilliard treatment of diffuse interface (although the interface is almost atomically sharp as pointed out at the end of subsection 2.3.2) by a non-local gradient term (as opposed to a classical interface energy σ^{ie}). In a quadratic free energy assumption

$$F(\eta, \nabla\eta) = F_0(\eta) + \kappa/2(\nabla\eta)^2 \quad (6.66)$$

κ is a gradient energy coefficient. Note that there is a multitude of functions describing the variation of the order parameter in a diffuse interface (sigmoidal shape), for which the associated variational functional (in which the free energy is contained, see Equation 6.22) is well-known. Note the strong similarity between generalized continuum mechanics and phase field models. For instance Forest et al. 2011 point out that the second gradient model of mechanics by R. D. Mindlin 1964 and the Cahn et al. 1958 diffusion theory were developed around the same time. A thermodynamical framework incorporating the order parameter was among others developed by Gurtin 1996 suggesting a scalar or tensorial microforce conjugate to gradient of order parameter.

6.7.2 Semi-empirical and Phenomenological Kinetics Fit Functions

Often the kinetics curve, i.e. the relation between the phase fraction of martensite and external driving forces, is provided as a fit. The most common fit function for fast quenching / athermal kinetics is due to Koistinen et al. 1959. It was initially obtained by fitting X-Ray diffraction measurements of volume-% fraction retained austenite as a function of the quenching temperature interval in ferrous martensite. The fit function is an exponential of the form:

$$\xi = 1 - \exp(-c_1(M_s - T)) \quad (6.67)$$

with M_s the martensite start temperature. Petersmann et al. 2017a explained the exponential saturation behavior as a consequence of elastic accommodation. For partially isothermal martensites or bainites showing a more sigmoidal kinetics curve, the most commonly used fit function is due to Johnson-Mehl-Avrami-Kolmogorov (JMAK) Johnson 1939; Avrami 1940. It stems from a statistical description and the following assumptions: i) random nucleation in the untransformed volume at ii) constant nucleation rate and iii) a constant radial growth (until impingement) in an infinite specimen. The fit function is of the form

$$\xi = 1 - \exp(-c_1 t^{c_2}) \quad (6.68)$$

A physical interpretation of the exponents can be found in Hömberg et al. 2016 for grain growth and H. K. D. H. Bhadeshia et al. 1990 for Bainite (section 6.10. therein). In Garrett et al. 2004; Mahnken et al. 2011 a constant value of coefficient c_2 is used for ferritic, pearlitic, and bainitic transformations, respectively. The coefficient $c_1(T)$ should

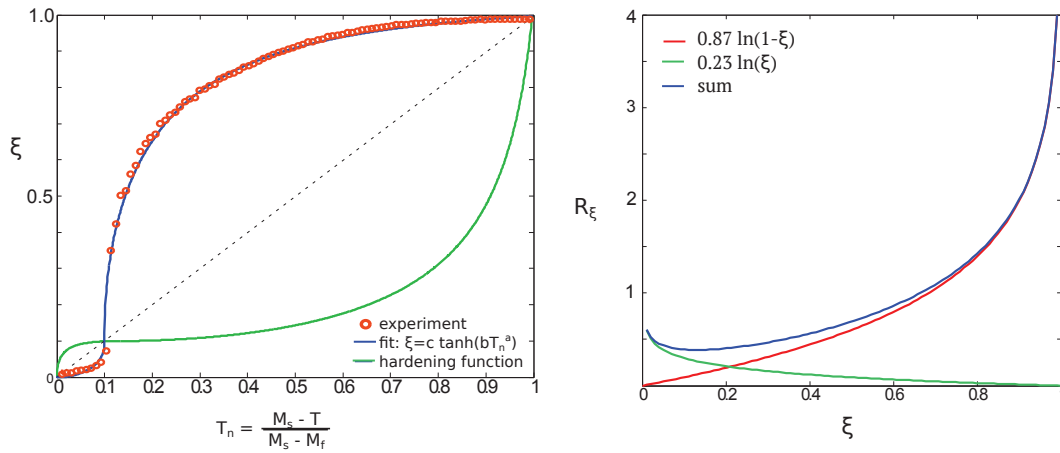


FIGURE 6.4: Phenomenological ways to macroscopically introduce hardening such that the transformation kinetics (by means of the Lever-rule) is depicted. Left: red points mark experimentally measured phase fraction. The abscissa shows the normalized transformation temperature T_n . The kinetics may be fitted with any function (blue line; here a piecewise fit joining at the saddle point is illustrated). A hardening function R_ξ that recovers the kinetics then for instance is the inverse of this function (green). Right: Construction of R_ξ with initial softening as in the model proposed by Fischlschweiger et al. 2013, see Appendix B.

map the form of the TTT diagram (e.g. a modified Gaussian function (cf. nucleation potency) is often used. Often even double exponential relations are found in the literature, see e.g. S. Kim et al. 2016. Note that upon directly providing a kinetics function the model automatically becomes non-associated.

For the burst-like kinetics of the MarvalX12 we found that most of the kinetics curve (apart the slow start) can be fitted better using a tanh. In the framework of driving and dragging forces the kinetics can be directly applied as well by providing e.g. the inverse of the fitted kinetics curve as a hardening variable. Compared to the double ln term by Fischlschweiger et al. 2012 it does not comprise initial softening before hardening to obtain the slow start and then very steep increase of phase fraction, see Figure 6.4.

6.7.3 Aspects of Discrete Transformation Strains in Mean Field Models

Govindjee et al. 2001 state that a well-posed model should automatically generate habit-plane variants (shape transformations) from lattice correspondence / orientational variants (structural stretch tensor plus 24 point group rotations) by “natural” evolution under appropriate loading conditions. Evidently, it is difficult to realize such a behavior in a mean field model that lacks a discrete microstructure. In the author’s opinion the closest this has been realized for dislocated lath martensites on the integration point level is the approach of Ma et al. 2015, who minimized the difference in shape strain between plastically deformed regions and full, a-priori determined shape strains of invariant habit planes by means of an optimization problem.

As pointed out by Cherkaoui et al. 1998; Cherkaoui et al. 2000b the main complexity is the description of the internal stresses on the progress of martensitic phase transition, i.e. the micromechanical point of view. Whereas in an integration point model nucleation and growth always take place inside a homogeneous stress field, in reality individual phase stresses differ significantly.

In the metallurgical literature a variety of variant selection models have been proposed, an overview of which is found in Ray et al. 1990:

(i) The shape-deformation / -strain model utilising a resolved shear stress on the full habit-plane shape variant as proposed by Patel et al. 1953. Quoting Christian 1965: "There is good evidence that the effects of stress on the transformation are correctly predicted by supposing the stress to interact with the strains of the shape deformation, rather than with those of the lattice deformation". However, as shown by Petersmann et al. 2017a the criterion does not lead to accommodation since it only considers the local as opposed to the global state of a representative volume element.

(ii) Strain induced nucleation models emphasising the interaction of slip systems and habit-plane variants. In most of these models favoured variants are those whose habit planes are nearly perpendicular to the active slip plane. In highly dislocated lath martensites this is reasonable since the lattice rotation due to the lattice invariant shear accomplishing the transformation compensates the necessary rotation of the laths so that the laths can approximately form an IPS, cf. Figure 3.8. (iii) The active slip model. In this model a set of habit plane deformations (variants) incorporating an arbitrary number of lattice invariant shears are calculated a-priori. In the model those variants are produced with slip

systems sustaining the maximum resolved shear stress. Particularly, in most cases only one LIS slip system is considered, which is often argued to be of the same nature as the twinning shear (first / twinning shear model).

(v) The Bain strain model. Often used with 24 instead of only three variants, which is not consistent with the actual nature of the Bain strain (produces unrealistically high lattice rotations).

(vi) The 'geometrical parameters' model, where those variants are selected which induce a maximum deformation along a certain direction (e.g. the normal direction of the sheet when the sheet is thin). The model utilised the fact that free surfaces are known to favour martensite formation because the shape strain can be accommodated most efficiently accommodated near them.

References on EBSD studies of variant selection can be found at the end of section 5.5.

6.7.4 Variant-Variant Interaction

The weakness of a constitutive integration point model incorporating both plasticity and the martensitic phase transformation in a coupled manner on the one hand is its inability to fully capture microstructural heterogeneity. On the other hand stands the problem finding the pertaining material parameters. Utilising a mere phenomenological formalism increasingly exacerbates the problem of ill-posedness of the inverse parameter determination. An example illustrating this problem is that the relative contributions of the overall deformation due to dislocation plasticity and accommodated lattice reorientation during the phase transformation are still controversially discussed.

The incorporation of crystallographic and morphological microstructural features like dislocation microstructure interactions and information about microstructural patterns/arrangements enables geometrically motivated interaction energies due to the transformation in the material which is a key factor in the transformation mechanism. Appropriate formulation of this interaction energy is very important and requires knowledge of the microstructural evolution.

Siredey et al. 1999 proposed to use interface operators (also see Walpole 1969; Hill 1983; Suvorov et al. 2002) to set up an interaction matrix between neighbouring variants. Niclaeys

et al. 2002 pointed out that this formulation holds preferentially if the number of variants within a grain is low.

In the case of lath martensite in steel the knowledge of the hierarchical arrangement of variants into blocks and packets can be used to quantify ratios of interactions and hence reduce the number of fitting parameters. Also it depends which set of transformation strains is used. For instance the set of 12 block strains is used and the sub-block evolution is neglected, or the full set of 24 laths is used. The interaction modes then are self (1), bivariant / intra block (0), block (2) and packet interactions (3). For the sake of simplicity also the case when 24 lath strains are used is written as a 12×12 matrix, i.e. half of the intra block and packet interactions are not given. If individual laths are considered then the matrix is as follows

$$h_{ij}^{vv} = \begin{bmatrix} 1 & 0 & 2 & 2 & 3 & 3 & 3 & 3 & 3 & 3 & 3 & 3 \\ 0 & 1 & 2 & 2 & 3 & 3 & 3 & 3 & 3 & 3 & 3 & 3 \\ 2 & 2 & 1 & 0 & 3 & 3 & 3 & 3 & 3 & 3 & 3 & 3 \\ 2 & 2 & 0 & 1 & 3 & 3 & 3 & 3 & 3 & 3 & 3 & 3 \\ 3 & 3 & 3 & 3 & 1 & 0 & 2 & 2 & 3 & 3 & 3 & 3 \\ 3 & 3 & 3 & 3 & 0 & 1 & 2 & 2 & 3 & 3 & 3 & 3 \\ 3 & 3 & 3 & 3 & 2 & 2 & 1 & 0 & 3 & 3 & 3 & 3 \\ 3 & 3 & 3 & 3 & 2 & 2 & 0 & 1 & 3 & 3 & 3 & 3 \\ 3 & 3 & 3 & 3 & 3 & 3 & 3 & 3 & 1 & 0 & 2 & 2 \\ 3 & 3 & 3 & 3 & 3 & 3 & 3 & 3 & 0 & 1 & 2 & 2 \\ 3 & 3 & 3 & 3 & 3 & 3 & 3 & 3 & 2 & 2 & 1 & 0 \\ 3 & 3 & 3 & 3 & 3 & 3 & 3 & 3 & 2 & 2 & 0 & 1 \end{bmatrix}$$

In the case where composite block strains are considered from the beginning the zeros just have to be replaced by twos.

For a large grain size ($> 150 \mu\text{m}$) and a transformation without external loading it has been suggested that packets equally partition grains on the argument that the grain deformation then is a mere volume change (Qi et al. 2014). If grains are not resolved explicitly, this fact can be exploited as a constraint in the formulation of the interaction matrix.

For microstructures with a higher degree of disorder than lath martensite the same form as in Equation 6.54 can be used.

6.7.5 Structural Model for Martensite Nuclei

The interface energy of coherently strained interfaces is in the range of 0.1 J m^{-2} and increases for incoherent interfaces up to about 0.8 J m^{-2} . The stacking fault energy (SFE) γ^{sf} for the MarvalX12 dealt with here is about $0.01 - 0.02 \text{ J m}^{-2}$. This is about as large as the twin boundary energy $\sigma^{\text{b.c.c.}}$, which on the contrary is relatively independent of temperature and steel composition (Ferreira et al. 1998; G. B. Olson et al. 1976a). In this range of SFE slip is dominant, but twinning is still possible.

In general, it seems that the SFE should be used as a model parameter, not only due to experimental evidence but also in order to compare several models utilizing it.

G. B. Olson et al. 1975; G. B. Olson et al. 1976a; G. B. Olson et al. 1976b; G. B. Olson et al. 1976c envisioned that martensite lath boundaries are formed by dislocation loops forming stacking faults, known as the defect dissociation model. They treated a stacking fault as a second phase embryo rather than a surface within a continuum coherency framework ($\gamma^{\text{sf}} = \Delta G$) comprising both volume energy and surface energy contributions. For the strain energy contribution they used Eshelby's solution for spherically shaped particles. The free energy of a nucleus ΔG^{nuc} then becomes

$$\Delta G^{\text{nuc}} = \Delta G_{\text{sf}} + \Delta G_{\text{work}} = A(w^{\text{sf}}, \text{etc}) \left[n(\gamma^{\text{sf}} - 2\sigma^{\text{hcp}}) + 2\sigma^{\text{hcp}} \right] + \text{Eshelby terms} \quad (6.69)$$

where $A(w^{\text{sf}}, \text{etc})$ describes the area of the the stacking fault depending on the separation distance of the partials w^{sf} and other geometrical parameters, n is the number of stacking fault layers and Eshelby terms for the strain energy dependence can be found in section 4.3. $\sigma^{\text{hcp}} \approx 0.0115 \text{ J m}^{-2}$ is the interface energy of stacking fault. Obviously, the problem is in the description of A and n . Roters 2011 formulates $A(w^{\text{sf}}, r)$ additionally considering the bowing of the partials with the bowing radius r . Commonly A is assumed to be a constant rectangular area (e.g Galindo-Nava et al. 2016).

Additionally it has been proposed to consider the pile up energy of overlapping partials forming the nucleus (Kibey et al. 2007, mainly for twins) and the dislocation interaction energy with the applied stress aiding in formation of the fault $\Delta G^\tau = A(w^{\text{sf}})b_p n \tau$, with τ the resolved shear stress obtained with the Schmid tensor of the partial dislocation system ($\langle\langle 211 \rangle\rangle\{111\}$) resulting in a critical nucleus thickness, i.e. the number of layers of

stacking faults n is still under debate. Usually the smallest values are taken, i.e. $n = 1$ for ε -martensite and $n = 3$ for twin formation. Staudhammer et al. 1983 reported a critical twin-fault thickness of 50 - 70 Å in a 18Cr-8Ni steel. For an overview of crystallographic twin nucleation models see Kibey et al. 2007; Steinmetz et al. 2013; Ojha et al. 2014 (nucleation of twins in b.c.c.) or the recent comprehensive review on TWIP steels by Cooman et al. 2018.

The equilibrium stress free separation distance of Shockley partials depending on γ^{sf} is

$$w^{\text{sf}} = \frac{Gb^2}{2\pi\gamma^{\text{sf}}} \quad (6.70)$$

see e.g. Cottrell 1964; A. Kelly et al. 2000. However, it has been shown that this width also strongly depends on the applied stress as derived by Byun 2003 and investigated by Talonen et al. 2007. Particularly, the influence of applied stress affects the separation width w^{sf} as follows:

$$w^{\text{sf}} = \frac{Gb^2}{\pi(2\gamma^{\text{sf}} - \tau b(\sin\theta_2 - \sin\theta_1))} f(\theta_1, \theta_2) \quad (6.71)$$

Where $\theta_{1,2} = \angle(\mathbf{b}, \boldsymbol{\xi}) \pm 30^\circ$ are the angles of the Burgers vectors of the leading and trailing partials with the dislocation line vector of the perfect dislocation respectively, i.e. $f(\theta_1, \theta_2) = 3/4 - 1/(4 - 4\nu)$. The angular and stress dependence of this expression is the following: There is no effect from the applied stress on pure edge dislocations and a maximum effect of dissociation with a stress for pure screw dislocations. Hence the effect must be important for the formation of lath martensite that is dominated by screw dislocations. For instance Polatidis et al. 2018 recently reported a suppressed martensitic transformation under biaxial loading in low stacking fault energy metastable austenitic steels.

6.7.6 Transformation Driving and Dragging Forces and "Flow" Formulation Incorporating Nucleation and Growth

Considering the effects of temperature, stress state, variant interactions and dissipative thresholds, reintroducing the notation from section 6.3, the driving force for the transformation is given by

$$\mathbf{K}^i - \mathbf{K}_c^i = \Delta G^i = \Delta s(T - T^0) + \boldsymbol{\sigma}^a : \boldsymbol{\varepsilon}^{*i} + \xi^i \xi^j h_{ij}^{vy} + \Delta \xi \mathcal{D}^{\text{growth}} \quad (6.72)$$

where $\boldsymbol{\sigma}^a$ is given by Equation 4.26 and incorporates the effect of external stress and a phenomenological contribution due to internal stresses. Additionally, for lath transformation strains it could be considered to add a term of the same kind for the composite blocks strain the lath is a part of. $\mathcal{D}^{\text{growth}}$ is a dissipative threshold given e.g. by the second term from Equation 4.15 and/or a plastic strain interaction term proposed by Cherkaoui et al. 2000b; Cherkaoui et al. 2000a of the form

$$\mathcal{D}^{\text{growth}} = \boldsymbol{\varepsilon}^{*j} : \underset{\sim}{\mathcal{C}} : \left(\underset{\sim}{\mathbf{S}}^{\text{P}j} - \underset{\sim}{\mathbf{S}}^{\text{I}i} \right) : \mathbf{m}^i \gamma^i \quad (6.73)$$

where $\underset{\sim}{\mathbf{S}}^{\text{P}j}$ is the Eshelby tensor of the plastic defect (or the initial shape of the martensite nucleus) and $\underset{\sim}{\mathbf{S}}^{\text{I}i}$ that of the fully grown variant.

Levitas et al. 2009b combining the Hadamard compatibility condition (??) and the traction continuity condition

$$[\boldsymbol{\sigma}] \cdot \mathbf{h} = 0 \quad (6.74)$$

derived the driving force for interface rotation $\mathbf{X}_{\text{introt}}^{ij}$ in the case of small strains as

$$\mathbf{X}_{\text{introt}}^{ij} = -\xi_i \xi_j \mathbf{d}_\tau [\boldsymbol{\sigma}] \quad (6.75)$$

where $\mathbf{d}_\tau = \mathbf{d} - d_h \mathbf{h}$ with $d_h \mathbf{h}$ collinear and \mathbf{d} orthogonal to \mathbf{h} . Hence only the shear component of the strain discontinuity contributes to $\mathbf{X}_{\text{introt}}^{ij}$. For the large strain case see Levitas et al. 2009b; Levitas et al. 2009a.

In terms of the flow function it is important to consider both the strain-induced and stress assisted effects. For the first commonly a factor N_s related to potent nucleation sites is

used. Often, it is also considered that any threshold property, e.g. the minimum driving forces for which nucleation sites will operate ("Potency", as proposed by G. B. Olson et al. 1975) or a nucleation threshold for void nucleation, see e.g. *Z-set Materials manual Version 8.6* n.d., are distributed by a Gaussian distribution. Similar approaches are followed by Stringfellow et al. 1992 and Iwamoto et al. 1998. The models were compared and extended by Zaera et al. 2012.

Commonly not much time is spent with the discussion of the flow function. Mainly simple power laws are used, such as by S. R. Kalidindi 2001. Turteltaub et al. 2005; Suiker et al. 2005 consider

$$\dot{\xi}^i = \dot{\xi}_0 \tanh\left(\frac{\mathbf{K}^i - \mathbf{K}_c^i}{c_1 \mathbf{K}_c^i}\right) \quad (6.76)$$

with fitting parameters $\dot{\xi}_0$ and c_1 interpreted as reference variant-strain-rate and a viscosity like parameter. Mahnken et al. 2015 construct the following function:

$$\dot{\xi}^i = \frac{1}{c_3} \langle \mathbf{K}^i - \mathbf{K}_c^i \rangle^{c_4} ((1 - \xi)^{c_1} (\xi^i)^{c_2})^{c_4} \quad (6.77)$$

The term in parentheses causes a slower formation of bainite for a decreasing amount of austenite. Also, small amounts of bainite lead to a slow formation of bainitic variants at the beginning of the simulation. Therefore, such an expression, though highly phenomenological depicts an easy way to capture the main characteristics of the kinetics incorporated in the flow function.

Here we combine classical and non-classical approaches into one to obtain a kinetics based flow function for the phase transformation. The critical step in martensitic nucleation is the barrierless growth of supercritical embryos, which does not appear to require the presence of soft-phonon modes. Afterwards the glissile interface moves without resistance once it is formed. The evolution of $\dot{\xi}^i$ should depend on both the nucleus (cf. Equation 6.69) and a fully grown variant Equation 6.72. Morsdorf et al. 2015 found that initially formed martensite domains are bigger since they grow with fewer constraints. This effect is accounted for in the interaction matrix ?? Additionally, a temperature dependency of the size and shape of the martensite blocks could be considered at this point.

$$\dot{\xi}^i = (1 - \xi) \left\langle \frac{\Delta G^{i-nuc} - \Delta G_c^{i-nuc}}{\Delta G_c^{i-nuc}} \right\rangle^{c_1} \left\langle \frac{\mathbf{K}^i - \mathbf{K}_c^i}{\mathbf{K}_c^i} \right\rangle^{c_2} \exp\left(-\frac{t}{t_{relax}}\right) \quad (6.78)$$

In Equation 6.78 solely reduced quantities are used and it is formulated in the spirit of critical exponents commonly used in the theory of continuous phase-transitions. The relaxation term incorporating t^{relax} can be used to consider the effect of momentary temperature increase due to local transformation without actually calculating the heat transfer. Generally nucleation occurs very rapidly, once the critical supercooling is reached. However, an inertial effect of the system arises due to the necessary heat flow considering that the latent heat of a typical metal is about one third of the total specific heat before the melting point. This can be taken into account with the relaxation term. An interesting approach in terms of extremisation is that of Levitas 2000a; Levitas 2000b who propose a time minimisation of transformation time in an Arrhenius type equation.

6.8 Model Parameter Calibration by Inverse Fitting

The challenge in modelling the TRIP effect is that models contain large numbers of parameters if the transformation and plasticity are considered independently (plus their coupled effect). Generally, uniform field model parameters may be obtained by fitting experimentally measured, macroscopic stress-strain behaviour under some convenient strain path. The fitting procedure is an inverse / backward problem i.e. given data from experiments and data from the model an optimization strategy is considered for the parameter identification (usually least squares), see e.g. Mahnken et al. 1996b; Mahnken et al. 1996a.

For uniform field models this modelling data is usually produced using a single integration point (as e.g. used by Z-sim). However, the mean-field model proposed here targets the micro (intra-grain) scale and aims to possess a certain sensitivity for microstructure formation (i.e. localized concentration of certain crystallographic martensite variants). Therefore it should at least be calibrated over a couple of grains to get some initial heterogeneity making the iterative parameter optimization a time-consuming task.

In any case, the inverse fitting problem is ill-posed in the sense of Hadamard 1923. Fitting simulation predictions to experimental data is often poorly conditioned, in the sense that a wide range of parameter values will fit the data.

Good / reliable / robust results will only be achieved with many (relative to the number of model coefficients) diverse experiment conditions, emphasizing complex experiments with

many interacting effects over simple ones. The effect of perturbations of the experimental data on the parameters should also be checked.

If the deviation of parameters is not relatively well-established (i.e. whenever a new equation is proposed) it is advised to start the optimization procedure using global optimizers such as simulated annealing, Monte Carlo, genetic algorithms and branch and bound strategies, since generally it must be assumed that the optimization surface is rough with many local minima. Afterwards local optimization schemes (utilizing gradients) can be used.

Dependable material parameters are one of the reasons why predictions using micromechanical methods tend to be a considerable challenge. Ghassemi-Armaki et al. 2013; Srivastava et al. 2015 utilizing micro-pillar compression tests, note the problem that the behavior is essentially influenced by the small dimension size of the test specimens (no bulk behavior). A similar situation occurs in nano-indentation and micro-cantilever testing (e.g. Mine et al. 2013). Bertin et al. 2016 proposes calibration of crystal plasticity parameters by an inverse optimization methodology on digital image correlation data.

Another point is that that temperature has the role of a driving force in a phase transformation model as opposed to its role in plasticity (except maybe for creep). Even if the temperature is assumed to evolve homogeneously over the whole model it becomes an additional parameter to take into account. A quantification of thermal / entropic and stress dependent contributions becomes necessary.

Chapter 7

Summary and Outlook

Integrated computational material engineering (ICME) and steel research have reached a state from where the next step must be to go beyond the concept of microstructure property relations, to a state where the evolution of microstructure can be anticipated using a combination of deterministic micromechanical finite element modelling as well as learning algorithm approaches. In order to achieve this goal highly interdisciplinary approaches of materials science (theoretic and experimental), computational mechanics, crystallography, physics and mathematics are necessary. In this work some established frameworks of these disciplines have been brought together in view of their usefulness for the martensitic transformation.

The main result of the current work is the generalized treatment of the martensite transformations as an optimization problem on the crystallographic scale. Although the key ingredients of the theory are by no means new their combination and generalization opens new possibilities. On the one hand, the framework permits to conduct sensitivity studies on various microstructural parameters, all included in a *crystallographic set*, that have been proven to play key-roles for the formation and stability of the microstructure. On the other hand, since the incremental framework proposed for the evaluation of lath habit planes and/or blocks resembles that of a crystal plasticity theory, it can also be incorporated as an integration point constitutive description in finite element codes.

An extension of the approach presented at the end of chapter 3 is to consider more than two deformation gradients in the minors rule such as in the case of a multiphase microstructure and investigate mixtures with varying phase fractions.

The next planned extension for the developed GUI is a plugin that enables to load OIM data (e.g. in conjunction with MTEX) and to plot habit plane traces at user specified positions (orientations).

In order to be able to compare and fit micromechanical models to variant statistics, the latter must first be rigorously available for highly hierarchical, highly dislocated lath martensite. Beside the generalized identification of the *crystallographic set* the demand on the variety of orientation imaging microscopy data for a full characterisation has been discussed.

It has been argued that the required data to achieve this goal must be comprised of lattice orientation data, interface statistics and some kind of characteristic three dimensional martensite domain morphology (e.g. characterised by a "grain-shape" distribution of blocks). In the case of external loading, all of this data should be characterised relative to critical stress directions. An emphasis has been laid on industrially relevant (practical) cooling rates, grain sizes etc. The next step would be to tackle the problem of austenite reconstruction using optimized crystallographic sets. Note that the scanned area for the statistical evaluation in this study is probably close to a lower bound for the required data. Verifications on a larger set of data are desirable. As far as future studies on sub-block features are concerned it would be interesting to study slip transfer effects on this scale, e.g. using the Matlab toolbox Stabix cf. section C.1. In terms of further experiments certainly, the most interesting question is the role of (especially martensite) sub-structure sliding on the overall deformation during loaded transformation. Considering size effects new experimental approaches should be explored.

If the role of substructure sliding was quantitatively characterised this would enable to naturally better calibrate phenomenological scale transition rules in both phases. Considering the importance of nucleation and defects, studies concerning the initial microstructure state should be carried out since commonly the initial microstructural state is highly simplified, e.g. stress free, no plastic deformation etc. In terms of model parameter verification it would in general be useful to model a full thermal transformation cycle i.e. heating and cooling, which requires to formulate relations for the reverse transformation of (reconstructive and displacive nature), recrystallization and recovery. Also, it is remarkable that to the best of the author's knowledge in the literature no modelling approaches of structural hardening tests such as the Satoh test can be found.

The β rule as finally stated in chapter 4 belongs to the general idea of a coupled pair of evolution equations between a force variable and its corresponding flux variable. In the same manner a geometrically motivated backstress relation has been deduced in subsection 6.6.2. A framework for studying the effect of parameters for a range of steel types for the structural nucleus model advised in subsection 6.7.5 must be set up.

The importance of generalized continuum mechanics concepts providing a valuable tool for bridging the necessary scales in finite element models for the martensite transformation is emphasised at this point.

The essence of modelling should be to be predictive in the sense to be able to draw conclusions for those domains where we do not have the required experimental data. In order to meet this requirement this work contributed to close the gap in understanding of how the transfer of information, across length scales, can be implemented effectively within a computational framework.

List of Figures

1.1	Redraw of highly idealised schematic commonly found in the literature, showing the hierarchical microstructure of dislocated lath martensite. Laths form (composite) blocks (bi-variant or single variant), blocks stack to packets and packets partition a grain. The variant notation (pairings) is that of Morito et al. 2003. A broader classification is found in Figure 1.3.	6
1.2	Lath structure of 18Cr-8Co-5Mo, see Table 1.1 Morito et al. 2006a. large block made up of sub-blocks V1 and V4 (alternating black and white contrast). The sub-block boundaries are marked as dashed red lines. Note the difference in the lath boundary directions in V1 and V4. The habit planes were identified as $(\bar{1}65)_\alpha$ and $(165)_\alpha \approx (575)_\gamma$ and $(775)_\gamma$ for V1 and V4, respectively.	8
1.3	Crystallographic characteristics of upper bainite and lath martensite sub-structures in Fe-9Ni-(0.15-0.5)C alloys according to Furuhashi et al. 2006 . . .	9
1.4	Exemplary orientation imaging microscopy image of hierarchic structure for small grain size of MarvalX12 (specimen TR32 see Table 1.1). Color code: inverse pole figure; grayscale: fit. One dominant packet (four visible blocks in the 2D representation) and a minor packet consisting of just one single block (redundant terminology). In the minor packet (single block) the inverse pole figure colour code contrast is zoomed on the left. Bright/dark regions indicate a bi-variant block structure, however, TEM is required to resolve it, see Figure 1.2.	11
1.5	Scales addressed in this work. Starting from considerations on the lattice kinematics and the 3D structure and arrangement of laths into blocks suitable strains are worked out. The idea is to construct a microstructure sensitive combination of a mean-field full-field model, that e.g. recovers the variant distribution into packets.	12
2.1	Comparison of schematic atomic movements according to notions of displacive (pure shear) and reconstructive transformation in the case of a simple shear. A controversy of this notion is that although twinning in steels is generally considered to be displacive the result is still a cubic crystal and not e.g. a rhombohedral (cf. for instance the cubic to monoclinic transformation in NiTi). The contraction due to the pure shear is compensated by a lattice stretch during transformation. ϵ_s are the shear magnitude. Lower-left: Schematic of two step dislocations producing a shear magnitude of two times their Burgers vector.	17

- 2.2 Structural classification after H. K. D. H. Bhadeshia et al. 1990. Note, that generally there is no strict boundary on these terms. For instance the term massive ferrite is rarely found in the literature and is normally called lath or dislocated martensite. The figure reflects the split of the scientific field into "displacivists" and "diffusionists". 19
- 2.3 Above: Strength-ductility trade-off in steels. Current research involves "How to get off the banana?" when referred to variety of steels. Below, typical vehicle body recoloured from Nanosteel 2017. The colouring of the individual parts corresponds to the diagram. Nowadays, illustrations of properties like the above one can easily be plotted with a larger variety of steels from any material selection software, such as CES (Cambridge Engineering Selector) see EduPack 2007 as has been done e.g. by S. Kalidindi 2015. 27
- 2.4 Three common processing routes for steels with $>\approx 0.2\text{wt}\%C$ content, entailing displacive or partially displacive transformations. All processes start with quenching (Q) to a certain temperature. If quenched under M_f , the fully martensitic part is tempered afterwards (Q & T). If quenched until slightly above M_s and transformed isothermally in the bainite region this is called "austempering" (Q & A). Quenching between M_s and M_f , followed by raising the temperature slightly below M_s (partitioning) to enrich the remaining austenite with carbon has been proposed by Speer et al. 2003; L. Wang et al. 2013 (Q & P) 30
- 2.5 Typical CCT of a steel with $< 0.2C$ and alloyed such that highly dislocated lath martensite occurs. (1)-(4) different cooling rates \dot{T} . (1) fully martensitic microstructure, (2) massive transformation, (3) Widmannstätten ferrite, (4) Slow cooling leads to precipitation of equiaxed ferritic grains. 33
- 2.6 The three different morphologies of ferrous martensites. Left: highly dislocated laths forming blocks and packets (Fe-9Ni-0.15C), Middle: Lenticular martensite (Fe-29Ni-0.26C), Right: Thin-plate, fully internally twinned morphology (Fe-31Ni-0.23C). (Images from Maki 1999; Maki 2012) 35
- 2.7 Schematic dependency of critical stress τ_c for deformation modes (slip and twinning) enabling the phase transformation. 36
- 2.8 Typical habit planes illustrated in the usual stereographic projection of the fundamental zone (equivalent by point group symmetry) highlighted in colour of the cubic system. Interestingly, habit planes of lath martensite are commonly found to be of the form (xyx) 39
- 2.9 Asymptotic behaviours under cyclic loading after Fouvry et al. 2001. Elastic shakedown: An elastic behaviour, after possibly an initial plastic strain. Plastic shakedown: An extended hysteresis loop, with a periodic plastic loading between two fixed values. Ratchetting: Accumulation of inelastic deformation, eventually leading to failure. 41
- 2.10 Schematic illustration of the critical stress σ_c to initiate martensitic transformation as a function of temperature after G. Olson et al. 1972. σ_y^A is the temperature dependent yield strength of austenite. The red line shows the behavior for martensites showing isothermal transformation characteristics. 43

2.11	Top: Top-down and bottom-up interactions arising from the interplay of industrial needs and scientific methods (according to G. B. Olson 1997). Bottom: Overview of ideas on various length scales treated in this thesis. Starting from considerations on the unit cell level a mean-field approach incorporating a detailed description of interactions between deformation mechanisms during the phase transformation and a suitable scale-transition rule is developed on the grain-scale. Simulation of a representative volume element (see section 4.1) enables to approach the macroscale.	51
3.1	Dislocation dissociations into partials to produce stacking faults. a) two Shockley partials, b) (immobile) pole mechanism for twinning.	61
3.2	Terminology of twinning elements. For a type I twin K_1 is the twin plane normal $\boldsymbol{\eta}_1$ the twinning shear direction. $\boldsymbol{\eta}_2$ points in the direction of the invariant line and is the twinning shear direction of a type II twin (K_2 is its twin plane normal).	62
3.3	Upper-left: asymmetric region of full Euler space (one-sixteenth) taken from Hansen et al. 1978. Upper-right: Surfaces representing the same misorientation of three symmetrically equivalent components of the orientation $\{123\} \langle 634 \rangle$ (taken from Hansen et al. 1978) illustrating the non-linearity of the Euler-space. Bottom: Major texture components of MarvalX12 (TR32 specimen see section 5.1).	67
3.4	Bain strain \mathbf{B} model. Golden atoms (f.c.c) remain invariant. Top: Initial b.c.t unit cell, that can be drawn into two neighbouring f.c.c unit cells (Bain OR, blue atoms coincide with golden ones). Lower-Left: $\langle 100 \rangle_{\text{bcc}}$ projection after application of \mathbf{B} morphing b.c.t \rightarrow b.c.c. Lower-right: Other view of right illustrating that a rotation around a specific $\langle 100 \rangle_{\text{bcc}}$ aligns $\{111\}_{\gamma} \parallel \{011\}_{\alpha'}$ (violet \parallel green plane), as e.g. pointed out by Maresca et al. 2017. Graphics have been produced with VESTA (Momma et al. 2011).	74
3.5	Two views of a Kurdjumov-Sachs OR, i.e. after application of the in-plane rotation aligning $\langle 110 \rangle_{\gamma} \parallel \langle 111 \rangle_{\alpha'}$ (violet \parallel green arrow). Experimentally, a distribution of the in-plane rotation angle θ_{KS} with a maximum between the KS and NW directions is observed. In the lower picture the correlation between row / edge matching between the phases as emphasised in subsection 3.5.5 and the KS directions is illustrated (slightly tilted projection along these directions).	75
3.6	Formal equivalence of an invariant plane strain on one side of an interface, constructed (left) by a twinned laminate of alternating stretches (modulated / adaptive martensite) or (right) by one homogeneously distributed, straight dislocation lines. In the former case an IPS can be obtained by varying ξ_1 (cf. Equation 3.30), in the latter by ε_s (cf. Equation 3.5). Generally, the variety of ILSs/ILPs solutions using shears is much larger, but the scale at which the concept of a homogeneous shear applies is much smaller than as a consequence of a twin laminate.	81

- 3.7 Traces of calculated habit planes of martensite with the surface recorded via EBSD (given in terms of a lattice vector) taken from Mayer et al. 2016. The color-code in the EBSD mapping and the traces correlates. U_1-U_6 denote the symmetry variants of the structural stretch tensor. Note, that in general four IPS solutions occur together. In this case the other phase easily enables a determination of the relative orientations and only a small amount of plastic slip is necessary in order to enable an invariant plane strain. 84
- 3.8 Left: modified from J. Hirth et al. 2016. Upper-left: low nucleation rate, high growth rate. Lower-left: high nucleation rate, low growth rate. According to J. Hirth et al. 2016 this tendency even applies for twinning. Right: magnification of glissile interface. Slip systems meet edge to edge along an invariant line. Also see Figure 3.10. 92
- 3.9 Interface terminology following J. Hirth et al. 2013. Indices of austenite (A) and martensite (M) lattice. For interfacial defects the suggested reference space is the dichromatic complex / pattern (union of the space groups of both A and B). Left column: Bicrystal, i.e. same as on the right but the atoms on the other side of the interface are not shown. Bottom: The total rotation, is partitioned between the two crystals with respect to the initial (coherently strained) terrace plane. The subscripts HP and TP mark the habit plane and terrace plane bases respectively. 94
- 3.10 Red, green and blue colors mark correspondences between the images. Upper-left: Habit structure of martensite laths along the lines of Christian 1965. Frank 1953 proposed a longitudinal growth by screw dislocations ($\mathbf{b} \parallel \xi_D = \xi_L$). Topological characterisation and notion of disconnection and terrace plane after J. Hirth et al. 2011. Recent MD simulations (e.g. Maresca et al. 2017 particularly Figure 5 therein) support this view and reveal the nature of the two shears. Upper-right: Characteristic dimensions of a lath. Center: Interface cross section showing orientation relation (terrace plane). Lower-left: Schematic of habit plane interface cross section as found in publications of J. Hirth et al. 2013. Lower-right: Habit-plane and terrace-plane systems. 97
- 3.11 Connections between the 24 KS-OR variants. The four triangles are the $\{111\}_\gamma$ slip planes oriented as an "unfolded" Thompson tetrahedron. The slip / KS-direction relation and variant number due to Morito et al. 2006a are shown on each plane. The lines mark special interfaces (CSL see subsection 3.5.5) between the variants: $\Sigma 1$ is a low angle boundary and $\Sigma 3$ a (coherent) twin boundary, see e.g. S. Zhang et al. 2012 for a Fe-13Cr-9Ni stainless steel similar to the MarvalX12. Variants connected by $\Sigma 1$ belong to the same Bain correspondence (see subsection 3.5.2). 99
- 3.12 Sketch of relative orientation between single laths (here illustrated as ellipsoids with half axis lengths $a < b \ll c$ with $a \parallel \mathbf{k}$ the close packed γ and invariant line direction and $b \parallel \mathbf{h}$ the habit plane) of a packet relative to austenite crystal system (also see Figure 3.11). The given pairs are actually twin pairs, which are related by a 60° rotation around $[1\bar{1}1]$ ($\Sigma 3$ boundary). However, the reported pairing in this block of lath martensite is V1-V4, V3-V6, V2-V5. The theoretical lattice misorientation between these pairs is 10.5° ($\Sigma 1$ boundary, experimentally smaller, see Stormvinter et al. 2012). . 102

- 3.13 Geometry of slip transfer across a grain boundary taken from Bieler et al. 2014. Horizontal (orange and blue) planes signify slip or twinning planes on either side of the boundary. κ is the angle between slip directions, Φ is the angle between plane normals, and θ is the angle between plane traces on the boundary. 103
- 3.14 The habit-plane (normal vector \mathbf{h}) is usually of type $\{xyx\}_\gamma$ and $10^\circ < \theta < 20^\circ$ from $\{111\}_\gamma$, i.e. between $\{557\}_\gamma$ and $\{112\}_\gamma$. \mathbf{n} terrace plane vector (usually $\{111\}_\gamma$). Illustration of different assumptions of relative slip plane alignment with stepped interface. The inter-penetrating lines indicate the general treatment as outlined in subsection 3.5.5. Accommodation of coherency strains is most efficient if the slip direction \mathbf{s} is parallel / \mathbf{m} is normal to the terrace plane. Conversely, the rotation necessary to achieve an invariant plane strain is most efficient if \mathbf{s} is normal / \mathbf{m} is parallel to the habit-plane. 106
- 3.15 Basic code structure of Martensite Calculator 117
- 3.16 Graphical user interface of written Matlab toolbox. Input parameters are the lattice parameters and possible slip systems (either in austenite or martensite). A default lattice correspondence is proposed but may also be changed. A set of predefined selection criteria with user defined tolerances can be specified. A log informs the user about errors or calculation activities. After lath solutions have been calculated, optionally composite solutions can be constructed from lath solutions. The results can be written to a text file. 119
- 3.17 Evolution of selected habit plane solutions dependent on the larger shear magnitude (right) as well as the sum of both plastic shear magnitudes respectively (left). Top: Correspondence update. Bottom: Constant Bain correspondence. In both cases the results indicate that for most solutions one shear is substantially larger than the other. Also both cases show a strong increase in solutions above a specific value. However, in the case of an updated lattice correspondence the total required shear magnitude is generally lower. 120
- 3.18 Progression of selected habit plane solutions depending on their shape strains ε_0^I as well as the rotation angle the inclusion must undergo in order to form an invariant plane strain. Top: Correspondence update. Bottom: Constant Bain correspondence. Due to the considered cost function that is optimized incrementally it can be seen that the shape strain has exactly the same progression as the rotation. The right column also illustrated the algorithms ability to find the same number of solutions due to opposite shear directions leading to opposite rotations, which may be interesting for lattices with lower symmetry. 121
- 3.19 Dependence of results on misorientation of CP planes (θ_{CP}) and deviation ideal KS direction parallelism θ_{KS} . θ_{CP} is reported to be almost zero. Top: Correspondence update. Bottom: Constant Bain correspondence. In both cases the calculations almost have a plateau for $\theta_{CP} > 0.5^\circ$, so it is reasonable to assume that it is smaller than 0.5° . As opposed to previous dependencies Right: The deviation of the ideal KS direction from the calculated one shows a continuous evolution in accordance with the continuous features of pole figures observed experimentally. 122

3.20	Left: Effect of misorientation between the laths' habit planes and the nearest close packed plane in austenite. Right-column: Smallest angle between preferred invariant line direction ($\langle 110 \rangle_\gamma$) and habit plane of solutions. Top: Correspondence update. Bottom: Constant Bain correspondence.	123
3.21	Visualization of combined property dependences of the number of total habit plane solutions on ε_0^L and θ_{HP}^L in the previous example. Left-column: $\varepsilon_0^L < \text{threshold}$ and $\theta_{HP}^L < \text{threshold}$. Right-column: $\varepsilon_0^L < \text{threshold}$ and $\theta_{Rot}^B < \text{threshold}$. Top: Correspondence update. Bottom: Constant Bain correspondence.	124
3.22	Overview of rotation angles of composite block deformations at a phase fraction of $\xi_1 = 0.5$. Left: All possible combinations of lath solutions. It can be seen that there are about 400 composite blocks with a rotation angle near 0° which can be seen as optimal in terms of accommodation. Right: Composite blocks reduced by minors relations with $\Delta d_{1_{\max}} = 0.003$ and $\Delta \det_{\max} = 0.003$ showing no blocks with low angles.	125
3.23	Left: Net rotation angle of linearly mixed block strain as a function of ξ_1 . It can be seen that almost all minima of the rotation angle are between $\xi_1 = 0.4$ to 0.6 . Right: Residuals of minors relations as a functions of ξ_1	126
3.24	Top: Evolution of block habit plane orientation (plane normal vector components) of two randomly selected linear mixtures of lath habit plane solutions. Bottom: Full spectrum of plots over all unrestricted linear mixtures of laths to blocks in the range of favourable rotation. The results indicate that there exists a continuous spectrum of block habit planes that are oriented similarly.	127
3.25	Block optimization by means of variation of ξ_1 . Three cost functions are considered. Top: Frobenius norm of the Green-Lagrange strain. Center: Minimized shape deformation magnitude. Bottom: Frobenius norm of the displacement gradient for verifying that the remaining small rotation has little influence on the results. The levels of the optimized quantities are still quite different, suggesting new limits for a further reduction of optimal solutions. Marked points are the only two remaining solutions without correspondence using the same constraints.	128
3.26	The previous calculations suggest the following microstructural arrangement of blocks. Shown are sections normal to the largest dimension of the blocks. Up to now a stacking in only one direction has been suggested since the blocks have been envisioned as plates.	130
4.1	Schematic, showing the influence of several kinds of boundary conditions on the effective bulk properties of a micromechanical model. An representative volume element is defined as the volume above which the effective properties obtained from KUBCs and SUBCs coincide.	133
4.2	Schematic interpretation of scale transition rules. Particularly, the evolution of this models under an evolving microstructure is emphasized.	142
5.1	Thin-walled tubular specimen used in the mechanic characterisation. Samples are machined with surfaces obtained from a longitudinal cut in the blue marked area of the gauge length. Dimensioning plan taken from Nagayama et al. 2001.	145

- 5.2 Top: Strain evolution due to transformation under various constant loading conditions. Bottom: Strain evolution of one thermal cycle without loading. 29 MPa additional tensile loading were found to be necessary to close the transformation loop for the 840° C prior annealing. 146
- 5.3 The kinetics of the MarvalX12 is relatively independent on the cooling rate, but varies strongly with the grain size and austenite heterogeneity both macroscopically characterised by an effective stress in the works cited at the beginning of section 5.2. In the experimental data available the kinetics varies between the upper-right (higher annealing temperature, measured via dilatometry) and upper-left (lower annealing temperature, transformation under load and lever-rule like calculation). The lower images taken from Loewy et al. 2014 illustrate that the transformation rate for a steel of similar composition and kinetics exhibit staggered rate maxima in the indicated temperature interval. This behavior indicates the presence of an elastic accommodation effect, although the transformation is strongly coupled with plasticity. 148
- 5.4 Strain evolution during thermal cycling (specimen TR32), without an applied load during transformation. Top: full temperature range. Bottom: Strain difference between start of heating and end of cooling for each cycle, respectively. 149
- 5.5 Taken from Hidalgo et al. 2016. Colour-code: inverse pole figure, grayscale: image quality. (a)-(d) Cycle 1-4. Note that in (a) a larger scale is used. White lines represent misorientation of rotating angle between 20° and 47° argued to represent prior austenite grain (PAG) boundaries. 151
- 5.6 Left: Schematic arrangement of electron source, specimen and with reference coordinate system in the used OIM software and EBSD detector (image taken from *TSL OIM Analysis Manual* n.d.). Terminology from the characterization of rolling texture: 1 - Rolling direction (RD), 2 - Transverse Direction (TD) and 3 - Normal direction (ND). Right: Orientation of the coordinate system in the images provided in this work and its relative alignment with the sample (indicated by an extract of the gauge length) and its external loading during transformation. 153
- 5.7 Sample T32, GS-IQ, lower left quarter of Figure 5.9. The sample surface is not very flat even after ion slicing. This indicates a high degree of dislocations and hence internal stresses. 154
- 5.8 Definition of grain shape in the OIM software is determined by fitting an ellipse to points making up a grain (red line marks the grain boundary). $0 < \theta < 180^\circ$ gives the grain shape orientation, i.e. the angle between the major axis of fitted ellipse and the horizontal direction (2 in Figure 5.6). 155
- 5.9 Specimen TR32 - transformation under 120 MPa torsion loading, CC: inverse pole figure (IPF), GS: fit. A visible orientation contrast from bottom right to top left can be noticed. Particularly, sub-block features oriented in this direction are more elongated than in any other direction. The torsion loading leads by far to the highest heterogeneity within individual blocks. 156
- 5.10 Specimen TR25 - transformation under 120 MPa tensile loading, CC: IPS, GS: fit. Contrary to the sheared sample no preferred block orientation is visible and heterogeneity within blocks is lower. 157

- 5.11 TA03 higher annealed, CC-IPF, GS:FIT - Same options for GS as for TR32 and TR25. The GS contrast of this image is distinctly different than from TR32 and TR25. This is due to the annealing at higher temperature significantly reducing the dislocation density. 158
- 5.12 $\langle 100 \rangle$ IPFs of specimen TA03. Top: IPFs constructed with one average orientation per reconstructed grain defined by a misorientation of 11° . Bottom: IPFs using all data points. It can be seen that the reduced texture evaluation reproduces the full texture very well. Interestingly, in the $3/ND/[001]$ direction corresponding to the tangential specimen direction there is a texture peak of $\langle 100 \rangle_\alpha$. One possibility is that this is the Bain compression axis, but this would be counter intuitive since without any other deformation mechanism this axis would preferably be oriented towards the free surface in $[010]$ sample direction. So it must be an artifact of the transformation texture developed during the thermal cycling. As expected in an unloaded transformation there is almost no difference between the $[010]$ and $[100]$ IPFs. 160
- 5.13 $\langle 100 \rangle$ IPFs of specimen TR32. Direction of maximum shear stress is $[001]$. Top: IPFs constructed with one average orientation per reconstructed grain defined by a misorientation of 11° . Bottom: IPFs using all data points. The two evaluations differ significantly indicating strong gradients within blocks. Therefore, evaluating all data points should be preferred. There is a preference of $\langle 111 \rangle_\alpha \approx \langle 110 \rangle_\gamma$ to align with the direction of maximum shear and $\langle 011 \rangle_\alpha \approx \langle 111 \rangle_\gamma$ to align with the direction of the free surface. 161
- 5.14 $\langle 100 \rangle$ IPFs of specimen TR25. Direction of tensile loading is $[100]$. Top: IPFs constructed with one average orientation per reconstructed grain defined by a misorientation of 11° . Bottom: IPFs using all data points. $\langle 111 \rangle_\alpha$ preferably is oriented in the loading direction and the absolute values of all the occurring maxima are much more pronounced than in the shear and unloaded samples. 161
- 5.15 Pole figures of sample TA03 (stereographic projections). Top row: one point per grain area weighted with grains defined by 5° misorientation. Middle row: one point per grain area weighted with grains defined by 11° . Note that the highest possible rank of 34 is used. Bottom row: fit of all scanned data points with harmonic series rank 16. The 11° resolution for the grains should be preferred over the 5° grain resolution since it depicts the overall state of texture much better. However, the 5° resolution is useful to identify bi-variant pairs forming blocks. Interestingly, maxima in the $\langle 001 \rangle_\alpha$ pole figure are concentrated on the left hand side, cf. the lack of inversion symmetry in Figure 5.12. 162
- 5.16 Pole figures of TR32 and TR25 (stereographic projections). Grain average orientation, with grains defined by a misorientation of 11° , weighted by the grain area for TR32 (top row) and TR25 (3rd row) respectively. Fit of all data points for TR32 (second row) and TR25 (bottom row). As for the IPFs for the torsion sample the reduced texture representation fails to be representative of the whole data. The texture for the tensile loaded sample is very sharp 164

- 5.17 Boundary/interface character distribution in the three samples. It is distinguished between low and high angle boundaries, where for the latter additionally coincidence site lattice boundaries are distinguished. In shear deformation significantly more low angle boundaries are formed and the number of CSL boundaries decreases most significantly. 165
- 5.18 Distributions of misorientations in the three samples. The sum of the number fractions of each of the individual intervals (0° - 2° , 2° - 5° , 5° - 60°) = 1, i.e. even small differences between the same intervals are very pronounced. Top: TR32, Middle: TR25, Bottom: TA03. Deviations in the second interval seem to be the lowest between the three specimen. Interestingly, all samples show a peak around 30° , where no special boundaries are reported (cf. Table 3.3). Therefore, this peak must be a result of the transformation cycling. 166
- 5.19 Distribution of grain shape orientation, cf. Figure 5.8. Grains are defined by connected regions with a misorientation of 5° . Several levels of discretisation are shown for a better characterisation. Left column: specimen transformed under 120 MPa tensile loading (TR25). Right-column: specimen transformed under 120 MPa shear loading (TR32). 167
- 5.20 Grain shape orientation, cf. Figure 5.8 with several discretisation levels. Left column: specimen transformed under 120 MPa tensile loading (TR25). Right-column: specimen transformed under 120 MPa shear loading (TR32). Grains are defined as connected regions with a misorientation of 11° 168
- 5.21 Left: Typical regular block arrangement of 18Cr-8Ni-5Mo with large $320 \mu\text{m}$ PAGS from Morito et al. 2006a. The data either has been coarsened or the resolution of common EBSD systems at the time of recording was significantly lower than for more modern systems. Right: according pole figure. Such pole figure representations are commonly used to reconstruct grains by comparing them with theoretical pole figures. 170
- 5.22 Specimen TR25 tensile specimen: Upper-left: GS: fit, CC: IPF. Upper-right: CC: [001] IPF with crystal direction $\langle 111 \rangle_{\alpha}$ and colouring up to 12° misorientation indicating bi-variant block-structure. The GND density is evaluated by first nearest neighbour analysis and considering misorientations up to 5° (larger misorientations are ignored). GND density is, given in multiples of $1 \times 10^{12} \text{ m}^{-2}$ 171
- 5.23 Specimen TR32 (shear loaded). Left: Local misorientation with maximum of 11° with respect to marked point in grain. Right: GND density evaluated with a maximum considered misorientation of 60° (larger misorientations are ignored) and second nearest neighbours analysis. The GND density is given, in multiples of $1 \times 10^{12} \text{ m}^{-2}$ 172
- 5.24 TA03: Left: Euler angle colouring background and local misorientation with maximum of 15° relative to marked point in the middle of the block. Right: GND density with maximum considered misorientation of 15° (larger misorientations are ignored) and first nearest neighbours gradient calculation. The GND density is given in multiples of $1 \times 10^{12} \text{ m}^{-2}$. Here the GND density is overlayed with an image quality gray-scale contrast Note that at this resolution the grain boundaries can be anticipated by the image quality contrast. 172

- 6.1 Terminology of generalized continua. Reproduced after Forest et. al: CISM 2017 - Mesoscale Models: From Micro-Physics to Macro Interpretation. Not explicitly drawn are microstrain theories (negligible micro rotations as a complementary to the Cosserat continuum). Second gradient approaches are probably necessary to describe the deformation of a martensite lath. A typical example of a gradient of internal variable is a gradient of the plastic strain in (phenomenological) strain gradient models. 175
- 6.2 Schematics of energy "wells" from Wilmanns 2010. Red lines indicate the general trend for various temperatures around the equilibrium temperature T_0 see subsection 6.4.1. The wells are separated by activation barriers. I stands for the untransformed parent phase, the U_i are structural stretch tensors or more generally shape strains (see section 3.5) of the product phase. 182
- 6.3 Parameter space for martensitic nucleation according to M. Cohen et al. 1992, chapter 9 therein. η is a strain order parameter, σ^{ie} a interface energy, m is a critical exponent. the initial substructure heterogeneity strongly varies depending on the processing history and evolves during transformation. Defect strength refers to the stabilization of a nucleus. Non-classical extensions depict softening phenomena. 208
- 6.4 Phenomenological ways to macroscopically introduce hardening such that the transformation kinetics (by means of the Lever-rule) is depicted. Left: red points mark experimentally measured phase fraction. The abscissa shows the normalized transformation temperature T_n . The kinetics may be fitted with any function (blue line; here a piecewise fit joining at the saddle point is illustrated). A hardening function R_ξ that recovers the kinetics then for instance is the inverse of this function (green). Right: Construction of R_ξ with initial softening as in the model proposed by Fischlschweiger et al. 2013, see Appendix B. 211

List of Tables

1.1	Top: Chemical compositions (wt%) of some steel types for which a hierarchical microstructure is reported. ¹ Nagayama et al. 2001, ² Shintani et al. 2011, ³ Morsdorf et al. 2015, ⁴ Morito et al. 2006a, ⁵ Morito et al. 2006a, ⁶ Kinney et al. 2014, ⁷ Kinney et al. 2017. Bottom: Emphasis on the difference on processing conditions of steel specimen for which a hierarchical microstructure is reported. Austenitization temperatures and holding times, approximate resulting grain sizes, specification of cooling process.	10
2.1	Characteristics of transformation product (low temperature phase) in steel. due to H. K. D. H. Bhadeshia et al. 1990; Christian 1965. consistency (✓) and inconsistency (x) of phenomenon or theory stated on the left. \approx means that both cases have been observed. Considered products are: martensite (α'), lower bainite (α_{lb}), upper bainite (α_{up}), acicular (chaotic) ferrite (α_{ac}), Widmanstätten ferrite (α_w), allotriomorphic ferrite (α), idiomorphic ferrite (α_i), pearlite (P)	22
2.2	Overview of typical habit planes, orientation relations and defect structures in steels (c.f Nishiyama et al. 1978; Porter et al. 2009). Note, that actually for a lath no definite plane is defined. From top to bottom: Dislocation density and M_s tendentially decrease. γ^{sf} ...stacking fault energy (SFE). Orientation relations (ORs) such as Kurdjumov-Sachs (KS) and Nishiyama-Wassermann (NW) are listed in section 3.4	38
3.1	Overview of commonly stated (idealised) orientation relationships between f.c.c. austenite, b.c.c. martensite and h.c.p ϵ -martensite in steel. Three dots indicate that the plane relation is the same, only that of the directions changes. Both Pitsch and NW are 5.26° from KS ($\{111\}_\gamma$ in-plane rotation). These relations are quite idealised considering that orientation relations are not discrete but follow some distribution and most interfaces are irrational.	65
3.2	Overview of terminology of dislocations at semi-coherent / commensurate interfaces.	91
3.3	Overview of the twenty-four KS orientation variants (orientational / lattice correspondence variants - LCVs). The individual Bains (compression axes), parallel plane (CP) relations defining packets and theoretical misorientations w.r.t. variant V1 are given. Note that all misorientations in a packet belong to a $\langle 110 \rangle_\alpha$ direction. The 10.5° and 14.9° misorientations are semi coherent $\Sigma 1$ coincidence side lattice CSL interfaces. $V_i - V_{i+1}$ are related by a 60° rotation around a specific $\{111\}_\gamma$ and form a $\Sigma 3$ twin boundary (this is the characteristic Type I twin solution).	100

3.4	Sub-block boundary sliding systems: each habit plane of a certain packet forms with a certain lath long direction a pseudo slip system. Note that within a block only two such systems are active due to the pairings forming coherent low angle CSL interfaces e.g. V1-V4, V3-V5, V2-V5 in packet $(111)_\gamma$, see Table 3.3	103
3.5	Overview of lattice invariant shear (LIS) systems proposed for the f.c.c. \rightarrow b.c.c. transformation in steels.	106
5.1	Alloying components of Marval X12 (wt%), $\Sigma \approx 24.2\%$ hence Fe-75.8 % . . .	143
6.1	Equivalent-Mises stress and strain in proportional / monotonic uniaxial tension/compression and and shear (approximately pure torsion) see Shrivastava et al. 2012; Pardis et al. 2017	196
6.2	Slip system interactions, naming convention after Franciosi et al. 1982. Slip planes $(\bar{1}11)$, (111) , $(\bar{1}\bar{1}1)$, $(1\bar{1}1)$ are named A, B, C, D respectively and slip directions $[011]$, $[0\bar{1}1]$, $[101]$, $[\bar{1}01]$, $[\bar{1}10]$, $[110]$, as 1 2 3 4 5 6 respectively. The 12 slip systems are A1, A3, A6, B2, B4, B5, C1, C3, C5, D1, D4, D6. SH: Self hardening, Copl: Coplanar / inplane reaction (same glide plane), CS: Colinear / cross slip (same Burgers vector), HL: Hirth Lock (orthogonal Burgers vectors) syst pair with normal slip directions, GJ: Glissile junctions formation, LC: Lomer-Cottrell sessile locks formation	205
6.3	Values of the dimensionless coefficients determining the critical stress and the storage rate in f.c.c. crystals for a reference dislocation density $\rho_{\text{ref}} = 1 \times 10^{12} m^{-2}$ as given by Devincre et al. 2008 and references therein.	207
B.1	Overview of residual derivatives - all internal variables are calculated at time $t + \Delta\Theta t$	245

Appendix A

Related Scale Bridging Concepts

A.1 Continuum Theory of Dislocations

For a large enough volume element, due to the ergodic hypothesis the ensemble average may be replaced by volume averaging. Then the result is identical to the dislocation density tensor, or Nye's tensor $\boldsymbol{\alpha}$ introduced subsequently, which is the basic variable of the continuum theory of dislocations and can directly be related to the densities of so-called geometrically necessary dislocations (GNDs) ρ_{gnd} , a terminology often attributed to Ashby 1970. Note that for a single, discrete dislocation: $\alpha_{ij} = \xi_i b_j \delta(\xi)$, where $\delta(\cdot)$ denotes the Dirac delta-function (for many dislocations summation can be applied). In the continuum case the Burgers vector content is given by

$$\mathbf{b} = \oint_{\partial S} \tilde{\mathbf{F}}^{e-1} d\mathbf{x} \quad (\text{A.1})$$

where ∂S is the closure contour surrounding an area S in the reference configuration. It should be kept in mind that the Burgers vector is a property of the reference lattice, and not the distorted medium. Application of Stokes theorem leads to the definition of the so-called dislocation density tensor.

$$\begin{aligned} \mathbf{b} &= \int_S \boldsymbol{\alpha} \cdot \mathbf{n} \, dS \quad \text{with} \\ \boldsymbol{\alpha} &= -\text{curl} \tilde{\mathbf{F}}^{e-1} = \tilde{\mathbf{F}}^{e-1} \times \nabla = -\varepsilon_{ikl} F_{ik,l}^{e-1} \mathbf{e}_i \otimes \mathbf{e}_j \end{aligned} \quad (\text{A.2})$$

If the surface is infinitesimal of normal \mathbf{n} , $d\mathbf{b} = \underline{\boldsymbol{\alpha}} \mathbf{n} dS$ is the resulting true Burgers vector of dislocations crossing the surface dS . Note that each component α_{ij} can be associated with a "super-dislocation". As a result, diagonal components represent screw dislocations and the off-diagonal components edge dislocations, see Forest 2012. While the density ρ_{gnd} can be computed approximately in some situations like plastic bending, see e.g. Ashby 1970 or punching, see e.g. Nix et al. 1998, in the continuum theory of dislocations a big enough RVE for allowing a volume average is required to compute the components of $\underline{\boldsymbol{\alpha}}$. Conventional plasticity laws tacitly assume that the density of GNDs is negligible $\rho_{\text{GND}} \ll \rho_S$ and no length scale enters.

Measurements from a plastically deformed material can only be performed in the deformed (current) configuration. Hence the following is actually used:

$$\begin{aligned} \mathbf{b} &= \oint_{\partial S} \underline{\mathbf{F}}^{e-1} d\mathbf{x} = \oint_{\partial S_0} \underline{\mathbf{F}}^{e-1} \underline{\mathbf{F}} d\mathbf{X} \stackrel{\text{Equation 6.2}}{=} \oint_{\partial S_0} \underline{\mathbf{F}}^p d\mathbf{X} \stackrel{\text{Stokes}}{=} - \int_S \nabla \times \underline{\mathbf{F}}^p \mathbf{N} dS = \dots \\ &\dots = - \int_S \nabla \times \underline{\mathbf{F}}^p J^{-1} \underline{\mathbf{F}}^T \mathbf{n} dS \quad \text{hence} \quad \underline{\boldsymbol{\alpha}} = \nabla \times \underline{\mathbf{F}}^p J^{-1} \underline{\mathbf{F}}^T \end{aligned} \tag{A.3}$$

Note the difference between spatial / current and reference frame. As apparent from Equation A.3 the spatial variation of the crystallographic slip throughout the domain is necessary to determine the GND densities. Either FEM elements collecting neighbouring information of the internal variable γ^i (see e.g. Han et al. 2007) or a generalized material treatment, which generally needs higher order (≥ 2) Ansatz functions (C_1 continuity connecting elements) is needed. For the latter, numerical problems due to gradients between neighbouring integration points are often reported (especially for non-uniform meshes).

Other names for α_{ij} are torsion-flexure tensor / Burgers tensor / Nye's dislocation density tensor after Nye 1953. He assumes negligible elastic strain and small (strain) elastic rotation, workign with an axial rotation vector of the lattice, which he calls lattice gradient / curvature (for a derivation, see Forest et al. 1997; Forest 2012).

As a next step the small-strain formalism is presented and connections with slip system vectors are given. Beforehand, as pointed out by Gurtin 2006: "The approximation of small deformations obscures much of the physics underlying the notion of a Burgers vector" (as will be elaborated after giving the equations for the small strain case that can be found

in the literature. With $\mathbf{H}^p = \mathbf{H} - \mathbf{H}^e$ and considering that $\text{curl } \mathbf{H} = 0$ due to the compatibility of the deformation gradient:

$$\boldsymbol{\alpha} \approx \text{curl } \mathbf{H}^e = -\text{curl } \mathbf{H}^p = -\nabla \times \boldsymbol{\xi}^p = -\epsilon_{ijk} \gamma_{lk,j} \quad (\text{A.4})$$

$${}^i \rho_{\text{gnd}}^{\text{edge}} b = {}^i \rho_{\text{gnd}}^{\perp} b = -(\nabla \cdot \boldsymbol{\gamma}^i) \cdot \mathbf{s}^i = -\text{grad } \boldsymbol{\gamma}^i \cdot \mathbf{s}^i = -\gamma_{,k} \cdot \mathbf{s}^i \quad (\text{A.5})$$

$${}^i \rho_{\text{gnd}}^{\text{screw}} b = {}^i \rho_{\text{gnd}}^{\odot} b = (\nabla \cdot \boldsymbol{\gamma}^i) \cdot \boldsymbol{\xi}^i \quad \text{next the index } i \text{ is replaced by a } \sum \quad (\text{A.6})$$

$$-\alpha_{ij} = -\sum \epsilon_{ijk} \gamma_{,j} s_l m_k = -\sum \gamma_{,j} s_l (s_j \xi_i - \xi_j s_i) \quad \text{Arsenlis et al. 1999} \quad (\text{A.7})$$

$$\boldsymbol{\alpha} = \sum_i \rho_{\text{gnd}}^{\odot} \mathbf{s} \otimes \mathbf{s} + \rho_{\text{gnd}}^{\perp} \boldsymbol{\xi} \otimes \mathbf{s} \quad \text{Gurtin 2006} \quad (\text{A.8})$$

From the above the dependence of α_{ij} upon the slip gradient in the slip direction \mathbf{s} , and the direction of the dislocation line $\boldsymbol{\xi}$ can be seen. Note that any slip gradient in the direction of the slip system normal \mathbf{m} does not contribute to α_{ij} . Also note that Gurtin 2006 uses the concept of a "macroscopic Burgers vector" as derived in their works, which is why b does not appear explicitly in Equation A.8.

The problems of such an approach are the following: In general $\boldsymbol{\alpha}$ is non-symmetric, i.e. a unique mapping would (theoretically) require nine independent slip systems (recall that the f.c.c structure has 5 independent systems, see section 3.2). A workaround in a large strain formalism, which utilizes the fact that dislocation densities can be considered as lengths of lines allowing certain variable substitutions, see Arsenlis et al. 1999 Equations 25-27 therein, has been developed by Ma et al. 2006 (Equations 20-27 therein). The most general form of dislocation density projections of GNDs and SSD (statistically stored dislocations) to forest and parallel sets can also be found in Ma et al. 2006 Equations 10-11 therein.

Due to the demanding numerics of a full crystallographic slip system treatment and the distinction of SSDs and GNDs (many additional variables) phenomenological strain gradient theories have been developed, starting with the works of N. Fleck et al. 1994; H. Gao et al. 1999; N. A. Fleck et al. 2014. Reducing the number of variables, while at the same time keeping as much flexibility as possible currently is a fruitful area of research, see e.g. Stupkiewicz et al. 2016; Petryk et al. 2016.

Next, the thermodynamical frameworks of GNDs are shortly outlined. A common assumption is that \mathbf{H}^p is fully accomplished by GNDs, hence it does not appear in the dissipation

inequality. For an overview of generalized balance laws as well as assumptions on boundary conditions see e.g. Bertram et al. 2014.

The derivative of the free energy w.r.t. the dislocation density tensor often is denoted as couple stress tensor (based on the early works of Koiter 1964, who introduced a gradient similar to Nye for the linear elastic case).

$$\Psi(\dots, \underline{\alpha} = \text{curl } \underline{\mathbf{H}}^p) \quad \frac{\partial \Psi}{\partial \underline{\alpha}} = \underline{\mathbf{M}} \quad (\text{couple stress tensor}) \quad (\text{A.9})$$

As usual, a first assumption for the thermodynamic contributions to the free energy is a linear relation resulting in a quadratic potential

$$\Psi = \dots + 1/2 c_1 \underline{\alpha} : \underline{\alpha} \quad (\text{A.10})$$

Based on dimensional considerations c_1 is interpreted as l^2 with l being a characteristic dimension of the microstructure. The problem is that it is not clear which value to choose for l .

A common feature of such generalized continuum dislocation theories is that they are associated with the existence of lattice curvature induced backstress and corresponding kinematic hardening. Steinmann 1996; Gurtin 2002; Forest 2008 (also see Cordero et al. 2012) assume a free energy of the form Equation A.10 using $\text{curl } \underline{\mathbf{M}} = \text{curl curl } \underline{\mathbf{H}}^p$ as projection tensor on the Schmidt tensor to obtain a GND based backstress x^i on slip system i . However it has been claimed that the scaling properties of this relation do not correspond to that obtained in large scale MD simulations (Zbib et al. 2017).

Next a relation to the density of GND was proposed, see e.g. Ohno et al. 2007; Neff et al. 2009

$$\Psi = \dots + c_1 \|\underline{\alpha}\| \sim \rho^{\text{gnd}} b \quad (\text{A.11})$$

with $\|\underline{\alpha}\| = \sqrt{\underline{\alpha} : \underline{\alpha}}$ being the Frobenius norm. Finally a logarithmic strain gradient energy based on the statistical theory of dislocations Groma et al. 2003 was proposed.

$$\underline{\mathbf{M}} \sim \ln \rho^{\text{gnd}} \Rightarrow \Psi \sim \dots + c_1 \rho^{\text{gnd}} (\ln \rho^{\text{gnd}} - 1) \quad (\text{A.12})$$

A.2 Relations between Thermodynamic Potentials, Kinetic Rate Factors and Statistical Mechanics

Note that in statistical physics (from where thermodynamics originates), as soon as any dynamic enters the description the notion of an ensemble (either in time or configuration space) is introduced. A statistical ensemble is a probability distribution for the state of the system over the system's phase space Gibbs 1902. If both time and space ensembles are equivalent the system is ergodic.

The inner energy $U = U(S, V, N)$ only depends on extensive variables. Absolute values of U cannot be directly measured but its chances. For fixed U, V and N , the entropy S becomes maximal (micro canonical ensemble). The according partition function (micro canonical partition function Z_m) is related to the entropy by $S = k_b \ln(Z_m)$.

The Helmholtz free energy $F = F(T, V$ or $\varepsilon, N)$ is given by $F = U - TS$. In the corresponding canonical ensemble the system can exchange energy, but no particles. The canonical Partition function is $F = -k_b T \ln(Z_k)$

If the change of particles is also considered one has the grand canonical potential that is related to the grand canonical partition function.

In the context of irreversible thermodynamics the Shannon entropy H ("information entropy") is noteworthy, see Jaynes 1957

$$H = - \sum p_i \ln p_i \quad (\text{A.13})$$

where p_i is the probability of an action and $\ln p_i$ is the so-called self-information. The motivation for the name of this quantity came from the close resemblance to the Gibbs-Boltzmann-entropy derived for an ideal gas.

$$S = k_B \ln p_i \quad (\text{A.14})$$

where p_i is the probability of a macroscopic state calculated from possible micro-states. In the habit plane the probability of each micro-state of an ideal gas is equal, hence the probability can be obtained by counting permutations (assumption of equal a priori probability of

micro-states / fundamental postulate of statistical mechanics). For solids this is not the case!

Note that $x \ln(x)$ is the first term of the Stirling approximation for $n!$ (James Stirling 1692-1770). The error of this approximation is only small if a large number of particles is considered (cf. law of large numbers and its limit the central limit theorem: empirical probability = theoretical probability; assumptions: same probability distribution, independent variables).

Also well known is the relation of the Helmholtz free energy and the canonical partition function Z_c .

$$F = -k_B T \ln Z_c \quad (\text{A.15})$$

Which, actually belongs to equilibrium thermodynamics, but is introduced here to bridge the gap to a coefficient often found in kinetic relations in the literature of classical nucleation theory (CNT), or thermal activation of dislocation motion.

$$\mathfrak{R} = \exp\left(-\frac{\Delta G}{k_B T}\right) = \ln\left(\frac{Z_c^1}{Z_c^2}\right) \quad (\text{A.16})$$

This obviously results from replacing F by G writing ΔG and rearranging. This term is widely known as Boltzmann Factor, or if k_B is (somewhat unjustified) replaced by $R = N_a k_B$ for molar quantities this is known as Arrhenius dependence. Relations with CNT, where ΔG is the change of free energy upon formation of a defect or small domain of new phase are discussed in subsection 6.7.5.

Depending on the specific problem at hand further, pre-exponential factors are commonly used. For instance a characteristic frequency and a mean free motion path for diffusion or thermally activated dislocation motion, see Equation 6.49 or a factor N_s related to the number of nucleation sites, see subsection 6.7.5.

In statistical mechanics phenomenologically motivated equations differential equations of first order for the time evolution of probability distributions, from which approximations and limits of easier equations can be derived are generally called master equations. For discrete states

$$\frac{dp_i}{dt} = \sum P_{ij} p_j - P_{ji} p_i \quad (\text{A.17})$$

where p_i is the probability that the system is in a state i and P_{ij} a (mainly constant) transition probability (cf. Markov-Process). Such an approach has e.g. been used by Govindjee et al. 2000; Achenbach 1989 for martensite. Another example is the Fokker-plank equation describing the velocity of a particle under the influence certain forces. A probabilistic model based on random events has been presented by J. M. Ball et al. 2015.

The use of the Boltzmann factor in nucleation-rate equations has been criticized since it stems from the customary assumption that the atoms can be regarded as separate oscillators having a characteristic frequency (see Kaufman et al. 1958). Crussard states that the energy for the thermally activated process under consideration is really supplied by statistical reinforcements of elastic waves are not considered and proposes an alternative probability factor based on quantum theory. Magee emphasized that the coordinated motion of large groups of atoms would involve much lower attempt frequencies as above, in the order $10^{10} - 10^{11} s^{-1}$ and G. B. Olson et al. 1986 even proposed $10^7 s^{-1}$.

Appendix B

Implicit Formulation of a Phenomenological Macro Model

In general the system of equations depicting the constitutive behavior can be expressed by much fewer variables than normally employed, e.g. in the case treated here σ and ξ . However, doing so would result in very long equations. Therefore the design of the system of equations itself constitutes some kind of optimization problem on its own.

Within the model code the number of mathematical operations should be optimized, e.g. by suitable setting of code sequences and brackets. For instance, let A and B be 3×3 matrices and c be a scalar, then $(cA): B$ and $c(A: B)$ in the first operation there are more operations than in the second.

Note that in Zebulon operator overloading is used for the various datatypes such as fourth order tensors. E.g. if a object is of type tensor then a tensor product is just the the overloaded multiplication symbol $*$.

Subsequently, the residual formulation and full Jacobian matrix necessary for an implicit implementation by the example of the model presented by Fischlschweiger et al. 2012 are presented. A similar model in a large-strain framework (intermediate config) has been presented by Hallberg et al. 2007

Scale transition rule

$$\underline{\sigma}^a = \underline{\sigma}^{\text{ext}} + \xi \mu (\underline{\beta}^{mo} - \underline{\beta}^a) + K \xi \delta / 3 \underline{\mathbf{I}}$$

$$\underline{\sigma}^m = \underline{\sigma}^{\text{ext}} - (1 - \xi) \mu (\underline{\beta}^{mo} - \underline{\beta}^a) - K(1 - \xi) \delta / 3 \underline{\mathbf{I}}$$

Residuals

Strain partitioning

$$\mathbf{R}^\varepsilon = -\Delta \underline{\varepsilon} + \Delta \underline{\varepsilon}^e + (1 - \xi) \Delta p^a \underline{\mathbf{n}}^a + \xi \Delta p^m \underline{\mathbf{n}}^m + \Delta \xi (\underline{\varepsilon}^{\text{vol}} + \underline{\varepsilon}^o)$$

Plasticity

$$\mathbf{R}^{p^a} = -\Delta p^a + \left\langle \frac{f(\underline{\mathbf{s}}^a, \underline{\mathbf{X}}^a, R^a)}{K^a} \right\rangle^{n^a} \Delta t$$

$$\mathbf{R}^{p^m} = -\Delta p^m + \left\langle \frac{f(\underline{\mathbf{s}}^m, \underline{\mathbf{X}}^m, R^m)}{K^m} \right\rangle^{n^m} \Delta t$$

Orientation strain

$$\mathbf{R}^{p^o} = -\Delta p^o + \left\langle \frac{f^o}{K^o} \right\rangle^{n^o} \Delta t$$

$$\mathbf{R}^{\varepsilon^o} = -\Delta \underline{\varepsilon}^o + \Delta p^o \underline{\mathbf{n}}^o$$

Kinetics

$$\mathbf{R}^\xi = -\Delta \xi + \left\langle \frac{f^\xi}{K^\xi} \right\rangle^{n^\xi} \Delta t$$

Scale transition rules

$$\mathbf{R}^{\beta^a} \cong -\Delta \underline{\beta}^a + \Delta p^a \underline{\mathbf{n}}^a - D^a \underline{\beta}^a \Delta p^a$$

$$\mathbf{R}^{\beta^{mo}} \cong -\Delta \underline{\beta}^{mo} + \Delta p^m \underline{\mathbf{n}}^m + \Delta p^o \underline{\mathbf{n}}^o - D^{mo} \underline{\beta}^{mo} (\Delta p^m + \Delta p^o)$$

Kinematic hardening

$$\mathbf{R}^{\alpha^a} = -\Delta \underline{\alpha}^a + \left(\underline{\mathbf{n}}^a - \frac{3}{2} \frac{D^a}{C^a} \underline{\mathbf{X}}^a \right) \Delta p^a$$

$$\mathbf{R}^{\alpha^m} = -\Delta \underline{\alpha}^m + \left(\underline{\mathbf{n}}^m - \frac{3}{2} \frac{D^m}{C^m} \underline{\mathbf{X}}^m \right) \Delta p^m$$

$$\mathbf{R}^{\alpha^o} = -\Delta \underline{\alpha}^o + \left(\underline{\mathbf{n}}^o - \frac{3}{2} \frac{D^o}{C^o} \underline{\mathbf{X}}^o \right) \Delta p^o$$

TABLE B.1: Overview of residual derivatives - all internal variables are calculated at time $t + \Delta\Theta t$

	$\frac{\partial}{\partial \Delta \tilde{\boldsymbol{\varepsilon}}^e}$	$\frac{\partial}{\partial \Delta p^a}$	$\frac{\partial}{\partial \Delta p^m}$	$\frac{\partial}{\partial \Delta p^o}$	$\frac{\partial}{\partial \Delta \tilde{\boldsymbol{\varepsilon}}^o}$	$\frac{\partial}{\partial \Delta \tilde{\boldsymbol{\beta}}^a}$	$\frac{\partial}{\partial \Delta \tilde{\boldsymbol{\beta}}^{mo}}$	$\frac{\partial}{\partial \Delta \tilde{\boldsymbol{\alpha}}^a}$	$\frac{\partial}{\partial \Delta \tilde{\boldsymbol{\alpha}}^m}$	$\frac{\partial}{\partial \Delta \tilde{\boldsymbol{\alpha}}^o}$	$\frac{\partial}{\partial \Delta \xi}$
\mathbf{R}^e	$\frac{\partial \mathbf{R}^e}{\partial \Delta \tilde{\boldsymbol{\varepsilon}}^e}$	$\frac{\partial \mathbf{R}^e}{\partial \Delta p^a}$	$\frac{\partial \mathbf{R}^e}{\partial \Delta p^m}$	$\frac{\partial \mathbf{R}^e}{\partial \Delta p^o}$	$\frac{\partial \mathbf{R}^e}{\partial \Delta \tilde{\boldsymbol{\varepsilon}}^o}$	$\mathbf{0}$	$\mathbf{0}$	$\frac{\partial \mathbf{R}^e}{\partial \Delta \tilde{\boldsymbol{\alpha}}^a}$	$\frac{\partial \mathbf{R}^e}{\partial \Delta \tilde{\boldsymbol{\alpha}}^m}$	$\frac{\partial \mathbf{R}^e}{\partial \Delta \tilde{\boldsymbol{\alpha}}^o}$	$\frac{\partial \mathbf{R}^e}{\partial \Delta \xi}$
\mathbf{R}^{p^a}	$\frac{\partial \mathbf{R}^{p^a}}{\partial \Delta \tilde{\boldsymbol{\varepsilon}}^e}$	$\frac{\partial \mathbf{R}^{p^a}}{\partial \Delta p^a}$	0	0	$\mathbf{0}$	$\mathbf{0}$	$\mathbf{0}$	$\frac{\partial \mathbf{R}^{p^a}}{\partial \Delta \tilde{\boldsymbol{\alpha}}^a}$	$\mathbf{0}$	$\frac{\partial \mathbf{R}^{p^a}}{\partial \Delta \tilde{\boldsymbol{\alpha}}^o}$	0
\mathbf{R}^{p^m}	$\frac{\partial \mathbf{R}^{p^m}}{\partial \Delta \tilde{\boldsymbol{\varepsilon}}^e}$	0	$\frac{\partial \mathbf{R}^{p^m}}{\partial \Delta p^m}$	0	$\mathbf{0}$	$\mathbf{0}$	$\mathbf{0}$	$\frac{\partial \mathbf{R}^{p^m}}{\partial \Delta \tilde{\boldsymbol{\alpha}}^m}$	$\mathbf{0}$	$\mathbf{0}$	0
\mathbf{R}^{p^o}	$\frac{\partial \mathbf{R}^{p^o}}{\partial \Delta \tilde{\boldsymbol{\varepsilon}}^e}$	0	0	$\frac{\partial \mathbf{R}^{p^o}}{\partial \Delta p^o}$	$\mathbf{0}$	$\mathbf{0}$	$\mathbf{0}$	$\frac{\partial \mathbf{R}^{p^o}}{\partial \Delta \tilde{\boldsymbol{\alpha}}^a}$	$\mathbf{0}$	$\frac{\partial \mathbf{R}^{p^o}}{\partial \Delta \tilde{\boldsymbol{\alpha}}^o}$	$\frac{\partial \mathbf{R}^{p^o}}{\partial \Delta \xi}$
$\mathbf{R}^{\varepsilon^o}$	$\frac{\partial \mathbf{R}^{\varepsilon^o}}{\partial \Delta \tilde{\boldsymbol{\varepsilon}}^e}$	$\mathbf{0}$	$\mathbf{0}$	$\frac{\partial \mathbf{R}^{\varepsilon^o}}{\partial \Delta p^o}$	$-\mathbf{I}$	$\mathbf{0}$	$\mathbf{0}$	$\frac{\partial \mathbf{R}^{\varepsilon^o}}{\partial \Delta \tilde{\boldsymbol{\alpha}}^a}$	$\mathbf{0}$	$\frac{\partial \mathbf{R}^{\varepsilon^o}}{\partial \Delta \tilde{\boldsymbol{\alpha}}^o}$	$\frac{\partial \mathbf{R}^{\varepsilon^o}}{\partial \Delta \xi}$
\mathbf{R}^{β^a}	$\frac{\partial \mathbf{R}^{\beta^a}}{\partial \Delta \tilde{\boldsymbol{\varepsilon}}^e}$	$\frac{\partial \mathbf{R}^{\beta^a}}{\partial \Delta p^a}$	$\mathbf{0}$	$\mathbf{0}$	$\mathbf{0}$	$\frac{\partial \mathbf{R}^{\beta^a}}{\partial \Delta \tilde{\boldsymbol{\beta}}^a}$	$\mathbf{0}$	$\frac{\partial \mathbf{R}^{\beta^a}}{\partial \Delta \tilde{\boldsymbol{\alpha}}^a}$	$\mathbf{0}$	$\frac{\partial \mathbf{R}^{\beta^a}}{\partial \Delta \tilde{\boldsymbol{\alpha}}^o}$	$\mathbf{0}$
$\mathbf{R}^{\beta^{mo}}$	$\frac{\partial \mathbf{R}^{\beta^{mo}}}{\partial \Delta \tilde{\boldsymbol{\varepsilon}}^e}$	$\mathbf{0}$	$\frac{\partial \mathbf{R}^{\beta^{mo}}}{\partial \Delta p^m}$	$\frac{\partial \mathbf{R}^{\beta^{mo}}}{\partial \Delta p^o}$	$\mathbf{0}$	$\mathbf{0}$	$\frac{\partial \mathbf{R}^{\beta^{mo}}}{\partial \Delta \tilde{\boldsymbol{\beta}}^{mo}}$	$\frac{\partial \mathbf{R}^{\beta^{mo}}}{\partial \Delta \tilde{\boldsymbol{\alpha}}^a}$	$\frac{\partial \mathbf{R}^{\beta^{mo}}}{\partial \Delta \tilde{\boldsymbol{\alpha}}^m}$	$\frac{\partial \mathbf{R}^{\beta^{mo}}}{\partial \Delta \tilde{\boldsymbol{\alpha}}^o}$	$\frac{\partial \mathbf{R}^{\beta^{mo}}}{\partial \Delta \xi}$
\mathbf{R}^{α^a}	$\frac{\partial \mathbf{R}^{\alpha^a}}{\partial \Delta \tilde{\boldsymbol{\varepsilon}}^e}$	$\frac{\partial \mathbf{R}^{\alpha^a}}{\partial \Delta p^a}$	$\mathbf{0}$	$\mathbf{0}$	$\mathbf{0}$	$\mathbf{0}$	$\mathbf{0}$	$\frac{\partial \mathbf{R}^{\alpha^a}}{\partial \Delta \tilde{\boldsymbol{\alpha}}^a}$	$\mathbf{0}$	$\frac{\partial \mathbf{R}^{\alpha^a}}{\partial \Delta \tilde{\boldsymbol{\alpha}}^o}$	$\mathbf{0}$
\mathbf{R}^{α^m}	$\frac{\partial \mathbf{R}^{\alpha^m}}{\partial \Delta \tilde{\boldsymbol{\varepsilon}}^e}$	$\mathbf{0}$	$\frac{\partial \mathbf{R}^{\alpha^m}}{\partial \Delta p^m}$	$\mathbf{0}$	$\mathbf{0}$	$\mathbf{0}$	$\mathbf{0}$	$\frac{\partial \mathbf{R}^{\alpha^m}}{\partial \Delta \tilde{\boldsymbol{\alpha}}^m}$	$\mathbf{0}$	$\mathbf{0}$	$\mathbf{0}$
\mathbf{R}^{α^o}	$\frac{\partial \mathbf{R}^{\alpha^o}}{\partial \Delta \tilde{\boldsymbol{\varepsilon}}^e}$	$\mathbf{0}$	$\mathbf{0}$	$\frac{\partial \mathbf{R}^{\alpha^o}}{\partial \Delta p^o}$	$\mathbf{0}$	$\mathbf{0}$	$\mathbf{0}$	$\frac{\partial \mathbf{R}^{\alpha^o}}{\partial \Delta \tilde{\boldsymbol{\alpha}}^a}$	$\mathbf{0}$	$\frac{\partial \mathbf{R}^{\alpha^o}}{\partial \Delta \tilde{\boldsymbol{\alpha}}^o}$	$\frac{\partial \mathbf{R}^{\alpha^o}}{\partial \Delta \xi}$
\mathbf{R}^ξ	$\frac{\partial \mathbf{R}^\xi}{\partial \Delta \tilde{\boldsymbol{\varepsilon}}^e}$	$\frac{\partial \mathbf{R}^\xi}{\partial \Delta p^a}$	0	0	$\frac{\partial \mathbf{R}^\xi}{\partial \Delta \tilde{\boldsymbol{\varepsilon}}^o}$	$\mathbf{0}$	$\mathbf{0}$	$\frac{\partial \mathbf{R}^\xi}{\partial \Delta \tilde{\boldsymbol{\alpha}}^a}$	$\mathbf{0}$	$\frac{\partial \mathbf{R}^\xi}{\partial \Delta \tilde{\boldsymbol{\alpha}}^o}$	$\frac{\partial \mathbf{R}^\xi}{\partial \Delta \xi}$

with

$$\begin{aligned}
 f^{a,m} &= J_2^{a,m} \left(\underline{\mathfrak{s}}^{a,m} - \underline{\mathfrak{X}}^{a,m} \right) - Q^{a,m} (1 - \exp(-b^{a,m} p^{a,m})) - R_0^{a,m} \\
 f^o &= J_2^o \left(\underline{\mathfrak{s}}^a - \underline{\mathfrak{X}}^o \right) \xi \left(1 + k_0 \frac{J_3^o}{(J_2^o)^3} \right)^{1/n} - H^o (J_{\varepsilon^o})^{b_o} \xi^2 - R_0^o \\
 f^\xi &= K_\sigma^\xi \left(\alpha \operatorname{tr}(\underline{\mathfrak{\sigma}}^a) + (1 - \alpha) J_2 \left(\underline{\mathfrak{\sigma}}^a - \underline{\mathfrak{X}}^a \right) A_a^{1/n} \right) - B(T - T_0) - R^\xi - R_0^\xi \\
 R^\xi &= -K_{\xi_1} \zeta \ln(1 - \xi) + K_{\xi_2} (1 - \zeta) \ln(\xi) + K_o^\xi (J_{\varepsilon^o})^{n_\delta^\xi} - K_p^\xi (p^a)^{n_p^\xi}
 \end{aligned}$$

$$J_2(\underline{\mathfrak{s}}) = \left(\frac{3}{2} \underline{\mathfrak{s}} : \underline{\mathfrak{s}} \right)^{1/2}$$

$$J_3(\underline{\mathfrak{s}}) = \det(\underline{\mathfrak{s}}) = \left(\frac{9}{2} \underline{\mathfrak{s}}^2 : \underline{\mathfrak{s}} \right)^{1/3}$$

$$J_{\varepsilon^o} = \left(\frac{2}{3} \underline{\mathfrak{\varepsilon}}^o : \underline{\mathfrak{\varepsilon}}^o \right)^{1/2}$$

$$\frac{\partial J_2^o}{\partial \underline{\mathfrak{\sigma}}} = \frac{\partial J_2 \left(\underline{\mathfrak{s}}^a - \underline{\mathfrak{X}}^o \right)}{\partial \underline{\mathfrak{\sigma}}} = \underline{\mathfrak{n}}_{J_2}^o$$

$$\frac{\partial J_3^o}{\partial \underline{\mathfrak{\sigma}}} = \underline{\mathfrak{n}}_{J_3}^o = \left(\underline{\mathfrak{s}}^a - \underline{\mathfrak{X}}^o \right)^2 - \frac{1}{3} (J_2^o)^2 \underline{\mathfrak{I}}$$

$$\frac{\partial \underline{\mathfrak{n}}_{J_3}^o}{\partial \underline{\mathfrak{\sigma}}} = \frac{1}{2} (\delta_{ik} s_{lj} + \delta_{il} s_{kj} + s_{ik} \delta_{jl} + s_{li} \delta_{kj}) - \frac{2}{3} J_2^o \underline{\mathfrak{I}} \otimes \underline{\mathfrak{n}}_{J_2}^o$$

$$J_{ijkl} = 1/2(\delta_{ik}\delta_{jl} + \delta_{kj}\delta_{li}) - 1/3\delta_{ij}\delta_{kl}$$

$$\underline{\mathfrak{X}}^a = \frac{2}{3} C_k^a \underline{\mathfrak{\alpha}}^a + \frac{2}{3} C_k^{ao} \underline{\mathfrak{\alpha}}^o$$

$$\underline{\mathfrak{X}}^m = \frac{2}{3} C_k^m \underline{\mathfrak{\alpha}}^m$$

$$\underline{\mathfrak{X}}^o = \frac{2}{3} C_k^o \underline{\mathfrak{\alpha}}^o + \frac{2}{3} C_k^{oa} \underline{\mathfrak{\alpha}}^a$$

$$\frac{\partial f^{a,m}}{\partial \underline{\sigma}} = \frac{\partial J_2^{a,m,o}(\underline{s}^{a,m} - \underline{X}^{a,m,o})}{\partial \underline{\sigma}} = \frac{\partial J_2}{\partial \underline{s}} : \frac{\partial \underline{s}}{\partial \underline{\sigma}} = \underline{n}^{a,m,o} = \frac{3}{2} \frac{(\underline{s}^{a,m} - \underline{X}^{a,m,o})}{J_2(\underline{\sigma}^{a,m} - \underline{X}^{a,m,o})}$$

$$\frac{\partial \underline{s}}{\partial \underline{\sigma}} = \underline{J} = \underline{I} - \frac{1}{3} \underline{I} \otimes \underline{I}$$

$$\frac{\partial \underline{n}^{a,m,o}}{\partial \Delta \bar{\xi}^e} = \frac{\partial \underline{n}^{a,m,o}}{\partial \underline{s}^{a,m,a}} : \frac{\partial \underline{s}^{a,m,a}}{\partial \underline{\sigma}^{a,m,a}} \frac{\partial \underline{\sigma}^{a,m,a}}{\partial \bar{\xi}^e} : \frac{\partial \bar{\xi}^e}{\partial \Delta \bar{\xi}^e} = \frac{1}{J_2} \left(\frac{3}{2} \underline{J} - \underline{n}^{a,m} \otimes \underline{n}^{a,m} \right) : \underline{C} : \Theta \underline{I}$$

$$\text{Note: } \frac{\partial \underline{n}^{a,m,o}}{\partial \underline{X}^{a,m,o}} = \frac{\partial \underline{n}^{a,m,o}}{\partial \underline{s}^{a,m,a}}$$

$$\text{using the abbreviations } A_o = \left(1 + k_0 \frac{J_3^o}{(J_2^o)^3} \right) ; \quad \frac{\partial A_o}{\partial \underline{\sigma}} = \frac{k_o}{(J_2^o)^3} \left(\underline{n}_{J_3}^o - \frac{3J_3^o \underline{n}_{J_2}^o}{J_2^o} \right)$$

$$\frac{\partial f^o}{\partial \underline{\sigma}} = \frac{\partial f^o}{\partial \underline{X}^o} : \underline{J} = \underline{n}^o = A_o^{1/n} \xi \left(\underline{n}_{J_2}^o + \frac{J_2^o}{n A_o} \frac{\partial A_o}{\partial \underline{\sigma}} \right) =$$

$$= A_o^{1/n} \xi \left[\underline{n}_{J_2}^o + \frac{k_0}{n A_o (J_2^o)^3} \left(\underline{n}_{J_3}^o J_2^o - 3J_3^o \underline{n}_{J_2}^o \right) \right]$$

$$\frac{\partial \underline{n}^o}{\partial \underline{\sigma}} = A_o^{1/n} \xi \left(\frac{1}{n A_o} \underline{n}_{J_2}^o \otimes \frac{\partial A_o}{\partial \underline{\sigma}} + \frac{\partial \underline{n}^o}{\partial \underline{\sigma}} + (1/n - 1) \frac{k_0}{n A_o^2 (J_2^o)^2} \underline{n}_{J_3}^o \otimes \frac{\partial A_o}{\partial \underline{\sigma}} + \dots \right.$$

$$\dots + \frac{k_0}{n A_o (J_2^o)^2} \frac{\partial \underline{n}^o}{\partial \underline{\sigma}} - \frac{2k_0}{n A_o (J_2^o)^3} \underline{n}_{J_3}^o \otimes \underline{n}_{J_2}^o - (1/n - 1) \frac{3k_0 J_3^o}{n A_o^2 (J_2^o)^3} \underline{n}_{J_2}^o \otimes \frac{\partial A_o}{\partial \underline{\sigma}} - \dots$$

$$\left. \dots - \frac{3k_0}{n A_o (J_2^o)^3} \underline{n}_{J_2}^o \otimes \underline{n}_{J_3}^o - \frac{3k_0 J_3^o}{n A_o (J_2^o)^3} \frac{\partial \underline{n}^o}{\partial \underline{\sigma}} + \frac{9k_0 J_3^o}{n A_o (J_2^o)^4} \underline{n}_{J_2}^o \otimes \underline{n}_{J_2}^o \right) : \underline{J}$$

Strain partitioning

$$\frac{\partial \mathbf{R}^\varepsilon}{\partial \Delta \bar{\varepsilon}^e} = \underline{\underline{\mathbf{I}}} + \left((1 - \xi) \Delta p^a \frac{\partial \underline{\underline{\mathbf{n}}}^a}{\partial \underline{\underline{\boldsymbol{\sigma}}}} + \xi \Delta p^m \frac{\partial \underline{\underline{\mathbf{n}}}^m}{\partial \underline{\underline{\boldsymbol{\sigma}}}} \right) : \underline{\underline{\mathbf{C}}} \Theta$$

$$\frac{\partial \mathbf{R}^\varepsilon}{\partial \Delta p^a} = (1 - \xi) \underline{\underline{\mathbf{n}}}^a$$

$$\frac{\partial \mathbf{R}^\varepsilon}{\partial \Delta p^m} = \xi \underline{\underline{\mathbf{n}}}^m$$

$$\frac{\partial \mathbf{R}^\varepsilon}{\partial \Delta \bar{\varepsilon}^o} = \Theta \Delta \xi \underline{\underline{\mathbf{I}}}$$

$$\frac{\partial \mathbf{R}^\varepsilon}{\partial \Delta \underline{\underline{\boldsymbol{\alpha}}}^a} = (1 - \xi) \Delta p^a \frac{\partial \underline{\underline{\mathbf{n}}}^a}{\partial \underline{\underline{\mathbf{X}}}^a} : \Theta (-1) \frac{2}{3} C_k^a \underline{\underline{\mathbf{I}}}$$

$$\frac{\partial \mathbf{R}^\varepsilon}{\partial \Delta \underline{\underline{\boldsymbol{\alpha}}}^m} = \xi \Delta p^m \frac{\partial \underline{\underline{\mathbf{n}}}^m}{\partial \underline{\underline{\mathbf{X}}}^m} : \Theta (-1) \frac{2}{3} C_k^m \underline{\underline{\mathbf{I}}}$$

$$\frac{\partial \mathbf{R}^\varepsilon}{\partial \Delta \underline{\underline{\boldsymbol{\alpha}}}^o} = (1 - \xi) \Delta p^a \frac{\partial \underline{\underline{\mathbf{n}}}^a}{\partial \underline{\underline{\mathbf{X}}}^a} : \Theta (-1) \frac{2}{3} C_k^{a,o} \underline{\underline{\mathbf{I}}}$$

$$\frac{\partial \mathbf{R}^\varepsilon}{\partial \Delta \xi} = -\Theta \underline{\underline{\mathbf{n}}}^a \Delta p^a + \Theta \underline{\underline{\mathbf{n}}}^m \Delta p^m + (\bar{\varepsilon}^{vol} + \bar{\varepsilon}^o)$$

Plasticity

$$\frac{\partial \mathbf{R}^{p^{a,m}}}{\partial \Delta \bar{\varepsilon}^e} = \Delta t \frac{\partial \phi}{\partial J_2} \frac{\partial J_2}{\partial \underline{\underline{\boldsymbol{\sigma}}}} : \frac{\partial \underline{\underline{\boldsymbol{\sigma}}}}{\partial \bar{\varepsilon}^e} : \frac{\partial \bar{\varepsilon}^e}{\partial \Delta \bar{\varepsilon}^e} = \Delta t \Theta \frac{n^{a,m}}{K^{a,m}} \left\langle \frac{f^{a,m}}{K^{a,m}} \right\rangle^{n^{a,m}-1} \underline{\underline{\mathbf{n}}}^{a,m} : \underline{\underline{\mathbf{C}}}$$

$$\begin{aligned} \frac{\partial \mathbf{R}^{p^{a,m}}}{\partial \Delta p^{a,m}} &= -1 + \Delta t \frac{\partial \phi}{\partial R^{a,m}} \frac{\partial R^{a,m}}{\partial \Delta p^{a,m}} = \\ &= -1 + \Theta \Delta t \frac{n^{a,m}}{K^{a,m}} \left\langle \frac{f^{a,m}}{K^{a,m}} \right\rangle^{n^{a,m}-1} (-b^{a,m} Q^{a,m} \exp(-b^{a,m} p^{a,m})) \end{aligned}$$

$$\frac{\partial \mathbf{R}^{p^a}}{\partial \Delta \underline{\underline{\boldsymbol{\alpha}}}^{a,o}} = \Delta t \frac{\partial \phi}{\partial f^a} \frac{\partial f^a}{\partial \underline{\underline{\mathbf{X}}}^a} : \frac{\partial \underline{\underline{\mathbf{X}}}^a}{\partial \underline{\underline{\boldsymbol{\alpha}}}^{a,o}} : \frac{\partial \underline{\underline{\boldsymbol{\alpha}}}^{a,o}}{\partial \Delta \underline{\underline{\boldsymbol{\alpha}}}^{a,o}} = \Delta t \Theta \frac{n^a}{K^a} \left\langle \frac{f^a}{K^a} \right\rangle^{n^a-1} \underline{\underline{\mathbf{n}}}^a : (-1) \frac{2}{3} C_k^{a,o} \underline{\underline{\mathbf{I}}}$$

$$\frac{\partial \mathbf{R}^{p^m}}{\partial \Delta \underline{\underline{\boldsymbol{\alpha}}}^m} = \text{see equation above with } f^a \rightarrow f^m, \quad \underline{\underline{\mathbf{X}}}^a \rightarrow \underline{\underline{\mathbf{X}}}^m, \quad \underline{\underline{\boldsymbol{\alpha}}}^{a,o} \rightarrow \underline{\underline{\boldsymbol{\alpha}}}^m, \quad C_k^{a,o} \rightarrow C_k^m$$

Orientation Strain

$$\begin{aligned} \frac{\partial \mathbf{R}^{p^o}}{\partial \Delta \bar{\varepsilon}^e} &= \Delta t \frac{\partial \phi}{\partial f^o} \frac{\partial f^o}{\partial \underline{\boldsymbol{\sigma}}} : \underline{\mathbf{C}} \Theta = \Delta t \Theta \frac{n^o}{K^o} \left\langle \frac{f^o}{K^o} \right\rangle^{n^o-1} \underline{\mathbf{n}}^o : \underline{\mathbf{C}} \\ \frac{\partial \mathbf{R}^{p^o}}{\partial \Delta \bar{\varepsilon}^o} &= -1 + \Delta t \frac{\partial \phi}{\partial R^o} \frac{\partial R^o}{\partial \Delta p^o} = -1 - \Delta t \Theta \frac{n^o}{K^o} \left\langle \frac{f^o}{K^o} \right\rangle^{n^o-1} H^o \xi^2 b^o (J_{\varepsilon^o})^{b^o-1} \\ \frac{\partial \mathbf{R}^{p^o}}{\partial \Delta \underline{\boldsymbol{\alpha}}^{a,o}} &= \Delta t \frac{\partial \phi^o}{\partial f^o} \frac{\partial f^o}{\partial \underline{\mathbf{X}}^o} : \frac{\partial \underline{\mathbf{X}}^o}{\partial \underline{\boldsymbol{\alpha}}^{a,o}} : \frac{\partial \underline{\boldsymbol{\alpha}}^{a,o}}{\partial \Delta \underline{\boldsymbol{\alpha}}^{a,o}} = \Delta t \frac{n^o}{K^o} \left\langle \frac{f^o}{K^o} \right\rangle^{n^o-1} \underline{\mathbf{n}}^o : (-1) \frac{2}{3} C_k^{oa,o} \underline{\mathbf{I}} \Theta \\ \frac{\partial \mathbf{R}^{p^o}}{\partial \Delta \xi} &= \Delta t \frac{\partial \phi}{\partial f^o} \frac{\partial f^o}{\partial \xi} \frac{\partial \xi}{\partial \Delta \xi} = \Delta t \Theta \frac{n^o}{K^o} \left\langle \frac{f^o}{K^o} \right\rangle^{n^o-1} \left(J_2^o A_o^{1/n} - 2 \xi H^o (J_{\varepsilon^o})^{b^o} \right) \\ \frac{\partial \mathbf{R}^{\varepsilon^o}}{\partial \Delta \bar{\varepsilon}^e} &= \Theta \Delta p^o \frac{\partial \underline{\mathbf{n}}^o}{\partial \underline{\boldsymbol{\sigma}}} : \underline{\mathbf{C}} \\ \frac{\partial \mathbf{R}^{\varepsilon^o}}{\partial \Delta p^o} &= \underline{\mathbf{n}}^o \\ \frac{\partial \mathbf{R}^{\varepsilon^o}}{\partial \Delta \xi} &= \Theta \Delta p^o \frac{\underline{\mathbf{n}}^o}{\xi} \end{aligned}$$

Kinetics

$$\begin{aligned} \frac{\partial \mathbf{R}^\xi}{\partial \Delta \bar{\varepsilon}^e} &= \Delta t \frac{\partial \phi}{\partial f^\xi} \frac{\partial f^\xi}{\partial \underline{\boldsymbol{\sigma}}} \frac{\partial \underline{\boldsymbol{\sigma}}}{\partial \bar{\varepsilon}^e} \frac{\partial \bar{\varepsilon}^e}{\partial \Delta \bar{\varepsilon}^e} = \\ &= \Delta t \Theta \frac{n^\xi}{K^\xi} \left\langle \frac{f^\xi}{K^\xi} \right\rangle^{n^\xi-1} K_\sigma^\xi \left[\alpha \underline{\mathbf{I}} + (1-\alpha) A^{1/n} \left(\underline{\mathbf{n}}^a + J_2^a \frac{1}{n A_o} \frac{\partial A_o}{\partial \underline{\boldsymbol{\sigma}}} \right) \right] : \underline{\mathbf{C}} \\ \frac{\partial \mathbf{R}^\xi}{\partial \Delta p^a} &= \Delta t \frac{\partial \phi}{\partial f^\xi} \frac{\partial f^\xi(R^\xi)}{\partial \Delta p^a} = \Delta t \Theta \frac{n^\xi}{K^\xi} \left\langle \frac{f^\xi}{K^\xi} \right\rangle^{n^\xi-1} K_p^\xi n_p^\xi (p^a)^{n_p^\xi-1} \\ \frac{\partial \mathbf{R}^\xi}{\partial \Delta \bar{\varepsilon}^o} &= \Delta t \frac{\partial \phi}{\partial f^\xi} \frac{\partial f^\xi(R^\xi)}{\partial J_{\varepsilon^o}} \frac{\partial J_{\varepsilon^o}}{\partial \bar{\varepsilon}^o} \frac{\partial \bar{\varepsilon}^o}{\partial \Delta \bar{\varepsilon}^o} = -\Delta t \Theta \frac{n^\xi}{K^\xi} \left\langle \frac{f^\xi}{K^\xi} \right\rangle^{n^\xi-1} K_o^\xi n_o^\xi (J_{\varepsilon^o})^{n_o^\xi-1} \frac{2}{3} \frac{\bar{\varepsilon}^o}{J_{\varepsilon^o}} : \underline{\mathbf{n}}^o \\ \frac{\partial \mathbf{R}^\xi}{\partial \Delta \underline{\boldsymbol{\alpha}}^{a,o}} &= \Delta t \frac{\partial \phi}{\partial f^\xi} \frac{\partial f^\xi}{\partial \underline{\mathbf{X}}^a} \frac{\partial \underline{\mathbf{X}}^a}{\partial \underline{\boldsymbol{\alpha}}^{a,o}} : \frac{\partial \underline{\boldsymbol{\alpha}}^{a,o}}{\partial \Delta \underline{\boldsymbol{\alpha}}^{a,o}} = \\ &= \Delta t \Theta \frac{n^\xi}{K^\xi} \left\langle \frac{f^\xi}{K^\xi} \right\rangle^{n^\xi-1} K_\sigma^\xi (1-\alpha) A^{1/n} (-1) \left(\underline{\mathbf{n}}^a \frac{2}{3} C_k^{a,ao} + J_2^a \frac{1}{n A_a} \frac{\partial A_a}{\partial \underline{\mathbf{X}}} \frac{2}{3} C_k^{ao,a} \right) \\ \frac{\partial \mathbf{R}^\xi}{\partial \Delta \xi} &= -1 + \Delta t \Theta \frac{n^\xi}{K^\xi} \left\langle \frac{f^\xi}{K^\xi} \right\rangle^{n^\xi-1} \left[-K_{\xi_1} \left(\frac{\zeta}{1-\xi} \right) + K_{\xi_2} \left(\frac{1-\zeta}{\xi} \right) \right] \end{aligned}$$

Scale transition

$$\frac{\partial \mathbf{R}^{\beta^a}}{\partial \Delta \bar{\boldsymbol{\varepsilon}}^e} = \Delta p^a \frac{\partial \underline{\mathbf{n}}^a}{\partial \underline{\boldsymbol{\sigma}}} : \underline{\underline{\mathbf{C}}} \Theta$$

$$\frac{\partial \mathbf{R}^{\beta^a}}{\partial \Delta p^a} = \underline{\mathbf{n}}^a - D^a \underline{\boldsymbol{\beta}}^a$$

$$\frac{\partial \mathbf{R}^{\beta^a}}{\partial \Delta \underline{\boldsymbol{\beta}}^a} = -\underline{\underline{\mathbf{I}}} - \Theta D^a \Delta p^a \underline{\underline{\mathbf{I}}}$$

$$\frac{\partial \mathbf{R}^{\beta^a}}{\partial \Delta \underline{\boldsymbol{\alpha}}^{a,o}} = \Delta p^a \frac{\partial \underline{\mathbf{n}}^a}{\partial \underline{\mathbf{X}}^a} : \frac{2}{3} C_k^{a,ao} \Theta \underline{\underline{\mathbf{I}}}$$

$$\frac{\partial \mathbf{R}^{\beta^{m,o}}}{\partial \Delta \bar{\boldsymbol{\varepsilon}}^e} = \left(\frac{\partial \underline{\mathbf{n}}^m}{\partial \underline{\boldsymbol{\sigma}}} \Delta p^m + \frac{\partial \underline{\mathbf{n}}^o}{\partial \underline{\boldsymbol{\sigma}}} \Delta p^o \right) : \underline{\underline{\mathbf{C}}} \Theta$$

$$\frac{\partial \mathbf{R}^{\beta^{m,o}}}{\partial \Delta p^{m,o}} = \underline{\mathbf{n}}^{m,o} - D^{m,o} \underline{\boldsymbol{\beta}}^{m,o}$$

$$\frac{\partial \mathbf{R}^{\beta^{m,o}}}{\partial \Delta \underline{\boldsymbol{\beta}}^{m,o}} = -\underline{\underline{\mathbf{I}}} - \Theta D^{m,o} (\Delta p^m + \Delta p^o) \underline{\underline{\mathbf{I}}}$$

$$\frac{\partial \mathbf{R}^{\beta^{m,o}}}{\partial \Delta \underline{\boldsymbol{\alpha}}^{a,o,m}} = \Delta p^{o,o,m} \frac{\partial \underline{\mathbf{n}}^{o,o,m}}{\partial \underline{\mathbf{X}}^{o,o,m}} : \frac{2}{3} C_k^{oa,o,m} \Theta \underline{\underline{\mathbf{I}}}$$

$$\frac{\partial \mathbf{R}^{\beta^{m,o}}}{\partial \Delta \xi} = \Theta \Delta p^o \frac{\underline{\mathbf{n}}^o}{\xi}$$

Kinematic hardening

$$\frac{\partial \mathbf{R}^{\alpha^{a,m,o}}}{\partial \Delta \bar{\boldsymbol{\varepsilon}}^e} = \Delta p^{a,m,o} \frac{\partial \underline{\mathbf{n}}^{a,m,o}}{\partial \Delta \bar{\boldsymbol{\varepsilon}}^e}$$

$$\frac{\partial \mathbf{R}^{\alpha^{a,m,o}}}{\partial \Delta p^{a,m,o}} = \underline{\mathbf{n}}^{a,m,o} - \frac{3}{2} \frac{D_k^{a,m,o}}{C_k^{a,m,o}} \underline{\mathbf{X}}^{a,m,o}$$

$$\frac{\partial \mathbf{R}^{\alpha^{a,m,o}}}{\partial \Delta \underline{\boldsymbol{\alpha}}^{a,m,o}} = -\underline{\underline{\mathbf{I}}} + \Theta \left(-\frac{\partial \underline{\mathbf{n}}^{a,m,o}}{\partial \underline{\boldsymbol{\alpha}}^{a,m,o}} - D_k^{a,m,o} \underline{\underline{\mathbf{I}}} \right) \Delta p^{a,m,o}$$

$$\frac{\partial \mathbf{R}^{\alpha^a}}{\partial \Delta \underline{\boldsymbol{\alpha}}^o} = \Theta \left(-\frac{\partial \underline{\mathbf{n}}^a}{\partial \underline{\mathbf{X}}^a} - \frac{3}{2} \frac{D_k^a}{C_k^a} \underline{\underline{\mathbf{I}}} \right) \Delta p^a : \frac{2}{3} C_k^{ao} \underline{\underline{\mathbf{I}}}$$

$$\frac{\partial \mathbf{R}^{\alpha^o}}{\partial \Delta \underline{\boldsymbol{\alpha}}^a} = \Theta \left(-\frac{\partial \underline{\mathbf{n}}^o}{\partial \underline{\mathbf{X}}^o} - \frac{3}{2} \frac{D_k^o}{C_k^o} \underline{\underline{\mathbf{I}}} \right) \Delta p^o : \frac{2}{3} C_k^{oa} \underline{\underline{\mathbf{I}}}$$

$$\frac{\partial \mathbf{R}^{\alpha^o}}{\partial \Delta \xi} = \Theta \Delta p^o \frac{\underline{\mathbf{n}}^o}{\xi}$$

Appendix C

Code

C.1 Programs, Codes, Libraries Related to the Topic

Artificial microstructure generation

- Neper: Quey et al. 2011 - *C++* code available on github, multiscale tessellation, supports periodic boundary conditions, mesh optimization, grain size statistics. <http://neper.sourceforge.net/>
- Dream3D: Groeber et al. 2014 - Program with GUI, supports non-convex meshing and a lot of statistics, no periodic boundary conditions
- MBuilder - Voxel mesh
- Alternatively combinations of codes can be used e.g. Voro++ to generate the geometry/tessellation and Gmsh to mesh it. For meshing also the CUBIT geometry and mesh generation toolkit developed in the Sandia National Laboratories seems to be very powerful.
- The geometries for the ellipsoidal inclusions have been produced using FreeCad. It supports python scripting. <https://www.freecadweb.org/>

EBSD data evaluation

- ARPGE: Cayron 2007 - python executable for PAG reconstruction (personal copy from the author via email request).
- MTEX: Hielscher et al. 2008 - matlab program EBSD data evaluation, code on github
- jtex / atom - Texture and Orientation imaging program "J.-J. Fundenberger, B. Beausir, Université de Lorraine - Metz, 2015, JTEX - Software for Texture Analysis, <http://www.atex-software.eu/> (formerly jtex-software)

Crystallography (mostly martensite specific)

- Martensite-Calculator - matlab code written for martensitic transformation strains during this thesis. Hosted on github: https://github.com/ManuelPetersmann/Martensite_Calculator.
- PTCLab, Gu et al. 2016 - program for many crystallographic compatibility calculations on the lattice level and their visualization. Also some PTMC models e.g. double shear solution,
- Lath Martensite: K. Koumatos et al. 2018: matlab toolbox for the calculation of martensitic microstructure considering hierarchical twinning, Available on mathworks.
- STABIX - Slip Transmission Matlab toolbox: Mercier et al. 2015, can be used in conjunction with MTEX to investigate OIM data <https://stabix.readthedocs.io/en/latest/references.html>
- VESTA, Momma et al. 2011 - programm for visualization of atomic arrangements

Programs to for the calculation of the structural stretch tensor

- OptLat, K. Koumatos et al. 2016 - matlab program for the calculation of the structural stretch tensor in orthogonal bases available on MathWorks File Exchange
- Chen et al. 2016 structrans: <http://www.structrans.org> - online calculation of structural stretch tensor U^S (e.g. Bain strain)

Selected finite element codes for materials modelling

- Z-set (Z-mat, Z-opt, Z-cracks, Z-sim)
- Code Aster - (supports Z-set, and free CAE / GUI Salome Mecca)
- Damask (Düsseldorf Advanced Modelling and Simulation Kit) - open source FFT solver and crystal plasticity routines.
- Abaqus, Feap (free, "light" version of Abaqus), Deal2, and many more...

C.2 Eshelby Tensor Ellipsoid - Matlab

```

1 function S = eshelby_tensor_ellipsoid( nu, a,b,c )
2 % call: eshelby_tensor_ellipsoid(nu,a,b,c)
3 % This function takes the Poissons ratio...nu and the half axis lengths
4 % of an ellipsoid: a > b > c and calculates the Eshelby tensor - see Eshelby 1957

6 a2 = a^2;
7 b2 = b^2;
8 c2 = c^2;
9 l2 = [a2,b2,c2];

11 theta = 1./sin( sqrt(1.- c2/a2) );
12 k = sqrt(a2 - b2) / sqrt(a2 - c2);

14 % solve incomplete elliptic integral of the second kind E(theta,k)
15 % https://de.mathworks.com/help/symbolic/mupad_ref/elliptice.html
16 E = ellipticE(theta,k);

18 % solve incomplete elliptic integral of the first kind F(theta,k)
19 % https://de.mathworks.com/help/symbolic/mupad_ref/ellipticf.html
20 F = ellipticF(theta,k);

22 pre = 4*pi*a*b*c;
23 Q = 3./(8*pi*(1.-nu));
24 R = (1.-2*nu) / (8*pi*(1.-nu));

26 %% ellipsoid
27 Ia = pre * (F-E) / ( (a2-b2)*sqrt(a2-c2) );
28 Ic = pre / ( (b2-c2)*sqrt(a2-c2) ) * ( b*sqrt(a2-c2) / (a*c) - E);
29 Ib = 4*pi - Ia - Ic;
30 I_i = [Ia, Ib, Ic];

32 % I_ij = [ Iab, Iac, Iba, Ibc, Ica, Icb ]
33 % indizes:  1  2  3  4  5  6
34 index = 0;
35 for i = 1:3
36     for j = 1:3
37         if abs(i-j) > 1.e-3 % if i-not-j
38             index = index + 1;
39             I_ij(index) = (I_i(j) - I_i(i) ) / (3*( l2(i) - l2(j) ) );
40         end
41     end
42 end

44 I_kk = [I_aa, I_bb, I_cc];
45 pre2 = 3.*pi / (3.*a2);
46 for k = 1:3
47     I_kk(k) = pre2 - I_ij( 2*k-1 ) - I_ij( 2*k );
48 end

50 %% elliptic cylinder after original paper eshelby 1957
51 % Ia = 4*pi*b / (a+b);
52 % Ib = 4*pi*a / (a+b);
53 % Ic = 0;
54 % I_ab = 4*pi/(3*(a+b)); % not sure in paper - could be 4*pi/3*(a+b)...
55 %
56 % I_aa = 4*pi/(3*a^2) - I_ab; % not sure - could be 4*pi/(3*a^2 - I_ab);
57 % I_bb = 4*pi/(3*b^2) - I_ab; % deto

```

```

58 % I_ac = 0.;
59 % I_bc = 0.;
60 % I_cc = 0.;
61 % I_kk = [I_aa, I_bb, I_cc];
62 % I_ij = [ I_ab, I_ac, 0, I_bc, 0, 0 ];

65 S = zeros(3,3,3,3); % all values are initialized with zero
66 % [ x1, x2, x3, x4, x5 ] = deal( 8 ); is equal to x1 = x2 = x3 = 8
67 S(1,1,1,1) = Q*a2*I_kk(1) + R*Ia;
68 S(2,2,2,2) = Q*b2*I_kk(2) + R*Ib;
69 S(3,3,3,3) = Q*c2*I_kk(3) + R*Ic;
70 % relations of the form S1122 = S2211 are not valid - check!
71 S(1,1,2,2) = Q* b2* I_ij(1) - R*Ia;
72 S(1,1,3,3) = Q* c2* I_ij(2) - R*Ia;
73 S(2,2,1,1) = Q* a2* I_ij(3) - R*Ib;
74 S(2,2,3,3) = Q* c2* I_ij(4) - R*Ib;
75 S(3,3,1,1) = Q* a2* I_ij(5) - R*Ic;
76 S(3,3,2,2) = Q* b2* I_ij(6) - R*Ic;
77 %
78 % The Eshelby tensor satisfies minor symmetries
79 % S_ijkl = S_jikl = S_ijlk
80 % but in general no major symmetries
81 % S_ijkl not S_klij - see e.g. Bower solidmechanics, Eshelby1957
82 %
83 [ S(1,2,1,2) , S(2,1,1,2) ] = deal( 0.5*Q*(a2+b2)*I_ij(1) + 0.5*R*(Ia + Ib) );
84 % S(1,2,2,1), S(2,1,2,1) - would have major symmetry

86 [ S(2,3,2,3) , S(3,2,2,3) ] = deal( 0.5*Q*(b2+c2)*I_ij(4) + 0.5*R*(Ib + Ic) );
87 % S(2,3,3,2) , S(3,2,3,2) - would have major symmetry

89 [ S(1,3,1,3) , S(3,1,1,3) ] = deal( 0.5*Q*(c2+a2)*I_ij(5) + 0.5*R*(Ic + Ia) );
90 % S(1,3,3,1) , S(3,1,3,1) - would have major symmetry
91 %
92 % Coefficients coupling an extension and a shear (S1112, S1123, S2311 ...)
93 % or one shear to another (S1223...) are zero. However same shears S1212 not 0!

95 voigt = [ S(1,1,1,1) , S(1,1,2,2) , S(1,1,3,3) , S(1,1,1,2) , S(1,1,1,3) , S(1,1,2,3) ;
96           S(2,2,1,1) , S(2,2,2,2) , S(2,2,3,3) , S(2,2,1,2) , S(2,2,1,3) , S(2,2,2,3) ;
97           S(3,3,1,1) , S(3,3,2,2) , S(3,3,3,3) , S(3,3,1,2) , S(3,3,1,3) , S(3,3,2,3) ;
98           S(1,2,1,1) , S(1,2,2,2) , S(1,2,3,3) , S(1,2,1,2) , S(1,2,1,3) , S(1,2,2,3) ;
99           S(1,3,1,1) , S(1,3,2,2) , S(1,3,3,3) , S(1,3,1,2) , S(1,3,1,3) , S(1,3,2,3) ;
100          S(2,3,1,1) , S(2,3,2,2) , S(2,3,3,3) , S(2,3,1,2) , S(2,3,1,3) , S(2,3,2,3) ];
101 end

```

C.3 Selected Zebfront Code

C.3.1 Micro-Meso Model Dislocation Densities Explicit in Zebfront

```

1 @Class Disdens2 : BASIC_NL_BEHAVIOR, BASIC_SIMULATOR {
2   @Name Disdens2;
3   @SubClass ELASTICITY elasticity;
4   @Coefs dgamma0,m,r0,mu;
5   @Coefs b111,disdens_forest_ref,disdens_start;
6   @Coefs K1,k0,kappa0,p0,K;
7   @Coefs a_ref,a_hirth,a_gliss,a_colin;
8   @tVarInt eel;
9   @sVarInt evcum;
10  @sVarInt plast_diss;
11  @sVarInt disdens_tot;
12  @sVarInt juncdens_tot;
13  @vVarInt gvcum [Nsyst];
14  @vVarInt disdens [Nsyst];
15  @vVarInt juncdens [Nsyst];
16  @tVarAux ev;
17  @vVarAux tau [Nsyst];
18  @sVarAux stored_ener;
19  @sVarAux sener;
20  @Criterion yield;
21  int Ngrain,Nsyst;
22  STRING forient,fsyst;
23  //void calc_torient(double,double,double,int);
24  void calc_torient();
25  void calc_hh(SMATRIX& hh,MATRIX& ss);
26  bool isforest(double);
27  MARRAY<TENSOR2> torient;
28  MARRAY<TENSOR2> torientg;
29  //@tVarUtil sigloc;
30  @tVarUtil devloc;
31  @tVarUtil devi;
32  SMATRIX hh;
33  MATRIX ss;
34  VECTOR densforest;
35  VECTOR l0;
36  VECTOR cf;
37 };

39 @UserRead {
40   if (str=="**system_number") Nsyst=file.getint();
41   else if (str=="**system_file") fsyst= file.getSTRING();
42   else return FALSE;
43   if(!file.ok)return FALSE;
44   return TRUE;
45 }

47 @SetUp {
48   int isyst,jsyst;
49   hh.resize(Nsyst);
50   ss.resize(12,6); // initialize matrix for hardcoded f.c.c. slip systems
51   densforest.resize(Nsyst);
52   l0.resize(Nsyst);
53   cf.resize(Nsyst);
54   calc_coef();

```

```

55  calc_hh(hh,ss);
56  Out <<"print ss "<<ss<<endl;
57  Out <<fsyst<<endl;
58  torientg.resize(Nsyst);
59  torient.resize(Nsyst);
60 //  ASCII_FILE syst; syst.open(fsyst());
61 //  Out <<"print syst.ok"<<(syst.ok)<<endl;
62 //  if (syst.ok) {
63  Out <<"Using hardcoded "<<Nsyst<< "Octahedral slip systems"<<fsyst<<endl;
64  TENSOR2 mm(tsz());
65  double n1,n2,n3,l1,l2,l3,nmag,lmag;
66  for(isyst=0;isyst<Nsyst;isyst++){
67      //density initialization here- does not work- NAN
68      //disdens[isyst] = disdens_start/12.;
69      //juncdens[isyst] = (disdens_start*kappa0)/12.;
70      //n1=syst.getdouble(); n2=syst.getdouble(); n3=syst.getdouble();
71      //l1=syst.getdouble(); l2=syst.getdouble(); l3=syst.getdouble();
72      n1 = ss(isyst,0); n2 = ss(isyst,1); n3 = ss(isyst,2);
73      l1 = ss(isyst,3); l2 = ss(isyst,4); l3 = ss(isyst,5);
74      lmag=sqrt(l1*l1 + l2*l2 + l3*l3); l1/=lmag; l2/=lmag; l3/=lmag;
75      nmag=sqrt(n1*n1 + n2*n2 + n3*n3); n1/=nmag; n2/=nmag; n3/=nmag;
76 //      if(!syst.ok) ERROR("error reading "+fsyst+" line "+itoa(isyst+1));
77      mm[0]=n1*l1;          // m11
78      mm[1]=n2*l2;          // m22
79      mm[2]=n3*l3;          // m33
80      mm[3]=(n1*l2 + n2*l1)/M_SQRT2; // m12 multiplied by sqrt(2)
81      mm[4]=(n2*l3 + n3*l2)/M_SQRT2; // m23 multiplied by sqrt(2)
82      mm[5]=(n3*l1 + n1*l3)/M_SQRT2; // m31 multiplied by sqrt(2)
83      torientg[isyst]=mm; }
84 //  Out<<"Read OK"<<endl;
85 //  }
86 }

88 @StrainPart {
89  sig = *elasticity*eel;
90  m_tg_matrix=*elasticity;
91  ev=eto-eel;
92 }

94 @Derivative {
95  int isyst,jsyst,ksyst,lsyst,msyst,nsyst;
96  double crit,stmx;
97  double deveq,cutoffl0,cutofftot;
98  double rsum_forest,rsum_copla,rsum_all,pkb,r_tot,active,cf_coef;
99  double a_gvcum,dd1,dd2,jd1,jd2;
100  devi = 0.;

102  sig = *elasticity*eel;
103  ev=eto-eel;

105  cf_coef = log(1./(b111*sqrt(a_ref*disdens_forest_ref)));
106  // determine dislocation density for line tension correction EQ 3 in Kubin,Devincre,Hoc 2008 Acta
107  for(ksyst=0;ksyst<Nsyst;ksyst++){
108      densforest[ksyst] = 0.;
109      for(lsyst=0;lsyst<Nsyst;lsyst++){
110          if(isforest(hh(ksyst,lsyst))){ densforest[ksyst] += (disdens[lsyst]+disdens_start/12.); }
111      }
112      cf[ksyst] = 0.2 + 0.8*(log(1./(b111*sqrt(a_ref*densforest[ksyst]))) / cf_coef);
113      // See EQ (4) Kubin,Devincre,Hoc 2008 Acta
114  }

```

```

116  pkb = p0 * k0 / b111;
117  active=0;
118  devloc=0.;
119  cutofftot = 0.;
120  for(isyst=0;isyst<Nsyst;isyst++){
121      rsum_forest=0.;
122      rsum_copla=0.;
123      rsum_all=0.;
124      dd1 = disdens[isyst] + disdens_start/12.;
125      // junction density about 30% of disdens - see Devincre 2008 Acta
126      jd1 = juncdens[isyst] + (disdens_start*kappa0)/12.;
127      for(jsyst=0;jsyst<Nsyst;jsyst++){
128          dd2 = disdens[jsyst] + disdens_start/12.;
129          jd2 = juncdens[jsyst] + (disdens_start*kappa0)/12.;
130          if(fabs(hh(isyst,jsyst)-(a_ref-0.001))<1.e-9){
131              //sum over coplanar interactions
132              rsum_copla +=sqrt(hh(isyst,jsyst)*dd2);
133          }
134          if(isforest(hh(isyst,jsyst))){
135              rsum_forest+=cf[isyst]*sqrt(hh(isyst,jsyst)*dd2);
136              rsum_all +=cf[isyst]*sqrt(hh(isyst,jsyst)*dd2);
137              l0[isyst]+= cf[isyst]*sqrt(hh(isyst,jsyst)*(dd2+jd2));
138          }
139          else{
140              rsum_all += sqrt(hh(isyst,jsyst)*dd2);
141              l0[isyst]+= sqrt(hh(isyst,jsyst)*(dd2+jd2));
142          }
143      }
144      tau[isyst]= sig | torientg[isyst];
145      rsum_all = rsum_all*mu*b111;
146      r_tot = r0 + rsum_all;
147      crit=fabs(tau[isyst]) - r_tot;

149      cutofff10 = (dd1 / (dd1+jd1)) / l0[isyst];
150      cutofftot += cutofff10;
151      if(crit<=0.){dgvcum[isyst]=0;}
152      else{
153          active+=1;
154          if((tau[isyst])>0.)stmx=1.; else stmx=-1.;
155          dgvcum[isyst] = dgamma0*pow((crit/r_tot),(1./m));
156          // dalpha[isyst]=dgvcum[isyst]*(stmx-d*alpha[isyst]); //dalpha[isyst]=0;
157          devloc += stmx*dgvcum[isyst]*torientg[isyst];
158          // Forest densities
159          // EQ 15 Kubin,Devincre,Hoc Acta 2008
160          ddisdens[isyst] = pkb * cutofff10 * rsum_forest*(1.-(jd1/densforest[isyst]))*fabs( dgvcum[isyst] );
161          // Self-hardening and coplanar interactions:
162          ddisdens[isyst] += (sqrt(a_ref*dd1) + rsum_copla) * fabs( dgvcum[isyst] ) / (b111*K1);
163          // total density (sum over all) and stored_energy (negative in dissipation inequality)
164          ddisdens_tot += ddisdens[isyst];
165      }
166  }
167  deveq=(devloc|devloc)/1.5; deveq= (deveq>0.0) ? sqrt(deveq) : 0.0;
168  devi=devloc;
169  devcum=sqrt((devi|devi)/1.5);
170  stored_ener = mu*pow(b111,2.)*disdens_tot * 6.; // see Begau,Hartmaier 2015Arxiv
171  dplast_diss += (sig|devloc);
172  sener = 0.5*(sig|eel);

174  // EVOLUTION OF JUNCTION DENSITIES
175  // MUST BE DONE SEPERATELY BECAUSE THE ACITIVE SYSTEMS & dgvcum HAVE TO BE DETERMINED BEFORE
176  //cout<<"active = "<<active<<endl;

```

```

177 for(msyst=0;msyst<Nsyst;msyst++){
178     dd1 = disdens[msyst] + disdens_start/12.;
179     jd1 = juncdens[msyst] + (disdens_start*kappa0)/12.;
180     a_gvcum = 0.;
181     for(nsyst=0;nsyst<Nsyst;nsyst++){
182         if(isforest(hh(msyst,nsyst))){
183             a_gvcum += fabs( dgvcum[msyst] ) * cf[nsyst]*sqrt(hh(msyst,nsyst));
184         }
185         else{
186             a_gvcum+= fabs( dgvcum[msyst] ) * sqrt(hh(msyst,nsyst));
187         }
188     }
189     // Evolution of Junctions formed by mobile forest dislocs
190     // EQ 16 Kubin,Devincre,Hoc Acta 2008
191     if(active > 1){ //kappa0*dd1 = jd1 !
192         djuncdens[msyst] = kappa0*dd1*(pkb / 10[msyst])* a_gvcum *(1.-jd1/((active-1)*dd1));
193     }
194     djuncdens_tot += djuncdens[msyst];
195 }

197 if(devcum==0.) resolve_flux_grad(*elasticity, deel, deto);
198 else resolve_flux_grad(*elasticity, deel, deto, devi);
199 } // end @Derivative

201 bool Disdens2::isforest(double a){
202     int i;
203     // forest interactions: Hirth          Lomer          glissle
204     // small correction to distinguish a_lomer as a forest-/junction forming type
205     // from a_ref (however same interaction value)
206     if( (fabs(a-a_hirth<1.e-9)) && (fabs(a-(a_ref+0.001)<1.e-9)) && (fabs(a-a_gliss<1.e-9)) ){
207         return true;}
208     else{
209         return false;
210     }
211 }

213 void Disdens2::calc_hh(SMATRIX& hh,MATRIX& ss){
214     int i,j;
215     for (i=0;i<Nsyst;i++) hh(i,i)=a_ref; // self interaction

217     hh(0,1) =hh(0,2) = hh(1,2) = hh(3,4) =hh(3,5)= hh(4,5) = hh(6,7) =hh(6,8) =
218     hh(7,8) = hh(9,10)= hh(9,11)= hh(10,11)= a_ref-0.001; // coplanar interaction

220     hh(0,3) = hh(1,6) = hh(2,9) = hh(4,11) = hh(5,7) = hh(8,10) = a_colin;

222     hh(0,8) =hh(0,10) = hh(1,4) =hh(1,11) = hh(2,5)= hh(2,7) = hh(3,8) =hh(3,10) =
223     hh(4,6) = hh(5,9)= hh(6,11) = hh(7,9) = a_hirth;

225     hh(0,4) =hh(0,5) =hh(0,6) =hh(0,9) = hh(1,3) =hh(1,7) =hh(1,8) =hh(1,9) =
226     hh(2,3) =hh(2,6) =hh(2,10) =hh(2,11) = hh(3,7) =hh(3,11) = hh(4,7) =hh(4,9) =hh(4,10) =
227     hh(5,6) =hh(5,8) =hh(5,11) = hh(6,10) = hh(7,10) = hh(8,9) =hh(8,11) = a_gliss;

229     hh(0,7) =hh(0,11) = hh(1,5) =hh(1,10) = hh(2,4) =hh(2,8) = hh(3,6) =hh(3,9) =
230     hh(4,8) = hh(5,10) = hh(6,9) = hh(7,11) = (a_ref+0.001); //Lomer lock

232     for (i=0;i<Nsyst;i++){ for (j=i+1;j<Nsyst;j++){ hh(j,i) = hh(i,j); }}

234     // hard coded slip systems for f.c.c.
235     ss(0,0) = ss(0,1) = ss(0,2) = ss(0,5) = ss(1,0) = ss(1,1) = ss(1,2) = ss(1,5) = ss(2,0) =
236     ss(2,1) = ss(2,2) = ss(2,4) = ss(3,0) = ss(3,2) = ss(3,5) = ss(4,0) = ss(4,2) = ss(4,4) =
237     ss(4,5) = ss(5,0) = ss(5,2) = ss(5,3) = ss(5,4) = ss(6,1) = ss(6,2) = ss(6,5) = ss(7,1) =

```

```

238  ss(7,2) = ss(7,3) = ss(7,4) = ss(8,1) = ss(8,2) = ss(8,3) = ss(8,5) = ss(9,0) = ss(9,1) =
239  ss(9,4) = ss(10,0) = ss(10,1) = ss(10,3) = ss(10,5) = ss(11,0) = ss(11,1) = ss(11,4) =
240  ss(11,5) = 1.;
241  ss(0,4) = ss(1,3) = ss(2,5) = ss(3,4) = ss(4,3) = ss(5,5) = ss(6,3) = ss(7,5) = ss(8,4) =
242  ss(9,5) = ss(10,4) = ss(11,3) = 0.;
243  ss(0,3) = ss(1,4) = ss(2,3) = ss(3,1) = ss(3,3) = ss(4,1) = ss(5,1) = ss(6,0) = ss(6,4) =
244  ss(7,0) = ss(8,0) = ss(9,2) = ss(9,3) = ss(10,2) = ss(11,2) = -1.;
245 }

```

Coefficient input file:

```

1  ***material
2  *rotation
3  x1 1. 1. 0.
4  x2 0. 0. 1.
5  *integration runge_kutta 1.e-4 1.e-4
6  % default is 1.e-3
7  ***save_energies
8  ***behavior Disdens2
9  **elasticity isotropic
10  young 174800.
11  poisson 0.33
12  **system_number 12
13  **system_file octa.sys
14  **model_coef
15  mu 73000.
16  dgamma0 0.001
17  m 0.01
18  r0 38.
19  b111 2.547e-7
20  disdens_forest_ref 1.e6
21  disdens_start 1.e2
22  kappa0 0.225
23  K1 180.
24  k0 1.08
25  p0 0.117
26  a_ref 0.122
27  a_hirth 0.07
28  a_gliss 0.137
29  a_colin 0.625
30  ***return

```

C.3.2 Macro Model Explicit and Implicit in Zebront

```

1  #include <iostream.h>
2  #include <string.h>
3  #include <Elasticity.h>
4  #include <Basic_nl_behavior.h>
5  #include <Basic_nl_simulation.h>
6  #include <External_parameter.h>
7  #include <stdlib.h>
8  #include <Print.h>
9  #define Id TENSOR2::unity(tsz())

```



```

11 //-----
12 //              Mean Field Model for TRIP                               -
13 //              Formalism and explicit code (@Derivative): M. Fischlschweiger 2012   -
14 //              Implicit implementation (@CalcGradF): M. Petersmann - Jan 2016     -
15 //-----

17 @Class MARAGING_full : BASIC_NL_BEHAVIOR, BASIC_SIMULATOR {
18 @Name      MARAGING_full;
19 @SubClass  ELASTICITY elasticity;
20 @Coefs     K, mu;
21 // kinetics and orientation
22 @Coefs     K_o, n_o;
23 @Coefs     K_T, K_P, K_Z, K_ZZ, K_S, B, alpha_t;
24 @Coefs     K_t, n_tt;
25 @Coefs     R0_t;
26 @Coefs     b_o, R_o0, H_o;
27 @Coefs     n_p, n_ot;
28 @Coefs     delta;
29 @Coefs     k_0, n_asym;
30 @Coefs     T0;
31 // plasticity
32 @Coefs     K_a, n_a;
33 @Coefs     K_m, n_m;
34 @Coefs     R0_a, R0_m;
35 @Coefs     Q_a, Q_m;
36 @Coefs     b_a, b_m;
37 // backstresses
38 @Coefs     C_a, D_a;
39 @Coefs     C_ao;
40 @Coefs     C_m, D_m;
41 @Coefs     C_o, D_o;
42 // scale transition
43 @Coefs     D_b_a, D_b_mo;

45 @tVarInt   eel;
46 @tVarInt   e_o;
47 @sVarInt   z;
48 @sVarInt   eocum;
49 @sVarInt   evcum_a, evcum_m;
50 @tVarInt   alpha_a, alpha_m, alpha_o;
51 @tVarInt   beta_a, beta_mo;

53 @Implicit

55 @tVarAux   norm_a, norm_m, norm_o, norm_o_dz, norm_J3_o, norm_J2_o, dAo_ds, dAon_ds;
56 @tVarAux   sigma_a, sigma_m;
57 @tVarAux   m1, m2, m3, z2, z3;
58 @tVarAux   devi, devo, ev;
59 @sVarAux   f_o, f_t, f_t1;
60 @sVarAux   Ao, R_t, R_a, R_m, R_o, J2_o_aux, J3_o_aux, Jeo_aux, J_a_aux;
61 @sVarAux   z1, test, dt2, hilf, TT;

63 Zfstream  my_file;
64 int  iter;
65 int  glob_counter;

67 static double fz_alpha_a_pert(MARAGING_full* b, const TENSOR2& );

69 static double fz(MARAGING_full* b, const TENSOR2& sig);
70 static double fz_eo_pert(MARAGING_full* b, const TENSOR2& e_o);

```

```

72 static double ff_o(MARAGING_full*, const TENSOR2& sig);
73 static double fp_o(MARAGING_full* b, const TENSOR2& e_o);

75 static TENSOR2 fnorm_o(MARAGING_full*, const TENSOR2& sig);
76 static TENSOR2 fnorm_o_part1(MARAGING_full*, const TENSOR2& sig);

78 static TENSOR2 dI3(MARAGING_full*, const TENSOR2& t);
79 static TENSOR4 d2I3(MARAGING_full*, const TENSOR2& t);

81 TENSOR4 d2_pert(const TENSOR2& e, TENSOR2 (*) (MARAGING_full*, const TENSOR2& ));
82 TENSOR2 d_pert(const TENSOR2& e, double (*func)(MARAGING_full*, const TENSOR2& ));
83 double s_pert_s(const double& e, double (*) (MARAGING_full*, double) );
84 double test1(const double& e);
85 double test2(const TENSOR2& e);

87 @Implicit
88 };

90 @PostStep {
91   ev = eto - eel;
92   sig = *elasticity*eel;
93   if (integration&LOCAL_INTEGRATION::THETA_ID) { // calculation of consistent tgmatt
94     TENSOR4 tmp(psz,f_grad,0,0);
95     if (Dtime>0.0) m_tg_matrix=*elasticity*tmp;
96     else          m_tg_matrix=*elasticity;
97   }
98   else{
99     m_tg_matrix=*elasticity;
100  }
101 }

103 @PreStep {
104   iter = 0;
105 }

107 @Derivative {
108   int rank_of_temp =EXTERNAL_PARAM::rank_of("temperature");
109   double T>(*curr_mat_data->param_set())[rank_of_temp];
110   double Tini>(*curr_mat_data->param_set_ini())[rank_of_temp];

112   sig=*elasticity*eel;

114   sigma_a = sig +      z * mu * (beta_mo - beta_a) + Id * K * z * delta/3.;
115   sigma_m = sig - (1.-z) * mu * (beta_mo - beta_a) - Id * K * (1.-z) * delta/3.;

117   double CCa=C_a/1.5; double CCm=C_m/1.5; double CCao=C_ao/1.5; double CCo=C_o/1.5;
118   TENSOR2 X_a      = CCa*alpha_a + CCao*alpha_o;
119   TENSOR2 X_m      = CCm*alpha_m;
120   TENSOR2 X_o      = CCao*alpha_a + CCo*alpha_o;

122   TENSOR2 sigeff_a = deviator(sigma_a) - X_a;
123   TENSOR2 sigeff_o = deviator(sigma_a) - X_o;
124   TENSOR2 sigeff_m = deviator(sigma_m) - X_m;

126   R_a      = R0_a + Q_a*( 1.0-exp(-b_a*evcum_a) );
127   R_m      = R0_m + Q_m*( 1.0-exp(-b_m*evcum_m) );

129   double Jeo  = sqrt(2./3.*(e_o|e_o));
130   Jeo_aux = Jeo;
131   R_o      = R_o0 + H_o*pow(Jeo,b_o)*pow(z,2.);

```

```

133 double eps1 = 1.e-12;
134 double eps = 0.0;
135 if (z < eps1){
136     R_t      = R0_t - K_Z*(log(1.-eps1)) + K_ZZ*log(eps1) + K_T*pow(Jeo,n_ot) - K_P*pow(evcum_a,n_p);
137 }
138 else if (z<(1.-eps1)){
139     R_t      = R0_t - K_Z*(log(1.-z)) + K_ZZ*log(z) + K_T*pow(Jeo,n_ot) - K_P*pow(evcum_a,n_p);
140 }
141 else{
142     R_t      = R0_t - K_Z*(log(eps1)) + K_ZZ*log((1.-eps1)) + K_T*pow(Jeo,n_ot) - K_P*pow(evcum_a,n_p);
143 }
144 if(R_t < 0.0) R_t = 0.0;

146 double J_a      = sqrt(1.5*(sigeff_a | sigeff_a));
147 J_a_aux = J_a;
148 double I_a      = trace(sigma_a);

150 double J2_o      = sqrt(1.5*(sigeff_o|sigeff_o));
151 J2_o_aux = J2_o;
152 double J2_o2     = pow(J2_o,2.);
153 double J2_o3     = pow(J2_o,3.);
154 double J2_o4     = pow(J2_o,4.);
155 double J2_o5     = pow(J2_o,5.);
156 double J3_o      = sigeff_o.determin();
157 J3_o_aux = J3_o;

159 if (J2_o > 0.0){
160     Ao = 1.0+k_0*J3_o/J2_o3;
161 }
162 else{
163     Ao = 1.;
164 }
165 double nAo_inv   = 1.0/(Ao*n_asym);
166 double Aon       = pow(Ao,(1.0/n_asym));

168 TENSOR2 titi = syme(sigeff_o * sigeff_o);
169 norm_J3_o = titi - (1./3.)*trace(titi)*Id;

171 f_t=0.;
172 f_o=0.;
173 if (J2_o > 0.){
174     f_t = K_S*(alpha_t*I_a + (1.-alpha_t)*Aon*J_a) - B*(T-T0) - R_t;
175     f_o = J2_o*z*Aon - R_o;

177     norm_J2_o = (1.5/J2_o)*sigeff_o;
178     dAo_ds = (k_0/J2_o3)*(norm_J3_o - (3.*J3_o/J2_o)*norm_J2_o);
179     dAon_ds = (Aon*nAo_inv)*dAo_ds;
180     norm_o_dz = Aon*norm_J2_o + J2_o*dAon_ds;
181     norm_o = z*norm_o_dz;
182 }
183 else {
184     f_t = K_S*alpha_t*I_a - B*(T-T0) - R_t;
185     norm_J2_o = 0.;
186     dAo_ds = 0.;
187     dAon_ds = 0.;
188     norm_o_dz = 0.;
189     norm_o = 0.;
190 }

192 double f_a      = J_a - R_a;

```

```

193 double J_m      = sqrt(1.5*(sigeff_m|sigeff_m));
194 double f_m      = J_m - R_m;

196 if (J_a > eps){
197     norm_a      = (1.5/J_a)*sigeff_a;
198 }
199 else {
200     norm_a      = 0.;
201 }
202 if (J_m > eps){
203     norm_m      = (1.5/J_m)*sigeff_m;
204 }
205 else {
206     norm_m      = 0.;
207 }

209 //Strain parts
210 devcum = devcum_a = devcum_m = dz = 0.;
211 dalpha_a = dalpha_m = dalpha_o = 0.;
212 dalpha_m = 0.0;
213 dbeta_a = dbeta_mo=0.;
214 devi = de_o = 0.;

216 if (f_a>0.) {
217     devcum_a      = pow(f_a/K_a,n_a);
218     if (CCa > 0.) { dalpha_a      = devcum_a*(norm_a - (D_a/CCa)*X_a); }
219     dbeta_a      = devcum_a*(norm_a - D_b_a*beta_a);
220 }
221 if (f_m>0.){
222     devcum_m      = pow(f_m/K_m,n_m);
223     if (CCm>0.) { dalpha_m      = devcum_m*(norm_m - (D_m/CCm)*X_m); }
224     dbeta_mo      = devcum_m*norm_m - (D_b_mo*devcum_m)*beta_mo;
225 }

227 if ((f_o>0.)&&(z<0.99)&&(z>0.)){
228     deocum      = pow(f_o/K_o,n_o);
229     if (CCo>0.){ dalpha_o      = deocum*(norm_o - (D_o/CCo)*X_o); }
230     de_o        = deocum*norm_o;
231     dbeta_mo      = deocum*norm_o - (D_b_mo*deocum)*beta_mo;
232 }

234 if ((f_t>0.)&&(z<=1.0)) {
235     dz = pow(f_t/K_t,n_tt);
236 }

238 //Strain formulation
239 devi= (devcum_m*z)*norm_m + (devcum_a*(1.0-z))*norm_a;
240 devo= devi + (dz*delta/3.)*Id + e_o*dz;
241 resolve_flux_grad(*elasticity,deel,deto,devo);
242 }

245 @CalcGradF {

247 f_vec_eel -= deto;

249 TENSOR4 dn_o_ds, dn_o_dX, dn_o_dsig;

251 int rank_of_temp =EXTERNAL_PARAM::rank_of("temperature");
252 double T=(*curr_mat_data->param_set())[rank_of_temp];
253 double Tini=(*curr_mat_data->param_set_ini())[rank_of_temp];

```

```

255 ELASTICITY& E=*elasticity;
256 sig = E*eel; // Update stress tensor

258 double tdv_o = theta*deocum;
259 double tdz   = theta*dz;
260 double tdv_a = theta*devcum_a;
261 double tdv_m = theta*devcum_m;

263 sigma_a      = sig +      z * mu * (beta_mo - beta_a) + Id * K * z * delta/3.;
264 sigma_m      = sig - (1.-z) * mu * (beta_mo - beta_a) - Id * K * (1.-z) * delta/3.;

266 double CCa=C_a/1.5; double CCm=C_m/1.5; double CCao=C_ao/1.5; double CCo=C_o/1.5;

268 TENSOR2 X_a      = CCa*alpha_a + CCao*alpha_o;
269 TENSOR2 X_m      = CCm*alpha_m;
270 TENSOR2 X_o      = CCao*alpha_a + CCo*alpha_o;

272 TENSOR2 sigeff_a = deviator(sigma_a) - X_a;
273 TENSOR2 sigeff_o = deviator(sigma_a) - X_o;
274 TENSOR2 sigeff_m = deviator(sigma_m) - X_m;

276 double Jeo      = sqrt(2./3.*(e_o|e_o));
277 Jeo_aux = Jeo;
278 R_o      = R_o0 + H_o*pow(Jeo,b_o)*pow(z,2.);

280 R_a      = R0_a + Q_a*( 1.0-exp(-b_a*evcum_a) );
281 R_m      = R0_m + Q_m*( 1.0-exp(-b_m*evcum_m) );

283 double eps1 = 1.e-12; // if too big problem with derivative,
284 //too small problem with badly conditioned tangent matrix
285 double eps = 1.e-10;
286 if (z < eps1){
287     R_t      = R0_t - K_Z*(log(1.-eps1)) + K_ZZ*log(eps1) + K_T*pow(Jeo,n_ot) - K_P*pow(evcum_a,n_p);
288 }
289 else if (z<(1.-eps1)){
290     R_t      = R0_t - K_Z*(log(1.-z)) + K_ZZ*log(z) + K_T*pow(Jeo,n_ot) - K_P*pow(evcum_a,n_p);
291 }
292 else{
293     R_t      = R0_t - K_Z*(log(eps1)) + K_ZZ*log((1.-eps1)) + K_T*pow(Jeo,n_ot) - K_P*pow(evcum_a,n_p);
294 }
295 if(R_t < 0.0) R_t = 0.0;

297 double I_a      = trace(sigma_a);
298 double J_a      = sqrt(1.5*(sigeff_a | sigeff_a));
299 J_a_aux = J_a;

301 double J2_o      = sqrt(1.5*(sigeff_o|sigeff_o));
302 J2_o_aux = J2_o;
303 double J2_o2     = pow(J2_o,2.);
304 double J2_o3     = pow(J2_o,3.);
305 double J2_o4     = pow(J2_o,4.);
306 double J2_o5     = pow(J2_o,5.);
307 double J3_o      = sigeff_o.determin();
308 J3_o_aux = J3_o;

310 if (J2_o > eps){
311     Ao = 1.0+k_0*J3_o/J2_o3;
312 }
313 else{
314     Ao = 1.;

```

```

315 }
316 double nAo_inv = 1.0/(Ao*n_asym);
317 double Aon = pow(Ao,(1.0/n_asym));

319 TENSOR2 titi = syme(sigeff_o * sigeff_o);
320 norm_J3_o = titi - (1./3.)*trace(titi)*Id;

322 double f_t=0.;
323 double f_o=0.;
324 if (J2_o > eps){
325     f_t = K_S*(alpha_t*I_a + (1.-alpha_t)*Aon*J_a) - B*(T-T0) - R_t;
326     f_o = J2_o*z*Aon - R_o;

328     norm_J2_o = (1.5/J2_o)*sigeff_o;
329     dAo_ds = (k_0/J2_o3)*(norm_J3_o - (3.*J3_o/J2_o)*norm_J2_o);
330     dAon_ds = (Aon*nAo_inv)*dAo_ds;
331     norm_o_dz = Aon*norm_J2_o + J2_o*dAon_ds;
332     norm_o = z*norm_o_dz;
333 }
334 else {
335     f_t = K_S*alpha_t*I_a - B*(T-T0) - R_t;
336     norm_J2_o = 0.;
337     dAo_ds = 0.;
338     dAon_ds = 0.;
339     norm_o_dz = 0.;
340     norm_o = 0.;
341 }

343 hilf = J2_o*z*Aon;
344 TT = T;
345 dt2 = dt;

347 double f_a = J_a - R_a;
348 double J_m = sqrt(1.5*(sigeff_m|sigeff_m));
349 double f_m = J_m - R_m;

351 if (J_a > eps){
352     norm_a = (1.5/J_a)*sigeff_a;
353 }
354 else {
355     norm_a = 0.;
356 }

358 // power n_o < 1 ==> (-x)^n_o = nan e.g. for z < 1.0
359 if ( ((( f_o > eps) && (deocum >= 0.0)) || (deocum > 0.0)) && (z < 0.99 && z > 0.) ) {
360     f_vec_eocum -= (f_o > 0.0) ? dt*pow(f_o/K_o , n_o) : 0.0;
361     f_vec_e_o -= deocum*norm_o;
362     double dv_o_df = (f_o > 0.0) ? tdt*(n_o/K_o)*pow(f_o/K_o , n_o-1.) : 0.0;
363     if( CCo > 0.) {
364         m3 = norm_o - (D_o/CCo)*X_o;
365         f_vec_alpha_o -= m3*deocum;
366     }
367     f_vec_beta_mo -= deocum*(norm_o - D_b_mo*beta_mo);

369     SMATRIX dn_J2o_ds = unit32; dn_J2o_ds -= norm_J2_o^norm_J2_o; dn_J2o_ds *= 1.0/J2_o;

371     TENSOR4 mix1 = 0.5*( TENSOR4::Tikjl(Id,sigeff_o) + TENSOR4::Tiljk(Id,sigeff_o) );
372     mix1 = mix1 + 0.5*( TENSOR4::Tikjl(sigeff_o,Id) + TENSOR4::Tiljk(sigeff_o,Id) );
373     SMATRIX mix11( shrink( mix1 ) );
374     TENSOR4 mix2 = ((2./3.)*sigeff_o) ^ Id;
375     TENSOR4 mix3 = ((2./3.)*Id) ^ sigeff_o;

```

```

376 TENSOR4 dn_J3o_ds = mix11 - mix2 - mix3;
377 TENSOR4 J = TENSOR4::J(tsz());

379 double nAo2_inv = nAo_inv/Ao;
380 double nf = (1./n_asym - 1.);
381 TENSOR4 t1 = (((nAo_inv)*norm_J2_o)^dAo_ds);
382 TENSOR4 t2 = dn_J2o_ds;
383 TENSOR4 t3 = (((nf*nAo2_inv/J2_o2)*norm_J3_o)^dAo_ds);
384 TENSOR4 t4 = (nAo_inv/J2_o2)*dn_J3o_ds;
385 TENSOR4 t5 = ((( - 2.*nAo_inv/J2_o3)*norm_J3_o)^norm_J2_o );
386 TENSOR4 t6 = ((( - 3.*nf*nAo2_inv*J3_o/J2_o3)*norm_J2_o)^dAo_ds);
387 TENSOR4 t7 = ((( - 3.*nAo_inv/J2_o3)*norm_J2_o)^norm_J3_o);
388 TENSOR4 t8 = ( - 3.*nAo_inv*J3_o/J2_o3)*dn_J2o_ds;
389 TENSOR4 t9 = ((( 9.*nAo_inv*J3_o/J2_o4)*norm_J2_o)^norm_J2_o);
390 dn_o_ds = (t1 + t2 + (t3 + t4 + t5 + t6 + t7 + t8 + t9) * k_0 ) * z * Aon;
391 // the derivative with respect to the backstresses the deviator must not be made here!
392 dn_o_dX = dn_o_ds* tdv_o; // added tdv_o
393 TENSOR4 dn_o_dXeel = dn_o_dX * E;
394 dn_o_dsig = dn_o_ds*J;
395 //prn("dn_o_dsig :", dn_o_dsig);
396 //prn("dn_o_dsig_pert :", d2_pert(sig, fnorm_o));
397 dn_o_dsig *= tdv_o;
398 TENSOR4 dn_o_deel = dn_o_dsig*E;
399 TENSOR2 df_o_fs = dv_o_df*norm_o;

401 deocum_deel -= df_o_fs*E;
402 if (Jeo > 0.){
403     deocum_de_o = dv_o_df* H_o*b_o*pow(Jeo,b_o-1.)*pow(z,2.)*(2./(3.*Jeo))*e_o;
404     //deocum_de_o = d_pert(e_o, fp_o); //using this changes nothing except its slower
405 }
406 deocum_dz = dv_o_df*( (-1.)*J2_o*Aon + 2.*H_o*pow(Jeo,b_o)*z );
407 de_o_deel -= dn_o_deel;
408 de_o_deocum -= norm_o;
409 de_o_dz -= tdv_o*norm_o_dz;

411 if ( (CCao > 0.) ) {
412     deocum_dalpha_a = df_o_fs * CCao;
413     de_o_dalpha_a = dn_o_dX * CCao;
414     dbeta_mo_dalpha_a = dn_o_dX*CCao;
415 }
416 if ( (CCo > 0.) ) {
417     deocum_dalpha_o = df_o_fs * CCo;
418     dalpha_o_deel -= dn_o_dXeel;
419     dalpha_o_deocum -= m3;
420     dalpha_o_dalpha_o += dn_o_dX * CCo; dalpha_o_dalpha_o.add_to_diagonal( tdv_o*D_o);
421     if ( (C_ao > 0.0) ) {
422         dalpha_o_dalpha_a += dn_o_dX * CCao; dalpha_o_dalpha_a.add_to_diagonal( D_o*C_ao*tdv_o/C_o);
423     }
424     dalpha_o_dz -= tdv_o * norm_o_dz;
425     de_o_dalpha_o = dn_o_dX * CCo;
426     dbeta_mo_deel -= dn_o_deel;
427     dbeta_mo_dalpha_o = dn_o_dX*CCo;
428 }
429 deocum_dbeta_a += df_o_fs* (z*mu);
430 deocum_dbeta_mo -= df_o_fs* (z*mu);
431 de_o_dbeta_a += dn_o_dsig* (z*mu);
432 de_o_dbeta_mo -= dn_o_dsig* (z*mu);

434 dbeta_mo_deocum -= (norm_o - D_b_mo*beta_mo);
435 dbeta_mo_dbeta_mo.add_to_diagonal( D_b_mo*tdv_o );
436 dbeta_mo_dz -= tdv_o*norm_o_dz;

```

```

438     dalpha_o_dbeta_a      += dn_o_dsig* (z*mu);
439     dalpha_o_dbeta_mo    -= dn_o_dsig* (z*mu);
440 }

442 if ( ((f_t > eps && dz >= 0.0) || (dz > 0.0) ) && (z<1.0) ) {

444     f_vec_z      -= (f_t > 0.0) ? dt*pow(f_t/K_t , n_tt) : 0.0;
445     f_vec_eel    += dz*((delta/3.)*Id + e_o);
446     double dv_t_df = (f_t > 0.0) ? tdt*(n_tt/K_t)*pow( f_t/K_t , n_tt-1.) : 0.0;

448     TENSOR2 J_a_Aon = Aon*norm_a + dAon_ds*J_a;

450     TENSOR2 z0 = dv_t_df* K_S*alpha_t*Id;
451     z1 = dv_t_df* K_S*(1.-alpha_t);
452     z3 = z1* J_a_Aon;

454     deel_dz      += (delta/3.)*Id + e_o;
455     deel_de_o    = tdz*(TENSOR4::I(tsz()));
456     dz_deel      -= (z0 + z3)*E ;

458     if(Jeo > 0.){
459         dz_de_o    = dv_t_df* K_T*n_ot*pow(Jeo,n_ot -1.)*(2./(3.*Jeo))*e_o;
460     }
461     if (z < eps1){
462         dz_dz      += dv_t_df * ( K_Z/(1.0-eps1) + K_ZZ/eps1 );
463     }
464     else if (z < (1.0-eps1)){
465         dz_dz      += dv_t_df * ( K_Z/(1.0-z) + K_ZZ/z );
466     }
467     else{
468         dz_dz      += dv_t_df * ( K_Z/(eps1) + K_ZZ/(1.0-eps1) );
469     }

471     if (z < (1.0-eps1)){
472         dz_dz      += (R_t > 0.0) ? dv_t_df * ( K_Z/(1.0-z) - K_ZZ/z ) : 0.0;
473     }
474     else{
475         dz_dz      += dv_t_df * ( K_Z/(eps1) - K_ZZ/(1.0-eps1) );
476     }
477     dz_devcum_a = (-1.0) * dv_t_df * K_P*n_p*pow( devcum_a , n_p-1.); // added at this level

479     if ( (CCa > 0.0) ) {
480         dz_dalpha_a = z1 *( norm_a*(CCa*Aon) + (J_a*CCao)*dAon_ds );
481         //prn("dz_dalpha_mine :", dz_dalpha_a );
482         //dz_dalpha_a = d_pert( alpha_a, fz_alpha_a_pert);
483         //prn("dz_dalpha_a_pert :", dz_dalpha_a );
484     }
485     if ( (CCao > 0.0) ) {
486         dz_dalpha_o = z1 *( norm_a*(CCao*Aon) + (J_a*CCo)*dAon_ds );
487     }

489     dz_dbeta_a  -= (z0 + z3)*mu*z; //added at this level
490     dz_dbeta_mo += (z0 + z3)*mu*z;
491 }

494 if ( (f_a > eps && devcum_a >= 0.0) || (devcum_a > 0.0) ) {
495     f_vec_eel    += ((1.-z)*devcum_a)*norm_a;
496     f_vec_evcum_a  -= (f_a > 0.0) ? dt*pow(f_a/K_a,n_a) : 0.0;
497     double dv_a_df = (f_a > 0.0) ? tdt*(n_a/K_a)*pow( f_a/K_a , n_a-1.) : 0.0;

```



```

498   if( C_a > 0.) {
499     m1      = norm_a - (D_a/CCa)*X_a;
500     f_vec_alpha_a  -= m1*devcum_a;
501   }
502   f_vec_beta_a  -= devcum_a*(norm_a - D_b_a*beta_a);

504   SMATRIX dn_a_ds = unit32; dn_a_ds -= norm_a^norm_a; dn_a_ds *= tdv_a/J_a; // contains p_dot !
505   SMATRIX dn_a_deel = dn_a_ds*E;
506   TENSOR2 df_a_fs  = dv_a_df*norm_a;

508   deel_deel      += (1.-z)*dn_a_deel;
509   deel_dz        -= tdv_a*norm_a;

511   deel_devcum_a  = (1.-z)*norm_a;
512   devcum_a_deel  -= df_a_fs*E;
513   devcum_a_devcum_a += dv_a_df* b_a*Q_a*exp( - b_a*devcum_a);

515   //added at this level
516   if ( (CCa > 0.0) ) {
517     deel_dalpha_a      -= ((1.-z)*CCa)*dn_a_ds;
518     devcum_a_dalpha_a  = df_a_fs*CCa; //inner derivative of -X is -CCa
519     dalpha_a_devcum_a  -= m1;
520     dalpha_a_dalpha_a  += dn_a_ds*CCa;    dalpha_a_dalpha_a.add_to_diagonal(tdv_a*D_a);
521     if ( (CCao > 0.0) ) {
522       dalpha_a_dalpha_o  = dn_a_ds*CCao;    dalpha_a_dalpha_o.add_to_diagonal( tdv_a*D_a*C_ao/C_a);
523     }
524     dalpha_a_deel      -= dn_a_deel;

526     dbeta_a_dalpha_a   = dn_a_ds*CCa;
527   }
528   if ( (CCao > 0.0) ) {
529     deel_dalpha_o      -= ((1.-z)*CCao)*dn_a_ds;
530     devcum_a_dalpha_o  = df_a_fs*CCao;
531     dbeta_a_dalpha_o   = dn_a_ds*CCao;
532   }
533   deel_dbeta_a        -= ((1.-z)*z*mu)* dn_a_ds; //added at this level
534   deel_dbeta_mo       += ((1.-z)*z*mu)*dn_a_ds;
535   devcum_a_dbeta_a    += df_a_fs* (z*mu);
536   devcum_a_dbeta_mo   -= df_a_fs* (z*mu);

538   dbeta_a_deel        -= dn_a_deel;
539   dbeta_a_devcum_a    -= (norm_a - D_b_a*beta_a);
540   dbeta_a_dbeta_a.add_to_diagonal( D_b_a*tdv_a );

542   dalpha_a_dbeta_a    += dn_a_ds* z*mu;
543   dalpha_a_dbeta_mo   -= dn_a_ds* z*mu;
544 }

546   if ( (f_m > eps && devcum_m >= 0.0) || (devcum_m > 0.0) ) {

548     norm_m           = (1.5/J_m)*sigeff_m;
549     f_vec_eel        += (z*devcum_m)*norm_m;
550     f_vec_evcum_m    -= (f_m > 0.0) ? dt*pow(f_m/K_m,n_m) : 0.0;
551     double dv_m_df   = (f_m > 0.0) ? tdt*(n_m/K_m)*pow(f_m / K_m,(n_m-1.)) : 0.0;
552     if( CCm > 0.) {
553       m2      = norm_m - (D_m/CCm)*X_m;
554       f_vec_alpha_m  -= m2*devcum_m;
555     }
556     f_vec_beta_mo  -= devcum_m*(norm_m - D_b_mo*beta_mo);

558     SMATRIX dn_m_ds  = unit32; dn_m_ds -= norm_m^norm_m; dn_m_ds *= tdv_m/J_m;

```

```

559 SMATRIX dn_m_deel = dn_m_ds*E;
560 TENSOR2 df_m_fs = dv_m_df*norm_m;

562 deel_deel += z*dn_m_deel;
563 deel_devcum_m = z*norm_m;
564 deel_dz += tdv_m*norm_m;
565 devcum_m_deel -= df_m_fs*E;
566 devcum_m_devcum_m += dv_m_df* b_m*Q_m*exp(- b_m*evcum_m);
567 if ( (CCm > 0.) ) {
568     deel_dalpha_m -= (z*CCm)*dn_m_ds;
569     devcum_m_dalpha_m = df_m_fs*CCm;
570     dalpha_m_devcum_m -= m2;
571     dalpha_m_dalpha_m += dn_m_ds*CCm;    dalpha_m_dalpha_m.add_to_diagonal(tdv_m*D_m);
572     dalpha_m_deel -= dn_m_deel;
573     dbeta_mo_dalpha_m += dn_m_ds*CCm;
574 }
575 deel_dbeta_a -= dn_m_ds*(z*(1.-z)*mu);
576 deel_dbeta_mo += dn_m_ds*(z*(1.-z)*mu);
577 devcum_m_dbeta_a -= df_m_fs* ((1.-z)*mu);
578 devcum_m_dbeta_mo += df_m_fs* ((1.-z)*mu);
579 dbeta_mo_deel -= dn_m_deel;
580 dbeta_mo_devcum_m -= (norm_m - D_b_mo*beta_mo);
581 dbeta_mo_dbeta_mo.add_to_diagonal( D_b_mo*tdv_m );

583 dalpha_m_dbeta_a -= dn_m_ds* (1.-z)*mu;
584 dalpha_m_dbeta_mo += dn_m_ds* (1.-z)*mu;
585 }

588 // For printing individual residual derivatives:
589 // STRING str;
590 // str = "\n--> Iteration: ";
591 // str += itoa(++iter);
592 // str += " Integration at time:"+dtoa(Time)+" dt:"+dtoa(Dtime)+" eto: ";
593 // for(int i=0;i<!eto;i++) str += dtoa(eto[i]) + " ";
594 // str += " deto: ";
595 // for(int i=0;i<!deto;i++) str += dtoa(deto[i]) + " ";
596 // prn(str);
597 // str = "var : ";
598 // for(int i=0;i<!chi_vec;i++) str += dtoa(chi_vec[i]) + " ";
599 // prn(str);
600 // str = "dvar : ";
601 // for(int i=0;i<!d_chi_vec;i++) str += dtoa(d_chi[i]) + " ";
602 // prn(str);
603 // str = "f_vec : ";
604 // for(int i=0;i<!f_vec;i++) str += dtoa(f_vec[i]) + " ";
605 // prn(str);
606 // prn("f_vec_evcum_a : ", f_vec_evcum_a);
607 // prn("f_vec_evcum_m : ", f_vec_evcum_m);
608 // prn("f_grad",f_grad);

611 //OTHER PARTS
612 //prn("dv_t_df : ", tdt*(n_tt/K_t)*pow( f_t/K_t , n_tt-1.));
613 //prn("K_Z/(1.-z) - K_ZZ/z ):", ( K_Z/(1.-z) - K_ZZ/z ));
614 // prn("sig = ",sig);
615 // prn("sigeff_o = ",sigeff_o);
616 // prn("sigeff_m = ",sigeff_m);
617 // prn("X_m = ",X_m);
618 // prn("f_t = ",f_t);
619 // prn("f_o = ",f_o);

```

```

620 // prn("f_a = ",f_a);
621 // prn("f_m = ",f_m);
622 // prn("z = ",z);
623 // prn("R_t = ", R_t);
624 // prn("eocum :", eocum);

626 // RESIDUAL DERIVATIVES

628 //prn("deel_dalpha_m      :", deel_dalpha_m  );
629 //prn("devcum_m_dalpha_m :", devcum_m_dalpha_m);
630 //prn("dalpha_m_devcum_m :", dalpha_m_devcum_m);
631 //prn("dalpha_m_dalpha_m :", dalpha_m_dalpha_m);
632 //prn("dalpha_m_deel     :", dalpha_m_deel   );
633 //
634 //prn("deel_dalpha_a      :", deel_dalpha_a  );
635 //prn("devcum_a_dalpha_a :", devcum_a_dalpha_a);
636 //prn("dalpha_a_devcum_a :", dalpha_a_devcum_a);
637 //prn("dalpha_a_dalpha_a :", dalpha_a_dalpha_a);
638 //prn("dalpha_a_dalpha_o :", dalpha_a_dalpha_o);
639 //prn("dalpha_a_deel     :", dalpha_a_deel   );
640 //prn("deel_dalpha_o     :", deel_dalpha_o  );
641 //prn("devcum_a_dalpha_o :", devcum_a_dalpha_o);
642 //
643 //prn("dz_dalpha_a      :", dz_dalpha_a);
644 //prn("dz_dalpha_a_pert :", d_pert( alpha_a, fz_alpha_a_pert) );
645 //prn("dz_dalpha_o     :", dz_dalpha_o);
646 //
647 //prn("deocum_dalpha_a   :", deocum_dalpha_a );
648 //prn("de_o_dalpha_a     :", de_o_dalpha_a );
649 //prn("deocum_dalpha_o   :", deocum_dalpha_o );
650 //prn("dalpha_o_deel     :", dalpha_o_deel );
651 //prn("dalpha_o_deocum   :", dalpha_o_deocum );
652 //prn("dalpha_o_dalpha_o :", dalpha_o_dalpha_o);
653 //prn("dalpha_o_dalpha_a :", dalpha_o_dalpha_a);
654 //prn("dalpha_o_dz       :", dalpha_o_dz );
655 //prn("de_o_dalpha_o     :", de_o_dalpha_o );

657 glob_counter++;
658 bool convergence = FALSE;
659 double conv_error;
660 convergence = ((THETA*m_inttn())->check_convergence(f_vec,d_chi,d_chi,conv_error));
661 my_file<<glob_counter<<" "<<conv_error<<endl;
662 // Out<<"res : "<<conv_error<<endl;

664 }

667 @PreRead {
668 my_file.open("convergence.txt", ios::out);
669 glob_counter = 0;
670 }

672 // FUNCTIONS FOR NUMERICALLY CHECKING THE DERIVATIVES
673 double MARAGING_full::fz_alpha_a_pert(MARAGING_full* b, const TENSOR2& alpha_a){
674 TENSOR2 fsigeff_o = deviator(b->sigma_a) - (b->C_ao/1.5)*alpha_a; // X_o(alpha_a)
675 TENSOR2 fsigeff_a = deviator(b->sigma_a) - (b->C_a/1.5)*alpha_a; // X_a(alpha_a)
676 double fI_a      = trace(b->sigma_a);
677 double fJ_a      = sqrt(1.5*(fsigeff_a|fsigeff_a));
678 double fJ2_o     = sqrt(1.5*(fsigeff_o|fsigeff_o));
679 double fJ2_o3    = pow(fJ2_o,3.);
680 double fJ3_o     = fsigeff_o.determin();

```

```

681 double fAo      = 1.0+b->k_0*fJ3_o/fJ2_o3;
682 double fnAo_inv = 1.0/(fAo*b->n_asym);
683 double fAon     = pow(fAo,(1.0/b->n_asym));
684 double f_t     = b->K_S*(b->alpha_t*fI_a + (1.-b->alpha_t)*fAon*fJ_a) - b->B*(b->TT-b->T0) - b->R_t;
685 double fz      = (-1.0) * b->dt2 * pow( f_t/b->K_t , b->n_tt);
686 return fz;
687 }

690 double MARAGING_full::fz(MARAGING_full* b, const TENSOR2& sig){
691 TENSOR2 fsigeff_o = deviator(sig) - (b->C_ao/1.5)*b->alpha_a;
692 TENSOR2 fsigeff_a = deviator(sig) - (b->C_a/1.5)*b->alpha_a; // add here the other backstress parts if needed
693 TENSOR2 fsigma_a  = sig;
694 double fI_a      = trace(fsigma_a);
695 double fJ2_o     = sqrt(1.5*(fsigeff_o|fsigeff_o));
696 double fJ_a      = sqrt(1.5*(fsigeff_a|fsigeff_a));
697 double fJ2_o3    = pow(fJ2_o,3.);
698 double fJ3_o     = fsigeff_o.determin();
699 double fAo       = 1.0+b->k_0*fJ3_o/fJ2_o3;
700 double fAon      = pow(fAo,(1.0/b->n_asym));
701 double f_t       = b->K_S*(b->alpha_t*fI_a + (1.-b->alpha_t)*fAon*fJ_a) - b->B*(b->TT-b->T0) - b->R_t;
702 double fz        = (-1.0) *pow( f_t/b->K_t , b->n_tt);
703 return fz;
704 }

706 double MARAGING_full::fz_eo_pert(MARAGING_full* b, const TENSOR2& e_o){
707 double J_eo      = sqrt(2./3.*(e_o|e_o));
708 double R_t       = b->R0_t - b->K_Z*(log(1.-b->z)) + b->K_ZZ*log(b->z) + b->K_T*pow(J_eo,b->n_ot);
709 double fz_pert   = (-1.0)*b->dt2 *pow( (b->f_t1 - R_t) / b->K_t , b->n_tt);
710 return fz_pert;
711 }

713 double MARAGING_full::fp_o(MARAGING_full* b, const TENSOR2& e_o){
714 double fJ_eo     = sqrt(2./3.*(e_o|e_o));
715 double fR_o      = b->H_o*pow(fJ_eo,b->b_o)*pow(b->z,2.);
716 double fp_o      = (-1.0) * pow(( b->hilf - fR_o)/b->K_o ,b->n_o);
717 return fp_o;
718 }

720 double MARAGING_full::ff_o(MARAGING_full* b, const TENSOR2& sig){
721 TENSOR2 fsigeff_o = deviator(sig);
722 double fJ2_o      = sqrt(1.5*(fsigeff_o|fsigeff_o));
723 double fJ2_o3    = pow(fJ2_o,3.);
724 double fJ3_o     = fsigeff_o.determin();
725 double fAo       = 1.0+b->k_0*fJ3_o/fJ2_o3;
726 double fAon      = pow(fAo,(1.0/b->n_asym));
727 double f_o_pert  = b->z*fAon*fJ2_o;
728 return f_o_pert;
729 }

731 TENSOR2 MARAGING_full::fnorm_o(MARAGING_full* b, const TENSOR2& sig){
732 TENSOR2 fsigeff_o = deviator(sig);
733 double fJ2_o      = sqrt(1.5*(fsigeff_o|fsigeff_o));
734 double fJ2_o3    = pow(fJ2_o,3.);
735 double fJ3_o     = fsigeff_o.determin();
736 double fAo       = 1.0+b->k_0*fJ3_o/fJ2_o3;
737 double fnAo_inv  = 1.0/(fAo*b->n_asym);
738 double fAon      = pow(fAo,(1.0/b->n_asym));
739 TENSOR2 ftiti    = syme(fsigeff_o * fsigeff_o);

741 TENSOR2 fnorm_J3_o = ftiti - (1./3.)*trace( ftiti )*TENSOR2::unity(b->tsz());

```

```

742 //TENSOR2 fnorm_J3_o = ftiti - (2./9.)*pow(fJ2_o,2.)* TENSOR2::unity(b->tsz());

744 TENSOR2 fnorm_J2_o = (1.5/fJ2_o)*fsigeff_o;
745 TENSOR2 fdAo_ds = (b->k_0/fJ2_o3)*(fnorm_J3_o - (3.*fJ3_o/fJ2_o)*fnorm_J2_o);
746 TENSOR2 fdAon_ds = (fAon*fnAo_inv)*fdAo_ds;
747 TENSOR2 fnorm_o_dz = fAon*fnorm_J2_o + fJ2_o*fdAon_ds;
748 TENSOR2 norm_o_pert = b->z*fnorm_o_dz;
749 return norm_o_pert;
750 }

752 TENSOR2 MARAGING_full::fnorm_o_part1(MARAGING_full* b, const TENSOR2& sig){
753 TENSOR2 fsigeff_o = deviator(sig);
754 double fJ2_o = sqrt(1.5*(fsigeff_o|fsigeff_o));
755 double fJ2_o3 = pow(fJ2_o,3.);
756 double fJ3_o = fsigeff_o.determin();
757 double fAo = 1.0+b->k_0*fJ3_o/fJ2_o3;
758 double fAon = pow(fAo,(1.0/b->n_asym));
759 TENSOR2 fnorm_J2_o = (1.5/fJ2_o)*fsigeff_o;
760 TENSOR2 norm_o_part1_pert = b->z*fAon*fnorm_J2_o;
761 return norm_o_part1_pert;
762 }

765 TENSOR2 MARAGING_full::dI3(MARAGING_full* b, const TENSOR2& t){ //here t is sig
766 TENSOR2 fsigeff_o = deviator(t);
767 TENSOR2 ftiti = syms(fsigeff_o * fsigeff_o);
768 TENSOR2 ret = ftiti - (1./3.)*trace( ftiti )*TENSOR2::unity(b->tsz());
769 return(ret);
770 }

772 //TENSOR2 function, derivative w.r.t TENSOR2
773 TENSOR4 MARAGING_full::d2_pert(const TENSOR2& e, TENSOR2 (*func)(MARAGING_full*, const TENSOR2& )){
774 int i;
775 //prn("NSYM d2g by perturbation = ");
776 SMATRIX dle_de(!e);

778 double perturb = 1.e-6*sqrt(e|e);

780 for (int j=0;j<!e;j++) {
781 TENSOR2 le2 = e;
782 le2[j] += perturb;
783 TENSOR2 dd2= (*func)(this,le2);

785 TENSOR2 le1 = e;
786 le1[j] -= perturb;
787 TENSOR2 dd1= (*func)(this,le1);

789 for (i=0;i<!e;i++) {
790 dle_de(i,j) = (dd2[i]-dd1[i])/(2.0*perturb);
791 }
792 }

794 TENSOR4 ret = dle_de;
795 //
796 //STRING str2;
797 //str2 = "perturbated: ";
798 //for(int i=0;i<!ret;i++) str2 += dtoa(ret[i]) + " "; // [] for TENSOR4 non existent
799 //prn(str2);
800 return(ret);
801 }

```

```

803 //scalar test2 function with TENSOR2 argument e, derivative w.r.t TENSOR2 argument by pertubation
804 TENSOR2 MARAGING_full::d_pert(const TENSOR2& e, double (*func)(MARAGING_full*, const TENSOR2& )){
805 //prn("NSYM dg by perturbation =");
806 VECTOR dle_de(!e);

808 double perturb = 1.e-4*sqrt(e|e); // eps must be in the size of the timestep investigated!!!

810 for (int j=0;j<!e;j++) {
811     TENSOR2 le2 = e;
812     le2[j] += perturb;
813     double dd2= (*func)(this,le2);

815     TENSOR2 le1 = e;
816     le1[j] -= perturb; // comment out for one sided perturbation
817     double dd1= (*func)(this,le1);

819     dle_de[j] = (dd2-dd1)/(2.0*perturb);
820     //dle_de[j] = (dd2-dd1)/(perturb); // one sided perturbation
821 }

823 TENSOR2 ret = dle_de;

825 // STRING str2;
826 // str2 = "perturbated: ";
827 // for(int i=0;i<!ret;i++) str2 += dtoa(ret[i]) + " ";
828 // prn(str2);
829 return(ret);
830 }

832 //scalar function, derivative w.r.t scalar
833 double MARAGING_full::s_pert_s(const double& e, double (*func)(MARAGING_full*,double) ){
834 //prn("NSYM dg by perturbation");

836 double perturb = 1.e-6;

838     double le2 = e;
839     le2 += perturb;
840     double dd2= (*func)(this,le2); //test1(le2);

842     double le1 = e;
843     le1 -= perturb;
844     double dd1= (*func)(this,le1); //test1(le1);

846     double dle_de = (dd2-dd1)/(2.0*perturb);

848     return(dle_de);
849 }

```

Bibliography

- Abdolrahim, N. and Demkowicz, M. (2016). “Determining coherent reference states of general semicoherent interfaces”. In: *Computational Materials Science* 118, pp. 297–308. ISSN: 0927-0256. DOI: [10.1016/j.commatsci.2016.02.002](https://doi.org/10.1016/j.commatsci.2016.02.002).
- Achenbach, M. (1989). “A model for an alloy with shape memory”. In: *International Journal of Plasticity* 5.4, pp. 371–395. ISSN: 0749-6419. DOI: [10.1016/0749-6419\(89\)90023-5](https://doi.org/10.1016/0749-6419(89)90023-5).
- Addessio, F. L., Bronkhorst, C. A., Bolme, C. A., Brown, D. W., Cerreta, E. K., Lebensohn, R. A., Lookman, T., Luscher, D. J., Mayeur, J. R., and Morrow, B. M. (2016). *A High-Rate, Single-Crystal Model including Phase Transformations, Plastic Slip, and Twinning*. Tech. rep. DOI: [10.2172/1312644](https://doi.org/10.2172/1312644).
- Allain, S., Chateau, J.-P., and Bouaziz, O. (2004). “A physical model of the twinning-induced plasticity effect in a high manganese austenitic steel”. In: *Materials Science and Engineering: A* 387-389, pp. 143–147. ISSN: 0921-5093. DOI: [10.1016/j.msea.2004.01.060](https://doi.org/10.1016/j.msea.2004.01.060).
- Altenbach, H., Bolchoun, A., and Kolupaev, V. A. (2014). “Phenomenological yield and failure criteria”. In: *Plasticity of Pressure-Sensitive Materials*. Springer, pp. 49–152.
- Altenbach, H., Forest, S., and Krivtsov, A. (2013). *Generalized Continua as Models for Materials*. Springer.
- Anand, L., Gurtin, M. E., and Reddy, B. D. (2015). “The stored energy of cold work, thermal annealing, and other thermodynamic issues in single crystal plasticity at small length scales”. In: *International Journal of Plasticity* 64, pp. 1–25. ISSN: 0749-6419. DOI: [10.1016/j.ijplas.2014.07.009](https://doi.org/10.1016/j.ijplas.2014.07.009).
- Arsenlis, A. and Parks, D. (1999). “Crystallographic aspects of geometrically-necessary and statistically-stored dislocation density”. In: *Acta Materialia* 47.5, pp. 1597–1611. ISSN: 1359-6454. DOI: [10.1016/S1359-6454\(99\)00020-8](https://doi.org/10.1016/S1359-6454(99)00020-8).

- Artemev, A., Jin, Y., and Khachaturyan, A. (2001). “Three-dimensional phase field model of proper martensitic transformation”. In: *Acta Materialia* 49.7, pp. 1165–1177. ISSN: 1359-6454. DOI: [10.1016/S1359-6454\(01\)00021-0](https://doi.org/10.1016/S1359-6454(01)00021-0).
- Ashby, M. F. (1970). “The deformation of plastically non-homogeneous materials”. In: *Philosophical Magazine* 21.170, pp. 399–424. DOI: [10.1080/14786437008238426](https://doi.org/10.1080/14786437008238426).
- Ask, A., Forest, S., Appolaire, B., Ammar, K., and Umut Salman, O. (2018). “A Cosserat crystal plasticity and phase field theory for grain boundary migration”. In: *Journal of the Mechanics and Physics of Solids* 115, pp. 167–194. DOI: [10.1016/j.jmps.2018.03.006](https://doi.org/10.1016/j.jmps.2018.03.006).
- Auricchio, F., Bonetti, E., Scalet, G., and Ubertini, F. (2014). “Theoretical and numerical modeling of shape memory alloys accounting for multiple phase transformations and martensite reorientation”. In: *International Journal of Plasticity* 59, pp. 30–54. ISSN: 0749-6419. DOI: [10.1016/j.ijplas.2014.03.008](https://doi.org/10.1016/j.ijplas.2014.03.008).
- Authier, A. (2003). *International Tables of Crystallography D: Physical Properties of Crystals*. Springer, Berlin.
- Avrami, M. (1940). “Transformation-time relations for random distribution of nuclei”. In: *Journal of Chemical Physics* 8, pp. 212–224.
- Bain, E. C. and Dunkirk, N. (1924). “The nature of martensite”. In: *trans. AIME* 70.1, pp. 25–47.
- Bain, E. C. and Paxton, H. W. (1966). “Alloying elements in steel”. In: *American society for metals*.
- Ball, J. (2004). “Mathematical models of martensitic microstructure”. In: *Material Science and Engineering A* 378, pp. 61–69. DOI: [10.1016/j.msea.2003.11.055](https://doi.org/10.1016/j.msea.2003.11.055).
- Ball, J. and James, R. (1987). “Fine phase mixtures as minimizers of energy”. In: *Archive for Rational Mechanics and Analysis* 100.1, pp. 13–52. DOI: [10.1007/BF00281246](https://doi.org/10.1007/BF00281246).
- Ball, J. M. (1976). “Convexity conditions and existence theorems in nonlinear elasticity”. In: *Archive for Rational Mechanics and Analysis* 63.4, pp. 337–403. ISSN: 1432-0673. DOI: [10.1007/BF00279992](https://doi.org/10.1007/BF00279992).
- Ball, J. M., Cesana, P., and Hambly, B. (2015). “A probabilistic model for martensitic avalanches”. In: *MATEC Web of Conferences*. Vol. 33. EDP Sciences.
- Balzani, D., Scheunemann, L., Brands, D., and Schröder, J. (2014). “Construction of two- and three-dimensional statistically similar RVEs for coupled micro-macro simulations”. In: *Computational Mechanics* 54.5, pp. 1269–1284. ISSN: 1432-0924. DOI: [10.1007/s00466-014-1057-6](https://doi.org/10.1007/s00466-014-1057-6).

- Banerjee, D. and Williams, J. (2013). “Perspectives on Titanium Science and Technology”. In: *Acta Materialia* 61.3, pp. 844–879. ISSN: 1359-6454. DOI: [10.1016/j.actamat.2012.10.043](https://doi.org/10.1016/j.actamat.2012.10.043).
- Banerjee, S. and Mukhopadhyay, P. (2010). *Phase Transformations: Examples from Titanium and Zirconium Alloys*. Pergamon Materials Series. Elsevier Science. ISBN: 9780080548791.
- Bargmann, S., Klusemann, B., Markmann, J., Schnabel, J., Schneider, K., Soyarslan, C., and Wilmers, J. (2018). “Generation of 3D representative volume elements for heterogeneous materials: a review”. In: *Progress in Materials Science*.
- Barlat, F., Gracio, J. J., Lee, M.-G., Rauch, E. F., and Vincze, G. (2011). “An alternative to kinematic hardening in classical plasticity”. In: *International Journal of Plasticity* 27.9, pp. 1309–1327. ISSN: 0749-6419. DOI: [10.1016/j.ijplas.2011.03.003](https://doi.org/10.1016/j.ijplas.2011.03.003).
- Bartel, T. and Hackl, K. (2009). “A micromechanical model for martensitic phase-transformations in shape-memory alloys based on energy-relaxation”. In: *Zeitschrift für angewandte Mathematik und Mechanik* 89.10, pp. 792–809. ISSN: 1521-4001. DOI: [10.1002/zamm.200900244](https://doi.org/10.1002/zamm.200900244).
- Bartel, T. and Hackl, K. (2010). “Multiscale modeling of martensitic phase transformations: on the numerical determination of heterogeneous mesostructures within shape-memory alloys induced by precipitates”. In: *Technische Mechanik* 30, pp. 324–342.
- Bartel, T., Menzel, A., and Svendsen, B. (2011). “Thermodynamic and relaxation-based modeling of the interaction between martensitic phase transformations and plasticity”. In: *Journal of the Mechanics and Physics of Solids* 59.5, pp. 1004–1019. ISSN: 0022-5096. DOI: [10.1016/j.jmps.2011.02.006](https://doi.org/10.1016/j.jmps.2011.02.006).
- Bartels, A., Bartel, T., Canadija, M., and Mosler, J. (2015). “On the thermomechanical coupling in dissipative materials: A variational approach for generalized standard materials”. In: *Journal of the Mechanics and Physics of Solids* 82, pp. 218–234. ISSN: 0022-5096. DOI: [10.1016/j.jmps.2015.04.011](https://doi.org/10.1016/j.jmps.2015.04.011).
- Bartels, S., Carstensen, C., Hackl, K., and Hoppe, U. (2004). “Effective relaxation for microstructure simulations: algorithms and applications”. In: *Computer Methods in Applied Mechanics and Engineering* 193.48-51, pp. 5143–5175. ISSN: 0045-7825. DOI: [10.1016/j.cma.2003.12.065](https://doi.org/10.1016/j.cma.2003.12.065).
- Baur, A. P., Cayron, C., and Logé, R. E. (2017). “ $\{225\}_\gamma$ habit planes in martensitic steels: from the PTMC to a continuous model”. In: *Scientific Reports* 7, p. 40938.
- Bayley, C., Brekelmans, W., and Geers, M. (2006). “A comparison of dislocation induced back stress formulations in strain gradient crystal plasticity”. In: *International Journal of*

- Solids and Structures* 43.24, pp. 7268–7286. ISSN: 0020-7683. DOI: [10.1016/j.ijsolstr.2006.05.011](https://doi.org/10.1016/j.ijsolstr.2006.05.011).
- Beese, A. M. and Mohr, D. (2012). “Anisotropic plasticity model coupled with Lode angle dependent strain-induced transformation kinetics law”. In: *Journal of the Mechanics and Physics of Solids* 60.11, pp. 1922–1940. DOI: [10.1016/j.jmps.2012.06.009](https://doi.org/10.1016/j.jmps.2012.06.009).
- Beissel, S. and Belytschko, T. (1996). “On patterns of deformation in phase transformations and Lüders bands”. In: *International Journal of Solids and Structures* 33.12, pp. 1689–1707. ISSN: 0020-7683. DOI: [10.1016/0020-7683\(95\)00120-4](https://doi.org/10.1016/0020-7683(95)00120-4).
- Ben Naceur, I., Saï, K., Hassan, T., and Cailletaud, G. (2016). “Micromechanical Modeling of the Ratcheting Behavior of 304 Stainless Steel”. In: *Journal of Engineering Materials and Technology* 138.2, 021005, 8 p. ISSN: 0094-4289. DOI: [10.1115/1.4032154](https://doi.org/10.1115/1.4032154).
- Berbenni, S., Paliwal, B., and Cherkaoui, M. (2013). “A micromechanics-based model for shear-coupled grain boundary migration in bicrystals”. In: *International Journal of Plasticity* 44, pp. 68–94. ISSN: 0749-6419. DOI: [10.1016/j.ijplas.2012.11.011](https://doi.org/10.1016/j.ijplas.2012.11.011).
- Berdichevsky, V. (2006). “On thermodynamics of crystal plasticity”. In: *Scripta Materialia* 54.5, pp. 711–716. ISSN: 1359-6462. DOI: [10.1016/j.scriptamat.2005.10.027](https://doi.org/10.1016/j.scriptamat.2005.10.027).
- Bernier, N., Bracke, L., Malet, L., and Godet, S. (2014). “An alternative to the crystallographic reconstruction of austenite in steels”. In: *Materials Characterization* 89, pp. 23–32. ISSN: 1044-5803. DOI: [10.1016/j.matchar.2013.12.014](https://doi.org/10.1016/j.matchar.2013.12.014).
- Bertin, M., Du, C., Hoefnagels, J. P., and Hild, F. (2016). “Crystal plasticity parameter identification with 3D measurements and Integrated Digital Image Correlation”. In: *Acta Materialia* 116, pp. 321–331. ISSN: 1359-6454. DOI: [10.1016/j.actamat.2016.06.039](https://doi.org/10.1016/j.actamat.2016.06.039).
- Bertram, A. and Glüge, R. (2015). *Solid Mechanics: Theory, Modeling, and Problems*. Springer International Publishing. ISBN: 9783319195667.
- Bertram, A. and Forest, S. (2014). “The thermodynamics of gradient elastoplasticity”. In: *Continuum Mechanics and Thermodynamics* 26.3, pp. 269–286. ISSN: 1432-0959. DOI: [10.1007/s00161-013-0300-2](https://doi.org/10.1007/s00161-013-0300-2).
- Berveiller, M. and Zaoui, A. (1978). “An extension of the self-consistent scheme to plastically-flowing polycrystals”. In: *Journal of the Mechanics and Physics of Solids* 26.5, pp. 325–344. ISSN: 0022-5096. DOI: [10.1016/0022-5096\(78\)90003-0](https://doi.org/10.1016/0022-5096(78)90003-0).
- Besson, J., Cailletaud, G., Chaboche, J., and Forest, S. (2009). *Non-Linear Mechanics of Materials*. Solid Mechanics and Its Applications. Springer Netherlands. ISBN: 9789048133567.

- Bever, M., Holt, D., and Titchener, A. (1973). "The stored energy of cold work". In: *Progress in Materials Science* 17, pp. 5–177. ISSN: 0079-6425. DOI: [10.1016/0079-6425\(73\)90001-7](https://doi.org/10.1016/0079-6425(73)90001-7).
- Bhadeshia, H. K. D. H. and Christian, J. (1990). "Bainite in steels". In: *Metallurgical transactions A* 21.3, pp. 767–797.
- Bhadeshia, H. (1987). *Worked examples in the geometry of crystals*. Book (The Institute of Metals). Institute of Materials. ISBN: 9780904357943.
- (2011). "Comments on - The mechanisms of the fcc - bcc martensitic transformation revealed by pole figures". In: *Scripta Materialia* 64.1, pp. 101–102. ISSN: 1359-6462. DOI: [10.1016/j.scriptamat.2010.07.044](https://doi.org/10.1016/j.scriptamat.2010.07.044).
- Bhadeshia, H. and Honeycombe, R. (2006). *Steels: Microstructure and Properties*. Metallurgy and Materials Science Series. Butterworth-Heinemann. ISBN: 9780750680844.
- Bhadeshia H.K.D.H. and Kundu, S. and Abreu, H. (2009). "Mathematics of Crystallographic Texture in Martensitic and Related Transformations". In: *Microstructure and Texture in Steels: and Other Materials*. Ed. by A. Halder, S. Suwas, and D. Bhattacharjee. London: Springer London, pp. 19–31. ISBN: 978-1-84882-454-6. DOI: [10.1007/978-1-84882-454-6_2](https://doi.org/10.1007/978-1-84882-454-6_2).
- Bhattacharya, K. (2003). *Microstructure of Martensite: why it forms and how it gives rise to the shape-memory effect*. Oxford Series on Materials Modelling. OUP Oxford. ISBN: 9780198509349.
- Bhattacharya, K., Conti, S., and Zanzotto, G. (2004). "Crystal symmetry and the reversibility of martensitic transformations". In: *Nature* 428, pp. 55–59. DOI: [doi:10.1038/nature02378](https://doi.org/10.1038/nature02378).
- Bhattacharya, K. (1992). "Self-accommodation in martensite". In: *Archive for Rational Mechanics and Analysis* 120.3, pp. 201–244. ISSN: 1432-0673. DOI: [10.1007/BF00375026](https://doi.org/10.1007/BF00375026).
- Bieler, T., Eisenlohr, P., Zhang, C., Phukan, H., and Crimp, M. (2014). "Grain boundaries and interfaces in slip transfer". In: *Current Opinion in Solid State and Materials Science* 18.4, pp. 212–226. ISSN: 1359-0286. DOI: [10.1016/j.cossms.2014.05.003](https://doi.org/10.1016/j.cossms.2014.05.003).
- Bigoni, D. (2012). *Nonlinear Solid Mechanics: Bifurcation Theory and Material Instability*. Cambridge University Press. ISBN: 9781139536981.
- Bilby, B. A., Bullough, R., and Smith, E. (1955). "Continuous Distributions of Dislocations: A New Application of the Methods of Non-Riemannian Geometry". In: *Proceedings of the*

- Royal Society of London A: Mathematical, Physical and Engineering Sciences* 231.1185, pp. 263–273. ISSN: 0080-4630. DOI: [10.1098/rspa.1955.0171](https://doi.org/10.1098/rspa.1955.0171).
- Bilby, B. and Frank, F. (1960). “The analysis of the crystallography of martensitic transformations by the method of prism matching”. In: *Acta Metallurgica* 8.4, pp. 239–248. ISSN: 0001-6160. DOI: [10.1016/0001-6160\(60\)90187-5](https://doi.org/10.1016/0001-6160(60)90187-5).
- Bishop, J. and Hill, R. (1951). “CXXVIII. A theoretical derivation of the plastic properties of a polycrystalline face-centred metal”. In: *The London, Edinburgh, and Dublin Philosophical Magazine and Journal of Science* 42.334, pp. 1298–1307. DOI: [10.1080/14786444108561385](https://doi.org/10.1080/14786444108561385).
- Bluthè, J., Weisz-Patrault, D., and Ehlacher, A. (2017). “Energetic approach for a sliding inclusion accounting for plastic dissipation at the interface, application to phase nucleation”. In: *International Journal of Solids and Structures* 121, pp. 163–173. ISSN: 0020-7683. DOI: [10.1016/j.ijsolstr.2017.05.023](https://doi.org/10.1016/j.ijsolstr.2017.05.023).
- Boehler, J.-P. (1987). *Applications of tensor functions in solid mechanics*. Vol. 292. Springer.
- Bogers, A. and Burgers, W. (1964). “Partial dislocations on the 110 planes in the B.C.C. lattice and the transition of the F.C.C. into the B.C.C. lattice”. In: *Acta Metallurgica* 12.2, pp. 255–261. ISSN: 0001-6160. DOI: [10.1016/0001-6160\(64\)90194-4](https://doi.org/10.1016/0001-6160(64)90194-4).
- Bohemen, S. van and Morsdorf, L. (2017). “Predicting the Ms temperature of steels with a thermodynamic based model including the effect of the prior austenite grain size”. In: *Acta Materialia* 125, pp. 401–415. ISSN: 1359-6454. DOI: [10.1016/j.actamat.2016.12.029](https://doi.org/10.1016/j.actamat.2016.12.029).
- Böhm, H. J. (1998). *A short introduction to basic aspects of continuum Micromechanics*. Cdl-fmd Report.
- Bollmann, W. (1971). “Crystal Defects and Crystalline Interfaces”. In: *Kristall und Technik* 6.3, p. 49. ISSN: 1521-4079. DOI: [10.1002/crat.19710060320](https://doi.org/10.1002/crat.19710060320).
- Bollmann, W., Michaut, B., and Sainfort, G. (1972). “Pseudo-subgrain-boundaries in stainless steel”. In: *physica status solidi (a)* 13.2, pp. 637–649. ISSN: 1521-396X. DOI: [10.1002/pssa.2210130236](https://doi.org/10.1002/pssa.2210130236).
- Bower, A. F. (2009). *Applied mechanics of solids*. CRC press. ISBN: 9781439802489.
- Bowles, J. and Mackenzie, J. (1954). “The crystallography of martensite transformations I”. In: *Acta metallurgica* 2.1, pp. 129–137. DOI: [10.1016/0001-6160\(54\)90102-9](https://doi.org/10.1016/0001-6160(54)90102-9).
- Boyce, B. and Dilmore, M. (2009). “The dynamic tensile behavior of tough, ultrahigh-strength steels at strain-rates from 0.0002s⁻¹ to 200s⁻¹”. In: *International Journal of*

- Impact Engineering* 36.2, pp. 263–271. ISSN: 0734-743X. DOI: [10.1016/j.ijimpeng.2007.11.006](https://doi.org/10.1016/j.ijimpeng.2007.11.006).
- Buerger, M. (1951). “Phase transformations in solids”. In: *John Wiley*, p. 183.
- Bullough, R. and Bilby, B. A. (1956). “Continuous Distributions of Dislocations: Surface Dislocations and the Crystallography of Martensitic Transformations”. In: *Proceedings of the Physical Society. Section B* 69.12, p. 1276.
- Bunge, H. J. (1970). “Some applications of the Taylor theory of polycrystal plasticity”. In: *Kristall und Technik* 5.1, pp. 145–175. ISSN: 1521-4079. DOI: [10.1002/crat.19700050112](https://doi.org/10.1002/crat.19700050112).
- Bunge, H. (1982). *Texture analysis in materials science: mathematical methods*. Butterworths. ISBN: 9780408106429.
- Bunge, H.-J. and Roberts, W. T. (1969). “Orientation distribution, elastic and plastic anisotropy in stabilized steel sheet”. In: *Journal of Applied Crystallography* 2.3, pp. 116–128. DOI: [10.1107/S0021889869006704](https://doi.org/10.1107/S0021889869006704).
- Burgers, W. (1934). “On the process of transition of the cubic-body-centered modification into the hexagonal-close-packed modification of zirconium”. In: *Physica* 1.7, pp. 561–586. ISSN: 0031-8914. DOI: [10.1016/S0031-8914\(34\)80244-3](https://doi.org/10.1016/S0031-8914(34)80244-3).
- Busso, E. P. and McClintock, F. A. (1996). “A dislocation mechanics-based crystallographic model of a B2-type intermetallic alloy”. In: *International Journal of Plasticity* 12.1, pp. 1–28. ISSN: 0749-6419. DOI: [10.1016/S0749-6419\(95\)00041-0](https://doi.org/10.1016/S0749-6419(95)00041-0).
- Byun, T. (2003). “On the stress dependence of partial dislocation separation and deformation microstructure in austenitic stainless steels”. In: *Acta Materialia* 51.11, pp. 3063–3071. ISSN: 1359-6454. DOI: [10.1016/S1359-6454\(03\)00117-4](https://doi.org/10.1016/S1359-6454(03)00117-4).
- Cahn, J. W. and Hilliard, J. E. (1958). “Free Energy of a Nonuniform System. I. Interfacial Free Energy”. In: *The Journal of Chemical Physics* 28.2, pp. 258–267. DOI: [10.1063/1.1744102](https://doi.org/10.1063/1.1744102).
- Caillard, D. and Martin, J. (2003). *Thermally Activated Mechanisms in Crystal Plasticity*. Pergamon Materials Series. Elsevier Science. ISBN: 9780080542782.
- Cailletaud, G. (1987). “Une approche micromécanique phénoménologique du comportement inélastique des métaux”. PhD thesis. Université Paris 6.
- (1992). “A micromechanical approach to inelastic behaviour of metals”. In: *International Journal of Plasticity* 8.1, pp. 55–73. ISSN: 0749-6419. DOI: [10.1016/0749-6419\(92\)90038-E](https://doi.org/10.1016/0749-6419(92)90038-E).

- Cailletaud, G. (2009). “An Overview of the Anatomy of Crystal Plasticity Models”. In: *Advanced Engineering Materials* 11.9, pp. 710–716. ISSN: 1527-2648. DOI: [10.1002/adem.200900064](https://doi.org/10.1002/adem.200900064).
- (2010). “Basic ingredients, development of phenomenological models and practical use of crystal plasticity”. In: *Multiscale Modelling of Plasticity and Fracture by Means of Dislocation Mechanics*. Springer, pp. 271–326.
- Cailletaud, G. and Coudon, F. (2016). “Scale Transition Rules Applied to Crystal Plasticity”. In: *Materials with Internal Structure: Multiscale and Multifield Modeling and Simulation*. Ed. by P. Trovalusci. Cham: Springer International Publishing, pp. 1–15. ISBN: 978-3-319-21494-8. DOI: [10.1007/978-3-319-21494-8_1](https://doi.org/10.1007/978-3-319-21494-8_1).
- Cailletaud, G., Forest, S., Jeulin, D., Feyel, F., Galliet, I., Mounoury, V., and Quilici, S. (2003). “Some elements of microstructural mechanics”. In: *Computational Materials Science* 27.3, pp. 351–374. ISSN: 0927-0256. DOI: [10.1016/S0927-0256\(03\)00041-7](https://doi.org/10.1016/S0927-0256(03)00041-7).
- Cailletaud, G. and Pilvin, P. (1994). “Utilisation de modèles polycristallins pour le calcul par éléments finis”. In: *Revue Européenne des éléments* 3.4, pp. 515–541. DOI: [10.1080/12506559.1994.10511147](https://doi.org/10.1080/12506559.1994.10511147).
- Cailletaud, G., Taleb, L., and Sai, K. (2018). *Multi-mechanism Modeling of Inelastic Material Behavior*. Iste Series. Wiley. ISBN: 9781848215801.
- Calcagnotto, M., Ponge, D., Demir, E., and Raabe, D. (2010). “Orientation gradients and geometrically necessary dislocations in ultrafine grained dual-phase steels studied by 2D and 3D EBSD”. In: *Materials Science and Engineering: A* 527.10 - 11, pp. 2738–2746. ISSN: 0921-5093. DOI: [10.1016/j.msea.2010.01.004](https://doi.org/10.1016/j.msea.2010.01.004).
- Canova, G., Kocks, U., Tomé, C., and Jonas, J. (1985). “The yield surface of textured polycrystals”. In: *Journal of the Mechanics and Physics of Solids* 33.4, pp. 371–397. ISSN: 0022-5096. DOI: [10.1016/0022-5096\(85\)90035-3](https://doi.org/10.1016/0022-5096(85)90035-3).
- Capriz, G. (2013). *Continua with Microstructure*. Springer Tracts in Natural Philosophy. Springer New York. ISBN: 9781461235842.
- Carson, R., Obstalecki, M., Miller, M., and Dawson, P. (2017). “Characterizing heterogeneous intragranular deformations in polycrystalline solids using diffraction-based and mechanics-based metrics”. In: *Modelling and Simulation in Materials Science and Engineering* 25.5, p. 055008.

- Carstensen, C., Hackl, K., and Mielke, A. (2002). “Non-convex potentials and microstructures in finite-strain plasticity”. In: *Proceedings of the Royal Society of London A: Mathematical, Physical and Engineering Sciences* 458.2018, pp. 299–317. ISSN: 1364-5021. DOI: [10.1098/rspa.2001.0864](https://doi.org/10.1098/rspa.2001.0864).
- Castelluccio, G. M. and McDowell, D. L. (2017). “Mesoscale cyclic crystal plasticity with dislocation substructures”. In: *International Journal of Plasticity* 98, pp. 1–26. ISSN: 0749-6419. DOI: [10.1016/j.ijplas.2017.06.002](https://doi.org/10.1016/j.ijplas.2017.06.002).
- Cayron, C. (2017). “Over the shear paradigm”. In: *arXiv*. DOI: [arXiv:1706.07750](https://doi.org/10.48550/arXiv.1706.07750).
- Cayron, C., Barcelo, F., and Carlan, Y. de (2010). “The mechanisms of the fcc - bcc martensitic transformation revealed by pole figures”. In: *Acta Materialia* 58.4, pp. 1395–1402. ISSN: 1359-6454. DOI: [10.1016/j.actamat.2009.10.046](https://doi.org/10.1016/j.actamat.2009.10.046).
- (2011). “Reply to "Comments on:~The mechanisms of the fcc - bcc martensitic transformation revealed by pole figures"”. In: *Scripta Materialia* 64.1, pp. 103–106. ISSN: 1359-6462. DOI: [10.1016/j.scriptamat.2010.09.004](https://doi.org/10.1016/j.scriptamat.2010.09.004).
- Cayron, C. (2006). “Groupoid of orientational variants”. In: *Acta Crystallographica Section A: Foundations of Crystallography* 62.1, pp. 21–40. DOI: [10.1107/S010876730503686X](https://doi.org/10.1107/S010876730503686X).
- (2007). “*ARPGE*: a computer program to automatically reconstruct the parent grains from electron backscatter diffraction data”. In: *Journal of Applied Crystallography* 40.6, pp. 1183–1188. DOI: [10.1107/S0021889807048777](https://doi.org/10.1107/S0021889807048777).
- (2015). “Continuous atomic displacements and lattice distortion during fcc–bcc martensitic transformation”. In: *Acta Materialia* 96, pp. 189–202. DOI: [10.1016/j.actamat.2015.06.010](https://doi.org/10.1016/j.actamat.2015.06.010).
- Cayron, C., Baur, A., and Loge, R. (2016). “Crystallography of low-alloy martensitic steels: {557} habit planes of the blocks and self-accommodation in the packets”. In: *arXiv preprint arXiv:1606.04257*.
- Cermelli, P. and Gurtin, M. E. (1994). “The dynamics of solid-solid phase transitions 2. Incoherent interfaces”. In: *Archive for Rational Mechanics and Analysis* 127.1, pp. 41–99. ISSN: 1432-0673. DOI: [10.1007/BF01845217](https://doi.org/10.1007/BF01845217).
- Chaboche, J. (1993). “Cyclic Viscoplastic Constitutive Equations, Part II: Stored Energy–Comparison Between Models and Experiments”. In: *Journal of Applied Mechanics* 60.4, pp. 822–828. ISSN: 0021-8936. DOI: [10.1115/1.2900990](https://doi.org/10.1115/1.2900990).

- Chaboche, J. (2008). “A review of some plasticity and viscoplasticity constitutive theories”. In: *International Journal of Plasticity* 24.10, pp. 1642–1693. ISSN: 0749-6419. DOI: [10.1016/j.ijplas.2008.03.009](https://doi.org/10.1016/j.ijplas.2008.03.009).
- Chen, X., Srivastava, V., Dabade, V., and James, R. D. (2013). “Study of the cofactor conditions: Conditions of supercompatibility between phases”. In: *Journal of the Mechanics and Physics of Solids* 61.12, pp. 2566–2587. ISSN: 0022-5096. DOI: [10.1016/j.jmps.2013.08.004](https://doi.org/10.1016/j.jmps.2013.08.004).
- Chen, X., Song, Y., Tamura, N., and James, R. D. (2016). “Determination of the stretch tensor for structural transformations”. In: *Journal of the Mechanics and Physics of Solids* 93, pp. 34–43. ISSN: 0022-5096. DOI: [10.1016/j.jmps.2016.02.009](https://doi.org/10.1016/j.jmps.2016.02.009).
- Cherkaoui, M. and Berveiller, M. (2000a). “Mechanics of materials undergoing martensitic phase change: A micro-macro approach for transformation induced plasticity”. In: *ZAMM-Journal of Applied Mathematics and Mechanics/Zeitschrift für Angewandte Mathematik und Mechanik* 80.4, pp. 219–232. DOI: [10.1002/\(SICI\)1521-4001\(200004\)80:4<219::AID-ZAMM219>3.0.CO;2-L](https://doi.org/10.1002/(SICI)1521-4001(200004)80:4<219::AID-ZAMM219>3.0.CO;2-L).
- Cherkaoui, M., Berveiller, M., and Lemoine, X. (2000b). “Couplings between plasticity and martensitic phase transformation: overall behavior of polycrystalline {TRIP} steels”. In: *International Journal of Plasticity* 16.10-11, pp. 1215–1241. ISSN: 0749-6419. DOI: [10.1016/S0749-6419\(00\)00008-5](https://doi.org/10.1016/S0749-6419(00)00008-5).
- Cherkaoui, M., Berveiller, M., and Sabar, H. (1998). “Micromechanical modeling of martensitic transformation induced plasticity (TRIP) in austenitic single crystals”. In: *International Journal of Plasticity* 14.7, pp. 597–626. DOI: [10.1016/S0749-6419\(99\)80000-X](https://doi.org/10.1016/S0749-6419(99)80000-X).
- Chiba, T., Shirazi, H., Miyamoto, G., and Furuhashi, T. (2017). “Grain Refinement by Cyclic Displacive Forward/Reverse Transformation in Fe-High-Ni Alloys”. In: *Metallurgical and Materials Transactions A* 48.9, pp. 4204–4210. ISSN: 1543-1940. DOI: [10.1007/s11661-017-4152-4](https://doi.org/10.1007/s11661-017-4152-4).
- Chintha, A. R., Sharma, V., and Kundu, S. (2013). “Analysis of Martensite Pole Figure from Crystallographic View Point”. In: *Metallurgical and Materials Transactions A* 44.11, pp. 4861–4865. ISSN: 1543-1940. DOI: [10.1007/s11661-013-1926-1](https://doi.org/10.1007/s11661-013-1926-1).
- Christian, J. (1965). *The Theory of Phase Transformations in Metals and Alloys*. Oxford: Pergamon Press. ISBN: 9780080542775.
- (1994). “Crystallographic theories, interface structures, and transformation mechanisms”. In: *Metallurgical and Materials Transactions A* 25 (9). DOI: [10.1007/bf02649031](https://doi.org/10.1007/bf02649031).

- Christian, J. (1997). "Lattice correspondence, atomic site correspondence and shape change in "diffusional-displacive" phase transformations". In: *Progress in materials science* 42.1 (1-4), pp. 101–108. DOI: [10.1016/s0079-6425\(97\)00009-1](https://doi.org/10.1016/s0079-6425(97)00009-1).
- Christian, J. and Mahajan, S. (1995a). "Deformation twinning". In: *Progress in Materials Science* 39.1-2, pp. 1–157. ISSN: 0079-6425. DOI: [10.1016/0079-6425\(94\)00007-7](https://doi.org/10.1016/0079-6425(94)00007-7).
- Christian, J., Olson, G., and Cohen, M. (1995b). "Classification of displacive transformations: What is a martensitic transformation?" In: *Le Journal de Physique IV* 5.C8, pp. C8–3. DOI: [10.1051/jp4:1995801](https://doi.org/10.1051/jp4:1995801).
- Christien, F., Telling, M., and Knight, K. (2013). "Neutron diffraction in situ monitoring of the dislocation density during martensitic transformation in a stainless steel". In: *Scripta Materialia* 68.7, pp. 506–509. ISSN: 1359-6462. DOI: [10.1016/j.scriptamat.2012.11.031](https://doi.org/10.1016/j.scriptamat.2012.11.031).
- Clayton, J. (2010). *Nonlinear Mechanics of Crystals*. Solid Mechanics and Its Applications. Springer Netherlands. ISBN: 9789400703506.
- Clayton, J., Hartley, C., and McDowell, D. (2014). "The missing term in the decomposition of finite deformation". In: *International Journal of Plasticity* 52, pp. 51–76. ISSN: 0749-6419. DOI: [10.1016/j.ijplas.2013.04.009](https://doi.org/10.1016/j.ijplas.2013.04.009).
- Cohen, J., Hinton, R., Lay, K., and Sass, S. (1962). "Partial dislocations on the {110} planes in the bcc lattice". In: *Acta metallurgica* 10.9, pp. 894–895.
- Cohen, M., Olson, G., and Owen, W. (1992). *Martensite: a tribute to Morris Cohen*. ASM International. ISBN: 9780871704344.
- Cohen, M. (1972). "Operational nucleation in martensitic transformations". In: *Metallurgical Transactions* 3.5, pp. 1095–1098. ISSN: 1543-1916. DOI: [10.1007/BF02642440](https://doi.org/10.1007/BF02642440).
- Conti, S. and Zanzotto, G. (2004). "A Variational Model for Reconstructive Phase Transformations in Crystals, and their Relation to Dislocations and Plasticity". In: *Archive for Rational Mechanics and Analysis* 173.1, pp. 69–88. ISSN: 1432-0673. DOI: [10.1007/s00205-004-0311-z](https://doi.org/10.1007/s00205-004-0311-z).
- Cooman, B. C. D., Estrin, Y., and Kim, S. K. (2018). "Twinning-induced plasticity (TWIP) steels". In: *Acta Materialia* 142, pp. 283–362. ISSN: 1359-6454. DOI: [10.1016/j.actamat.2017.06.046](https://doi.org/10.1016/j.actamat.2017.06.046).
- Cordero, N., Forest, S., Busso, E., Berbenni, S., and Cherkaoui, M. (2012). "Grain size effects on plastic strain and dislocation density tensor fields in metal polycrystals". In:

- Computational Materials Science* 52.1, pp. 7–13. ISSN: 0927-0256. DOI: [10.1016/j.commatsci.2011.02.043](https://doi.org/10.1016/j.commatsci.2011.02.043).
- Cosserat, E. and Cosserat, F. (1909). *Théorie des corps déformables*. Paris, Librairie Scientifique A. Hermann et fils 6, Rue de la Sorbonne, 6.
- Cottrell, A. (1964). *Theory of crystal dislocations*. Documents on modern physics. Gordon and Breach.
- Crocker, A. (1965). “Shear resolution applied to the martensite reaction in steel”. In: *Acta Metallurgica* 13.7, pp. 815–825.
- Curtze, S. and Kuokkala, V.-T. (2010). “Dependence of tensile deformation behavior of TWIP steels on stacking fault energy, temperature and strain rate”. In: *Acta Materialia* 58.15, pp. 5129–5141. ISSN: 1359-6454. DOI: [10.1016/j.actamat.2010.05.049](https://doi.org/10.1016/j.actamat.2010.05.049).
- Cyril, C. (2018). “A one-step mechanism for new twinning modes in magnesium and titanium alloys modelled by the obliquity correction of a (58° , $\mathbf{a} + 2\mathbf{b}$) prototype stretch twin”. In: *Acta Crystallographica Section A* 74.1, pp. 44–53. DOI: [10.1107/S2053273317015042](https://doi.org/10.1107/S2053273317015042).
- Dacorogna, B. (1982). “Quasiconvexity and relaxation of nonconvex problems in the calculus of variations”. In: *Journal of Functional Analysis* 46.1, pp. 102–118. ISSN: 0022-1236. DOI: [10.1016/0022-1236\(82\)90046-5](https://doi.org/10.1016/0022-1236(82)90046-5).
- Dacorogna, B. (2007). *Direct Methods in the Calculus of Variations*. Springer. ISBN: 9780387552491.
- Dahmen, U. (1982). “Orientation relationships in precipitation systems”. In: *Acta Metallurgica* 30.1, pp. 63–73. ISSN: 0001-6160. DOI: [10.1016/0001-6160\(82\)90045-1](https://doi.org/10.1016/0001-6160(82)90045-1).
- Davies, R. G. and Magee, C. L. (1971). “Influence of austenite and martensite strength on martensite morphology”. In: *Metallurgical Transactions* 2.7, pp. 1939–1947. ISSN: 1543-1940. DOI: [10.1007/BF02913427](https://doi.org/10.1007/BF02913427).
- Davies, R. and Magee, C. (1970). “Austenite ferromagnetism and martensite morphology”. In: *Metallurgical Transactions* 1.10, pp. 2927–2931. ISSN: 1543-1916. DOI: [10.1007/BF03037832](https://doi.org/10.1007/BF03037832).
- Daw, M. S. and Baskes, M. I. (1984). “Embedded-atom method: Derivation and application to impurities, surfaces, and other defects in metals”. In: *Physics Reviews B* 29 (12), pp. 6443–6453. DOI: [10.1103/PhysRevB.29.6443](https://doi.org/10.1103/PhysRevB.29.6443).
- Devincre, B. and Gatti, R. (2015). “Physically Justified Models for Crystal Plasticity Developed with Dislocation Dynamics Simulations”. In: *AerospaceLab* 9, pp. 1–7. DOI: [10.12762/2015.AL09-02](https://doi.org/10.12762/2015.AL09-02).

- Devincre, B., Hoc, T., and Kubin, L. (2008). “Dislocation Mean Free Paths and Strain Hardening of Crystals”. In: *Science* 320.5884, pp. 1745–1748. ISSN: 0036-8075. DOI: [10.1126/science.1156101](https://doi.org/10.1126/science.1156101).
- Devincre, B., Kubin, L., and Hoc, T. (2006). “Physical analyses of crystal plasticity by DD simulations”. In: *Scripta Materialia* 54.5, pp. 741–746. ISSN: 1359-6462. DOI: [10.1016/j.scriptamat.2005.10.066](https://doi.org/10.1016/j.scriptamat.2005.10.066).
- (2007). “Collinear superjogs and the low-stress response of fcc crystals”. In: *Scripta Materialia* 57.10, pp. 905–908. ISSN: 1359-6462. DOI: [10.1016/j.scriptamat.2007.07.026](https://doi.org/10.1016/j.scriptamat.2007.07.026).
- Djaziri, S., Li, Y., Nematollahi, G. A., Grabowski, B., Goto, S., Kirchlechner, C., Kostka, A., Doyle, S., Neugebauer, J., Raabe, D., and Dehm, G. (2016). “Deformation-Induced Martensite: A New Paradigm for Exceptional Steels”. In: *Advanced Materials* 28.35, pp. 7753–7757. ISSN: 1521-4095. DOI: [10.1002/adma.201601526](https://doi.org/10.1002/adma.201601526).
- Dong, Z., Schönecker, S., Chen, D., Li, W., Long, M., and Vitos, L. (2017). “Elastic properties of paramagnetic austenitic steel at finite temperature: Longitudinal spin fluctuations in multicomponent alloys”. In: *Physical Review B* 96 (17), p. 174415. DOI: [10.1103/PhysRevB.96.174415](https://doi.org/10.1103/PhysRevB.96.174415).
- Drucker, D. C. (1957). *A definition of stable inelastic material*. Tech. rep. DTIC Document.
- Du, C., Hoefnagels, J., Vaes, R., and Geers, M. (2016a). “Block and sub-block boundary strengthening in lath martensite”. In: *Scripta Materialia* 116, pp. 117–121. ISSN: 1359-6462. DOI: [10.1016/j.scriptamat.2016.01.043](https://doi.org/10.1016/j.scriptamat.2016.01.043).
- (2016b). “Plasticity of lath martensite by sliding of substructure boundaries”. In: *Scripta Materialia* 120, pp. 37–40. ISSN: 1359-6462. DOI: [10.1016/j.scriptamat.2016.04.006](https://doi.org/10.1016/j.scriptamat.2016.04.006).
- Dudarev, S. L., Bullough, R., and Derlet, P. M. (2008). “Effect of the $\alpha-\gamma$ Phase Transition on the Stability of Dislocation Loops in bcc Iron”. In: *Physical Reviews Letters* 100 (13), p. 135503. DOI: [10.1103/PhysRevLett.100.135503](https://doi.org/10.1103/PhysRevLett.100.135503).
- Düsing, M. and Mahnken, R. (2016). “Simulation of lower bainitic transformation with the phase-field method considering carbide formation”. In: *Computational Materials Science* 111, pp. 91–100. ISSN: 0927-0256. DOI: [10.1016/j.commatsci.2015.08.043](https://doi.org/10.1016/j.commatsci.2015.08.043).
- Dvorak, G. (2012). *Micromechanics of Composite Materials*. Solid Mechanics and Its Applications. Springer Netherlands. ISBN: 9789400741010.
- Edalati, K., Toh, S., Furuta, T., Kuramoto, S., Watanabe, M., and Horita, Z. (2012). “Development of ultrahigh strength and high ductility in nanostructured iron alloys

- with lattice softening and nanotwins”. In: *Scripta Materialia* 67.5, pp. 511–514. ISSN: 1359-6462. DOI: [10.1016/j.scriptamat.2012.06.019](https://doi.org/10.1016/j.scriptamat.2012.06.019).
- EduPack, C. (2007). *The Cambridge Engineering Selector*.
- Ehrenfest, P. (1933a). “Phase changes in the ordinary and extended sense classified according to the corresponding singularities of the thermodynamic potential”. In: *Proc Acad Sci Amsterdam*. Vol. 36, pp. 153–157.
- (1933b). *Phasenumwandlungen im üblichen und erweiterten Sinn, classifiziert nach den entsprechenden Singularitäten des thermodynamischen Potentials*. NV Noord-Hollandsche Uitgevers Maatschappij.
- Ericksen, J. (2008). “On the Cauchy - Born Rule”. In: *Mathematics and Mechanics of Solids* 13.3-4, pp. 199–220. DOI: [10.1177/1081286507086898](https://doi.org/10.1177/1081286507086898).
- Eringen, A. and Edelen, D. (1972). “On nonlocal elasticity”. In: *International Journal of Engineering Science* 10.3, pp. 233–248. ISSN: 0020-7225. DOI: [10.1016/0020-7225\(72\)90039-0](https://doi.org/10.1016/0020-7225(72)90039-0).
- Erinosho, T., Collins, D., Wilkinson, A., Todd, R., and Dunne, F. (2016). “Assessment of X-ray diffraction and crystal plasticity lattice strain evolutions under biaxial loading”. In: *International Journal of Plasticity* 83, pp. 1–18. ISSN: 0749-6419. DOI: [10.1016/j.ijplas.2016.03.011](https://doi.org/10.1016/j.ijplas.2016.03.011).
- Esfahani, S. E., Ghamarian, I., Levitas, V. I., and Collings, P. C. (2018). “Microscale Phase Field Modeling of the Martensite Transformation during cyclic loading of NiTi Single Crystal”. In: *International Journal of Solids and Structures*. ISSN: 0020-7683. DOI: [10.1016/j.ijsolstr.2018.03.022](https://doi.org/10.1016/j.ijsolstr.2018.03.022).
- Eshelby, J. D. (1999). “Energy Relations and the Energy-Momentum Tensor in Continuum Mechanics”. In: *Fundamental Contributions to the Continuum Theory of Evolving Phase Interfaces in Solids: A Collection of Reprints of 14 Seminal Papers*. Ed. by J. M. Ball, D. Kinderlehrer, P. Podio-Guidugli, and M. Slemrod. Berlin, Heidelberg: Springer Berlin Heidelberg, pp. 82–119. ISBN: 978-3-642-59938-5. DOI: [10.1007/978-3-642-59938-5_5](https://doi.org/10.1007/978-3-642-59938-5_5).
- Eshelby, J. (1961). “Elastic inclusions and inhomogeneities”. In: *Progress in solid mechanics* 2.1, pp. 89–140.
- Eshelby, J. D. (1957). “The determination of the elastic field of an ellipsoidal inclusion, and related problems”. In: *Proceedings of the Royal Society of London A: Mathematical, Physical and Engineering Sciences*. Vol. 241. The Royal Society, pp. 376–396.

- Ferreira, P. and Müllner, P. (1998). “A thermodynamic model for the stacking-fault energy”. In: *Acta Materialia* 46.13, pp. 4479–4484. ISSN: 1359-6454. DOI: [10.1016/S1359-6454\(98\)00155-4](https://doi.org/10.1016/S1359-6454(98)00155-4).
- Feyel, F. (2003). “A multilevel finite element method (FE2) to describe the response of highly non-linear structures using generalized continua”. In: *Computer Methods in Applied Mechanics and Engineering* 192.28, pp. 3233–3244. ISSN: 0045-7825. DOI: [10.1016/S0045-7825\(03\)00348-7](https://doi.org/10.1016/S0045-7825(03)00348-7).
- Field, D., Trivedi, P., Wright, S., and Kumar, M. (2005). “Analysis of local orientation gradients in deformed single crystals”. In: *Ultramicroscopy* 103.1, pp. 33–39. ISSN: 0304-3991. DOI: [10.1016/j.ultramic.2004.11.016](https://doi.org/10.1016/j.ultramic.2004.11.016).
- Fischer, A. (1992). “A special newton-type optimization method”. In: *Optimization* 24.3-4, pp. 269–284. DOI: [10.1080/02331939208843795](https://doi.org/10.1080/02331939208843795).
- Fischer, F. D., Antretter, T., Azzouz, F., Cailletaud, G., Pineau, A., Tanaka, K., and Nagayama, K. (2000). “The role of backstress in phase transforming steels”. In: *Archives of Mechanics* 52.4-5, pp. 569–588.
- Fischer, F., Svoboda, J., and Petryk, H. (2014). “Thermodynamic extremal principles for irreversible processes in materials science”. In: *Acta Materialia* 67, pp. 1–20. ISSN: 1359-6454. DOI: [10.1016/j.actamat.2013.11.050](https://doi.org/10.1016/j.actamat.2013.11.050).
- Fischlschweiger, M., Cailletaud, C., and T., A. (2012). “A mean-field model for transformation induced plasticity including backstress effects for non-proportional loadings”. In: *International journal of plasticity*, pp. 53–71. ISSN: 0749-6419. DOI: [10.1016/j.ijplas.2012.04.001](https://doi.org/10.1016/j.ijplas.2012.04.001).
- Fischlschweiger, M., Antretter, T., and Cailletaud, G. (2013). “Transformation hardening and kinetics for stress assisted and temperature driven martensitic transformation in steels”. In: *Mechanics Research Communications* 47, pp. 84–88. ISSN: 0093-6413. DOI: [10.1016/j.mechrescom.2012.09.007](https://doi.org/10.1016/j.mechrescom.2012.09.007).
- Fleck, N. A., Hutchinson, J. W., and Willis, J. R. (2014). “Strain gradient plasticity under non-proportional loading”. In: *Proceedings of the Royal Society of London A: Mathematical, Physical and Engineering Sciences* 470.2170. ISSN: 1364-5021. DOI: [10.1098/rspa.2014.0267](https://doi.org/10.1098/rspa.2014.0267).
- Fleck, N., Muller, G., Ashby, M., and Hutchinson, J. (1994). “Strain gradient plasticity: Theory and experiment”. In: *Acta Metallurgica et Materialia* 42.2, pp. 475–487. ISSN: 0956-7151. DOI: [10.1016/0956-7151\(94\)90502-9](https://doi.org/10.1016/0956-7151(94)90502-9).

- Forest, S. (2008). “Some links between Cosserat, strain gradient crystal plasticity and the statistical theory of dislocations”. In: *Philosophical Magazine* 88.30-32, pp. 3549–3563. DOI: [10.1080/14786430802154815](https://doi.org/10.1080/14786430802154815).
- Forest, S., Cailletaud, G., and Sievert, R. (1997). “A Cosserat theory for elastoviscoplastic single crystals at finite deformation”. In: *Arch. Mech* 49, pp. 705–736.
- Forest, S. (2012). “Generalized Continuum Modelling of Crystal Plasticity”. In: *Generalized Continua and Dislocation Theory: Theoretical Concepts, Computational Methods and Experimental Verification*. Ed. by C. Sansour and S. Skatulla. Vienna: Springer Vienna, pp. 181–287. ISBN: 978-3-7091-1222-9. DOI: [10.1007/978-3-7091-1222-9_3](https://doi.org/10.1007/978-3-7091-1222-9_3).
- Forest, S., Ammar, K., and Appolaire, B. (2011). “Micromorphic vs. phase-field approaches for gradient viscoplasticity and phase transformations”. In: *Advances in extended and multifield theories for continua* 59, pp. 69–88.
- Fouvry, S., Kapsa, P., and Vincent, L. (2001). “An elastic - plastic shakedown analysis of fretting wear”. In: *Wear* 247.1, pp. 41–54. ISSN: 0043-1648. DOI: [10.1016/S0043-1648\(00\)00508-1](https://doi.org/10.1016/S0043-1648(00)00508-1).
- Franciosi, P. (1983). “Glide mechanisms in b.c.c. crystals: An investigation of the case of α -iron through multislip and latent hardening tests”. In: *Acta Metallurgica* 31.9, pp. 1331–1342. ISSN: 0001-6160. DOI: [10.1016/0001-6160\(83\)90004-4](https://doi.org/10.1016/0001-6160(83)90004-4).
- (1985). “The concepts of latent hardening and strain hardening in metallic single crystals”. In: *Acta Metallurgica* 33.9, pp. 1601–1612. ISSN: 0001-6160. DOI: [10.1016/0001-6160\(85\)90154-3](https://doi.org/10.1016/0001-6160(85)90154-3).
- Franciosi, P. and Zaoui, A. (1982). “Multislip in f.c.c. crystals a theoretical approach compared with experimental data”. In: *Acta Metallurgica* 30.8, pp. 1627–1637. ISSN: 0001-6160. DOI: [10.1016/0001-6160\(82\)90184-5](https://doi.org/10.1016/0001-6160(82)90184-5).
- Frank, F. (1951). “LXXXIII. Crystal dislocations - Elementary concepts and definitions”. In: *The London, Edinburgh, and Dublin Philosophical Magazine and Journal of Science* 42.331, pp. 809–819. DOI: [10.1080/14786445108561310](https://doi.org/10.1080/14786445108561310).
- Frank, F. (1953). “Martensite”. In: *Acta Metallurgica* 1.1, pp. 15–21. ISSN: 0001-6160. DOI: [10.1016/0001-6160\(53\)90005-4](https://doi.org/10.1016/0001-6160(53)90005-4).
- Frederick, C. and Armstrong, P. (2007). “A mathematical representation of the multiaxial Bauschinger effect”. In: *Materials at High Temperatures* 24.1, pp. 1–26. DOI: [10.1179/096034007X207589](https://doi.org/10.1179/096034007X207589).
- Fressengeas, C. (2017). *Mechanics of Dislocation Fields*. Iste Series. Wiley. ISBN: 9781848213753.

- Friedel, G. (1964). *Dislocations*. Pergamon Press Paris.
- Fritzen, F. and Böhlke, T. (2010). “Three-dimensional finite element implementation of the nonuniform transformation field analysis”. In: *International Journal for Numerical Methods in Engineering* 84.7, pp. 803–829. DOI: [10.1002/nme.2920](https://doi.org/10.1002/nme.2920).
- Fritzen, F. and Hodapp, M. (2016). “The finite element square reduced (FE2R) method with GPU acceleration: towards three-dimensional two-scale simulations”. In: *International Journal of Numerical Methods in Engineering* 107.10, pp. 853–881. ISSN: 1097-0207. DOI: [10.1002/nme.5188](https://doi.org/10.1002/nme.5188).
- Fullman, R. L. (1953). “Measurement of Particle Sizes in Opaque Bodies”. In: *JOM* 5.3, pp. 447–452. ISSN: 1543-1851. DOI: [10.1007/BF03398971](https://doi.org/10.1007/BF03398971).
- Fullwood, D. T., Niezgodka, S. R., Adams, B. L., and Kalidindi, S. R. (2010). “Microstructure sensitive design for performance optimization”. In: *Progress in Materials Science* 55.6, pp. 477–562. ISSN: 0079-6425. DOI: [10.1016/j.pmatsci.2009.08.002](https://doi.org/10.1016/j.pmatsci.2009.08.002).
- Furuhara, T., Kawata, H., Morito, S., and Maki, T. (2006). “Crystallography of upper bainite in Fe-Ni-C alloys”. In: *Materials Science and Engineering: A* 431.1-2, pp. 228–236. ISSN: 0921-5093. DOI: [10.1016/j.msea.2006.06.032](https://doi.org/10.1016/j.msea.2006.06.032).
- Furuhara, T., Miyamoto, G., and Takayama, N. (2010). “Key Factors in Grain Refinement of Martensite and Bainite”. In: *THERMEC 2009*. Vol. 638. Materials Science Forum. Trans Tech Publications, pp. 3044–3049. DOI: [10.4028/www.scientific.net/MSF.638-642.3044](https://doi.org/10.4028/www.scientific.net/MSF.638-642.3044).
- Galindo-Nava, E. and Rivera-Díaz-del-Castillo, P. (2015). “A model for the microstructure behaviour and strength evolution in lath martensite”. In: *Acta Materialia* 98, pp. 81–93. ISSN: 1359-6454. DOI: [10.1016/j.actamat.2015.07.018](https://doi.org/10.1016/j.actamat.2015.07.018).
- (2016). “Understanding the factors controlling the hardness in martensitic steels”. In: *Scripta Materialia* 110, pp. 96–100. ISSN: 1359-6462. DOI: [10.1016/j.scriptamat.2015.08.010](https://doi.org/10.1016/j.scriptamat.2015.08.010).
- Gao, H., Huang, Y., Nix, W., and Hutchinson, J. (1999). “Mechanism-based strain gradient plasticity - I. Theory”. In: *Journal of the Mechanics and Physics of Solids* 47.6, pp. 1239–1263. ISSN: 0022-5096. DOI: [10.1016/S0022-5096\(98\)00103-3](https://doi.org/10.1016/S0022-5096(98)00103-3).
- Gao, X., Huang, M., and Brinson, C. (2000). “A multivariant micromechanical model for SMAs Part 1. Crystallographic issues for single crystal model”. In: *International Journal of Plasticity* 16, pp. 1345–1369. DOI: [10.1016/S0749-6419\(00\)00014-0](https://doi.org/10.1016/S0749-6419(00)00014-0).

- Gao, Y., Shi, R., Nie, J.-F., Dregia, S. A., and Wang, Y. (2016). “Group theory description of transformation pathway degeneracy in structural phase transformations”. In: *Acta Materialia* 109, pp. 353–363. ISSN: 1359-6454. DOI: [10.1016/j.actamat.2016.01.027](https://doi.org/10.1016/j.actamat.2016.01.027).
- Garrett, R., Xu, S., Lin, J., and Dean, T. (2004). “A model for predicting austenite to bainite phase transformation in producing dual phase steels”. In: *International Journal of Machine Tools and Manufacture* 44.7-8, pp. 831–837. ISSN: 0890-6955. DOI: [10.1016/j.ijmachtools.2004.01.004](https://doi.org/10.1016/j.ijmachtools.2004.01.004).
- Geissler, D., Freudenberger, J., Kauffmann, A., Martin, S., and Rafaja, D. (2014). “Assessment of the thermodynamic dimension of the stacking fault energy”. In: *Philosophical Magazine* 94.26, pp. 2967–2979. DOI: [10.1080/14786435.2014.944606](https://doi.org/10.1080/14786435.2014.944606).
- Gelfand, I., Fomin, S., and Silverman, R. (2000). *Calculus of Variations*. Dover Books on Mathematics. Dover Publications. ISBN: 9780486414485.
- Germain, L., Gey, N., Mercier, R., Blaineau, P., and Humbert, M. (2012). “An advanced approach to reconstructing parent orientation maps in the case of approximate orientation relations: Application to steels”. In: *Acta Materialia* 60.11, pp. 4551–4562. ISSN: 1359-6454. DOI: <http://10.1016/j.actamat.2012.04.034>.
- Germain, P. (1973). *Cours de mécanique des milieux continus*. Cours de mécanique des milieux continus Bd. 1. Masson.
- Ghassemi-Armaki, H., Chen, P., Bhat, S., Sadagopan, S., Kumar, S., and Bower, A. (2013). “Microscale-calibrated modeling of the deformation response of low-carbon martensite”. In: *Acta Materialia* 61.10, pp. 3640–3652. ISSN: 1359-6454. DOI: [10.1016/j.actamat.2013.02.051](https://doi.org/10.1016/j.actamat.2013.02.051).
- Ghosh, C., Aranas, C., and Jonas, J. J. (2016). “Dynamic transformation of deformed austenite at temperatures above the Ae3”. In: *Progress in Materials Science* 82.Supplement C, pp. 151–233. ISSN: 0079-6425. DOI: [10.1016/j.pmatsci.2016.04.004](https://doi.org/10.1016/j.pmatsci.2016.04.004).
- Gibbs, J. (1902). *Elementary Principles in Statistical Mechanics: Developed with Especial Reference to the Rational Foundations of Thermodynamics*. Elementary Principles in Statistical Mechanics: Developed with Especial Reference to the Rational Foundation of Thermodynamics. C. Scribner’s sons. DOI: [10.1017/CB09780511686948](https://doi.org/10.1017/CB09780511686948).
- Ginzburg, V. L. and Landau, L. D. (1950). “On the theory of superconductivity”. In: *Journal of Experimental and Theoretical Physics* 20.1064-1082, p. 35.

- Giri, S. K., Biswas, P., and Kundu, S. (2017). “Prediction of Transformation Strain Using Microtexture Data”. In: *Metallurgical and Materials Transactions A* 48.7, pp. 3175–3180. ISSN: 1543-1940. DOI: [10.1007/s11661-017-4098-6](https://doi.org/10.1007/s11661-017-4098-6).
- Glüge, R. and Bucci, S. (2017). “Does convexity of yield surfaces in plasticity have a physical significance?” In: *Mathematics and Mechanics of Solids*, p. 1081286517721599. DOI: [10.1177/1081286517721599](https://doi.org/10.1177/1081286517721599).
- Goto, D. M., Garrett, R. K., Bingert, J. F., Chen, S. R., and Gray, G. T. (2000). “The mechanical threshold stress constitutive-strength model description of HY-100 steel”. In: *Metallurgical and Materials Transactions A* 31.8, pp. 1985–1996. ISSN: 1543-1940. DOI: [10.1007/s11661-000-0226-8](https://doi.org/10.1007/s11661-000-0226-8).
- Govindjee, S., Hackl, K., and Heinen, R. (2007). “An upper bound to the free energy of mixing by twin-compatible lamination for n-variant martensitic phase transformations”. In: *Continuum Mechanics and Thermodynamics* 18.7, pp. 443–453. ISSN: 1432-0959. DOI: [10.1007/s00161-006-0038-1](https://doi.org/10.1007/s00161-006-0038-1).
- Govindjee, S. and Hall, G. J. (2000). “A computational model for shape memory alloys”. In: *International Journal of Solids and Structures* 37.5, pp. 735–760. ISSN: 0020-7683. DOI: [10.1016/S0020-7683\(99\)00048-7](https://doi.org/10.1016/S0020-7683(99)00048-7).
- Govindjee, S. and Miehe, C. (2001). “A multi-variant martensitic phase transformation model: formulation and numerical implementation”. In: *Computer Methods in Applied Mechanics and Engineering* 191.3, pp. 215–238. DOI: [10.1016/S0045-7825\(01\)00271-7](https://doi.org/10.1016/S0045-7825(01)00271-7).
- Greenwood, G. W. and Johnson, R. H. (1965). “The Deformation of Metals Under Small Stresses During Phase Transformations”. In: *Proceedings of the Royal Society of London A: Mathematical, Physical and Engineering Sciences* 283.1394, pp. 403–422. ISSN: 0080-4630. DOI: [10.1098/rspa.1965.0029](https://doi.org/10.1098/rspa.1965.0029).
- Greninger, A. B. and Troiano, A. R. (1949). “The mechanism of martensite formation”. In: *Trans. AIME* 185.9, pp. 590–598.
- Grinfeld, M. (1991). *Thermodynamic Methods in the Theory of Heterogeneous Systems*. Longman Scientific and Technical.
- Groeber, M. A. and Jackson, M. A. (2014). “DREAM.3D: A Digital Representation Environment for the Analysis of Microstructure in 3D”. In: *Integrating Materials and Manufacturing Innovation* 3.1, p. 5. ISSN: 2193-9772. DOI: [10.1186/2193-9772-3-5](https://doi.org/10.1186/2193-9772-3-5).

- Groma, I. (1997). “Link between the microscopic and mesoscopic length-scale description of the collective behavior of dislocations”. In: *Phys. Rev. B* 56 (10), pp. 5807–5813. DOI: [10.1103/PhysRevB.56.5807](https://doi.org/10.1103/PhysRevB.56.5807).
- (2017). *private communication*.
- Groma, I., Csikor, F., and Zaiser, M. (2003). “Spatial correlations and higher-order gradient terms in a continuum description of dislocation dynamics”. In: *Acta Materialia* 51.5, pp. 1271–1281. ISSN: 1359-6454. DOI: [10.1016/S1359-6454\(02\)00517-7](https://doi.org/10.1016/S1359-6454(02)00517-7).
- Gu, X.-F., Furuhashi, T., and Zhang, W.-Z. (2016). “PTCLab: free and open-source software for calculating phase transformation crystallography”. In: *Journal of Applied Crystallography* 49.3, pp. 1099–1106. DOI: [10.1107/S1600576716006075](https://doi.org/10.1107/S1600576716006075).
- Gu, X.-F., Zhang, W.-Z., and Qiu, D. (2011). “A systematic investigation of the development of the orientation relationship in an fcc/bcc system”. In: *Acta Materialia* 59.12, pp. 4944–4956. ISSN: 1359-6454. DOI: [10.1016/j.actamat.2011.04.039](https://doi.org/10.1016/j.actamat.2011.04.039).
- Gueninchault, N. (2017). “Experimental and numerical investigation of incipient plasticity in FCC polycrystals by X-ray synchrotron topotomography and CPFEM”. PhD thesis. PSL Research University.
- Guo, Z., Lee, C., and Jr., J. M. (2004). “On coherent transformations in steel”. In: *Acta Materialia* 52.19, pp. 5511–5518. ISSN: 1359-6454. DOI: [10.1016/j.actamat.2004.08.011](https://doi.org/10.1016/j.actamat.2004.08.011).
- Gurtin, M. E. (1996). “Generalized Ginzburg-Landau and Cahn-Hilliard equations based on a microforce balance”. In: *Physica D: Nonlinear Phenomena* 92.3, pp. 178–192. ISSN: 0167-2789. DOI: [10.1016/0167-2789\(95\)00173-5](https://doi.org/10.1016/0167-2789(95)00173-5).
- (2002). “A gradient theory of single-crystal viscoplasticity that accounts for geometrically necessary dislocations”. In: *Journal of the Mechanics and Physics of Solids* 50.1, pp. 5–32. ISSN: 0022-5096. DOI: [10.1016/S0022-5096\(01\)00104-1](https://doi.org/10.1016/S0022-5096(01)00104-1).
- (2006). “The Burgers vector and the flow of screw and edge dislocations in finite-deformation single-crystal plasticity”. In: *Journal of the Mechanics and Physics of Solids* 54.9, pp. 1882–1898. ISSN: 0022-5096. DOI: [10.1016/j.jmps.2006.03.003](https://doi.org/10.1016/j.jmps.2006.03.003).
- Hackl, K. and Heinen, R. (2008a). “A micromechanical model for pretextured polycrystalline shape-memory alloys including elastic anisotropy”. In: *Continuum Mechanics and Thermodynamics* 19.8, pp. 499–510. DOI: [10.1007/s00161-008-0067-z](https://doi.org/10.1007/s00161-008-0067-z).

- Hackl, K. (1997). “Generalized standard media and variational principles in classical and finite strain elastoplasticity”. In: *Journal of the Mechanics and Physics of Solids* 45.5, pp. 667–688. ISSN: 0022-5096. DOI: [10.1016/S0022-5096\(96\)00110-X](https://doi.org/10.1016/S0022-5096(96)00110-X).
- Hackl, K. and Fischer, F. D. (2008b). “On the relation between the principle of maximum dissipation and inelastic evolution given by dissipation potentials”. In: *Proceedings of the Royal Society of London A: Mathematical, Physical and Engineering Sciences* 464.2089, pp. 117–132. ISSN: 1364-5021. DOI: [10.1098/rspa.2007.0086](https://doi.org/10.1098/rspa.2007.0086).
- Hackl, K., Hoppe, U., and Kochmann, D. M. (2014). “Variational modeling of microstructures in plasticity”. In: *Plasticity and Beyond: Microstructures, Crystal-Plasticity and Phase Transitions*. Ed. by J. Schröder and K. Hackl. Vienna: Springer Vienna, pp. 65–129. ISBN: 978-3-7091-1625-8. DOI: [10.1007/978-3-7091-1625-8_2](https://doi.org/10.1007/978-3-7091-1625-8_2).
- Hadamard, J. (1923). *Lectures on Cauchy’s Problem in Linear Partial Differential Equations*. Dover Books on Science. Yale University Press.
- Hahn, T. (1987). *Space-group symmetry*. International Tables for Crystallography. D. Reidel Pub. Co. ISBN: 9789027722805.
- Haldar, A., Suwas, S., and Bhattacharjee, D. (2009). *Microstructure and Texture in Steels: and Other Materials*. Springer London. ISBN: 9781848824546.
- Hallberg, H., Håansson, P., and Ristinmaa, M. (2007). “A constitutive model for the formation of martensite in austenitic steels under large strain plasticity”. In: *International Journal of Plasticity* 23.7, pp. 1213–1239. ISSN: 0749-6419. DOI: [10.1016/j.ijplas.2006.11.002](https://doi.org/10.1016/j.ijplas.2006.11.002).
- Halphen, B. and Nguyen, Q. S. (1975). “Sur les matériaux standard généralisés”. In: *Journal de mécanique* 14, pp. 39–63.
- Han, C.-S., Ma, A., Roters, F., and Raabe, D. (2007). “A finite element approach with patch projection for strain gradient plasticity formulations”. In: *International Journal of Plasticity* 23.4, pp. 690–710. DOI: [10.1016/j.ijplas.2006.08.003](https://doi.org/10.1016/j.ijplas.2006.08.003).
- Hane, K. F. and Shield, T. W. (1998). “Symmetry and microstructure in martensites”. In: *Philosophical Magazine* 78.6, pp. 1215–1252. DOI: [10.1080/01418619808239984](https://doi.org/10.1080/01418619808239984).
- Hansen, J., Pośpiech, J., and Lücke, K. (1978). *Tables for Texture Analysis of Cubic Crystals*. Springer-Verlag. ISBN: 9780387086897.
- Hasan, H. S. and Peet, M. J. (2012). “Heat transfer coefficient and latent heat of martensite in a medium-carbon steel”. In: *International Communications in Heat and Mass Transfer*

- 39.10, pp. 1519–1521. ISSN: 0735-1933. DOI: [10.1016/j.icheatmasstransfer.2012.09.008](https://doi.org/10.1016/j.icheatmasstransfer.2012.09.008).
- Hata, S., Sato, K., Murayama, M., Tsuchiyama, T., and Nakashima, H. (2015). “An Experimental Protocol Development of Three-Dimensional Transmission Electron Microscopy Methods for Ferrous Alloys: Towards Quantitative Microstructural Characterization in Three Dimensions”. In: *ISIJ International* 55.3, pp. 623–631. DOI: [10.2355/isijinternational.55.623](https://doi.org/10.2355/isijinternational.55.623).
- He, Y., Godet, S., and Jonas, J. J. (2005). “Representation of misorientations in Rodrigues-Frank space: application to the Bain, Kurdjumov-Sachs, Nishiyama-Wassermann and Pitsch orientation relationships in the Gibeon meteorite”. In: *Acta Materialia* 53.4, pp. 1179–1190. ISSN: 1359-6454. DOI: [10.1016/j.actamat.2004.11.021](https://doi.org/10.1016/j.actamat.2004.11.021).
- Heinen, R. and Hackl, K. (2007). “On the calculation of energy-minimizing phase fractions in shape memory alloys”. In: *Computer Methods in Applied Mechanics and Engineering* 196.21, pp. 2401–2412. ISSN: 0045-7825. DOI: [10.1016/j.cma.2007.01.001](https://doi.org/10.1016/j.cma.2007.01.001).
- Hidalgo, J. and Santofimia, M. J. (2016). “Effect of Prior Austenite Grain Size Refinement by Thermal Cycling on the Microstructural Features of As-Quenched Lath Martensite”. In: *Metallurgical and Materials Transactions A* 47.11, pp. 5288–5301. ISSN: 1543-1940. DOI: [10.1007/s11661-016-3525-4](https://doi.org/10.1007/s11661-016-3525-4).
- Hielscher, R. and Schaeben, H. (2008). “A novel pole figure inversion method: specification of the MTEX algorithm”. In: *Journal of Applied Crystallography* 41.6, pp. 1024–1037. DOI: [10.1107/S0021889808030112](https://doi.org/10.1107/S0021889808030112).
- Hill, R. (1958). “A general theory of uniqueness and stability in elastic-plastic solids”. In: *Journal of the Mechanics and Physics of Solids* 6.3, pp. 236–249. ISSN: 0022-5096. DOI: [10.1016/0022-5096\(58\)90029-2](https://doi.org/10.1016/0022-5096(58)90029-2).
- (1965). “Continuum micro-mechanics of elastoplastic polycrystals”. In: *Journal of the Mechanics and Physics of Solids* 13.2, pp. 89–101. ISSN: 0022-5096. DOI: [10.1016/0022-5096\(65\)90023-2](https://doi.org/10.1016/0022-5096(65)90023-2).
- (1983). “Interfacial operators in the mechanics of composite media”. In: *Journal of the Mechanics and Physics of Solids* 31.4, pp. 347–357. ISSN: 0022-5096. DOI: [10.1016/0022-5096\(83\)90004-2](https://doi.org/10.1016/0022-5096(83)90004-2).
- (1990). “Constitutive modelling of orthotropic plasticity in sheet metals”. In: *Journal of the Mechanics and Physics of Solids* 38.3, pp. 405–417. ISSN: 0022-5096. DOI: [10.1016/0022-5096\(90\)90006-P](https://doi.org/10.1016/0022-5096(90)90006-P).

- Hillert, M. and Agren, J. (2006). “Extremum principles for irreversible processes”. In: *Acta Materialia* 54.8, pp. 2063–2066. ISSN: 1359-6454. DOI: [10.1016/j.actamat.2005.12.033](https://doi.org/10.1016/j.actamat.2005.12.033).
- Hirth, J. P. and Lothe, J. (1968). *Theory of Dislocations. Second Edition*. Vol. 1. McGraw-Hill, New York.
- Hirth, J. (1994). “Dislocations, steps and disconnections at interfaces”. In: *Journal of Physics and Chemistry of Solids* 55.10, pp. 985–989. DOI: [10.1016/0022-3697\(94\)90118-X](https://doi.org/10.1016/0022-3697(94)90118-X).
- Hirth, J. and Pond, R. (1996). “Steps, dislocations and disconnections as interface defects relating to structure and phase transformations”. In: *Acta Materialia* 44.12, pp. 4749–4763. ISSN: 1359-6454. DOI: [10.1016/S1359-6454\(96\)00132-2](https://doi.org/10.1016/S1359-6454(96)00132-2).
- (2011). “Compatibility and accommodation in displacive phase transformations”. In: *Progress in Materials Science* 56.6, pp. 586–636. ISSN: 0079-6425. DOI: [10.1016/j.pmatsci.2011.01.003](https://doi.org/10.1016/j.pmatsci.2011.01.003).
- Hirth, J., Pond, R., Hoagland, R., Liu, X.-Y., and Wang, J. (2013). “Interface defects, reference spaces and the Frank–Bilby equation”. In: *Progress in Materials Science* 58.5, pp. 749–823. DOI: [10.1016/j.pmatsci.2012.10.002](https://doi.org/10.1016/j.pmatsci.2012.10.002).
- Hirth, J., Wang, J., and Tomé, C. (2016). “Disconnections and other defects associated with twin interfaces”. In: *Progress in Materials Science* 83, pp. 417–471. DOI: [10.1016/j.pmatsci.2016.07.003](https://doi.org/10.1016/j.pmatsci.2016.07.003).
- Hlilou, A., Naceur, I. B., Saï, K., Gérard, C., and G. Cailletaud, S. F. an (2009). “Generalization of the polycrystalline β -model: Finite element assessment and application to softening material behavior”. In: *Computational Materials Science* 45 (4), pp. 1104–1112. DOI: [10.1016/j.commatsci.2009.01.015](https://doi.org/10.1016/j.commatsci.2009.01.015).
- Hoc, T. and Forest, S. (2001). “Polycrystal modelling of IF-Ti steel under complex loading path”. In: *International Journal of Plasticity* 17.1, pp. 65–85. ISSN: 0749-6419. DOI: [10.1016/S0749-6419\(00\)00019-X](https://doi.org/10.1016/S0749-6419(00)00019-X).
- Hochrainer, T., Zaiser, M., and Gumbsch, P. (2007). “A three-dimensional continuum theory of dislocation systems: kinematics and mean-field formulation”. In: *Philosophical Magazine* 87.8-9, pp. 1261–1282. DOI: [10.1080/14786430600930218](https://doi.org/10.1080/14786430600930218).
- Hochrainer, T., Sandfeld, S., Zaiser, M., and Gumbsch, P. (2014). “Continuum dislocation dynamics: Towards a physical theory of crystal plasticity”. In: *Journal of the Mechanics*

- and Physics of Solids* 63, pp. 167–178. ISSN: 0022-5096. DOI: [10.1016/j.jmps.2013.09.012](https://doi.org/10.1016/j.jmps.2013.09.012).
- Holmquist, M., Nilsson, J.-O., and Stigenberg, A. (1995). “Isothermal formation of martensite in a 12Cr-9Ni-4Mo maraging stainless steel”. In: *Scripta Metallurgica et Materialia* 33.9, pp. 1367–1373. ISSN: 0956-716X. DOI: [10.1016/0956-716X\(95\)00386-A](https://doi.org/10.1016/0956-716X(95)00386-A).
- Holzer, I. (2010). *Modelling and Simulation of Strengthening in Complex Martensitic 9-12% Cr Steel and a Binary Fe-Cu Alloy*. Advanced materials science. Verlag der Technischen Universität Graz. ISBN: 9783851251227.
- Hömborg, D., Patachini, F. S., Sakamoto, K., and Zimmer, J. (2016). “A revisited Johnson-Mehl-Avrami-Kolmogorov model and the evolution of grain-size distributions in steel”. In: *ArXiv e-prints*, pp. 763–780. DOI: [10.1093/imamat/hxx012](https://doi.org/10.1093/imamat/hxx012).
- Horstemeyer, M. (2012). *Integrated Computational Materials Engineering (ICME) for Metals: Using Multiscale Modeling to Invigorate Engineering Design with Science*. Wiley. ISBN: 9781118342657.
- Houlsby, G. T. and Puzrin, A. M. (2007). *Principles of hyperplasticity: an approach to plasticity theory based on thermodynamic principles*. Springer Science & Business Media. ISBN: 9781846282409.
- Howe, J. M. (1997). *Interfaces in materials: atomic structure, thermodynamics and kinetics of solid-vapor, solid-liquid and solid-solid interfaces*. Wiley-Interscience. ISBN: 9780471138303.
- Howe, J. M. (2006). “Comparison of the atomic structure, composition, kinetics and mechanisms of interfacial motion in martensitic, bainitic, massive and precipitation face-centered cubic-hexagonal close-packed phase transformations”. In: *Materials Science and Engineering: A* 438-440, pp. 35–42. ISSN: 0921-5093. DOI: [10.1016/j.msea.2006.02.120](https://doi.org/10.1016/j.msea.2006.02.120).
- Hull, D. and Bacon, D. (2001). *Introduction to Dislocations*. Elsevier Science. ISBN: 9780080524900.
- Hutchinson, J. (1976). “Bounds and self-consistent estimates for creep of polycrystalline materials”. In: *Proceedings of the Royal Society of London A: Mathematical, Physical and Engineering Sciences*. Vol. 348. 1652. The Royal Society, pp. 101–127. DOI: [10.1098/rspa.1976.0027](https://doi.org/10.1098/rspa.1976.0027).
- Idesman, A., Levitas, V., Preston, D., and Cho, J.-Y. (2005). “Finite element simulations of martensitic phase transitions and microstructures based on a strain softening model”. In: *Journal of the Mechanics and Physics of Solids* 53.3, pp. 495–523. ISSN: 0022-5096. DOI: [10.1016/j.jmps.2004.10.001](https://doi.org/10.1016/j.jmps.2004.10.001).

- Itskov, M. (2015). *Tensor Algebra and Tensor Analysis for Engineers: With Applications to Continuum Mechanics*. Mathematical Engineering. Springer International Publishing. ISBN: 9783319163420.
- Iwamoto, T. and Tsuta, T. (2000). “Fraction tensor measured from micrographs for evaluating the geometrical orientation of martensite in TRIP steel”. In: *Journal of the Society of Materials Science, Japan* 49.9Appendix, pp. 173–179. DOI: [10.2472/jsms.49.9Appendix_173](https://doi.org/10.2472/jsms.49.9Appendix_173).
- Iwamoto, T. and Tsuta, T. (2002). “Assessment of Geometrical Orientation of Martensitic Particles in TRIP Steel by Fourier and Wavelet Transformation Image Analysis”. In: *Engineering Plasticity from Macroscale to Nanoscale*. Vol. 233. Key Engineering Materials. Trans Tech Publications, pp. 627–636. DOI: [10.4028/www.scientific.net/KEM.233-236.627](https://doi.org/10.4028/www.scientific.net/KEM.233-236.627).
- Iwamoto, T., Tsuta, T., and Tomita, Y. (1998). “Investigation on deformation mode dependence of strain-induced martensitic transformation in trip steels and modelling of transformation kinetics”. In: *International Journal of Mechanical Sciences* 40.2, pp. 173–182. ISSN: 0020-7403. DOI: [10.1016/S0020-7403\(97\)00047-7](https://doi.org/10.1016/S0020-7403(97)00047-7).
- Iwashita, K., Murata, Y., Tsukada, Y., and Koyama, T. (2011). “Formation mechanism of the hierarchic structure in the lath martensite phase in steels”. In: *Philosophical Magazine* 91.35, pp. 4495–4513. DOI: [10.1080/14786435.2011.610763](https://doi.org/10.1080/14786435.2011.610763).
- James, R. and Hane, K. (2000). “Martensitic transformations and shape-memory materials”. In: *Acta Materialia* 48.1, pp. 197–222. ISSN: 1359-6454. DOI: [10.1016/S1359-6454\(99\)00295-5](https://doi.org/10.1016/S1359-6454(99)00295-5).
- Jänicke, R., Diebels, S., Sehlhorst, H.-G., and Düster, A. (2009). “Two-scale modelling of micromorphic continua”. In: *Continuum Mechanics and Thermodynamics* 21.4, pp. 297–315. ISSN: 1432-0959. DOI: [10.1007/s00161-009-0114-4](https://doi.org/10.1007/s00161-009-0114-4).
- Jaswon, M. and Wheeler, J. (1948). “Atomic displacements in the austenite–martensite transformation”. In: *Acta Crystallographica* 1.4, pp. 216–224.
- Jaynes, E. T. (1957). “Information Theory and Statistical Mechanics”. In: *Phys. Rev.* 106 (4), pp. 620–630. DOI: [10.1103/PhysRev.106.620](https://doi.org/10.1103/PhysRev.106.620).
- Jirasek, M. and Bazant, Z. (2002). *Inelastic Analysis of Structures*. John Wiley & Sons. ISBN: 9780471987161.

- J.M. Howe R.C. Pond, J. H. (2009). “The role of disconnections in phase transformations”. In: *Progress in Materials Science* 54, pp. 792–838. DOI: [doi:10.1016/j.pmatsci.2009.04.001](https://doi.org/10.1016/j.pmatsci.2009.04.001).
- Johnson, W. A. (1939). “Reaction kinetics in process of nucleation and growth”. In: *Transaction of AIME* 135, pp. 416–458.
- Jonas, J. J. (2009). “Transformation Textures Associated with Steel Processing”. In: *Microstructure and Texture in Steels: and Other Materials*. Ed. by A. Haldar, S. Suwas, and D. Bhattacharjee. London: Springer London, pp. 3–17. ISBN: 978-1-84882-454-6. DOI: [10.1007/978-1-84882-454-6_1](https://doi.org/10.1007/978-1-84882-454-6_1).
- Jonas, J. J., He, Y., and Godet, S. (2005). “The possible role of partial dislocations in facilitating transformations of the Nishiyama - Wassermann type”. In: *Scripta Materialia* 52.3, pp. 175–179. ISSN: 1359-6462. DOI: [10.1016/j.scriptamat.2004.09.031](https://doi.org/10.1016/j.scriptamat.2004.09.031).
- K. Verbeke, D. R. (2009). “Evaluation of the Crystallographic Orientation Relationships between FCC and BCC PPhase in TRIP Steels”. In: *ISIJ International* 49.10, pp. 1601–1609. DOI: [DOI:10.2355/isijinternational.49.1601](https://doi.org/10.2355/isijinternational.49.1601).
- Kalidindi, S. (2015). *Hierarchical Materials Informatics: Novel Analytics for Materials Data*. Elsevier Science. ISBN: 9780124104556.
- Kalidindi, S., Bronkhorst, C., and Anand, L. (1992). “Crystallographic texture evolution in bulk deformation processing of FCC metals”. In: *Journal of the Mechanics and Physics of Solids* 40.3, pp. 537–569. ISSN: 0022-5096. DOI: [10.1016/0022-5096\(92\)80003-9](https://doi.org/10.1016/0022-5096(92)80003-9).
- Kalidindi, S. R. (2001). “Modeling anisotropic strain hardening and deformation textures in low stacking fault energy fcc metals”. In: *International Journal of Plasticity* 17.6, pp. 837–860. ISSN: 0749-6419. DOI: [10.1016/S0749-6419\(00\)00071-1](https://doi.org/10.1016/S0749-6419(00)00071-1).
- Kallend, J., Morris, P., and Davies, G. (1976). “Texture transformations-the misorientation distribution function”. In: *Acta Metallurgica* 24.4, pp. 361–370. DOI: [10.1016/0001-6160\(76\)90011-0](https://doi.org/10.1016/0001-6160(76)90011-0).
- Karaman, I., Sehitoglu, H., Gall, K., Chumlyakov, Y., and Maier, H. (2000). “Deformation of single crystal Hadfield steel by twinning and slip”. In: *Acta Materialia* 48.6, pp. 1345–1359. ISSN: 1359-6454. DOI: [10.1016/S1359-6454\(99\)00383-3](https://doi.org/10.1016/S1359-6454(99)00383-3).
- Karewar, S., Sietsma, J., and Santofimia, M. (2018). “Effect of pre-existing defects in the parent fcc phase on atomistic mechanisms during the martensitic transformation in pure Fe: A molecular dynamics study”. In: *Acta Materialia* 142.Supplement C, pp. 71–81. ISSN: 1359-6454. DOI: [10.1016/j.actamat.2017.09.049](https://doi.org/10.1016/j.actamat.2017.09.049).

- Kaufman, L. and Cohen, M. (1958). “Thermodynamics and kinetics of martensitic transformations”. In: *Progress in Metal Physics* 7, pp. 165–246. DOI: [10.1016/0502-8205\(58\)90005-4](https://doi.org/10.1016/0502-8205(58)90005-4).
- Kelly, A., Groves, G., and Kidd, P. (2000). *Crystallography and Crystal Defects*. Wiley. ISBN: 9780471720447.
- Kelly, P. M. (1992). “Crystallography of Lath Martensite in Steels”. In: *Materials Transactions* 33.3, pp. 235–242. DOI: [10.2320/matertrans1989.33.235](https://doi.org/10.2320/matertrans1989.33.235).
- Kelly, P., Jostsons, A., and Blake, R. (1990). “The orientation relationship between lath martensite and austenite in low carbon, low alloy steels”. In: *Acta Metallurgica et Materialia* 38.6, pp. 1075–1081. ISSN: 0956-7151. DOI: [10.1016/0956-7151\(90\)90180-0](https://doi.org/10.1016/0956-7151(90)90180-0).
- Khachaturyan, A. (1983). *Theory of Structural Transformations in Solids*. Mineola, New York: Dover Publications Inc. ISBN: 9780486783444.
- Kibey, S., Liu, J., Johnson, D., and Sehitoglu, H. (2007). “Predicting twinning stress in fcc metals: Linking twin-energy pathways to twin nucleation”. In: *Acta Materialia* 55.20, pp. 6843–6851. ISSN: 1359-6454. DOI: [10.1016/j.actamat.2007.08.042](https://doi.org/10.1016/j.actamat.2007.08.042).
- Kienzler, R. and Herrmann, G. (2000). *Mechanics in Material Space: With Applications to Defect and Fracture Mechanics*. Engineering online library. Springer Berlin Heidelberg. ISBN: 9783540669654.
- Kim, D., Lee, S.-J., and De Cooman, B. C. (2012). “Microstructure of Low C Steel Isothermally Transformed in the M S to M f Temperature Range”. In: *Metallurgical and Materials Transactions A* 43.13, pp. 4967–4983. ISSN: 1543-1940. DOI: [10.1007/s11661-012-1338-7](https://doi.org/10.1007/s11661-012-1338-7).
- Kim, S., Lee, J., Barlat, F., and Lee, M.-G. (2016). “Transformation kinetics and density models of quenching and partitioning (Q&P) steels”. In: *Acta Materialia* 109, pp. 394–404. ISSN: 1359-6454. DOI: [10.1016/j.actamat.2015.11.051](https://doi.org/10.1016/j.actamat.2015.11.051).
- Kinney, C., Pytlewski, K., Khachaturyan, A., and Jr., J. M. (2014). “The microstructure of lath martensite in quenched 9Ni steel”. In: *Acta Materialia* 69, pp. 372–385. ISSN: 1359-6454. DOI: [10.1016/j.actamat.2014.01.058](https://doi.org/10.1016/j.actamat.2014.01.058).
- Kinney, C., Yi, I., Pytlewski, K., Khachaturyan, A., Kim, N., and Morris, J. J. (2017). “The microstructure of as-quenched 12Mn steel”. In: *Acta Materialia* 125, pp. 442–454. ISSN: 1359-6454. DOI: [10.1016/j.actamat.2016.12.001](https://doi.org/10.1016/j.actamat.2016.12.001).

- Kinney, C., Pytlewski, K., Qi, L., Khachaturyan, A. G., and Morris, J. W. (2016). “An Investigation Into 6-Fold Symmetry in Martensitic Steels”. In: *Metallurgical and Materials Transactions A* 47.11, pp. 5266–5270. ISSN: 1543-1940. DOI: [10.1007/s11661-016-3710-5](https://doi.org/10.1007/s11661-016-3710-5).
- Kisko, A., Misra, R., Talonen, J., and Karjalainen, L. (2013). “The influence of grain size on the strain-induced martensite formation in tensile straining of an austenitic 15Cr-9Mn-Ni-Cu stainless steel”. In: *Materials Science and Engineering: A* 578, pp. 408–416. ISSN: 0921-5093. DOI: [10.1016/j.msea.2013.04.107](https://doi.org/10.1016/j.msea.2013.04.107).
- Kitahara, H., Ueji, R., Tsuji, N., and Minamino, Y. (2006). “Crystallographic features of lath martensite in low-carbon steel”. In: *Acta Materialia* 54.5, pp. 1279–1288. ISSN: 1359-6454. DOI: [10.1016/j.actamat.2005.11.001](https://doi.org/10.1016/j.actamat.2005.11.001).
- Kitayama, K., Tomé, C., Rauch, E., Gracio, J., and Barlat, F. (2013). “A crystallographic dislocation model for describing hardening of polycrystals during strain path changes. Application to low carbon steels”. In: *International Journal of Plasticity* 46, pp. 54–69. ISSN: 0749-6419. DOI: [10.1016/j.ijplas.2012.09.004](https://doi.org/10.1016/j.ijplas.2012.09.004).
- Kochmann, J., Wulfinghoff, S., Reese, S., Mianroodi, J. R., and Svendsen, B. (2016). “Two-scale FE-FFT-and phase-field-based computational modeling of bulk microstructural evolution and macroscopic material behavior”. In: *Computer Methods in Applied Mechanics and Engineering* 305, pp. 89–110. ISSN: 0045-7825. DOI: [10.1016/j.cma.2016.03.001](https://doi.org/10.1016/j.cma.2016.03.001).
- Kocks, U. F. (1976). “Laws for Work-Hardening and Low-Temperature Creep”. In: *Journal of Engineering Materials and Technology* 98.1, pp. 76–85. ISSN: 0094-4289. DOI: [10.1115/1.3443340](https://doi.org/10.1115/1.3443340).
- Kocks, U. and Mecking, H. (2003). “Physics and phenomenology of strain hardening: the FCC case”. In: *Progress in Materials Science* 48.3, pp. 171–273. ISSN: 0079-6425. DOI: [10.1016/S0079-6425\(02\)00003-8](https://doi.org/10.1016/S0079-6425(02)00003-8).
- Kocks, W. F. (1975). “Thermodynamics and kinetics of slip”. In: *Progress in Materials Science* 19, p. 291.
- Kohn, R. V. (1991). “The relaxation of a double-well energy”. In: *Continuum Mechanics and Thermodynamics* 3.3, pp. 193–236. ISSN: 1432-0959. DOI: [10.1007/BF01135336](https://doi.org/10.1007/BF01135336).
- Koistinen, D. and Marburger, R. (1959). “A general equation prescribing the extent of the austenitic-martensitic transformation in pure iron-carbon alloys and plain carbon steels”. In: *Acta Metall. Mater.* 7, pp. 59–60.

- Koiter, W. (1964). “Couple-stresses in the theory of elasticity, I & II”. In: *Proceedings of the Koninklijke Nederlandse Akademie van Wetenschappen* 67, pp. 17–44.
- Konijnenberg, P., Zaefferer, S., and Raabe, D. (2015). “Assessment of geometrically necessary dislocation levels derived by 3D EBSD”. In: *Acta Materialia* 99, pp. 402–414. ISSN: 1359-6454. DOI: [10.1016/j.actamat.2015.06.051](https://doi.org/10.1016/j.actamat.2015.06.051).
- Kords, C. (2013). *On the Role of Dislocation Transport in the Constitutive Description of Crystal Plasticity*. epubli GmbH. ISBN: 9783844277418.
- Kostorz, G., Calderon, H., and Martin, J. (2013). *Fundamental Aspects of Dislocation Interactions: Low-Energy Dislocation Structures III*. Elsevier Science. ISBN: 9781483274928.
- Koumatos, K. and Muehlemann, A. (2016). “Optimality of general lattice transformations with applications to the Bain strain in steel”. In: *Proceedings of the Royal Society of London A: Mathematical, Physical and Engineering Sciences* 472.2188. ISSN: 1364-5021. DOI: [10.1098/rspa.2015.0865](https://doi.org/10.1098/rspa.2015.0865).
- (2018). “A Parameter Free Double Shear Theory for Lath Martensite”. In: *ArXiv e-prints*. DOI: [arXiv:1802.01196v1](https://arxiv.org/abs/1802.01196v1).
- Kouznetsova, V. G. and Geers, M. (2007). “Modeling the Interaction between Plasticity and the Austenite-Martensite Transformation”. In: *International Journal for Multiscale Computational Engineering* 5.2, pp. 129–140. ISSN: 1543-1649.
- Kratochvíl, J. (2014). “Formation of deformation substructures observed in ductile materials”. In: *Plasticity and Beyond: Microstructures, Crystal-Plasticity and Phase Transitions*. Ed. by J. Schröder and K. Hackl. Vienna: Springer Vienna, pp. 199–304. ISBN: 978-3-7091-1625-8. DOI: [10.1007/978-3-7091-1625-8_4](https://doi.org/10.1007/978-3-7091-1625-8_4).
- Krauss, G. (2015). *Steels: Processing, Structure, and Performance, Second Edition: EngineeringPro collection*. ASM International. ISBN: 9781627080842.
- Krauss, G. and Marder, A. R. (1971). “The morphology of martensite in iron alloys”. In: *Metallurgical Transactions* 2.9, pp. 2343–2357. ISSN: 1543-1916. DOI: [10.1007/BF02814873](https://doi.org/10.1007/BF02814873).
- Krieg, R. and Key, S. (1976). “Implementation of a time independent plasticity theory into structural computer programs”. In: *Constitutive equations in viscoplasticity: Computational and engineering aspects*, pp. 125–137.
- Kröner, E. (1958). *Kontinuumstheorie der Versetzungen und Eigenspannungen*. Vol. 5. Springer.

- Kröner, E. (1961). “Zur plastischen Verformung des Vielkristalls”. In: *Acta Metallurgica* 9.2, pp. 155–161. ISSN: 0001-6160. DOI: [10.1016/0001-6160\(61\)90060-8](https://doi.org/10.1016/0001-6160(61)90060-8).
- Kröner, E. (1969). “Initial studies of a plasticity theory based upon statistical mechanics”. In: *Inelastic behaviour of solids*, pp. 137–147.
- Kröner, E. (1972). *Statistical continuum mechanics*. 92. Springer.
- Kubin, L. (2013). *Dislocations, Mesoscale Simulations and Plastic Flow*. Oxford Series on Materials Modelling. OUP Oxford. ISBN: 9780198525011.
- Kubin, L., Devincere, B., and Hoc, T. (2008). “Modeling dislocation storage rates and mean free paths in face-centered cubic crystals”. In: *Acta Materialia* 56.20, pp. 6040–6049. ISSN: 1359-6454. DOI: [10.1016/j.actamat.2008.08.012](https://doi.org/10.1016/j.actamat.2008.08.012).
- Kubin, L., Hoc, T., and Devincere, B. (2009). “Dynamic recovery and its orientation dependence in face-centered cubic crystals”. In: *Acta Materialia* 57.8, pp. 2567–2575. ISSN: 1359-6454. DOI: [10.1016/j.actamat.2009.02.013](https://doi.org/10.1016/j.actamat.2009.02.013).
- Kurdjumov, G. and Khachaturyan, A. (1975). “Nature of axial ratio anomalies of the martensite lattice and mechanism of diffusionless $\gamma - \alpha$ transformation”. In: *Acta Metallurgica* 23.1077. DOI: [10.1016/0001-6160\(75\)90112-1](https://doi.org/10.1016/0001-6160(75)90112-1).
- Kurdjumov, G. and Sachs, G. (1930). “Über den Mechanismus der Stahlhärtung”. In: *Zeitschrift für Physik* 64.5, pp. 325–343. ISSN: 0044-3328. DOI: [10.1007/BF01397346](https://doi.org/10.1007/BF01397346).
- Kurth, J. and Haupt, P. (2013). *Continuum Mechanics and Theory of Materials*. Advanced Texts in Physics. Springer Berlin Heidelberg. ISBN: 9783662041093.
- Kwak, K., Mayama, T., Mine, Y., and Takashima, K. (2016). “Anisotropy of strength and plasticity in lath martensite steel”. In: *Materials Science and Engineering: A* 674, pp. 104–116. ISSN: 0921-5093. DOI: [10.1016/j.msea.2016.07.047](https://doi.org/10.1016/j.msea.2016.07.047).
- Lagoudas, D. (2008). *Shape Memory Alloys Modeling and Engineering Applications*. New York: Springer press. ISBN: 9780387476858.
- Lambert-Perlade, A., Gourgues, A., and Pineau, A. (2004). “Austenite to bainite phase transformation in the heat-affected zone of a high strength low alloy steel”. In: *Acta Materialia* 52.8, pp. 2337–2348. ISSN: 1359-6454. DOI: [10.1016/j.actamat.2004.01.025](https://doi.org/10.1016/j.actamat.2004.01.025).
- Landau, L. D. (1937). “On the theory of phase transitions. II.” In: *Journal of Experimental and Theoretical Physics* 11, p. 627.

- Lange, S. and Ricoeur, A. (2015). “A condensed microelectromechanical approach for modeling tetragonal ferroelectrics”. In: *International Journal of Solids and Structures* 54, pp. 100–110. ISSN: 0020-7683. DOI: [10.1016/j.ijsolstr.2014.11.004](https://doi.org/10.1016/j.ijsolstr.2014.11.004).
- Laverroux, M. and Pineau, A. (1974). “Influence of precipitation in austenite on the morphology of martensite in Fe-Ni-Co-Ta alloys”. In: *Scripta Metallurgica* 8.4, pp. 351–356. ISSN: 0036-9748. DOI: [10.1016/0036-9748\(74\)90137-9](https://doi.org/10.1016/0036-9748(74)90137-9).
- Lebensohn, R. A. (2001). “N-site modeling of a 3D viscoplastic polycrystal using Fast Fourier Transform”. In: *Acta Materialia* 49.14, pp. 2723–2737. ISSN: 1359-6454. DOI: [10.1016/S1359-6454\(01\)00172-0](https://doi.org/10.1016/S1359-6454(01)00172-0).
- Leblond, J. B., Devaux, J., and Devaux, J. (1989). “Mathematical modelling of transformation plasticity in steels I: case of ideal-plastic phases”. In: *International journal of plasticity* 5.6, pp. 551–572. DOI: [10.1016/0749-6419\(89\)90001-6](https://doi.org/10.1016/0749-6419(89)90001-6).
- Leblond, J. (1989). “Mathematical modelling of transformation plasticity in steels II: coupling with strain hardening phenomena”. In: *International journal of plasticity* 5.6, pp. 573–591. DOI: [10.1016/0749-6419\(89\)90002-8](https://doi.org/10.1016/0749-6419(89)90002-8).
- Lecroisey, F. and Pineau, A. (1972). “Martensitic transformations induced by plastic deformation in the Fe-Ni-Cr-C system”. In: *Metallurgical Transactions* 3.2, pp. 391–400. ISSN: 1543-1916. DOI: [10.1007/BF02642042](https://doi.org/10.1007/BF02642042).
- Leem, D.-S., Lee, Y.-D., Jun, J.-H., and Choi, C.-S. (2001). “Amount of retained austenite at room temperature after reverse transformation of martensite to austenite in an Fe-13Cr-7Ni-3Si martensitic stainless steel”. In: *Scripta Materialia* 45.7, pp. 767–772. ISSN: 1359-6462. DOI: [10.1016/S1359-6462\(01\)01093-4](https://doi.org/10.1016/S1359-6462(01)01093-4).
- Leitner, H., Schober, M., Schnitzer, R., and Zinner, S. (2011). “Strengthening behavior of Fe-Cr-Ni-Al-(Ti) maraging steels”. In: *Materials Science and Engineering: A* 528.15, pp. 5264–5270. ISSN: 0921-5093. DOI: [10.1016/j.msea.2011.03.058](https://doi.org/10.1016/j.msea.2011.03.058).
- Lemaitre, J. (2001). *Handbook of Materials Behavior Models, Three-Volume Set: Nonlinear Models and Properties*. Elsevier Science. ISBN: 9780080533636.
- Lemaitre, J. and Chaboche, J.-L. (1994). *Mechanics of solid materials*. Cambridge university press. ISBN: 9780521477581.
- Levitas, V. I. (1998). “Thermomechanical theory of martensitic phase transformations in inelastic materials”. In: *International Journal of Solids and Structures* 35.9, pp. 889–940. ISSN: 0020-7683. DOI: [10.1016/S0020-7683\(97\)00089-9](https://doi.org/10.1016/S0020-7683(97)00089-9).

- Levitas, V. I. (2000a). “Structural changes without stable intermediate state in inelastic material. Part I. General thermomechanical and kinetic approaches”. In: *International Journal of Plasticity* 16.7-8, pp. 805–849. DOI: [10.1016/S0749-6419\(99\)00084-4](https://doi.org/10.1016/S0749-6419(99)00084-4).
- (2000b). “Structural changes without stable intermediate state in inelastic material. Part II. Applications to displacive and diffusional–displacive phase transformations, strain-induced chemical reactions and ductile fracture”. In: *International Journal of Plasticity* 16.7-8, pp. 851–892. DOI: [10.1016/S0749-6419\(99\)00083-2](https://doi.org/10.1016/S0749-6419(99)00083-2).
- Levitas, V. I. (2014). “Phase field approach to martensitic phase transformations with large strains and interface stresses”. In: *Journal of the Mechanics and Physics of Solids* 70, pp. 154–189. ISSN: 0022-5096. DOI: [10.1016/j.jmps.2014.05.013](https://doi.org/10.1016/j.jmps.2014.05.013).
- (2018). “Effect of the ratio of two nanosize parameters on the phase transformations”. In: *Scripta Materialia* 149, pp. 155–162. ISSN: 1359-6462. DOI: [10.1016/j.scriptamat.2017.08.035](https://doi.org/10.1016/j.scriptamat.2017.08.035).
- Levitas, V. I., Idesman, A., and Preston, D. (2004). “Microscale simulation of evolution of martensitic microstructure”. In: *Physical Reviews Letters* 93.10, pp. 105701–1. DOI: [10.1103/PhysRevLett.93.105701](https://doi.org/10.1103/PhysRevLett.93.105701).
- Levitas, V. I. and Ozsoy, I. B. (2009a). “Micromechanical modeling of stress-induced phase transformations. Part 1. Thermodynamics and kinetics of coupled interface propagation and reorientation”. In: *International Journal of Plasticity* 25.2, pp. 239–280. ISSN: 0749-6419. DOI: [10.1016/j.ijplas.2008.02.004](https://doi.org/10.1016/j.ijplas.2008.02.004).
- (2009b). “Micromechanical modeling of stress-induced phase transformations. Part 2. Computational algorithms and examples”. In: *International Journal of Plasticity* 25.3, pp. 546–583. ISSN: 0749-6419. DOI: [10.1016/j.ijplas.2008.02.005](https://doi.org/10.1016/j.ijplas.2008.02.005).
- Levitas, V. I. and Warren, J. A. (2016). “Phase field approach with anisotropic interface energy and interface stresses: Large strain formulation”. In: *Journal of the Mechanics and Physics of Solids* 91, pp. 94–125. ISSN: 0022-5096. DOI: [10.1016/j.jmps.2016.02.029](https://doi.org/10.1016/j.jmps.2016.02.029).
- Lin, J., Balint, D., and Pietrzyk, M. (2012). *Microstructure evolution in metal forming processes*. Elsevier. ISBN: 9780857096340.
- Liu, B., Eisenlohr, P., Roters, F., and Raabe, D. (2012). “Simulation of dislocation penetration through a general low-angle grain boundary”. In: *Acta Materialia* 60.13, pp. 5380–5390. ISSN: 1359-6454. DOI: [10.1016/j.actamat.2012.05.002](https://doi.org/10.1016/j.actamat.2012.05.002).

- Liu, J., Feng, Q., Fang, X., Wang, H., Lu, J., Raabe, D., and Yang, W. (2017). “Dislocation Activities at the Martensite Phase Transformation Interface in Metastable Austenitic Stainless Steel: An In-situ TEM Study”. In: *arXiv*. DOI: [arXiv:1612.08282](https://doi.org/10.1101/1612.08282).
- Lode, W. (1926). “Versuche über den Einfluß der mittleren Hauptspannung auf das Fließen der Metalle Eisen, Kupfer und Nickel”. In: *Zeitschrift für Physik A Hadrons and Nuclei* 36.11, pp. 913–939.
- Loewy, S., Hjordt, L., Rheingans, B., and Mittemeijer, E. J. (2016). “Modulated formation of lath martensite: Influence of uniaxial compressive load and transformation-induced plasticity”. In: *Acta Materialia* 109, pp. 46–54. ISSN: 1359-6454. DOI: [10.1016/j.actamat.2016.02.047](https://doi.org/10.1016/j.actamat.2016.02.047).
- Loewy, S., Rheingans, B., Meka, S. R., and Mittemeijer, E. J. (2014). “Unusual martensite-formation kinetics in steels: Observation of discontinuous transformation rates”. In: *Acta Materialia* 64, pp. 93–99. ISSN: 1359-6454. DOI: [10.1016/j.actamat.2013.11.052](https://doi.org/10.1016/j.actamat.2013.11.052).
- Lu, J., Hultman, L., Holmström, E., Antonsson, K. H., Grehk, M., Li, W., Vitos, L., and Golpayegani, A. (2016). “Stacking fault energies in austenitic stainless steels”. In: *Acta Materialia* 111, pp. 39–46. ISSN: 1359-6454. DOI: [10.1016/j.actamat.2016.03.042](https://doi.org/10.1016/j.actamat.2016.03.042).
- Luscher, D. J. (2010). *A Hierarchical Framework for the Multiscale Modeling of Microstructure Evolution in Heterogeneous Materials*. Department of Energy, Los Alamos National Laboratory, and United States.
- Luscher, D. J., McDowell, D. L., and Bronkhorst, C. A. (2010). “A second gradient theoretical framework for hierarchical multiscale modeling of materials”. In: *International Journal of Plasticity* 26.8, pp. 1248–1275. ISSN: 0749-6419. DOI: [10.1016/j.ijplas.2010.05.006](https://doi.org/10.1016/j.ijplas.2010.05.006).
- Ma, A. and Hartmaier, A. (2012). *Scale bridging modeling of plastic deformation and damage initiation in polycrystals, Polycrystalline Materials Theoretical and Practical Aspects*. DOI: [10.5772/30508](https://doi.org/10.5772/30508).
- Ma, A., Roters, F., and Raabe, D. (2006). “A dislocation density based constitutive model for crystal plasticity FEM including geometrically necessary dislocations”. In: *Acta Materialia* 54.8, pp. 2169–2179. ISSN: 1359-6454. DOI: [10.1016/j.actamat.2006.01.005](https://doi.org/10.1016/j.actamat.2006.01.005).
- Ma, A. and Hartmaier, A. (2015). “A study of deformation and phase transformation coupling for TRIP-assisted steels”. In: *International Journal of Plasticity* 64, pp. 40–55. ISSN: 0749-6419. DOI: [10.1016/j.ijplas.2014.07.008](https://doi.org/10.1016/j.ijplas.2014.07.008).

- Magee, C. L. (1966). *Transformation Kinetics, microplasticity and aging of martensite in Fe-31-Ni*. Tech. rep. DTIC Document.
- Mahajan, S. and Chin, G. (1973). “Formation of deformation twins in f.c.c. crystals”. In: *Acta Metallurgica* 21.10, pp. 1353–1363. ISSN: 0001-6160. DOI: [10.1016/0001-6160\(73\)90085-0](https://doi.org/10.1016/0001-6160(73)90085-0).
- Mahnken, R., Schneidt, A., Antretter, T., Ehlenbröcker, U., and Wolff, M. (2015). “Multi-scale modeling of bainitic phase transformation in multi-variant polycrystalline low alloy steels”. In: *International Journal of Solids and Structures* 54, pp. 156–171. ISSN: 0020-7683. DOI: [10.1016/j.ijsolstr.2014.10.021](https://doi.org/10.1016/j.ijsolstr.2014.10.021).
- Mahnken, R., Schneidt, A., Tschumak, S., and Maier, H. (2011). “On the simulation of austenite to bainite phase transformation”. In: *Computational Materials Science* 50.6, pp. 1823–1829. ISSN: 0927-0256. DOI: [10.1016/j.commatsci.2010.12.032](https://doi.org/10.1016/j.commatsci.2010.12.032).
- Mahnken, R. and Stein, E. (1996a). “A unified approach for parameter identification of inelastic material models in the frame of the finite element method”. In: *Computer Methods in Applied Mechanics and Engineering* 136.3, pp. 225–258. ISSN: 0045-7825. DOI: [10.1016/0045-7825\(96\)00991-7](https://doi.org/10.1016/0045-7825(96)00991-7).
- (1996b). “Parameter identification for viscoplastic models based on analytical derivatives of a least-squares functional and stability investigations”. In: *International Journal of Plasticity* 12.4, pp. 451–479. ISSN: 0749-6419. DOI: [10.1016/S0749-6419\(95\)00016-X](https://doi.org/10.1016/S0749-6419(95)00016-X).
- Mahnken, R. and Wilmanns, S. (2008). “Simulation of asymmetric effects for shape memory alloys by decomposition of transformation strains”. In: *Computational Materials Science* 42.2, pp. 295–305. ISSN: 0927-0256. DOI: [10.1016/j.commatsci.2007.07.042](https://doi.org/10.1016/j.commatsci.2007.07.042).
- Mahon, G. J., Howe, J. M., and Mahajan, S. (1989). “HRTEM study of the $\{252\}_\gamma$ austenite - martensite interface in an Fe-8Cr-1C alloy”. In: *Philosophical Magazine Letters* 59.6, pp. 273–279. DOI: [10.1080/09500838908206355](https://doi.org/10.1080/09500838908206355).
- Maki, T. (1999). “Ferrous shape memory alloys”. In: ed. by K. Otsuka and C. M. Wayman. Cambridge University Press. Chap. 4, pp. 117–132.
- Maki, T. (2012). “2 - Morphology and substructure of martensite in steels”. In: *Phase Transformations in Steels*. Ed. by E. Pereloma and D. V. Edmonds. Vol. 2. Woodhead Publishing Series in Metals and Surface Engineering. Woodhead Publishing, pp. 34–58. ISBN: 978-1-84569-971-0. DOI: [10.1533/9780857096111.1.34](https://doi.org/10.1533/9780857096111.1.34).

- Malet, L., Barnett, M., Jacques, P., and Godet, S. (2009). “Variant selection during the γ -to- α phase transformation in hot-rolled bainitic TRIP-aided steels”. In: *Scripta Materialia* 61.5, pp. 520–523. ISSN: 1359-6462. DOI: [10.1016/j.scriptamat.2009.05.015](https://doi.org/10.1016/j.scriptamat.2009.05.015).
- Malvern, L. (1969). *Introduction to the mechanics of a continuous medium*. Prentice-Hall series in engineering of the physical sciences. Prentice-Hall. ISBN: 0134876032.
- Man, T., Liu, T., Ping, D., and Ohmura, T. (2018). “TEM investigations on lath martensite substructure in quenched Fe-0.2C alloys”. In: *Materials Characterization* 135, pp. 175–182. ISSN: 1044-5803. DOI: [10.1016/j.matchar.2017.11.039](https://doi.org/10.1016/j.matchar.2017.11.039).
- Mandel, J. (1972). *Plasticité classique et viscoplasticité: course held at the Department of Mechanics of Solids, September-October, 1971*. Springer. ISBN: 9783211811979.
- Maresca, F. (2015). “Multi-scale modeling of plasticity and damage of lath martensite in multi-phase steels”. PhD thesis. technische universiteit eindhoven.
- Maresca, F. and Curtin, W. (2017). “The austenite/lath martensite interface in steels: Structure, athermal motion, and in-situ transformation strain revealed by simulation and theory”. In: *Acta Materialia*, pp. 302–323. ISSN: 1359-6454. DOI: [10.1016/j.actamat.2017.05.044](https://doi.org/10.1016/j.actamat.2017.05.044).
- Maresca, F., Kouznetsova, V., and Geers, M. (2014). “Subgrain lath martensite mechanics: A numerical-experimental analysis”. In: *Journal of the Mechanics and Physics of Solids* 73, pp. 69–83. ISSN: 0022-5096. DOI: [10.1016/j.jmps.2014.09.002](https://doi.org/10.1016/j.jmps.2014.09.002).
- Mason, J. and Schuh, C. (2008). “Hyperspherical harmonics for the representation of crystallographic texture”. In: *Acta Materialia* 56.20, pp. 6141–6155. ISSN: 1359-6454. DOI: [10.1016/j.actamat.2008.08.031](https://doi.org/10.1016/j.actamat.2008.08.031).
- Massalski, T. B., Laughlin, D. E., and Soffa, W. A. (2006). “The nature and role of incoherent interphase interfaces in diffusional solid-solid phase transformations”. In: *Metallurgical and Materials Transactions A* 37.3, pp. 825–831. ISSN: 1543-1940. DOI: [10.1007/s11661-006-0055-5](https://doi.org/10.1007/s11661-006-0055-5).
- Matouš, K., Geers, M. G., Kouznetsova, V. G., and Gillman, A. (2017). “A review of predictive nonlinear theories for multiscale modeling of heterogeneous materials”. In: *Journal of Computational Physics* 330, pp. 192–220. ISSN: 0021-9991. DOI: [10.1016/j.jcp.2016.10.070](https://doi.org/10.1016/j.jcp.2016.10.070).
- Maugin, G. A. (1980). “The method of virtual power in continuum mechanics: Application to coupled fields”. In: *Acta Mechanica* 35.1, pp. 1–70. ISSN: 1619-6937. DOI: [10.1007/BF01190057](https://doi.org/10.1007/BF01190057).

- Maugin, G. A. (1993). *Material Inhomogeneities in Elasticity*. Applied Mathematics. Taylor & Francis. ISBN: 9780412495205.
- (2016). *Non-Classical Continuum Mechanics: A Dictionary*. Advanced Structured Materials. Springer Singapore. ISBN: 9789811024344.
- Maugin, G. A. (1992). *The thermomechanics of plasticity and fracture*. Vol. 7. Cambridge University Press. ISBN: 9780521397803.
- Maugin, G. A. (1990). “Internal variables and dissipative structures”. In: *Journal of Non-Equilibrium Thermodynamics* 15.2, pp. 173–192.
- (2013). “Continuum mechanics through the twentieth century”. In: *Springer, Berlin*. doi 10, pp. 978–94.
- Mayer, S., Petersmann, M., Fischer, F. D., Clemens, H., Waitz, T., and Antretter, T. (2016). “Experimental and theoretical evidence of displacive martensite in an intermetallic Mo-containing γ -TiAl based alloy”. In: *Acta Materialia* 115, pp. 242–249. ISSN: 1359-6454. DOI: [10.1016/j.actamat.2016.06.006](https://doi.org/10.1016/j.actamat.2016.06.006).
- Mazière, M., Luis, C., Marais, A., Forest, S., and Gasperini, M. (2017). “Experimental and numerical analysis of the Lüders phenomenon in simple shear”. In: *International Journal of Solids and Structures* 106-107, pp. 305–314. ISSN: 0020-7683. DOI: [10.1016/j.ijsolstr.2016.07.026](https://doi.org/10.1016/j.ijsolstr.2016.07.026).
- Mazière, M. and Forest, S. (2015). “Strain gradient plasticity modeling and finite element simulation of Lüders band formation and propagation”. In: *Continuum Mechanics and Thermodynamics* 27.1-2, p. 83. DOI: [10.1007/s00161-013-0331-8](https://doi.org/10.1007/s00161-013-0331-8).
- McDowell, D. L. (2008). “Viscoplasticity of heterogeneous metallic materials”. In: *Materials Science and Engineering: R: Reports* 62.3, pp. 67–123. ISSN: 0927-796X. DOI: [10.1016/j.mser.2008.04.003](https://doi.org/10.1016/j.mser.2008.04.003).
- (2010). “A perspective on trends in multiscale plasticity”. In: *International Journal of Plasticity* 26.9, pp. 1280–1309. ISSN: 0749-6419. DOI: [10.1016/j.ijplas.2010.02.008](https://doi.org/10.1016/j.ijplas.2010.02.008).
- Mercier, D., Zambaldi, C., and Bieler, T. R. (2015). “A Matlab toolbox to analyze slip transfer through grain boundaries”. In: *IOP Conference Series: Materials Science and Engineering* 82.1, p. 012090. DOI: [10.1088/1757-899X/82/1/012090](https://doi.org/10.1088/1757-899X/82/1/012090).
- Méric, L., Poubanne, P., and Cailletaud, G. (1991). “Single Crystal Modeling for Structural Calculations: Part 1 - Model Presentation”. In: *Journal of Engineering Materials and Technology* 113.1, pp. 162–170. ISSN: 0094-4289. DOI: [10.1115/1.2903374](https://doi.org/10.1115/1.2903374).

- Mesarovic, S. D. (2016). “Lattice continuum and diffusional creep”. In: *Proceedings of the Royal Society of London A: Mathematical, Physical and Engineering Sciences* 472.2188. ISSN: 1364-5021. DOI: [10.1098/rspa.2016.0039](https://doi.org/10.1098/rspa.2016.0039).
- Michel, J. and Suquet, P. (2003). “Nonuniform transformation field analysis”. In: *International Journal of Solids and Structures* 40.25, pp. 6937–6955. ISSN: 0020-7683. DOI: [10.1016/S0020-7683\(03\)00346-9](https://doi.org/10.1016/S0020-7683(03)00346-9).
- Michel, J.-C. and Suquet, P. (2016). “A model-reduction approach to the micromechanical analysis of polycrystalline materials”. In: *Computational Mechanics* 57.3, pp. 483–508. ISSN: 1432-0924. DOI: [10.1007/s00466-015-1248-9](https://doi.org/10.1007/s00466-015-1248-9).
- Miehe, C., Göktepe, S., and Lulei, F. (2004). “A micro-macro approach to rubber-like materials - Part I: the non-affine micro-sphere model of rubber elasticity”. In: *Journal of the Mechanics and Physics of Solids* 52.11, pp. 2617–2660. ISSN: 0022-5096. DOI: [10.1016/j.jmps.2004.03.011](https://doi.org/10.1016/j.jmps.2004.03.011).
- Miehe, C. (2011). “A multi-field incremental variational framework for gradient-extended standard dissipative solids”. In: *Journal of the Mechanics and Physics of Solids* 59.4, pp. 898–923. ISSN: 0022-5096. DOI: [10.1016/j.jmps.2010.11.001](https://doi.org/10.1016/j.jmps.2010.11.001).
- Mindlin, R. D. (1964). “Micro-structure in linear elasticity”. In: *Archive for Rational Mechanics and Analysis* 16.1, pp. 51–78. ISSN: 1432-0673. DOI: [10.1007/BF00248490](https://doi.org/10.1007/BF00248490).
- Mindlin, R. (1965). “Second gradient of strain and surface-tension in linear elasticity”. In: *International Journal of Solids and Structures* 1.4, pp. 417–438. ISSN: 0020-7683. DOI: [10.1016/0020-7683\(65\)90006-5](https://doi.org/10.1016/0020-7683(65)90006-5).
- Mine, Y., Hirashita, K., Takashima, H., Matsuda, M., and Takashima, K. (2013). “Micro-tension behaviour of lath martensite structures of carbon steel”. In: *Materials Science and Engineering: A* 560, pp. 535–544. ISSN: 0921-5093. DOI: [10.1016/j.msea.2012.09.099](https://doi.org/10.1016/j.msea.2012.09.099).
- Mishiro, Y., Nambu, S., Inoue, J., and Koseki, T. (2013). “Effect of Stress on Variant Selection in Lath Martensite in Low-carbon Steel”. In: *ISIJ International* 53.8, pp. 1453–1461. DOI: [10.2355/isijinternational.53.1453](https://doi.org/10.2355/isijinternational.53.1453).
- Miyamoto, G., Iwata, N., Takayama, N., and Furuhashi, T. (2012). “Quantitative analysis of variant selection in ausformed lath martensite”. In: *Acta Materialia* 60.3, pp. 1139–1148. ISSN: 1359-6454. DOI: [10.1016/j.actamat.2011.11.018](https://doi.org/10.1016/j.actamat.2011.11.018).
- Miyamoto, G., Iwata, N., Takayama, N., and Furuhashi, T. (2010). “Mapping the parent austenite orientation reconstructed from the orientation of martensite by {EBSD} and

- its application to ausformed martensite”. In: *Acta Materialia* 58.19, pp. 6393–6403. ISSN: 1359-6454. DOI: [10.1016/j.actamat.2010.08.001](https://doi.org/10.1016/j.actamat.2010.08.001).
- Miyamoto, G., Iwata, N., Takayama, N., and Furuhashi, T. (2013). “Variant selection of lath martensite and bainite transformation in low carbon steel by ausforming”. In: *Journal of Alloys and Compounds* 577, S528–S532. ISSN: 0925-8388. DOI: [10.1016/j.jallcom.2011.12.111](https://doi.org/10.1016/j.jallcom.2011.12.111).
- Momma, K. and Izumi, F. (2011). “VESTA3 for three-dimensional visualization of crystal, volumetric and morphology data”. In: *Journal of Applied Crystallography* 44.6, pp. 1272–1276. DOI: [10.1107/S0021889811038970](https://doi.org/10.1107/S0021889811038970).
- Moreau, J. J. (1977). “Evolution problem associated with a moving convex set in a Hilbert space”. In: *Journal of differential equations* 26.3, pp. 347–374.
- Moritani, T., Miyajima, N., Furuhashi, T., and Maki, T. (2002). “Comparison of interphase boundary structure between bainite and martensite in steel”. In: *Scripta Materialia* 47.3, pp. 193–199. ISSN: 1359-6462. DOI: [10.1016/S1359-6462\(02\)00128-8](https://doi.org/10.1016/S1359-6462(02)00128-8).
- Morito, S., Adachi, Y., and Ohba, T. (2009). “Morphology and Crystallography of Sub-Blocks in Ultra-Low Carbon Lath Martensite Steel”. In: *Materials Transactions* 50.8, pp. 1919–1923. DOI: [10.2320/matertrans.MRA2008409](https://doi.org/10.2320/matertrans.MRA2008409).
- Morito, S., Huang, X., Furuhashi, T., Maki, T., and Hansen, N. (2006a). “The morphology and crystallography of lath martensite in alloy steels”. In: *Acta Materialia* 54, pp. 5323–5331. DOI: [10.1016/j.actamat.2006.07.009](https://doi.org/10.1016/j.actamat.2006.07.009).
- Morito, S., Pham, A., Hayashi, T., and Ohba, T. (2015). “Block Boundary Analyses to Identify Martensite and Bainite”. In: *Materials Today: Proceedings* 2, S913–S916. ISSN: 2214-7853. DOI: [10.1016/j.matpr.2015.07.430](https://doi.org/10.1016/j.matpr.2015.07.430).
- Morito, S., Saito, H., Ogawa, T., Furuhashi, T., and Maki, T. (2005). “Effect of Austenite Grain Size on the Morphology and Crystallography of Lath Martensite in Low Carbon Steels”. In: *ISIJ International* 45.1, pp. 91–94. DOI: [10.2355/isijinternational.45.91](https://doi.org/10.2355/isijinternational.45.91).
- Morito, S., Tanaka, H., Konishi, R., Furuhashi, T., and Maki, T. (2003). “The morphology and crystallography of lath martensite in Fe-C alloys”. In: *Acta Materialia* 51, pp. 1789–1799. DOI: [10.1016/S1359-6454\(02\)00577-3](https://doi.org/10.1016/S1359-6454(02)00577-3).
- Morito, S., Yoshida, H., Maki, T., and Huang, X. (2006b). “Effect of block size on the strength of lath martensite in low carbon steels”. In: *Materials Science and Engineering: A* 438-440, pp. 237–240. ISSN: 0921-5093. DOI: [10.1016/j.msea.2005.12.048](https://doi.org/10.1016/j.msea.2005.12.048).

- Morito, S., Edamatsu, Y., Ichinotani, K., Ohba, T., Hayashi, T., Adachi, Y., Furuhashi, T., Miyamoto, G., and Takayama, N. (2013). “Quantitative analysis of three-dimensional morphology of martensite packets and blocks in iron-carbon-manganese steels”. In: *Journal of Alloys and Compounds* 577, S587–S592. ISSN: 0925-8388. DOI: [10.1016/j.jallcom.2012.02.004](https://doi.org/10.1016/j.jallcom.2012.02.004).
- Morito, S., Igarashi, R., Kamiya, K., Ohba, T., and Maki, T. (2010). “Effect of Cooling Rate on Morphology and Crystallography of Lath Martensite in Fe-Ni Alloys”. In: *Thermec 2009*. Vol. 638. Materials Science Forum. Trans Tech Publications, pp. 1459–1463. DOI: [10.4028/www.scientific.net/MSF.638-642.1459](https://doi.org/10.4028/www.scientific.net/MSF.638-642.1459).
- Morrey, C. (2009). *Multiple Integrals in the Calculus of Variations*. Classics in Mathematics. Springer Berlin Heidelberg. ISBN: 9783540699521.
- Morrey, C. B. et al. (1952). “Quasi-convexity and the lower semicontinuity of multiple integrals”. In: *Pacific J. Math* 2.1, pp. 25–53.
- Morris Jr, J. W. (2017). “Maraging steels: Making steel strong and cheap”. In: *Nature Materials* 16.8, pp. 787–789. ISSN: 1476-1122. DOI: [10.1038/nmat4949](https://doi.org/10.1038/nmat4949).
- Morris, J. (2016). “The Microstructure of Dislocated Martensitic Steel: Microscopy and Microanalysis”. In: *Microscopy and Microanalysis* 22.S3, pp. 1226–1227. DOI: [10.1017/s1431927616006978](https://doi.org/10.1017/s1431927616006978).
- Morsdorf, L., Jeannin, O., Barbier, D., Mitsuhara, M., Raabe, D., and Tasan, C. (2016). “Multiple mechanisms of lath martensite plasticity”. In: *Acta Materialia* 121, pp. 202–214. ISSN: 1359-6454. DOI: [10.1016/j.actamat.2016.09.006](https://doi.org/10.1016/j.actamat.2016.09.006).
- Morsdorf, L., Tasan, C., Ponge, D., and Raabe, D. (2015). “3D structural and atomic-scale analysis of lath martensite: Effect of the transformation sequence”. In: *Acta Materialia* 95, pp. 366–377. ISSN: 1359-6454. DOI: [10.1016/j.actamat.2015.05.023](https://doi.org/10.1016/j.actamat.2015.05.023).
- Mosler, J. and Bruhns, O. T. (2009a). “On the implementation of rate-independent standard dissipative solids at finite strain”. In: *Computer Methods in Applied Mechanics and Engineering*, 9-12:417-429, 2009 9.12, pp. 417–429. DOI: [10.1016/j.cma.2009.07.006](https://doi.org/10.1016/j.cma.2009.07.006).
- Mosler, J. and Bruhns, O. (2009b). “Towards variational constitutive updates for non-associative plasticity models at finite strain: Models based on a volumetric-deviatoric split”. In: *International Journal of Solids and Structures* 46.7, pp. 1676–1684. ISSN: 0020-7683. DOI: [10.1016/j.ijsolstr.2008.12.008](https://doi.org/10.1016/j.ijsolstr.2008.12.008).
- Moulinec, H. and Suquet, P. (1995). “A FFT-Based Numerical Method for Computing the Mechanical Properties of Composites from Images of their Microstructures”. In: *IUTAM*

- Symposium on Microstructure-Property Interactions in Composite Materials: Proceedings of the IUTAM Symposium held in Aalborg, Denmark, 22–25 August 1994*. Ed. by R. Pyrz. Dordrecht: Springer Netherlands, pp. 235–246. ISBN: 978-94-011-0059-5. DOI: [10.1007/978-94-011-0059-5_20](https://doi.org/10.1007/978-94-011-0059-5_20).
- Muehlemann, A. and Koumatos, K. (2016). “A Theoretical Investigation of Orientation Relationships and Transformation Strains in Steels”. In: *arXiv preprint arXiv:1604.05270*.
- Muehlemann, A. . and Koumatos, K. (2015). “The morphology of lath martensite: a new perspective”. In: *arXiv*. DOI: [10.1051/mateconf/20153307003](https://doi.org/10.1051/mateconf/20153307003).
- Müller, U. (2013). *Symmetry Relationships between Crystal Structures: Applications of Crystallographic Group Theory in Crystal Chemistry*. International Union of Crystallography Texts on Crystallography. OUP Oxford. ISBN: 9780191648809.
- Mura, T. (1987). *Micromechanics of Defects in Solids*. Mechanics of Elastic and Inelastic Solids. Springer Netherlands. ISBN: 9789024732562.
- Nagayama, K., Kitajima, Y., Kigami, S., Tanaka, K., Fischer, F. D., and Cailletaud, G. (2000). “Transformation induced plasticity in maraging steel: An experimental study”. In: *Key Engineering Materials*. Vol. 177. Trans Tech Publ, pp. 443–448. DOI: [10.4028/www.scientific.net/KEM.177-180.443](https://doi.org/10.4028/www.scientific.net/KEM.177-180.443).
- Nagayama, K., Terasaki, T., Goto, S., Tanaka, K., Antretter, T., Fischer, F., Cailletaud, G., and Azzouz, F. (2002). “Back stress evolution and iso-volume fraction lines in a Cr–Ni–Mo–Al–Ti maraging steel in the process of martensitic transformation”. In: *Materials Science and Engineering: A* 336.1, pp. 30–38. DOI: [10.1016/S0921-5093\(01\)01920-7](https://doi.org/10.1016/S0921-5093(01)01920-7).
- Nagayama, K., Terasaki, T., Tanaka, K., Fischer, F., Antretter, T., Cailletaud, G., and Azzouz, F. (2001). “Mechanical properties of a Cr–Ni–Mo–Al–Ti maraging steel in the process of martensitic transformation”. In: *Materials Science and Engineering: A* 308.1, pp. 25–37. DOI: [10.1016/S0921-5093\(00\)01999-7](https://doi.org/10.1016/S0921-5093(00)01999-7).
- Nambu, S., Shibuta, N., Ojima, M., Inoue, J., Koseki, T., and Bhadeshia, H. (2013). “In situ observations and crystallographic analysis of martensitic transformation in steel”. In: *Acta Materialia* 61.13, pp. 4831–4839. ISSN: 1359-6454. DOI: [10.1016/j.actamat.2013.04.065](https://doi.org/10.1016/j.actamat.2013.04.065).
- Nanosteel (2017). <https://nanosteelco.com> - Accessed: 2017-09-30.
- Nayak, G. C., Zienkiewicz, O. C., et al. (1972). “Convenient form of stress invariants for plasticity”. In: *Proceedings of the ASCE Journal of the Structural Division*. Vol. 98, pp. 949–953.

- Neff, P., Sydow, A., and Wieners, C. (2009). “Numerical approximation of incremental infinitesimal gradient plasticity”. In: *International Journal for Numerical Methods in Engineering* 77.3, pp. 414–436. ISSN: 1097-0207. DOI: [10.1002/nme.2420](https://doi.org/10.1002/nme.2420).
- Nemat-Nasser, S. and Hori, M. (2013). *Micromechanics: overall properties of heterogeneous materials*. Vol. 37. Elsevier. ISBN: 9781483291512.
- Niclaeys, C., Zineb, T. B., Arbab-Chirani, S., and Patoor, E. (2002). “Determination of the interaction energy in the martensitic state”. In: *International Journal of Plasticity* 18.11, pp. 1619–1647. ISSN: 0749-6419. DOI: [10.1016/S0749-6419\(02\)00032-3](https://doi.org/10.1016/S0749-6419(02)00032-3).
- Nishiyama, Z. (1934). “X-ray investigation of the mechanism of the transformation from face centered cubic lattice to body centered cubic”. In: *Sci. Rep. Tohoku Univ* 23, pp. 637–664.
- Nishiyama, Z., Fine, M., Meshii, M., and Wayman, C. (1978). *Martensitic transformation*. Materials science and technology. Academic Press. ISBN: 9780125198509.
- Nix, W. D. and Gao, H. (1998). “Indentation size effects in crystalline materials: A law for strain gradient plasticity”. In: *Journal of the Mechanics and Physics of Solids* 46.3, pp. 411–425. ISSN: 0022-5096. DOI: [10.1016/S0022-5096\(97\)00086-0](https://doi.org/10.1016/S0022-5096(97)00086-0).
- Nolze, G. and Hielscher, R. (2016). “Orientations - Perfectly colored”. In: *Journal of Applied Crystallography* 49.5, pp. 1786–1802. DOI: [10.1107/S1600576716012942](https://doi.org/10.1107/S1600576716012942).
- Novikov, V. (2002). *Concise Dictionary of Materials Science: Structure and Characterization of Polycrystalline Materials*. CRC Press. ISBN: 9781420041149.
- Nye, J. (1953). “Some geometrical relations in dislocated crystals”. In: *Acta metallurgica* 1.2, pp. 153–162. DOI: [10.1016/0001-6160\(53\)90054-6](https://doi.org/10.1016/0001-6160(53)90054-6).
- Oberaigner, E. (1993). “Festkörperphasenumwandlungen aus der Sicht der Thermodynamik - Analytische Modelle und numerische Studien”.
- Oberaigner, E. R. and Fischlschweiger, M. (2011). “A statistical mechanics approach describing martensitic phase transformation”. In: *Mechanics of Materials* 43.9, pp. 467–475. ISSN: 0167-6636. DOI: [10.1016/j.mechmat.2011.06.001](https://doi.org/10.1016/j.mechmat.2011.06.001).
- Ogawa, K. and Kajiwara, S. (2004). “High-resolution electron microscopy study of ledge structures and transition lattices at the austenite-martensite interface in Fe-based alloys”. In: *Philosophical Magazine* 84.27, pp. 2919–2947. DOI: [10.1080/14786430410001701751](https://doi.org/10.1080/14786430410001701751).
- Ohno, N. and Okumura, D. (2007). “Higher-order stress and grain size effects due to self-energy of geometrically necessary dislocations”. In: *Journal of the Mechanics and Physics of Solids* 55.9, pp. 1879–1898. ISSN: 0022-5096. DOI: [10.1016/j.jmps.2007.02.007](https://doi.org/10.1016/j.jmps.2007.02.007).

- Ojha, A., Sehitoglu, H., Patriarca, L., and Maier, H. J. (2014). “Twin nucleation in Fe-based bcc alloys - modeling and experiments”. In: *Modelling and Simulation in Materials Science and Engineering* 22.7, p. 075010. DOI: [10.1088/0965-0393/22/7/075010](https://doi.org/10.1088/0965-0393/22/7/075010).
- Olson, G. B. (1997). “Computational Design of Hierarchically Structured Materials”. In: *Science* 277.5330, pp. 1237–1242. ISSN: 0036-8075. DOI: [10.1126/science.277.5330.1237](https://doi.org/10.1126/science.277.5330.1237).
- Olson, G. B. and Cohen, M. (1975). “Kinetics of strain-induced martensitic nucleation”. In: *Metallurgical Transactions A* 6.4, p. 791. ISSN: 1543-1940. DOI: [10.1007/BF02672301](https://doi.org/10.1007/BF02672301).
- (1976a). “A general mechanism of martensitic nucleation: Part I. General concepts and the FCC \rightarrow HCP transformation”. In: *Metallurgical Transactions A* 7.12, pp. 1897–1904. ISSN: 1543-1940. DOI: [10.1007/BF02659822](https://doi.org/10.1007/BF02659822).
- (1976b). “A general mechanism of martensitic nucleation: Part II. FCC \rightarrow BCC and other martensitic transformations”. In: *Metallurgical Transactions A* 7.12, pp. 1905–1914. ISSN: 1543-1940. DOI: [10.1007/BF02659823](https://doi.org/10.1007/BF02659823).
- (1976c). “A general mechanism of martensitic nucleation: Part III. Kinetics of martensitic nucleation”. In: *Metallurgical Transactions A* 7.12, pp. 1915–1923. ISSN: 1543-1940. DOI: [10.1007/BF02659824](https://doi.org/10.1007/BF02659824).
- (1979). “Interphase-boundary dislocations and the concept of coherency”. In: *Acta Metallurgica* 27.12, pp. 1907–1918. ISSN: 0001-6160. DOI: [10.1016/0001-6160\(79\)90081-6](https://doi.org/10.1016/0001-6160(79)90081-6).
- (1981). “A perspective on martensitic nucleation”. In: *Annual Review of Materials Science* 11.1, pp. 1–32.
- (1986). “Dislocation theory of martensitic transformations”. In: *Dislocations in solids* 7, pp. 297–407.
- Olson, G. and Cohen, M. (1972). “A mechanism for the strain-induced nucleation of martensitic transformations”. In: *Journal of the Less Common Metals* 28.1, pp. 107–118. ISSN: 0022-5088. DOI: [10.1016/0022-5088\(72\)90173-7](https://doi.org/10.1016/0022-5088(72)90173-7).
- Onsager, L. (1931). “Reciprocal Relations in Irreversible Processes. I.” In: *Physical Review* 37 (4), pp. 405–426. DOI: [10.1103/PhysRev.37.405](https://doi.org/10.1103/PhysRev.37.405).
- Ortiz, M. and Stainier, L. (1999). “The variational formulation of viscoplastic constitutive updates”. In: *Computer Methods in Applied Mechanics and Engineering* 171.3, pp. 419–444. ISSN: 0045-7825. DOI: [10.1016/S0045-7825\(98\)00219-9](https://doi.org/10.1016/S0045-7825(98)00219-9).

- Osipov, N., Gourgues-Lorenzon, A.-F., Marini, B., Mounoury, V., N’Guyen, F., and Cailletaud, G. (2009). “FE modelling of bainitic steels using crystal plasticity”. In: *Philosophical Magazine* 88.30-32, pp. 3757–3777. DOI: [10.1080/14786430802566380](https://doi.org/10.1080/14786430802566380).
- Ostwald, R., Bartel, T., and Menzel, A. (2010). “A computational micro-sphere model applied to the simulation of phase-transformations”. In: *ZAMM - Journal of Applied Mathematics and Mechanics / Zeitschrift für Angewandte Mathematik und Mechanik* 90.7-8, pp. 605–622. ISSN: 1521-4001. DOI: [10.1002/zamm.200900390](https://doi.org/10.1002/zamm.200900390).
- Ottosen, N. and Ristinmaa, M. (2005). *The Mechanics of Constitutive Modeling*. Elsevier Science. ISBN: 9780080525693.
- Ou, X., Sietsma, J., and Santofimia, M. J. (2016). “Molecular dynamics simulations of the mechanisms controlling the propagation of bcc/fcc semi-coherent interfaces in iron”. In: *Modelling and Simulation in Materials Science and Engineering* 24.5, p. 055019. DOI: [10.1088/0965-0393/24/5/055019](https://doi.org/10.1088/0965-0393/24/5/055019).
- Pardis, N., Ebrahimi, R., and Kim, H. S. (2017). “Equivalent strain at large shear deformation: Theoretical, numerical and finite element analysis”. In: *Journal of Applied Research and Technology* 15.5, pp. 442–448. ISSN: 1665-6423. DOI: [10.1016/j.jart.2017.05.002](https://doi.org/10.1016/j.jart.2017.05.002).
- Patala, S., Mason, J. K., and Schuh, C. A. (2012). “Improved representations of misorientation information for grain boundary science and engineering”. In: *Progress in Materials Science* 57.8, pp. 1383–1425. ISSN: 0079-6425. DOI: [10.1016/j.pmatsci.2012.04.002](https://doi.org/10.1016/j.pmatsci.2012.04.002).
- Patel, J. and Cohen, M. (1953). “Criterion for the action of applied stress in the martensitic transformation”. In: *Acta Metallurgica* 1.5, pp. 531–538. DOI: [10.1016/0001-6160\(53\)90083-2](https://doi.org/10.1016/0001-6160(53)90083-2).
- Peigney, M. (2016). “Improved bounds on the energy-minimizing strains in martensitic polycrystals”. In: *Continuum Mechanics and Thermodynamics* 28.4, pp. 923–946. ISSN: 1432-0959. DOI: [10.1007/s00161-015-0427-4](https://doi.org/10.1007/s00161-015-0427-4).
- Peirce, D., Asaro, R., and Needleman, A. (1982). “An analysis of nonuniform and localized deformation in ductile single crystals”. In: *Acta Metallurgica* 30.6, pp. 1087–1119. ISSN: 0001-6160. DOI: [10.1016/0001-6160\(82\)90005-0](https://doi.org/10.1016/0001-6160(82)90005-0).
- Pereloma, E. and Edmonds, D. (2012). *Phase Transformations in Steels: Diffusionless Transformations, High Strength Steels, Modelling and Advanced Analytical Techniques*. Woodhead Publishing Series in Metals and Surface Engineering. Elsevier Science. ISBN: 9780857096111.

- Petegem, S. V., Wagner, J., Panzner, T., Upadhyay, M., Trang, T., and Swygenhoven, H. V. (2016). “In-situ neutron diffraction during biaxial deformation”. In: *Acta Materialia* 105, pp. 404–416. ISSN: 1359-6454. DOI: [10.1016/j.actamat.2015.12.015](https://doi.org/10.1016/j.actamat.2015.12.015).
- Petersmann, M., Antretter, T., Waitz, T., and Fischer, F. (2017a). “A new approach predicting the evolution of laminated nanostructures - Martensite in NiTi as an example”. In: *Modelling and Simulation in Materials Science and Engineering* 25.3, p. 035004. DOI: [10.1088/1361-651X/aa5ab4](https://doi.org/10.1088/1361-651X/aa5ab4).
- Petersmann, M., Pranger, W., Waitz, T., and Antretter, T. (2017b). “An Energy Approach to Determine the Martensite Morphology in Nanocrystalline NiTi”. In: *Advanced Engineering Materials*, p. 1600684. ISSN: 1527-2648. DOI: [10.1002/adem.201600684](https://doi.org/10.1002/adem.201600684).
- Petryk, H. and Stupkiewicz, S. (2016). “A minimal gradient-enhancement of the classical continuum theory of crystal plasticity. Part I: The hardening law”. In: *Archives of Mechanics* 68.6, pp. 459–485.
- Phillips, R. (2001). *Crystals, Defects and Microstructures: Modeling Across Scales*. Cambridge University Press. ISBN: 9780521790055.
- Phillips, R. (1998). “Multiscale modeling in the mechanics of materials”. In: *Current Opinion in Solid State & Materials Science* 3 (6), pp. 526–532. DOI: [10.1016/s1359-0286\(98\)80020-x](https://doi.org/10.1016/s1359-0286(98)80020-x).
- Pietrzyk, M. and Kuziak, R. (2012). “6 - Modelling phase transformations in steel”. In: *Microstructure Evolution in Metal Forming Processes*. Ed. by J. Lin, D. Balint, and M. Pietrzyk. Woodhead Publishing Series in Metals and Surface Engineering. Woodhead Publishing, pp. 145–179. ISBN: 978-0-85709-074-4. DOI: [10.1533/9780857096340.2.145](https://doi.org/10.1533/9780857096340.2.145).
- Ping, D., Ohnuma, M., Hirakawa, Y., Kadoya, Y., and Hono, K. (2005). “Microstructural evolution in 13Cr-8Ni-2.5Mo-2Al martensitic precipitation-hardened stainless steel”. In: *Materials Science and Engineering: A* 394.1-2, pp. 285–295. ISSN: 0921-5093. DOI: [10.1016/j.msea.2004.12.002](https://doi.org/10.1016/j.msea.2004.12.002).
- Pitsch, W. (1962). “Der Orientierungszusammenhang zwischen Zementit und Austenit”. In: *Acta Metallurgica* 10.9, pp. 897–900. ISSN: 0001-6160. DOI: [10.1016/0001-6160\(62\)90108-6](https://doi.org/10.1016/0001-6160(62)90108-6).
- Pitteri, M. and Zanzotto, G. (1998). *Continuum Models for Phase Transitions and Twinning in Crystals*. London: Chapman and Hall.
- Polatidis, E., Hsu, W.-N., Smid, M., Panzner, T., Chakrabarty, S., Pant, P., and Swygenhoven, H. V. (2018). “Suppressed martensitic transformation under biaxial loading in low

- stacking fault energy metastable austenitic steels”. In: *Scripta Materialia* 147, pp. 27–32. ISSN: 1359-6462. DOI: [10.1016/j.scriptamat.2017.12.026](https://doi.org/10.1016/j.scriptamat.2017.12.026).
- Pond, R. C. and Celotto, S. (2003). “Special interfaces: military transformations”. In: *International Materials Reviews* 48.4, pp. 225–245. DOI: [10.1179/095066003225010245](https://doi.org/10.1179/095066003225010245).
- Pond, R. C. and Vlachavas, D. S. (1983). “Bicrystallography”. In: *Proceedings of the Royal Society of London A: Mathematical, Physical and Engineering Sciences* 386.1790, pp. 95–143. ISSN: 0080-4630. DOI: [10.1098/rspa.1983.0028](https://doi.org/10.1098/rspa.1983.0028).
- Pond, R., Celotto, S., and Hirth, J. (2003). “A comparison of the phenomenological theory of martensitic transformations with a model based on interfacial defects”. In: *Acta materialia* 51.18, pp. 5385–5398. DOI: [10.1016/S1359-6454\(03\)00395-1](https://doi.org/10.1016/S1359-6454(03)00395-1).
- Pond, R. and Hirth, J. (2015). “The Frank-Bilby Equation and Invariant-plane Interfaces”. In: *Materials Today: Proceedings* 2, pp. 541–544. DOI: [10.1016/j.matpr.2015.07.342](https://doi.org/10.1016/j.matpr.2015.07.342).
- Pond, R., Ma, X., Chai, Y., and Hirth, J. (2007). “Topological modelling of martensitic transformations”. In: *Dislocations in solids* 13, pp. 225–261. DOI: [10.1016/S1572-4859\(07\)80006-4](https://doi.org/10.1016/S1572-4859(07)80006-4).
- Porter, D., Easterling, K., and Sherif, M. (2009). *Phase Transformations in Metals and Alloys, Third Edition (Revised Reprint)*. CRC Press. ISBN: 9781439883570.
- Prager, W. (1949). “Recent Developments in the Mathematical Theory of Plasticity”. In: *Journal of Applied Physics* 20.3, pp. 235–241. DOI: [10.1063/1.1698348](https://doi.org/10.1063/1.1698348).
- Prigogine, I. (1955). *Introduction to thermodynamics of irreversible processes*.
- Qi, L., Khachaturyan, A., and Morris, J. J. (2014). “The microstructure of dislocated martensitic steel: Theory”. In: *Acta Materialia* 76, pp. 23–39. ISSN: 1359-6454. DOI: [10.1016/j.actamat.2014.04.038](https://doi.org/10.1016/j.actamat.2014.04.038).
- Qiu, D. and Zhang, M. (2014). “A simple and inclusive method to determine the habit plane in transmission electron microscope based on accurate measurement of foil thickness”. In: *Materials Characterization* 94.Supplement C, pp. 1–6. ISSN: 1044-5803. DOI: [10.1016/j.matchar.2014.04.008](https://doi.org/10.1016/j.matchar.2014.04.008).
- Qu, J. and Cherkaoui, M. (2006). *Fundamentals of micromechanics of solids*. Wiley Hoboken. ISBN: 978-0-471-46451-8.
- Quey, R., Dawson, P., and Barbe, F. (2011). “Large-scale 3D random polycrystals for the finite element method: Generation, meshing and remeshing”. In: *Computer Methods in Applied Mechanics and Engineering* 200, pp. 1729–1745. DOI: [10.1016/j.cma.2011.01.002](https://doi.org/10.1016/j.cma.2011.01.002).

- Quey, R. and Renversade, L. (2018). “Optimal polyhedral description of 3D polycrystals: Method and application to statistical and synchrotron X-ray diffraction data”. In: *Computer Methods in Applied Mechanics and Engineering* 330, pp. 308–333. ISSN: 0045-7825. DOI: [10.1016/j.cma.2017.10.029](https://doi.org/10.1016/j.cma.2017.10.029).
- Queyreau, S., Monnet, G., and Devincere, B. (2010). “Orowan strengthening and forest hardening superposition examined by dislocation dynamics simulations”. In: *Acta Materialia* 58.17, pp. 5586–5595. ISSN: 1359-6454. DOI: [10.1016/j.actamat.2010.06.028](https://doi.org/10.1016/j.actamat.2010.06.028).
- Queyreau, S., Monnet, G., and Devincere, B. (2009). “Slip systems interactions in α -iron determined by dislocation dynamics simulations”. In: *International Journal of Plasticity* 25.2, pp. 361–377. ISSN: 0749-6419. DOI: [10.1016/j.ijplas.2007.12.009](https://doi.org/10.1016/j.ijplas.2007.12.009).
- Raabe, D., Sandlöbes, S., Millán, J., Ponge, D., Assadi, H., Herbig, M., and Choi, P. (2013). “Segregation engineering enables nanoscale martensite to austenite phase transformation at grain boundaries: A pathway to ductile martensite”. In: *Acta Materialia* 61.16, pp. 6132–6152. ISSN: 1359-6454. DOI: [10.1016/j.actamat.2013.06.055](https://doi.org/10.1016/j.actamat.2013.06.055).
- Ray, R. K. and Jonas, J. J. (1990). “Transformation textures in steels”. In: *International Materials Reviews* 35.1, pp. 1–36. DOI: [10.1179/095066090790324046](https://doi.org/10.1179/095066090790324046).
- Rémy, L., Pineau, A., and Thomas, B. (1978). “Temperature dependence of stacking fault energy in close-packed metals and alloys”. In: *Materials Science and Engineering* 36.1, pp. 47–63. ISSN: 0025-5416. DOI: [10.1016/0025-5416\(78\)90194-5](https://doi.org/10.1016/0025-5416(78)90194-5).
- Rice, J. R. (1971). “Inelastic constitutive relations for solids: an internal-variable theory and its application to metal plasticity”. In: *Journal of the Mechanics and Physics of Solids* 19.6, pp. 433–455. DOI: [10.1016/0022-5096\(71\)90010-X](https://doi.org/10.1016/0022-5096(71)90010-X).
- Roitburd, A. (1990). “On the thermodynamics of martensite nucleation”. In: *Materials Science and Engineering: A* 127.2, pp. 229–238. ISSN: 0921-5093. DOI: [10.1016/0921-5093\(90\)90313-R](https://doi.org/10.1016/0921-5093(90)90313-R).
- Roitburd, A. and Kurdjumov, G. (1979). “The Nature of martensitic transformations”. In: *Materials Science and Engineering* 39, pp. 141–167. DOI: [10.1016/0025-5416\(79\)90055-7](https://doi.org/10.1016/0025-5416(79)90055-7).
- Roters, F., Eisenlohr, P., Kords, C., Tjahjanto, D., Diehl, M., and Raabe, D. (2012). “DAMASK: the Düsseldorf Advanced MATERIAL Simulation Kit for studying crystal plasticity using an FE based or a spectral numerical solver”. In: *Procedia IUTAM* 3, pp. 3–10. ISSN: 2210-9838. DOI: [10.1016/j.piutam.2012.03.001](https://doi.org/10.1016/j.piutam.2012.03.001).

- Roters, F. (2011). *Advanced material models for the crystal plasticity finite element method: development of a general CPFEM framework*. Tech. rep. Fachgruppe für Materialwissenschaft und Werkstofftechnik.
- Sachs, G. (1928). “Zur Ableitung einer Fließbedingung”. In: *Mitteilungen der deutschen Materialprüfungsanstalten: Sonderheft IX: Arbeiten aus dem Kaiser Wilhelm-Institut für Metallforschung und dem Staatlichen Materialprüfungsamt zu Berlin-Dahlem*. Berlin, Heidelberg: Springer Berlin Heidelberg, pp. 94–97. ISBN: 978-3-642-92045-5. DOI: [10.1007/978-3-642-92045-5_12](https://doi.org/10.1007/978-3-642-92045-5_12).
- Sai, K., Cailletaud, G., and Forest, S. (2006). “Micro-mechanical modeling of the inelastic behavior of directionally solidified materials”. In: *Mechanics of Materials* 38.3, pp. 203–217. ISSN: 0167-6636. DOI: [10.1016/j.mechmat.2005.06.007](https://doi.org/10.1016/j.mechmat.2005.06.007).
- San Martin, D., Jiménez-Melero, E., Duffy, J. A., Honkimäki, V., Zwaag, S. van der, and Dijk, N. H. van (2012). “Real-time synchrotron X-ray diffraction study on the isothermal martensite transformation of maraging steel in high magnetic fields”. In: *Journal of Applied Crystallography* 45.4, pp. 748–757. DOI: [10.1107/S0021889812024892](https://doi.org/10.1107/S0021889812024892).
- Sandvik, B. and Wayman, C. (1983). “Characteristics of lath martensite: Part I. Crystallographic and substructural features”. In: *Metallurgical transactions A* 14.4, pp. 809–822. DOI: [10.1007/BF02644284](https://doi.org/10.1007/BF02644284).
- Sargent, C. (1974). “Texture transformations”. In: *Scripta Metallurgica* 8.7, pp. 821–823. ISSN: 0036-9748. DOI: [10.1016/0036-9748\(74\)90301-9](https://doi.org/10.1016/0036-9748(74)90301-9).
- Satoh, K. (1972). “Transient thermal stresses of weld heat-affected zone by both-ends-fixed bar analogy”. In: *Transactions of the Japan Welding Society* 3.1, pp. 125–134.
- Sauzay, M. and Kubin, L. (2011). “Scaling laws for dislocation microstructures in monotonic and cyclic deformation of fcc metals”. In: *Progress in Materials Science* 56.6, pp. 725–784. ISSN: 0079-6425. DOI: [10.1016/j.pmatsci.2011.01.006](https://doi.org/10.1016/j.pmatsci.2011.01.006).
- Savage, D. J. and Knezevic, M. (2015). “Computer implementations of iterative and non-iterative crystal plasticity solvers on high performance graphics hardware”. In: *Computational Mechanics* 56.4, pp. 677–690. ISSN: 1432-0924. DOI: [10.1007/s00466-015-1194-6](https://doi.org/10.1007/s00466-015-1194-6).
- Scardi, P., Leoni, M., and Delhez, R. (2004). “Line broadening analysis using integral breadth methods: a critical review”. In: *Journal of Applied Crystallography* 37.3, pp. 381–390. DOI: [10.1107/S0021889804004583](https://doi.org/10.1107/S0021889804004583).

- Schastlivtsev, V., Rodionov, D., Khlebnikova, Y., and Yakovleva, I. (1999). “Peculiarity of structure and crystallography of plastic deformation of lath martensite in structural steels”. In: *Materials Science and Engineering: A* 273-275, pp. 437–442. ISSN: 0921-5093. DOI: [10.1016/S0921-5093\(99\)00323-8](https://doi.org/10.1016/S0921-5093(99)00323-8).
- Schmid, E. and Boas, W. (1968). *Plasticity of crystals: with special reference to metals*. Chapman & Hall.
- Schmidt-Baldassari, M. (2003). “Numerical concepts for rate-independent single crystal plasticity”. In: *Computer Methods in Applied Mechanics and Engineering* 192.11, pp. 1261–1280. ISSN: 0045-7825. DOI: [10.1016/S0045-7825\(02\)00563-7](https://doi.org/10.1016/S0045-7825(02)00563-7).
- Schneider, K., Klusemann, B., and Bargmann, S. (2017). “Fully periodic RVEs for technological relevant composites: not worth the effort”. In: *Journal of Mechanics and Materials of Structures* 12, pp. 471–484. DOI: [10.2140/jomms.2017.12.471](https://doi.org/10.2140/jomms.2017.12.471).
- Schoen, F. J., Nilles, J. L., and Owen, W. S. (1971). “Crystallographic aspects of Fe-Ni and Fe-Ni-C dilute alloy martensites”. In: *Metallurgical Transactions* 2.9, pp. 2489–2494. ISSN: 1543-1916. DOI: [10.1007/BF02814887](https://doi.org/10.1007/BF02814887).
- Schröder, J., Neff, P., and Ebbing, V. (2008). “Anisotropic polyconvex energies on the basis of crystallographic motivated structural tensors”. In: *Journal of the Mechanics and Physics of Solids* 56.12, pp. 3486–3506. ISSN: 0022-5096. DOI: [10.1016/j.jmps.2008.08.008](https://doi.org/10.1016/j.jmps.2008.08.008).
- Schröder, J., Balzani, D., and Brands, D. (2011). “Approximation of random microstructures by periodic statistically similar representative volume elements based on lineal-path functions”. In: *Archive of Applied Mechanics* 81.7, pp. 975–997. ISSN: 1432-0681. DOI: [10.1007/s00419-010-0462-3](https://doi.org/10.1007/s00419-010-0462-3).
- Sedláček, R., Blum, W., Kratochvíl, J., and Forest, S. (2002). “Subgrain formation during deformation: Physical origin and consequences”. In: *Metallurgical and Materials Transactions A* 33.2, pp. 319–327. ISSN: 1543-1940. DOI: [10.1007/s11661-002-0093-6](https://doi.org/10.1007/s11661-002-0093-6).
- Seiner, H., Stoklasová, P., Sedlák, P., Mušálek, M., Janovská, M., Landa, M., Fukuda, T., Yamaguchi, T., and Kakeshita, T. (2016). “Evolution of soft-phonon modes in Fe-Pd shape memory alloy under large elastic-like strains”. In: *Acta Materialia* 105, pp. 182–188. ISSN: 1359-6454. DOI: [10.1016/j.actamat.2015.12.025](https://doi.org/10.1016/j.actamat.2015.12.025).
- Shaw, J. and Kyriakides, S. (1997). “On the nucleation and propagation of phase transformation fronts in a NiTi alloy”. In: *Acta Materialia* 45.2, pp. 683–700. ISSN: 1359-6454. DOI: [10.1016/S1359-6454\(96\)00189-9](https://doi.org/10.1016/S1359-6454(96)00189-9).

- Shaw, J. A. (2000). “Simulations of localized thermo-mechanical behavior in a NiTi shape memory alloy”. In: *International Journal of Plasticity* 16.5, pp. 541–562. ISSN: 0749-6419. DOI: [10.1016/S0749-6419\(99\)00075-3](https://doi.org/10.1016/S0749-6419(99)00075-3).
- Shi, B. and Mosler, J. (2013). “On the macroscopic description of yield surface evolution by means of distortional hardening models: application to magnesium”. In: *International Journal of Plasticity* 44, pp. 1–22. DOI: [10.1016/j.ijplas.2012.11.007](https://doi.org/10.1016/j.ijplas.2012.11.007).
- Shibata, A., Morito, S., Furuhashi, T., and Maki, T. (2009). “Substructures of lenticular martensites with different martensite start temperatures in ferrous alloys”. In: *Acta Materialia* 57.2, pp. 483–492. ISSN: 1359-6454. DOI: [10.1016/j.actamat.2008.09.030](https://doi.org/10.1016/j.actamat.2008.09.030).
- Shibata, A., Murakami, T., Morito, S., Furuhashi, T., and Maki, T. (2008). “The origin of midrib in lenticular martensite”. In: *Materials transactions* 49.6, pp. 1242–1248. DOI: [10.2320/matertrans.MRA2007296](https://doi.org/10.2320/matertrans.MRA2007296).
- Shibata, A., Nagoshi, T., Sone, M., Morito, S., and Higo, Y. (2010). “Evaluation of the block boundary and sub-block boundary strengths of ferrous lath martensite using a micro-bending test”. In: *Materials Science and Engineering: A* 527.29-30, pp. 7538–7544. ISSN: 0921-5093. DOI: [10.1016/j.msea.2010.08.026](https://doi.org/10.1016/j.msea.2010.08.026).
- Shiflet, G. and Merwe, J. van der (1994). “The role of structural ledges at phase boundaries-II. F.C.C.-B.C.C. interfaces in Nishiyama-Wasserman orientation”. In: *Acta Metallurgica et Materialia* 42.4, pp. 1189–1198. ISSN: 0956-7151. DOI: [10.1016/0956-7151\(94\)90135-X](https://doi.org/10.1016/0956-7151(94)90135-X).
- Shintani, T. and Murata, Y. (2011). “Evaluation of the dislocation density and dislocation character in cold rolled Type 304 steel determined by profile analysis of X-ray diffraction”. In: *Acta Materialia* 59.11, pp. 4314–4322. ISSN: 1359-6454. DOI: [10.1016/j.actamat.2011.03.055](https://doi.org/10.1016/j.actamat.2011.03.055).
- Shrivastava, S., Ghosh, C., and Jonas, J. J. (2012). “A comparison of the von Mises and Hencky equivalent strains for use in simple shear experiments”. In: *Philosophical Magazine* 92.7, pp. 779–786. DOI: [10.1080/14786435.2011.634848](https://doi.org/10.1080/14786435.2011.634848).
- Silhavy, M. (1997). *The Mechanics and Thermodynamics of Continuous Media*. Theoretical and Mathematical Physics. Springer Berlin Heidelberg. ISBN: 9783662033890.
- Simo, J. C., Kennedy, J. G., and Govindjee, S. (1988). “Non-smooth multisurface plasticity and viscoplasticity. Loading/unloading conditions and numerical algorithms”. In: *Int. J. Numer. Meth. Engng.* 26.10, pp. 2161–2185. ISSN: 1097-0207.

- Simo, J. and Hughes, T. (2006). *Computational Inelasticity*. Interdisciplinary Applied Mathematics. Springer New York. ISBN: 9780387227634.
- Siredey, N., Patoor, E., Berveiller, M., and Eberhardt, A. (1999). “Constitutive equations for polycrystalline thermoelastic shape memory alloys.: Part I. Intragranular interactions and behavior of the grain”. In: *International Journal of Solids and Structures* 36.28, pp. 4289–4315. ISSN: 0020-7683. DOI: [10.1016/S0020-7683\(98\)00196-6](https://doi.org/10.1016/S0020-7683(98)00196-6).
- Song, Y., Chen, X., Dabade, V., Shield, T. W., and James, R. D. (2013). “Enhanced reversibility and unusual microstructure of a phase-transforming material”. In: *Nature* 502.7469, pp. 85–88. ISSN: 0028-0836. DOI: [10.1038/nature12532](https://doi.org/10.1038/nature12532).
- Sowa, H. (2017). “Sphere packings as a tool for the description of martensitic phase transformations”. In: *Acta Crystallographica Section A* 73.1, pp. 39–45. DOI: [10.1107/S2053273316013425](https://doi.org/10.1107/S2053273316013425).
- Speer, J., Matlock, D., Cooman, B. D., and Schroth, J. (2003). “Carbon partitioning into austenite after martensite transformation”. In: *Acta Materialia* 51.9, pp. 2611–2622. ISSN: 1359-6454. DOI: [10.1016/S1359-6454\(03\)00059-4](https://doi.org/10.1016/S1359-6454(03)00059-4).
- Spitzig, W., Sober, R., and Richmond, O. (1975). “Pressure dependence of yielding and associated volume expansion in tempered martensite”. In: *Acta Metallurgica* 23.7, pp. 885–893. ISSN: 0001-6160. DOI: [10.1016/0001-6160\(75\)90205-9](https://doi.org/10.1016/0001-6160(75)90205-9).
- Srivastava, A., Ghassemi-Armaki, H., Sung, H., Chen, P., Kumar, S., and Bower, A. F. (2015). “Micromechanics of plastic deformation and phase transformation in a three-phase TRIP-assisted advanced high strength steel: Experiments and modeling”. In: *Journal of the Mechanics and Physics of Solids* 78, pp. 46–69. ISSN: 0022-5096. DOI: [10.1016/j.jmps.2015.01.014](https://doi.org/10.1016/j.jmps.2015.01.014).
- Staudhammer, K., Murr, L., and Hecker, S. (1983). “Nucleation and evolution of strain-induced martensitic (b.c.c.) embryos and substructure in stainless steel: A transmission electron microscope study”. In: *Acta Metallurgica* 31.2, pp. 267–274. ISSN: 0001-6160. DOI: [10.1016/0001-6160\(83\)90103-7](https://doi.org/10.1016/0001-6160(83)90103-7).
- Stefanou, G. (2009). “The stochastic finite element method: Past, present and future”. In: *Computer Methods in Applied Mechanics and Engineering* 198.9, pp. 1031–1051. ISSN: 0045-7825. DOI: [10.1016/j.cma.2008.11.007](https://doi.org/10.1016/j.cma.2008.11.007).
- Steinmann, P. (1996). “Views on multiplicative elastoplasticity and the continuum theory of dislocations”. In: *International Journal of Engineering Science* 34.15, pp. 1717–1735. ISSN: 0020-7225. DOI: [10.1016/S0020-7225\(96\)00062-6](https://doi.org/10.1016/S0020-7225(96)00062-6).

- Steinmetz, D. R., Jäpel, T., Wietbrock, B., Eisenlohr, P., Gutierrez-Urrutia, I., Saeed-Akbari, A., Hickel, T., Roters, F., and Raabe, D. (2013). “Revealing the strain-hardening behavior of twinning-induced plasticity steels: Theory, simulations, experiments”. In: *Acta Materialia* 61.2, pp. 494–510. ISSN: 1359-6454. DOI: [10.1016/j.actamat.2012.09.064](https://doi.org/10.1016/j.actamat.2012.09.064).
- Stibitz, G. (1936). “Energy of lattice distortion”. In: *Phys. Rev* 49, p. 859.
- Stormvinter, A., Miyamoto, G., Furuhashi, T., Hedström, P., and Borgenstam, A. (2012). “Effect of carbon content on variant pairing of martensite in $Fe - C$ alloys”. In: *Acta Materialia* 60.20, pp. 7265–7274. ISSN: 1359-6454. DOI: [10.1016/j.actamat.2012.09.046](https://doi.org/10.1016/j.actamat.2012.09.046).
- Stringfellow, R., Parks, D., and Olson, G. (1992). “A constitutive model for transformation plasticity accompanying strain-induced martensitic transformations in metastable austenitic steels”. In: *Acta Metallurgica et Materialia* 40.7, pp. 1703–1716. ISSN: 0956-7151. DOI: [10.1016/0956-7151\(92\)90114-T](https://doi.org/10.1016/0956-7151(92)90114-T).
- Stukowski, A., Bulatov, V. V., and Arsenlis, A. (2012). “Automated identification and indexing of dislocations in crystal interfaces”. In: *Modelling and Simulation in Materials Science and Engineering* 20.8, p. 085007. DOI: [10.1088/0965-0393/20/8/085007](https://doi.org/10.1088/0965-0393/20/8/085007).
- Stupkiewicz, S. and Petryk, H. (2016). “A minimal gradient-enhancement of the classical continuum theory of crystal plasticity. Part II: Size effects”. In: *Archives of Mechanics* 68.6, pp. 487–513.
- Suiker, A. S. J. and Turteltaub, S. (2005). “Computational modelling of plasticity induced by martensitic phase transformations”. In: *International Journal for Numerical Methods in Engineering* 63.12, pp. 1655–1693. ISSN: 1097-0207. DOI: [10.1002/nme.1327](https://doi.org/10.1002/nme.1327).
- Sun, F., Meade, E. D., and O’Dowd, N. P. (2018). “Microscale modelling of the deformation of a martensitic steel using the Voronoi tessellation method”. In: *Journal of the Mechanics and Physics of Solids* 113, pp. 35–55. ISSN: 0022-5096. DOI: [10.1016/j.jmps.2018.01.009](https://doi.org/10.1016/j.jmps.2018.01.009).
- Suquet, P. (1997). *Continuum Micromechanics*. CISM International Centre for Mechanical Sciences. Springer Vienna. ISBN: 9783709126622.
- Sutton, A. and Balluffi, R. (1995). *Interfaces in crystalline materials*. Monographs on the physics and chemistry of materials. Clarendon Press. ISBN: 9780198513858.

- Suvorov, A. P. and Dvorak, G. J. (2002). “Rate form of the Eshelby and Hill tensors”. In: *International Journal of Solids and Structures* 39.21-22, pp. 5659–5678. ISSN: 0020-7683. DOI: [10.1016/S0020-7683\(02\)00369-4](https://doi.org/10.1016/S0020-7683(02)00369-4).
- Tabourot, L., Fivel, M., and Rauch, E. (1997). “Generalised constitutive laws for f.c.c. single crystals”. In: *Materials Science and Engineering: A* 234, pp. 639–642. ISSN: 0921-5093. DOI: [10.1016/S0921-5093\(97\)00353-5](https://doi.org/10.1016/S0921-5093(97)00353-5).
- Tadmor, E. and Miller, R. (2011). *Modeling Materials: Continuum, Atomistic and Multi-scale Techniques*. Cambridge University Press. ISBN: 9781139500654.
- Takayama, N., Miyamoto, G., and Furuhashi, T. (2012). “Effects of transformation temperature on variant pairing of bainitic ferrite in low carbon steel”. In: *Acta Materialia* 60.5, pp. 2387–2396. ISSN: 1359-6454. DOI: [10.1016/j.actamat.2011.12.018](https://doi.org/10.1016/j.actamat.2011.12.018).
- Taleb, L. and Petit, S. (2006). “New investigations on transformation induced plasticity and its interaction with classical plasticity”. In: *International journal of plasticity* 22.1, pp. 110–130. ISSN: 0749-6419. DOI: [10.1016/j.ijplas.2005.03.012](https://doi.org/10.1016/j.ijplas.2005.03.012).
- Taleb, L. and Petit-Grostabussiat, S. (2002). “Elastoplasticity and phase transformations in ferrous alloys: Some discrepancies between experiments and modeling”. In: 12, pp. 187–194. DOI: [10.1051/jp4:20020492](https://doi.org/10.1051/jp4:20020492).
- Talonen, J. and Hänninen, H. (2007). “Formation of shear bands and strain-induced martensite during plastic deformation of metastable austenitic stainless steels”. In: *Acta Materialia* 55.18, pp. 6108–6118. ISSN: 1359-6454. DOI: [10.1016/j.actamat.2007.07.015](https://doi.org/10.1016/j.actamat.2007.07.015).
- Talonen, J. (2007). *Effect of strain-induced α' -martensite transformation on mechanical properties of metastable austenitic stainless steels*.
- Tanaka, K., Terasaki, T., Goto, S., Antretter, T., Fischer, F., and Cailletaud, G. (2003). “Effect of back stress evolution due to martensitic transformation on iso-volume fraction lines in a Cr–Ni–Mo–Al–Ti maraging steel”. In: *Materials Science and Engineering: A* 341.1, pp. 189–196. DOI: [10.1016/S0921-5093\(02\)00202-2](https://doi.org/10.1016/S0921-5093(02)00202-2).
- Taylor, G. I. (1938). “Analysis of plastic strain in a cubic crystal”. In: *Stephen Timoshenko 60th Anniversary Volume*, pp. 218–224.
- Taylor, G. I. and Quinney, H. (1932). “The plastic distortion of metals”. In: *Philosophical Transactions of the Royal Society of London. Series A, Containing Papers of a Mathematical or Physical Character* 230, pp. 323–362.

- Taylor, G. I. and Quinney, H. (1934). “The latent energy remaining in a metal after cold working”. In: *Proceedings of the Royal Society of London. Series A, Containing Papers of a Mathematical and Physical Character* 143.849, pp. 307–326.
- Teodosiu, C. (1997). “Dislocation modelling of crystalline plasticity”. In: *Large plastic deformation of crystalline aggregates*. Springer, pp. 21–80. ISBN: 978-3-7091-2672-1. DOI: [10.1007/978-3-7091-2672-1_2](https://doi.org/10.1007/978-3-7091-2672-1_2).
- Thadhani, N. N. and Meyers, M. A. (1986). “Kinetics of isothermal martensitic transformation”. In: *Progress in Materials Science* 30.1, pp. 1–37. DOI: [10.1016/0079-6425\(86\)90002-2](https://doi.org/10.1016/0079-6425(86)90002-2).
- Tian, Y., Lienert, U., Borgenstam, A., Fischer, T., and Hedström, P. (2017). “Martensite formation during incremental cooling of Fe-Cr-Ni alloys: An in-situ bulk X-ray study of the grain-averaged and single-grain behavior”. In: *Scripta Materialia* 136.Supplement C, pp. 124–127. ISSN: 1359-6462. DOI: [10.1016/j.scriptamat.2017.04.020](https://doi.org/10.1016/j.scriptamat.2017.04.020).
- Timoshenko, S., Timoshenko, S. P., Timoshenko, S. P., and Timoshenko, S. P. (1940). *Strength of materials*. Vol. 210. van Nostrand New York. DOI: [10.1.1.57:8888/dspace/handle/hau/4597](https://doi.org/10.1.1.57:8888/dspace/handle/hau/4597).
- Toji, Y., Matsuda, H., Herbig, M., Choi, P.-P., and Raabe, D. (2014). “Atomic-scale analysis of carbon partitioning between martensite and austenite by atom probe tomography and correlative transmission electron microscopy”. In: *Acta Materialia* 65, pp. 215–228. ISSN: 1359-6454. DOI: [10.1016/j.actamat.2013.10.064](https://doi.org/10.1016/j.actamat.2013.10.064).
- Tomida, T., Wakita, M., Yasuyama, M., Sugaya, S., Tomota, Y., and Vogel, S. (2013). “Memory effects of transformation textures in steel and its prediction by the double Kurdjumov-Sachs relation”. In: *Acta Materialia* 61.8, pp. 2828–2839. ISSN: 1359-6454. DOI: [10.1016/j.actamat.2013.01.015](https://doi.org/10.1016/j.actamat.2013.01.015).
- Tomida, T. (2018). “Variant selection mechanism by elastic anisotropy and double K-S relation for transformation texture in steel; difference between martensite and ferrite”. In: *Acta Materialia* 146, pp. 25–41. ISSN: 1359-6454. DOI: [10.1016/j.actamat.2017.12.033](https://doi.org/10.1016/j.actamat.2017.12.033).
- Tong, H. and Wayman, C. (1974). “Characteristic temperatures and other properties of thermoelastic martensites”. In: *Acta Metall.* 22, pp. 887–896. DOI: [10.1016/0001-6160\(74\)90055-8](https://doi.org/10.1016/0001-6160(74)90055-8).
- Torquato, S. (2013). *Random Heterogeneous Materials: Microstructure and Macroscopic Properties*. Interdisciplinary Applied Mathematics. Springer New York. ISBN: 9781475763553.

- Totten, G. E. and Howes, M. A. (1997). *Steel heat treatment handbook*. CRC Press.
- Truesdell, C. and Noll, W. (1965). *The non-linear field theories of mechanics*. The non-linear field theories of mechanics Bd. 2. Springer-Verlag. ISBN: 9783540550983.
- Truesdell, C. A. and Noll, W. (1965). *Handbuch der physik*. Springer.
- Truesdell, C. and Toupin, R. (1960). “The classical field theories”. In: *Principles of Classical Mechanics and Field Theory/Prinzipien der Klassischen Mechanik und Feldtheorie*. Springer, pp. 226–858. ISBN: 9783540055358.
- Tschopp, M. A., Spearot, D. E., and McDowell, D. L. (2008). “Influence of Grain Boundary Structure on Dislocation Nucleation in f.c.c. Metals”. In: *A Tribute to F.R.N. Nabarro*. Ed. by J. Hirth. Vol. 14. Dislocations in Solids. Elsevier. Chap. Chapter 82, pp. 43–139. DOI: [10.1016/S1572-4859\(07\)00002-2](https://doi.org/10.1016/S1572-4859(07)00002-2).
- TSL OIM Analysis Manual*. 7th ed. EDAX.
- Turteltaub, S. and Suiker, A. (2005). “Transformation-induced plasticity in ferrous alloys”. In: *Journal of the Mechanics and Physics of Solids* 53.8, pp. 1747–1788. ISSN: 0022-5096. DOI: [10.1016/j.jmps.2005.03.004](https://doi.org/10.1016/j.jmps.2005.03.004).
- Ungár, G. and Borbély, A. (1996). “The effect of dislocation contrast on X-ray line broadening: A new approach to line profile analysis”. In: *Applied Physics Letters* 69.21, pp. 3173–3175. DOI: [10.1063/1.117951](https://doi.org/10.1063/1.117951).
- Upadhyay, M., Petegem, S. V., Panzner, T., Lebensohn, R., and Swygenhoven, H. V. (2016). “Study of lattice strain evolution during biaxial deformation of stainless steel using a finite element and fast Fourier transform based multi-scale approach”. In: *Acta Materialia* 118, pp. 28–43. ISSN: 1359-6454. DOI: [10.1016/j.actamat.2016.07.028](https://doi.org/10.1016/j.actamat.2016.07.028).
- Van der Zwaag, S. (2012). “4 - Kinetics of phase transformations in steels”. In: *Phase Transformations in Steels*. Ed. by E. Pereloma and D. V. Edmonds. Vol. 1. Woodhead Publishing Series in Metals and Surface Engineering. Woodhead Publishing, pp. 126–156. ISBN: 978-1-84569-970-3. DOI: [10.1533/9780857096104.1.126](https://doi.org/10.1533/9780857096104.1.126).
- Vattré, A. and Demkowicz, M. (2014). “Effect of interface dislocation Burgers vectors on elastic fields in anisotropic bicrystals”. In: *Computational Materials Science* 88, pp. 110–115. ISSN: 0927-0256. DOI: [10.1016/j.commatsci.2014.02.044](https://doi.org/10.1016/j.commatsci.2014.02.044).
- Venables, J. A. (1962). “The martensite transformation in stainless steel”. In: *Philosophical Magazine* 7.73, pp. 35–44. DOI: [10.1080/14786436208201856](https://doi.org/10.1080/14786436208201856).

- Venables, J. (1964). “The electron microscopy of deformation twinning”. In: *Journal of Physics and Chemistry of Solids* 25.7, pp. 685–692. ISSN: 0022-3697. DOI: [10.1016/0022-3697\(64\)90177-5](https://doi.org/10.1016/0022-3697(64)90177-5).
- Villa, M., Niessen, F., and Somers, M. A. J. (2018a). “In Situ Investigation of the Evolution of Lattice Strain and Stresses in Austenite and Martensite During Quenching and Tempering of Steel”. In: *Metallurgical and Materials Transactions A* 49.1, pp. 28–40. ISSN: 1543-1940. DOI: [10.1007/s11661-017-4387-0](https://doi.org/10.1007/s11661-017-4387-0).
- Villa, M. (2013). “Isothermal martensite formation”. PhD thesis. The Technical University of Denmark, Lyngby, Denmark.
- Villa, M., Pantleon, K., and Somers, M. A. (2014). “Evolution of compressive strains in retained austenite during sub-zero Celsius martensite formation and tempering”. In: *Acta Materialia* 65, pp. 383–392. ISSN: 1359-6454. DOI: [10.1016/j.actamat.2013.11.007](https://doi.org/10.1016/j.actamat.2013.11.007).
- Villa, M. and Somers, M. A. (2018b). “Thermally activated martensite formation in ferrous alloys”. In: *Scripta Materialia* 142, pp. 46–49. ISSN: 1359-6462. DOI: [10.1016/j.scriptamat.2017.08.024](https://doi.org/10.1016/j.scriptamat.2017.08.024).
- Voss, J., Baaser, H., Martin, R., and Neff, P. (2018). “Again anti-plane shear”. In:
- Wakasa, K. and Wayman, C. (1981). “The morphology and crystallography of ferrous lath martensite. Studies of Fe-20% Ni-5%Mn - I. Optical microscopy”. In: *Acta Metallurgica* 29.6, pp. 973–990. ISSN: 0001-6160. DOI: [10.1016/0001-6160\(81\)90051-1](https://doi.org/10.1016/0001-6160(81)90051-1).
- Walpole, L. (1969). “On the overall elastic moduli of composite materials”. In: *Journal of the Mechanics and Physics of Solids* 17.4, pp. 235–251. ISSN: 0022-5096. DOI: [10.1016/0022-5096\(69\)90014-3](https://doi.org/10.1016/0022-5096(69)90014-3).
- Wang, B. and Urbassek, H. M. (2013). “Molecular dynamics study of the $\alpha - \gamma$ phase transition in Fe induced by shear deformation”. In: *Acta Materialia* 61.16, pp. 5979–5987. ISSN: 1359-6454. DOI: [10.1016/j.actamat.2013.05.045](https://doi.org/10.1016/j.actamat.2013.05.045).
- Wang, L. and Speer, J. G. (2013). “Quenching and Partitioning Steel Heat Treatment”. In: *Metallography, Microstructure, and Analysis* 2.4, pp. 268–281. ISSN: 2192-9270. DOI: [10.1007/s13632-013-0082-8](https://doi.org/10.1007/s13632-013-0082-8).
- Wang, M.-M., Tasan, C., Ponge, D., Kostka, A., and Raabe, D. (2014). “Smaller is less stable: Size effects on twinning vs. transformation of reverted austenite in TRIP-maraging steels”. In: *Acta Materialia* 79.Supplement C, pp. 268–281. ISSN: 1359-6454. DOI: [10.1016/j.actamat.2014.07.020](https://doi.org/10.1016/j.actamat.2014.07.020).

- Wang, Y. U., Jin, Y. M., Cuitino, A. M., and Khachaturyan, A. G. (2001). “Phase field microelasticity theory and modeling of multiple dislocation dynamics”. In: *Applied Physics Letters* 78.16, pp. 2324–2326. DOI: [10.1063/1.1366370](https://doi.org/10.1063/1.1366370).
- Wayman, C. (1964). *Introduction to the crystallography of martensitic transformations*. New York: Macmillan.
- (1972). “Crystallographic theories of martensitic transformations”. In: *Journal of the Less Common Metals* 28.1, pp. 97–105. ISSN: 0022-5088. DOI: [10.1016/0022-5088\(72\)90172-5](https://doi.org/10.1016/0022-5088(72)90172-5).
- Wechsler, M., Liebermann, D., and Read, T. (1953). “On the theory of the formation of martensite”. In: *Trans AIME J. Metals* 197, pp. 1503–1521.
- Weinberger, C., Cai, W., and Barnett, D. (2005). “Lecture Notes–Elasticity of Microscopic Structures”. In: *ME340–Stanford University*.
- Wiessner, M., Gamsjäger, E., Zwaag, S. van der, and Angerer, P. (2017). “Effect of reverted austenite on tensile and impact strength in a martensitic stainless steel–An in-situ X-ray diffraction study”. In: *Materials Science and Engineering: A* 682, pp. 117–125. ISSN: 0921-5093. DOI: [10.1016/j.msea.2016.11.039](https://doi.org/10.1016/j.msea.2016.11.039).
- Wilkinson, A. J., Meaden, G., and Dingley, D. J. (2006). “High-resolution elastic strain measurement from electron backscatter diffraction patterns: New levels of sensitivity”. In: *Ultramicroscopy* 106.4, pp. 307–313. ISSN: 0304-3991. DOI: [10.1016/j.ultramicro.2005.10.001](https://doi.org/10.1016/j.ultramicro.2005.10.001).
- Wilmanns, S. (2010). “Phänomenologische und mikroskopische Modellierung von Formgedächtnislegierungen”. PhD thesis. University of Paderborn.
- Wittridge, N. J., Jonas, J. J., and Root, J. H. (2001). “A dislocation-based model for variant selection during the γ -to- α transformation”. In: *Metallurgical and Materials Transactions A* 32.4, pp. 889–901. ISSN: 1543-1940. DOI: [10.1007/s11661-001-0346-9](https://doi.org/10.1007/s11661-001-0346-9).
- Wong, S. L., Madivala, M., Prahl, U., Roters, F., and Raabe, D. (2016). “A crystal plasticity model for twinning- and transformation-induced plasticity”. In: *Acta Materialia* 118, pp. 140–151. ISSN: 1359-6454. DOI: [10.1016/j.actamat.2016.07.032](https://doi.org/10.1016/j.actamat.2016.07.032).
- Yalcinkaya, T., Brekelmans, W., and Geers, M. (2011). “Deformation patterning driven by rate dependent non-convex strain gradient plasticity”. In: *Journal of the Mechanics and Physics of Solids* 59.1, pp. 1–17. ISSN: 0022-5096. DOI: [10.1016/j.jmps.2010.10.002](https://doi.org/10.1016/j.jmps.2010.10.002).

- (2012). “Non-convex rate dependent strain gradient crystal plasticity and deformation patterning”. In: *International Journal of Solids and Structures* 49.18, pp. 2625–2636. ISSN: 0020-7683. DOI: [10.1016/j.ijsostr.2012.05.029](https://doi.org/10.1016/j.ijsostr.2012.05.029).
- Yang, X.-S., Sun, S., Ruan, H.-H., Shi, S.-Q., and Zhang, T.-Y. (2017). “Shear and shuffling accomplishing polymorphic fcc $\gamma \rightarrow$ hcp ε bct α martensitic phase transformation”. In: *Acta Materialia* 136, pp. 347–354. ISSN: 1359-6454. DOI: [10.1016/j.actamat.2017.07.016](https://doi.org/10.1016/j.actamat.2017.07.016).
- Yang, X.-S., Sun, S., and Zhang, T.-Y. (2015). “The mechanism of bcc α' nucleation in single hcp ε laths in the fcc $\gamma \rightarrow$ hcp ε bcc α' martensitic phase transformation”. In: *Acta Materialia* 95, pp. 264–273. ISSN: 1359-6454. DOI: [10.1016/j.actamat.2015.05.034](https://doi.org/10.1016/j.actamat.2015.05.034).
- Yeddu, H. K., Shaw, B. A., and Somers, M. A. (2017). “Effect of thermal cycling on martensitic transformation and mechanical strengthening of stainless steels - A phase-field study”. In: *Materials Science and Engineering: A* 690. Supplement C, pp. 1–5. ISSN: 0921-5093. DOI: [10.1016/j.msea.2017.02.085](https://doi.org/10.1016/j.msea.2017.02.085).
- Zachrisson, J., Börjesson, J., and Karlsson, L. (2013). “A new EBSD based methodology for the quantitative characterisation of microstructures formed by displacive fcc - bcc transformations”. In: *Micron* 45, pp. 45–54. ISSN: 0968-4328. DOI: [10.1016/j.micron.2012.10.012](https://doi.org/10.1016/j.micron.2012.10.012).
- Zaera, R., Rodríguez-Marínez, J., Casado, A., Fernández-Sáez, J., Rusinek, A., and Pesci, R. (2012). “A constitutive model for analyzing martensite formation in austenitic steels deforming at high strain rates”. In: *International Journal of Plasticity* 29, pp. 77–101. ISSN: 0749-6419. DOI: [10.1016/j.ijplas.2011.08.003](https://doi.org/10.1016/j.ijplas.2011.08.003).
- Zaiser, M. (2001). “Statistical modelling of dislocation systems”. In: *Materials Science and Engineering: A* 309-310, pp. 304–315. ISSN: 0921-5093. DOI: [10.1016/S0921-5093\(00\)01676-2](https://doi.org/10.1016/S0921-5093(00)01676-2).
- Zaiser, M. and Hochrainer, T. (2006). “Some steps towards a continuum representation of 3D dislocation systems”. In: *Scripta Materialia* 54.5, pp. 717–721. ISSN: 1359-6462. DOI: [10.1016/j.scriptamat.2005.10.060](https://doi.org/10.1016/j.scriptamat.2005.10.060).
- Zaiser, M. and Sandfeld, S. (2014). “Scaling properties of dislocation simulations in the similitude regime”. In: *Modelling and Simulation in Materials Science and Engineering* 22.6, p. 065012. DOI: [10.1088/0965-0393/22/6/065012](https://doi.org/10.1088/0965-0393/22/6/065012).
- Zbib, H., Mesarovic, S., and Forest, S. (2017). *Mesoscale models: From Micro-Physics to Macro-Interpretation*. CISM International Centre for Mechanical Sciences.

- Zener, C. (1948). “Theory of Strain Interaction of Solute Atoms”. In: *Phys. Rev.* 74 (6), pp. 639–647. DOI: [10.1103/PhysRev.74.639](https://doi.org/10.1103/PhysRev.74.639).
- Zener, C. and Hollomon, J. H. (1944). “Effect of Strain Rate Upon Plastic Flow of Steel”. In: *Journal of Applied Physics* 15.1, pp. 22–32. DOI: [10.1063/1.1707363](https://doi.org/10.1063/1.1707363).
- Zhang, M.-X. and Kelly, P. M. (2009). “Crystallographic features of phase transformations in solids”. In: *Progress in Materials Science* 54.8, pp. 1101–1170.
- Zhang, M.-X. and Kelly, P. (2005). “Edge-to-edge matching and its applications: Part I. Application to the simple HCP/BCC system”. In: *Acta Materialia* 53.4, pp. 1073–1084. ISSN: 1359-6454. DOI: [10.1016/j.actamat.2004.11.007](https://doi.org/10.1016/j.actamat.2004.11.007).
- Zhang, P., Chen, Y., Xiao, W., Ping, D., and Zhao, X. (2016). “Twin structure of the lath martensite in low carbon steel”. In: *Progress in Natural Science: Materials International* 26.2, pp. 169–172. ISSN: 1002-0071. DOI: [10.1016/j.pnsc.2016.03.004](https://doi.org/10.1016/j.pnsc.2016.03.004).
- Zhang, R., Wang, J., Beyerlein, I., and Germann, T. (2011). “Dislocation nucleation mechanisms from fcc/bcc incoherent interfaces”. In: *Scripta Materialia* 65.11, pp. 1022–1025. ISSN: 1359-6462. DOI: [10.1016/j.scriptamat.2011.09.008](https://doi.org/10.1016/j.scriptamat.2011.09.008).
- Zhang, R., Wang, J., Beyerlein, I., Misra, A., and Germann, T. (2012). “Atomic-scale study of nucleation of dislocations from fcc - bcc interfaces”. In: *Acta Materialia* 60.6, pp. 2855–2865. ISSN: 1359-6454. DOI: [10.1016/j.actamat.2012.01.050](https://doi.org/10.1016/j.actamat.2012.01.050).
- Zhang, S., Morito, S., and Komizo, Y.-i. (2012). “Variant Selection of Low Carbon High Alloy Steel in an Austenite Grain during Martensite Transformation”. In: *ISIJ International* 52.3, pp. 510–515. DOI: [10.2355/isijinternational.52.510](https://doi.org/10.2355/isijinternational.52.510).
- Zhang, W.-Z., Gu, X.-F., and Dai, F.-Z. (2016). “Faceted interfaces: a key feature to quantitative understanding of transformation morphology”. In: *Npj Computational Materials* 2, pp. 16021–.
- Zhang, W.-Z. and Purdy, G. R. (1993a). “O-lattice analyses of interfacial misfit. I. General considerations”. In: *Philosophical Magazine A* 68.2, pp. 279–290. DOI: [10.1080/01418619308221205](https://doi.org/10.1080/01418619308221205).
- (1993b). “O-lattice analyses of interfacial misfit. II. Systems containing invariant lines”. In: *Philosophical Magazine A* 68.2, pp. 291–303. DOI: [10.1080/01418619308221206](https://doi.org/10.1080/01418619308221206).
- Zhang, W.-Z. and Weatherly, G. (2005). “On the crystallography of precipitation”. In: *Progress in Materials Science* 50.2, pp. 181–292. ISSN: 0079-6425. DOI: [10.1016/j.pmatsci.2004.04.002](https://doi.org/10.1016/j.pmatsci.2004.04.002).

- Zhang, Z. and Farrar, R. A. (1995). *Atlas of continuous cooling transformation (CCT) diagrams applicable to low carbon low alloy weld metals*. Woodhead.
- Zheng, Q.-S. (1994). “Theory of Representations for Tensor Functions—A Unified Invariant Approach to Constitutive Equations”. In: *Applied Mechanics Reviews* 47.11, pp. 545–587. ISSN: 0003-6900. DOI: [10.1115/1.3111066](https://doi.org/10.1115/1.3111066).
- Ziegler, H. (1987). “Advances in Applied Mechanics”. In: vol. 25. Chap. The Derivation of Constitutive Relations from the Free Energy and the Dissipation Function. ISBN: 9780120020256. DOI: [10.1016/S0065-2156\(08\)70278-3](https://doi.org/10.1016/S0065-2156(08)70278-3).
- Z-set Materials manual Version 8.6*. ARMINES, ONERA, NWNumerics. Centre des Matériaux B.P. 87 - 91003 Evry Cedex, France. URL: <http://www.zset-software.com>.
- Z-set: Multiscale Materials Modelling V8.6*. Centre des Matériaux B.P. 87 - 91003 Evry Cedex, France. URL: <http://www.zset-software.com>.